Fatigue damage in wood composites

Hacker, Clare Lyndall

Award date:
1995

Awarding institution:
University of Bath

FATIGUE DAMAGE IN WOOD COMPOSITES

submitted by Clare Lyndall Hacker
for the degree of PhD
of the University of Bath
1995

COPYRIGHT

Clare Lyndall Hacker

ProQuest LLC
789 East Eisenhower Parkway
P.O. Box 1346
Ann Arbor, MI 48106-1346

SUMMARY

Fatigue damage accumulation mechanisms and property changes in a Khaya-epoxy wood composite were investigated. The effect on the fatigue response of normal operation, controlled- and emergency-stops experienced by a wind turbine blade in service was also determined.

Stress-strain hysteresis loop capture was used to obtain data from constant amplitude tests [tension, compression and reverse loading modes] and complex loading fatigue tests. Changes in strain, modulus and loop area were calculated for each test and the general trends determined for each loading mode. Hysteresis loop shape was considered, property trend curves were compared and the overall trends summarised. An environmental scanning electron microscope (ESEM) was used to investigate the microscopic damage caused by the different fatigue modes. Small samples of Khaya [prefatigued in tension, compression and reverse loading] were loaded inside the microscope to reveal their damage states.

The fatigue response of wood composite was found to depend on the loading mode. In compression the peak strain became more negative progressively. At high stress levels in tension, insignificant property changes were observed. At low stresses, large irregular decreases in modulus were observed. A mixed response, depending on stress level, was seen in reversed loading. Prediction of fatigue life using dynamic and fatigue modulus approaches was only applicable in compression fatigue. In complex loading the load reversals associated with controlled and emergency stops increased the damage rate. Tensile excursions above the elastic limit were also significant. All tensile test samples showed increase in stiffness, probably due to a decrease in the S2 cell wall winding angle. The ESEM investigation revealed fatigue damage in the form of S2 helical cracking and ray bundle splitting in tension and reverse loading. Fatigue damage was also seen to weaken individual fibres and the middle lamella, reducing the notch insensitivity of Khaya.

Alternatives to epoxy adhesive were investigated and although epoxy performed best, differences in fatigue life were less significant in high cycle tests. Therefore cheaper adhesives could be used successfully in blade manufacture.

In conclusion, the fatigue damage accumulation mechanisms in the wood composite have been thoroughly investigated and the wood composite has been seen to perform extremely well in fatigue making it an excellent wind turbine blade material.

CONTENTS

ACKNOWLEDGEMENTS

As is always the case, many people have been involved with this work in a wide variety of different ways. There is a range of people to whom I wish to express my thanks and gratitude for their input and support. Firstly, I would like to acknowledge the Energy Technology Support Unit, part of the Department of Trade and Industry, for their financial support of the project, and Dr. Martin Ward for his overall supervision.

At work, my prime debt of gratitude goes to Dr Martin Ansell, my supervisor, who has consistently encouraged me and particularly helped me see the wood for the trees in the knotty business of data analysis. His generous hand in the daily running of the project has also enhanced its smooth and successful running. The ability to attend wind energy conferences and European project meetings has greatly added to the enjoyment and learning experience of this research.

All the technical staff in the School of Materials Science have been involved in the work at some stage, whether it was providing computer support [thank you Simon] or helping with machine maintenance [thank you Ian]. Further afield I also wish to thank Mark Hancock at WEG for manufacturing the wood composite. Finally, I would like to thank Dr. Andy Horsewell, from Risø in Denmark, for enabling me to use their environmental scanning electron microscope for what turned out to be a most helpful series of tests. It was great fun too!

On a more personal note, I am keen to express my deep gratitude and thanks to my parents, without whose unconditional love and support I would never have made it thus far. The unswerving interest in my work expressed by my Grandparents over the years has also meant more to me than I can write down. Thank you.

This page would not be complete if I was to omit to thank my dearest friend, Ron. He has consistently encouraged me in numerous ways and generously provided the practical support I needed, not least in the use of his computer and in the reading of many thesis chapters.

As a Christian, I want to thank the Lord for His hand on my life over the past years, without whose strength and joy to draw on I would have been a much poorer person.

You have made known to me the path of life; you will fill me with joy in your presence, with eternal pleasures at your right hand.

Psalm 16:11

1.0. INTRODUCTION

With the increasing commercialisation of the wind energy industry over the last fifteen years, it has been increasingly important to refine designs on a scientific basis, in order to gain competitive advantage. This includes the design of wind turbine blades. Wind Energy Group Ltd. (WEG), the only manufacturer of wind turbine generators (WTGs) in the UK, use a wood composite system for the manufacture of their blades.

Since 1982 the School of Materials Science has provided research and development support for WEG in the development of wood composite blade materials. The project under which this research was undertaken was funded by the Energy Technology Support Unit (ETSU), in conjunction with WEG, under contract number W/44/00287.

1.1. Aims of the research

In the early days the aim of the research was to provide WEG with fatigue design data for their Khaya-epoxy wood composite. However, as the understanding of the fatigue of wood has increased, the scope of the work has broadened into three areas. Firstly, alternative materials and manufacturing methods have been investigated, with a view to reducing the cost of wood composite blades. Secondly, life prediction methods, based on S-N data and Miner's rule of linear damage accumulation, have been developed which can be used in the blade design process. Thirdly, alternative methods for fatigue life prediction have been developed which are based on the property changes which occur as a result of fatigue damage accumulation.

It is the third area of interest which comprises the bulk of the work presented in this thesis. In addition, alternative adhesives have also been evaluated as part of the work carried out to improve the cost efficiency and competitiveness of wood composite WTG blades.

The primary aim of this research is to increase the understanding of the way in which fatigue damage accumulates in wood composites under different fatigue loading modes and how the properties are affected. In order to do this, axial fatigue testing of a Khaya-epoxy wood composite has been carried out in constant amplitude tension, compression and reversed loading modes. Stress-strain hysteresis loop capture has been used to record the property changes in the wood composite throughout its fatigue life and these changes have been analysed. Two fatigue life prediction methods have been developed and applied to the results.

A second aim of the work was to contrast fatigue damage during normal operation with damage from controlled- and emergency-stops. Changes in the fatigue response of the wood composite was again determined by stress-strain hysteresis loop capture.

The understanding of fatigue damage accumulation under different fatigue loading configuration modes has been complimented by the investigation of fatigue damage in wood using in-situ loading techniques in an environmental scanning electron microscope (ESEM).

1.2. Layout of thesis

The first four chapters (2-5) provide background information on the wind energy industry, wood, fatigue and fatigue life prediction methods respectively. Particular attention is paid to fatigue damage accumulation and life prediction in fibre reinforced plastics as wood is also a fibre-reinforced polymeric composite. Experimental methods are presented in Chapter 6 for both constant amplitude and complex load-time history fatigue tests. Data from static tests are given in Chapter 7, followed by basic S-N data (stress plotted against log(cycles to failure)) in Chapter 8. Typical stress-strain hysteresis loops from tension, compression and reverse loading fatigue are discussed in Chapter 9 and the property change trends which can be distiled from them are discussed in Chapter 10. In Chapters 11 and 12 the property changes are summarised and analysed so that trends in the fatigue response under the three loading modes becomes apparent. Chapter 13 contains a fatigue life prediction method based on the concept of a fatigue modulus. An attempt is made to use changes in dynamic modulus alone to predict life in Chapter 14 before the complex load-time history work is tackled in Chapter 15. The ESEM results are presented in Chapter 16, followed by the alternative adhesives investigation in Chapter 17. In Chapter 18 an overall discussion is presented which pulls together the important themes and results which run through the work. Chapter 19 contains the most important conclusions and the references follow in Chapter 20. Appendices A to E contain supporting information, mostly in the form of a complete set of stress-strain hysteresis loops and property change graphs for the constant amplitude and complex loading results.

2. THE UK. ELECTRICITY SUPPLY INDUSTRY AND WIND ENERGY GENERATION

In this section the wind energy industry is set in the wider context of the UK electricity supply industry (ESI). The environmental implications of current generating practices are highlighted and the role of renewable energy sources in the reduction of harmful emission gases is presented. It becomes clear that a more urgent response to the changes in our environment must be adopted and that the use of benign energy sources, such as wind, has an essential part to play.

2.1. The UK. electricity supply industry

The recent privatisation of the UK ESI and the deregulation of the use of natural gas in 1989 has dramatically changed the face of electricity generation and exposed it to market forces. As a result the industry is now driven by short term profits rather than long-term objectives relating to the balance of supply and environmental goals such as those recommended by the Rio Summit Treaty in 1993.

2.1.1. UK. generation profile

The UK supply of electrical power is characterised by a heavy dependence on fossil fuels. In 1989, prior to privatisation, the UK ESI's generating capacity totalled 72.3GW. This breaks down as shown in table 2.1.

Generation method	GW	% total
Coal fired	35.5	49.2
Dual coal/oil	4.5	6.3
Oil	14.5	20.0
Nuclear	10.4	14.3
Gas turbine peaking sets	3.1	4.3
Hydro and pumped storage	4.1	5.7
Diesel and wind	0.2	0.2
Total	72.3	100.0

Table 2.1. Sources of energy for UK electricity power generation in 1989 (Chesshire, 1993).

79.8% of the country's generating capacity relies on fossil fuels. This corresponds to 75.2% of all energy used. Of the remaining kWhrs, 23% are produced from nuclear

and 1.8% from renewable fuels. This is in marked contrast to the rest of Europe where an appreciably higher proportion of energy needs is met by renewable sources [Germany, 5%, USA, 9%, France 13% and Japan, 14%]. The difference is mainly due to the UK's small size and less favourable topography for hydroelectric development. However, it demonstrates the unbalanced nature of UK electricity supply and the its sensitivity to future fossil fuel price increases.

A second characteristic of our ESI is the age of the current generating capacity. The commissioning of large coal fired power stations was concentrated in a short period of time between the early 60s and 70s. It is expected that the majority will have reached the end of their economic lives during the next 10 years (Chesshire, 1993). With regard to the nuclear industry, in 1989 the government decided to order no further nuclear power stations until the nuclear power review in 1994. This, coupled with the fact that all but one of the Magnox stations were commissioned later than 1971, means that the UK nuclear generating capacity will fall steadily from the mid-1990s as the older existing stations are retired.

At present the ESI is dominated by a 'dash for gas'. There is great interest in combined cycle gas turbine (CCGT) generation technology and it is estimated that between 8 and 16GW of capacity will be installed in the next decade. Such a significant investment in gas turbine generation will radically alter the UK's ESI fuel mix. CCGTs have low specific capital costs (£350-400 per kW installed capacity), permit lower manning levels, can be built quickly, have higher thermal efficiencies and possess significant environmental advantages, namely reductions in NO_x, SO_2 and CO_2 emissions.

However, there are several reasons which suggest that natural gas should not be used so extensively in the ESI. Until recently the use of natural gas for crude heat applications such as bulk power generation was discouraged by successive UK governments and the European Commission, due to the inherently irreplaceable nature of the resource. Although there is at present an abundance of gas in Northern Europe and the supply could be expanded significantly via greater dependence on Norwegian, CIS and Algerian pipeline supplies it is expected that towards the turn of the century prices will be forced to rise as a result of depletion of the UK Continental Shelf gas reserves. As the extent of price rises is uncertain it would seems unwise to rely too heavily on CCGT-generated supply, and as a result a balance of generating technologies should be encouraged.

It is well known that all fossil fuel reserves have a finite lifetime and the time will come when they are exhausted. According to the BP Statistical Review of World Energy,

proven and extractable reserves of fossil fuels stood at 39.19 X 10^{15} MJ in 1987. The estimates of the undiscovered reserves vary by up to four-times this amount (O'Callaghan, 1993). Table 2.2 shows how this breaks down for the different parts of the world. The values for the UK are presented at the bottom of the table below the totals for each fossil fuel. These values become more meaningful when the rate at which they are being depleted is considered. In 1850, before industrialisation, there was an estimated 5.2 10^{16} MJ of energy in fossil fuel reserves. 21.3% of this had been used up by 1977 and 28.5% by 1987. The annual rate of increase in fossil fuel consumption has averaged 2.6% since 1850. Between 1968 and 1973 this rose as high as 5.88%. This was cut as a result of the first energy crisis stemming from the Arab - Israeli war in 1973 and again in 1983 because of the Iran - Iraq war. However, this highlights the significant oil supply problems which can arise as a result our dependence on OPEC countries.

Region or country	**OIL**	**COAL**	**GAS**	**Total**
North America	0.236	7.788	0.311	8.335
Latin America	0.731	0.201	0.250	1.182
Western Europe	0.132	2.747	0.238	3.116
Middle East	3.473	0	1.179	4.652
Africa	0.336	1.898	0.269	2.503
Asia and Australasia	0.114	2.721	0.242	3.077
China	0.109	4.896	0.035	5.040
USSR	0.363	7.047	1.578	8.989
Others	0.009	2.254	0.031	2.294
Totals	5.502	29.553	4.132	39.187
UK	0.032	0.274	0.02304	0.328

Table 2.2. Energy locked up in proven world reserves of fossil fuels in 1987 (10^{15}MJ) (O'Callaghan, 1993).

The length of time the reserves will last can be calculated for various scenarios. In table 2.3 the year in which the reserves would run out is presented, assuming a steady 2.79% increase in the annual consumption of fossil fuels at the 1987 rate. It is clear that under this scenario the UK would run out of its reserves in 2013 and would therefore be totally dependent on imported fuels. More significantly, from a global perspective, all known, extractable reserves would be exhausted by 2041. However, if we assume that a positive effort is made to reduce the rate of fossil fuel consumption by 1% each year, it can be seen from table 2.4 that the total world reserves of fossil fuels

becomes, in effect, infinite. In the case of the UK however, dependence on imported fossil fuels would be delayed by only 17 years, until the year 2031.-

Region or country	OIL	COAL	GAS	Total
North America	1992	2073	1999	2036
Latin America	2027	2054	2027	2030
Western Europe	1991	2060	2006	2024
Middle East	2096	1987	2085	2093
Africa	2031	2091	2053	2068
Asia and Australasia	1997	2066	2036	2044
China	2005	2054	2022	2049
Japan	1987	1987	1987	1987
USSR	2001	2079	2025	2046
Others	1988	2046	1993	2032
Totals	2014	2065	2022	2041
UK	1995	2032	1996	2013

Table 2.3. Depletion year for a consumption rate increasing at the 1987 level (O'Callaghan, 1993).

Region or country	OIL	COAL	GAS	Total
North America	1993	infinite	2002	2199
Latin America	2095	infinite	2100	2120
Western Europe	1992	infinite	2015	2078
Middle East	infinite	1987	infinite	infinite
Africa	2137	infinite	infinite	infinite
Asia and Australasia	1998	infinite	2203	infinite
China	2012	infinite	2067	infinite
Japan	1987	1987	1987	1987
USSR	2006	infinite	2082	infinite
Others	1988	infinite	1993	2144
Totals	2036	infinite	2065	infinite
UK	1996	2143	1997	2031

Table 2.4. Depletion year for a consumption rate decreasing at a rate of 1% per year (O'Callaghan, 1993).

However, this is in many ways still an optimistic scenario. The increase in demand from third world countries is likely to increase significantly as they seek to alleviate poverty and catch up with the developed countries. This will be made worse by the expected increase in population that is predicted in many of these countries (Berrie, 1992). It is predicted that 90% of the world population growth and that 85% of the increasing demand for energy services will occur in the third world (Jefferson, 1993).

In summary, the UK ESI fuel mix is dominated by dependence on fossil fuels. Whilst the use of oil and coal is being replaced by cleaner, more efficient CCGT technology, finite reserves are being depleted and the combustion of these fossil fuels has important environmental implications.

2.1.2. Environmental aspects

The principle environmental concerns which currently have a direct bearing on the ESI are those of acid rain and global warming. The affects of acid rain are clearly defined whereas the occurrence of global warming continues to be extensively debated (O'Callaghan, 1993).

2.1.2.1. Acid rain

The acidification of Scandinavian Lakes and dieback in German forests became major environmental problems in the 70s and early 80s respectively. Intense scientific research lead to the discovery that acid rain is caused by the dissolution of the acid gases, SO_2 and NO_x, and hydrocarbons in rainwater. Moreover, these gases can be transported long distances in the atmosphere and affect countries other than the producers. International action was, therefore, essential to control this problem and in 1988 the UK agreed to control emissions of the main acidic gases produced in fossil-fuel power stations and large industrial plants in accordance with the European Community's Large Combustion Plant Directive. The target is for the UK to reduce SO_2 emissions by 20% below the 1980 level by 1993, 40% by 1988 and 60% by 2003. Similarly, NO_x emissions must be reduced by 15% by 1993 and 30% by 1998. All targets are subject to review and may be increased if it is felt necessary (Chesshire, 1993).

The main result of this directive has been that higher costs for energy have been passed on to the users but the directive has also stimulated technological development, such as the development of flue gas desulphurisation equipment, retro-fitting of low NO_x burners to coal-fired stations and imports of low sulphur coal.

2.1.2.2. Global warming

The temperature of our atmosphere is the result of a balance between the energy gained by the planet from solar radiation and radiative energy losses into space. The greenhouse gases, CO_2, N_2O, CFCs, methane, ozone and water vapour, all impede the transmission of long wavelength radiation from the earth. Stratospheric ozone also protects us from damaging short wave uv radiation from the sun. Any changes in the composition of the tropospheric atmosphere change the thermal balance of the earth (O'Callaghan, 1993).

The concentration of CO_2 in the atmosphere has increased from 270ppm (parts per million) before industrialisation to 350ppm today. The argument for global warming states that, even though the carbon released with fossil fuel combustion is small compared with the fluxes of the natural carbon cycle, the extra CO_2 emitted is enough to disturb the thermal equilibrium of the earth from its global mean of 15° C in pre-industrial times. In Europe, approximately 1/3 of CO_2 emissions come from electricity generation. As it was agreed at the Toronto conference in 1988 that all industrialised nations should reduce their CO_2 emissions by 20% from 1988 levels by the year 2005, so there is a significant role for renewable sources to play, along with energy efficiency.

There is much debate as to the extent of global warming and many would argue that the fluctuation in world temperatures is not outside the ±0.2°C boundaries of expected variations (O'Callaghan, 1993). Clearly it is difficult to prove exactly what the increases might be because of the complexity of the atmosphere, its slow response to changes in composition and the wide variety of influencing factors. Instead predictions have to be made using simplified computer models. These models predict increases of between 1.5 and 4°C. Unfortunately, the inability of these models to predict known historical changes in temperature has enabled sceptics to dismiss the predicted increases and any need for remedial action. However, more recently the inclusion in such a model of the effect of sulphate particles injected into the atmosphere as a result of fossil fuel combustion has enabled it to predict the historical changes much more accurately as well as the future increase in global temperature. This makes it much more difficult for sceptics to dismiss the validity of global warming (Matthews, 1994).

Irrespective of the global warming rate it is common sense to reduce the rate of change of the atmosphere's composition so that potentially damaging changes are minimised. This will allow more time for the development of a renewable energy economy and, if significant global warming is occurring, for the world's climate to stabilize by natural processes.

2.1.3. The role of renewables

At present the UK electricity market is dominated by fossil fuel generation. As the decade proceeds the older coal - fired generators are likely to be retired early to make way for the cleaner, more convenient CCGT generated electricity. However, at some stage, possibly in the second half of the next century, UK fossil fuel reserves will run out. This, coupled with population growth and increasing living standards expected in the third world, suggests that there will be an increasing shortfall between the world-wide supply of, and demand for, electrical energy as the next century progresses. Alternatives must be found!

Nuclear energy is one such alternative and large sums of money have been spent on its development. It has been suggested that the fast breeder reactor is likely to be the main thrust of electricity generation in the UK and USA (Taylor, 1983). However, nuclear energy is no longer a popular option with the general public due to environmental concerns such as increased levels of radioactivity and possible links with cancer, major disasters, eg. Chernobyl and radioactive waste disposal. The cost of electricity from nuclear power stations has also turned out to be much higher than expected while the decommissioning costs are not yet determined, and are likely to be considerably higher than first thought (Milborrow, 1993).

It is in this setting that renewable energy sources have a positive contribution to make. Renewable energy sources cover a wide range of technologies and include wind, wave, tidal, geothermal, solar and biomass. They are not dependent on imported fuel and they do not cause harmful gas emissions. Given that the UK government is holding back on expanding nuclear generating capacity, it is likely that, if not in the immediate short term, there will be a great need for electricity generated by renewable means. Of the available technologies wind is the most economically viable (Taylor, 1983). In this context it must also be said that the UK has the best wind resource in Europe.

2.1.3.1. Costs

When considering the implementation of renewable generation technologies the question of costs in comparison with conventional sources always arises. There are three types of opinion regarding the cost of wind energy generation. Firstly, it is cheaper than conventional sources; secondly it is cheaper when the total environmental costs for all generation systems are taken into account and thirdly it is more expensive. There are many issues affecting the price of electricity generated from wind, most importantly, the wind speed at the site, the cost of the technology and the method of financing.

Table 2.5 shows the effect of wind speed and rate of return on the capital loans on the price of wind generated electricity. It is clear that low rates of return and higher wind speeds result in the cheapest electricity.

Type of site	Wind speed	Required internal rates of return (ECUc/kWh)			
	m/s	5%	8%	10%	15%
fairly good	6.5	6.1	7.4	8.3	10.8
Good	7.5	5.0	6.0	6.7	8.8
Very good	8.5	3.4	4.1	4.6	6.0

Table 2.5. The cost of electricity as a function of mean wind speed at hub height and required rate of return net of inflation using a 20 year loan (Garrad, 1991).

The values are compared with costs for other generation plant in table 2.6. In all cases wind is cheaper than nuclear but is, on the whole, more expensive than other methods. Gipe (1991) reported that wind energy not only leads most renewable alternatives but also competes well against conventional sources including coal with an estimated levelised cost of a new, utility owned, wind plant of about 5c/kWhr in constant dollars. When the total environmental costs associated with electricity generation systems were included in the cost of generation it was found that wind energy generation had the lowest total costs associated with it (Goddard and Goddard, 1993). The parameters included in this investigation were capital and externality costs, air emissions of NO_x, SO_x, particulate matter, CO_2, water use and liquid waste disposal, wastes from emission control systems, eg. fly ash and scrubber materials, fuel residues such as bottom ash and the production and disposal of noxious and hazardous wastes, eg. asbestos, heavy metals, radioactivity and air toxics. Unfortunately the paper did not give any figures which could be used for direct comparison.

Power plant	ECUc/kWhr
Nuclear	8.5 - 1000
CCGT	2.8 - 4.2
Hydro	2.0 - 4.0
Coal	4.2 - 5.6
Wind	4.1 - 7.4

Table 2.6. Comparison of the cost per kWhr for different generating technologies (Garrad, 1991).

The last opinion, namely that wind generated electricity is more expensive, is decreasing in frequency as the cost of the technology has dramatically decreased. This is a result of improved machine design leading to better efficiency and reliability. Today the cost of wind farm plant stands at between £850 and £1200/kWhr for a 7.5m/s site. It is expected to fall to between £650 and £850/KWHR in 2000 (Milborrow, 1993). This capital cost is less than the cost of nuclear and coal but is still greater than CCGT.

2.1.3.2. Energy policy and renewables. The Non Fossil Fuels Obligation

It would appear that the stimulation of a renewable energy industry in the UK happened somewhat by accident. In 1989 the Electricity Act introduced the Non-Fossil Fuels Obligation (NFFO) to increase diversity of supply and guarantee a market for non-privatised nuclear power. It took the form of a levy collected on each unit of electricity generated by fossil fuel power stations which is used to pay a premium price for electricity generated by nuclear power. Of the £1200 million collected annually by this levy 2% [£24 million] has been set aside to stimulate renewable energy technologies in England and Wales (Halliday, 1993). There have been three calls for proposals under NFFO, the first in 1989, the second in 1990 and the third in 1994. In each case developers submitted proposals for the generation of clean energy [not only wind]. These were evaluated and the successful projects awarded contracts to supply a certain amount of power to the National Grid for a premium price. As a result, 22 wind farms are now operational with an installed capacity of 137.5MW (Lindley, 1994).

If the wind energy industry is to continue to develop, market incentive will need to be used to help the industry become an accepted generation technology [within clear goals set by the government for the levels of implementation required].

2.1.3.3. Targets for the implementation of wind energy

In 1992 the Renewable Energy Advisory Group (REAG) published its recommendations for the targets which should be set for renewable energy development. It was felt that their target of 1500MW in the year 2000 was disappointingly low since in April 1992 the House of Commons Energy Select Committee recommended a target of 3-4000MW by 2000 (Watts, 1992). In fact the government decided to underwrite only 1000MW of renewable energy by the year 2000 (Halliday, 1993).

Other countries have published targets for the implementation specifically for wind and are presented in table 2.7.

Country	Target, MW	year
China	100-200	2000
Denmark	1000 2000	2000 2010
Finland	25-30 800	2000 2010
Germany	250	1995
Greece	150	2000
Italy	300	2000
Jordan	50	2010
The Netherlands	1000 2000	2000 2010
Spain	100	1993
Sweden	100	1996
USA	4000-8000	2000

Table 2.7. National targets for installed wind turbine capacity (Halliday, 1993).

On a European front, the targets presented in table 2.8 have been proposed, taking into account the programmes already approved by governments and assuming that the utilities play a significant part in this development. This corresponds to a realistic goal for wind energy to meet 10% of the EEC's electricity requirements by the year 2030.

Installed capacity [Wind], MW	year
4000	2000
11500	2005
25000	2010
100000	2030

Table 2.8. Proposed European medium term targets (Garrad, 1991).

2.1.4. Conclusions

The demand for electricity in the developed world will continue to increase as we move into the next century The expected massive increase in the third world population and its need for energy suggests that there will be a shortfall in energy supply over demand at the start of the next century if the current dependence on fossil fuel generated electricity continues. The ESI will need to significantly reduce its dependence on fossil fuel generation if current fossil fuel reserves are to be conserved and environmental catastrophe via global warming is to be avoided.

If all the costs associated with electricity generation are taken into account wind energy is the least environmentally damaging and should be priced accordingly. Increasing targets have been set for its use in a number of countries and implementation of wind programmes is growing world-wide.

2.2. Wind

The kinetic energy associated with the wind is enormous. It has been estimated that 10% of the energy potentially available from wind would meet the planet's entire electrical energy needs. A more realistic figure of 1% of the wind's energy would still provide 10% of world wide energy requirements (Garrad, 1991).

The driving force behind the wind is the solar radiation incident on the earth's atmosphere and, in particular, the pattern of heat transfer between the surface and the atmosphere. Unequal heating of the earth's surface establishes a pressure gradient and the air is subject to a force leading to acceleration in the direction of the gradient. Because of the relative position of the earth and sun, the earth is hotter near the equator than at the poles. This causes cold surface winds to blow from the poles to the equator to replace the hot air that rises in the tropics and moves through the upper atmosphere to the poles. The rotation of the earth also plays a major part in establishing global patterns of air flow (Taylor, 1983). A simplified representation of the general world wind circulation patterns is shown in fig.2.1.

At the earth's surface frictional forces slow the air down. As height above the ground increases wind speed increases. This can be shown as a profile, see fig.2.2 for wind speed with height above the sea and smooth land. It is clear that smooth land slows the air down more than water. α is a measure of the roughness of each surface with the lowest value indicating the smoothest surface.

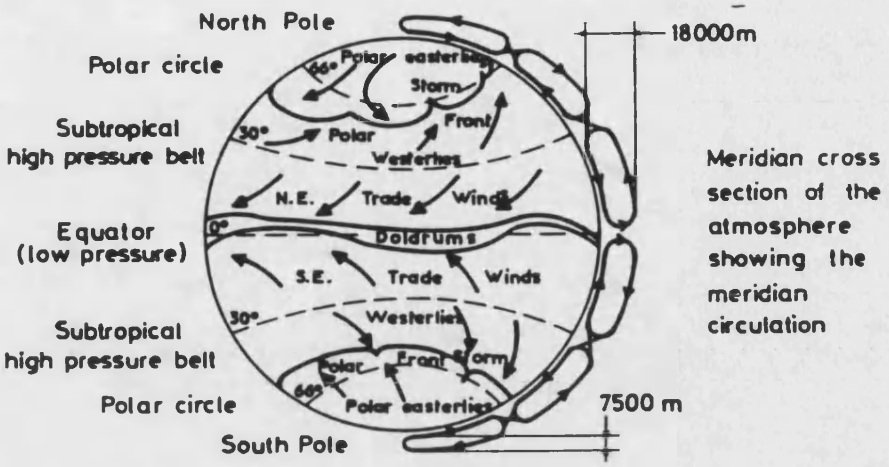

Fig.2.1. General world wind circulation (Le Gougiérès, 1982).

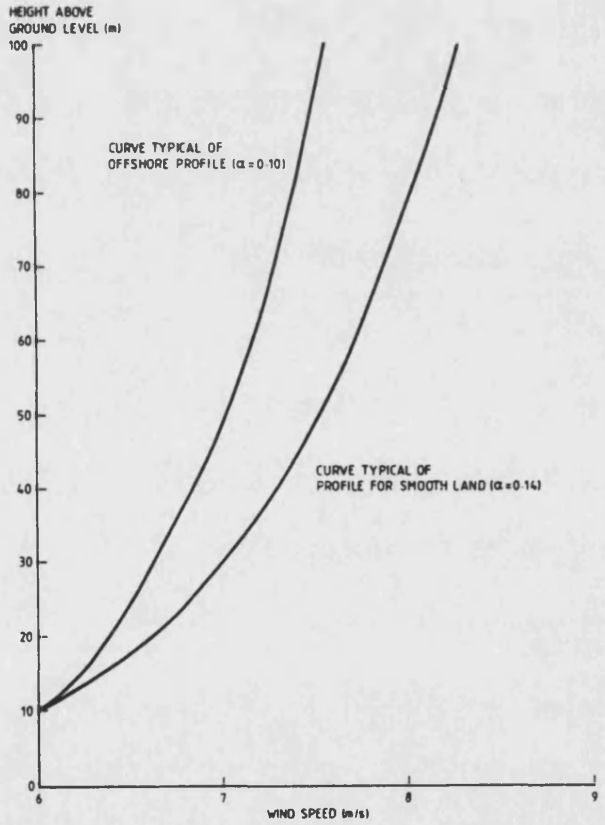

Fig.2.2. Typical variations of wind speed within the boundary layer (Taylor, 1982).

The gradient of these curves is known as the wind shear factor and is significant in wind turbine design. A taller WTG tower exposes the generator to higher wind speeds resulting in higher energy capture. Secondly, there are different wind speeds from top to bottom across the swept rotor area which cause additional forces on the blades.

Topographical features influence the way the wind blows. Wind tends to follow the direction of valleys, estuaries and tracts of water. Exposed hills and coastlines tend to have the highest wind speeds, particularly where the wind is forced up over rising ground, see fig.2.3 (Freris, 1990). Because air has a low viscosity its flow tends to become broken and turbulent leading to gusts and non-steady flow. This causes short term variations which greatly affect the performance of a wind turbine generator.

As weather fronts tend to dominate the weather patterns in the UK the wind flow changes every few days. Wind speed patterns also vary on a daily basis due to the heating and cooling of the earth's surface by the sun. Finally, there are seasonal variations in wind speeds tending to result in a large output in energy from wind turbine generators in the winter months (Taylor, 1983). Ideally the times of the day and year when the wind is strongest would coincide with the times of peak electricity demand.

All these variations in wind conditions must be accounted for by the designer of a wind farm in order to maximise power output and to ensure the wind turbines can survive the expected levels of turbulence, storms and gusting. Particular care must be taken as wind conditions are extremely site-specific.

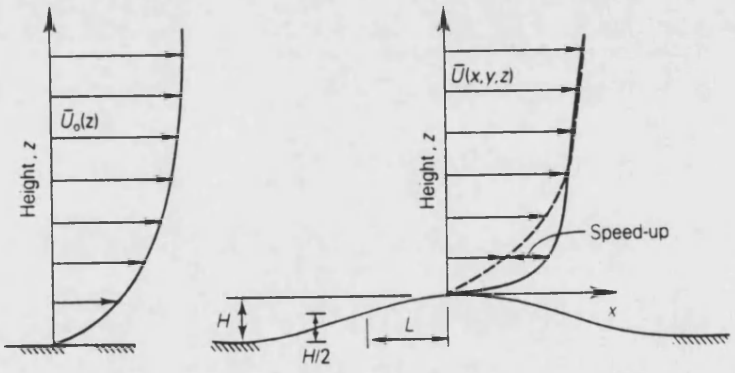

Fig.2.3. Windflow over a hill showing the resulting increase in wind speed (Freris, 1990).

The distribution of the wind energy resource in Europe is presented in fig.2.4. The darker areas have the higher mean annual wind speeds. It is clear that these regions are most abundant over the UK, highlighting our excellent wind energy resource. It would be more than a shame if this resource was not exploited.

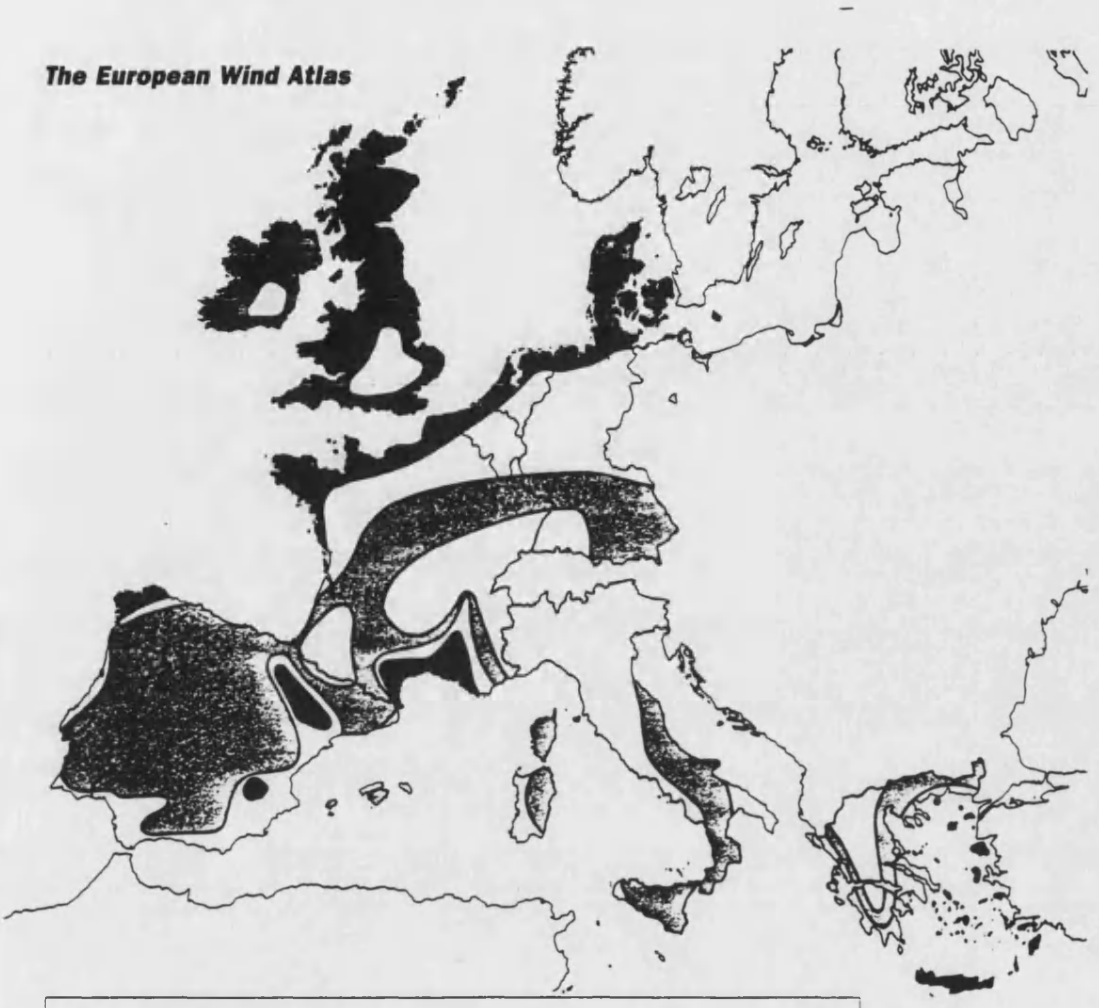

Wind speed at 50 metres above ground level for four different topographic conditions

	Open Plain m/s	At sea coasts m/s	Open sea m/s	Hill and ridges m/s
	> 7.5	> 8.5	> 9.0	> 11.5
	6.5 - 7.5	7.0 - 8.5	8.0 - 9.0	10.0 - 11.5
	5.5 - 6.5	6.9 - 7.0	7.0 - 8.0	8.5 - 11.0
	4.5 - 5.5	5.0 - 6.0	5.5 - 7.0	7.0 - 8.5
	< 4.5	< 5.0	< 5.5	< 7.0

The darker shades indicate higher wind speeds.

Reproduced from the European Wind Energy Atlas. Troen and Pedersen. 1989. The atlas was prepared before the unification of Germany

Fig.2.4. The European wind resource (Garrad, 1991)

2.3. The wind energy industry

As of June 1994 there are 21 operational wind farms in the UK. Their locations are indicated in fig.2.5 along with the name of the developer for each site. The sites have a total capacity of approximately 140MW and will generate about 360GWh of electricity in a full year. This is equivalent to the electricity needs of a town of 250 000 people, and reduces emissions of CO_2 by about 400 000 tonnes each year. Further details for

each wind farm are given in table 2.8. A further 40MW of capacity is currently under construction.

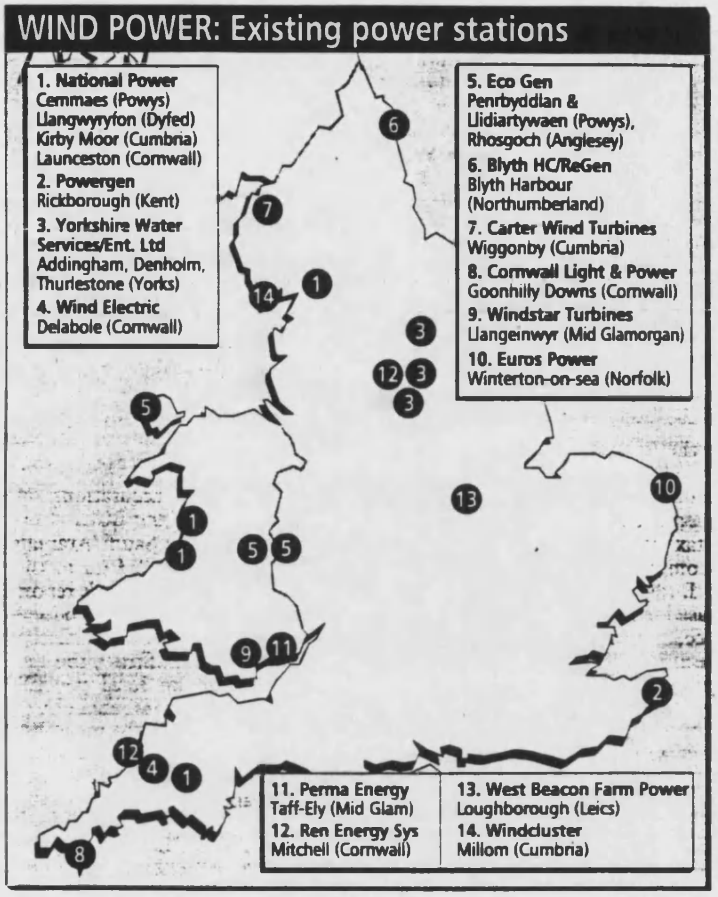

Fig.2.5. Existing wind farms as of February 1994 (Gillie, 1994)

	Sites	Developer	Turbine type	No. turbines	installed MW	Start date
1	Delabole, Cornwall	Windelectric	Vestas	10	4.0	11-91
2	Carland Cross, Cornwall	Renewable Energy Systems	Vestas	15	6.0	8-92
3	Cemmaes, Powys	National Wind Power	WEG	24	7.2	11-92
4	Chelker, Yorkshire	Yorkshire Water	WEG	4	1.2	12-92
5	Haverigg, Cumbria	Windcluster	Vestas	5	1.1	10-92
6	Rhyd-y-Groes, Anglesey	Ecogen	Bonus	24	7.2	12-92

Table 2.8. Details of major wind farm projects in the UK (Lindley, 1994b).

	Sites	Developer	Turbine type	No. turbines	installed MW	Start date
7	Blyth Harbour, Northumberland	Blyth Harbour	HMZ	9	2.7	1-93
8	Winterton on Sea, Norfolk	Euros Power	Vestas	10	2.3	12-92
9	Great Orton, Cumbria	Carter Wind Turbines	Carter	10	3.0	1-93
10	Coal Clough, Lancs.	Renewable Energy Systems	Vestas	12	4.8	2-93
11	Penrhyddlan, Powys	Ecogen	Mitsu-bishi	43	12.9	1-93
12	Llidiartywaun, Powys	Ecogen	Mitsu-bishi	60	18.0	1-93
13	Cold Northcote, Cornwall	National Wind Power	WEG	21	6.3	4-93
14	Llangwyryfon, Dyfed	National Wind Power	WEG	20	6.0	6-93
15	Ovenden Moor, Yorks.	Yorkshire Wind Power	Vestas	23	9.2	6-93
16	Goonhilly, Cornwall	Cornwall Light & Power	Vestas	14	5.6	4-93
17	Kirby Moor, Cumbria	National Wind Power	Vestas	12	4.8	9-93
18	Taff Ely, Mid Glamorgan	Perma Energy	Nordtank	20	9.0	8-93
19	Royd Moor, Yorks	Yorkshire Water	Bonus	13	5.9	12-93
20	Bryn Titly	National Wind Power	Bonus	22	9.9	7-94
21	St Breock, Cornwall	Ecogen	Bonus	11	5.0	7-94
22	Canton Moor, Lancs	New World Power	Wind-harvester	10	3.0	constrn.
23	Corkey, Antrim	B9 Energy Services	Nordtank	10	5.0	constrn.

Table 2.8 cont. Details of major wind farm projects in the UK (Lindley, 1994b).

	Sites	Developer	Turbine type	No. turbines	installed MW	Start date
24	Dyffryn Brodyn, Dyfed	New World Power	Nordtank	11	5.5	constrn.
25	Four Burrows, Cornwall	New World Power	Bonus	15	4.5	constrn.
26	Rigged Hill, Limavady	B9 Energy Services	Nordtank	10	5.0	constrn.
27	Slieve Rushen, Fermanagh	Sean Quinn Group	Vestas	10	5.0	constrn.
28	Werfa, Mid Glam,	Windstar Turbines	Windstar	10	0.5	constrn.
	Totals			**458**	**160.5**	

Table 2.8 cont. Details of major wind farm projects in the UK (Lindley, 1994b).

So far, these developments have required an investment of £140 million, mostly provided by banks and large corporate investors. A framework for the financing of such projects has been built around the use of NFFO contracts. Statutory and other bodies have responded to the rapid development of wind farms by issuing guide-lines which, together with Public Enquiry documentation, provide essential guidance for the industry (Lindley, 1994).

At present, the industry is poised to hear the outcome of the selection procedure in the NFFO 3 round of contracts. Once this has been announced there will be a renewed bout of building activity. It is expected that approximately 20 wind farms will be built under the next round of NFFO, out of the 230 wind energy projects submitted by wind farm developers (Massy, 1994).

2.3.1. A brief history of the industry

Wind power has been used in sailing ships for at least 4000 years. Its use to produce rotary power is more recent, with vertical axis machines existing in Persia from around the 7th century AD. These were used for irrigation and milling grain and despite their inefficiency their use spread to China and throughout the domain of Islam.

The first windmills appeared in Europe in the 12th century. Evidence suggests that the first use of the windmill probably occurred in the Low Countries since they have very little water power (Calvert, 1979). In Crete windmills were introduced by the Venetians along with their fortresses in the 13th century. Fig.2.6 shows the remains of

such windmills aligned along the main pass into the Lassithi Plain. The use of windmills was widespread across Europe, for such diverse tasks as draining polders in the Netherlands and making snuff tobacco, until the Industrial Revolution when it was progressively replaced by the steam engine, internal combustion engine and electrical power.

Fig.2.6. Early windmills: Corn-grinding mills along the pass into the Lassithi plain. The mills face in the direction of the prevailing wind only.

The first 'modern' windmills were developed in the late 19th century for pioneer agricultural use in the USA and Australia. These were originally developed for water pumping and were generally of a multi-bladed design. They are still widely used in rural areas today.

In the first decades of this century, as the use of windpower was generally decreasing, there were some key applications of wind energy from which the modern industry has stemmed. In Denmark a man named La Cour developed windmills for electricity production. To overcome the variations in power he stored the energy by electrolysing water to produce hydrogen which he then used to light his laboratories. As a result, a Royal Commission was set up in Denmark to develop windmills for agricultural use and several hundred such machines were produced, notably by the Lyddegaard Company (Taylor, 1982). The first really large scale modern windmill was built in 1941 on a hill

in Vermont called Grandpa's Knob. It had a diameter of 55m and gave an output of 1.25MW in a 13.5m/s wind. It rotated at a constant speed of 29rpm and the blades, which were made of steel and weighed 8 tonnes, could be pitched.

After the second world war there was an increase in demand for electricity, coupled with a shortage of fossil fuel, and attention was turned to windpower. This led to the production of several machines in the 1950s: the Enfield Andreau machine (100kW in a 15m/s wind), a prototype by the John Brown Company, (also 100kW) and a machine run by the Electrical Research Foundation on the Isle of Man (100kW in 18m/s wind). This was the most successful of the three (Taylor, 1983).

Such development continued in the UK and Europe during the '50s and '60s. The oil crisis of the 1970s led to renewed research into applications of windpower, ranging from the large 3MW demonstration turbine at Burgar Hill on Orkney to small machines used in battery charging. In the early '80s several countries, namely the USA and Denmark, actively encouraged the erection of a large number of wind turbines through programmes of subsidies and tax credits. Between 1982 and 1990 over 20 000 machines were connected to national grids with a total rating of 2000MW (Halliday, 1993).

2.3.2. The technology

A broad outline of the technology associated with modern wind turbine generators (WTG) is presented in this section.

Wind turbines generate power by converting the momentum of the wind into mechanical power and converting this rotating mechanical power into electrical power via standard a.c. generation techniques. A theoretical maximum of 59.3% of the power in the wind can be converted to electrical power and modern utility grade wind turbines operate with a maximum aerodynamic efficiency of approximately 50% (Richardson, 1993). The design of a wind turbine is determined by the balance between its ability to withstand mechanical loads and cost. Fig.2.7. is a schematic representation of the main components in a typical WTG and shows how they relate to each other. They include the structural elements of the system, the aerodynamics, the electrical generation system and the control system. There are many variations in these features between machines. These include the machine's size, the number of blades, the type of aerodynamic control, fixed or variable speed and the type of yaw control.

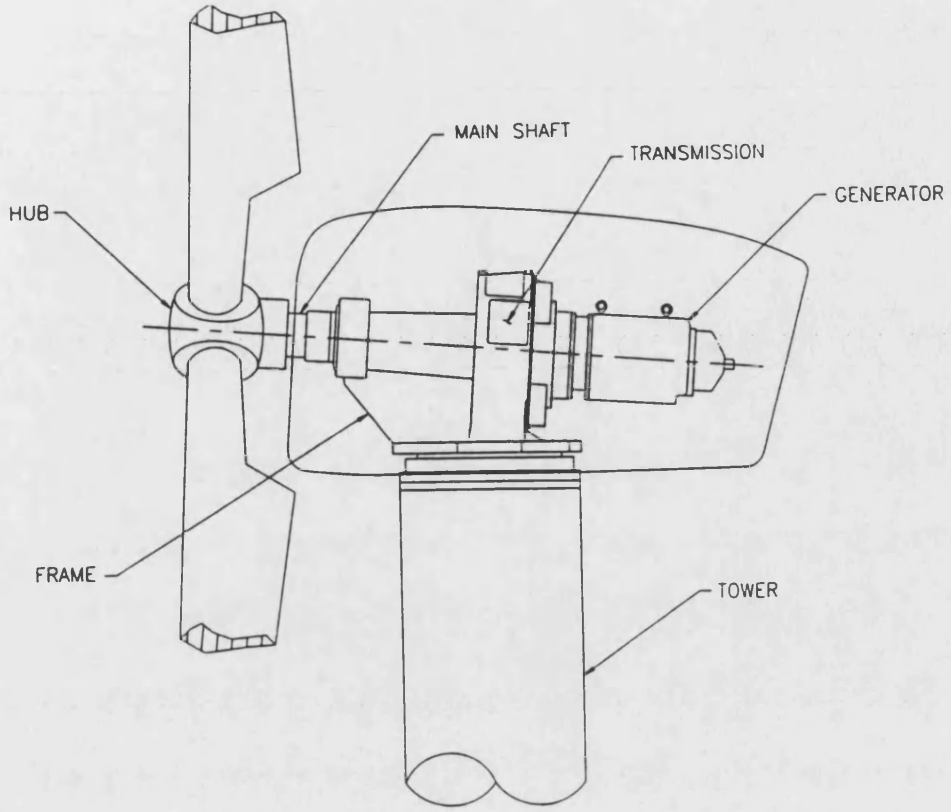

Fig.2.7. Schematic of a typical wind turbine illustrating the major components (Richardson, 1993).

A typical power output curve is presented in fig.2.8. It can be seen that a WTG has a cut in point, below which the wind is too light for power production and a cut out speed where the winds are so strong that the machine is shut down and turned out of the wind to prevent damage. The power output increases with wind speed until it reaches the rated wind speed above which the power output becomes constant. WTG power output is either controlled aerodynamically, where the blade goes into increasing amounts of aerodynamic stall which reduces the power output and protects the electrical equipment, or mechanically where the blades are progressively twisted or pitched out of the wind.

Over the last decade a huge amount of research effort has been invested in WTG technology, with particular attention being paid to the aerodynamics and structural dynamics of the system. This has paid off with improved machine efficiency, availability and a reduction in capital and generation costs.

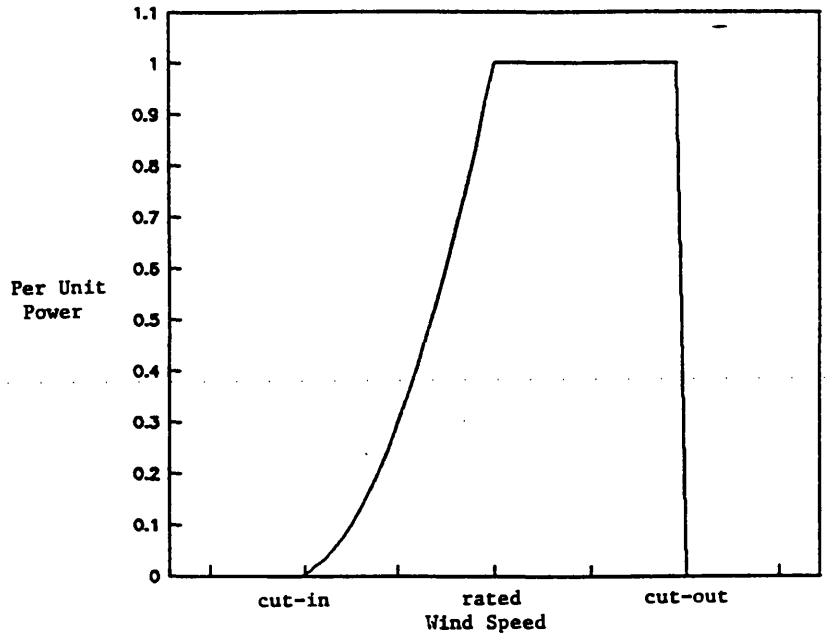

Fig.2.8. A typical design power curve for a commercial wind turbine (Richardson, 1993).

Much remains to be done to reduce costs and increase efficiency. The future likely trends in technology include:

- advanced airfoils
- variable speed operation
- taller towers
- teetered rotors
- planetary gearboxes
- electrodynamic breaks
- downwind orientation (Poore and Lynette, 1991).

By employing a combination of these it has been suggested that cost reductions of the order of 20-30% can be made along with a 25-30% increase in energy production. Fig.2.9 illustrates the possible cost reductions graphically.

Other suggestions include moving to increasingly larger machines and developing offshore wind farms (Simpson, 1994). A totally different approach has been presented by Jamieson et al. (1994) who proposed a machine in which the blades hinged as the wind speed increased thus reducing the rotor area and controlling the power. This, combined with other features, eg. very tall towers, has the potential to offer substantial reductions in the cost of wind generated electricity.

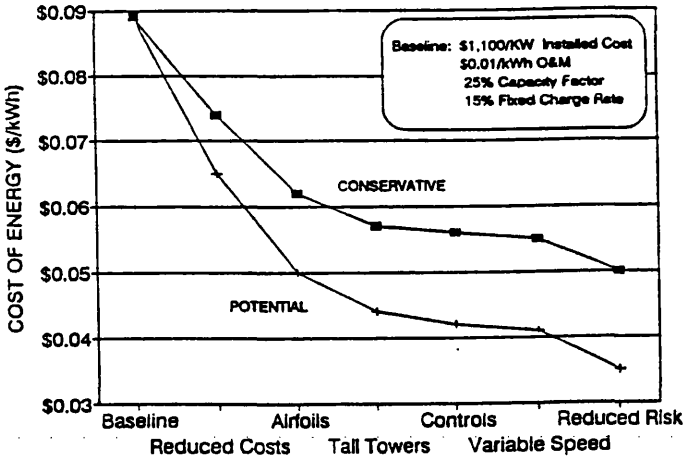

Fig.2.9. Potential system turnkey cost reductions (Poore and Lynette, 1991).

2.3.3. Barriers constraining wind energy development

Whilst there are important financial and policy barriers which must be overcome in the process of developing a wind farm (Clarke, 1991), the problem of greatest relevance to the general public is that of wind farm siting, and the extent to which wind farms are perceived as intrusive on the landscape.

As a result of the price constraints enforced by NFFO, developers are forced to concentrate their efforts on the highest wind speed sites. These tend to be in remote, and often beautiful areas such as the Welsh hills, the Yorkshire moors and the Lake District. Such places are valued for there wildness and are often also designated as sites of special scientific interest (SSSI), or are National Parks. The opponents of windpower in Britain fear that there will be so many wind farms developed in upland landscapes the opportunity for enjoying unspoilt countryside will be lost (Massey, 1994b). To satisfy these and other concerns all proposed wind farm developments are subjected to a rigorous planning procedures often involving Public Enquiries. Best practice guide-lines have been recommended (Trinick, 1994 and Weightman, 1994) to ensure that all interested parties are fully informed and can express their concerns.

However, the extent to which a wind farm despoils a landscape is highly subjective and Inspectors at Public Enquiries have generally taken the view that wind turbines are elegant structures (Lindley, 1994). It has been found that local consultation/involvement is essential to minimise the possible levels of opposition. Public opinion surveys have shown that the numbers of people in favour of wind farm development increases once a proposed site has been built. A good example of this is public attitudes in Mynydd y Cemmaes, adjacent to the Cemmaes wind farm, where

high levels of public support were demonstrated on a wide range of wind farm issues (Carver and Page, 1994).

Other issues which are important include noise levels, safety requirements, electromagnetic interference and wildlife disturbance.

Noise originates from two main sources. Rotating mechanical and electrical equipment produces tonal hums while aerodynamic noise is caused by the blades moving through the air [a swishing noise]. The former can be reduced by using special gear mountings and damping materials and the latter is minimised by optimising the blade design (Halliday, 1993). However, the significance of WTG noise depends on its level with respect to the background sounds. The impact of noise depends on the turbines used and the local topography, as well as on proximity to the WTG. Residents of the Llandinam Valley complain that its peace has been broken by incessant noise from the nearby wind farm (Underhill, 1993) but the residents in Haverigg state that the noise is minimal (Aubrey, 1994).

The main safety concern arises from the danger of a WTG shedding a blade should it fail to stop in high wind conditions. The likelihood of this happening is minimised by the application of design and operational standards and has been equated to the probability of being struck by lightning (1 in 10 million) at a distance up to 210m from the turbine.

In the majority of circumstances it is unlikely that there will be a problem with electromagnetic interference to radio transmissions if turbines are not installed immediately adjacent to the transmitter or receiver. However, terrestrial television broadcasts are more likely to be a problem. Such problems can fortunately be cured by the use of an extra repeater station, or cable television, without undue additional expense (Halliday, 1993).

It has been found that in California an appreciable number of birds of prey have been killed as a result of being struck by a wind turbine blade and an influential organisation has called for a moratorium on further wind farm development in bird migratory areas (Davidson, 1994). Bird deaths have also caused fury at the Spanish Tarifa wind farm which is situated above the Straits of Gibraltar. Birds stop over at Tarifa to rest and feed before crossing from Europe to Africa and use the same updrafts to soar away as do the wind turbines. Collisions are the inevitable result (Luke, 1994). This result was identified in a Dutch survey of the effect of WTGs on birdlife (Benner, 1993). It was found that WTGs disturb migrating and resting birds but that their impact on breeding

birds is negligible. Closer to home, a study was conducted in Blyth harbour to determine the effect of the wind farm on the large bird population (Still et al., 1994). Nineteen birds have been killed by collision with wind turbines in the 18 months since the wind farm was commissioned. During the study over 423 dead birds were recovered which had died from a variety of natural and unnatural causes in the vicinity of the wind farm. Consequently it was concluded that there is not a significant threat to the local bird population.

2.3.4. Conclusions

Whilst there are many reasons why the UK should be investing heavily in wind farm development for the production of clean energy the perceived negative impact of wind energy must be taken into account. If best practice is followed, and public consultation is maximised at the planning stage to take account of local concerns regarding visual intrusion, noise and impact on the landscape, the affected communities are much more supportive of new wind farms.

2.4. Wind turbine generator blades

Blades are the most obvious and critical component of a wind turbine generator. They suffer severe stresses in high wind speed conditions and will experience in the order of 10^8 rotations, and hence fatigue cycles, in their lifetime (Taylor, 1983).

2.4.1. Blade profiles

Blade technology has evolved considerably over the last 15 years. There are two major aspects of blade design: blade profiles and blade materials, and these are discussed in the paragraphs below.

The profile of the blade airfoil controls the aerodynamic efficiency of a WTG. An enormous number of blade profiles have been developed which give a good lift to drag ratio and consequently good performance. A good lift to drag ratio results from little or no separation in the air as it passes over the upper surface of the blade (Calvert, 1979). Fig.2.10 shows two typical blade profiles.

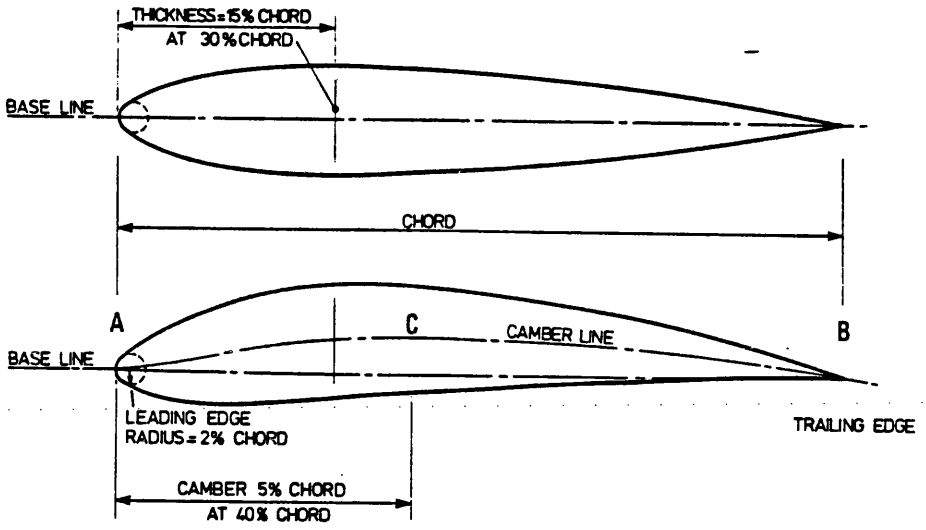

Fig.2.10. Two typical blade profiles. A symmetrical and a cambered aerofoil (Calvert, 1979).

2.4.2. Blade materials

A wide range of materials have been used in the manufacture of wind turbine blades. The most common are steel, GRP and wood. There is wide variation within these groups and all have their specific disadvantages and disadvantages.

Steel was commonly used on the early prototype machines such as the Boeing Mod-2 machine (Gipe, 1993). However, steel blades are very heavy [a 25m blade weighs 1700kg (Freris, 1990)] and no machines are now made with steel blades. The other metal which has been used in blade manufacture is aluminium, which can be extruded in constant cross section lengths (Andreä, 1993), giving mass production advantages, which result in appreciable cost savings. However aluminium has two disadvantages: it is expensive and prone to fatigue cracking (Gipe, 1993).

By far the most common blade material today is GRP with two thirds of manufacturers using it for their blades (Simpson, 1994). The blades may be produced by pultrusion, hand lay-up into female moulds or by tape or filament winding (Gipe, 1993). There is scope for tremendous variation, with different resins and glass as single fibres, tape or cloth (Lowe, 1993). This can lead to large variations in blade properties for essentially similar blades. Although GRPs are generally found to have good weathering properties, the effects of moisture on fatigue are not negligible with the greatest effects being noticed at high stress levels in tension (Bach, 1993). Blade weight has been reduced enormously by the use of composite blade materials. However, it is still felt that GRP blades, are overdesigned (Corbett, 1993). Heavy blades result in the need for more robust components such as bearings and gears to withstand the greater rotational forces.

Consequently, if blade weight is reduced other savings are also made in the components further down the drive train. For this reason there has always been interest in reducing the mass of WTG blades. Other glass-reinforced plastic blades include glass reinforced epoxy and carbon reinforced epoxy. Both are high performance materials and as such are more expensive than the traditional GRP materials.

Wooden blades have been used for many centuries and consequently may have a 'low tech' image. Solid wood is used for blades of small machines with a rotor diameter of less than 5m. Such blades are machined from planks or laminated blocks and then varnished to protect them from the environment (Gipe, 1993). Hollow laminated blades are used on larger machines. This technology developed from wooden boat-building techniques where thick wood veneers were glued together in a female mould and consolidated to produce two halves of a blade which could then be joined together (Corbett, 1993). The use of wood in the production of such blades has many advantages. It is a low density material with the optimum combinations of stiffness and strength to produce high solidity, light blades at reasonable prices (Hacker, 1993) [a 25m blade weighs 400kg (Freris, 1990)]. It uses a minimum amount of energy to produce a blade and therefore reduces the energy payback period (the time taken to generate the energy expended in the production of the WTG) (Knight, 1993). The main constraint on the manufacture and use of wood composite blades is the low level of automation currently used in the manufacturing process.

A study was conducted to attempt to resolve the lack of consensus regarding the most suitable blade material. It was shown that wood composite blades are indeed the optimum blade material (Corbett, 1993). This view is also supported by Ansell et al, (1991).

The most unusual materials cited in the literature on blade manufacture were titanium and its alloys and concrete. The former was dismissed on grounds of expense and the latter on the grounds of weight (Taylor, 1983).

2.4.3. Manufacture of wood-epoxy wind turbine blades

A schematic diagram of the Wind Energy Group's wood composite blade is presented in fig.2.11, showing the position of all the structural features. These are the wood veneers bonded together with epoxy resin, the lightweight glass foam trailing edge, inner and outer layers of GRE for complete moisture protection, the smooth gelcoat and the high strength SG (spheroidal graphite) iron studs bonded into the root of the blade with graphite-filled epoxy.

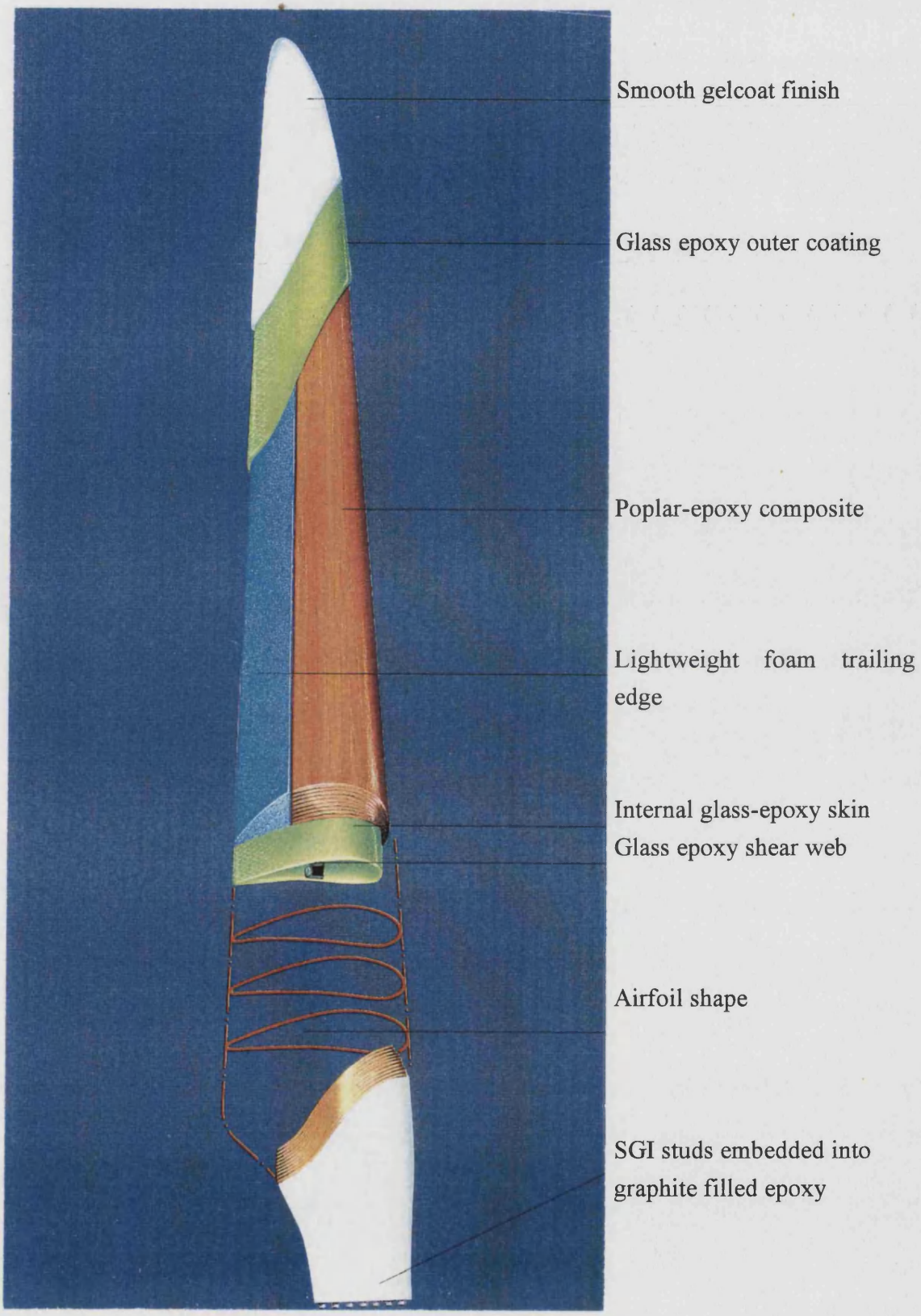

Fig.2.11. Schematic of the WEG wood composite wind turbine blade (WEG Blade literature).

The wood which is currently used in production is the European hardwood Poplar (*Populus nigra*). This is the result of a switch away from the African mahogany (*Khaya ivorensis*) in an effort to produce the most environmentally friendly blades. Poplar was selected because its mechanical performance was almost as high as that of Khaya, it was easy to glue and was readily available in thick veneers. Douglas fir was used by Gougeon Brothers because of its ready availability in the USA. Other wood species investigated as a substitute for Khaya include birch, Baltic pine, and beech (Bonfield et al., 1992).

The manufacture of a wood composite blade is shown in figs.2.12 and 2.13. Each half of the blade is laid up by coating the pre-cut and jointed sheets of 5mm thick rotary cut poplar with room temperature curing epoxy resin and laying them up in a mould, fig.2.12. The mould has been prepared by lining it with the blade's outer protective coating of glass reinforced epoxy (GRE). The moisture content of the wood is about 8% and any large defects have been removed. Once the wood has been laid in the mould the leading edge is also laid in the mould and consists of structural foam. A polythene sheet is sealed over the uncured blade and the air evacuated, fig.2.13. This consolidates the blade and it is allowed to cure under a pressure of approximately 7psi for 6 hours. The edges of the blade are smoothed before the GRE shear web is bonded into place and the two halves of the blade are joined.

The blades are attached to the hub by conical SG iron studs which are bonded directly into the root using a carbon fibre filled epoxy grout. The studs are conical in shape to reduce the shear stresses between the high modulus steel and low modulus wood composite.

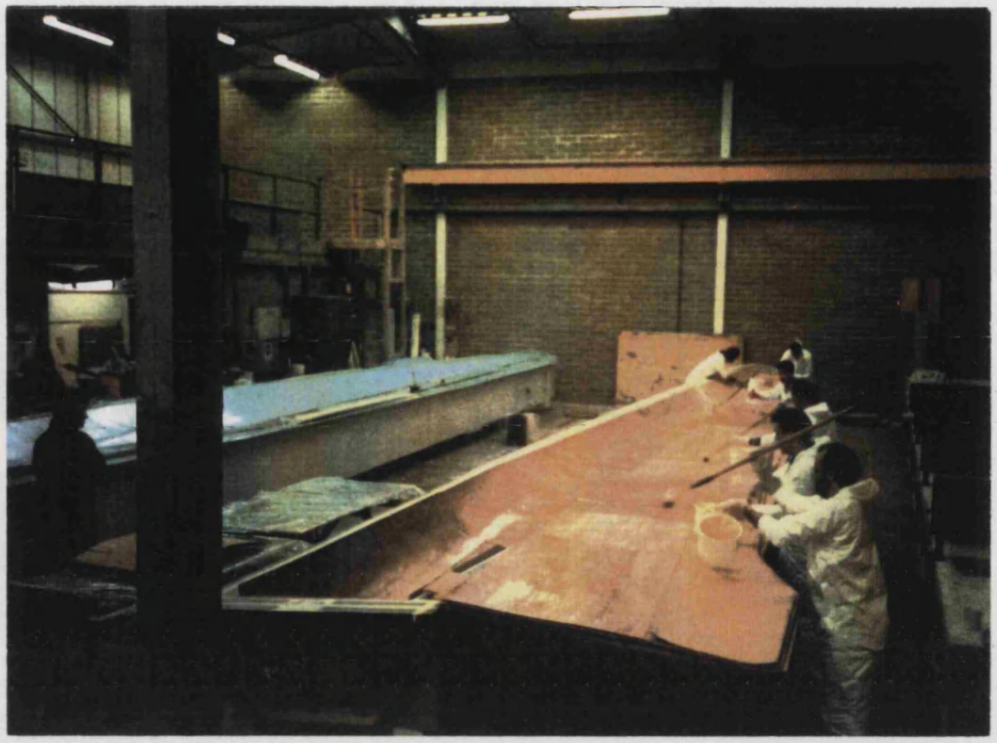

Fig.2.12 The wood veneers are laid into prepared female moulds using an epoxy adhesive.

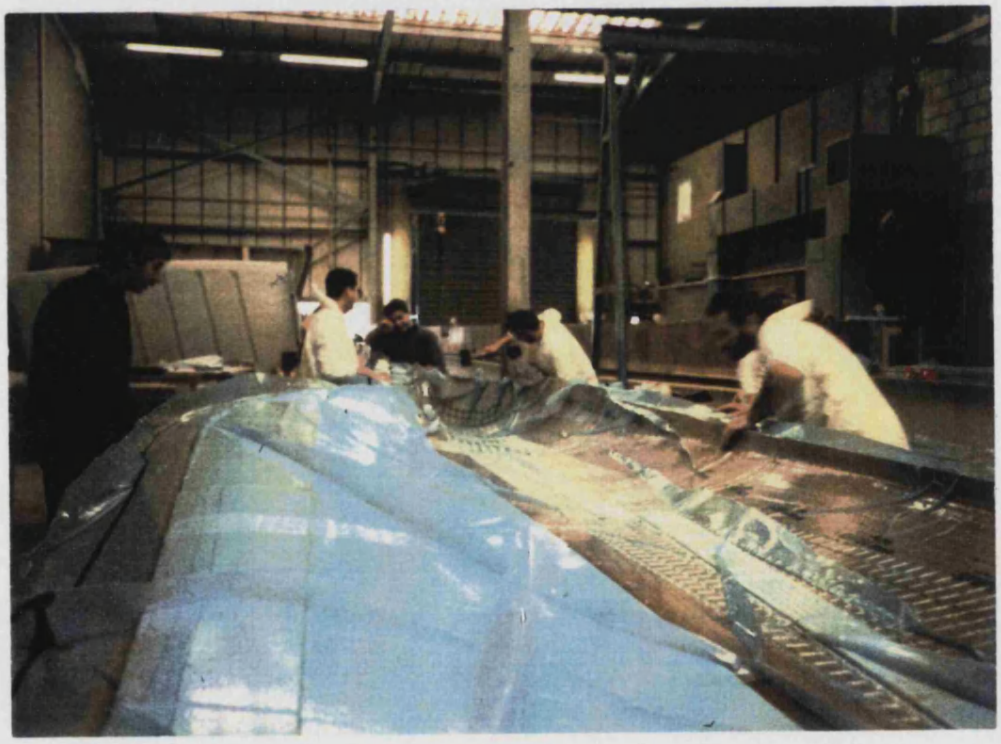

Fig.2.13. The blade is covered with a polythene sheet for blade consolidation by atmospheric pressure following the evacuation of air.

2.5. Conclusions

In overall conclusion it can be said that:

- The use of renewable electricity generation sources will increase by necessity over the next 50 years.

- Wind energy is at present the most developed technology available and its implementation is growing world-wide.

- The UK has the best wind resource in Europe but its development must be pursued using best practice guide-line and with sensitivity to the local commumity's concerns.

- Research has shown that wood composites are an optimum solution in the choice of wind turbine blade material.

3. WOOD

Wood has been used in a wide range of applications for many centuries. Early uses include weapons, canoes, furniture, housing, musical instruments, water-wheels and gear wheels. Although the use of wood in many of these applications has been replaced by other, more modern materials, the mass of wood consumed annually is comparable with that of iron and steel (Dinwoodie, 1981), with the construction industry as the primary consumer.

The properties of wood vary enormously. There are over 30000 different species of tree ranging from *Lignum vitae*, the densest wood (1249kg/m^3), to Balsa with the lowest density (160kg/m^3). Variation also occurs within species and here differences in density can vary by up to 300%. This is largely due to differences in the proportions of earlywood and latewood (Everett, 1994). The complexity of wood structure is eloquently summed up by Dinwoodie (1981) who states that 'wood as a material can be defined as a low density, cellular, polymeric composite'. As such it does not fall into any one class of material but overlaps a number of classes. In terms of its high strength performance and low cost, wood remains the world's most successful fibre composite.

In this chapter the overall structure of wood is reviewed, ranging from the complete tree to the molecular level. Most attention is directed to the cellular level, covering both micro- and macro-levels of the structure. The factors affecting the mechanical properties of wood are covered along with common defects which contribute to the variability of wood and its mechanical properties. A subsection is devoted to the structural features of *Khaya ivorensis* as it is the material which has been used in the research.

3.1. Wood structure

Fig.3.1 summarises the overall structure of a tree and draws attention to the important features. Essentially the tree is a complex plant which uses salts form the soil and CO_2 from the atmosphere to manufacture food materials by the action of sunlight on chlorophyll in the leaves. To do this the tree sometimes grows to a height of 90m and to support the weight of the crown the trunk is, by necessity, an excellent structural unit.

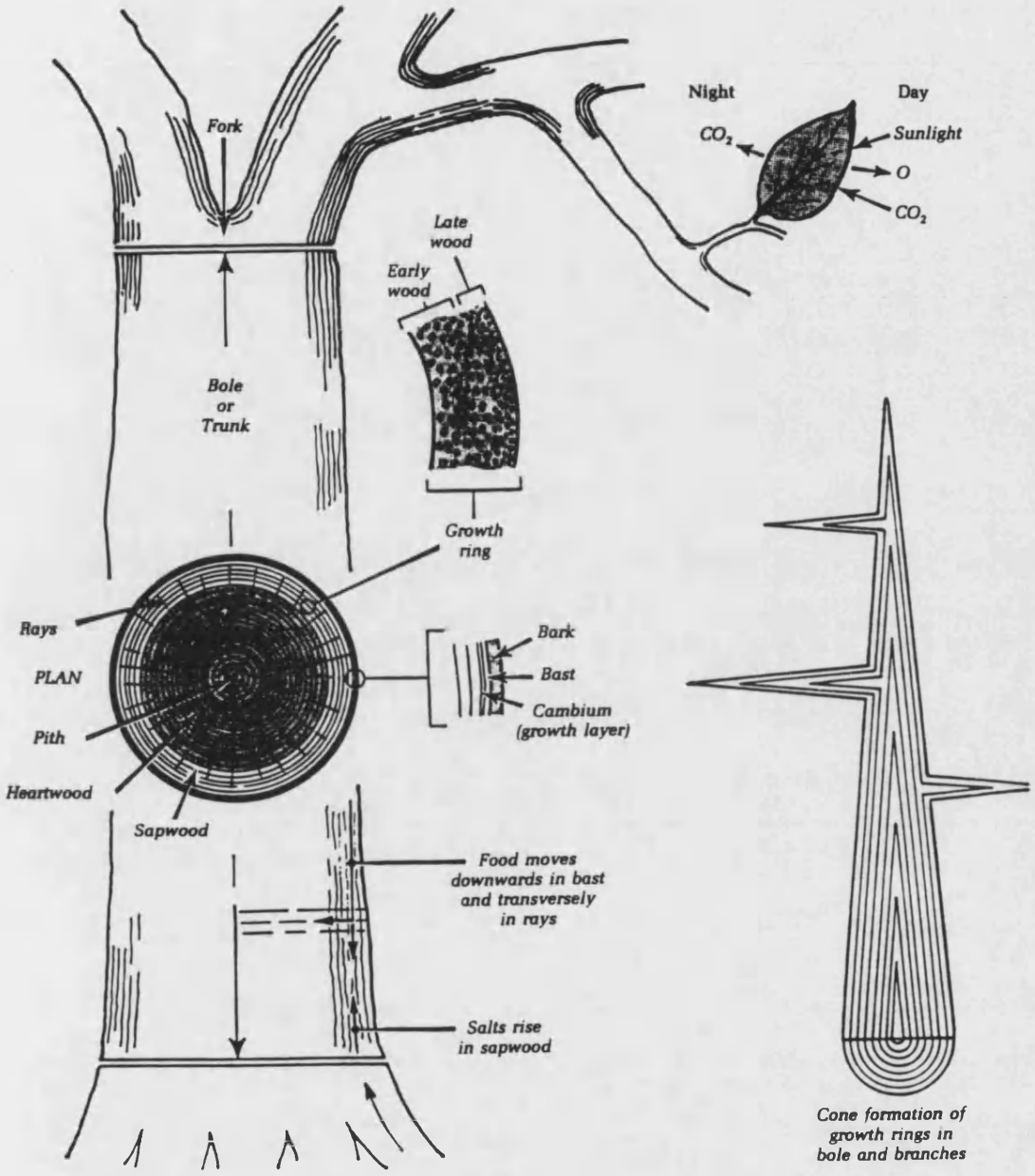

Fig.3.1. The tree - a schematic of its structural features (Everett, 1994).

3.1.1. Microstructure

The microstructure of wood relates primarily to the constitution of the wood cell walls. At this level wood consists of several types of molecular species which are bound together to form microfibrils which are, in turn, built into cell walls in a complex spiral orientation. There are four primary chemical constituents of wood cells - cellulose I, hemicelluloses, lignin and extractives which are discussed below. The relative proportions of each are shown in table 3.1 for both softwoods and hardwoods.

Principal constituent	% (mass)	
	softwoods	hardwoods
Cellulose I	40-45	45-50
Hemicelluloses:		
• galactoglucomannans	15-20	---
• arabinoglucuronoxylan	10	---
• glucuronoxylan	---	20-30
• glucomannan	---	1-5
Lignin	26-34	22-30
Extractives	0-5	0-10

Table 3.1. Chemical constituents of wood (Bodig and Jayne, 1982).

Cellulose, hemicellulose and lignin together form the basic building unit known as a microfibril, fig.3.1. Cellulose forms the central core of a microfibril, fig. 3.2. This is surrounded by a paracrystalline mixture of cellulose and hemicellulose. A thin, 1nm, layer of amorphous lignin forms the outer layer of the microfibril.

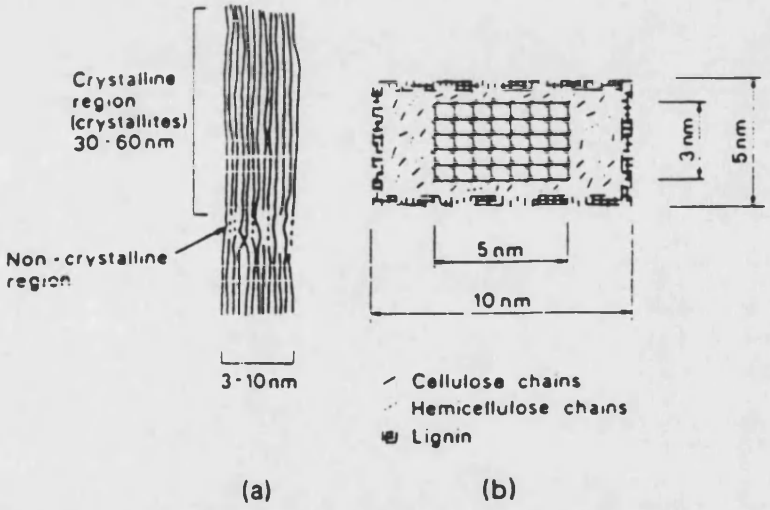

Fig.3.2. The microfibril: a) crystalline core in longitudinal section and b) transverse section of surrounding core and matrix (Dinwoodie, 1989).

Cellulose $(C_6H_{10}O_6)_n$ is a chain molecule with a high degree of polymerization - usually containing 8000-10 000 units, fig.3.3. Up to 70% of the cellulose present in wood is of the crystalline form, cellulose I. Although there has been much controversy over the structure of cellulose, the most widely accepted view is that of Gardener and Blackwell (1974) and is shown in fig.3.4.

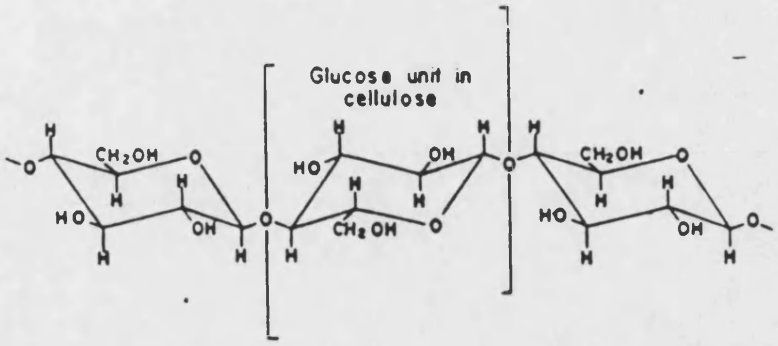

Fig.3.3. Portion of a cellulose molecule (Bodig and Jayne, 1982).

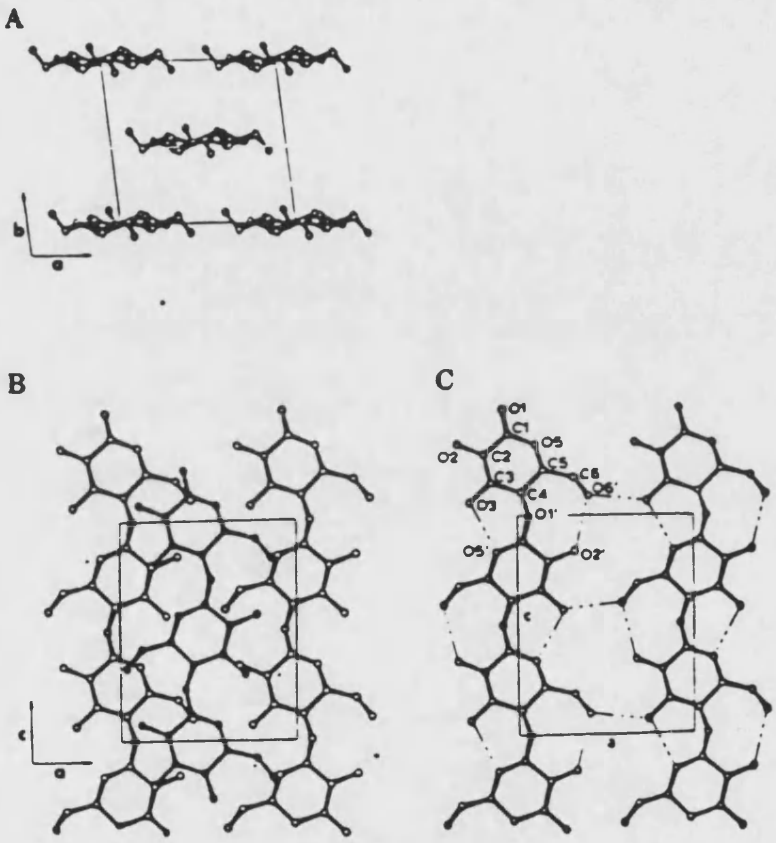

Fig.3.4. Crystal structure of cellulose I. A. ab-projection; B. ac-projection; C. network of hydrogen bonds in the ac-plane (Gardener and Blackwell, 1974).

The cellulose molecules line up and hydrogen bonds form between them, resulting in distinct planar layers. No hydrogen bonding occurs between these layers and they are held together by Van der Waals forces in a regular crystalline structure. A cellulose molecule passes through regions where it is aligned with adjacent cellulose molecules and is, therefore, crystalline. Where cellulose molecules fail to line up and form hydrogen bonds with adjacent molecules amorphous cellulose regions result. Because the hydrogen bonding is incomplete in the amorphous region the cellulose molecules will bond with water. This is detrimental to the mechanical properties of cellulose.

Hemicellulose is a carbohydrate of low crystallinity and has a degree of polymerization between 150 and 200 units. It stiffens the cellulose core of the microfibril and acts as a coupling agent between the crystalline cellulose and the amorphous lignin.

Lignin encases each microfibril and is a large, irregularly substituted phenylpropane-based molecule. It is important in stiffening the microfibril and in protecting the hydrophillic non-crystalline cellulose and hemicellulose from water. Since it coats each microfibril it is responsible for binding them together and transferring stress between them.

Extractives, organic or inorganic compounds deposited in the heartwood, have little or no direct effect on the mechanical properties of wood but are responsible for increasing specific gravity and decreasing equilibrium moisture content. They can also control durability, colour, odour and taste. In some species, phenolic extractives provide resistance to decay and insect attack. The type and amount of extractives vary enormously. Sapwood, except for food reserves, is usually extractive free, rendering it light in colour and less durable than extractive rich heartwood. Examples of extractives include silica, calcium salts and tannin.

When a wood cell grows microfibrils are laid down to form the cell walls. There are several distinct layers to a cell wall, primary secondary and tertiary, which are distinguished from each other by the angles of the microfibrils. Fig.3.5 shows the structure of a wood cell and the complex way in which microfibrils comprise cell walls.

In the primary wall the cellulose fibres are arranged in thin crossing layers of random orientation and are the first fibrils to be laid down in a new cell. The secondary wall comprises up to three parts. In the first part, S1, the fibrils have a gentle helical slope [50°-70°]; the second, S2 layer is the thickest wall layer and the fibrils run at a steep angle [10°-30°]. The tertiary wall [sometimes termed the S3 wall] consists of fibres arranged with a gentle slope but not in a very strict parallel order [60°-90°]. This layer has a higher concentration of non-structural substances, giving the lumen a smooth appearance. Helical thickening is an integral part of the tertiary wall structure. In some woods the central lumen is lined with a warty layer which is composed mainly of lignin-like materials. Between individual cells there is a thin layer called the middle lamella which glues the cells together. It is composed mainly of lignin and is cellulose-free.

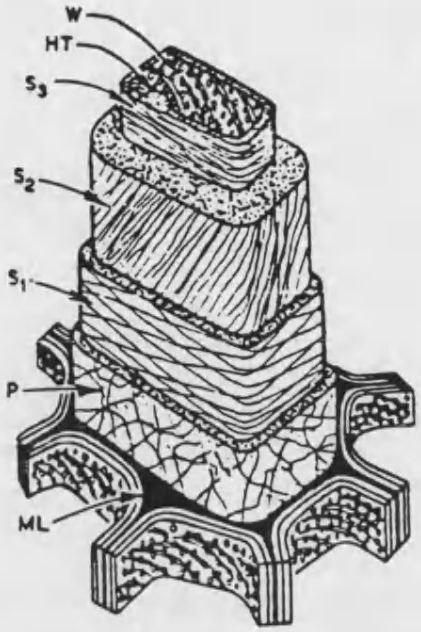

Fig.3.5. A schematic diagram illustrating the general structure of the cell wall layer showing the helical orientation of the microfibrils in each layer. ML, middle lamella; P, primary wall; S1, S2, S3, constituents of secondary wall; HT, helical thickening; W, warty layer (Butterfield and Meylan, 1980).

In all types of cell the secondary wall, S2, accounts for the main portion of the cell wall. In all types of cells it constitutes at least 50% of the cell wall and can be up to 90% of the total thickness in late wood (Fengel and Wegner, 1984).

The system of sloping fibrils in combination with the non-structural solidifying substances gives wood cells a sturdy and flexible construction which can resist a wide range of applied stresses. Due to the steep running fibrils the S2 layer is strong in tension, whereas the gentle sloped S1 layer provides the cell with compression and torsion resistance.

3.1.2. Macrostructure

The macrostructural level of wood structure is above the cellular level and relates to the way in which different cell types are arranged to form the tree trunk. There are up to four types of cell which together perform all the functions necessary for the survival of the tree.

The types of cells present in the wood determine whether it is a 'softwood' or a 'hardwood'. Softwoods (Gymnosperms) are comprised of only two of the four types of cell, tracheids and parenchyma. In hardwoods, (Angiosperms) two additional types of

cell are present, namely vessels and fibres. Table 3.2 summarises the different cell types and their function for both softwoods and hardwoods.

Cells	Softwood	Hardwood	Function	Relative wall thickness
Parenchyma	+	+	Storage	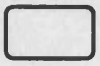
Tracheids	+	+	Support Conduction	
Fibres		+	Support	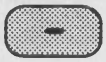
Vessels		+	Conduction	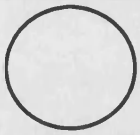

Table 3.2. The functions and wall thicknesses of the various types of cell found in softwoods and hardwoods (Dinwoodie, 1981).

Tracheids constitute 90-95% of a softwood and are responsible for the conduction of mineral solutions up the tree and the support of the crown. The parenchyma are groups of horizontally aligned cells which form rays and act as a store for food produced in the leaves. Parenchyma, like tracheids, are connected to each other by minute openings called pits.

In the case of a hardwood, the support of the tree is primarily effected by fibres which are long (2.5-7mm), slender (17-60μm radius) cells with tapered ends. Conduction of nutrients occurs in vessels which are stacks of large diameter cells (20-350mm diameter, 0.2-1.3mm long) whose interconnecting walls have been dissolved away to form a tube.

The following features of the macrostructure can be seen in fig.3.1 (p.43).

1. *Cambium*. A thin layer under the bark where all the cell growth occurs.

2a. *Inner bark*. The living portion of the bark through which food is conducted from the leaves.

2b. *Outer bark*. The dead, corky, outer protective layer.

3. *Sapwood*. A living band of wood under the cambium through which sap passes up to the leaves. It also acts as a food storage zone and transfer area.

4. *Heartwood.* This comprises the bulk of the wood in mature trees with its sole function being the mechanical support of the tree. Its darker colour is due to the infiltration of extractives.
5. *Pith.* The very centre of the tree. It consists of thin, pulpy strands which were the tree's first years of rapid growth.
6. *Ray cells.* Radial groups of thin walled parenchyma cells.
7. *Annual rings.* Occur in wood grown in temperate climates. Cells formed in the early part of the year, where growth is rapid, are thin walled and large in diameter. As the season advances, growth slows and cells become smaller in diameter with thicker cell walls. If the transition from earlywood to latewood is abrupt, distinct rings of the two types of wood are visible.

3.2. Defects and variability in wood

As was mentioned earlier, there is a huge range of woods with widely different properties. In addition to the genetic differences between species, other factors cause variation. Some of these are detrimental to the wood and others add character and distinctiveness and are highly prized. The most important of these are outlined below.

There are distinct patterns of variation in macrostructure within every tree depending on the height and the distance from its centre. Features exhibiting such variations include cell length, cell wall thickness, grain angle and S2 microfibrillar angle. Such patterns result in the formation of a core of wood, in the centre of the tree, approximately 10 growth rings thick with many undesirable properties such as low strength and high shrinkage.

The main defects are knots, reaction wood and brittleheart. Knots are disturbances in the grain caused by the presence of branches. If the grain is continuous the knot is termed a live knot, but if there is a discontinuity, due to the presence of bark from the branch, the knot is said to be dead because it is liable to fall out.

Reaction wood occurs as a result of differential loading on the tree during growth, usually because of a prevailing wind or growing on a slope, and has different properties from normal wood. In softwoods reaction wood develops in the region of compressive stress and is known as compression wood. Such wood is characterised by having a higher than normal lignin content, a higher microfibrillar S2 angle resulting in increased longitudinal shrinkage and a darker appearance. Compression wood tends to be more brittle than usual and cracks appear during drying. In hardwoods reaction wood develops in the region of tensile stress and is known as tension wood. Such wood

is characterised by a higher than normal cellulose content which gives a rubbery characteristic to the fibres resulting in difficulties in sawing and machining.

Brittleheart occurs in many low density tropical hardwoods. It is caused by the slight shrinkage of cells after their formation which puts the core of the tree into compression. When the stresses reach the compressive yield point shear lines are formed through the wood which cause considerable weakening, especially when a piece of such wood is loaded in tension.

The variations in wood which add character and distinctiveness and enhance its appearance include its texture, figure, grain and colour. All, except colour are a result of the size, shape and orientation of the individual cells in the wood tissue interacting with the way in which the wood is cut.

3.3. Factors affecting the mechanical properties of wood

It has been seen that there is enormous scope for variation in wood and this section deals with the effects of such variations [density and wood structure] and external factors [moisture, temperature and time] on the mechanical properties of wood. The effects of such parameters on wood strength and stiffness are, on the whole, as expected and are presented graphically.

The density of wood is a function of the cell wall thickness which, in turn, is directly related to the area of microfibrillar reinforcement in a section of wood. Therefore a fairly linear relationship between density and strength and stiffness is to be expected. This is illustrated for the compressive strength of both air dried and green woods in fig.3.6.

Before considering other mechanical properties of wood it must be stressed that wood is an orthotropic material with different properties in the different grain directions. Fig.3.7 shows how the different planes of wood are defined and table 3.3 shows the variation of stiffness and strength for each direction for Khaya, beech and Douglas fir. Although Dinwoodie's data (1981) has been supplemented by similar data from other sources none of the data sets are complete and density and moisture contents vary between workers. This anisotropy is partly due to the cellular nature of wood and partly to the structure and orientation of microfibrils within the cell walls. Bonding along the direction of the microfibrils is covalent and much stronger than the hydrogen bonding between adjacent microfibrils. Since the majority of microfibrils are orientated along the cell wall, wood is stronger and stiffer in the longitudinal direction than in the transverse directions.

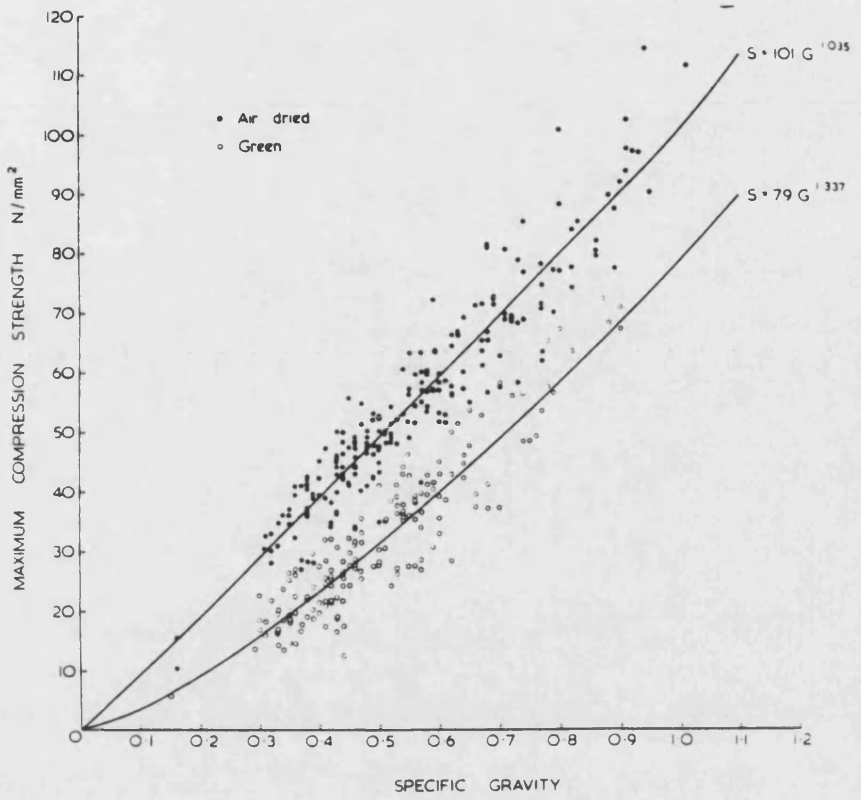

Fig.3.6. The relationship between maximum compression strength and specific gravity for 200 wood species tested in the green and dried states (Dinwoodie, 1981).

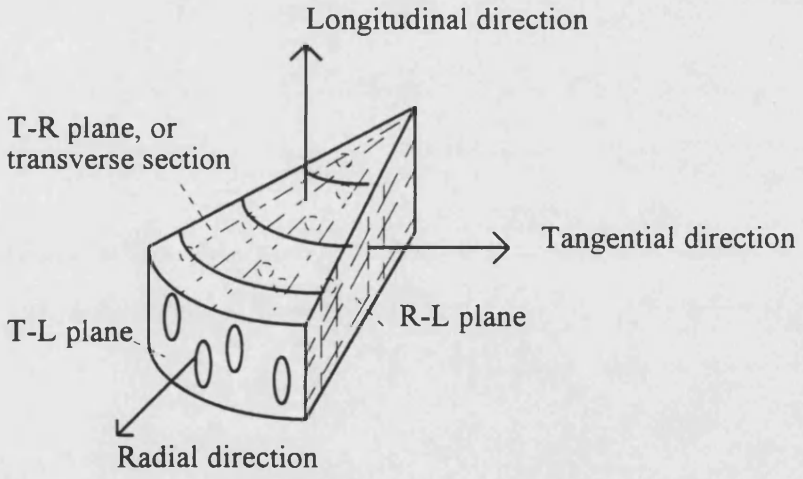

Fig.3.7. Planes and directions defined for wood

Species	Density kg/m^3	MC %	E_L, GPa	E_R	E_T	Tension MPa //	Tension MPa ⊥	Compression MPa //	Compression MPa ⊥
Khaya	440	11	10.2	1.13	0.51				
	530[c]	6[c]				85[c]		52[c]	
Beech	750	11	13.7	2.24	1.14				
	673[b]	12[b]				100[c]	12.5[b]	51.8[b]	9.41[b]
Douglas fir	590	9	16.4	1.3	0.9				
		12				138	2.9	49.6	6.9
	545[b]	12[b]				138[b]	2.9[b]	52.1[b]	5.48[b]

Table 3.3. The orthotropic properties of wood. MC = % moisture content by weight; E_L, longitudinal stiffness; E_R, radial stiffness; E_T, tangential stiffness; //, strength parallel to grain; ⊥, strength perpendicular to the grain (Dinwoodie, 1981). [b] Desch and Dinwoodie (1981). [c] data collected at Bath University.

As one would expect with any fibre reinforced composite, if a load is applied off-axis from the fibre reinforcement direction stiffness and strength properties fall off rapidly. This is illustrated in fig.3.8 where the modulus of elasticity for beech is plotted against the grain angle.

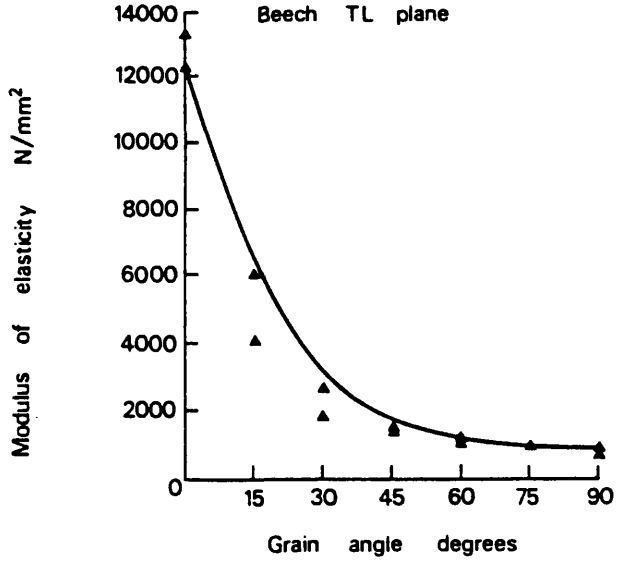

Fig.3.8. Effect of grain angle of the modulus of elasticity of beech (Dinwoodie, 1981).

Similar effects are observed on the microstructural level with regard to the microfibrillar angle within a cell wall. Fig.3.9 shows how the stiffness of the cell wall decreases with increasing microfibrillar angle. It can be seen that the stiffness of a perfectly aligned microfibril is over 40GPa. The mean microfibrillar angle can be

roughly estimated for Khaya to be between 10° and 15°as follows (assuming that the cell wall material is of the same strength):

- % cellulose cell walls in Khaya = 530/1500=35%
- assume 75% of this is in the form of axial microfibrils
- The axial stiffness of Khaya is approximately 10GPa
- The stiffness of the cell walls in Khaya = 10/(0.35 X 0.75) = 37GPa
- Measured from fig.3.9, the mean microfibrillar angle = 12°.

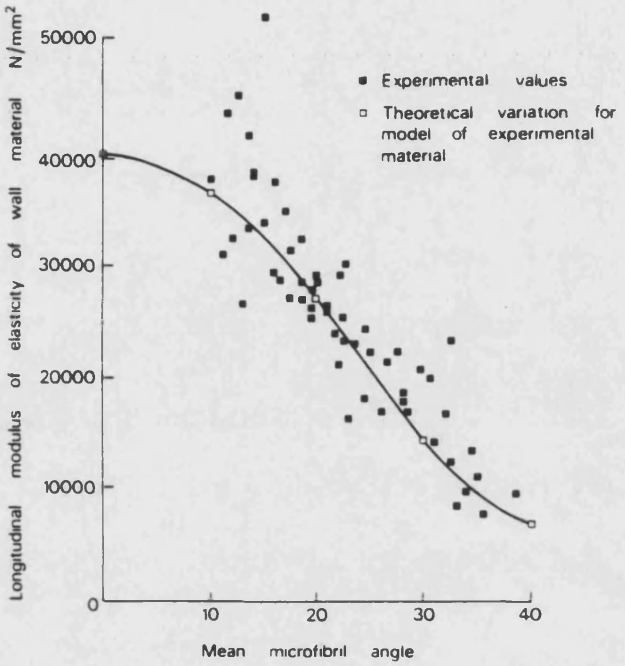

Fig.3.9. Effect of mean microfibrillar angle of the modulus of elasticity of the cell wall material in *Pinus radiata*. Predicted stiffnesses are also included (Dinwoodie, 1981).

Moisture content has a similar effect on the strength and stiffness of wood, although the changes in properties are more significant for the strength. When a fibre is saturated its stiffness decreases by 30% from its dry state and further increases in moisture content have no effect. The radial and tangential stiffnesses of solid wood are much more sensitive to moisture content than the axial stiffness. Fig.3.10 shows the relationship between longitudinal compressive strength and moisture content. The curve falls into two distinct regions, below and above ~ 25% moisture content. Above this value the strength is unaffected by additional moisture. The wood is fully saturated and the extra water just fills up the cell lumens. The point between the two regions of response is known as the fibre saturation point and corresponds to the moisture content where all available hydrogen bonds in and between the microfibrils are occupied by a water molecule. If the moisture content is decreased sites become available for hydrogen bonding to be re-established between microfibrils, the structure becomes more coherent and the strength increases dramatically. In practice there is always water present in the

cell walls and at 20°C and 65% relative humidity wood contains, on average, 14wt% of water.

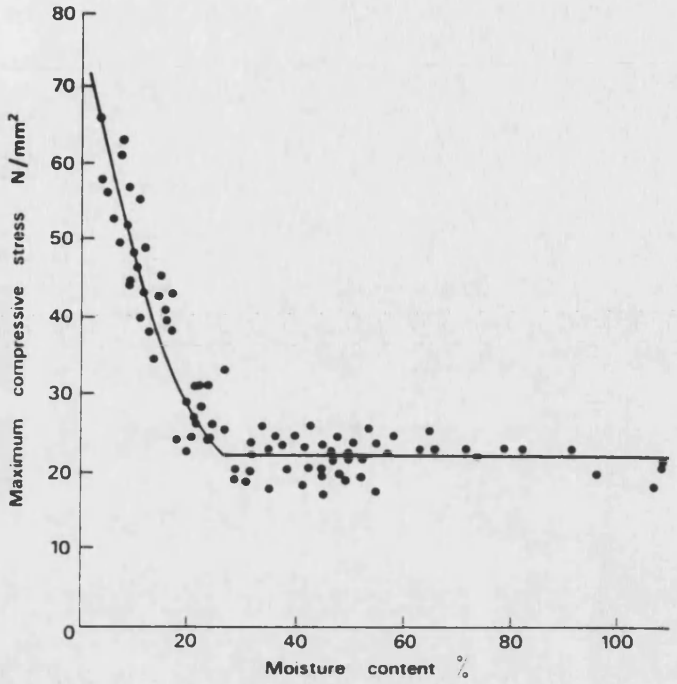

Fig.3.10. Relationship between longitudinal compressive strength and moisture content (Dinwoodie, 1981).

The effect of temperature on wood, as in other materials, is to increase the magnitude of molecular vibrations and to enlarge the crystal lattice. This results in a decrease in strength and stiffness of the material, as can be seen in fig.3.11. It is also apparent that the moisture content of the wood affects the sensitivity of the wood to temperature changes where high water content wood exhibits greater changes in properties with temperature than a low water content sample.

In addition the duration of loading must also be taken into account. This is because wood is a viscoelastic material, exhibiting a combination of elastic and viscous responses to the application of an applied load. A typical response to the application and removal of a load is shown in fig.3.12 and it can be seen to consist of three parts. There is elastic strain which develops the moment the load is applied and returns to zero when it is removed. The delayed elastic strain is a time dependent response to the load and increases with time but then slowly reduces to zero again after stress removal. The plastic response is also time-dependent and increases gradually during the loading period. When the stress is removed however no change in strain occurs and irrecoverable creep has occurred.

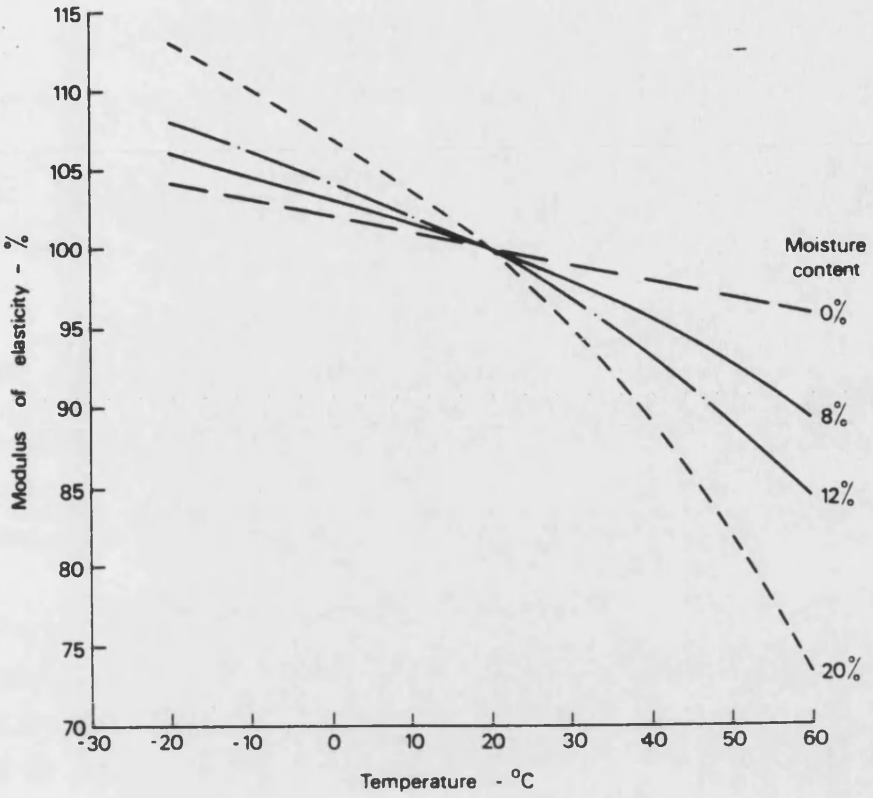

Fig.3.11. The interaction of temperature and moisture content on the modulus of elasticity. Results are averaged for six specimens of wood and the modulus at 20°C and 0% moisture content is taken as unity (Dinwoodie, 1981).

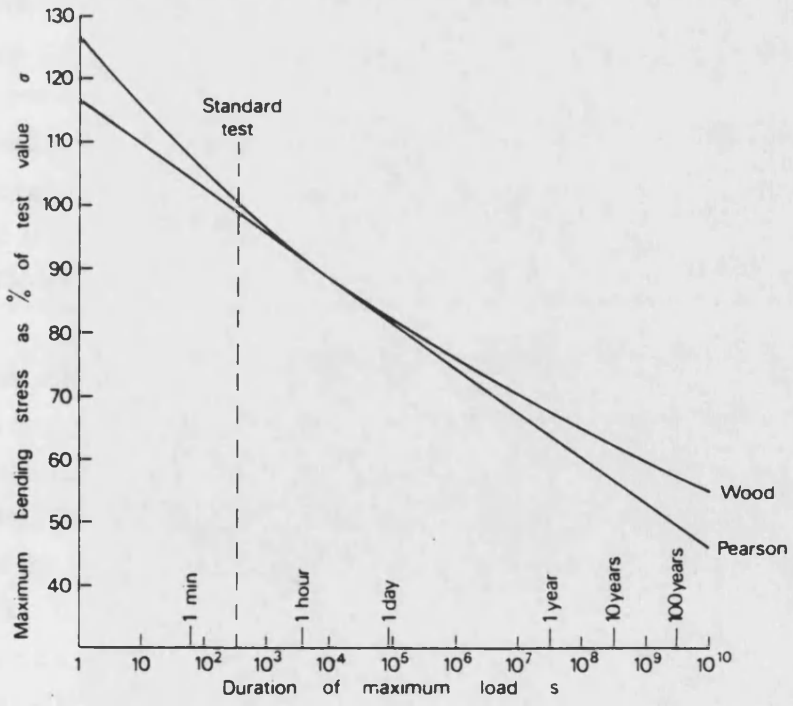

Fig.3.12. The effect of duration on load in the bending strength of wood, according to workers Wood and Pearson (Dinwoodie, 1981).

The result of this time-dependence manifests itself primarily in the form of creep and time-dependent strength. Fig.3.12 illustrates the effect of time on the strength of wood. The shorter the test rate, the less time there is available for creep rupture to occur, and the higher the measured strength of the wood. It is clear that where wood is used in long term applications this fall off in strength must be accounted for if failure is to be avoided.

3.4. *Khaya ivorensis*

In this section more information is given on *Khaya ivorensis*, the African Mahogany used, until recently, in the manufacture of wood - epoxy wind turbine blades and as a consequence it is the material investigated in this project.

Khaya ivorensis was selected by British blade manufacturers because of its relative cheapness and availability in thick, 4mm, veneers (Bonfield and Ansell, 1991). It was supplied to WEG Ltd. from sustainable forests in Cameroon, Africa and originally imported by Reliance Veneer. It is a hardwood of intermediate density (~530kg/m^3) and does not have annual growth rings as it is grown in the tropics. It contains a high volume proportion of medium to moderately large vessels regularly spaced throughout the wood tissue [diffuse porous]. These are commonly filled with dark coloured gum-like deposits and allow the easy passage of resin adhesives into the wood structure during lamination of veneers, ensuring high quality, thin gluelines. Its parenchyma cells [storage cells] are defined as 'sparsely paratracheal' which means that the parenchyma are associated with the vessels. Traumatic resin canals are not uncommon and are formed as a result of damage to the tree. Its grain is interlocked, meaning that fibres of successive growth layers are inclined in opposite directions, producing the characteristic ribbon figure when quarter sawn. It varies in colour from pink to dark red-brown (Desch and Dinwoodie, 1981).

Fig.3.13 is an electron micrograph of the transverse and T-L planes (see fig.3.7) of Khaya taken in a SEM. The top part of the picture is the transverse section. The most prominent features are the large vessels [dark circles] and the ray parenchyma [pale bands of cells]. It is clear that it is sparsely paratracheal. The other cells are fibres and tracheids. In the T-L plane the ray bundles have been cut and show up as pale ellipses of small cells. To the left of the picture a vessel has been cut longitudinally and the position of the dissolved cell walls can be seen clearly. Fine detail on the lumen is also present. The cells running vertically are the fibres and tracheids. At the extreme right of the picture a glueline between two veneers can be seen because of the difference in

orientation of the wood cells. A second feature associated with the glueline is the resin-filled vessels at the centre of the picture.

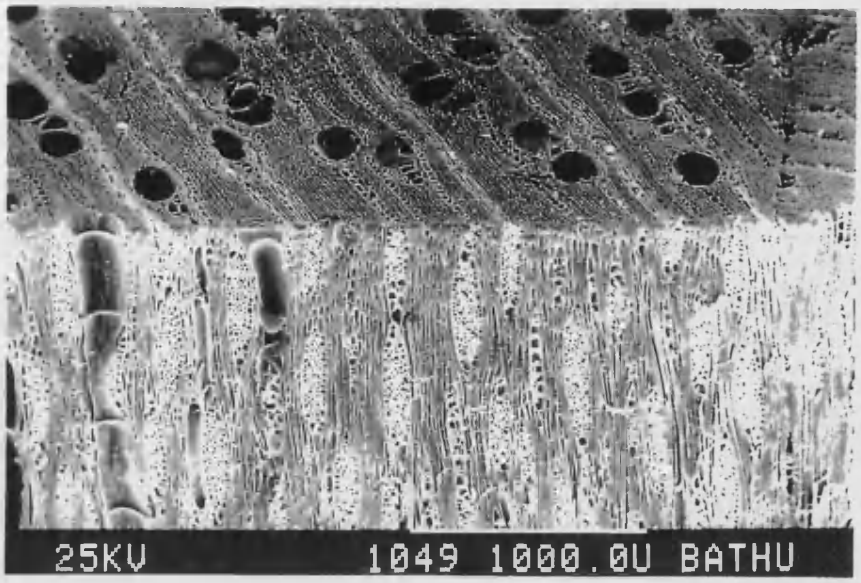

Fig.3.13. Transverse and T-L sections through a Khaya laminate, showing a glue line on the far right (Tsai and Ansell, 1990).

In terms of mechanical properties Khaya is described as having moderate durability, with strength between beech and obeche and with good working properties. It dries fairly rapidly with low shrinkage and does not move more than a small amount with changing moisture content (Desch and Dinwoodie, 1981).

The veneers (as used in wind turbine blade manufacture) are rotary cut from a tree trunk by mounting a log on its centres in a lathe and rotating it against a heavy horizontal knife which peels off a continuous spiral sheet of veneer from the surface of the log (Panshin and De Zeeuw, 1970). The advantage of using veneers is that knots and regions of inferior quality can be cut out and replaced with clear wood, resulting in improved mechanical properties over solid wood. The veneers are stacked flat and seasoned to a moisture content of approximately 6wt% of water. Once fully seasoned they are sealed in polythene to maintain the moisture content for shipping.

3.5. Summary

In this chapter:

- the overall structure of wood has been reviewed, ranging from the complete tree to the molecular level;
- particular attention has been directed to the cellular level, covering both micro and macro levels of the structure;
- the factors affecting the mechanical properties of wood have been covered along with common defects which contribute to the variability of wood and its mechanical properties; and
- a subsection has been devoted to the structural features of *Khaya ivorensis*, the material used in this research.

4. FATIGUE

4.1. Introduction

The problem of fatigue in engineering components is a serious one. Harris (1986) defines fatigue as failure under the influence of a cyclically varying load which is much lower in amplitude than the ultimate short term strength of the material. Two examples of fatigue loading are presented in fig.4.1, random and constant amplitude loading. The former is typical of the stresses seen on a component in service and the latter is more typical of a laboratory fatigue test. A high proportion of mechanical failures have been attributed to fatigue and it has widespread design implications. Any system experiencing a varying cyclical load is susceptible to fatigue.

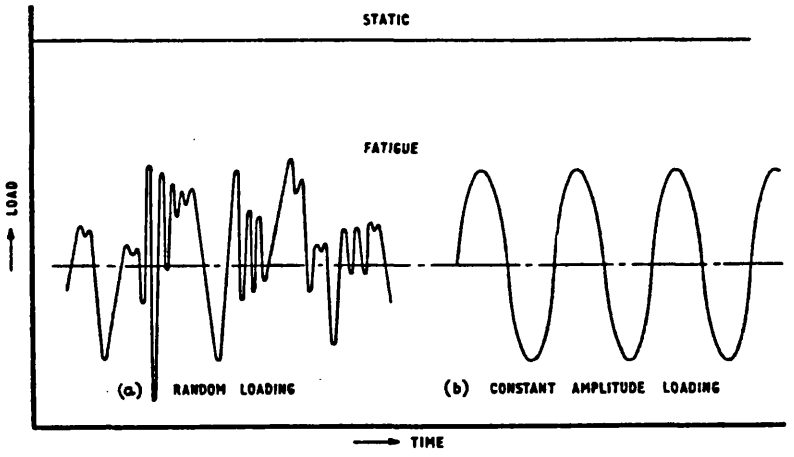

Fig.4.1. Random and constant amplitude fatigue loading conditions (Mann, 1967)

In order to be able to predict how a material will behave in fatigue, laboratory tests must be carried out under known conditions and design rules formulated based on the results. Ideally these rules should take into account the different processes involved in the build-up of damage and should be applicable over a wide range of service conditions.

In this section the basic fatigue behaviour of metals and organic matrix fibre reinforced composites is covered. The fatigue of metals is covered because it is the original work upon which the appreciation of composite fatigue is based. Wood is a natural fibre reinforced composite material and consequently work on the fatigue of organic matrix fibre reinforced composites is highly relevant to the fatigue performance of wood.

Fatigue testing

The main purposes of most fatigue tests are firstly to determine the relationship between the applied load and the number of cycles to failure and, secondly, to obtain an estimate of the likelihood of failure under certain loading conditions.

Fatigue testing is a complex subject not least because of the wide range of testing machines available and the large number of possible variables which can be used in any series of tests. This variability is reflected in very general guide-lines for fatigue testing in BS 3518 (1962). The scope of variation in test parameters includes:

- sample geometry or component shape
- type of loading: 3 or 4 point bending, axial, shear, torsion, rotating bending
- frequency and shape of applied waveform
- the use of constant amplitude, block loading or random waveform sequences
- atmospheric conditions: temperature, humidity etc
- load or displacement control of the fatigue machine.

A typical constant amplitude fatigue loading regime is presented in fig.4.2 along with the associated terms which define such a regime.

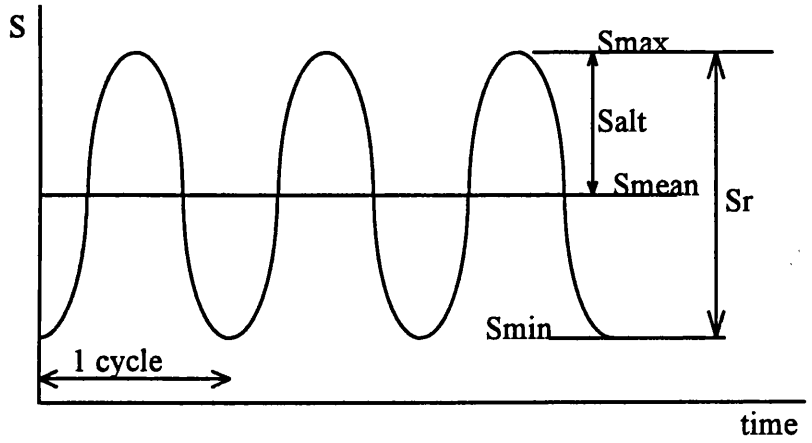

S = stress
S_{max} = maximum sinusoidal stress
S_{min} = minimum sinusoidal stress
S_{mean} = mean sinusoidal stress
S_{alt} = alternating stress
S_r = stress range

Fig.4.2. Sinusoidal fatigue loading cycles and definition of associated terms

An important term which defines the stresses applied during constant amplitude fatigue is the R ratio. This is defined as the ratio of the minimum stress to the maximum stress, eq.4.1, and can also be defined as in eq.4.2:

$$R = \frac{S_{min}}{S_{max}} \qquad \text{Eq.4.1}$$

$$R = \frac{S_{mean} - S_{alt}}{S_{mean} + S_{alt}} \qquad \text{Eq.4.2}$$

For completely reversed loading [S_{mean}=0] R=-1; if the loading regime is completely tensile then $0 \leq R \leq 1$ and if it is totally compressive $1 \leq R \leq \infty$.

The relationship between stress (S) and number of cycles to failure (N_f) is commonly presented in what is known as the S-N diagram. An example of such a curve is presented in fig.4.3 for both metals and thermoplastics (Harris and Bunsell, 1977). The curve for the Cr/Mo steel flattens out after about 10^6 cycles which indicates that below a certain stress no fatigue damage occurs. This is known as an endurance limit, S_e, and is very useful because if a component is designed to experience stresses always lower than S_e no fatigue damage will occur. Commercial aluminium-based alloys containing zinc, magnesium and copper (UTS = 617MNm^{-2}) do not have an endurance limit and at 10^8 cycles their fatigue strength is as low as 154MNm^{-2}.

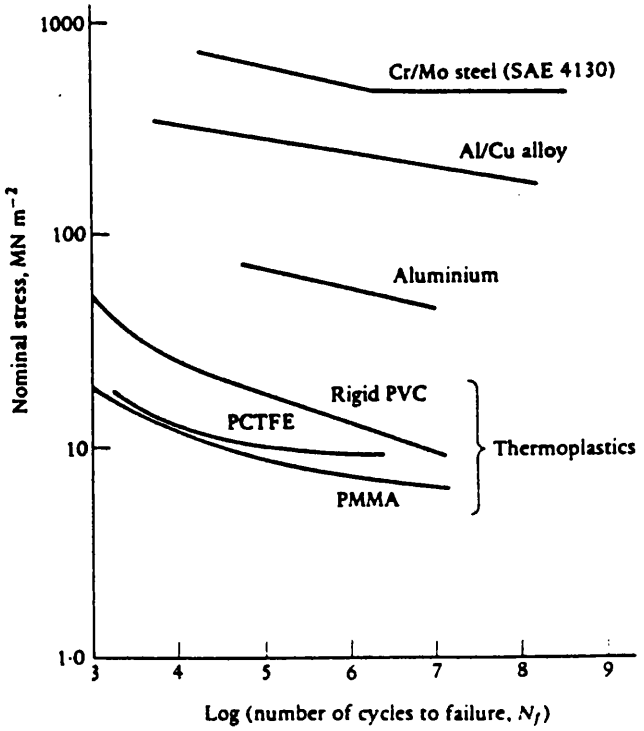

Fig.4.3. S-N curves for some typical engineering materials (Harris and Bunsell, 1977).

S-N curves can be produced for each R ratio at which the material is tested and from these curves a constant life diagram can be developed. S_{alt} is plotted against S_{mean} for fatigue lives of, eg. logN=5, 6, and 7. Such a plot is presented in fig.4.4. An envelope is created within which any combination of mean and alternating stresses will not cause failure within logN=5, 6, or 7 cycles. The higher the number of cycles, the lower the allowed stresses. Such a diagram can be used to predict the expected fatigue lifetime of a material under any combination of mean and alternating stresses. In conjunction with Miner's rule (Miner, 1945) it can be used to predict the fatigue life of materials subjected to complex loading regimes (Bond, 1994).

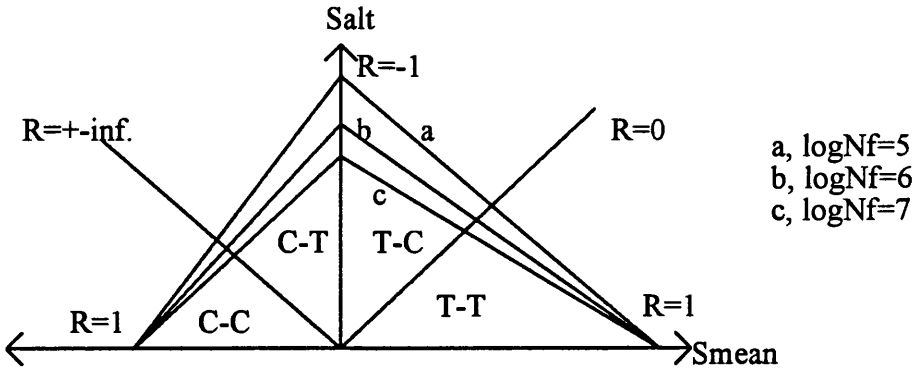

T-T = tension-tension fatigue
T-C = tension-compression fatigue
C-T = compression-tension fatigue
C-C = compression-compression fatigue

Fig.4.4. Constant life diagram for both tensile and compressive stresses.

4.2. Fatigue in metals

The existence of metal fatigue has been known since the mid 1800s when failures in stage coach and locomotive axles were common (Mann, 1967). Metal fatigue is dangerous because it develops as localised damage, which is often invisible on the surface of the component and can cause a catastrophic, brittle type of failure. In many cases fatigue failures can be avoided by careful design which minimises stress concentrations from features such as notches, holes and rapid changes in section in the component.

4.2.1. Variables affecting the fatigue behaviour of metals

The stress amplitude seen by a sample is the most important variable in determining its fatigue life but there are other factors which are highly significant (Smallman, 1985, Harris and Bunsell, 1987). These include:

- *Surface preparation.* Fatigue cracks are usually initiated at the surface of the component because of stress concentrations at machining marks, dents etc. The initiation of cracks is delayed if such marks are removed by polishing or if the surface layers are put under compression by shot peening or other surface treatments.

- *Temperature.* Temperature affects the UTS and fatigue strength of metals and the fatigue strength decreases with increasing temperature. This is due to the increased mobility of the metal ions.

- *Frequency.* This has little overall effect on fatigue. At lower frequencies fatigue life is slightly shorter due to creep effects and at higher frequencies adiabatic heating can cause degradation. At higher temperatures failure becomes more dependent on the duration of loading due to creep rather than loading frequency. Corrosion fatigue is affected by frequency where lower frequency loading causes an increased rate of fatigue.

- *Mean stress.* Under conditions where the mean stress does not exceed the yield stress, σ_y, a relationship known as Basquin's law holds for high cycle fatigue, eq.4.3.

$$S_r \cdot N_f^a = \text{const} \qquad \text{Eq.4.3.}$$

It is valid over a range of about 10^2 to 10^5 cycles, less than the knee of the S-N curve for metal alloys, where a is a constant $\cong 0.1$, fig.4.5. When the stress range $S_r > \sigma_y$ Basquin's law no longer holds but a reasonable relationship, known as the Coffin-Manson law is valid for low cycle fatigue, eq.4.4, fig.4.6.

$$\Delta\varepsilon_p \cdot N_f^b = \text{const} \qquad \text{Eq.4.4.}$$

$\Delta\varepsilon_p$ is the plastic strain range and $b \cong 0.6$.

- *Environment.* Fatigue occurring in a corrosive environment is referred to as corrosion fatigue. The presence of a corrosive medium can not only produce pits on the

surface of a metal which may subsequently initiate fatigue cracking but can also greatly increase the crack growth rate by localised corrosive attack.

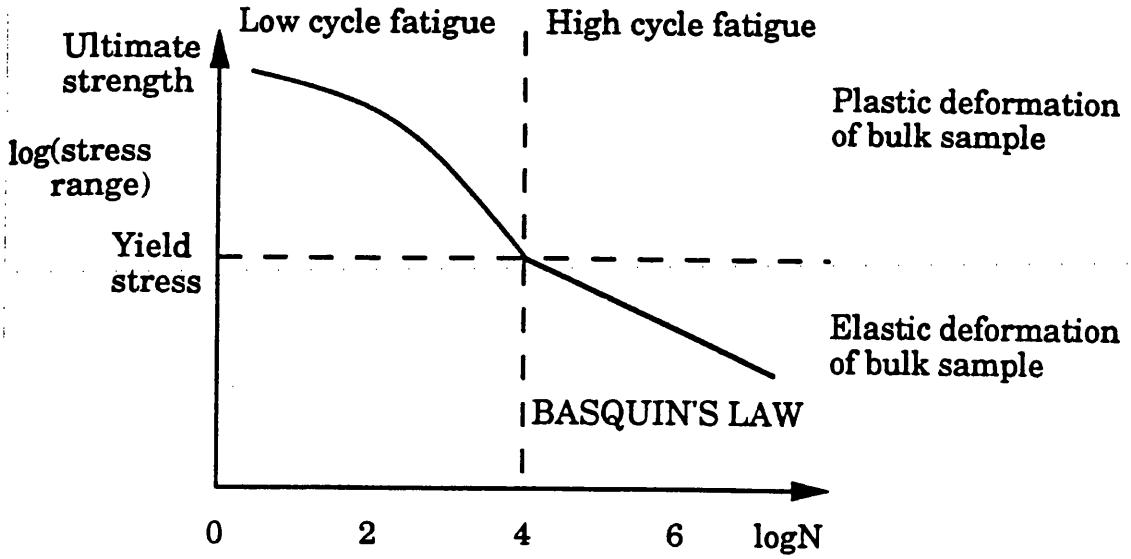

Fig.4.5. Graphical representation of Basquin's law for high cycle fatigue.

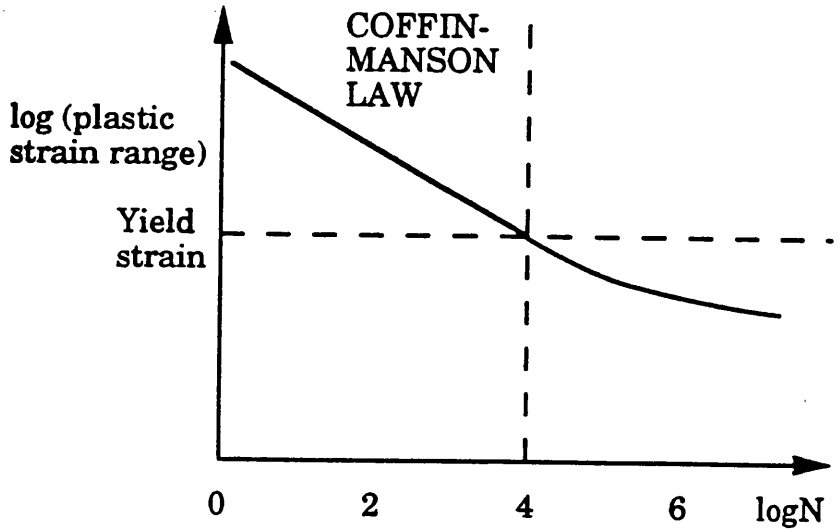

Fig.4.6. Graphical representation of the Coffin-Manson law for low cycle fatigue.

4.2.2. Metallurgical factors affecting fatigue life

It is well known that fatigue crack growth initiates at the surface of a metal because surfaces are un-constrained and often contain stress-concentrating flaws which initiate dislocation glide. Environmental attack can occur and in bending the stresses are greatest at the surface. The best fatigue resistance is found in metals with a worked surface layer, eg. by shot peening, skin rolling, nitriding and carburising. The main benefit is due to compression at the surface, hindering crack opening when under tensile loading, with the secondary benefit of work hardening, leading to an increase in the metal's UTS.

Alloy composition and the thermal and mechanical history of a component are also significant in influencing fatigue performance as both affect the yield strength. Any increase in the yield stress, S_y or hardness leads to an increase in the stress necessary for slip to occur and consequently increases fatigue life. Grain size is also important and a small grained sample has a superior fatigue life to a large grained sample of the same composition, at the same temperature.

If an alloy is thermodynamically stable then its fatigue performance will be essentially the same as that of the pure metal. If the alloy has a higher UTS than the pure metal then the alloy's fatigue strength will also be proportionally higher. However, unstable alloys and those exhibiting a yield point will respond differently to fatigue. Fatigue loading drives the system towards equilibrium. A solution treated age-hardening alloy will become harder, and a fully aged specimen will become softer due to overaging. Such changes are localised at regions of fatigue damage because they are enhanced by the increased vacancy concentrations leading to higher diffusion rates of solute atoms.

The presence of a fatigue endurance limit in ferrous alloys has been attributed to the effect of dislocations being pinned by solute carbon atoms (Smallman, 1985). This is also the reason for the presence of a yield point in such alloys. It is interesting to note that non-ferrous alloys which do not have yield points have not got an endurance limit either. This supports the view that the two phenomena are linked. When a cyclic stress exceeds S_y dislocations are unlocked and glide adding to the build up of fatigue damage in the sample. If S_y is not exceeded no dislocations are unlocked by the stress cycle and no damage results. Fig.4.7 supports this theory because the decarburised iron has a lower fatigue strength and no distinct endurance limit.

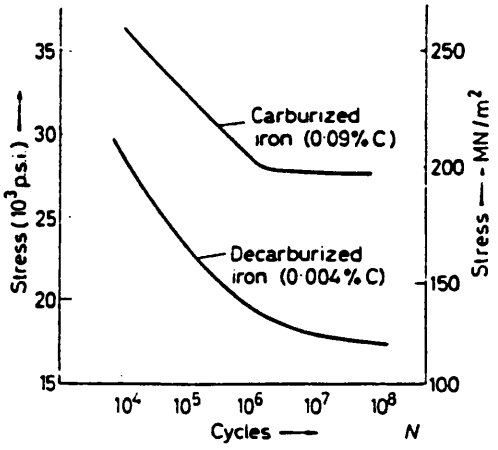

Fig.4.7. SN curves for carburised and decarburised iron (Smallman, 1985)

4.2.3. The stages associated with the fatigue process

The fatigue behaviour of a smooth metallic specimen falls into three stages: crack initiation, crack propagation and catastrophic failure. Each stage is considered briefly (Anderson et al., 1989, Smallman, 1985).

1. *Crack initiation.* Initiation involves localised movement of dislocations on slip planes at approximately 45° to the applied stress, where the shear stress is a maximum. At the start of fatigue loading initial slip bands comprise essentially primary dislocations but as the sample work hardens and dislocation concentration increases, persistent slip bands develop which have a different dislocation structure and are the active regions in fatigue damage. This process is illustrated in figs 4.8 and 4.9.

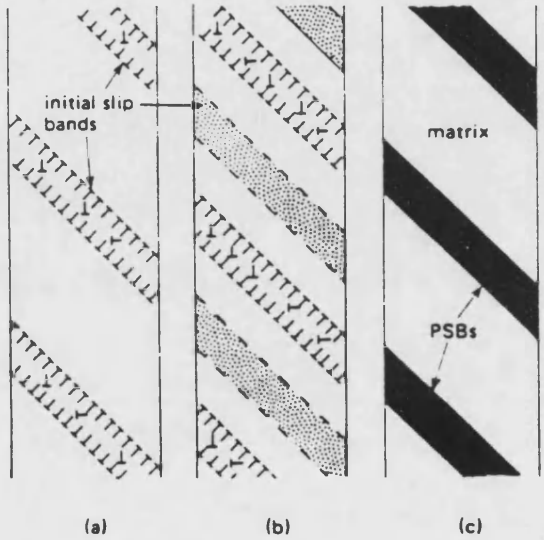

Fig.4.8. Formation of persistent slip bands (PSBs) during fatigue (Smallman, 1985)

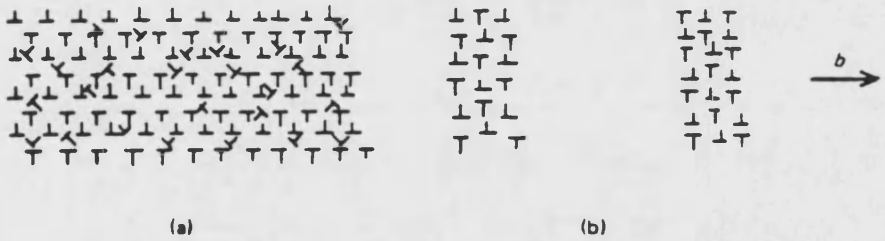

Fig.4.9. Schematic diagram showing (a) vein structure of the matrix, (b) ladder structure of PSBs (Smallman, 1985)

The interaction of the dislocation movement under cyclic loading has the effect of producing extrusions and intrusions at the sample surface. This does not depend on either chemical or thermal action but is a purely geometrical process which depends on cyclic stressing, and although two general mechanisms have been suggested, neither

fully explain the physical observations (Smallman, 1985). The formation of surface roughness leads to stress concentrations which cause the initiation of fatigue cracks at 45° to the sample's axis.

2. *Propagation.* The fatigue cracks change direction after a few grain diameters and start to grow perpendicular to the direction of the applied stress. One crack tends to predominate. Fatigue striations are formed in the crack with one ridge being produced each cycle due to blunting and resharpening of the crack tip by plastic deformation, fig.4.10.

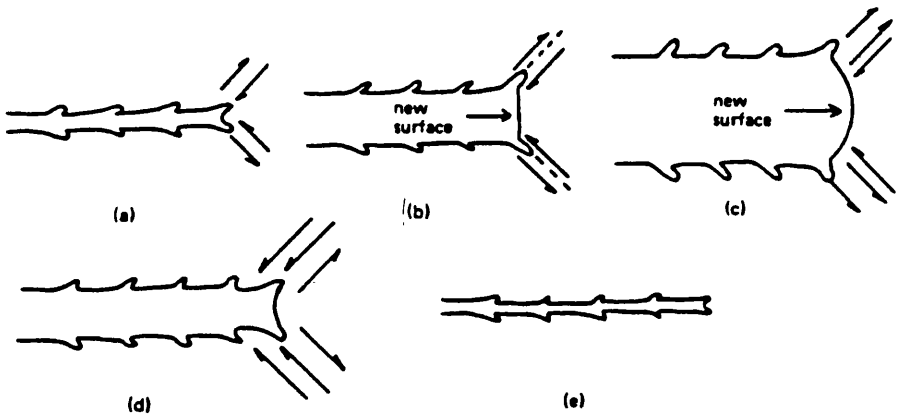

Fig.4.10. Schematic illustration of the formation of fatigue striations (Smallman, 1985)

The fatigue crack growth rate is related to the stress intensity factor range, ΔK, at the crack tip. The critical stress intensity factor K_c is defined in eq.4.5, where S_f = failure stress and a = crack length at failure.

$$K_c = S_f\sqrt{\pi a} \qquad \text{eq.4.5}$$

The relationship between the fatigue crack growth rate, da/dN, and the stress intensity factor range, ΔK, is presented in eq.4.6,

$$\frac{da}{dN} = A(\Delta K)^m \qquad \text{eq.4.6}$$

where $\Delta K = K_{max} - K_{min} = (S_{max} - S_{min})\sqrt{\pi a}$. S_{max} is the maximum fatigue stress and S_{min} in the minimum fatigue stress. $K_{min} = 0$ for compression because the crack closes under compression loading and no crack growth occurs. A and m are constants.

This empirical relationship is known as the Paris-Erdogen law and is valid for ductile metals and polymers. It is shown graphically in fig.4.11 (Reiter, 1992).

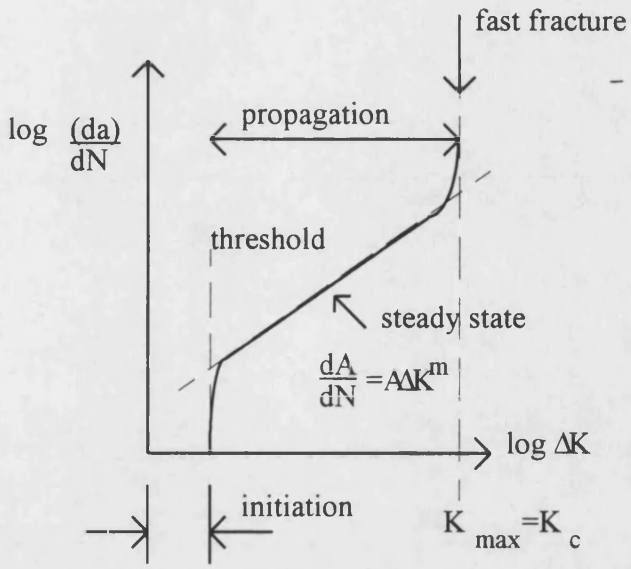

Fig.4.11. Fatigue crack growth rates for a pre-cracked material illustrating the Paris-Erdogen law (Reiter, 1992).

3. *Catastrophic failure*. The fatigue crack has grown so much that catastrophic failure occurs. It happens either by simple ductile overload due to the reduction in cross sectional area of the component or by brittle cleavage when $K_{max}=K_c$, the critical stress intensity factor.

A fatigue failure has a typical appearance, as shown in fig.4.12. There is a relatively smooth area due to the repeated rubbing together of the crack faces during each cycle of stable crack growth. The rough part corresponds to rapid transcrystalline failure. The initiation site can usually be seen because the concentric striations centre on it.

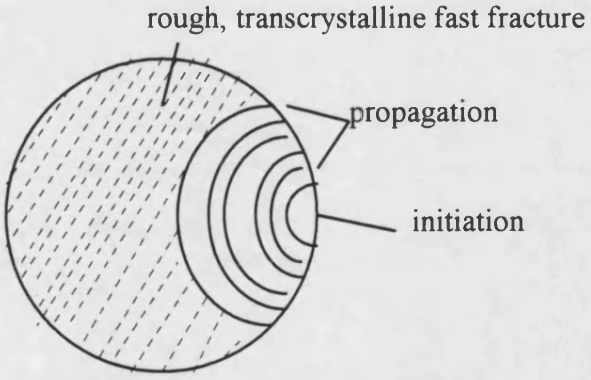

Fig.4.12. A schematic fatigue fracture (Smallman, 1985)

4.3. Fatigue in organic matrix composites

4.3.1. Introduction

Organic matrix composites, reinforced with long fibres aligned parallel to the axis of loading, are generally accepted as behaving well in tensile fatigue (Bathias, 1989, Curtis, 1989). They have other desirable properties such as high strength and stiffness with low density. The scope for designing with composite materials is wide because their properties can be tailored to suit the application (a) by selection of fibre and resin and (b) by the orientation of fibres and lay-up of the composite.

The main problem which hinders the development of new composite applications is the lack of available design data. Unlike metals composite systems have only relatively recently been tested and applied in engineering systems. They are very different from metals in that they are anisotropic and inhomogeneous and consequently behave very differently in fatigue. Although the conventional approaches to fatigue damage in metals have been applied widely to composites they are not necessarily best suited to these materials.

Composite damage builds up through the bulk of the material as opposed to the localised damage observed in metals. This results in a gradual deterioration of properties rather than a catastrophic failure. Consequently it can often be difficult to determine when a sample has failed.

The range of composites is huge and each system may behave differently in fatigue. Composites are inherently variable and it would be impossible to test every combination of resin, matrix and lay-up in enough orientations to characterise the fatigue response completely. Consequently when testing a composite system it is necessary to rigorously specify all the material variables and the failure criteria used.

Another problem which presents itself in the fatigue of composites is that they are often sensitive to rate effects. If they are tested at high frequencies, hysteretic heating will occur which will affect the mechanical properties of the resin and may even cause thermal degradation. Consequently, it is necessary to test at frequencies just low enough to avoid too much heating. A better approach is to test at a constant rate of load application rather than frequency to minimise any heating during high stress range tests and to avoid viscoelastic effects (Harris, 1986).

4.3.2. Types of fatigue damage

Fatigue damage accumulates progressively in composite materials during cyclic loading and failure occurs when the damage exceeds a critical level. The basic failure mechanisms in a composite are matrix cracking, fibre breakage, debonding, splitting and delamination (Ye, 1989, Stinchcomb and Reifsnider, 1979). The damage accumulates in a bulk, as opposed to a local, manner and failure is not usually due to the propagation of a single crack. The different mechanisms occur both independently and interactively according to the materials variables and testing conditions.

The simplest system to consider is a unidirectional composite, comprising long fibres aligned parallel to the direction of loading in an organic matrix. The damage occurring in the matrix and fibres is explained below:

1. Matrix damage. The fatigue of a polymer consists of two stages, crack initiation and crack growth (Talreja, 1987). In fibre reinforced polymers the matrix is subjected to strain controlled fatigue due to the higher stiffness of the fibres. Cracks initiate from flaws in the polymer and grow until they hit an interface. This delays further growth if the stress at the crack tip is too low to cause fibre fracture. If the stresses are low no fibre breakage occurs and the increasing concentration of cracks is confined to the matrix. This is termed the dispersed matrix failure mode. At higher applied strains the fibres at the crack tip may fail allowing the matrix cracks to grow. If the stress concentration at the crack tip increases sufficiently the shear stress may be sufficient to cause a weak matrix-fibre interface to debond, leading to a diversion of the crack. This is known as a localised failure mode, fig.4.13.

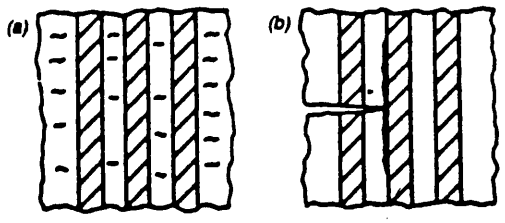

Fig.4.13. Ductile (polymer) matrix damage. a) Dispersed failure mode: cracks confined to matrix only. b) Localised failure mode: cracks grow by breaking fibres and, at a later stage, interfacially (Talreja, 1987).

2. *Fibre damage.* Brittle fibres do not show fatigue behaviour but crack instantaneously due to overstressing. A fibre may break either at its weakest point or at the site of a stress concentration. When a fibre breaks, shear stresses are set up at the interface adjacent to the break. Some delamination will result, depending on the

strength of the interfacial bond. The stress concentration caused by a fibre break is likely to cause damage in the matrix, as shown in fig.4.14, depending on whether the matrix is already damaged.

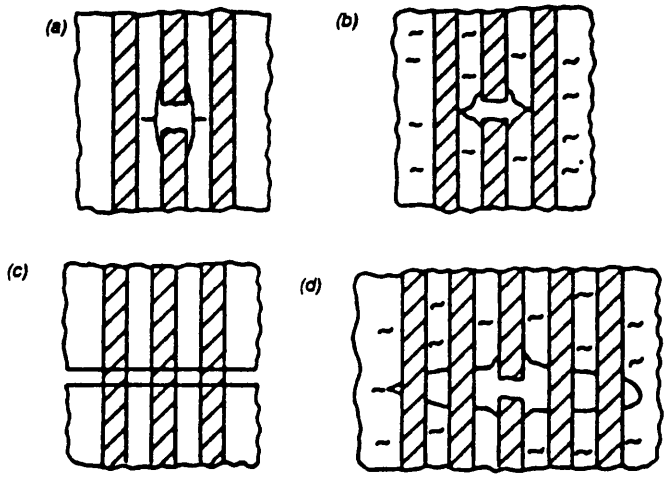

Fig.4.14. Fibre damage: a) fibre break causing interfacial debonding, b) fibre break increasing size of matrix crack, c) fibres bridging a matrix crack, and d) a combination of a), b) and c) (Talreja, 1987).

These mechanisms can be portrayed schematically on a fatigue-life diagram as shown in fig.4.15. The maximum applied strain is used for the y-axis because the fibre and matrix both see the same strains whereas the stress levels vary, with the fibres carrying most of the stress. The shaded regions show where the different mechanisms are operative. The horizontal band centred about the mean composite fracture strain, ε_c, corresponds to fibre breakage and the resulting interfacial debonding. The band is hatched to show the scatter in fracture strain. The lower limit corresponds to the fatigue limit of the resin. Below this strain no resin cracking will occur so no damage will build up in the composite. In the sloping band matrix cracking and interfacial shear occur. These 2 mechanisms are considered together as they may occur simultaneously, particularly towards the end of their fatigue life.

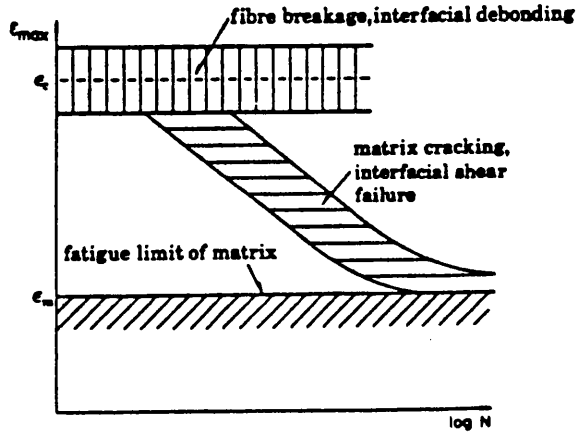

Fig.4.15. A schematic fatigue life diagram for tensile fatigue of unidirectional polymer composite (Talreja, 1987).

This model, which appears to be widely acceptable, explains the results shown in fig.4.16 obtained for carbon fibre reinforced plastic, CFRP, glass reinforced plastic, GRP and Kevlar fibre reinforced plastic, KFRP (Harris, 1986). The high initial strains experienced by the GRP soon lead to matrix cracking and interfacial shear, whereas in CFRP the strains are insufficient to exceed the matrix fatigue limit and therefore the strain-life plot remains flat (Reiter, 1992).

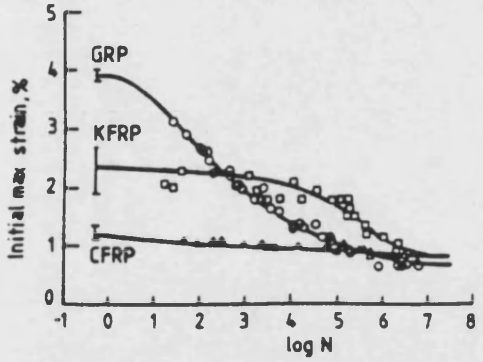

Fig.4.16. Strain-logN curves for comparable 0°/90° laminates of HTS carbon, E-glass and Kevlar-49 in Code-69 epoxy resin. R=0.1 (Harris, 1986).

The above example of a unidirectional material is the most simple. Often composite laminates are used where the layers are laid up at other angles to the direction of the applied stress and 45° and 90° are the most common orientations. When these laminates are fatigued, delamination and cross-ply cracking become important and the damage process is more complex. Stinchcomb (1986) looked at the surface damage on the edge of graphite-epoxy laminates containing off-axis plies using microscopy and edge replication techniques. An example of the damage development process he observed is given in fig.4.17. The damage parameter, D is based on the change in stiffness of the laminate.

4.3.3. Factors affecting fatigue damage

There are a wide range of factors which affect the fatigue properties of composite systems. Firstly, there are the materials variables. Fig.4.18 shows how different fibres set in the same epoxy resin exhibit different fatigue responses (Reiter, 1992). However, the results for different types of carbon fibre in the same resin matrix are all of a similar form, fig.4.19. This is likely to be a consequence of the fatigue behaviour being dependent on the matrix and interfacial characteristics rather than the fibre strength (Curtis, 1989). Fig.4.20 compares the fatigue behaviour of two carbon fibre reinforced composites, one made with toughened epoxy. Although the toughened epoxy has a higher static strength its fatigue curve is much steeper. This poorer fatigue response has been attributed to the inferior fatigue behaviour of the toughened matrix.

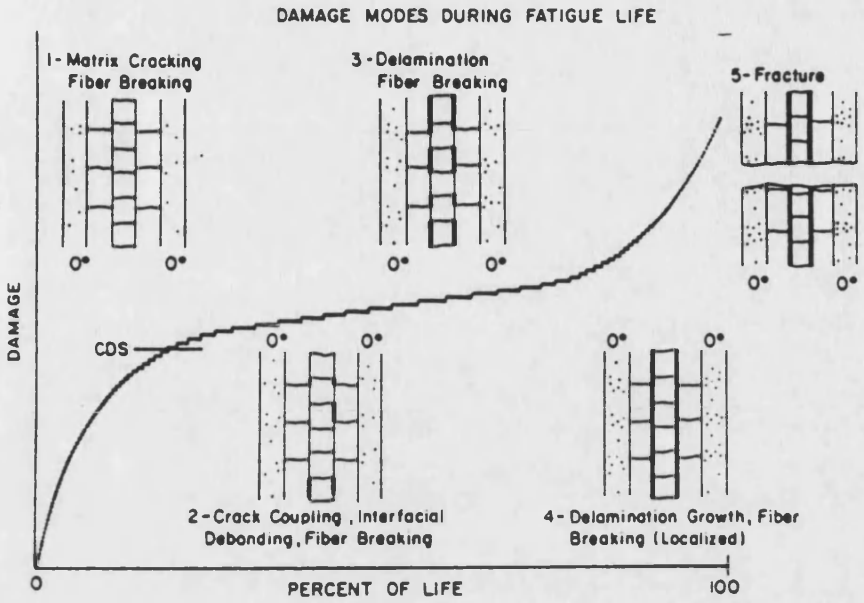

Fig.4.17. Schematic representation of the damage accumulation process in composite laminates (Stinchcomb, 1986).

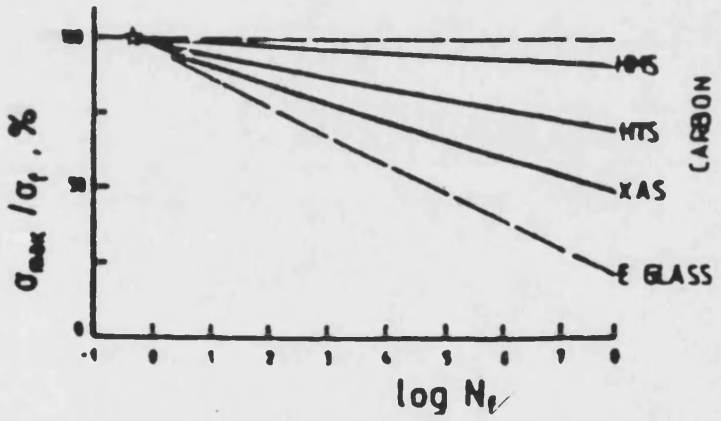

Fig.4.18. S-N curve for composites made with different fibres but the same epoxy resin (Reiter, 1992).

When multi-directional laminates are fatigued their properties will be inferior to their unidirectional counterparts. Fibres with other orientations are included in composites to improve their properties in other directions, eg. ±45° fibres to carry torsional loads and 90° fibres to impart transverse rigidity. On increasing the percentage of non-axial fibres in a laminate, the static tensile strength and stiffness are reduced since fewer fibres are available to support the applied loads. The slope of the tensile SN curve increases in relation to the static strength as the proportion of off-axis plies is increased, since the mechanical properties of these layers are resin-dependent and are more easily damaged in fatigue, fig.4.19 (Curtis, 1989).

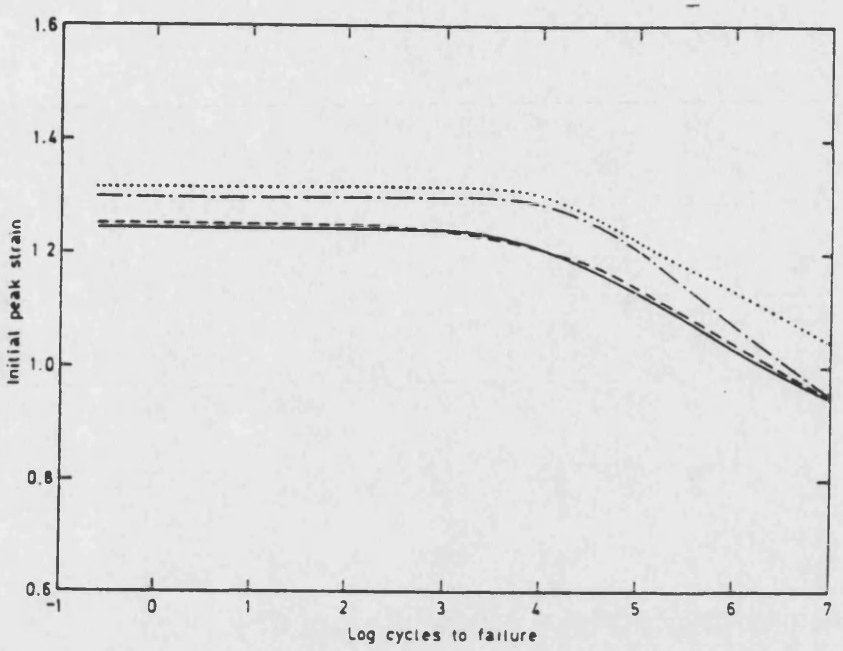

Fig.4.19. Fatigue strain-life data for unidirectional carbon fibre composites with different fibre types in the same basic epoxy resin (—— standard CFRP, the rest are high performance fibres in a standard resin). (Curtis, 1989).

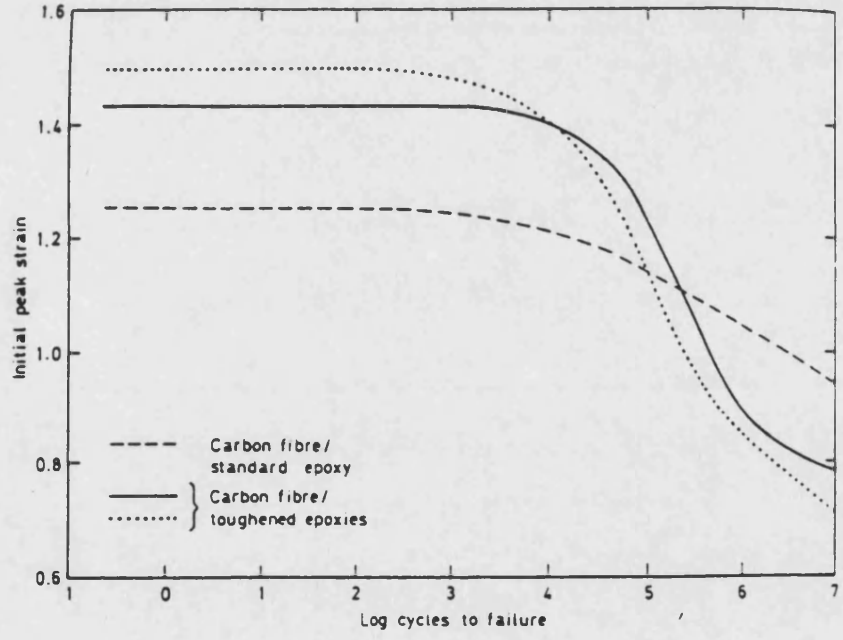

Fig.4.20. Fatigue strain-life data for unidirectional carbon fibre composites with the same high strain fibre in different epoxy matrices (Curtis, 1989).

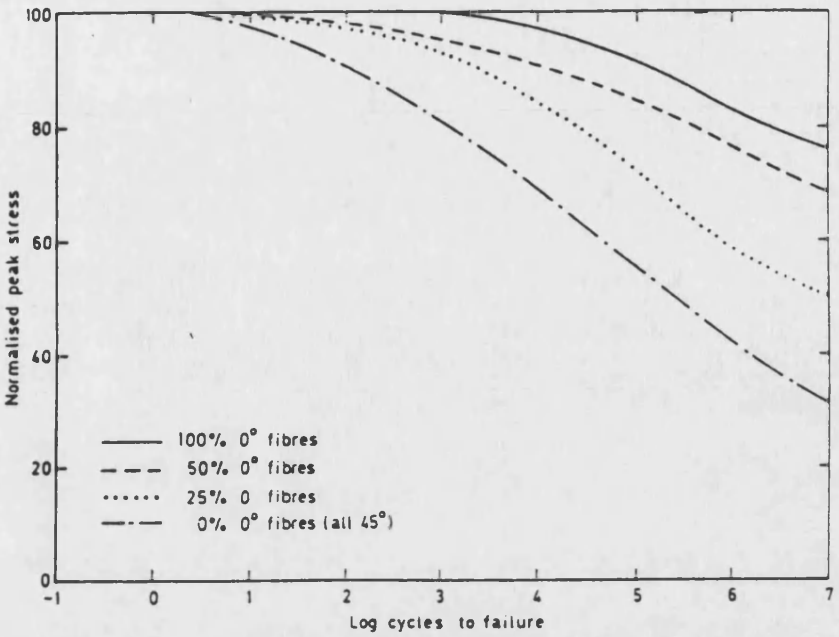

Fig.4.21. S-N curves for carbon fibre epoxy laminates with varying percentages of 0° fibres, normalised with respect to their static strength (Curtis, 1989).

Loading factors such as R ratio and mean stress will also affect the fatigue response of composite materials. Fig.4.22 shows a Goodman, or constant life, diagram for CFRP/KFRP hybrid materials for a lifetime of 10^5 cycles (Adam et al., 1989) It can be seen that the curves are not symmetrical about the zero mean stress. This is because fibre reinforced composites are weaker in compression than in tension with compression fatigue much more damaging than tension fatigue. Compression loading tends to produce fibre buckling which causes local delamination, leading to crack propagation and large scale delamination (Stinchcomb and Reifsnider, 1978).

The effect of environmental exposure on fatigue behaviour depends on the sensitivity of the laminate to matrix properties, since it is usually the matrix or fibre/matrix interface that is affected by the absorbed moisture. Water has the effect of plasticising epoxy resin which reduces its elastic modulus. Although this is a reversible effect there is direct evidence for micromechanical breakdown associated with matrix and interface cracking when the exposure times are prolonged (Hull, 1981). The presence of electrolytes in ingressed water can increase the rate of attack of the matrix and may also degrade the fibres. Temperature effects are also likely to be significant although the extent will depend on the thermal sensitivity of the matrix. Fig.4.23 shows the poorer behaviour of moist (1 wt % water) at high temperatures (Curtis, 1989).

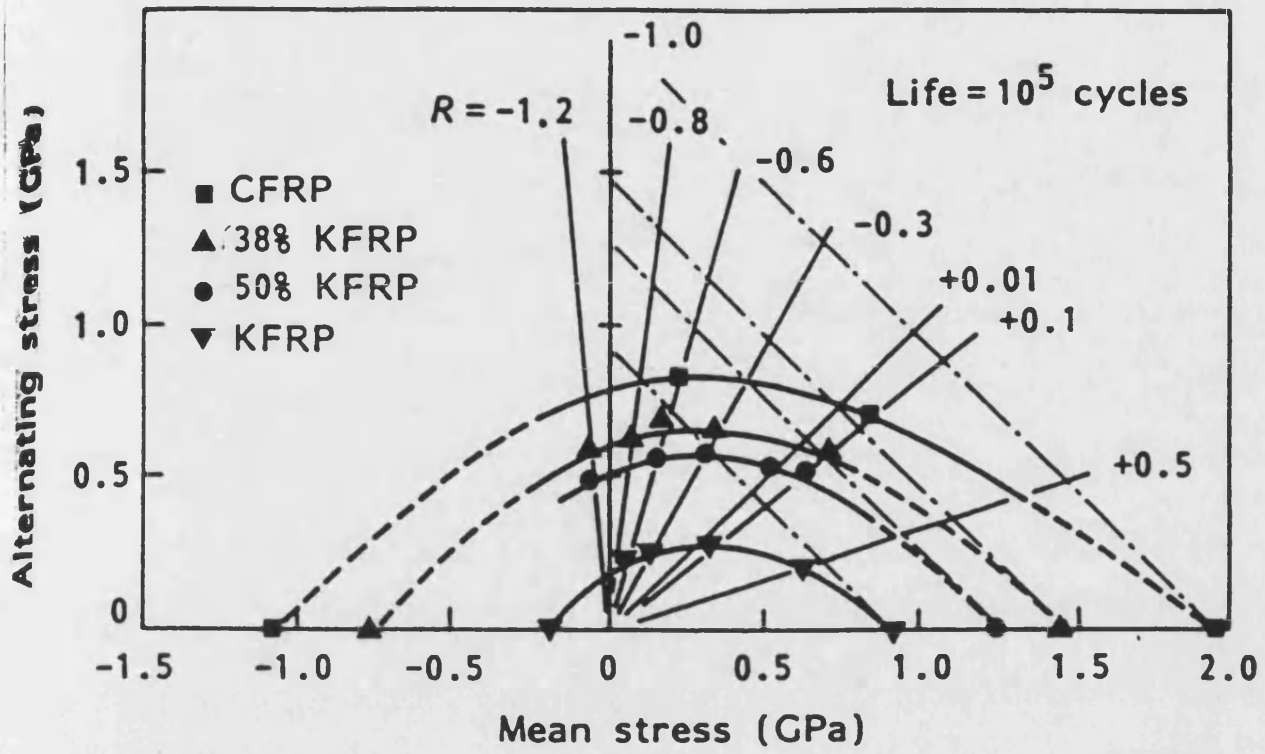

Fig.4.22. Constant life, or Goodman diagram, showing the effect of mean stress on the fatigue response of unidirectional CFRP/KFRP hybrids. The alternating stresses plotted represent the peak stresses for failure in 10^5 cycles. The broken line at 45° represents the limits for tensile failure (Adam et al., 1989).

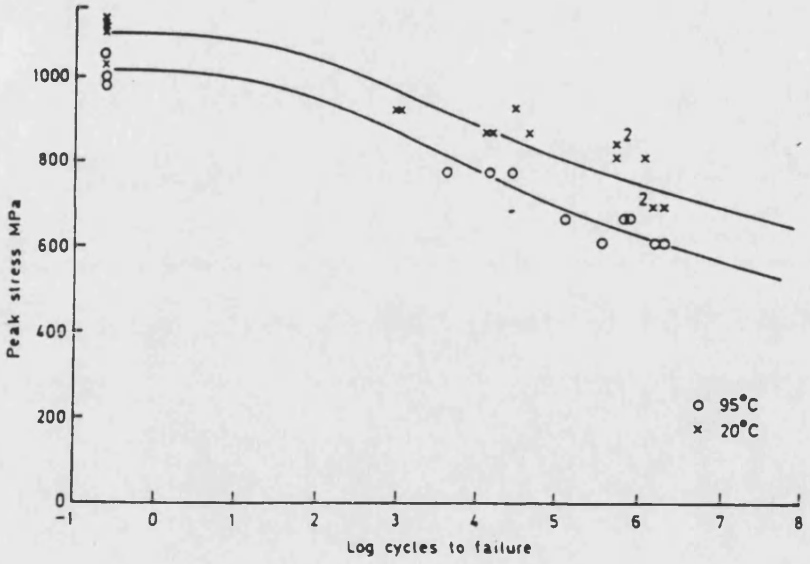

Fig.4.23. Reversed axial fatigue data for carbon fibre with a [0°, ±45°] lay up containing 1% moisture, tested at 20° and 90°C (Curtis, 1989).

4.3.4. The effect of notches and holes

There is uncertainty over how much the presence of notches and holes affects the fatigue strength of composite materials. This is very different from metals where flaws are likely to initiate cracks which lead to failure of the component. Stress concentrations at notches and holes may lead to increased damage in their vicinity but the damage alleviates the stress concentration so the hole does not always affect the final failure. Fig.4.24 illustrates the difference in response between metals and composites.

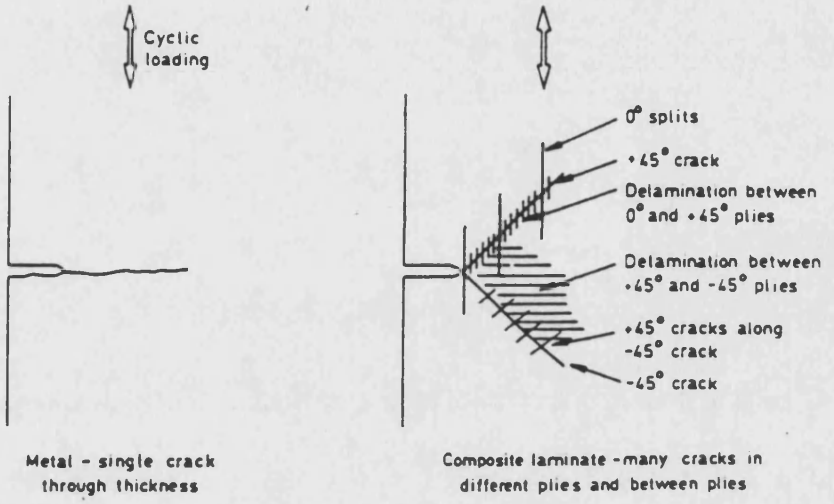

Fig.4.24. Comparison of typical damage zones at notches in metal and composite materials (Curtis, 1989).

The crack stopping ability of a fibre reinforced composite means that fracture mechanics is not easy to apply for design purposes, particularly in unidirectional, continuous, non-woven fibre composites. In woven cloth and chopped strand mat short fibre composites, cracks and notches do, however, propagate more normally (Harris, 1989). The effect of crack geometry on notch sensitivity is shown in fig.4.25. In (a) and (b) a unidirectional lamina is tested in longitudinal tension with (b) showing the presence of cracks parallel to the fibre direction causing blunting of the notch resulting in notch-insensitive behaviour. In (c) the lamina is being tested perpendicularly to the fibres which causes no crack blunting and crack growth occurs along the matrix-fibre interface. Thus in this orientation the lamina is notch sensitive. (d) and (e) illustrate the growth of a damage zone in a sheet of dough moulding compound, DMC, [short glass fibre reinforced polyester] by debonding and matrix cracking at the root of the notch, leading to the formation of a crack. A ±45° angle ply laminate is illustrated in (f) showing damage zones comprising cracking along the fibre directions.

4.4. Fatigue in wood

Wood, like other fibre reinforced composite materials, when subjected to repeated loading fails at a stress lower than its short term ultimate strength. However, the extent of this reduction is much lower than that which occurs in other materials (Dinwoodie, 1989). The reason wood performs well in fatigue is that its complex structure contains many weak interfaces which provide effective barriers to crack propagation. The chain polymer structure of the cellulose and its microfibrillar aggregation are especially well suited to resist this type of stressing. Tests on air dried wood in tension, reversed bending and rotation at a maximum stress of 30% UTS have shown an endurance limit of approximately 30 million cycles (Pashin and de Zeeuw, 1970).

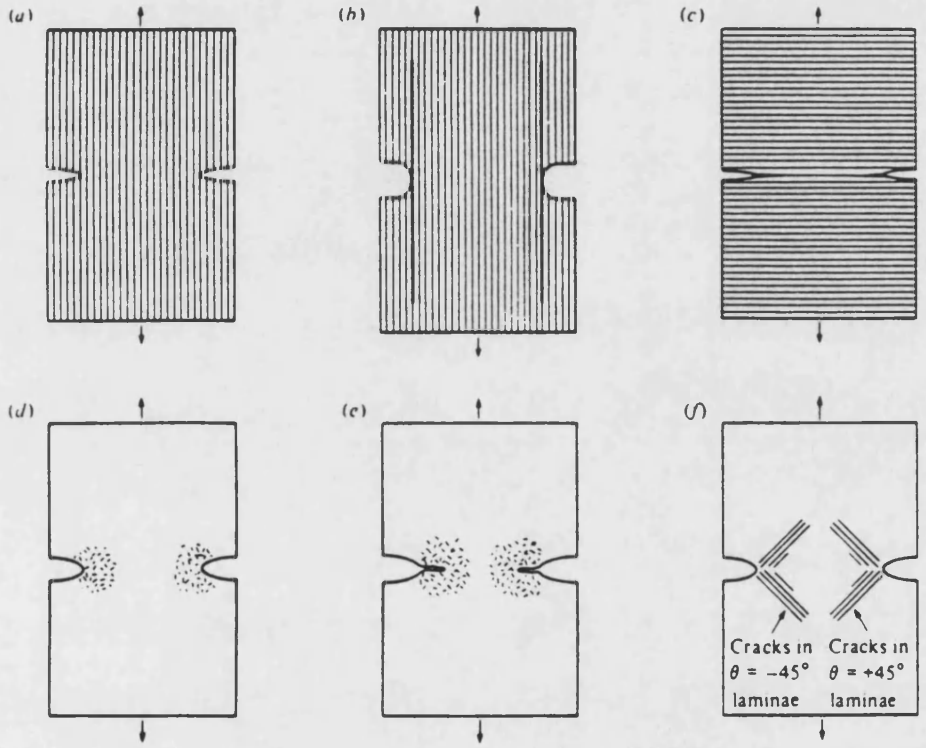

Fig.4.25. Effect of fibre geometry on notch sensitivity. (a) Unidirectional lamina tested in longitudinal tension. (b) As for (a) showing cracks parallel to fibres and blunting of the notch (notch insensitive). (c) Unidirectional lamina tested in transverse tension (notch sensitive). (d) DMC damage zone has grown and crack has formed at the root of the notch. (e) as for (d). (f) ±45° angle ply laminate tested in uniaxial tension showing damage zones due to cracking parallel to the fibres (Talreja, 1987).

In comparison to the amount of work carried out on the fatigue of metals and organic matrix fibre reinforced composites, very little research has been done on wood and wood composites (Tsai and Ansell, 1990). Although wood has been used for large scale boat building for over 400 years, it was only in the 1940s where it was used by the

rapidly expanding aircraft industry [eg. in the De Haviland Mosquito bomber] that preliminary work on the fatigue of wood was carried out (Bonfield, 1991). However, after the war the use of wood died out because of the problem of rotting of wood in high moisture content environments and the development of aluminium alloys (Spera et al., 1990). The key to the more recent use of wood's excellent structural properties in a range of high performance applications [racing boats, catamaran hulls, ice-boats and wind turbine generator blades] has been primarily due to the advent of epoxy resin adhesives. Epoxy is not only an excellent adhesive for laminating and joining, but it is also a sealant and an effective barrier to moisture penetration, and consequently biological decay.

Although wood is being tested and evaluated world-wide, the extent of fatigue testing is limited. Out of 54 laboratories in twelve European countries only four cite fatigue as an important area of their research (Seoane, 1992). The effect of live loads on wood flooring in buildings has initiated fatigue research, with wood and wood composite boards being tested in bending (Tsai, 1987, Hacker et al. 1993).

With the increased use of wood in dynamic applications its fatigue performance has been more thoroughly investigated, in particular as a result of the use of wood composites in WTG blades. Extensive research has been carried out in the USA on Douglas fir/epoxy laminates, the material used by Gougeon Brothers in the production of blades. The effects of moisture, size, joint design, veneer grade, and R ratio were all investigated on samples of 0.1" thick veneers bonded with the WEST epoxy system (Spera et al., 1990).

The work at Bath has concentrated on Khaya/epoxy laminates, the material used by WEG in their blade manufacture. The scope of the investigations has been wide ranging. The effect of moisture content on fatigue performance was investigated (Tsai and Ansell, 1984) and fig.4.26 shows how increasing moisture content decreases the fatigue strength of Khaya laminates. Tests were also carried out in axial tension and compression and fig.4.27 shows how R ratio affects fatigue life (Bonfield and Ansell, 1988). From these tests a constant life diagram for axially loaded Khaya was developed, fig.4.28 (Bonfield and Ansell, 1990).

More recent research has included the evaluation of joints, alternative species (Bonfield et al, 1992) and adhesives (Hacker, 1993). Complex load-time histories taken from instrumented blades have also been used in conjunction with life prediction models (Bond and Ansell, 1994).

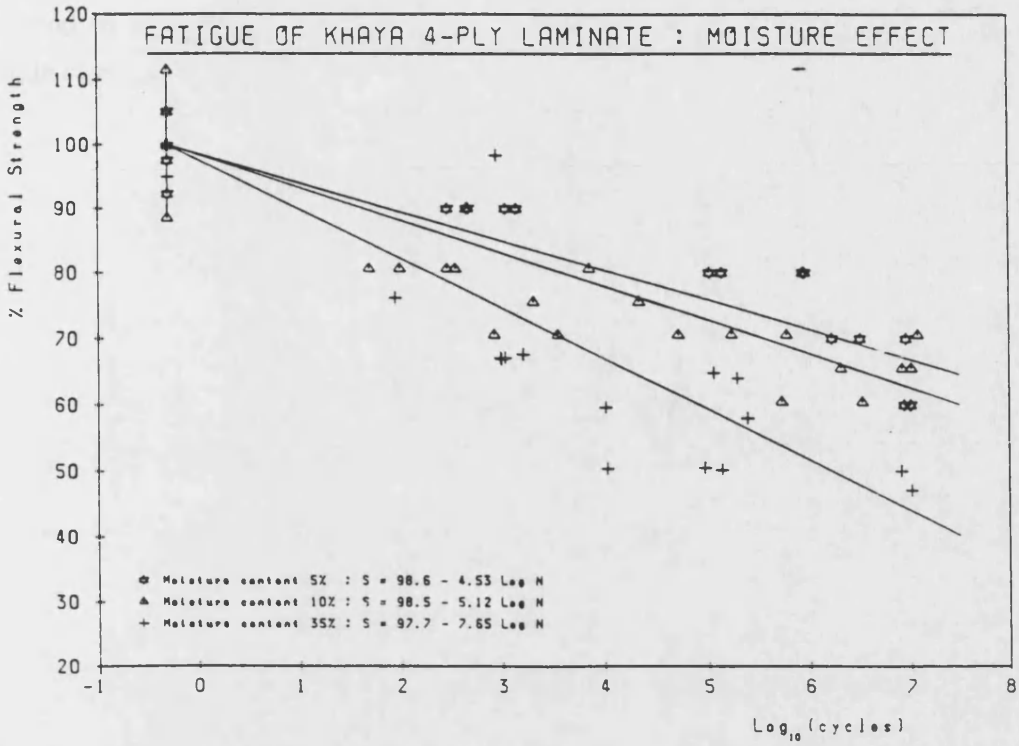

Fig.4.26. S-N characteristics for Khaya ivorensis laminate fatigued in four point flexure at moisture contents of 5%, 10% and 35% at R=0.1. Stress is expressed as % flexural strength (Tsai and Ansell, 1984).

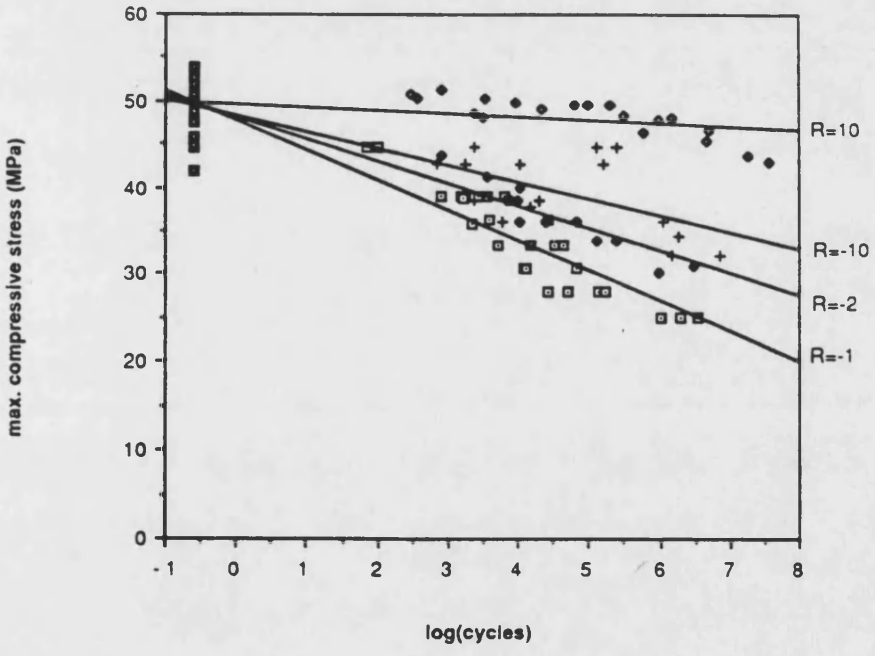

Fig.4.27. SN data for Khaya laminate axially loaded at R=-1, -2, -10 and 10 (Bonfield and Ansell, 1988).

According to Tsai and Ansell (1990), the effect of temperature on fatigue has not been investigated, although they did find that at frequencies above 8Hz adiabatic heating

occurred in wood which reduced its moisture content and consequently increased its fatigue strength.

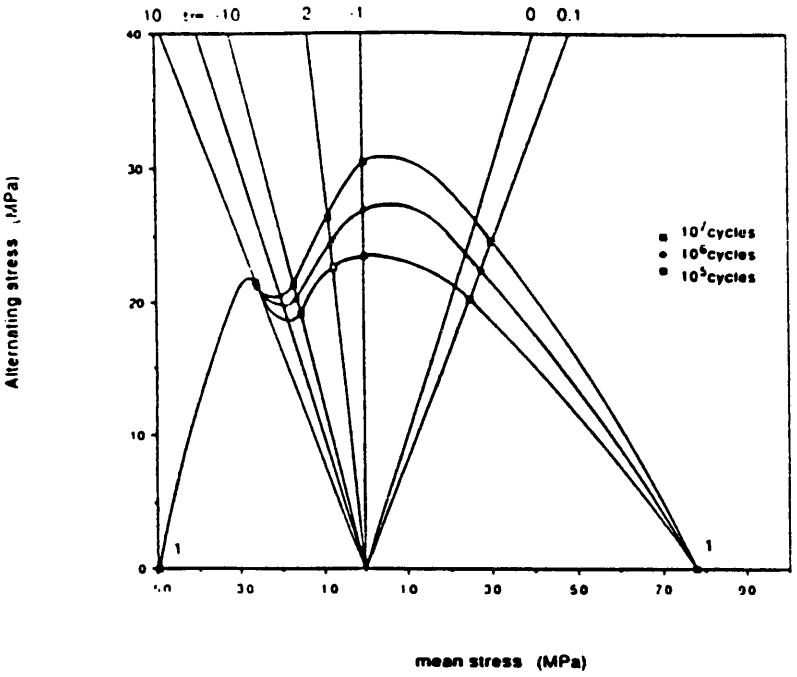

Fig.4.28. Constant life diagram for Khaya ivorensis (Bonfield and Ansell, 1990).

In the Netherlands research has centred on the evaluation of alternative species to Khaya as part of their national programme of research into WTG rotor materials, in conjunction with the manufacturer Windmaster Nederland (Rink and van Delft, 1994). They concluded that it is possible to use non-tropical hardwood species from moderate climates in the production of wood-epoxy rotor blades. Fig.4.29 shows the fatigue responses of all-scarf jointed samples for the different woods tested.

In order to investigate the fatigue failure mechanisms associated with wood fatigue, Bonfield (1991) inspected fracture faces of Khaya-epoxy samples in a scanning electron microscope (SEM). In tension fatigue at R=0.1 failure was observed to be nearly instantaneous with fracture following only a few cycles after crack initiation. The fracture surfaces were clean with the cellular structure clearly visible. Bunches of cells had been pulled apart, giving rise to a stepped fracture surface, fig.4.30. In contrast, the fracture surface of a sample tested in compression at R=10 consisted of crushed cell ends where gross cell buckling had occurred at failure, fig.4.31. The fracture surfaces of samples tested at intermediate R ratios contained a mixture of the two failure modes, the proportions of each depending on the relative proportions of the tensile and compressive load.

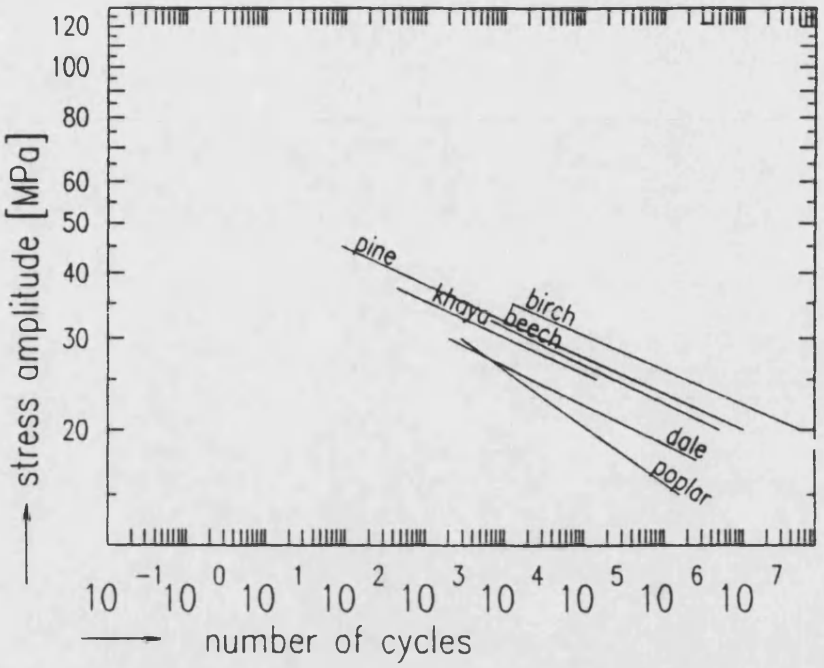

Fig.4.29. Fatigue response of alternative wood species samples, containing all scarf joints (Rink and van Delft, 1994).

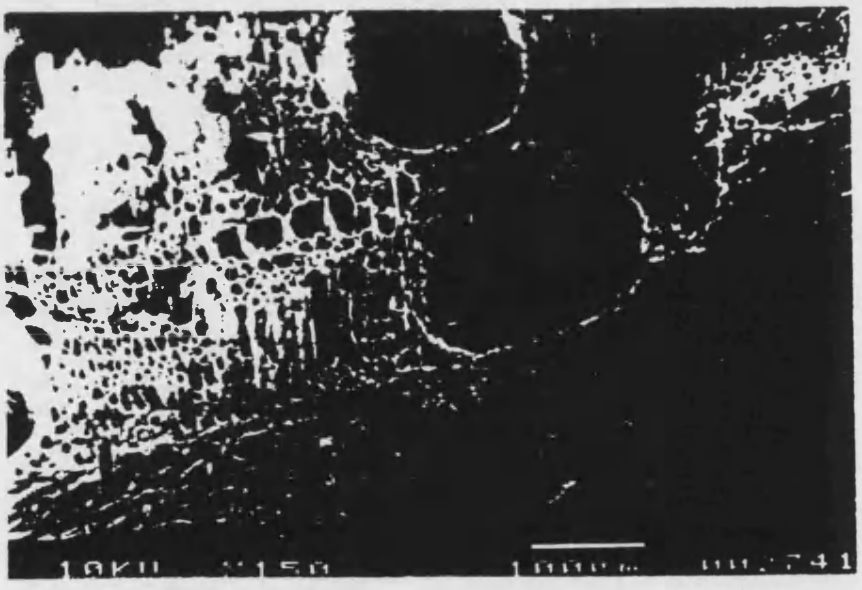

Fg.4.30. Stepped fracture of Khaya in tension fatigue at R=0.1 (Bonfield, 1991).

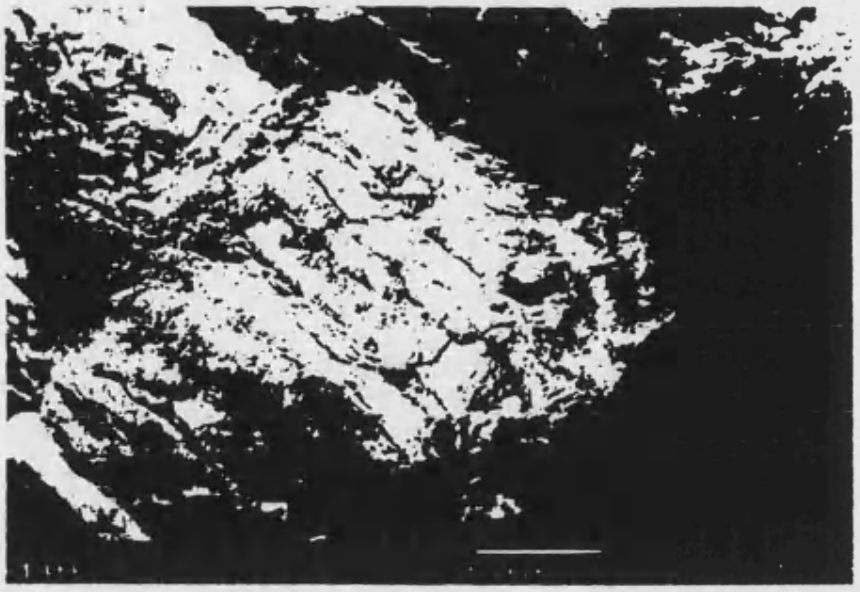

Fig.4.31. Compressive crushing of cell ends at R=10 (Bonfield, 1991).

Tsai and Ansell (1990) observed damage accumulating throughout the fatigue process in Sitka spruce under flexural loading. Thin shavings of wood from the compression side of the sample were carefully microtomed off and observed under a polarised light microscope. From as early as 500 cycles compression creases were observed in the cell walls. These increased in number with increasing cycles as well as growing in depth toward the centre of the specimen and along the length of the cell wall, until macroscopic creases were visible to the naked eye at 100 000 cycles, fig.4.32.

Fig.4.32. Compression kinks and a macroscopic crease which is visible to the naked eye on a radial-longitudinal section of Sitka spruce after 100 000 cycles at 75% UTS (Tsai and Ansell, 1990).

Reversed loading fatigue is the most damaging mode for wood because compression creases are repeatedly subjected to tensile loads where they concentrate stress in the

adjacent cells, thus accelerating the rate at which damage occurs. As wood is weaker in compression it is the compression damage which initiates the failure. However, it is tensile damage which is most obvious and it is manifested as splinters forming on the sample surface.

4.5. Summary

Fatigue failure is a serious problem with about 80% of all engineering failures attributed to it annually. It is particularly assiduous in metals and the volume of research in the area reflects this. Composites respond differently to fatigue with a gradual accumulation of damage at a microscopic level throughout the bulk of the material. This causes gradual decay in the properties of materials as opposed to catastrophic failure. The mechanisms of fatigue damage development and factors affecting fatigue performance in both metals and composites are well-known and have been surveyed.

Wood, a natural polymeric fibre reinforced composite, performs well in fatigue and the background to the current research at Bath has been presented. As far as they are known, the mechanisms of fatigue damage in wood have been described.

5. FATIGUE DAMAGE PREDICTION

The development of life prediction techniques for composites in fatigue is again based on extensive research applied to metals. A brief summary of the main techniques is included in this section.

5.1. Life prediction in metals

The most widely used life prediction method is that which was proposed by Miner (1945). Miner's rule is based on the assumption that the cumulative fatigue damage is related linearly to the nett energy absorbed by the specimen during fatigue. He suggested that if the number of stress cycles applied to a material, n, is divided by the predicted life from constant amplitude S-N data, N, then this is the fraction of life which is used up. When the sum of the fractions equals one, then the sample should fail, eq.5.1.

$$\sum \frac{n}{N} = 1 \qquad \text{eq.5.1.}$$

Miner validated his hypothesis by testing Alcad 24S-T samples under different block loading regimes and obtained an average $\Sigma n/N$ ratio of 1.015. This led him to suggest that his rule was applicable to this alloy and that it should be investigated for other materials. Although it has been used widely in design to predict the safe life of a component, further investigation has shown that damage does not accumulate linearly as Miner suggested. Neither does his rule take into account the effects of mean stress, loading sequence effects or the presence of surface defects such as notches etc. Many workers have modified Miner's rule so that it models the fatigue behaviour of metals more closely (eg. Leipholtz, 1992 and Heuler and Schutz, 1986).

A second safe life technique called the local strain approach was proposed by Morrow (1970). It is based on the assumption that the material in highly strained areas such as notches and grooves behaves in the same way as the material would in an unnotched sample under the same stress-strain history. Only materials data, namely the cyclic stress-strain and the strain-life curves are required to estimate a component's life (Heuler and Schutz, 1986). The stresses and strains at the root of the notch are calculated and the damage contribution of each cycle summed in a similar way to Miner's rule. From this the number of cycles to crack initiation is calculated. Everett (1990) used this analysis for metals used in helicopter components which were tested under the standard spectrum, Felix 28, and found that the estimated lives followed the experimental data closely but slightly conservatively.

Fracture mechanics approaches which correlate crack propagation rates with the range of the stress intensity factor, eq.4.5 (p.67), are numerous. Such damage tolerance approaches have great potential because a measurable quantity, the fatigue crack length, is involved. The Paris relationship is integrated with respect to crack length over the interval from the maximum defect present in the material to the critical crack length when the stress intensity factor is high enough to cause catastrophic failure. In calculating the stress intensity factor it is necessary to incorporate crack closure considerations because only part of a loading cycle produces an increase in crack length (Heuler and Schutz, 1986, and Everett, 1990).

5.2. Life prediction in composites

The study of damage accumulation in composites has been the subject of recent intensive study (Ye, 1989, Yang, Lee and Sheu, 1992, O'Brien, Rigamonti and Zanotti, 1989 and Spearing and Beaumont, 1992 (a), (b), (c) and (d)). The objectives of such work are firstly to understand more fully the physical processes involved in composite fatigue and secondly to develop methods of modelling damage accumulation which would be useful for life prediction and for design purposes. Some of the methods used in metal fatigue life prediction can be applied with varying degrees of success, eg. Miner's rule and fracture mechanics, but since the damage accumulation mechanisms in composites are so different from those in metals it is not surprising that existing rules need to be refined and new ones developed.

Physical indications of fatigue damage can be followed in composites such as matrix cracking, fibre breakage, debonding etc. Changes in properties such as stiffness and residual strength can also be followed throughout a composite's fatigue life. All these have the possibility of being used to characterise damage and then, hopefully, to predict the fatigue life time of components in service. The ultimate accuracy and success of modelling damage accumulation in a material depends greatly on the understanding of the microscopic mechanisms that produce damage and affect the strength and life of the material (Ye, 1989). One basic problem in the development of a damage accumulation model is in the definition of a damage variable. Such a variable needs to have a direct physical meaning and, secondly, should phenomenologically describe the physical process of damage accumulation and correlate well with damage states in the composite material. These types of variable are not easy to find!

5.2.1. Methods of measuring damage

There is a range of nondestructive experimental techniques used for measuring matrix cracking, fibre breakage and delamination as it occurs during the fatigue process. The major methods are outlined below (Curtis, 1989).

1. *Microscopy and edge replication.* Microscopy can be used to examine damage at the edges of samples and inside notches and holes. Usually this involves polishing the edge of the sample by conventional metallographic techniques. Ideally it should be carried out without removing the sample from the machine. Edge replication avoids any need to remove the sample. A polymer solution is applied to the edge of the sample which is allowed to dry before being peeled away. The film reproduces in fine detail the surface state of the sample and it can then be inspected under a microscope. It also serves as a permanent record of the damage state and can be used to follow the development of specific defects under the influence of fatigue loading.

Stinchcomb (1986) used replication techniques to good effect in the investigation of damage in a $[0,\pm45°]_{2s}$ graphite epoxy laminate, fig.5.1. He found that matrix cracks developed in a series of sequential events to form a series of regularly spaced cracks in the off-axis plies. These then caused the initiation of interfacial debonding between plies. He also found that fibre breaks occurred throughout the fatigue life and that a large percentage were associated with other damage modes and the resulting stress concentrations.

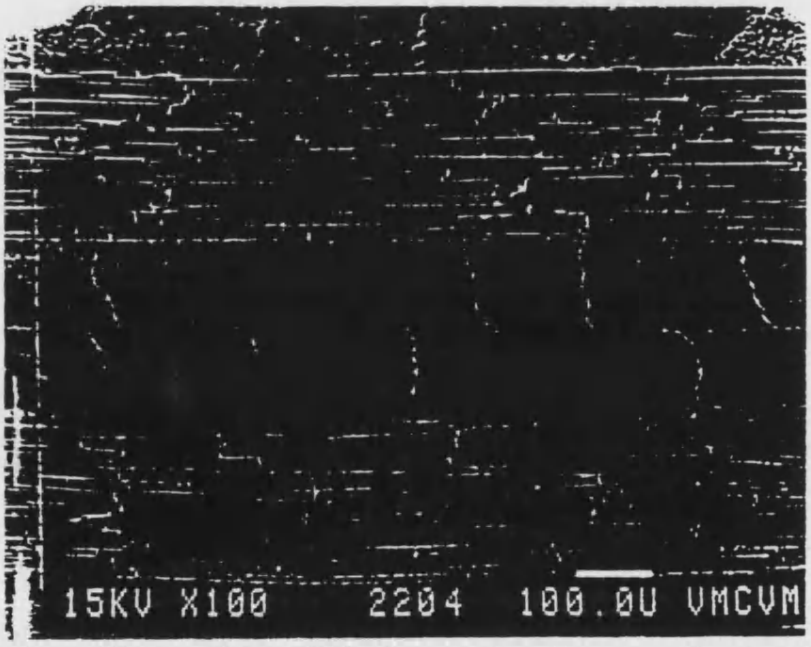

Fig.5.1. Scanning electron micrograph of a replica showing matrix cracks and broken fibres in a graphite epoxy laminate (Stinchcomb, 1986).

2. *Ultrasonic C-Scanning.* This technique relies on measuring the attenuation of an ultrasonic beam passed through the specimen and relating the signal to the damage present. The disadvantage of this method is that it requires the presence of a transfer medium for the beam which is usually water and it is inevitable that the sample will need to be removed from the test machine. Ultrasonic inspection is particularly useful for detecting and studying the growth of interlaminar damage such as edge cracks and delaminations.

3. *X-ray radiography.* A dye which is opaque to X-rays, commonly zinc oxide in an organic solvent, is introduced to the specimen which leaches into cracks and delaminations which are open to the sample surface. An X-ray photograph is then taken which reveals the distribution and size of the damage.

4. *Infra-red thermography.* The advantage of this technique is that the inspection requires no interruption of the fatigue test. Heat is generated in a sample during fatigue either by hysteresis losses in the resin or by frictional heating as a result of differential movement at cracks. The resolution of this method is about 1mm, similar to ultrasonics but worse than x-ray radiography (0.1mm).

5. *Measuring the change in stiffness and residual strength.* Both these techniques have been used in following the build-up of fatigue damage in composites (Hashin, 1985 and Rotem, 1988). As fatigue loading proceeds fatigue damage builds up throughout the bulk of the material and causes a reduction in strength and stiffness of the composite. Rotem (1988) found that the residual strength of laminated composite materials exhibit a degradation in residual strength that starts only within the last 10% of the fatigue life. Hashin (1985) suggests that the stiffness of a composite is a much better parameter to relate to damage build-up under fatigue because it involves non-destructive measurement and exhibits less statistical scatter than the residual strength. Fig.5.2. shows a typical normalised stiffness reduction curve for composite materials. Changes in dynamic modulus can be measured without interrupting the test by capturing stress-strain hysteresis loops.

5.2.2. Life prediction methods

In a survey of recent literature concerning the fatigue of composite materials the dominant approach to damage and life prediction appears to involve relating physical changes in the composite material, eg. edge delaminations and matrix cracking to changes in stiffness. It has been widely accepted that using a linear cumulative damage

rule such as Miner's rule is inadequate for composites because it is non-conservative and consequently dangerous (Poursartip and Beaumont, 1986 and Bonfield, 1991).

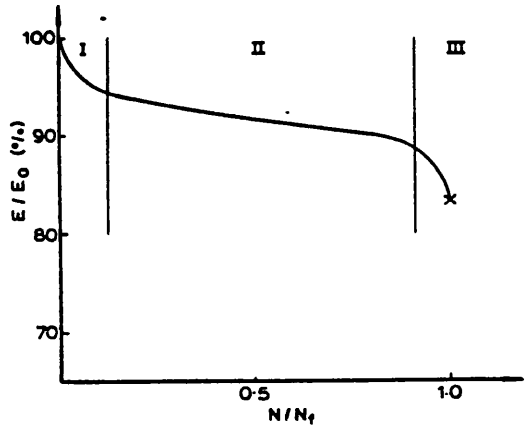

Fig.5.2. Typical normalised stiffness reduction curve for composite materials (Ye, 1989).

O'Brien et al. (1989) carried out tension fatigue tests on glass epoxy, graphite epoxy, and glass/graphite epoxy hybrid laminates. In order to predict stiffness loss they characterised the growth of matrix cracks and delaminations using the strain energy release rate, G, associated with each process. Stiffness was also measured at regular intervals throughout the fatigue tests. Failure was predicted by comparing the increase in global strain, ε_{max}, resulting from stiffness loss to the decrease in laminate failure strain resulting from delaminations forming at matrix cracks through the lamiante thickness. Fig.5.3 shows how ε_{max} increases with increasing number of cycles and how the failure strain ε_F is expected (according to strain energy release rate considerations) to decrease as matrix cracking and delaminations occur. Failure occurs at the number of cycles where the global strain and the failure strain coincide. The scatter in experimental results is shown by ε_{max} being represented as a shaded band rather than a single line.

Spearing and Beaumont (1992a, b, c, and d) have presented a new approach to modelling the fatigue performance of notched carbon fibre-epoxy composite materials. By using x-ray radiography to measure the shape of the damage zone at the notch tip throughout the fatigue lives of the samples, they observed a characteristic triangular shaped delamination zone at the $(90/0)_s$ interface of the composite as shown schematically in fig.5.4. They found that the residual strength and stiffness of the laminates could be related directly to the size of damage, expressed as the normalised split length, l/a. Fig.5.5 shows that regardless of the applied loading, the stiffness of each specimen tested had the same dependence on damage zone size. This evidence confirms that the nature of the damage is similar at all load levels.

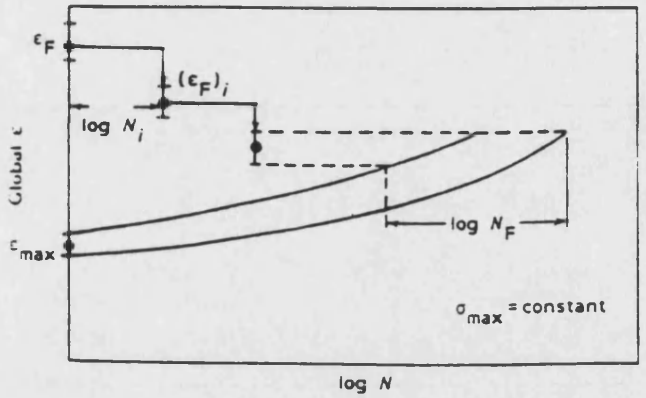

Fig.5.3. Tension fatigue life prediction for composite materials based on a reduction in global ε_F caused by delamination through the thickness (O'Brien et al., 1989).

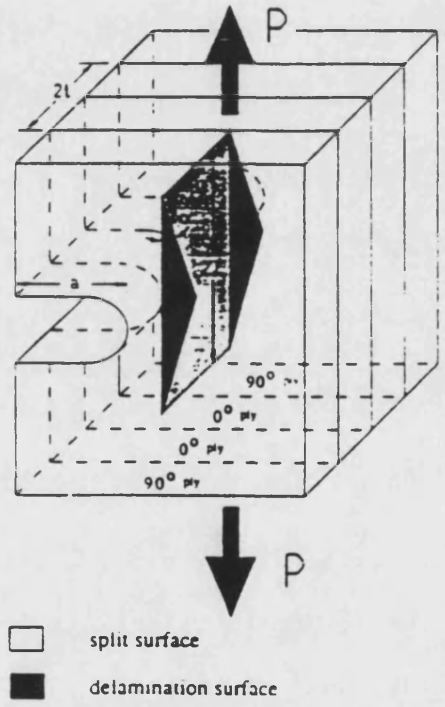

Fig.5.4. Schematic of notch tip damage in a $(90/0)_s$ notched specimen (Spearing and Beaumont, 1992a).

In their subsequent paper (1992b) they produce a damage growth model based on an energy balance between the decrease in the global strain energy of the system and the energy absorbed when split growth occurs. By using a finite element model of the stresses at the crack tip and a Paris law type expression, an equation was obtained relating the damage (normalised split length) to the number of cycles seen by the sample. Fig.5.6 shows how well the curve fits the data obtained.

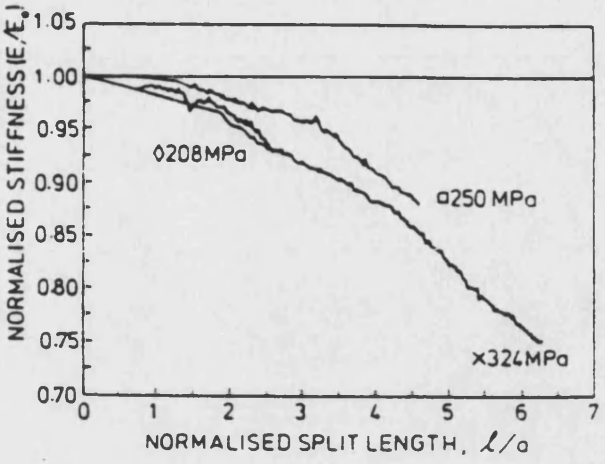

Fig.5.5. Residual stiffness of a $(90/0)_S$ laminate as a function of split length in cyclic loading (initial crack length, a=4mm, sample width, W=24mm) (Spearing and Beaumont, 1992a).

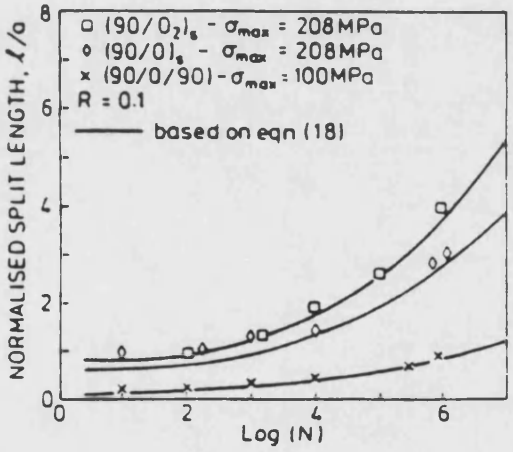

Fig.5.6. Normalised split length as a function of load cycles for (90°/0°) laminates (Spearing et al, 1992b).

In the final two parts in the series of papers (Spearing and Beaumont, 1992c and 1992d) models are presented which predict the residual strength and stiffness of carbon-epoxy laminates. Both require that the damage and its effect on the stress distribution can be quantified. Despite this constraint they found that the effect of damage propagation on stiffness can be predicted from a small initial database.

Ye (1989) states that the ultimate success of modelling damage accumulation in a material depends greatly on the understanding of the microscopic mechanisms that

produce damage and affect the properties and fatigue life. However, he believes that micromechanical models, which may be based on a large number of parameters are difficult to apply in practical situations and that, as a result, phenomenological characterisation is nearly always required. He states that stiffness change appears to be an excellent damage parameter to describe the damage development in composite materials under fatigue loading as it decreases in direct relation to microscopic damage and is easy to measure frequently without degrading the material. Consequently he defines a damage variable, D, eq.5.1:

$$D = 1 - \frac{E}{E_0} \qquad \text{eq.5.1.}$$

where E_0 is the initial stiffness of the material and E is the instantaneous stiffness. The variation of such a variable with number of cycles has already been seen in fig.4.17 (Stinchcomb, 1986), although Ye (1989) defines the critical damage state (CDS) as being just before the damage begins to build up to final failure, typically after 80% of the fatigue life.

Ye (1989) proposes a damage accumulation law by analogy with Paris' law for fatigue crack growth, eq.5.2.

$$\frac{dD}{dN} = C\left\{\frac{S_{max}^2}{D}\right\}^n \qquad \text{eq.5.2.}$$

where C and n are material constants to be determined experimentally. Eq.5.2 can be integrated to give a simple damage function. If the critical damage level can be determined by a proper criterion then the duration of the first part of damage development which normally takes up most of the total lifetime can be predicted. By substituting eq.5.1 into eq.5.2 an expression can be obtained which relates the current value of stiffness, E/E0, the number of cycles, N, and the fatigue stress level σ_{max}. This theory was evaluated using data from tests of a random short fibre SMC composite. Fig.5.7 shows how the predicted SN behaviour (solid line) compares to experimental data. A critical damage level Dc=0.3 was assumed. Although the fit is reasonable, Ye (1989) feels that the prediction could be improved if a proper criterion could be developed to define the critical damage.

Picasso and Priolo (1988) have also used a modulus degradation technique in fatigue life predictions for graphite/PEEK composites. The fatigue life of quasi-isotropic material was fairly well predicted using fatigue data from the unidirectional material and by adopting a linear criterion such as the maximum stress or strain criterion in the fibre direction.

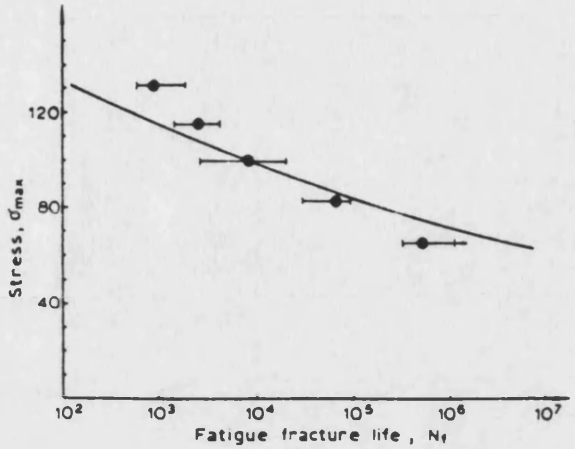

Fig.5.7. The cyclic stress-life diagram for SMC-R50 composite subjected to tensile fatigue (Ye, 1989).

Yang, Lee and Sheu (1992) apply a fatigue modulus degradation model which predicts the statistical distributions of fatigue modulus reduction for matrix-dominated composites. In a matrix dominated material the stress-strain relationship is not linear and this is why the fatigue modulus is used, see fig.5.8 for modulus definitions.

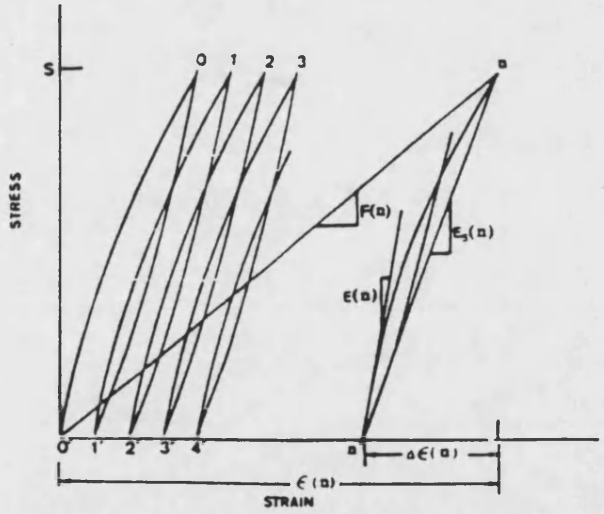

Fig.5.8. Definitions of stiffness, E(n), secant modulus, Es(n) and fatigue modulus F(n) (Yang, Lee and Sheu, 1992)

The fatigue degradation model can be written as in eq.5.3:

$$F(n) = g(S)E(0)[1 - Q n^{v}] \qquad \text{eq.5.3.}$$

where F(n) is the fatigue modulus after n cycles; g(S) is a function of stress level, S; E(0) is the initial modulus, Q is a random variable and v is a linear function of the applied stress level, S. Eq.5.3, regression analysis and a Bayesian statistical approach were used to predict the fatigue modulus reduction for individual specimens. An experimental program was carried out using graphite/epoxy $[\pm 45°]_{2s}$ laminates to generate statistically meaningful data to verify proposed models. The correlations between experimental results and the predictions were found to be quite reasonable.

Hwang and Han (1989) also used a fatigue modulus approach to predict the fatigue life of composite materials. First they established a fatigue modulus degradation model which they used to develop a fatigue life equation as a function of fatigue modulus. Finally they calculated the fatigue life using a strain failure criteria, fig.5.9. The model was used to predict the fatigue life of short carbon fibre reinforced nylon 6 when subjected to 2 stress level block loading and the predictions were found to fit reasonably closely to the experimental data.

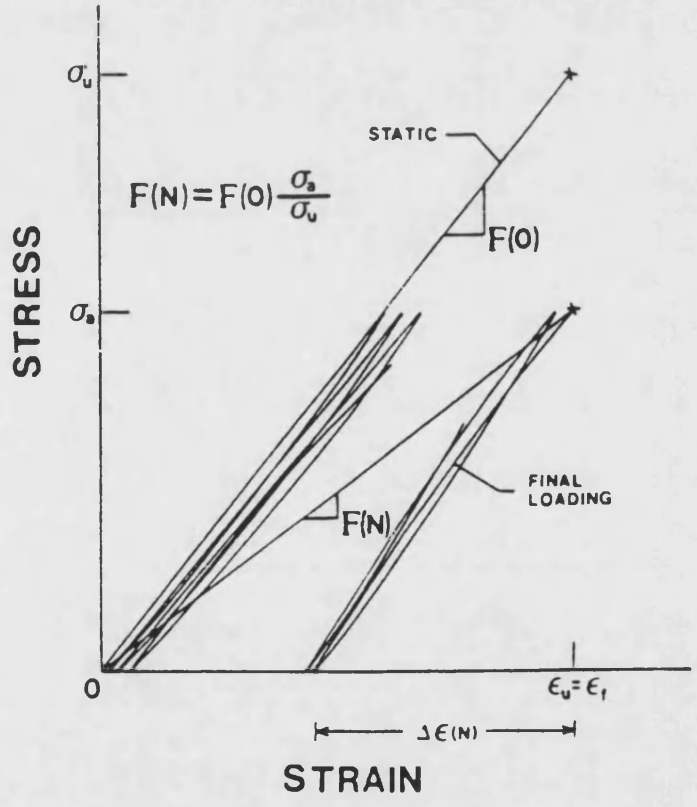

Fig.5.9. Resultant strain failure criterion (Hwang and Han, 1989)

Continuum damage mechanics has also been used in the fatigue life prediction of composite materials. (Talreja, 1987 and Jessen and Plumtree, 1991). Continuum damage mechanics is concerned with the creation of new surfaces in the form of

microcracks and voids on any plane of representative volume of the material, fig.5.10. Fatigue damage develops in an anisotropic manner in reinforced composites which means that in order to give a reasonable representation of damage the damage variables must be tensorial in nature. Jessen and Plumtree (1991) express the effective stress tensor on a damaged body in a general form, eq.5.4:

$$\{\hat{s}\} = [M(D)]\{s\} \qquad \text{eq.5.4.}$$

where [M(D)] is a general damage tensor transformation. Their model was produced using a strain energy criterion and used to predict the decrease in stiffness of the composite. The model was verified by experiment on GRP pultruded rods and accurate fatigue lives were predicted for single stress and 2 stress level block loading tests.

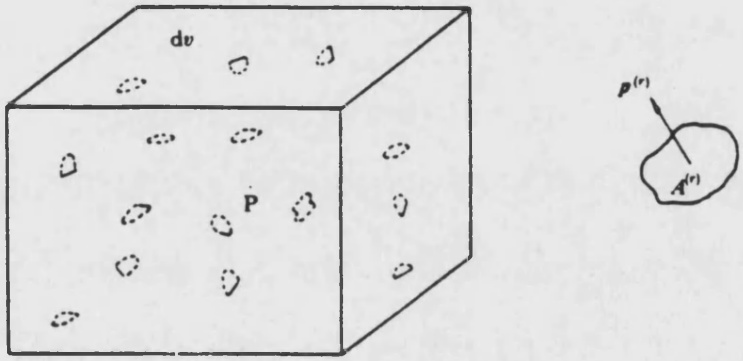

Fig.5.10. Vector field characterisation of damage (Talreja, 1987).

5.2.3. Application to wood composites

As mentioned in chapter 4 the amount of published work on wood fatigue is small and consequently work on fatigue life prediction for wood and wood composites is even more scarce. Fatigue life prediction has been carried out for wood composites by Bonfield and Ansell (1988, 1989, 1990) for block- and complex-loading regimes. The life prediction method was based on Miner's rule of linear damage summation which proved conservative under certain block loading regimes (Bonfield and Ansell, 1988) but optimistic under others (Bonfield and Ansell, 1989).

Bonfield (1991) presents a fatigue life prediction method based on Miner's rule for a complex loading spectrum known as WISPERX which is a standardised load sequence for horizontal axis wind turbine blades (Poppen and Bach, 1991). The WISPERX spectrum is depicted in fig.5.11. The spectrum can be broken down into cycles of different mean stress and stress range and sorted into bins, fig.5.12, by rainflow counting. The damage caused by each bin of cycles was calculated using interpolatetd SN data for the material and Miner's rule. The calculated number of passes through the spectrum are compared with those obtained by experiment in fig.5.13. It can be seen

that the actual lives of the samples exceed the predicted lives by up to 1.4 decades of loading cycles.

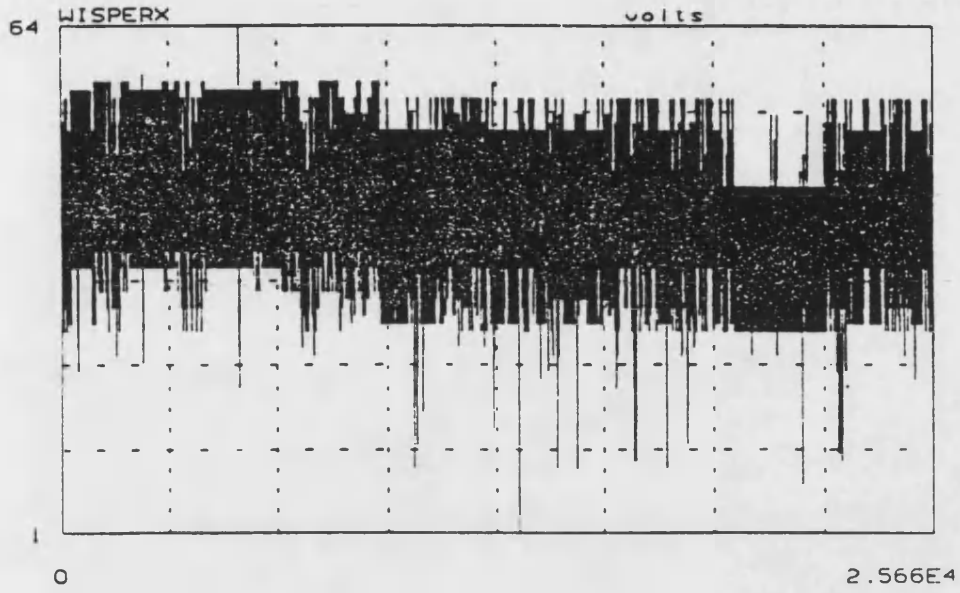

Fig.5.11. The WISPERX spectrum (Bonfield, 1991)

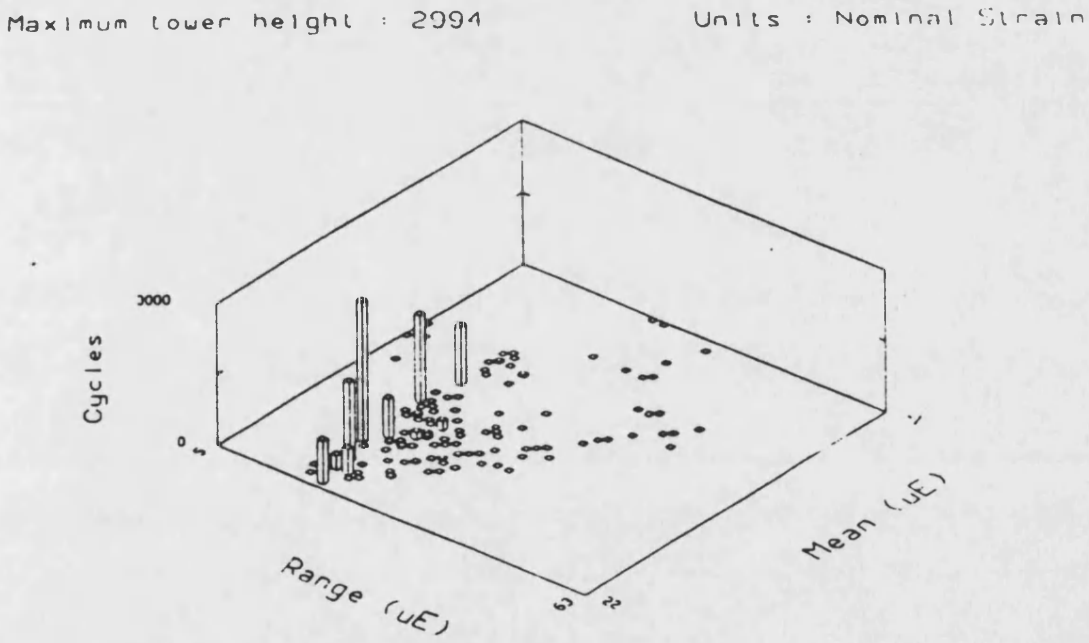

Fig.5.12. Results of a rainflow analysis of WISPERX (Bonfield, 1991).

In section 5.2 a range of methods for predicting the fatigue life of composite materials was outlined. However, it is unlikely that methods which relate a distinct damage mechanism (matrix cracking, fibre breakage, delamination) to changes in stiffness are applicable to wood fatigue. This is because the fibrous content (microfibrils) of wood

is so finely related to its matrix of hemicellulose and lignin that it is not possible to detect any of the damage mechanisms mentioned above. The situation is also complicated by the fact that wood has a cellular structure which fails in compression by cell wall buckling.

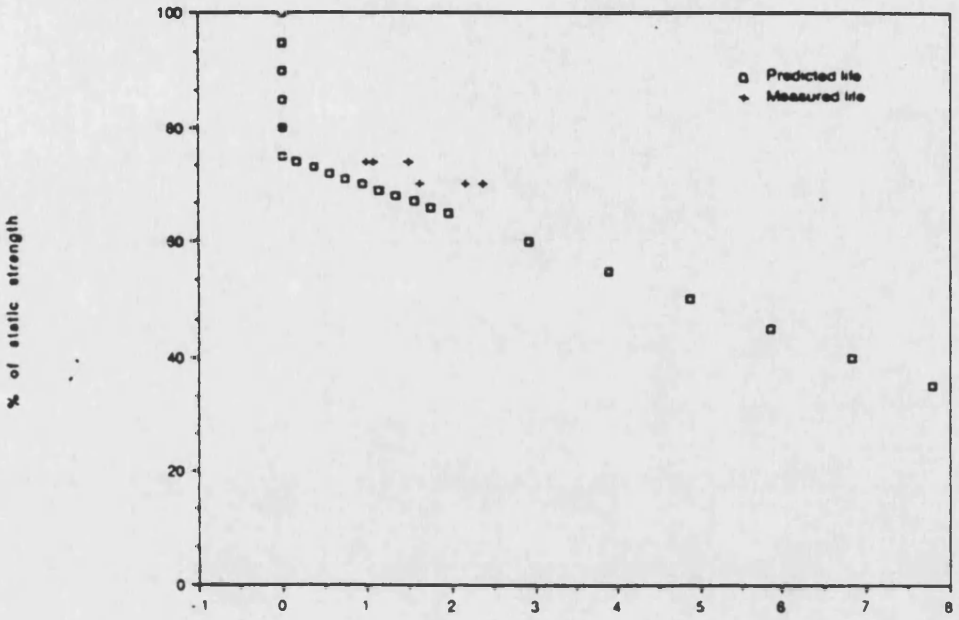

Fig.5.13. Predicted and measured lives for Khaya tested using WISPERX (Bonfield, 1991).

It is also uncertain whether many of the conventional non destructive techniques for measuring microscopic damage are applicable to wood because of its open cellular structure. Infra-red thermography has been used on a whole wood laminate wind turbine blade and on coupon testing of wood laminate samples (Dutton et al, 1992 and Bond et al, 1992) and marked increases in temperature were observed at the sites of joints in the blade/coupon. A rapid increase in temperature was observed close to failure and it was possible to determine the joint from which the failure had initiated. As yet no predictive model has been developed using infra-red thermography and it is essentially a qualitative technique at this stage. As mentioned earlier, the technique has a resolution of about 5mm which makes it unable to distinguish individual damage events taking place in the cell walls. Consequently it is an inappropriate technique to follow damage accumulation in unjointed laminates.

The technique of edge replication was investigated for use with wood composites but it was found that the plasticised cellulose acetate film was drawn deep into the wood cells. Consequently the film could not be removed or left the wood structure full of plastic and preventing the production of any further meaningful replicas (Bond et al., 1992) A second technique involving the application of plastic films is the use of photoelastic

coatings to show up changes in stress distribution as a result of fatigue damage. A final year project was conducted into this method and it was found that only changes in stress distribution around very obvious joints at high stress levels were detected (James, 1993). This makes this method unsuitable to follow the subtle changes in wood structure at a cellular level.

Ye (1989) developed a model for predicting fatigue lives based purely on measurements of decreasing stiffness in a composite as he felt that models based on micromechanical damage events were too complex to apply in practical situations. Such an approach is applicable to wood as it avoids the necessity of making quantitative measurements of microscopic damage. Data relating to the decrease in stiffness of wood have been obtained by Bonfield (1991) and the curves obtained are similar to those obtained by Ye (1989).

5.3. Hysteresis loop capture and fatigue life prediction

The capture of hysteresis loops is a very useful technique with which to follow property changes in a material during fatigue. Its primary attraction is that damage can be collected throughout a test without interrupting the loading regime. In addition to being used to follow decrease in stiffness, it also provides information on the creep strains in the sample and the energy dissipated per fatigue loading cycle.

5.3.1. Introduction

When a linear elastic material is loaded and unloaded the stress-strain plot is linear and the loading and unloading portions of the curve coincide, fig.5.14a. The elastic energy absorbed by the material on loading is evolved on unloading and is equal to the energy under the stress-strain curve. Consequently, no energy is lost in the material as a result of cyclic loading. Most real materials do not exhibit linear elastic behaviour, fig.5.14b, but have some degree of time-dependent response. As the frequency of loading is increased the resultant strain begins to lag behind the applied stress as mechanical energy is converted into heat by internal friction. The stress-strain unloading part of the curve does not follow the loading part, fig.5.14c, and the energy evolved on unloading is less than that absorbed during loading. The energy absorbed in a complete loading and unloading cycle is known as the hysteresis energy and is equal to the energy enclosed between the two curves (Reinhart, 1988 and Ashby and Jones, 1987).

Typically, a strain gauge or extensometer is attached to the sample surface and the output fed to a fatigue data system which allows hysteresis loop capture. As the sample

is cycled, paired values for stress and strain are recorded and saved at set intervals throughout a test, as specified by the operator.

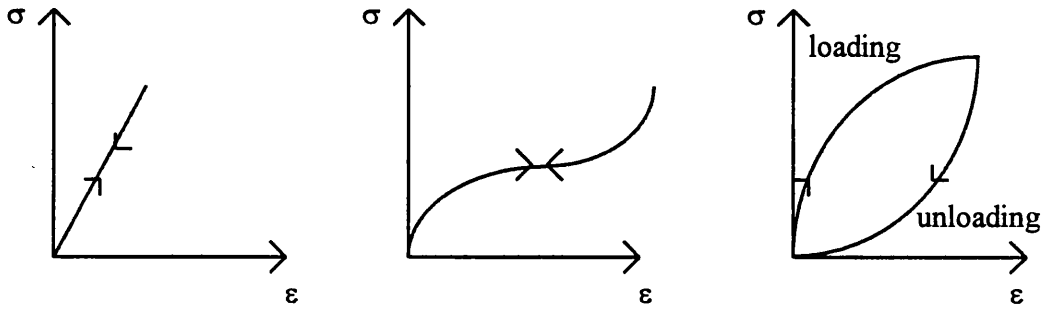

(a) Linear elastic response (b) Non-linear elastic response (c) Non-linear elastic response at high frequency

Fig.5.14. Stress-strain response of (a) ideal linear elastic material and (b), (c) non-linear elastic materials.

As well as providing information on changes in dynamic modulus, creep strain and energy dissipated per cycle, a series of hysteresis loops can provide information about other features such as the development of different tensile and compressive moduli. All the above are linked to the damage state of the material and may be used to measure fatigue damage accumulation and in fatigue life prediction models.

5.3.2. Work on metals and composites

Hysteresis loop capture has been used as a method of investigating the fatigue of metals, composites and other materials such as ceramics and bolted joints. Xiao-Yan et al. (1989) investigated four types of steel in strain controlled reversed loading and found that the hysteresis energy absorbed by the metal is not all used up in the crack initiation process but that some is dissipated as heat, acoustic emission or absorbed by immobile defects. Linde and Henderson (1992) used hysteresis loop capture to investigate thermomechanical fatigue of a Ni-Cr oxide dispersion strengthened alloy, and in particular its yielding behaviour.

Picasso and Priolo (1988) and Jessen and Plumtree (1991) used hysteresis loop capture as a method of measuring the change in stiffness of fibre reinforced composites. Fig.5.15 shows loops obtained for isotropic and unidirectional graphite-PEEK laminates. Picasso and Priolo (1988) found that, although the measurements of dynamic modulus were satisfactory, the loop area varied too much to be of any practical use. Carswell (1985) considered the fatigue damage in glass- and graphite-reinforced nylon by measuring the maximum deflection and deflection range of the sample during fatigue. Loop rotation and drift were observed, the former due to damage accumulation

in the material and the latter due to creep caused by the mean load on the sample. From analysis of the loops a single expression relating stress, deflection and endurance was obtained which allowed fatigue lives to be predicted.

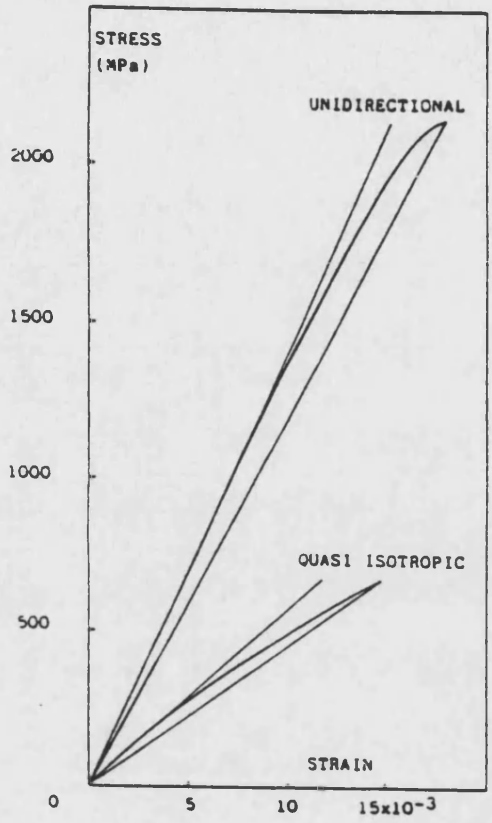

Fig.5.15. Stress-strain curves for the quasi-isotropic and unidirectional laminates (Picasso and Priolo, 1989)

Fig.5.16 shows a series of hysteresis loops obtained for tightly woven carbon/carbon composites by Ozturk and Moore (1992). The loop area is clearly seen to decrease throughout the fatigue life of the sample and the modulus decreases by just under 3%. They attribute the decrease in loop area to changes in loading and unloading modulus which occur as a result of fatigue damage in the composite. As the two moduli become more similar the loop area correspondingly decreases. At 10^5 cycles they are both the same and the loop area is zero. This behaviour is unexpected because there is usually an increase in energy absorbed by the material as fatigue damage accumulates due to internal friction and an increase in hysteresis loop area results.

Bonnee (1989) used hysteresis loop capture to determine the behaviour of pre-stressed bolted joints in glass fibre reinforced polyester, as used in the hub connection of some wind turbine blades. Fig.5.17 shows a series of hysteresis loops captured when there was no tension in the bolt. The points of inflection in the curves are where the bolt

slipped in the hole as the direction of loading was reversed. The amount of slipping increased throughout the test as a result of ovalisation of the hole as localised damage built up in the GRP. In fig.5.18 hysteresis loops are shown for a pre-stressed joint. All, except the first loop, have no region of inflection because the load on the bolt mates the metal and GRP surfaces together so no slipping can occur. The decrease in loop area exists because at the start of the test initial large displacements of the composite under the smooth steel pressure rings generate heat. As fatigue proceeds and fretting occurs a more fixed joint results and less heat is generated, leading to narrower hysteresis loops. It is not surprising that the pre-stressed joints were found to have a superior fatigue life, a hundred times greater than the unstressed joints.

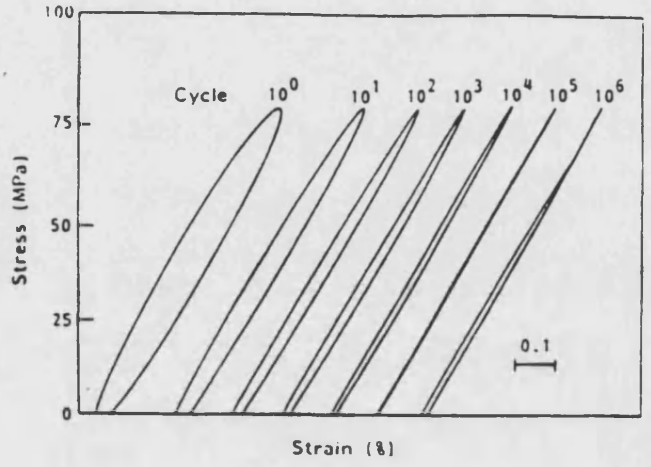

Fig.5.16. Stress/strain relations with increasing number of fatigue cycles (Ozturk and Moore, 1992).

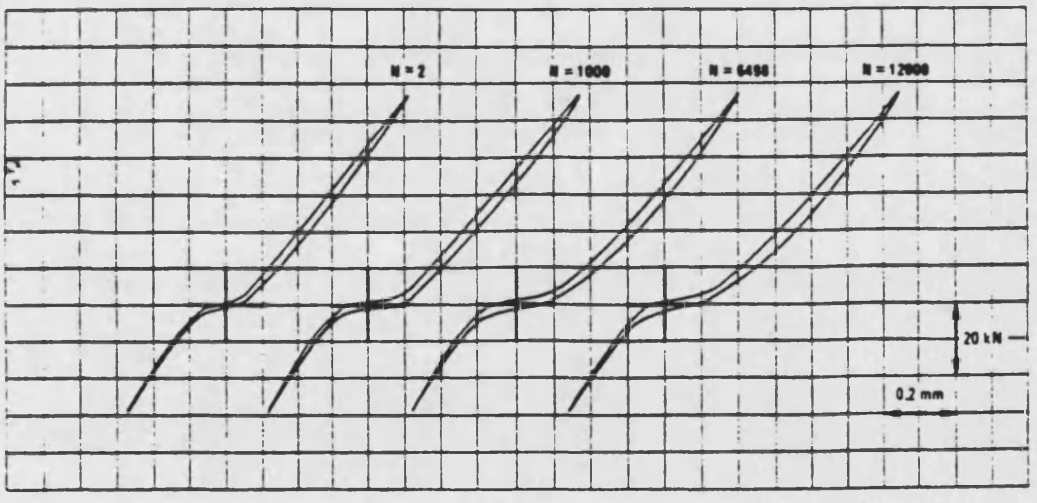

Fig.5.17. Hysteresis loops for an unpre-stressed bolted joint specimen (Bonnee, 1989)

Hysteresis loop capture has also been used to investigate the fatigue damage mechanisms of zirconia ceramics by Liu and Chen (1992). They identified two

mechanisms: microcracking and transformation plasticity, and by considering the shapes of hysteresis loops captured at different loads and frequencies found that transformation plasticity predominated at low frequencies but could be suppressed at higher frequencies, leaving microcracking as the main damage mechanism.

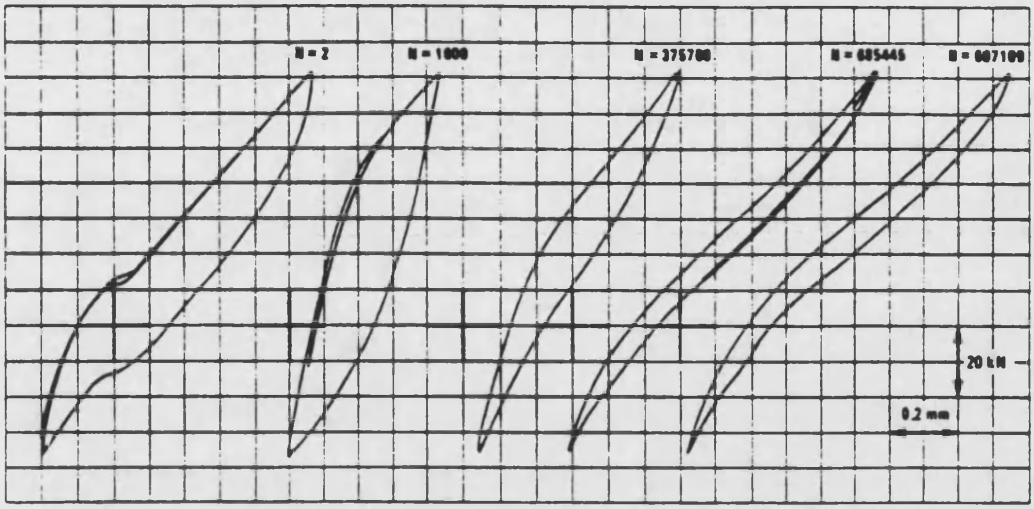

Fig.5.18. Hysteresis loops for a pre-stressed bolted joint specimen (Bonnee, 1989).

5.3.3. Loop capture in wood

With the exception of a team of Japanese workers [Kohara and Okuyama, 1993], Bonfield and Ansell (1990) are the only workers known to have carried out hysteresis loop capture on wood. Laminated Khaya samples were loaded axially and stress-strain hysteresis data captured throughout tests carried out at R=-1. In all tests a decrease in dynamic modulus and an increase in loop area were observed. Fig.5.19 shows typical loops captured at the start and end of a test. The narrow loop was captured after only 10 cycles and the wider, flatter one was captured after 13840 cycles. The increase in loop area and decrease in sample stiffness indicated that a large amount of permanent damage occurred in the wood. The larger loop was also bent, indicating that the dynamic tensile modulus is higher than the dynamic compressive modulus. The overall trends in dynamic modulus and loop area can be seen in figs.5.20 and 5.21 respectively. The data have been normalised by the initial property and are presented as a function of percentage of fatigue life (Bonfield, 1991). The dynamic modulus and loop area both change significantly after 70-80% of the fatigue life.

Bonfield (1991) states that the conclusions drawn from this part of his work are based on only a few successful tests and that there was wide scatter in the data which suggested the need for further investigation.

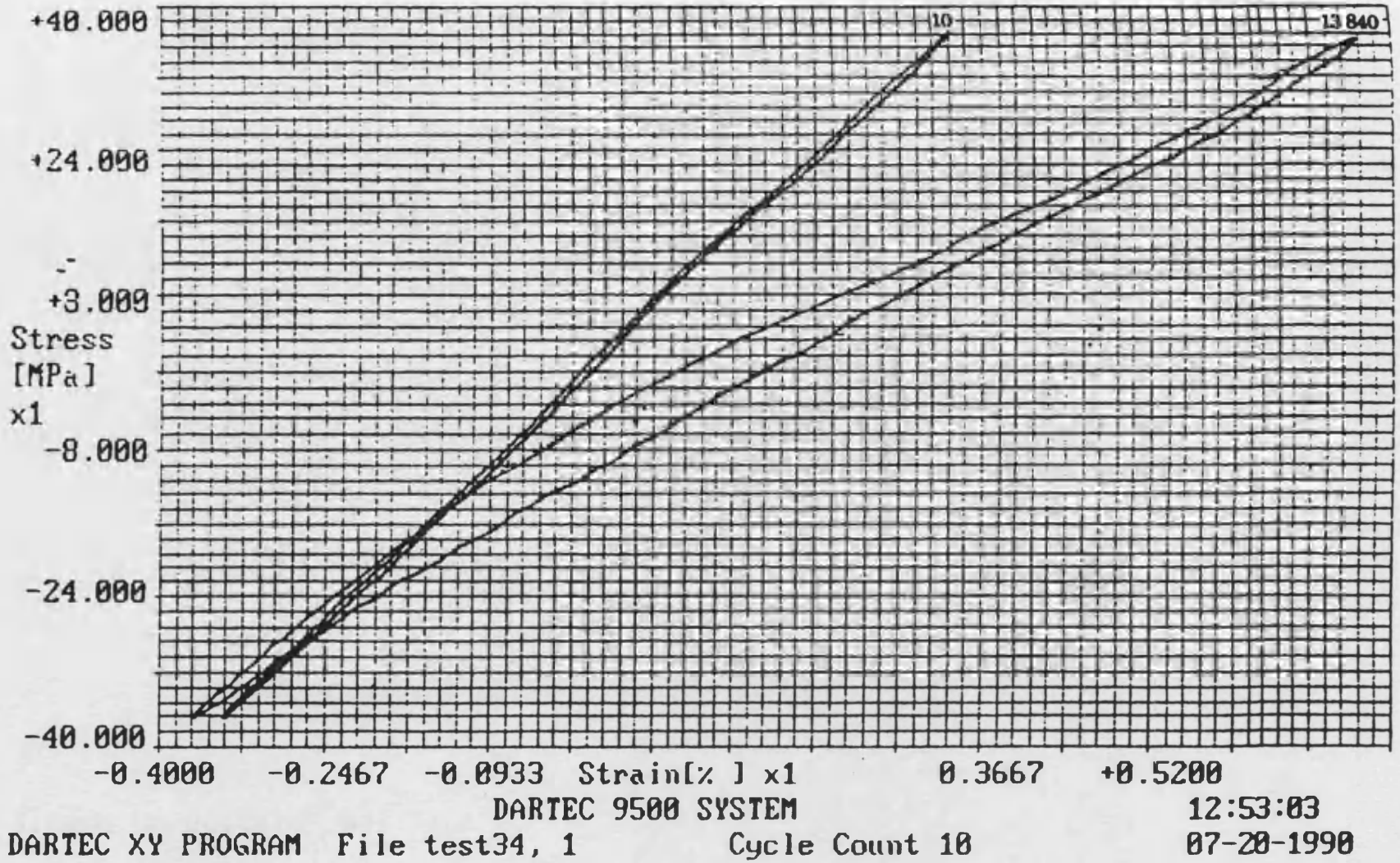

Fig.5.19. Hysteresis loops captured after 10 and 13840 cycles at ±37.5MPa, R=-1 (Bonfield, 1991).

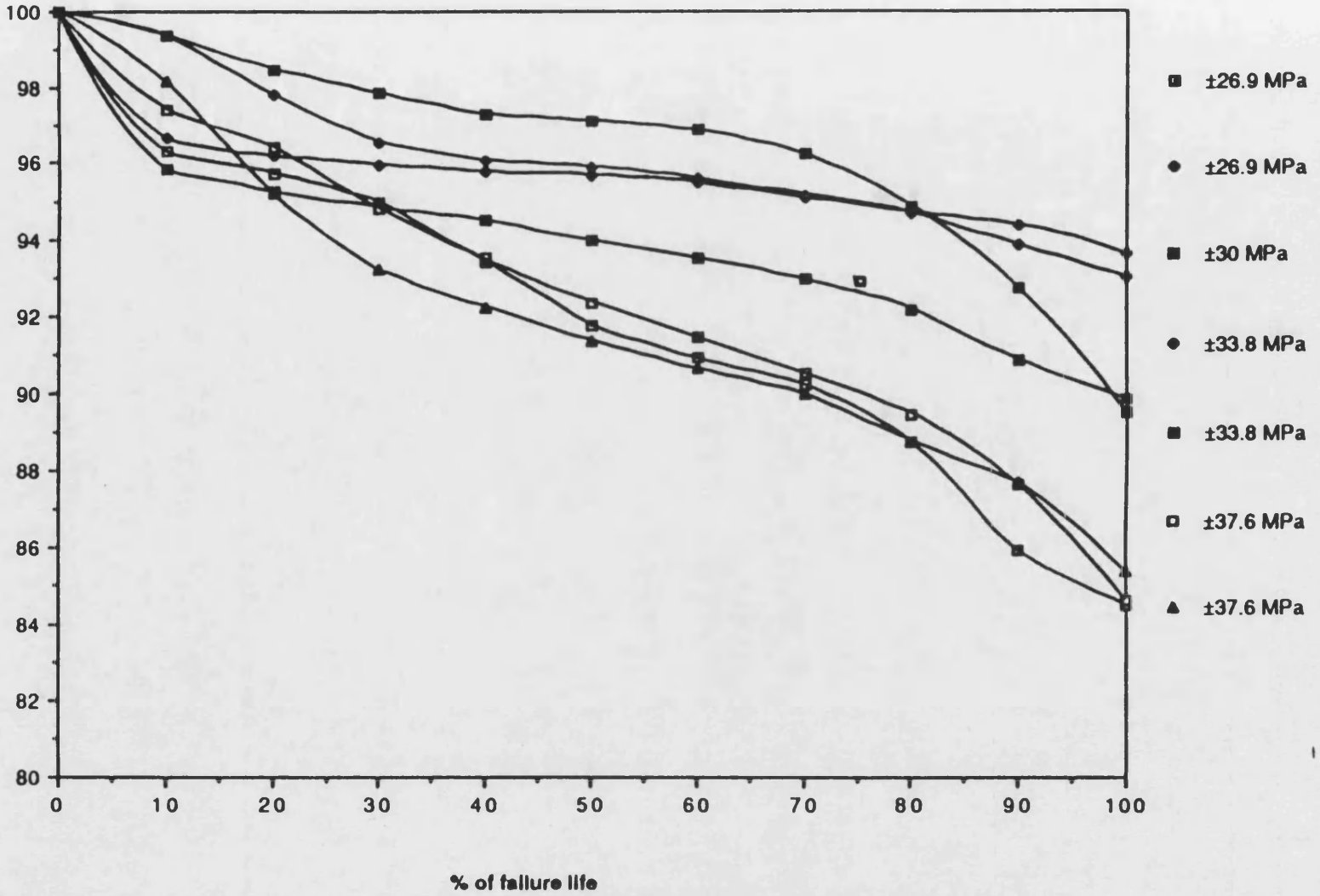

Fig.5.20. Normalised dynamic modulus versus normalised life (Bonfield, 1991).

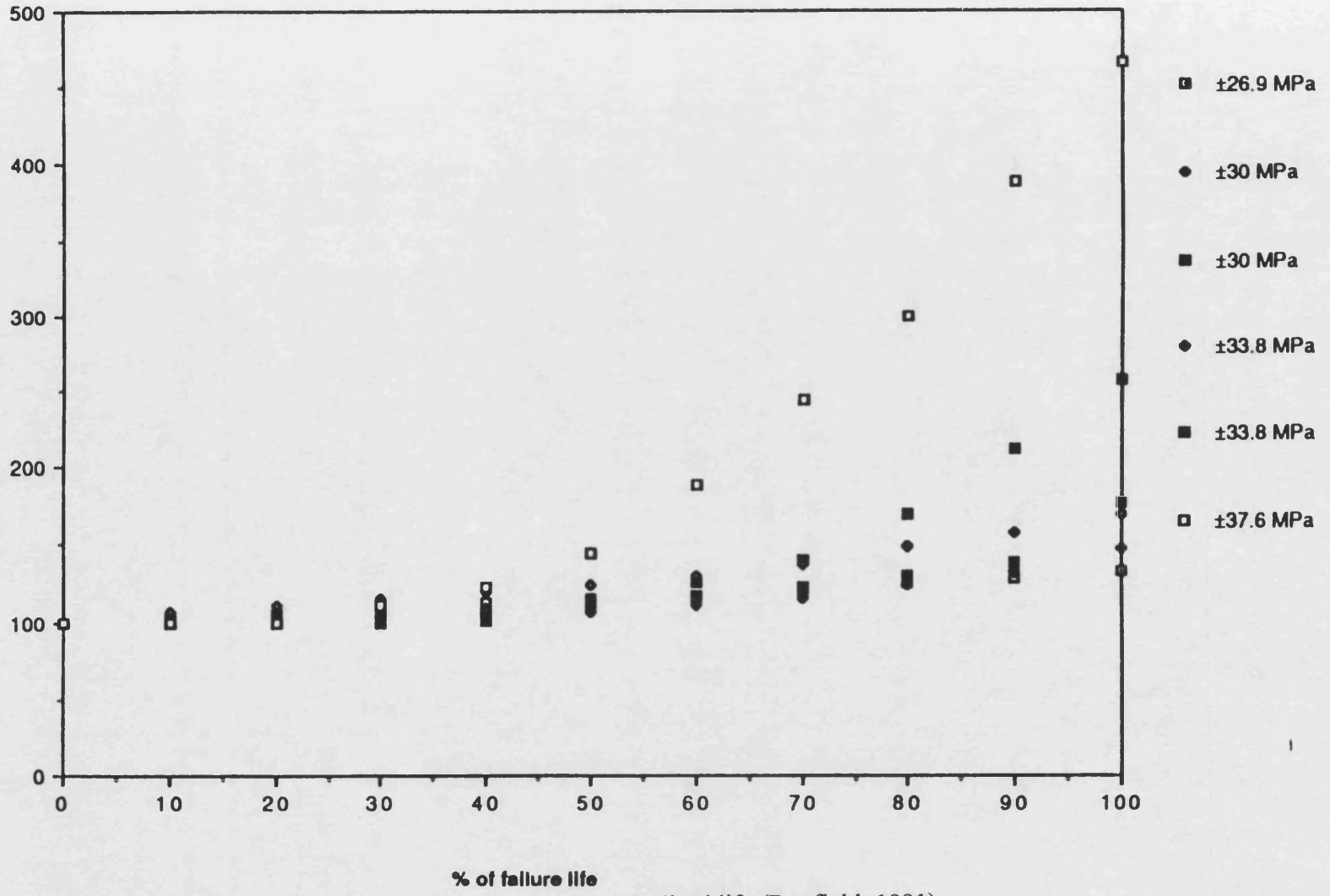

Fig.5.21. Normalised loop area versus normalised life (Bonfield, 1991).

5.4. Summary

A survey of fatigue life prediction has been presented. This includes important work on metals, namely Miner's rule of linear damage accumulation and fracture mechanics approaches, upon which composite fatigue life prediction techniques have been established. Methods of measuring the damage state of fibre reinforced organic matrix composites have also been presented and their relevance to fatigue damage measurement in wood assessed. The use of changes in properties such as stiffness were seen to be a common approach for composite materials and was identified as a suitable technique for wood and wood composites.

A background into stress-strain hysteresis loop capture has been presented along with its application in the study of fatigue damage accumulation for a wide range of materials, including composites and wood.

6. EXPERIMENTAL TECHNIQUE

6.1. Materials

The African mahogany *Khaya ivorensis* was used in this study as its fatigue performance has been extensively documented in previous work at Bath University (Ansell and Tsai, 1984; Bonfield, 1991; Bonfield and Ansell, 1992) and the intention was to build on the knowledge already gained. It is also the wood which has, until recently, been used in the production of Wind Energy Group's wood composite wind turbine blades (Ansell et al, 1991). It has been widely used in wind turbine blades for the following reasons:

- it is fairly cheap and available in thick veneers (4mm)
- its variability is relatively low as it is equatorially grown thus reducing density changes due to seasonal variations
- it contains vessels allowing the penetration of surplus resin into the wood structure enabling the formation of thin gluelines.

Wood composite panels (approx. 600mm x 900mm) were manufactured by WEG Ltd. at their blade manufacturing plant in Southampton using the same wood and adhesives used in the production of their blades. The techniques applied in the manufacture of their blades were emulated as closely as possible in panel manufacture, for example the adhesive was applied using rollers to one side of each veneer only and a vacuum was applied whilst the adhesive cured to ensure the same level of consolidation. When the panels were fully cured they were sent to be cut into 'dog bone' shaped samples at, Flower and Hayes Ltd and Bath Precision Joinery in Bath. About 10 samples were produced from each panel.

In order to investigate the manner in which damage accumulates in wood composites during fatigue the simplest possible sample configuration was adopted. The samples did not contain any joints and were not coated with glass reinforced epoxy. Fig.6.1 shows the sample geometry which was developed by Bonfield (1991). Each sample comprises eight 4mm thick rotary cut Khaya veneers laminated with a structural grade two part room temperature curing epoxy resin [filled SPS Ampreg 20]. All 8 veneers were aligned with their longitudinal grain direction as closely parallel with the sample axis as possible [natural variations in the grain direction within each veneer were frequent].

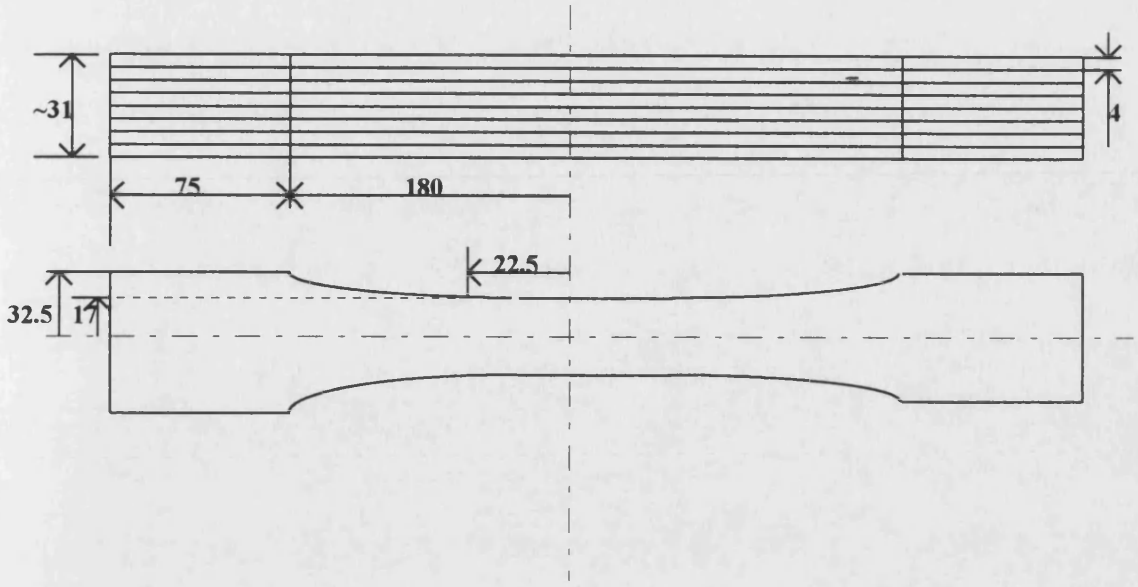

Fig.6.1. Sample geometry, dimensions in mm.

The samples are reasonably substantial because in order to avoid sample splitting from the parallel gauge length it is necessary to have a large radius of curvature in the region between the end tabs and the gauge length. Secondly, they have a high cross sectional area in order to avoid buckling problems when loaded in compression.

Because the mechanical properties of wood are very sensitive to moisture content (Dinwoodie, 1981) the veneers used both in blades and sample panels were conditioned at 65% relative humidity and then stored in sealed bags before laminating. The samples were kept in constant humidity conditions by storage in a cupboard containing large beakers of saturated sodium nitrite solution. This has a vapour pressure such that the air above it has a relative humidity of 65%. After the samples had been cut they were kept in the conditioning cupboard for at least one week before they were tested.

6.2. Equipment

6.2.1. Fatigue rigs

Two servohydraulic fatigue machines were used in the fatigue evaluation of wood composites. One was a four column model, the other had two columns. Both could apply a maximum of 20 tonnes force. The four column Mayes machine can be seen in fig.6.2. The four column machine was equipped with a Dartec 9500 controller which enabled tests to be computer controlled. This was essential for stress-strain hysteresis loop capture and for complex load-time history testing. The two column machine was used exclusively for constant amplitude testing without loop capture, for example, in

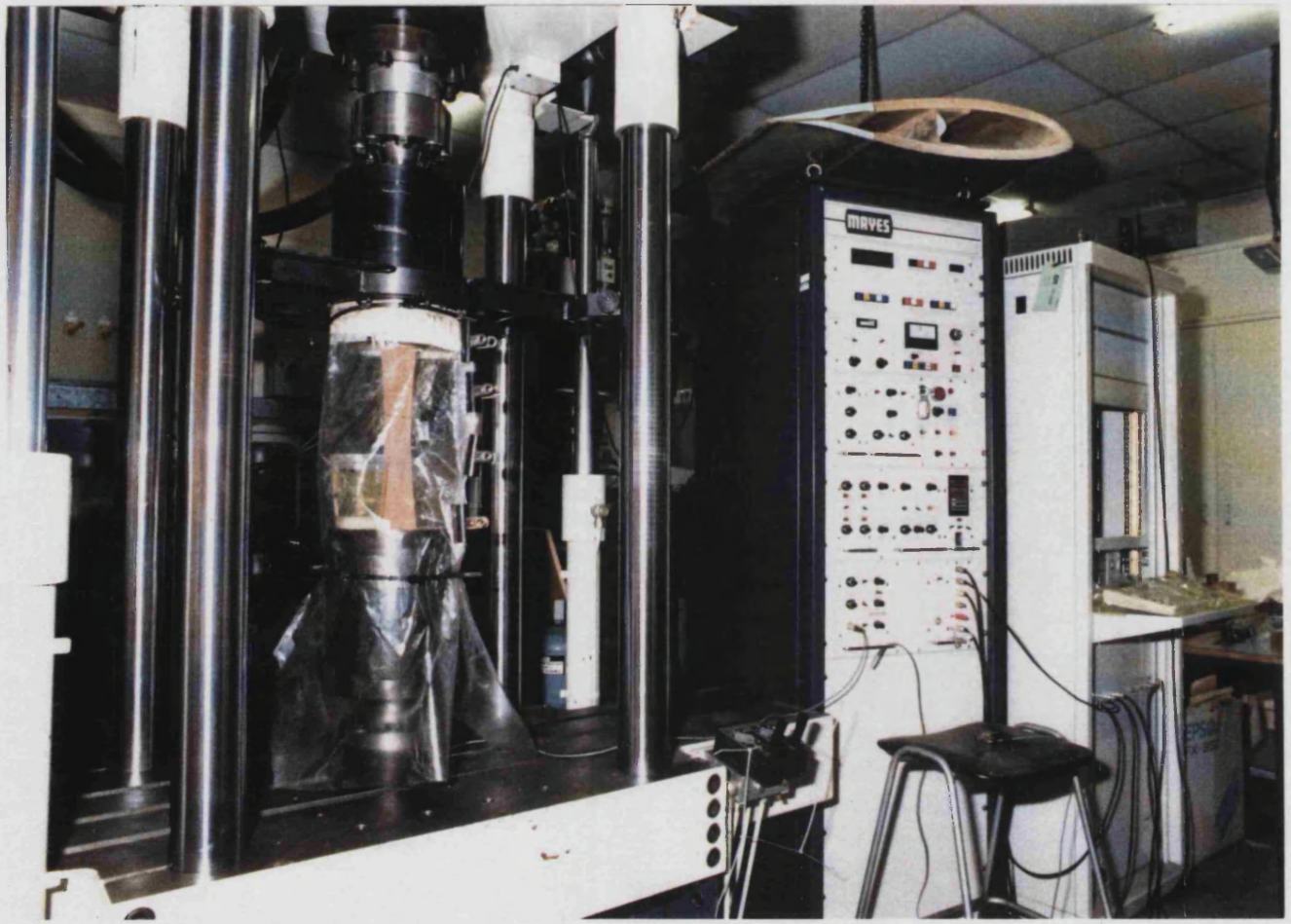

Fig.6.2. The four column Mayes 20 tonne servohydraulic fatigue machine. The photograph shows a sample in position, the control panel and the Dartec 9500 controller at the extreme right.

the evaluation of alternative laminating adhesives (Chapter 17). At the end of the project money was awarded by the Energy Technology Support Unit (ETSU) to purchase a second controller for the second machine enabling it to perform the same range of tests as the four column Mayes.

When the Mayes is controlled by the Dartec it is necessary to stop the cycle generator in the Dartec when a sample fails in order to record the number of cycles to failure. To achieve this a flip flop circuit was designed and installed by Simon Bowman to send a pulse to the Dartec at failure when the Mayes overtravel trips were activated and the test stopped. This pulse was used to stop the cycle generator.

6.2.2. Dartec 9500 controller

The Dartec 9500 controller is a multifunctional system which enables fatigue tests on the Mayes to be driven via a personal computer and allows the recording of data as a test proceeds.

Two types of tests can be run using the Dartec controller via the 'complex' and 'profile' options. In the complex option constant amplitude and block loading test sequences can be constructed. The maximum and minimum loads, frequency and number of cycles are required for each block of loading cycles. These can be the same for a constant amplitude test or vary for block loading sequences. An example of a complex file written to perform a constant amplitude test at R=10 with a maximum compressive stress of 50MPa is given in table 6.1. In all four stages the wave form generated is sinusoidal and the mode is 'load standalone'. This means that the test is run in load control on a fatigue rig which is not an integral part of the Dartec machine. The first two stages are low amplitude cycles which allow the wood to bed into the grips before the maximum load is applied. Without these initial cycles the samples often slipped in the grips. Level A is the minimum compressive load applied to the sample and level B is the maximum. The values in stage 3 have been calculated for a particular sample so that the applied stresses are -5MPa and -50MPa [R=10]. The frequency depends on the load levels and is calculated to give a constant rate of loading of $400MPa.s^{-1}$. In all tests the frequency was between 4 and 7Hz, low enough to avoid the sample warming up and affecting its moisture content and mechanical properties. Stage 3 consists of 50000 cycles which are repeated 200 times. If the sample has not failed by this stage (10^7 cycles) it is termed a runout and stage 4 stops the test. In practise very long term tests were stopped between 10^6 and 10^7 cycles, a testing time of about one month.

```
DARTEC SOFTWARE                                          COMPLEX DATA

Date  08-03-1994
Time  11:06:34

File: R1050B                  1st stage  1  Last stage  4  Repeats   1
Cell status  MAIN CELL        Load scaling   100 kN

                                  Stage : 1
                                  ---------

Waveform  : Sine                          Hold      : No hold
Mode      : Load Standalone               Delay     : 0 ms
Level A   :   1.000 %                    A[max]    :   0.000 %
Level B   :  10.000 %                    A[min]    :   0.000 %
Freq      :    4.44 Hz                   B[max]    :   0.000 %
Cycles    :     2                        B[min]    :   0.000 %
Sync is OFF                             Branch to   0
                                        Next stage  2
                                        Branches    0

                                  Stage : 2
                                  ---------

Waveform  : Sine                          Hold      : No hold
Mode      : Load Standalone               Delay     : 0 ms
Level A   :   3.000 %                    A[max]    :   0.000 %
Level B   :  30.000 %                    A[min]    :   0.000 %
Freq      :    4.44 Hz                   B[max]    :   0.000 %
Cycles    :     2                        B[min]    :   0.000 %
Sync is OFF                             Branch to   0
                                        Next stage  3
                                        Branches    0

                                  Stage : 3
                                  ---------

Waveform  : Sine                          Hold      : No hold
Mode      : Load Standalone               Delay     : 0 ms
Level A   :   5.540 %                    A[max]    :   0.000 %
Level B   :  55.350 %                    A[min]    :   0.000 %
Freq      :    4.44 Hz                   B[max]    :   0.000 %
Cycles    : 50000                        B[min]    :   0.000 %
Sync is OFF                             Branch to   3
                                        Next stage  4
                                        Branches    200

                                  Stage : 4
                                  ---------

Waveform  : Sine                          Hold      : No hold
Mode      : Load Standalone               Delay     : 0 ms
Level A   :   0.000 %                    A[max]    :   0.000 %
Level B   :   1.000 %                    A[min]    :   0.000 %
Freq      :    0.00 Hz                   B[max]    :   0.000 %
Cycles    :     1                        B[min]    :   0.000 %
Sync is OFF                             Branch to   0
                                        Next stage  1
                                        Branches    0
```

Table 6.1. A 'complex' file, written to perform constant amplitude loading at R=10 with a minimum stress of -50MPa.

The 'profile' option enables complex load-time histories to be played through a sample until failure occurs. The complex load-time history can correspond to a standard

complex testing sequence, e.g. WISPER (Poppen and Bach, 1991) or can be based on data captured from an instrumented blade when in service (Chapter 15). The load-time history is inputted into the 9500 controller in the form of a .dac file which is generated by a routine in the nCode software from an ASCII data file. Once in the 9500 controller it can be modified by adding extra cycles and changing the scaling to suit the particular test.

Table 6.2 shows the common data page for a complex load-time (l-t) history test. The data it contains applies to all the turning points in a l-t history. The features of note are that the waveform is sinusoidal, the control mode is load standalone and the test is rate controlled, as in 'complex' driven tests. The sequence repeats itself 100000 times before stopping.

Data is	: 16 Bit Normal/Inverted	: Inverted Fullscale	: 100.000 %
Scale	: 100.002 %	Offset	: 0.000 %
Waveform	: Sine	Sync is	: OFF
Control Mode is	: Load Standalone	Rate/Frequency	: Rate
Peak Hold is	: OFF	Peak Feedback is	: Stroke
Peak Error Band	: 0.000 %	Peak Delay Time	: 0 mS
Repeat count	: 100000	Channel Number	: 1
Created	: 13:16 08-03-1994	Last Update	: 13:17 08-03-1994

Table 6.2. Common data page for a complex load time history test.

Once a profile or complex data file is loaded into the 9500 controller the test can be run within the 'advanced capture' mode in order to collect stress-strain hysteresis loop data. An example of a data capture table is given in table 6.3. Such a file can have up to 200 loop captures programmed. This example is a capture table from a complex load-time history test. The 'cycle trigger' is set to initiate data capture at certain points in a test. In this case data capture is calculated to occur at four consecutive constant amplitude cycles every few passes through the load time history so that a direct comparison can be made of the wood properties as fatigue progresses. The Dartec is programmed to capture load and extension data every 2.00ms until 200 or 400 data points have been recorded. The load data comes from an output on the load cell and the extension data is collected via a clip gauge attached to the sample surface.

Before the hysteresis loop capture facility was used in tests, characterisation of its performance was carried out. In particular, it was necessary to determine which loop was actually captured when a trigger was reached and also the time delay between the

trigger and the start of data capture. The details of this characterisation are contained in Appendix A.

```
**********************************************************************
   D A R T E C   S O F T W A R E  - - - - - - -  D A T A   C A P T U R E
**********************************************************************

TEST            08-03-1994     11:12:29
```

Capt. No.	Cycle Trigger	Storage Interval	Store Size	Cyclic Store	Store Flags: Load	Stroke	Extn	Ex-
1	18	2.00mS	200	No	Yes	No	Yes	No
2	42	2.00mS	200	No	Yes	No	Yes	No
3	67	2.00mS	400	No	Yes	No	Yes	No
4	11998	2.00mS	200	No	Yes	No	Yes	No
5	12022	2.00mS	200	No	Yes	No	Yes	No
6	12047	2.00mS	400	No	Yes	No	Yes	No
7	23978	2.00mS	200	No	Yes	No	Yes	No
8	24002	2.00mS	200	No	Yes	No	Yes	No
9	24027	2.00mS	400	No	Yes	No	Yes	No
10	59918	2.00mS	200	No	Yes	No	Yes	No
11	59942	2.00mS	200	No	Yes	No	Yes	No
12	59967	2.00mS	400	No	Yes	No	Yes	No
13	119818	2.00mS	200	No	Yes	No	Yes	No
14	119842	2.00mS	200	No	Yes	No	Yes	No
15	119867	2.00mS	400	No	Yes	No	Yes	No
16	179718	2.00mS	200	No	Yes	No	Yes	No
17	179742	2.00mS	200	No	Yes	No	Yes	No
18	179767	2.00mS	400	No	Yes	No	Yes	No
19	239618	2.00mS	200	No	Yes	No	Yes	No
20	239642	2.00mS	200	No	Yes	No	Yes	No
21	239667	2.00mS	400	No	Yes	No	Yes	No
22	479218	2.00mS	200	No	Yes	No	Yes	No
23	479242	2.00mS	200	No	Yes	No	Yes	No
24	479267	2.00mS	400	No	Yes	No	Yes	No
25	718818	2.00mS	200	No	Yes	No	Yes	No
26	718842	2.00mS	200	No	Yes	No	Yes	No
27	718867	2.00mS	400	No	Yes	No	Yes	No
28	958418	2.00mS	200	No	Yes	No	Yes	No
29	958442	2.00mS	200	No	Yes	No	Yes	No
30	958467	2.00mS	400	No	Yes	No	Yes	No
31	1198018	2.00mS	200	No	Yes	No	Yes	No
32	1198042	2.00mS	200	No	Yes	No	Yes	No
33	1198167	2.00mS	400	No	Yes	No	Yes	No

Table 6.3. Data capture table.

In the constant amplitude tests hysteresis loop capture was also triggered to great effect using the 'window trips' option in the 'advanced capture' menu. Fig.6.3 shows the principle by which the window trips function, using a reverse loading test as an example. Once the test has been started a window is set around the maximum and minimum strain gauge outputs of, for example, 2.5% full scale deflection. As the test proceeds creep and fatigue damage occur and the strain values change. The moment one value exceeds the trip values hysteresis loop capture is triggered. The window then resets itself around the most recent trigger value. In this way data capture is triggered at the point in the test where the strains are changing rapidly, namely at the end of the test, enabling changes in properties to be followed which would otherwise be missed. At the start of testing the window trips were not functioning correctly so large and rapid

changes in properties were missed on some of the early tests. However, they can be assumed to have existed as they were clearly seen in the later tests.-

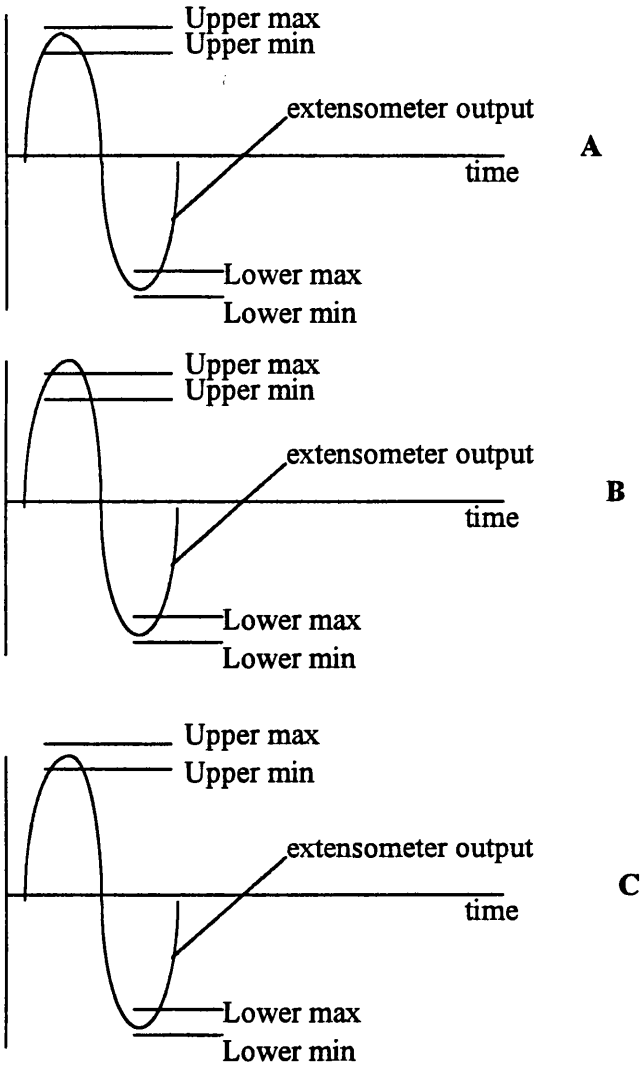

A. The window trips are set above and below the maximum and minimum extensometer strain output.

B. As creep and fatigue damage builds up the maximum extensometer output increases and exceeds the upper max level. As a result a hysteresis loop is captured.

C. The upper window trip levels reset themselves around the new max extensometer output.

Fig.6.3. Diagram showing operation of the window trips

Before a test was started it was necessary to run a complex routine to set the output signal on the cable from the Dartec to zero volts. This was essential because unless the zero routine was run the signal on the Dartec output cable would be the one at the point

of failure of the sample in the previous test. Otherwise an instantaneous load could be applied to the sample and cause damage or failure.

6.2.3. Clip gauges

Two clip gauges were used during the course of the testing to measure the strains experienced by the wood composite. They had knife edge blades and were located into small steel grooved tabs which were attached to the centre of each sample using 'Araldite Rapide' prior to each test. The steel tabs served to locate the clip gauges securely throughout a test and prevented the sharp blades damaging the sample surface and consequently initiating failure. The gauge was held onto the sample using two steel springs and elastic bands at each end of the gauge, fig.6.4. Both gauges were calibrated regularly throughout their use in order to obtain an accurate calibration coefficient to convert the gauge's output into a strain value. Fig.6.5 shows a typical calibration curve for one of the gauges. This also required an accurate measurement of the gauge length for each sample and was achieved to 0.01mm using a digital micrometer.

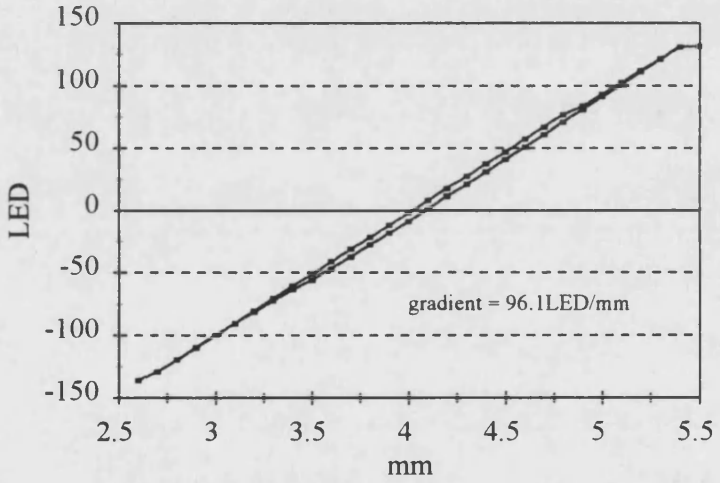

Fig.6.5. Typical extensometer calibration curve.

6.2.4. nCode analysis software

Fatigue analysis software supplied by nCode International Ltd. was used to process the stress-strain hysteresis loops. The nCode software package had been developed primarily for metal fatigue but an extra routine, LPA, was written to deal with the loop analysis. The LPA program enabled the Dartec data files containing raw hysteresis loops to be read, the scaling factors applied and important values calculated for each loop. Table 6.4 shows a typical output for a constant amplitude reverse loading test. The values of most importance are the loop areas (Jm^{-3}), moduli (GPa), strains (dimensionless) and stresses (Pa). The data are imported into the spreadsheet package

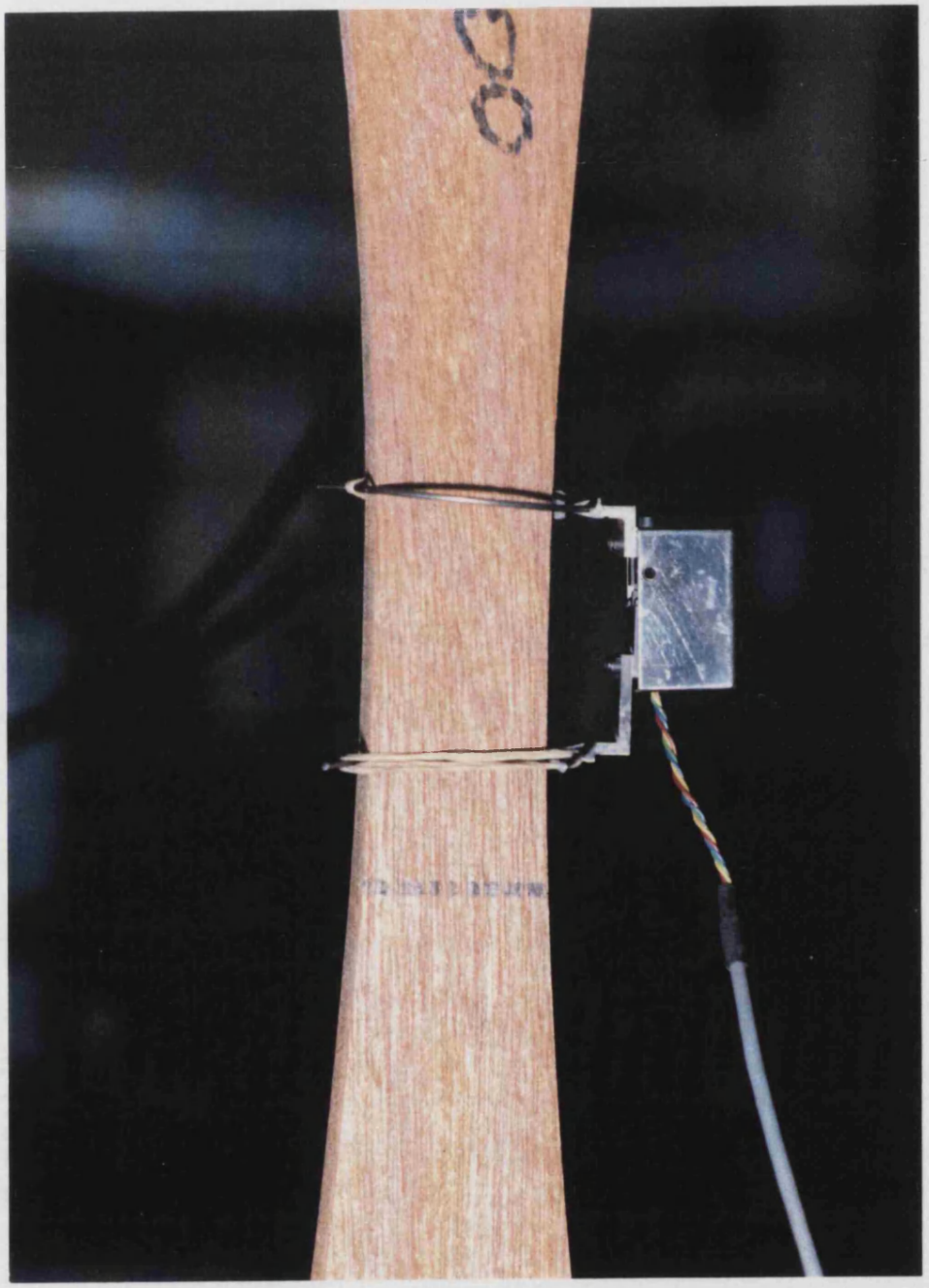

Fig.6.4. Detail of the extensometer attachment to the sample.

'Quattro Pro for Windows' where the data can be further manipulated and the properties displayed graphically.

Loop	Intercept	Corr coef	e at mean S		Area	Modulus	emin	Smin	emax	Smax
1	1.5E+07	0.9983	-0.00182	-0.00136	29887	9.1118	-0.00704	-4.9E+07	0.003724	5E+07
2	1.6E+07	0.9979	-0.00186	-0.00132	33487	8.9914	-0.00715	-4.9E+07	0.003761	5E+07
3	1.6E+07	0.9975	-0.00192	-0.00132	36144	8.898	-0.00724	-4.9E+07	0.003774	5E+07
4	1.6E+07	0.9972	-0.00194	-0.00133	38560	8.8161	-0.00733	-4.9E+07	0.003784	5E+07
5	1.6E+07	0.9968	-0.00199	-0.00132	40925	8.7387	-0.00741	-4.9E+07	0.003787	5E+07
6	1.6E+07	0.9964	-0.00204	-0.00132	43193	8.6632	-0.00749	-4.9E+07	0.003793	5E+07
7	1.6E+07	0.996	-0.00208	-0.00133	45472	8.5921	-0.00757	-4.9E+07	0.0038	5E+07
8	1.6E+07	0.9957	-0.00214	-0.00131	47738	8.5286	-0.00764	-4.9E+07	0.003805	5E+07
9	1.6E+07	0.9952	-0.00216	-0.00131	50070	8.4553	-0.00772	-4.9E+07	0.003805	5E+07
10	1.7E+07	0.9947	-0.00222	-0.00133	52396	8.3865	-0.00779	-4.9E+07	0.003809	5E+07
11	1.7E+07	0.9944	-0.00228	-0.00132	54945	8.3165	-0.00787	-4.9E+07	0.003816	5E+07
12	1.7E+07	0.9941	-0.00231	-0.00133	57506	8.2434	-0.00796	-4.9E+07	0.00382	5E+07
13	1.7E+07	0.993	-0.00236	-0.00132	60257	8.1665	-0.00805	-4.9E+07	0.003821	5E+07
14	1.7E+07	0.9927	-0.00246	-0.00133	63193	8.0855	-0.00815	-4.9E+07	0.003825	5E+07
15	1.7E+07	0.9921	-0.00251	-0.00134	66350	8.0005	-0.00825	-4.9E+07	0.003829	5E+07
16	1.8E+07	0.9916	-0.00257	-0.00133	69733	7.9051	-0.00837	-4.9E+07	0.00383	5E+07
17	1.8E+07	0.9902	-0.00264	-0.00132	73725	7.8118	-0.00849	-4.9E+07	0.003835	5E+07
18	1.8E+07	0.9889	-0.00273	-0.00133	78137	7.7125	-0.00863	-4.9E+07	0.003839	5E+07
19	1.8E+07	0.9878	-0.00282	-0.00133	83161	7.5971	-0.0088	-4.9E+07	0.003839	5E+07
20	-5274000	0.000697	0.02255	0.02255	7.055	0.26475	0.02255	481900	0.02256	904000

Table 6.4. Typical output for a constant amplitude test at R=-1.

At the start of the work there were considerable problems in getting the LPA program to work in the desired manner. This centred on the manner in which the program read the Dartec data file and how it calculated the loop area of each hysteresis loop. After numerous attempts by nCode to modify the program two days were spent at nCode International Ltd. in Sheffield to oversee the complete re-writing of the program so that it could accurately and reliably calculate the hysteresis loop area.

6.3. Summary

In this section the following have been presented:

- The sample lay-up, manufacture and geometry.
- The Mayes servohydraulic fatigue rigs.
- The Dartec 9500 controller, and in particular, the functioning of the window trips and clip gauges.
- The nCode software and the format of the data it generates.

The manner in which the equipment is used for particular types of test is given in the relevant chapters. [Chapter 7 for axial static testing, Chapter 8 for constant amplitude stress-strain hysteresis loop capture and Chapter 15 for complex loading.]

7. AXIAL STATIC TESTING

Tensile and compressive axial static tests were carried out on samples from a range of panels for inclusion with the fatigue data in S-logN plots (Chapter 8) and to compare their ultimate static tensile and compressive strengths with those obtained previously (Bonfield, 1991). Ten samples were tested in tension and twelve in compression using the Mayes servohydraullic fatigue machines. The tests were controlled via the Dartec 9500 using a 'complex' routine which applied a single cycle in a triangular waveform up to ±100kN, a load considerably greater than the expected tensile and compressive strengths of the Khaya-epoxy composite. The load was applied to the sample at a rate of $10MPas^{-1}$. This is much slower than the rate used in fatigue tests ($400MPas^{-1}$), and was adopted so that the samples did not pull out of the grips but had sufficient time to 'bed in'. A data capture file was written with a single capture calculated to last the whole of the loading portion of the triangular wave so that data were captured until after failure had occurred. The applied load was recorded in all tests and used to calculate the ultimate tensile stress (UTS) or ultimate compressive stress (UCS) for each sample. The cross head displacement was recorded in six of the tensile tests and all of the compressive tests. It was used to estimate the modulus of the sample.

In seven of the compressive tests the clip gauge was attached so the strain could be measured directly. This enabled the production of complete stress-strain curves for a representative number of samples tested in compression. This could not be done in the tensile tests because the clip gauge was likely to be pulled apart when the sample failed. However, the tensile modulus was measured on a second set of samples which were loaded up to a stress of 20MPa. This was well below both the UTS and the elastic limit of the wood so the clip gauge could be used without any likelihood of damaging it. The elastic modulus of each sample was measured from the stress-strain data captured.

The Dartec data files obtained from each test were converted directly to ASCII format using a modified Dartec basic program and manipulated in 'Quattro Pro for Windows'.

7.1. Results and discussion

7.1.1. 'Stress-strain' curves

Data from two static tensile tests are presented in figs.7.1 and 7.2. [The full set of curves are contained in Appendix B]. In fig.7.1. only the applied load was recorded by the Dartec and it is clear that the load increases at the set rate of $10MPas^{-1}$. It can be

appreciated that once the sample has failed the Mayes trips operate almost instantaneously and the load drops to zero extremely rapidly.

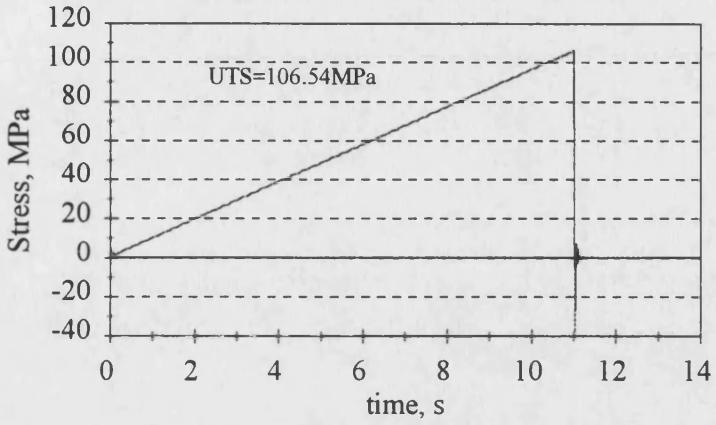

Fig.7.1. A typical static tensile loading curve where only the load was recorded, test t_st_1.

In fig.7.2. stress is plotted against cross-head movement (stroke). The cross-head movement equals the total change in length of the sample and includes the change in strain in the gauge length and in the necked portion of the sample as well as any movement in the sample grips. It is important to appreciate that a stress-stroke curve is not the same as a stress-strain curve since the former is a combination of the basic material response to loading and additional features caused by the sample geometry and gripping arrangement, while the latter is the basic material response.

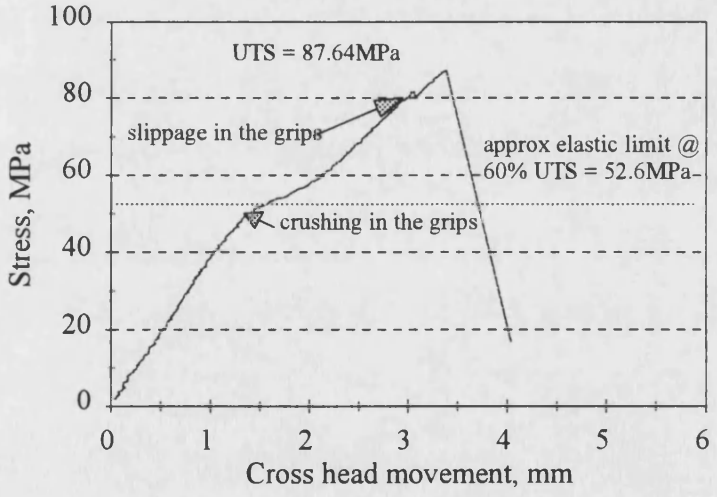

Fig.7.2. A typical static loading curve where the load and cross head movement were recorded, test t_st_2.

The stroke increases linearly with stress up to about 40MPa, after which point a departure from linearity was observed. This was seen in all samples where cross-head

movement was recorded at between 40MPa and 52MPa (except sample t_st_5, at 33MPa). The curve returns to being linear again at between 56MPa and 59MPa (except sample t_st_5, at 39MPa) as the stress increases, and remains linear until failure occurs. The gradient of this second linear portion is lower than at the start of loading. When the sample fails the stroke increases rapidly by several mm. It is this movement which could damage a clip gauge if it was attached.

It is well established that wood exhibits an approximately linear response to a rapidly applied load, fig.7.3 (Dinwoodie, 1981) and fig.7.4 (Sun, 1992), so the unusual features in fig.7.2 can be attributed with certainty to other external factors. Dinwoodie (1981) states that wood behaves linearly up to about 60% of the ultimate tensile stress (UTS). 60% UTS falls between the two linear portions of the stress-stroke curves for all samples, except t_st_5, so it is likely that the change in gradient of the stress-stroke curves is associated with the combination of the elastic limit of proportionality of the wood and increased movement in the grips. Sun, 1992, reported a limit of elasticity for Khaya of 45±5MPa, slightly lower than 60% UTS but comparable to the stress at which initial departure from the linear loading response occurred.

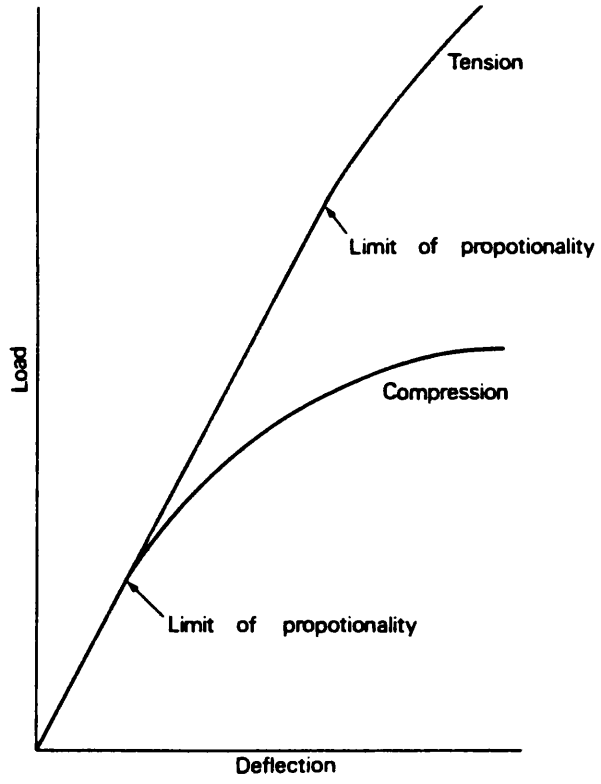

Fig.7.3. Load-deflection graphs for timber stressed in tension and compression parallel to the grain. The assumed limit of proportionality for each graph is indicated (Dinwoodie, 1981).

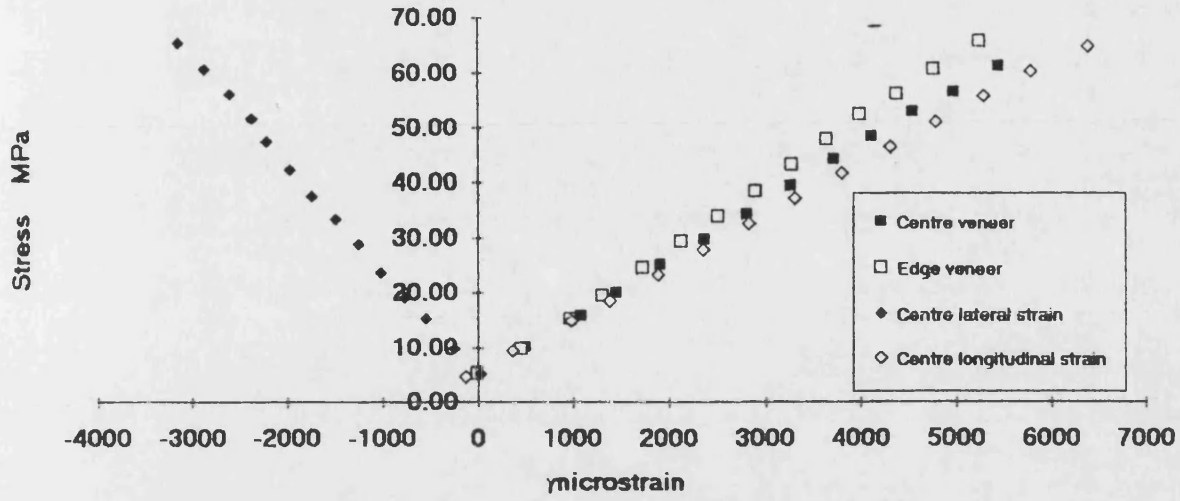

Fig.7.4. Stress-strain relationship in unjointed Khaya with no GRP skin (Sun, 1993).

Figs.7.5 and 7.6 contain data from the static compressive tests. Fig.7.5 shows a typical stress vs. cross-head movement trace and fig.7.6 shows a stress-strain plot. The full set of plots are presented in Appendix B. In fig.7.6 the compressive stress increases linearly up to approximately 75% UCS and the maximum load is reached at a strain of -0.86%. At this point a macroscopic compression crease is formed which grows rapidly and causes the compressive strain to increase. The load falls to zero at the point when the Mayes overtravel trip operates and stops the test. It is clear that the sample can still sustain a compressive load even though it contains a compression crease and the failed wood is weaker than in its undamaged state. However, once the crease has formed it makes the wood unstable and the compression crease develops quickly. For the sample in fig.7.6. the load falls from the maximum to zero in 0.2 seconds.

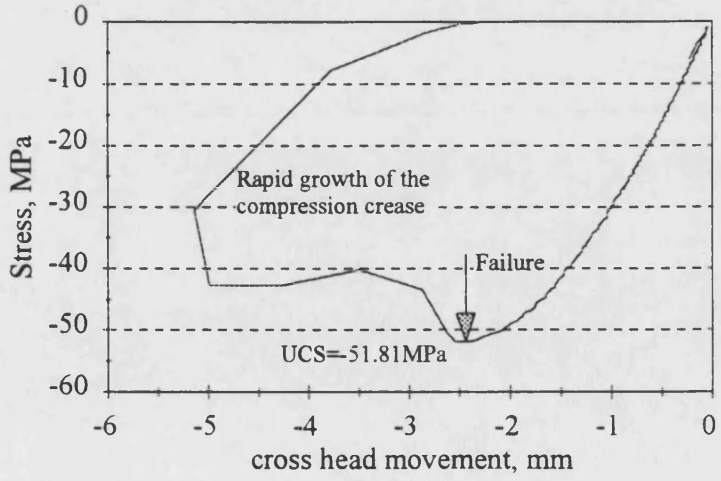

Fig.7.5. A typical static compressive loading curve where load and cross head movement were recorded, test c_st_1.

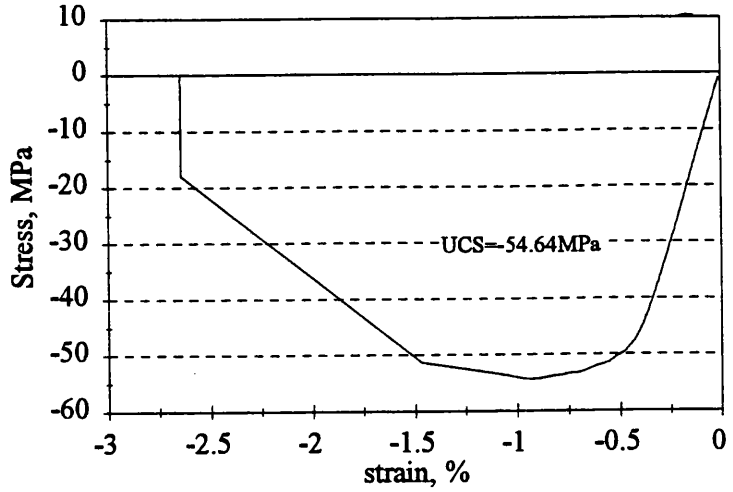

Fig.7.6. A typical static compressive loading curve where the load and strain were recorded, test c_st_3.

Dinwoodie (1981) stated that in compression the initial stages of damage appear at as low as 25% UCS and that the stress-strain curve departs from linearity at between 30 to 50% of the failure stress. He attributes a failure to observe this to a lack of sensitivity in the testing equipment. In these tests the departure from linearity was observed to occur between 56% and 86% with a mean of 74%. It would be surprising if these high values were due to a lack of sensitivity on the part of the testing equipment since strain data were taken from a clip gauge attached to the sample which is capable of measuring a 0.001% strain change. Therefore, it must be assumed that the composite does behave linearly up to between 56% and 86% UTS.

The mean strain to failure (taken as the point where the maximum load was sustained) for the samples tested with the clip gauge attached was -1.03%, very close to the expected value of -1%.

7.1.2. Tensile and compressive strengths

A mean tensile strength of 85.41MPa, with a standard deviation of 10.22MPa, was obtained, table 7.1. This is similar to, but slightly higher than, the value obtained by Bonfield (1991) who found a mean value of 81.8±9.3MPa. Sun (1993) found a mean tensile strength for unjointed Khaya samples of 67.7MPa. This considerably lower value was likely to be because failure occurred in the tabs at the grips. Sun's samples coated with glass reinforced epoxy (GRE) had a higher mean tensile strength of 76.7MPa, probably because the GRE protected the wood from being cut by the grips.

Sample	UTS, MPa	Calculated tensile tangential modulus, GPa	Comments
1. Old board	83.02	---	
2. Board B3	74.55	9.53	
3. Board B4	90.07	7.67	
4. New pale coloured board	66.63	9.25	Contained 2 highly angled grain veneers
5. New pale coloured board	106.54	8.55	
6. New pale coloured board	82.64	---	
2. Board B4	94.21	---	
8. Board B4	83.27	---	
9. Board B3	86.17	9.27	
10. Board B3	81.97	10.38	
mean value	**85.41**	**9.11**	
Std. dev.	**±10.22**	**±0.92**	

Table 7.1. Static tensile strength data and calculated stiffness for the wood composite.

Table 7.2 contains the compression test results. A mean ultimate compressive stress of 52.69MPa, with a standard deviation of 4.86MPa, was obtained. This compares with the value obtained by Bonfield (1991) who tested 32 samples and obtained a mean value of 49.47±2.77MPa.

Although the static strengths are slightly higher than those obtained by Bonfield (1991) the ratio of the ultimate compressive to tensile strengths (UCS/UTS) are approximately the same. UCS/UTS for the current tests is 0.617 compared to the tests carried out by Bonfield (1991) where UCS/UTS = 0.605. This suggests that the samples tested in this programme have the same cellular structure as those tested previously but are of a slightly higher density than those tested by Bonfield, probably because the wood has slightly thicker cell walls (Dinwoodie, 1981).

The modulus values presented in tables 7.1 and 7.2 are discussed in section 7.2.3.

Sample	UCS, MPa	Ult. compressive strain, %	Compressive - modulus, GPa	
			measured	estimated
1. Old board	54.64	---	---	9.14
2. Board B4	45.25	---	---	8.11
3. Board B4	51.81	-0.93	12.00	11.90
4. Pale board	58.16	-0.86	11.00	11.26
5. Old board	64.31	-0.84	11.03	7.58
6. Old board	54.27	-1.55	11.10	10.25
7. Board B4	52.67	-1.04	9.68	11.07
8. Board with GRE coated end tabs	49.02	-0.82	8.89	11.45
9. Board with GRE coated end tabs	54.12	-1.14	12.00	7.17
10. Board with GRE coated end tabs	50.54		---	7.80
11. Board with GRE coated end tabs	50.43		---	5.48
12. Board B3	42.1		---	5.98
Mean value	**52.69**	**-1.03**	**10.81**	**8.93**
Std. deviation	**±4.86**	**±0.240**	**±1.15**	**±2.22**

Table 7.2. Static compressive strength, stiffness and strain data for the composite.

7.1.3. Estimated and measured tangential moduli

Tangential moduli values have been determined from one or more of the following, depending on the data captured during the test:

- direct measurement from a stress-strain curve,
- estimation from a load-stroke curve, or
- measurement from a low stress level test.

For the compression tests where the clip gauge was attached to the sample the tangential modulus was measured directly from the stress-strain curve and these results are

presented in table 7.2. For these measured values a mean compressive modulus of 10.81±1.15GPa was obtained. The compressive modulus was estimated for all samples according to the method outlined below and a mean value of 8.93±2.22GPa was obtained.

In order to calculate the tangential modulus of a sample from the cross head movement it was necessary to make an estimate of the strain in the gauge length during the linear portion of the loading curve. This was done according to the method presented in appendix B. An equation was developed which accounted for the sample geometry and could be solved for the modulus using a crosshead movement data point within the linear response part of the curve. A data point at an applied load of 10kN and its corresponding cross-head movement were used. This method was applied to all tests where cross-head movement had been recorded, see tables 7.1. and 7.2.

For the tensile tests a mean modulus of 9.11±0.92GPa was calculated, lower than Sun's measured mean value of 11.54GPa (1992).

It can be seen that in several cases the calculated and measured moduli values are similar, but that in others there are several GPa between the two. These differences may arise from two sources: slippage in the grips from the start of the test and variations in sample geometry. In the case where the calculated values are lower than the measured values slippage in the grips is most likely, as this would give rise to an increased cross head movement. This is backed by the fact that the low calculated moduli values tended to occur for the samples with GRP coated end tabs which were seen to cause slipping in the grips even at low stress levels. The average modulus value is lower than expected on account of the samples where slipping in the grips occurred. If the samples with GRP end tabs are omitted an average value of 9.71±1.73GPa is obtained.

The tensile elastic moduli values measured on a second set of samples, without loading to failure, are presented in table 7.3. A mean value of 8.67±0.93GPa was calculated from the stress-strain plots obtained. This is 19.8% lower than the measured stiffness in compression and is a significant difference and must be attributed to variations between batches of samples. Conners and Medvecz (1991) found that on average hardwoods were slightly stiffer in tension than in compression with an average ratio of stiffnesses of 1.08 although they did report a 0.84 ratio which is similar to the results presented here.

Sample	Measured tensile modulus, GPa
Board B2	7.99
Board B2	8.02
Old board	9.59
Old board	10.00
Old board	7.77
Mean value Std. deviation	**8.67** **±0.93**

Table 7.3. Measured tensile elastic modulus values

7.1.4. Normalised modulus changes in compression

The gradient of the stress-strain curve was calculated between adjacent stress and strain data points throughout each test for samples where the extensometer was attached, seven samples in all. A typical plot is presented in fig.7.7 for sample c_st_6. The fluctuations in the calculated moduli values are due to fluctuation in the load cell output voltage.

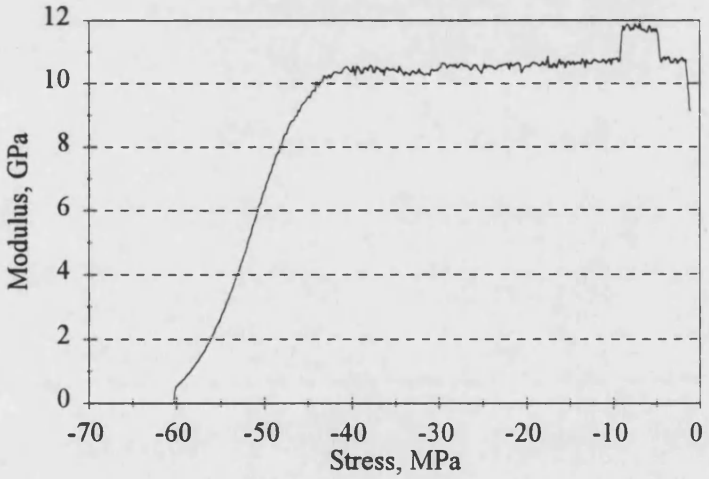

Fig.7.7. Typical plot of modulus vs stress level.

These plots were normalised on the x- and y-axes by dividing by the UCS and the initial modulus respectively. The curves all overlay each other as is shown schematically in fig.7.8. Up to 80% UCS the moduli remained inside the 0.9 to 1.1 mod/mod_0 range. In the last 20% of the sample's life the modulus fell fairly linearly to,

on average, 20% of its initial value at failure. This is a useful plot with which to compare the changes in dynamic modulus as a result of fatigue damage accumulation.

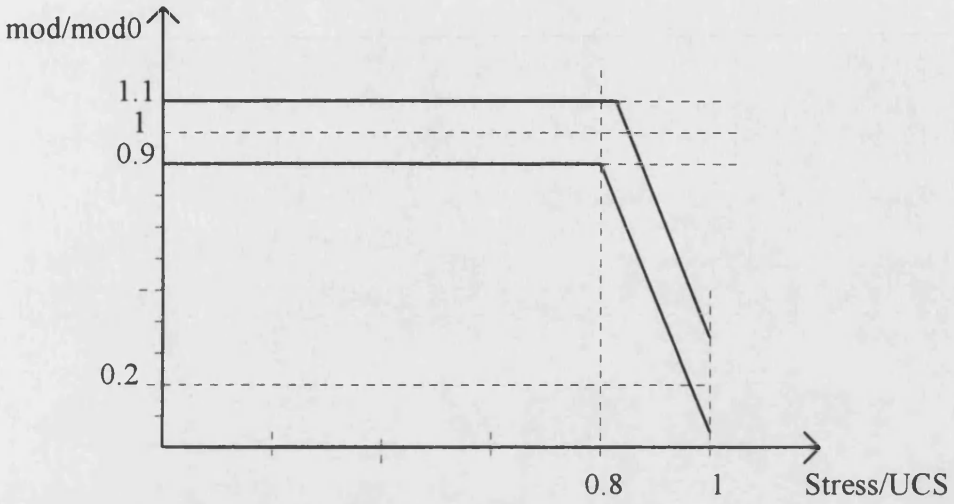

Fig.7.8. Normalised curve for change in modulus with stress for wood composite under static compression loading.

7.1.5. Strength-stiffness correlation for compression loading

Both strength and stiffness have a high dependency on the density of wood and, therefore, there exists a direct correlation between strength and stiffness (Dinwoodie, 1981). Strength was plotted as a function of stiffness for the samples tested in compression where both the stiffness and strength had been measured. Fig.7.9 shows this relationship and it can be seen that the stiffer samples tend to have the most negative UCS, as expected. A best fit line was calculated for the data and it is given in eq.7.1.

$$\text{Strength} = -2.47 \times (\text{Stiffness}) - 28 \qquad \text{eq.7.1.}$$

The units of strength and stiffness are MPa and GPa respectively. Although the number of data points is small and the scatter associated with wood properties this equation will give a rough estimate of the UCS of a sample from its modulus. It is anticipated that this could be useful in the normalising of S-N data in subsequent chapters.

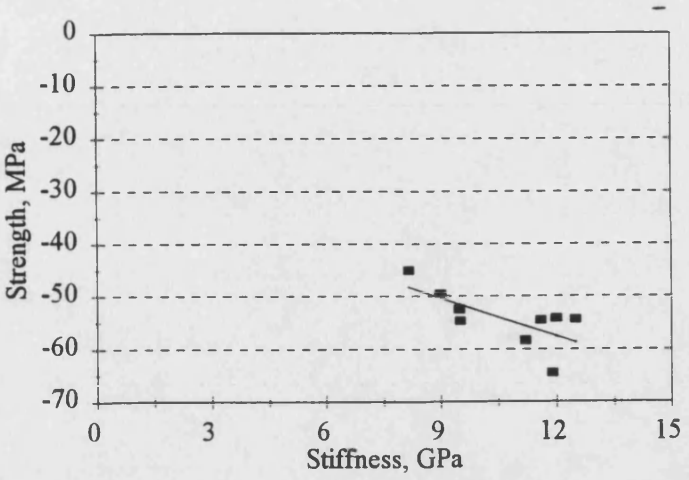

Fig.7.9. Stiffness-strength correlation for Khaya in compression.

7.2. Conclusions

Axial static tensile and compressive tests were carried out and the data captured were used to calculate the ultimate tensile and compressive strengths of the Khaya - epoxy laminate. The tangential tensile and compressive moduli were also measured and calculated. In addition the ultimate compressive strain was measured. These results are summarised in table 7.4.

	Ultimate strength, MPa	Strain at failure, %	Measured elastic modulus, GPa
Tension ± 1 std.dev.	85.41±10.22	---	8.67±0.93
Compression ± 1 std.dev.	52.69±4.86	1.03±0.24	10.81±1.15

Table 7.4. Summary of static test results.

The values obtained are close to the expected values obtained elsewhere. Although the material stiffness can be calculated using the method in Appendix B it was found to be somewhat unreliable due to slippage in the grips during the test.

It was observed that the modulus stayed within ±10% of the initial modulus for loads of up to 80% UCS after which the load dropped off linearly to 20±10% of the initial value at failure.

A linear relationship was found for stiffness and strength of Khaya in compression. The lower modulus samples tended to have lower UCS values, as would be expected.

8. CONSTANT AMPLITUDE STRESS-STRAIN HYSTERESIS LOOP CAPTURE

8.1. Introduction

The rationale behind the experimental programme for the capture of constant amplitude, stress-strain hysteresis loops is discussed in this section.

In addition, the S-logN curves obtained at each R ratio are presented, along with the different fracture morphologies observed. Although these results are not taken from stress-strain hysteresis loops, they are relevant to the discussion regarding the fatigue of wood.

The results and analysis of stress-strain hysteresis loop data have been divided into smaller sections and are presented in Chapters 9 to 14.

8.2. Experimental design

By capturing stress-strain hysteresis loops throughout the duration of a fatigue test it is possible to follow the changes in the wood composite's behaviour as fatigue damage accumulates. The trends in property changes can then be compared for different loading situations and stress levels.

Constant amplitude fatigue tests were carried out on standard geometry samples, fig.6.1, at R ratios of R=10 (compression fatigue), R=0.1 (tension fatigue) and R=-1 (reversed loading), fig.8.1. The tests at R=0.1 and R=10 were carried out so that it would be possible to identify the property changes associated with tension and compression fatigue respectively. Reverse loading fatigue was also used because it is the most damaging loading mode on account of the interaction of tension and compression fatigue damage.

Between three and five tests were carried out at the majority of load levels, with a maximum stress of 30MPa, 40MPa, 45MPa, 50MPa, 55MPa, 60MPa and 65MPa at R=0.1; a minimum stress of -45MPa, -47.4MPa, -50MPa, -52.5MPa and -55MPa at R=10 and maximum and minimum stresses of ±25MPa, ±30MPa, ±35MPa, ±40MPa, ±45MPa and ±50MPa at R=-1. These stress levels were chosen so that all the samples survived for between 10^2 and 10^7 cycles. In the compression tests these stresses were very close to the UCS because the S-N curve at R=10 is very flat. At R=0.1 the maximum fatigue stresses are much lower in proportion to the UTS.

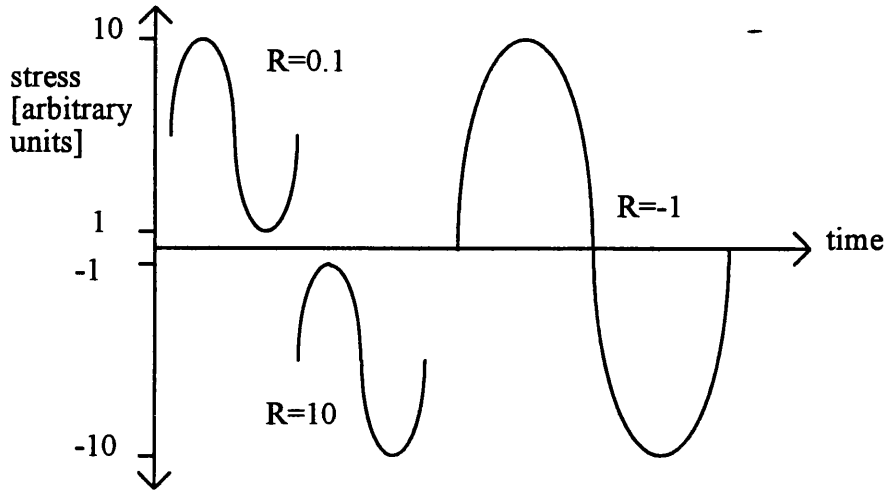

Fig.8.1. Diagram of R ratios used.

A minimum of 20 stress-strain hysteresis loops were captured per decade of loading cycles throughout each test. Capture times were either pre-set using the Dartec controller's advanced data capture facility or the window trips were used to trigger data capture when the properties were changing rapidly at the end of a test. The hysteresis loops were then processed using nCode's LPA routine and manipulated in 'Quattro Pro for Windows'. As the number of sets of hysteresis loops is large they are all presented in Appendix C. All property change data are shown graphically and the full complement of curves are assembled in Appendix D.

8.3. Basic results and discussion

8.3.1. S-N data

S-N data for tests at R=0.1, R=10 and R=-1 are presented in tables 8.1 to 8.3 and figs.8.2 to 8.6. The static data are included at logN=-0.602, one quarter of a loading cycle, as a static test is assumed to be a fatigue test where the maximum load is equal to the UTS or UCS of that sample. A line of best linear fit has been calculated for all fatigue data points, excluding run out samples [ones which did not fail]. The runout samples are indicated by the attachment of an arrow to the data point.

In tension fatigue up to 10^7 cycles to failure, the data points all fall below the range of UTS data, fig.8.2. The best linear fit line for the fatigue failure data points cuts the range of scatter in UTS values but falls above the cluster of run out values. The linear fit line is steeper than for R=10 which shows that wood is more sensitive to fatigue damage in tension than in compression.

valid tests	N		logN	Stress, MPa
rp130a	4036009	run out	6.61	29.6
rp130b	10000000	run out	7	30.8
rp140a	5758720	run out	6.76	40.5
rp140b	2464614	run out	6.39	40.3
rp140c	10000000	run out	7	40.7
rp145b	3137897		6.50	45
rp145c	2466211		6.39	45
rp150d	286528		5.46	50.6
rp150h	1286427		6.11	50.2
rp150i	100572		5.00	50.6
rp150j	113286		5.05	50.4
rp155b	72588		4.86	55.1
rp155c	664156		5.82	55.4
rp155d	281600		5.45	56.2
rp155e	278774		5.45	55
rp160a	2629		3.42	59.9
rp160d	43631		4.64	60.2
rp160e	6126		3.79	60.1
rp160f	45260		4.66	60.1
rp165a	227		2.36	66.47
rp165b	178		2.26	63.81
rp165c	716		2.85	63.74
rp165d	778		2.89	64.76

Table 8.1. S-N data at R=0.1.

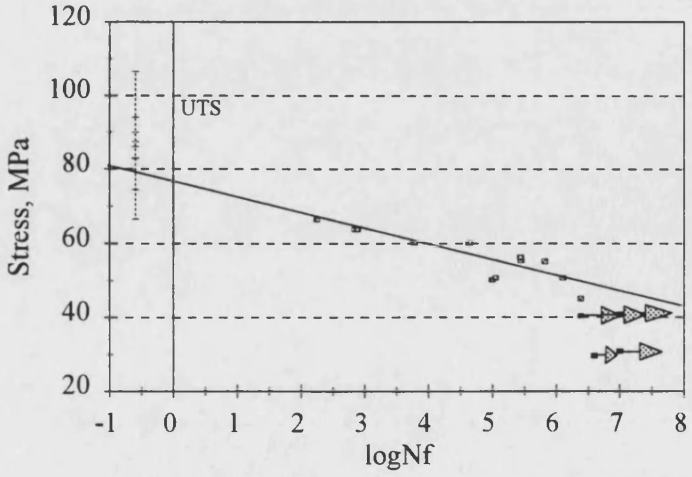

Fig.8.2. S-logN plot for tension fatigue at R=0.1.

valid tests	N		logN	Stress, MPa
r1045a	8267182		6.92	45
r1047a	2750		3.44	46.2
r1047b	3750		3.57	46.5
r1047c	2864773	run out	6.46	45.9
r1047d	5007214	run out	6.70	46.9
r1050a	1144386	run out	6.06	47.9
r1050b	25002		4.40	47.2
r1050d	4300000		6.63	46.9
r1050f	845		2.93	48.2
r1050g	10000000	run out	7	48.3
r1050h	11465		4.06	49.4
r1052a	25002		4.40	50.7
r1052b	845		2.93	49.6
r1052c	2203		3.34	50.2
r1052d	654		2.82	51.2
r1052e	12684		4.102	51.2
r1052f	1288		3.11	51.8
r1055a	5024		3.70	51.8
r1055b	191		2.28	53.9
r1055c	1278		3.11	53.9
r1055d	1527		3.18	54.5
r1055e	1366		3.14	54.6
r1055f	64		1.81	54.2

Table 8.2. S-N data at R=10.

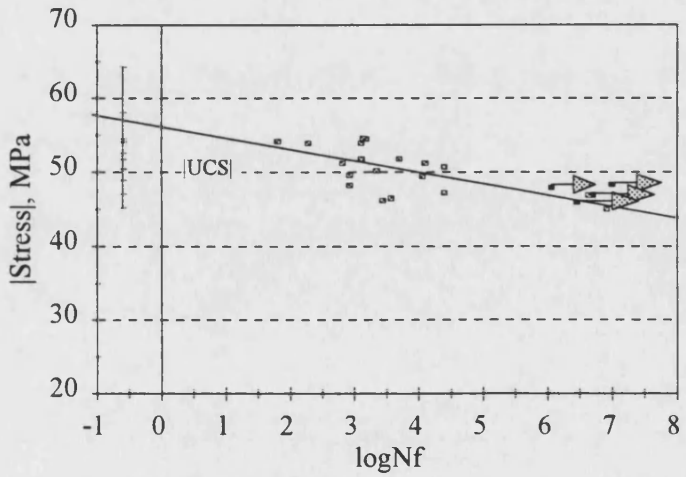

Fig.8.3. S-logN plot for compression fatigue at R=10.

In compression fatigue, fig.8.3, the data points fall within a small stress range and consequently the gradient of the linear fit is shallow. The linear fit passes through the range of UCS data at logN=-0.602 and also intersects the cluster of runout points. All the fatigue data points fall within the scatter of the UCS values. Similarly, at long lifetimes failed and runout samples are in close proximity to each other. It can be concluded that wood is unaffected by compression fatigue at stresses much below the UCS and consequently, the fatigue lifetime must be dependent on the UCS.

In order to try and reduce the amount of scatter in the data, the relationship presented in eq.7.1 was used to determine the expected UCS of each sample tested at R=10, using the dynamic modulus of the first hysteresis loop captured. The applied stress was then normalised by the expected UCS for each sample and the resultant S-logN curve is presented in fig.8.4. It has been overlaid by the same data also normalised by the mean UCS value of -52.69MPa. It is clear that there appears to be little significant difference between the two sets of fatigue data. The best fit lines for both normalisations are very similar and it must be concluded that although there is a relationship between modulus and UCS in static loading it is not necessarily beneficial to use it in fatigue situations.

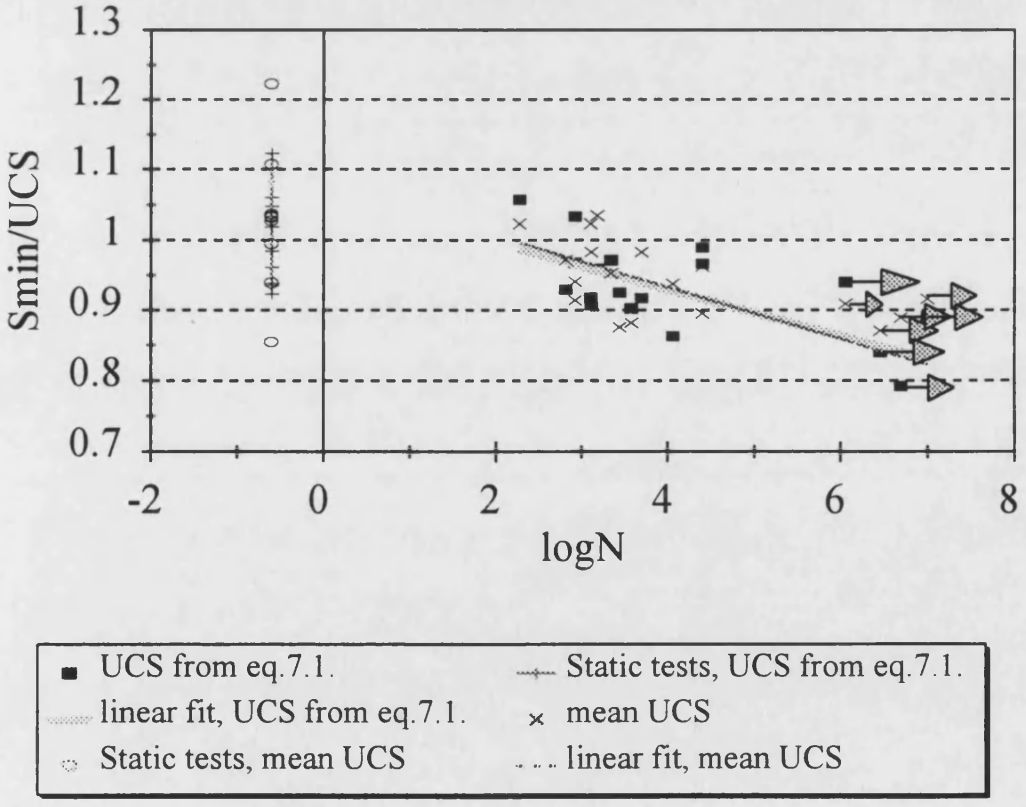

Fig.8.4. Normalised S-logN plot for compression fatigue at R=10. The UCS has been taken as the mean value measured in Chapter 7 and estimated from eq.7.1.

valid tests	N		logN	|Smax|
rm125a	4527983	run out	6.66	23.2
rm130c	613554		5.79	28
rm130f	1349103	run out	6.13	28.3
rm130g	156481		5.19	27.1
rm130h	631441		5.80	26.4
rm135a	8880		3.95	33
rm135b	6195		3.79	32.6
rm135c	193667		5.29	31.5
rm140a	5198		3.72	38.5
rm140b	4751		3.68	37.8
rm140e	1799		3.26	37
rm145a	499		2.70	42.7
rm145b	683		2.83	42.8
rm145c	1683		3.23	43.5
rm150a	678		2.83	48
rm150b	222		2.35	50.7
rm150c	125		2.10	50.3

Table 8.3. S-N data at R=10.

In reverse loading fatigue, fig.8.5, the best fit line falls in between the static and compressive strength values and passes close to the runout data points. The range of stress levels over which failure occurred is the largest of the three loading regimes and the best fit line has the steepest gradient. This shows that reverse loading fatigue is the most damaging.

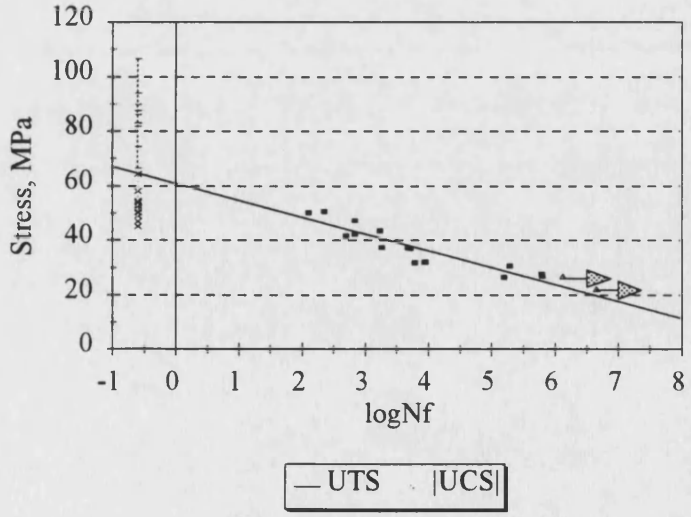

Fig.8.5. S-logN plot for reverse loading fatigue tests at R=-1.

All the data from tests at R=0.1, R=10, R=-1, and the static tests are presented in fig.8.6. The difference in gradients of the best line fits is apparent, with the steepest gradient at R=-1 and the shallowest at R=10.

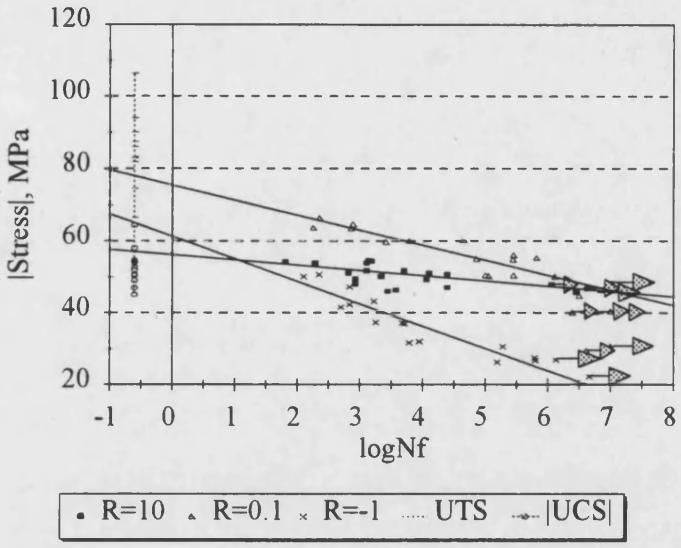

Fig.8.6. S-logN data for all samples tested at R=0.1, R=10 and R=-1.

It is unexpected that at $\log N_f$=-0.603 the line for R=-1 should fall between the UTS and UCS values. Bonfield (1991) found that in reverse loading fatigue the best fit line fell through the UCS data points, suggesting that fatigue failure at R=-1 was controlled by the build up of compression fatigue damage. However, in all but three tests at R=-1 the minimum applied stress was smaller in magnitude than the lowest UCS value, the minimum stress level at which compression fatigue was seen to occur. Given that fatigue damage does not appear to accumulate in wood at stresses below the UCS range it is not surprising that there is no relationship between the UCS and the reverse loading best fit line.

It cannot be denied, however, that the gradient of the best fit line at R=-1 is steeper than both at R=0.1 and R=10, showing that fatigue damage accumulates most rapidly when the loading regime contains both tension and compression components.

In fig.8.7 the data for reversed loading has been compared with that collected by Bonfield (1991). It can be seen that the linear fit lines for each set of data are fairly similar. There is some difference in the data though, with the recent samples performing slightly better at higher stress levels. It is probable that the differences observed are due to variation between the batches of samples.

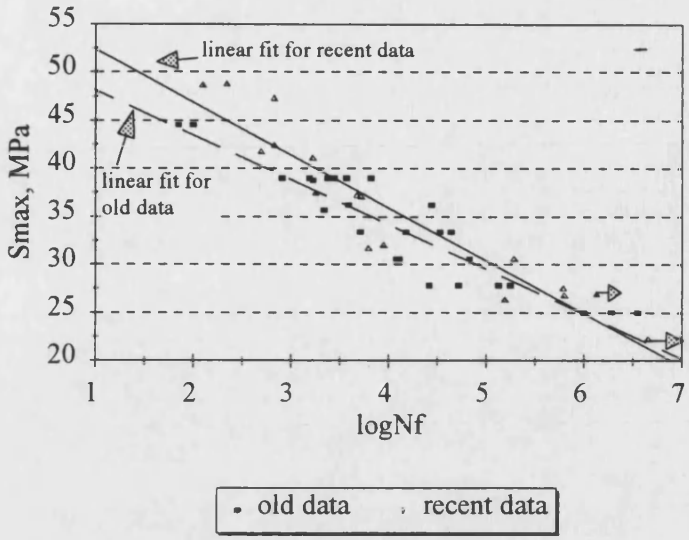

Fig.8.7. Comparison with data from Bonfield (1991).

Typically, fibre reinforced polymer composites show a decrease in fatigue strength of the order of 9-13% of static strength per decade of fatigue cycles (Reifsnider, 1991). The gradients of the best fit lines were calculated and normalised to the static strength, and are presented in table 8.4.

R ratio	Decrease in fatigue strength per decade of loading cycles	
R=0.1	4.4%	[normalised by UTS]
R=10	2.8%	[normalised by UCS]
R=-1	11.8%	[normalised by UCS]
	7.3%	[normalised by UTS]

Table 8.4. Gradients of S-logN curves.

It is clear that in tension and compression fatigue the decrease in fatigue strength per decade of loading cycles is much lower than the values for fibre reinforced plastics, highlighting the superior performance of wood composites. As expected, the lowest gradient is in compression fatigue at R=10, followed by tension at R=0.1. Only when the gradient is normalised by the UCS at R=-1 does it fall into the range more commonly observed for fibre reinforced plastics.

8.3.2. Failure modes

The failure mode is, understandably, different for each R ratio. In compression fatigue the sample fails via the formation of a macroscopic compression crease which runs

diagonally across the sample, for example fig.8.8. The crease is straight, apart from at each end, and is at an angle of approximately 60° to the grain of the wood which is parallel to the sample axis. The edge view shows several creases running through the sample in the vicinity of the main crease. This shows that compression damage has accumulated throughout the gauge length of the sample and not just at the site of the main crease. The metal tabs indicate the position of the gauge length between them. All samples tested at R=10 failed by the formation of a macroscopic compression crease.

The failure mode observed in tension is completely different. Large amounts of longitudinal cracking can be seen in fig.8.9. In most cases the cracks run along the T-L plane of the wood in close proximity to the laminating gluelines. However, at the bottom of fig.8.9 the cracks can be seen to follow the grain angle in a veneer which is not parallel to the sample and runs at a shallow angle (3.5°). The position of the steel tabs is marked by patches of slightly darker epoxy resin. Not surprisingly, the tabs became detached during the progressive growth of cracks through the veneers at the end of the test. Fig.8.9 typifies tensile fatigue damage. However, in some cases failure occurred with little or no crack development producing a flatter fracture surface, more typical of a static tensile test.

In reversed loading failure is essentially a combination of the tensile and compressive elements of damage seen in pure tension and compression fatigue. Fig.8.10 shows a more localised, but jagged, failure from a sample fatigued at R=-1. The sample has broken into two pieces and there is evidence of cellular crushing on each side of the fracture. There is some evidence of longitudinal crack growth on the side of the sample but failure had clearly occurred before this developed to the extent seen in fig.8.9.

8.4. Conclusions

S-logN plots were produced for each R ratio and revealed differences in the sensitivity of wood to the different modes of fatigue loading as follows:

- At R=0.1 fatigue failure occurred at between approximately 50% and 75% UTS and the fatigue strength decreased at a rate of 4.4% UTS per decade of loading cycles.

- At R=10 fatigue failure only occurred within the scatter of the UCS values measured in Chapter 7. Below this level, fatigue failure did not occur within 10^7 cycles, the maximum limit of testing. The fatigue strength decreased at a low rate of 2.8% UCS per decade of fatigue cycles.

Fig.8.8. A typical compression fatigue failure at R=10.

Fig.8.9. A typical tension fatigue failure at R=0.1.

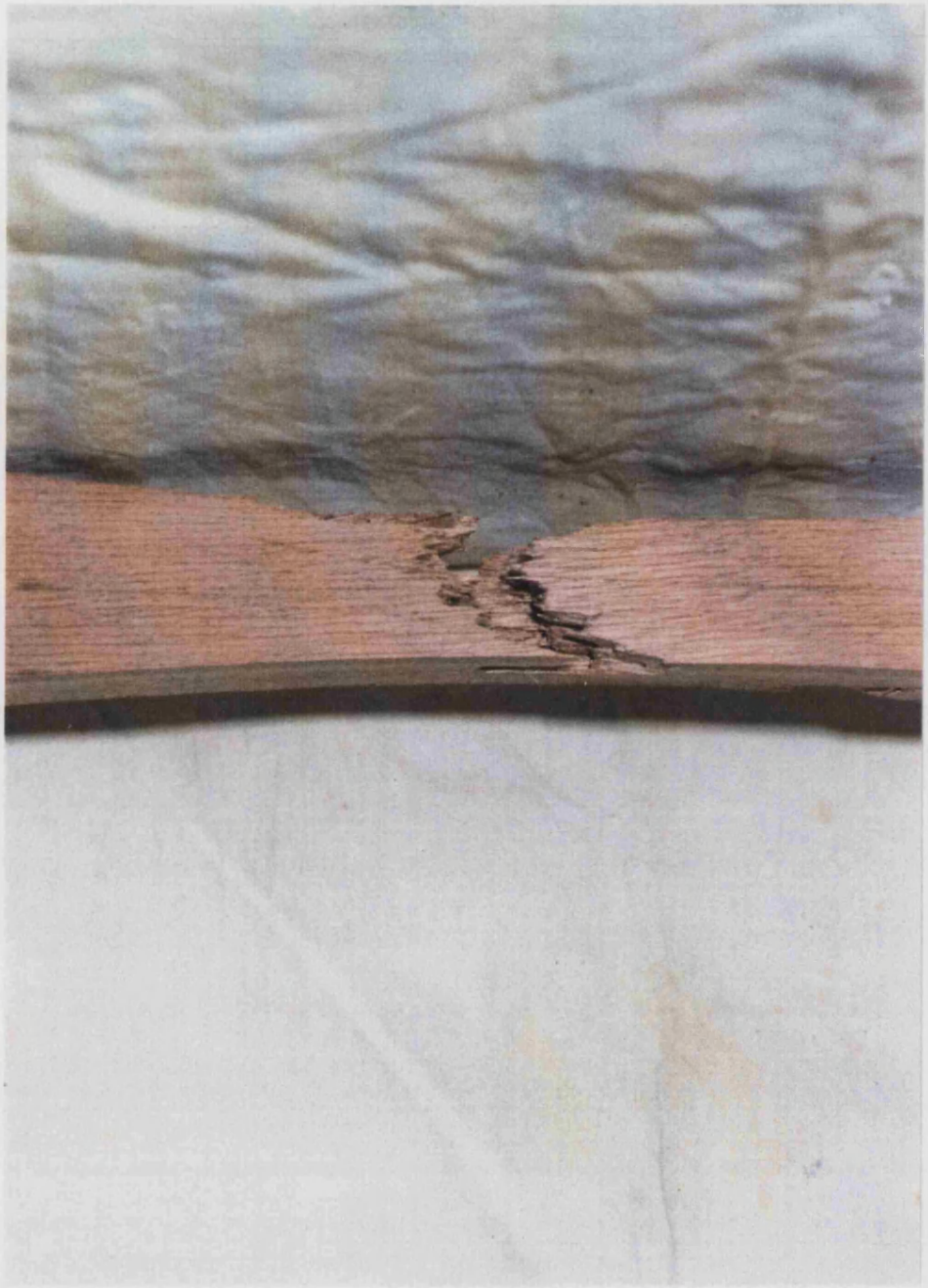

Fig.8.10. A typical reversed loading fatigue failure at R=-1.

- At R=-1 the fatigue strength decreased at by far the fastest rate, at 7.3% per decade when normalised by the UTS and 11.8% per decade when normalised by the UCS, showing reverse loading to be the most damaging loading mode.

Using a UCS value calculated according to eq.7.1 to normalise compression fatigue data did not significantly reduce the scatter in S-N data at R=10.

Distinctly different failure modes were observed at each R ratio, and the modes are summarised as follows:

- R=0.1. Tension fatigue damage was typified by high degrees of longitudinal splitting, primarily on the T-L planes of the veneers with cracks growing throughout the length of the sample. However, in some cases the sample failed without extensive crack growth.

- R=10. Failure occurred by the formation of a macroscopic compression crease running diagonally across the sample. No evidence of damage was observed elsewhere in the sample, except in the form of small regions of buckling in the vicinity of the main compression crease. All samples failed in this manner.

- R=-1. Reverse loading fatigue resulted in a failure mode which was a mixture of tensile and compressive fatigue damage. In general there was less longitudinal splitting and the damage was more localised.

9. FIRST AND LAST HYSTERESIS LOOPS

For every test, shown as a data point on the S-N curves in Chapter 8, a series of between twenty and several hundred stress-strain hysteresis loops were captured. These have been analysed using nCode's LPA program and the spreadsheet package, 'Quattro Pro'. As fatigue damage accumulation and consequent changes in properties in wood composite are encapsulated in the hysteresis loop shape, these loops provide a useful indication of the damage process. In this chapter typical hysteresis loops are presented from tests at R=0.1, R=10 and R=-1, and their features discussed. The full set of loops are presented in Appendix C.

9.1. R=10

A series of stress strain hysteresis loops captured during a compression fatigue test are presented in fig.9.1. A static loading curve from a different sample has also been included for comparison. The first hysteresis loop approximately follows the static loading curve [small differences arise due to the slight difference in modulus of the two samples]. As fatigue proceeds creep occurs under the action of the compressive fatigue load and the hysteresis loops move in the compression direction. The last loop captured before failure has a minimum strain of under -1%, close to the expected static strain at failure. The last loop is also less steep and fatter than the first loop. This is indicative of the accumulation of fatigue damage in the composite.

It can be appreciated that the minimum stress in the fatigue test is close to the static ultimate compressive strength (UCS) [53MPa] of the composite. It is necessary to test at such high stress levels in compression fatigue because the S-N curve is very shallow (Bonfield, 1991) and at stress levels a few MPa below the mean static UCS failure would not have occurred within the runout limit of 10^7 cycles. When testing so close to the UCS it is not surprising that there is great scatter in the fatigue lifetimes because the minimum stress is within the range of variation in UCS. Furthermore, at these stress levels the fatigue response of an individual sample is likely to be determined, for the most part, by its static strength.

9.2. R=0.1

First and last hysteresis loops for tension fatigue are presented in figs.9.2 and 9.3. They represent the two different types of fatigue response which were observed. At low and very high stress level tests only a small change in the loop shape was observed, eg. fig.9.2 where S_{max}=65MPa. At intermediate stresses the changes were pronounced, with tensile creep, a decrease in modulus and an increase in loop area all apparent, eg. fig.9.3 where S_{max}=55MPa.

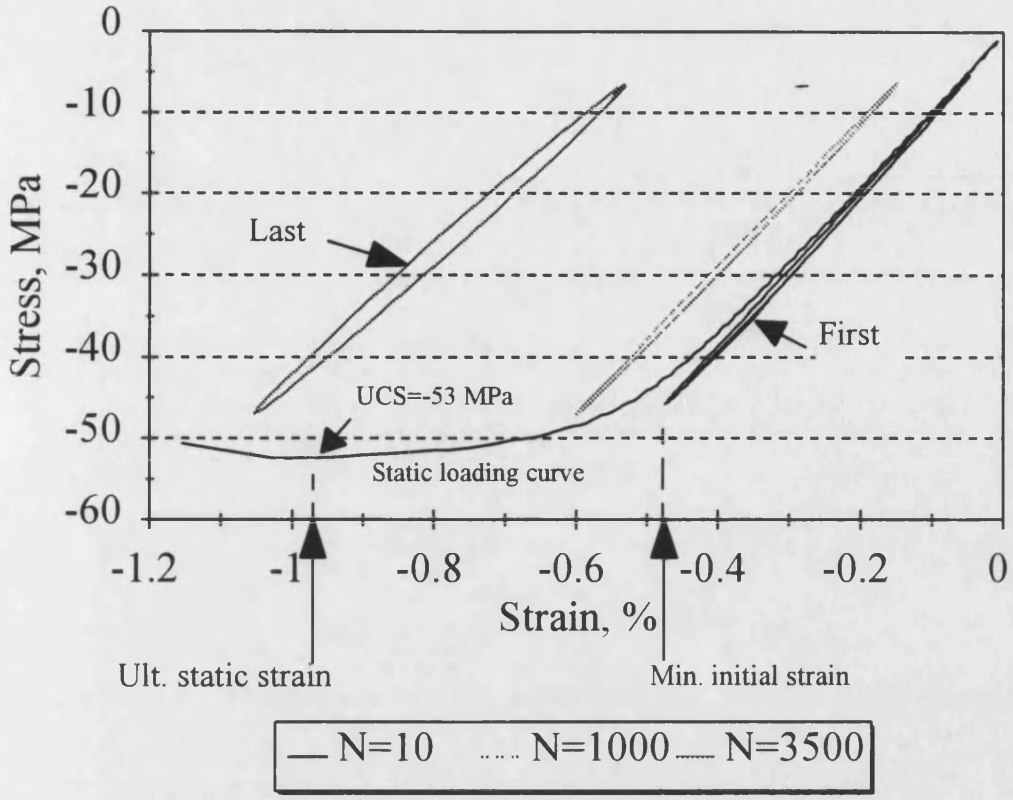

Fig.9.1. Stress-strain hysteresis loops at R=10, minimum stress =-47.5MPa. A static stress-strain curve has been overlaid for comparison.

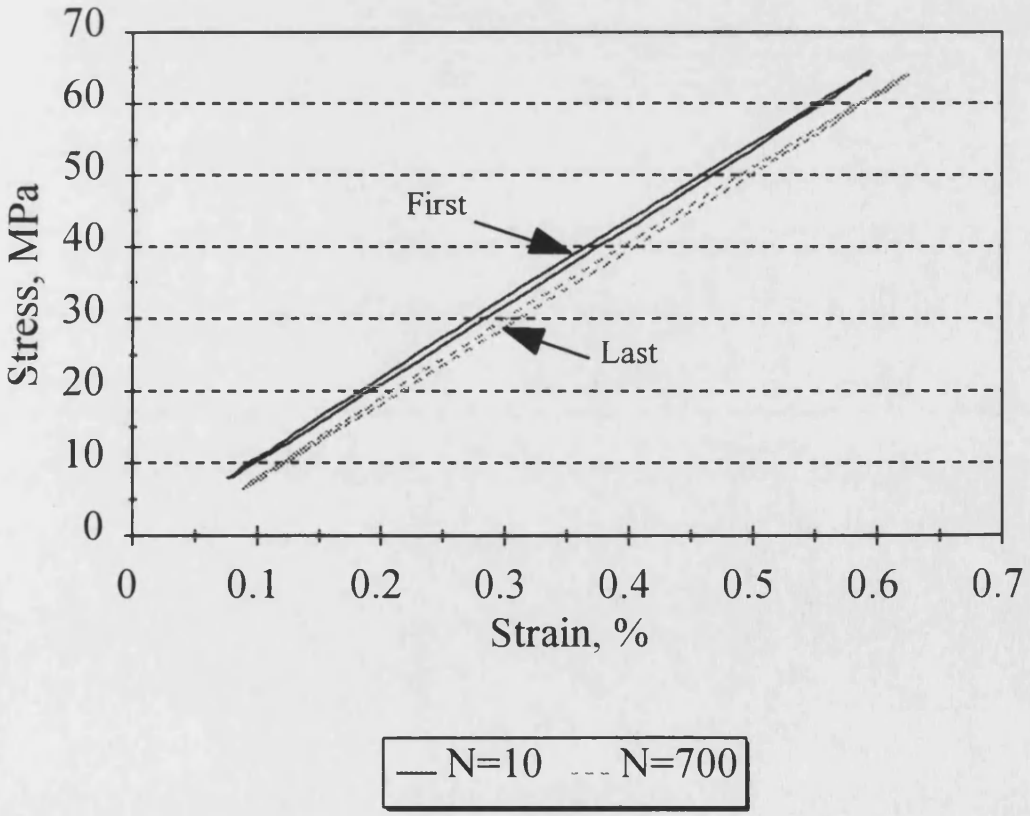

Fig.9.2. Stress-strain hysteresis loop from a high stress level test, R=0.1, S_{max}=65MPa.

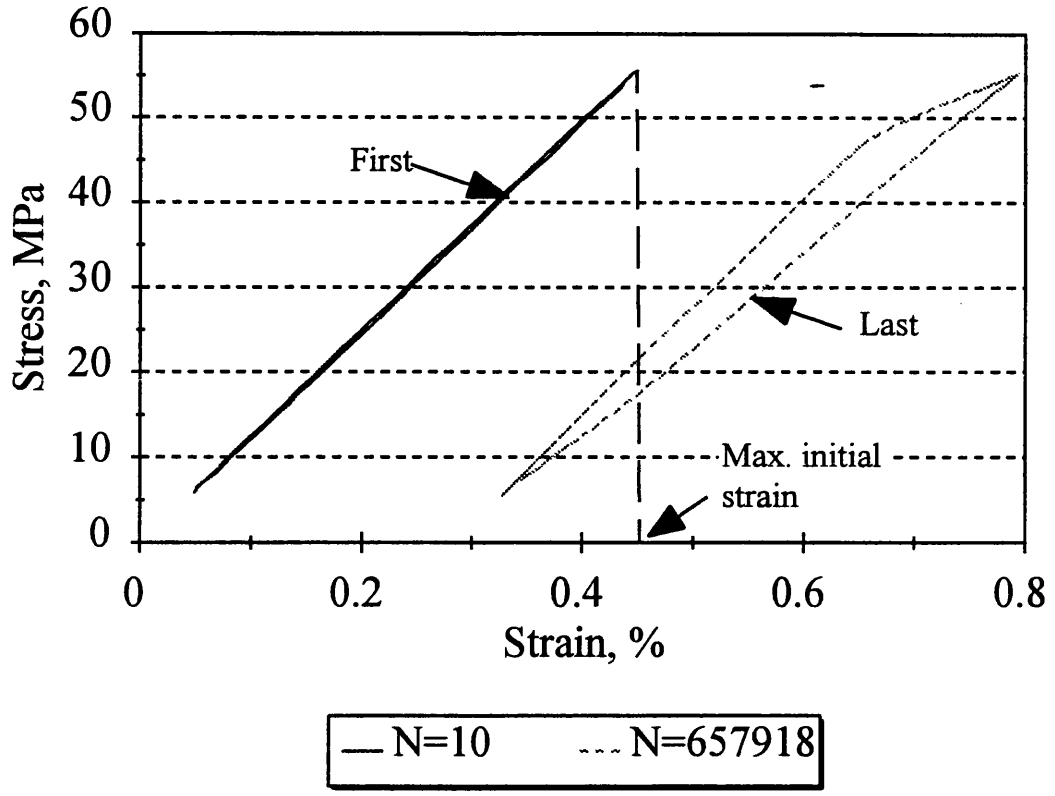

Fig.9.3. Stress-strain hysteresis loops from an intermediate stress level test, S_{max}=55MPa, at R=0.1.

All the samples tested at S_{max}=30MPa and 40MPa are runouts and, as such, have suffered negligible fatigue damage. Dinwoodie (1981) states that in tension wood behaves elastically up to 60% UTS but Sun (1993) found the departure from linearity to be lower at 45±5%. The stress levels of the runout samples correspond to 35% and 47% UTS, close to or below the elastic limit. The marked difference in behaviour of the runout samples compared with those tested at intermediate stress levels suggests that fatigue damage does not build up in samples cycled below the elastic limit. At intermediate levels, close to or above the elastic limit, where pronounced changes in loop shape were observed, longitudinal cracks were seen to build up in the composite as fatigue proceeded. At high stress levels failure occurs without any dramatic changes in properties. The gradual build up of cracks is not evident and failure is instantaneous. It is likely that at the high stress levels once a crack in a veneer is formed it leads to immediate failure but at lower stress levels the cracks are not critical and grow gradually, causing a decrease in modulus and increase in loop area until failure.

9.3. R=-1

The changes in properties under reverse loading fatigue are, not surprisingly, the most complicated of the three loading regimes as they are determined by both the tension and compression fatigue damage accumulation in the composite. Three different types of

fatigue response were identified, compression dominated, fig.9.4, tension dominated, fig.9.5, a combination of the two, fig.9.6.

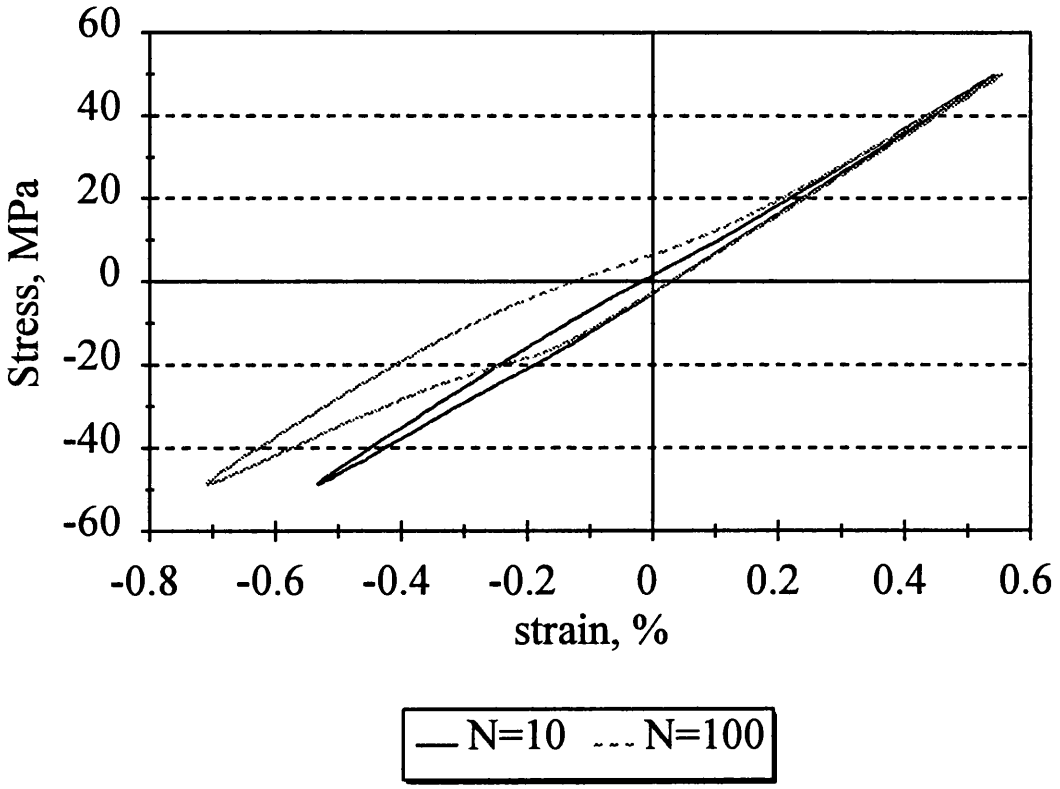

Fig.9.4. First and last hysteresis loops showing compression dominated fatigue damage at R=-1, S_{max}=50MPa.

In a compression dominated fatigue response, fig.9.4, the maximum tensile strain has not changed but the minimum compressive strain has decreased considerably. In fig.9.5 the tensile strain has increased considerably whilst the compressive minimum has hardly changed at all. In both cases the dynamic modulus has also decreased and loop area increased. Both these responses are observed in fig.9.6 where both the maximum tensile and minimum compressive strains have changed considerably. The maximum tensile strain on the last loop is very close to the expected ultimate static tensile strain of 1%. The decrease in the compressive strains is less pronounced than the increase in tension, and the result is that the hysteresis loop becomes bent. The tensile and compressive moduli are different from each other. Some samples only showed small indistinct changes in loop shape and were defined as having exhibited an intermediate response.

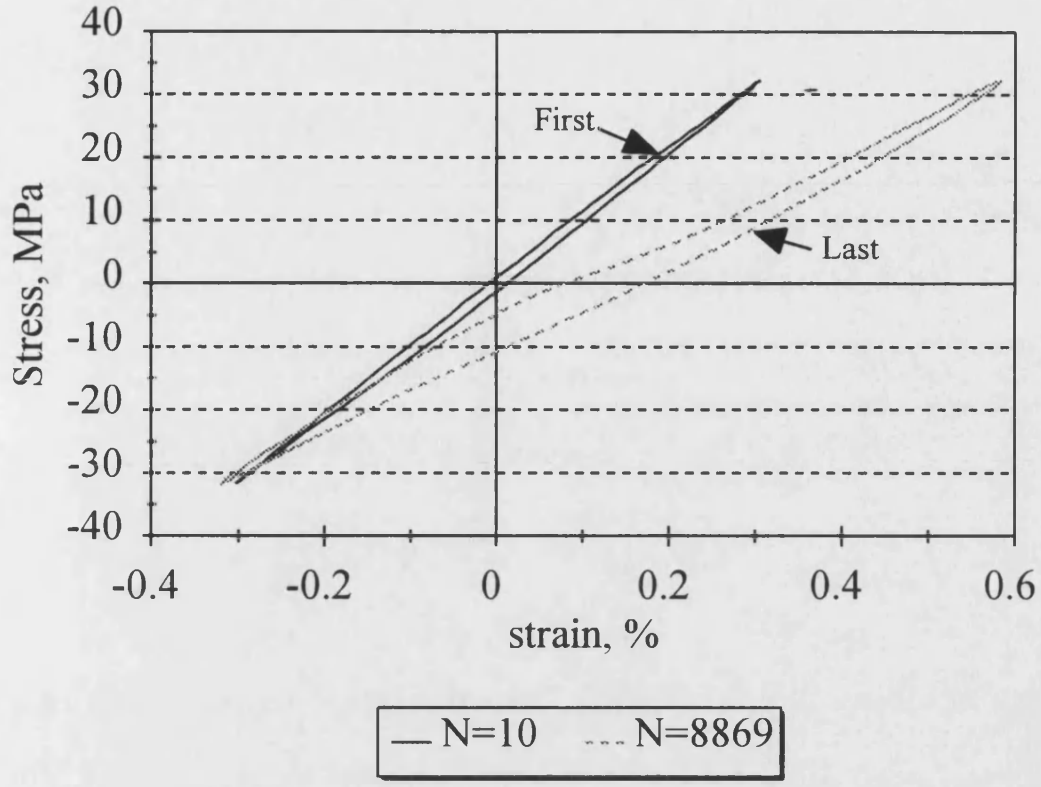

Fig.9.5. First and last hysteresis loops showing tension-dominated fatigue damage at R=-1, S_{max}=35MPa.

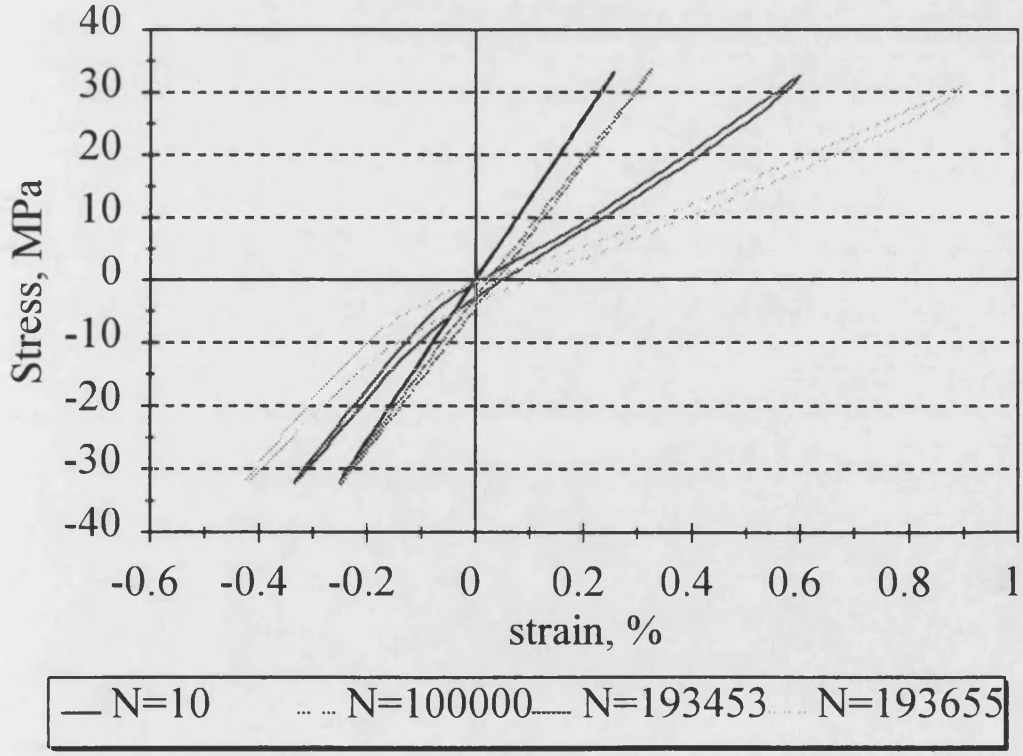

Fig.9.6. Stress-strain hysteresis loops showing tension- and compression-dominated fatigue damage accumulation at R=-1, S_{max}=35MPa.

Fractured samples of each type were inspected and distinct differences in the way failure had occurred were observed. Samples which exhibited large degrees of loop bending before failure contained many longitudinal cracks, following the radial - longitudinal wood plane. This was particularly noticeable where the outer veneers were at a shallow angle to the axis of the sample. Samples failing without loop bending contained more evidence of compression damage in the form of compression creases on the sample surfaces with a greatly reduced level of lifting of the grain to form splinters which is a feature of tension-tension fatigue damage.

9.4. Conclusions

Stress strain hysteresis loop capture has been used successfully to follow fatigue damage accumulation in wood composites in compression, tension and reversed loading fatigue. Different fatigue responses have been observed under each loading regime.

At R=10 the minimum stress level must be within the scatter of the ultimate static strength of the composite if fatigue failure is to occur. This is a result of wood's excellent fatigue performance in compression and as a result the fatigue response of any individual sample is likely to be linked to the ultimate compressive strength of that particular sample.

At R=0.1 two types of fatigue response were observed. In one case the changes in loop shape were small and in the second the changes in tensile creep, loop area and dynamic modulus were pronounced. The former behaviour occurred in the runout samples where negligible fatigue damage occurred and at high stress levels where failure was almost instantaneous. The latter occurred at intermediate stress levels where progressive crack growth was observed in the wood composite.

At R=-1 three distinct modes of fatigue damage accumulation were observed: compression-dominated, tension-dominated and both compression- and tension-dominated. Compression-dominated damage occurred at high stress levels where S_{min} was close to the UCS. Tension and mixed mode damage occurred in similar proportions at lower stress levels.

10. PROPERTY CHANGES DURING FATIGUE

The stress-strain hysteresis loops presented in Chapter 9 have been analysed and values for the strain, stiffness and energy loss calculated for every hysteresis loop. This enables the changes which occur in the wood composite as a result of fatigue to be followed. These property changes are presented for the Khaya-epoxy composite loaded in tension, compression and reversed loading fatigue in this chapter. Differences in the fatigue response of the composite under the different loading regimes become apparent.

10.1. Changes in strain, dynamic modulus and loop area

nCode's hysteresis loop analysis program, LPA, was used to process the hysteresis loop data associated with each test. The dynamic modulus, loop area and maximum and minimum strains were calculated for each loop. From these values other parameters could also be generated. The volume of data associated with each test is considerable and a comprehensive set is included in Appendix D. Typical examples of the data obtained at each R ratio are presented in figs.10.1 to 10.9. The figures have been plotted in large format because several curves are presented on each graph. Although there are important differences in the data obtained at each R ratio the following general trends are observed:

- the strain increases in the direction of the applied stress [figs.10.1, 10.4 and 10.7]
- the significant changes in strain occur at the end of a sample's fatigue life [figs.10.1, 10.4 and 10.7]
- the dynamic modulus decreases [figs.10.2, 10.5 and 10.8]
- the loop area increases [figs. 10.3, 10.6 and 10.9]
- the loop area decreases at the start of a test before increasing to failure [figs. 10.3, 10.6 and 10.9]
- during the initial part of the fatigue life the property remains unchanged or varies in a linear fashion [figs.10.1 to 10.9].

If the strain vs. log(N) plots are compared more carefully [figs.10.1, 10.4 and 10.7] variations in the wood composite's response to compression, tension and reverse loading fatigue become apparent. At R=10 [fig.10.1] the maximum and minimum strains decrease by similar amounts [except sample f] which suggests that creep is significant, due to the proximity of the minimum fatigue stress to the UCS. At R=0.1 [fig.10.4] the maximum strain changes much more significantly than the minimum strain in samples b and d. This indicates that there has been a large decrease in modulus in these samples. At R=-1 [fig.10.7] the maximum strain always increases by more than the minimum

Fig.10.1. Maximum and minimum strains for samples tested at R=10, Smin=-52.5 MPa

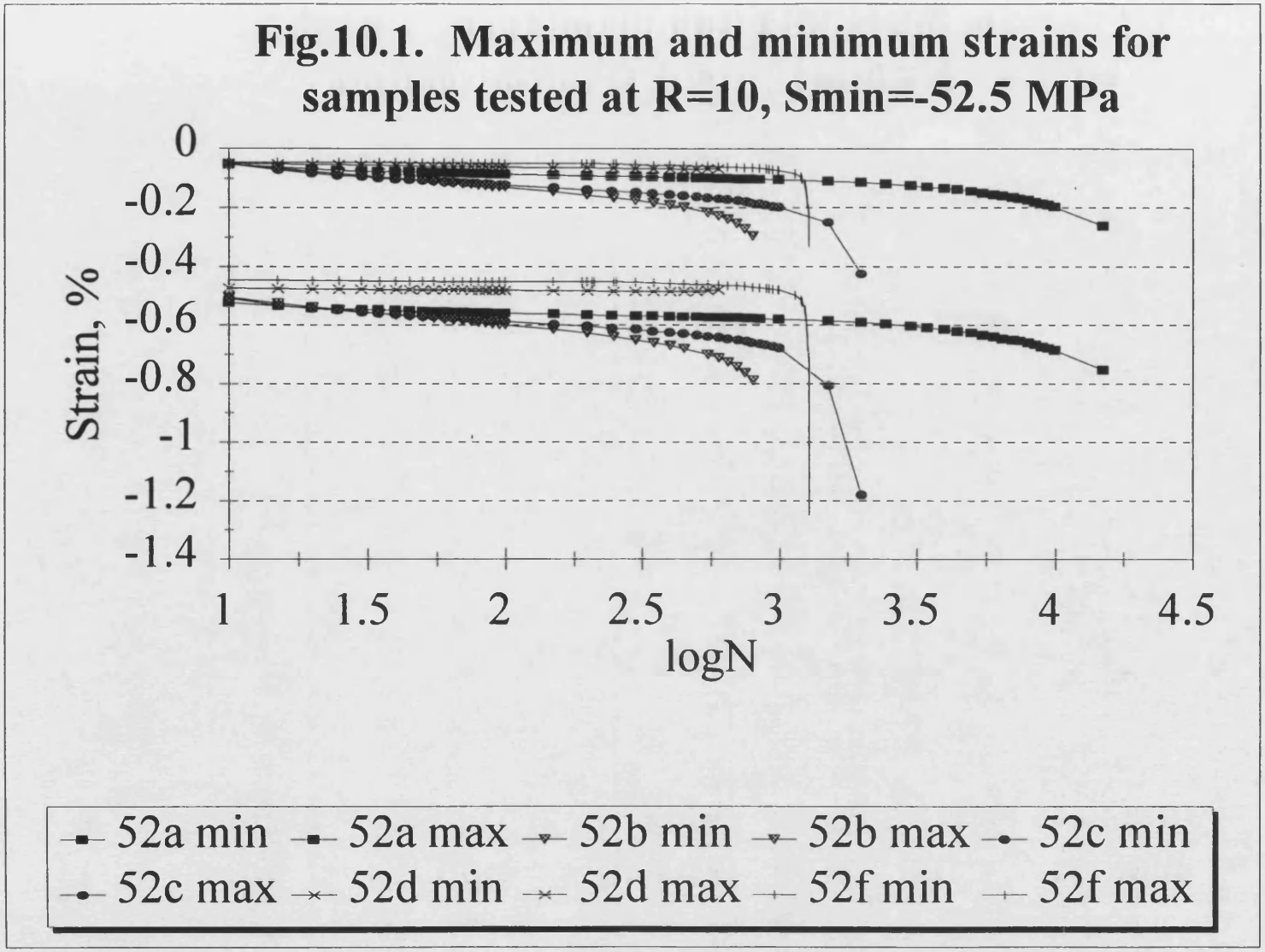

Fig.10.2. Dynamic moduli for samples tested at R=10, Smin=-52.5 MPa

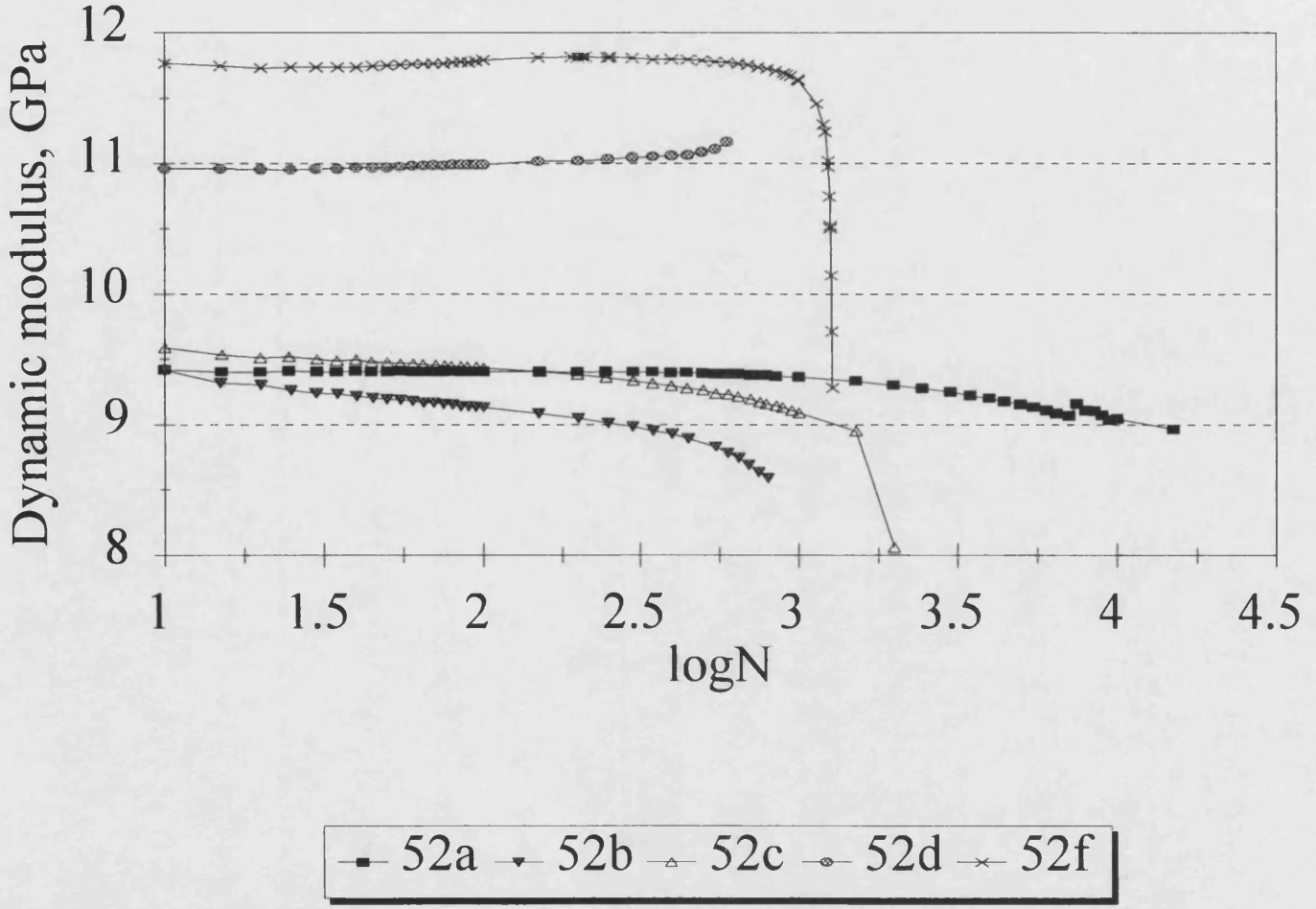

Fig.10.3. Hysteresis loop area for samples tested at R=10, Smin=-52.5 MPa

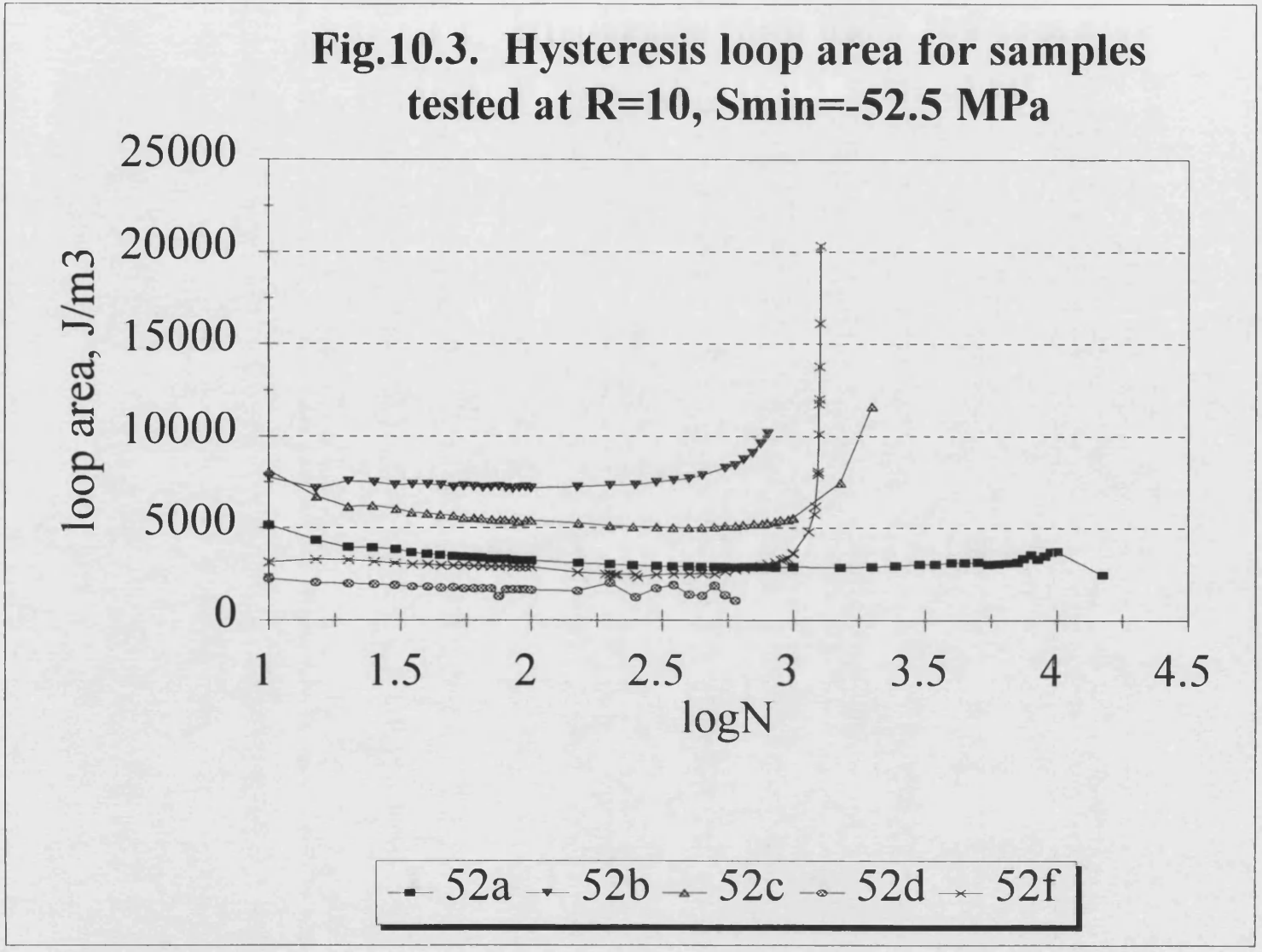

Fig.10.4 Maximum and minimum strains for samples tested at R=0.1, Smax=55 MPa

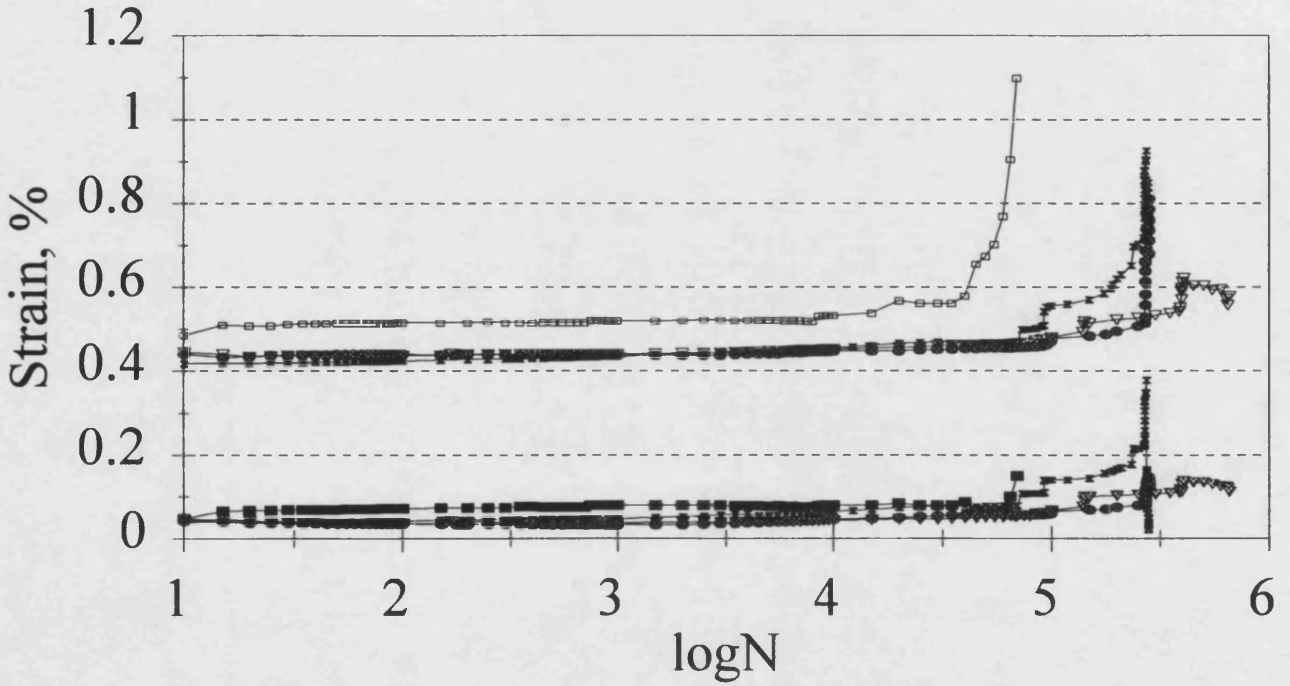

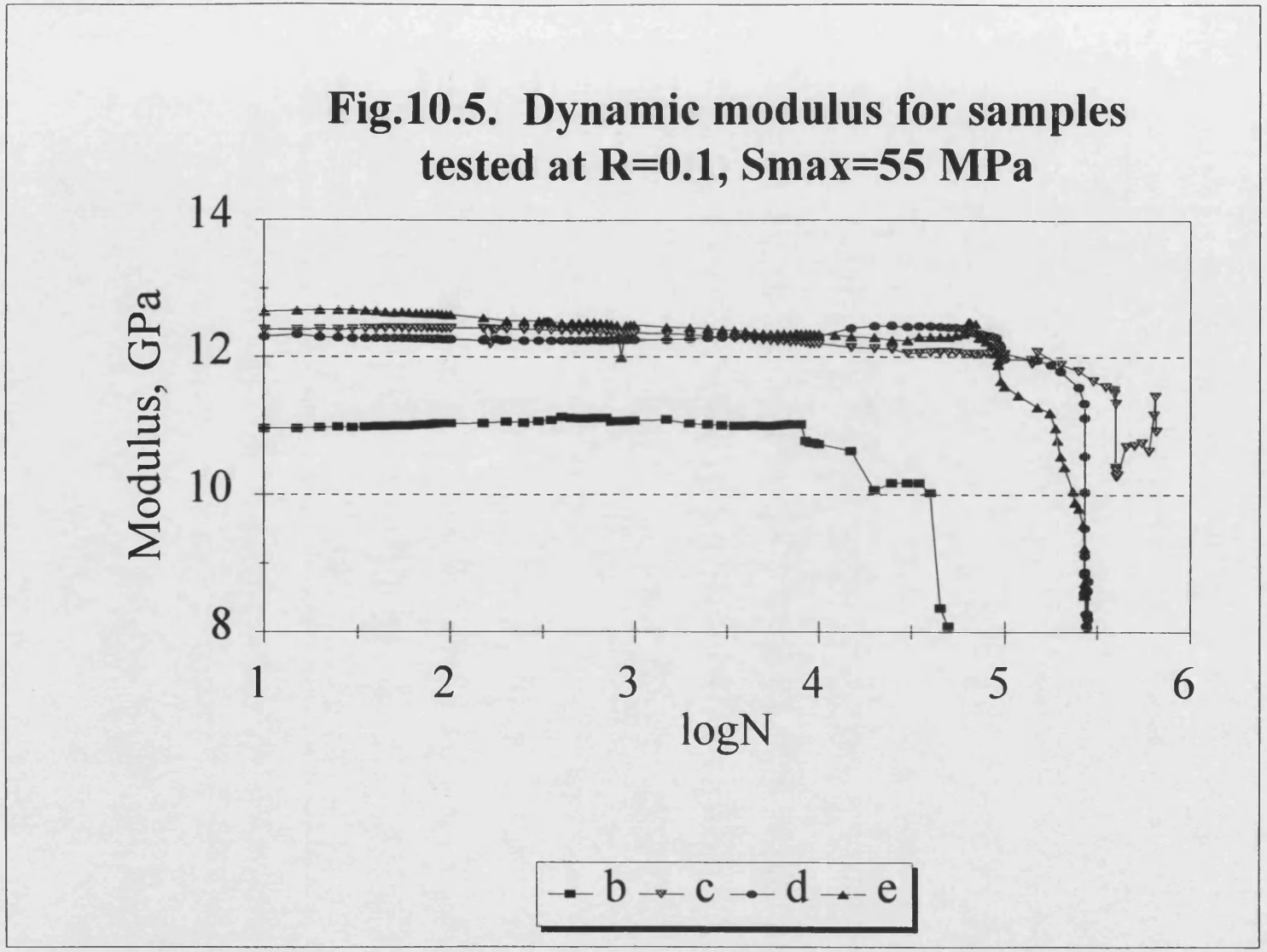
Fig.10.5. Dynamic modulus for samples tested at R=0.1, Smax=55 MPa
Modulus, GPa
14
12
10
8
1
2
3
4
5
6
logN
b
c
d
e

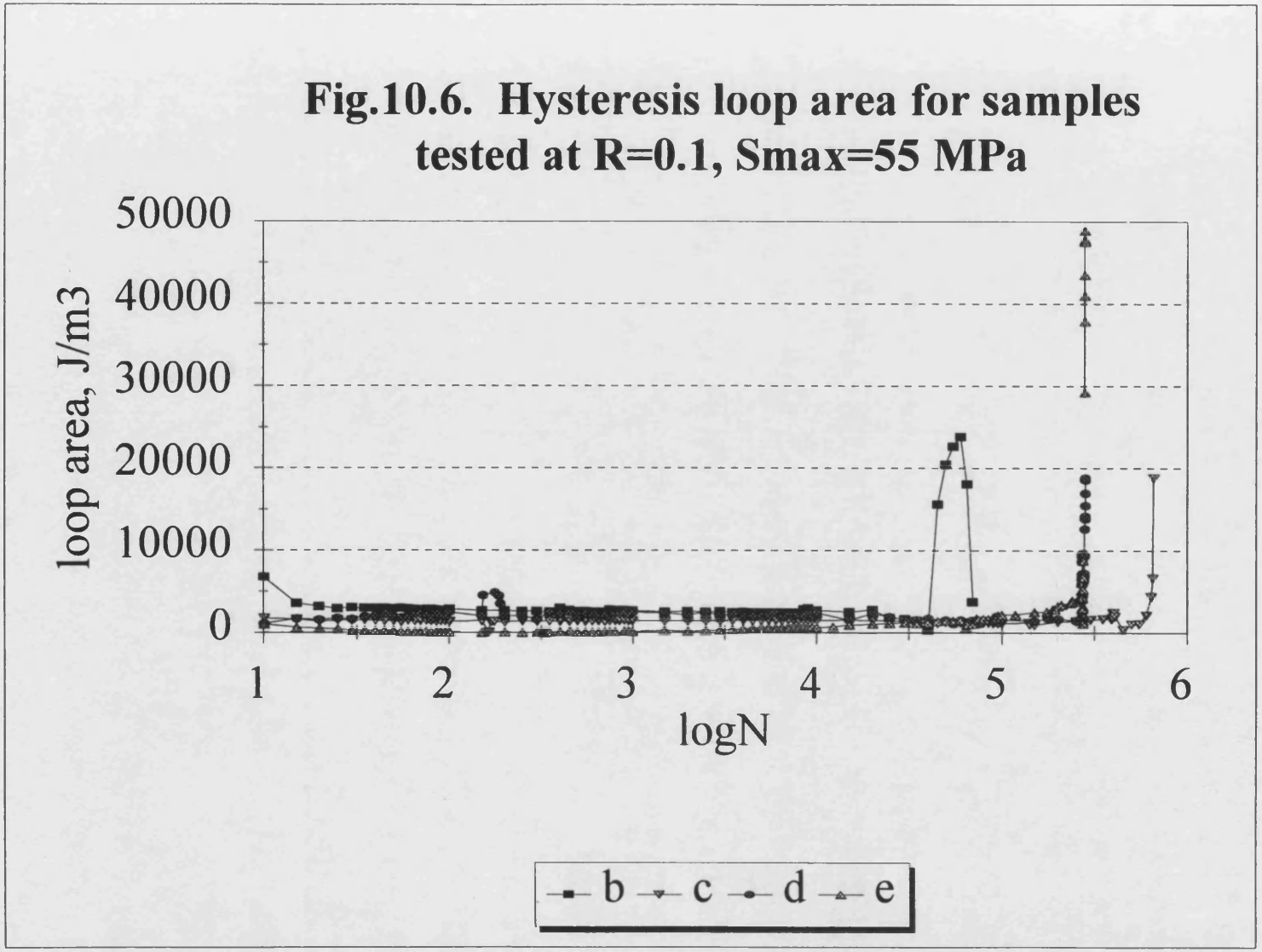
Fig.10.6. Hysteresis loop area for samples tested at R=0.1, Smax=55 MPa
loop area, J/m3
50000
40000
30000
20000
10000
0
1
2
3
4
5
6
logN
b
c
d
e

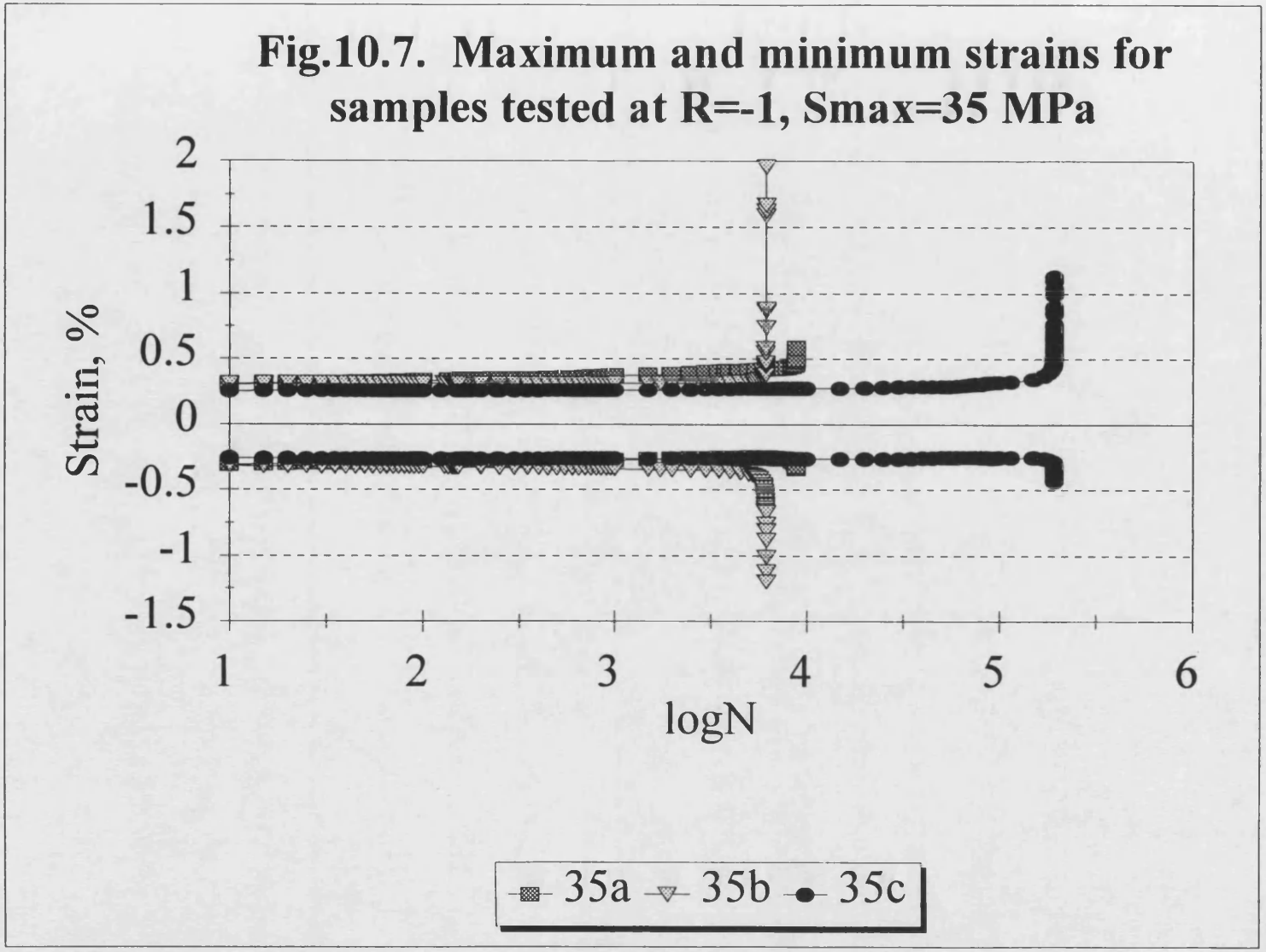
Fig.10.7. Maximum and minimum strains for samples tested at R=-1, Smax=35 MPa
Strain, %
2
1.5
1
0.5
0
-0.5
-1
-1.5
1
2
3
4
5
6
logN
35a
35b
35c

Fig.10.8. Dynamic modulus for samples tested at R=-1, Smax=35 MPa

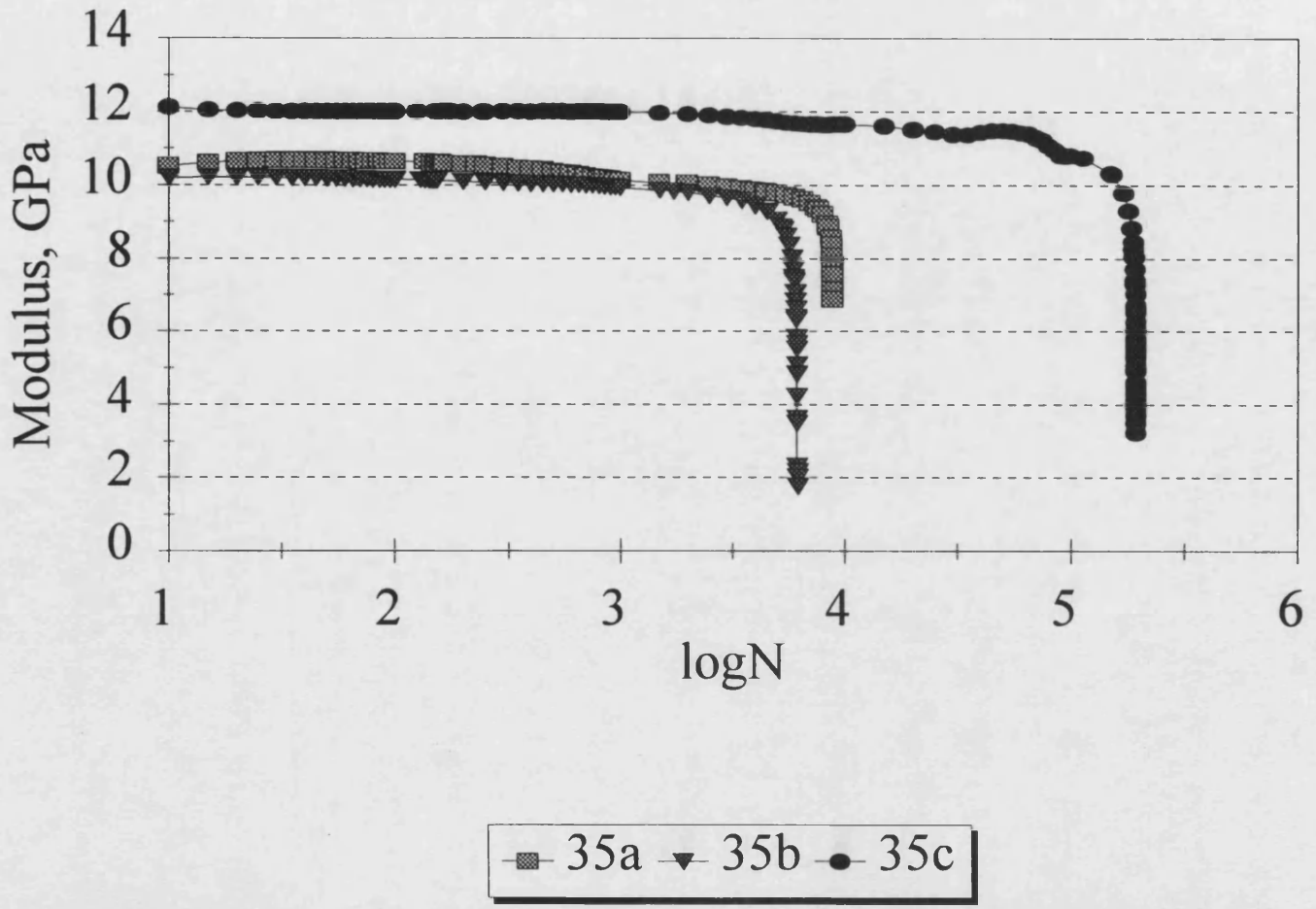

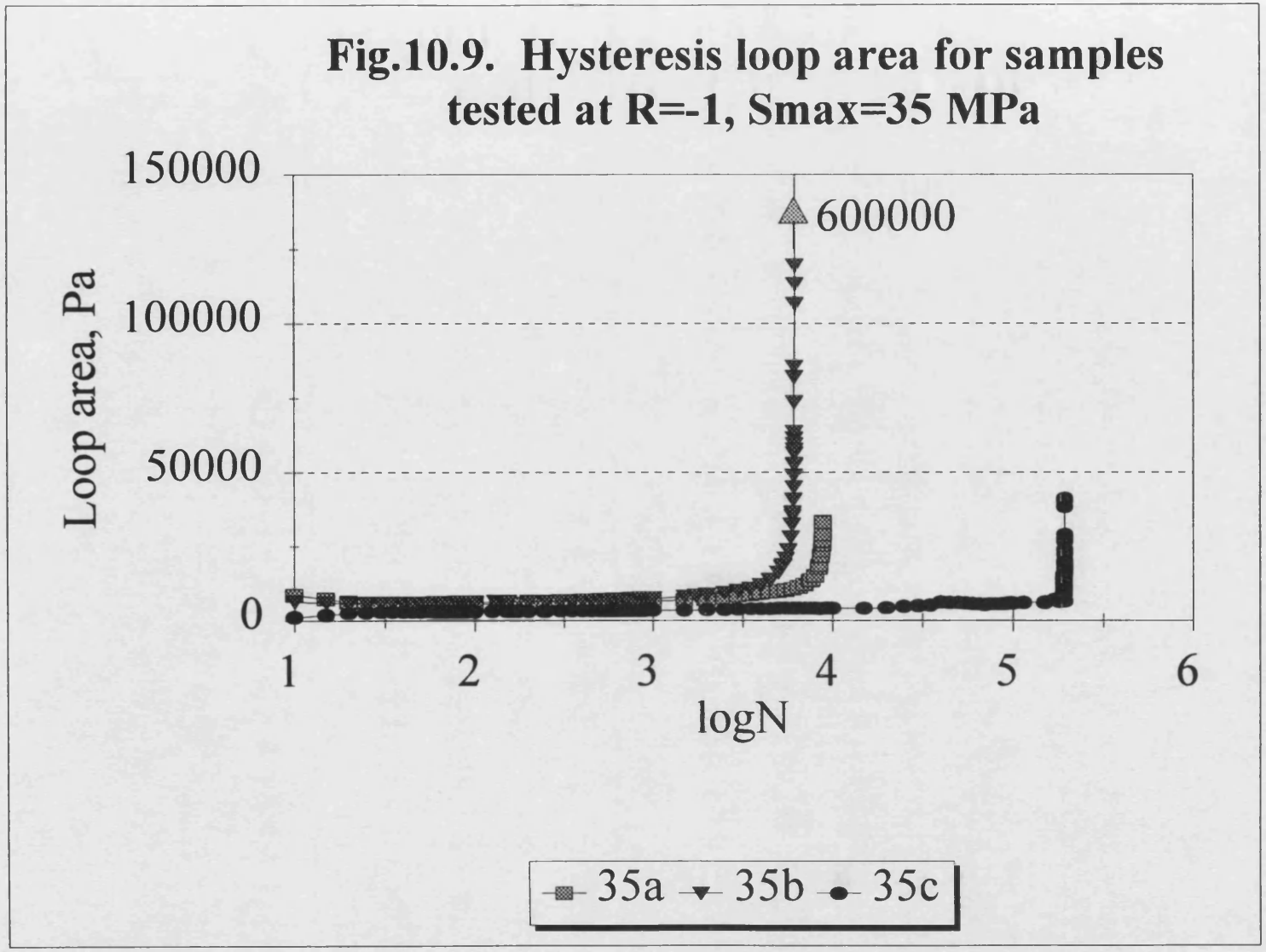
Fig.10.9. Hysteresis loop area for samples tested at R=-1, Smax=35 MPa
150000
100000
50000
0
Loop area, Pa
600000
1
2
3
4
5
6
logN
35a
35b
35c

strain decreases and shows that hysteresis loop bending has occurred in each sample [see section 10.2].

None of the plots for tension fatigue [figs. 10.4 to 10.6] exhibit smooth changes in properties. This is due to the initiation and growth of fatigue cracks along the wood grain causing irregular increases in the strain seen by the sample. It is possible that when a crack is initiated there is a step increase in the strain [samples b, c and e] but at the end of the test the jerky changes in properties are also likely to be due to the lifting of the clip gauge from the sample surface as the cracked wood is loaded.

By comparing the dynamic modulus and loop area plots it can be seen that the most marked changes are observed in the reverse loading case.

10.2. Normalised property changes

An informative way of presenting the above data is to normalise it by dividing by the initial value. This facilitates comparison between samples and loading regimes as it minimises the inherent variation associated with wood. Figs.10.10 to 10.18 show the normalised plots of figs.10.1 to 10.9.

Figs.10.10 to 10.12 show some interesting features. Sample 52f exhibits different behaviour to the rest of the samples tested at this stress level. In all the other samples there is a relationship between the rate of change of a property and the fatigue lifetime. For example, in fig.10.10, the samples showing the slowest change in minimum strain survives longest and the one where the strain changes most rapidly fails first. Sample 52f, however, shows no change in minimum strain until the rapid changes occur immediately prior to failure. This is also evident in fig.10.11 where there is no change in modulus until the rapid decrease before failure. However, the normalised area curve for sample 52f fits in with the trend and does not cut across the curves belonging to the other samples, fig.10.12. Sample 52d is one which failed without exhibiting any significant property changes.

A comparison of figs.10.10, 10.13 and 10.16 reveal differences in the strain changes under compression, tension and reverse loading fatigue. In compression the maximum and minimum strains tend to increase almost linearly throughout the majority of the samples' lifetime. The tension and reverse loading responses are more similar with the strains hardly changing during all but the last half decade of loading cycles.

The largest and most rapid changes in dynamic modulus occur in reverse loading at the very end of a test (fig.10.17). This is also true for tension fatigue (fig.10.14). In

Fig.10.10. Normalised maximum and minimum strains, R=10, Smin=-52.5 MPa

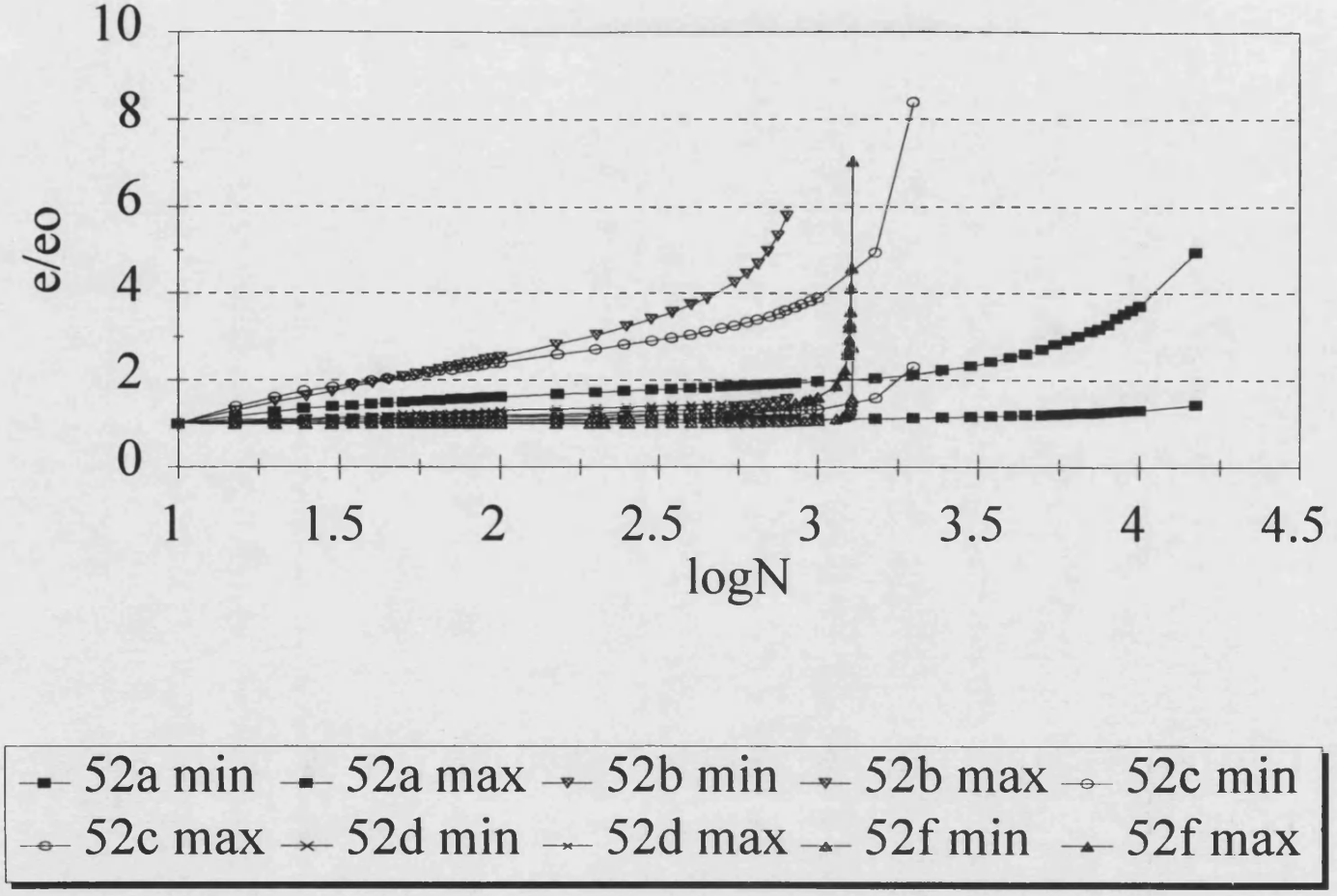

Fig.10.11. Normalised dynamic modulus for samples tested at R=10, Smin=-52.5 MPa

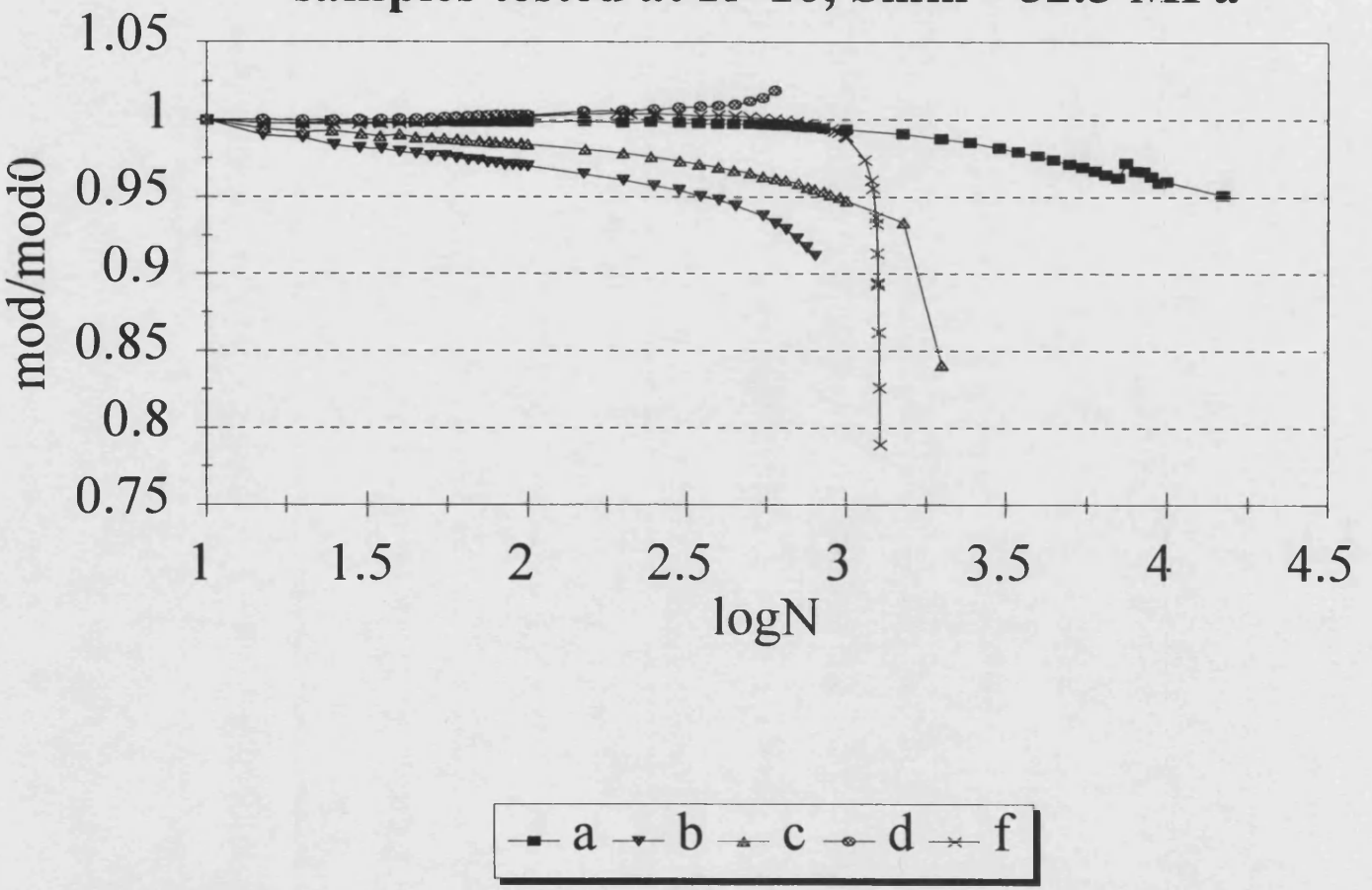

Fig.10.12. Normalised hysteresis loop area for samples tested at R=10, Smin=-52.5 MPa

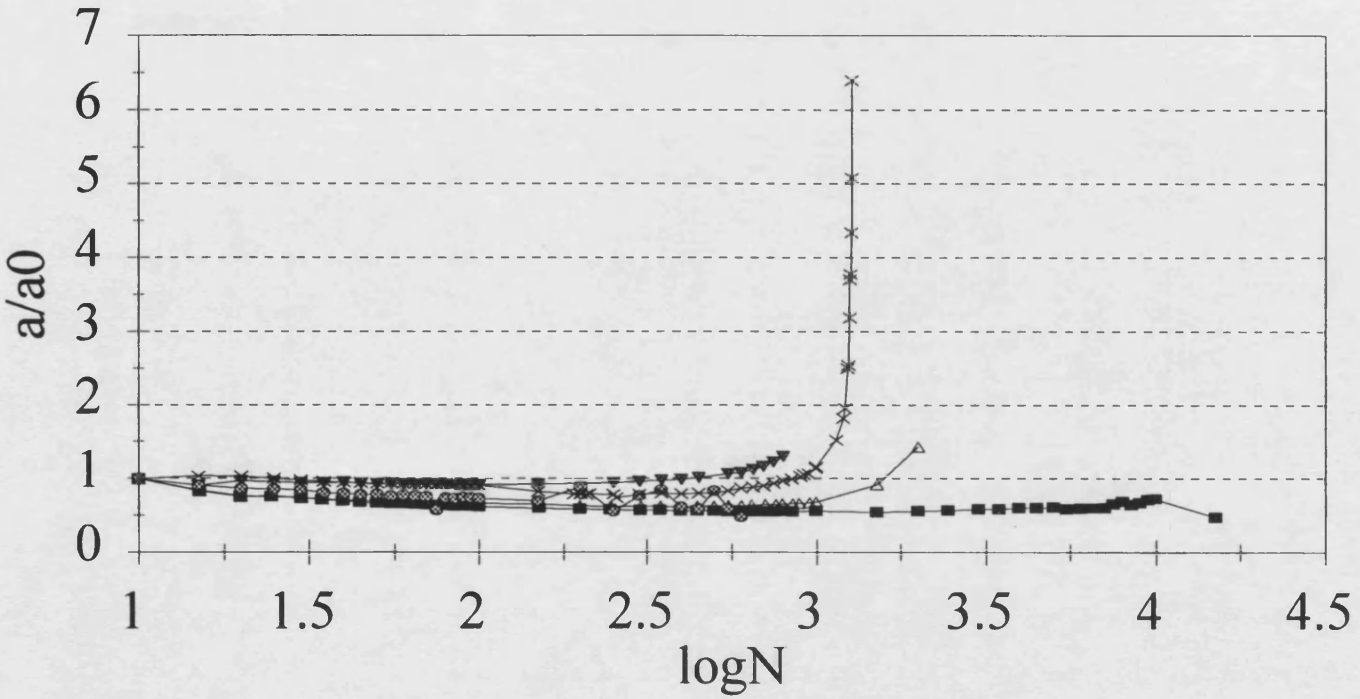

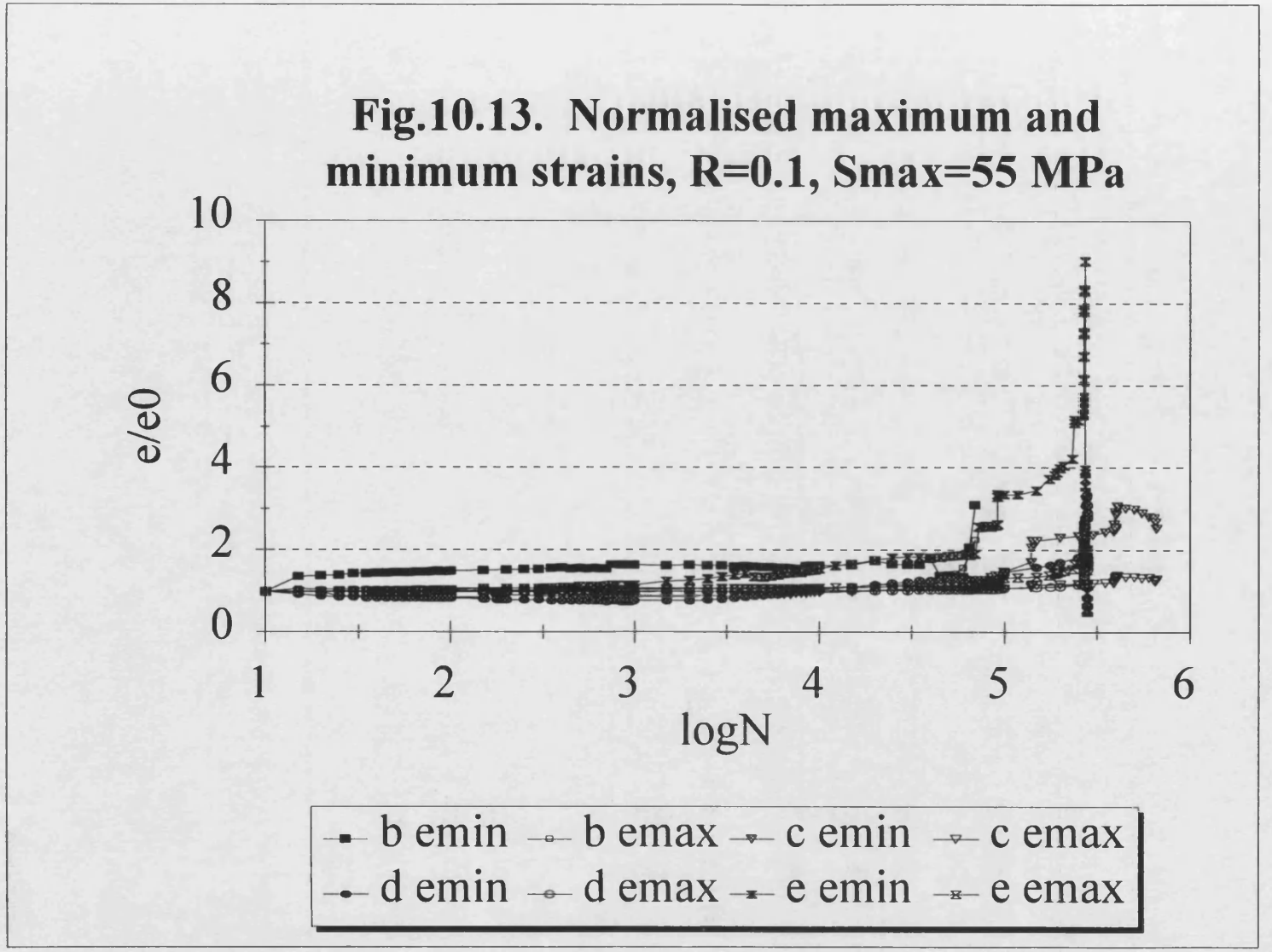
Fig.10.13. Normalised maximum and minimum strains, R=0.1, Smax=55 MPa
10
8
6
4
2
0
e/e0
1
2
3
4
5
6
logN
b emin
b emax
c emin
c emax
d emin
d emax
e emin
e emax

Fig.10.14. Normalised dynamic modulus for samples tested at R=0.1, Smax=55 MPa

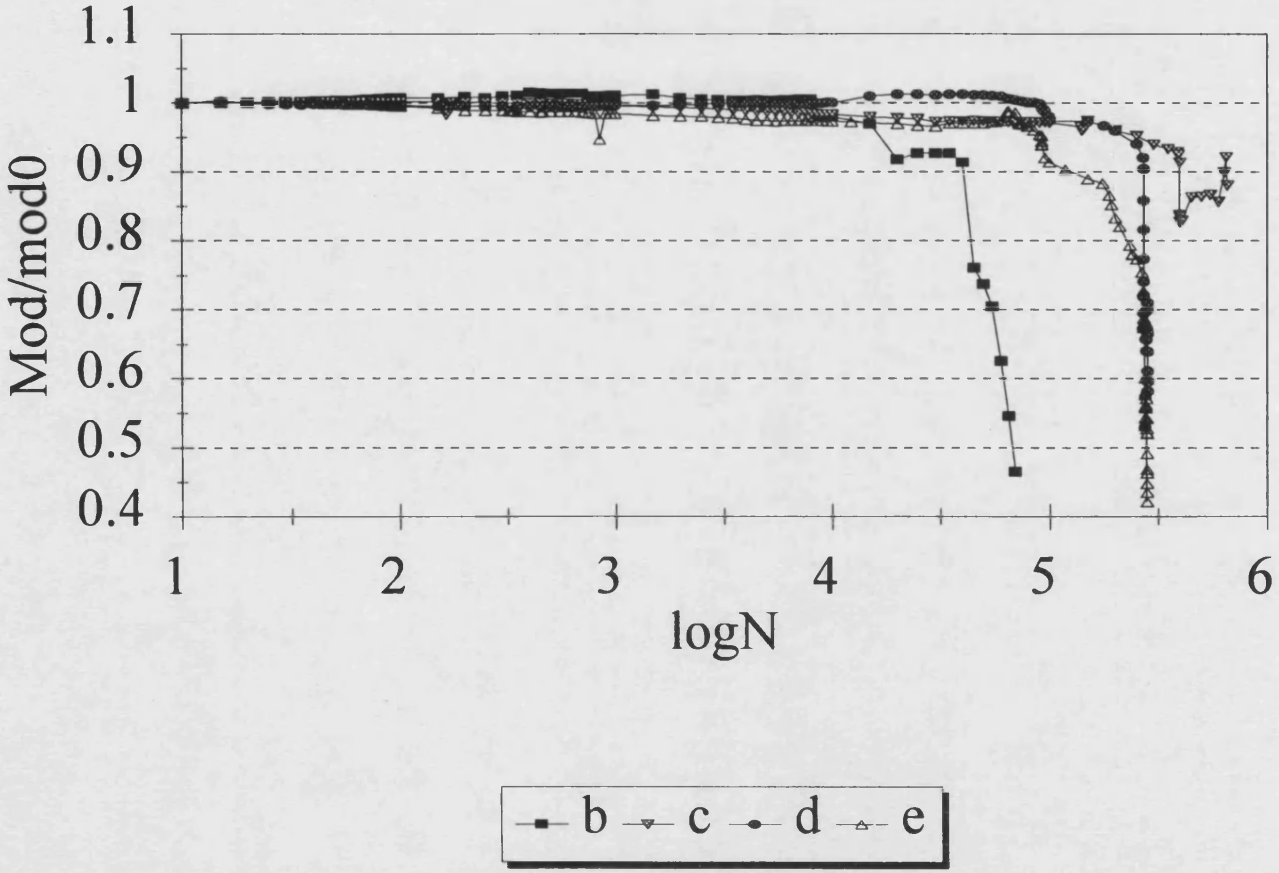

Fig.10.15. Normalised hysteresis loop area for samples tested at R=0.1, Smax=55 MPa

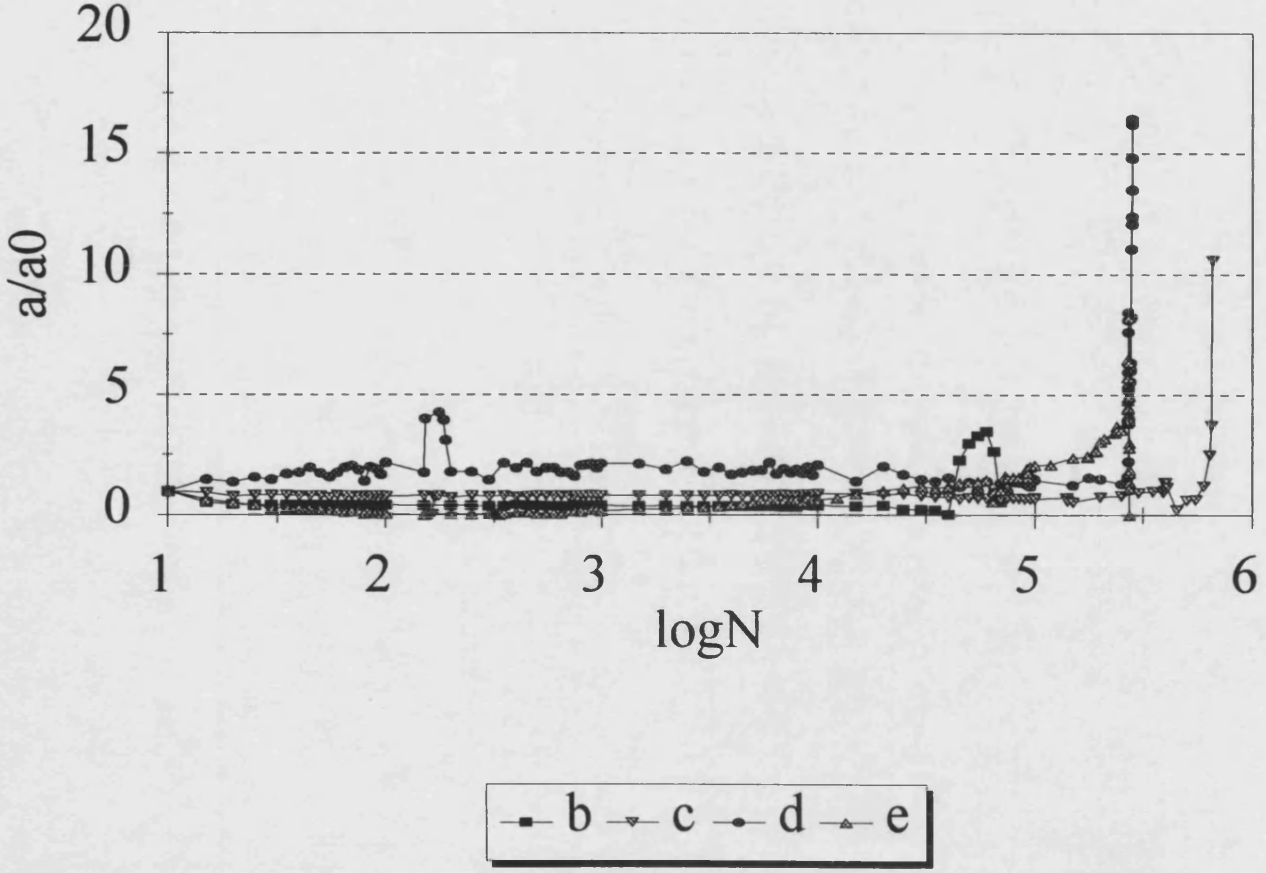

Fig.10.16. Normalised maximum and minimum strains, R=-1, Smax=35 MPa

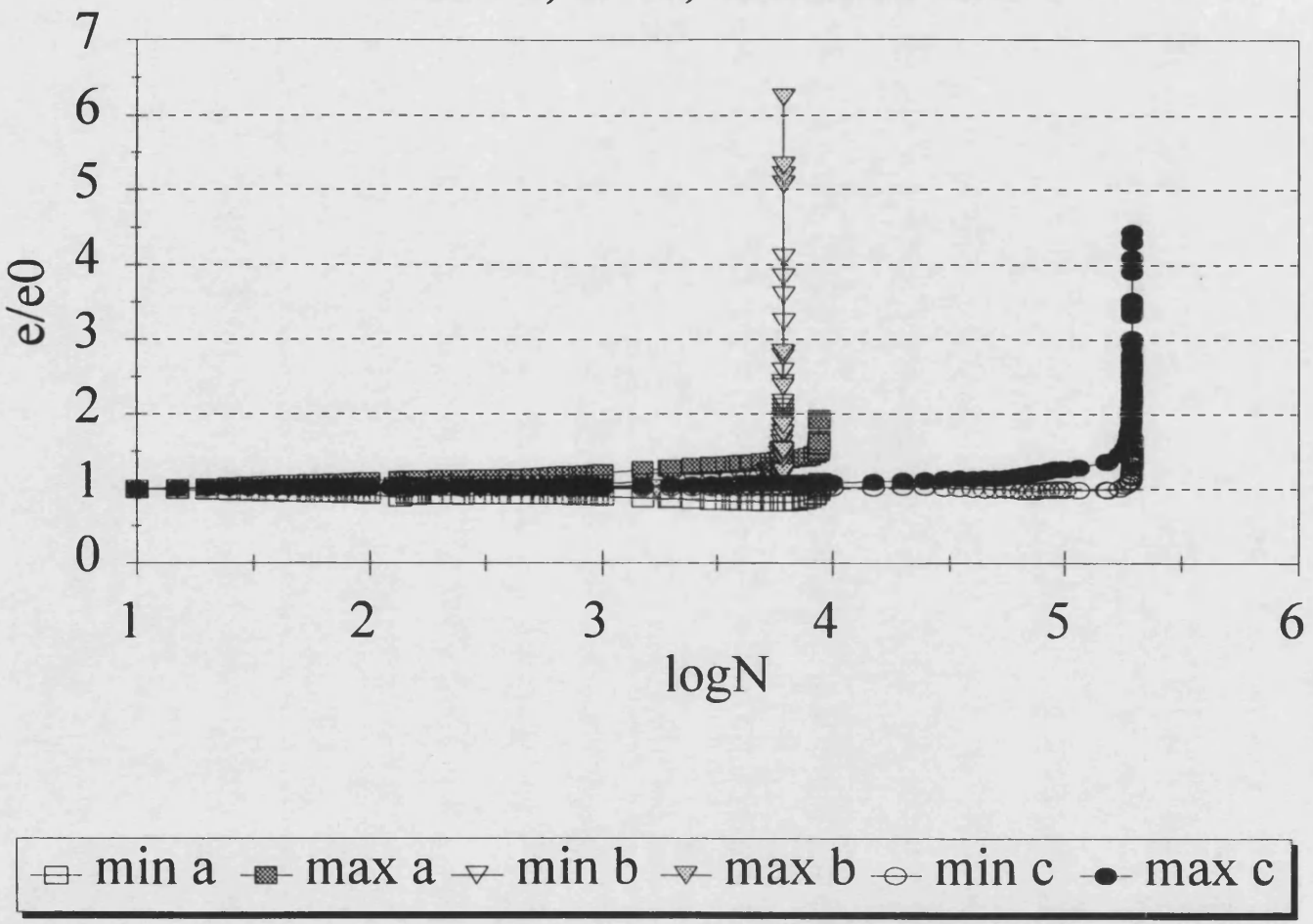

Fig.10.17. Normalised dynamic modulus for samples tested at R=-1, Smax=35 MPa

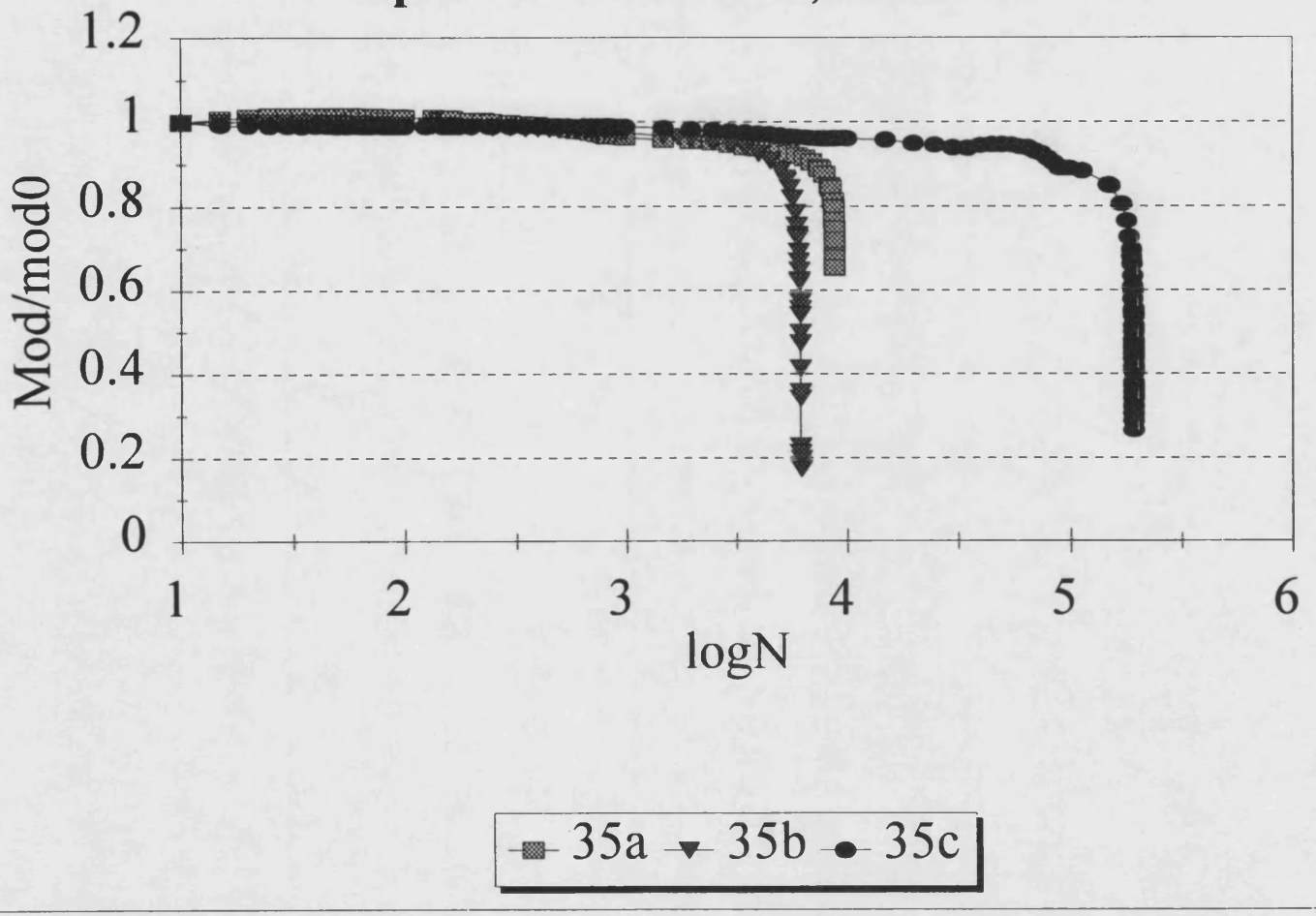

Fig.10.18. Normalised hysteresis loop area for samples tested at R=-1, S,ax=35 MPa

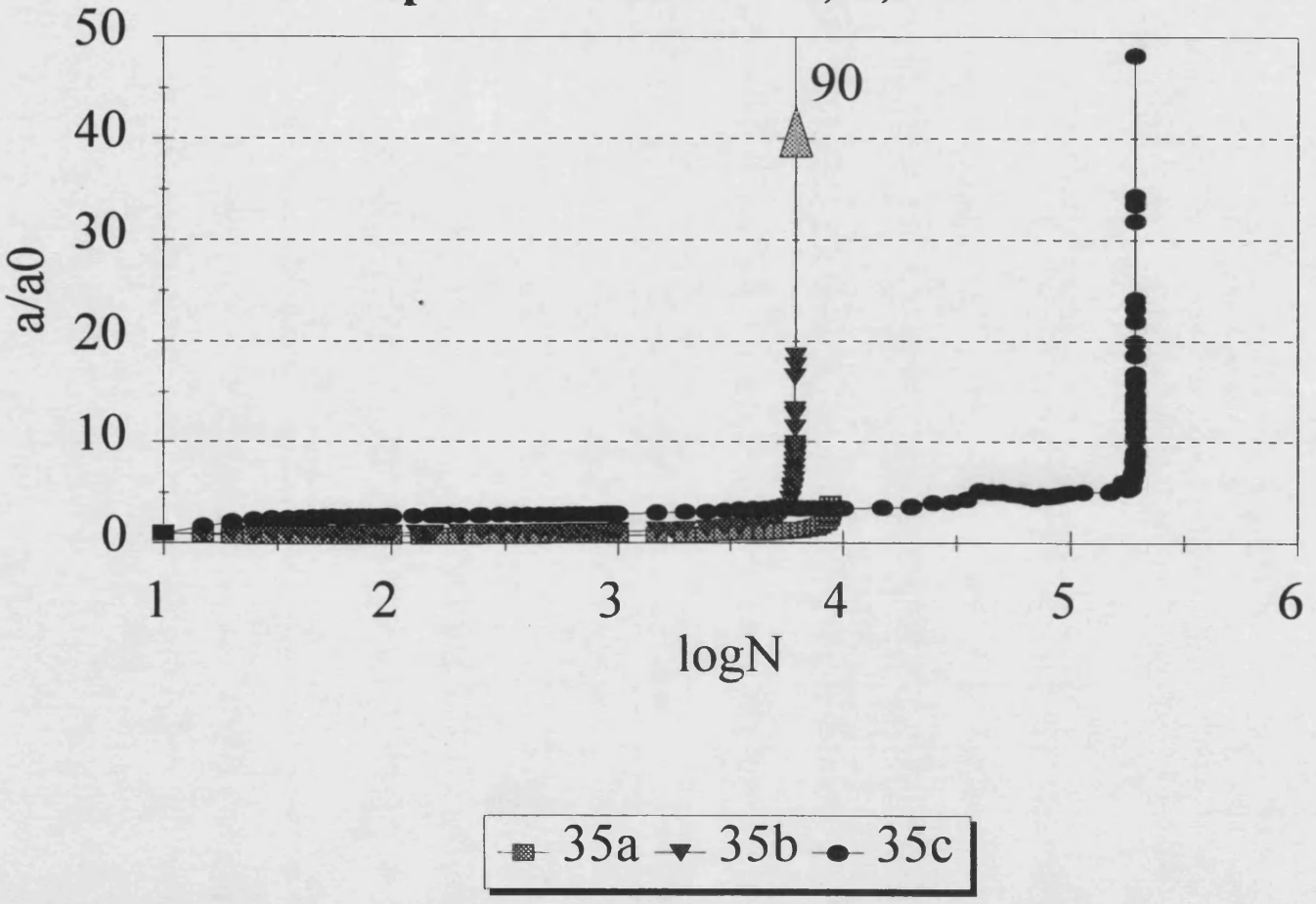

compression, however, the changes accumulate more steadily as a test proceeds and the large changes are not observed (fig.10.11).

Changes in loop area are least significant at R=10 (fig.10.12) where the loop area decreases before increasing [except 52a]. The extent of the increases is small and the most marked change in sample 52f only shows an increase of seven times. Fig.10.15 shows more significant levels of increase associated with energy losses as cracks are formed and grow in the veneers. Very large loop area changes are observed in reverse loading (fig.10.18) where loop bending due to the presence of tensile fatigue damage [cracks along the grain] is also observed.

In order to determine at what proportion of the fatigue life changes in properties occur, the data are also plotted against N/N_f, where N_f is the number of cycles to failure [as opposed to log(N)]. These plots are presented in figs.10.19 to 10.27 and show various differences in the fatigue response of the wood composite under the different loading modes. In some cases the graphs have been plotted twice on a larger scale so the trends show up more clearly, e.g. fig.10.21.

Fig.10.19 contains strain data for compression fatigue and two fatigue responses are clearly visible. In samples a, b and c the maximum strain increases rapidly whilst the minimum strain remains fairly constant or increases slowly. These samples show a rapid increase in max strain during the first 5 - 10 % of the fatigue life. The other two samples show little change in either strain value until the last 10% of life. In the samples where the minimum strain (close to zero) changes more than the maximum strain, creep is occurring under the influence of the mean fatigue stress. This is also observed to a lesser extent in tension fatigue, indicating the occurrence of tensile creep, fig.10.22. None of the curves are smooth and step increments are present in each. In between steps the rate of increase in normalised strain is much less than for the compression fatigue tests. It seems that there is no significant change in maximum and minimum strains at R=-1 until 95% of the fatigue life is expended, fig.10.25.. However, on a magnified scale this value is closer to 80% and follows a linear portion which begins at about 5% of life.

Fig.10.19. Normalised max. and min. strains vs. normalised fatigue life, R=10, Smin=-52.5 MPa

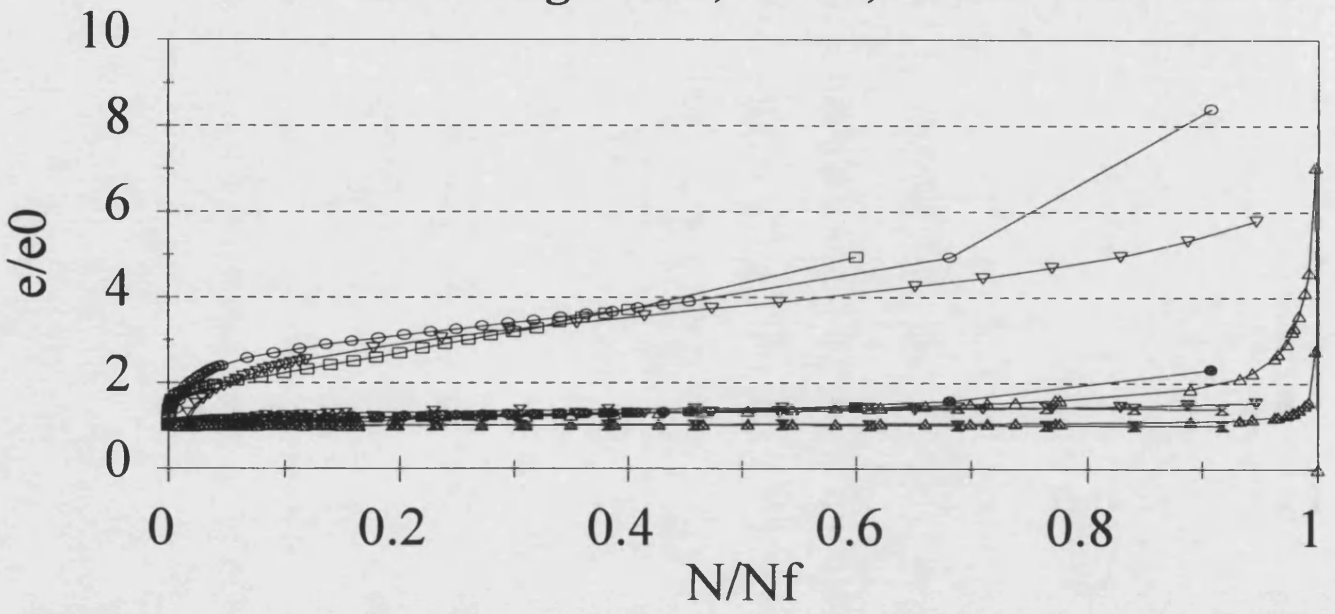

52a min — 52a max — 52b min — 52b max — 52c min
52c max — 52d min — 52d max — 52f min — 52f max

Fig.10.20. Normalised dynamic modulus vs. normalised fatigue life, R=10, Smin=-52.5 MPa

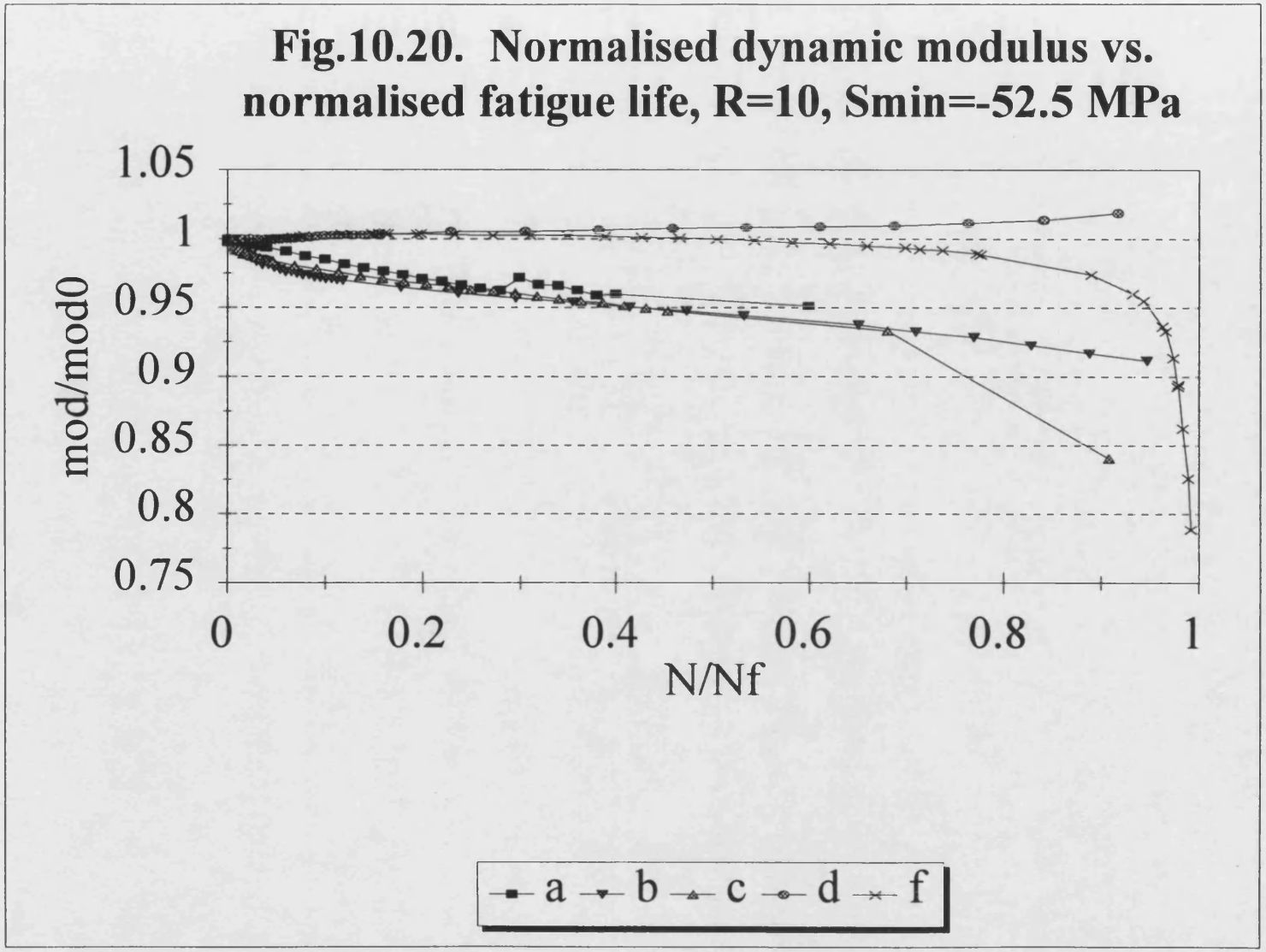

Fig.10.21a. Normalised hysteresis loop area vs. normalised fatigue life, R=10, Smin=-52.5 MPa

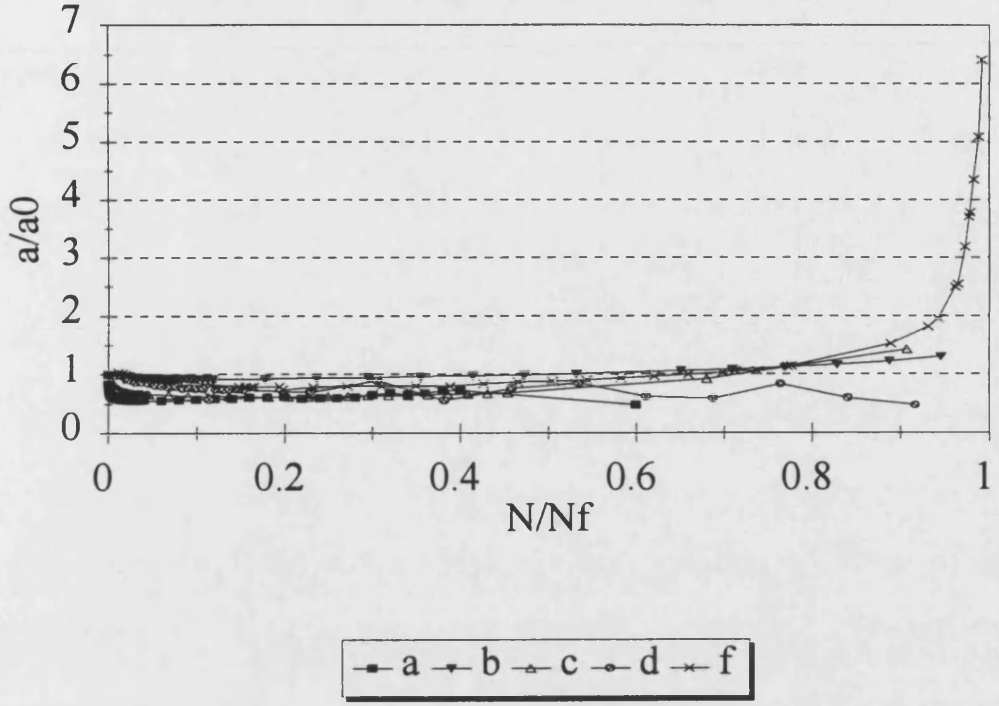

Fig.10.21b. Normalised hysteresis loop area vs. normalised fatigue life, R=10, Smin=-52.5 MPa

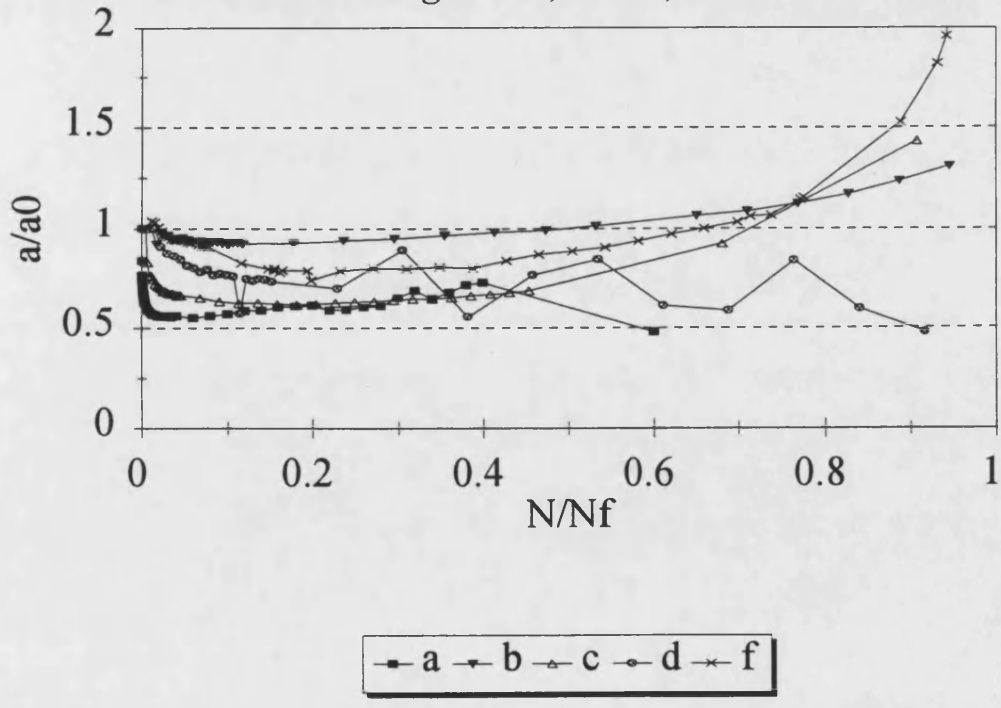

Fig.10.22a. Normalised max. and min. strains vs. normalised fatigue life, R=0.1, Smax=55 MPa

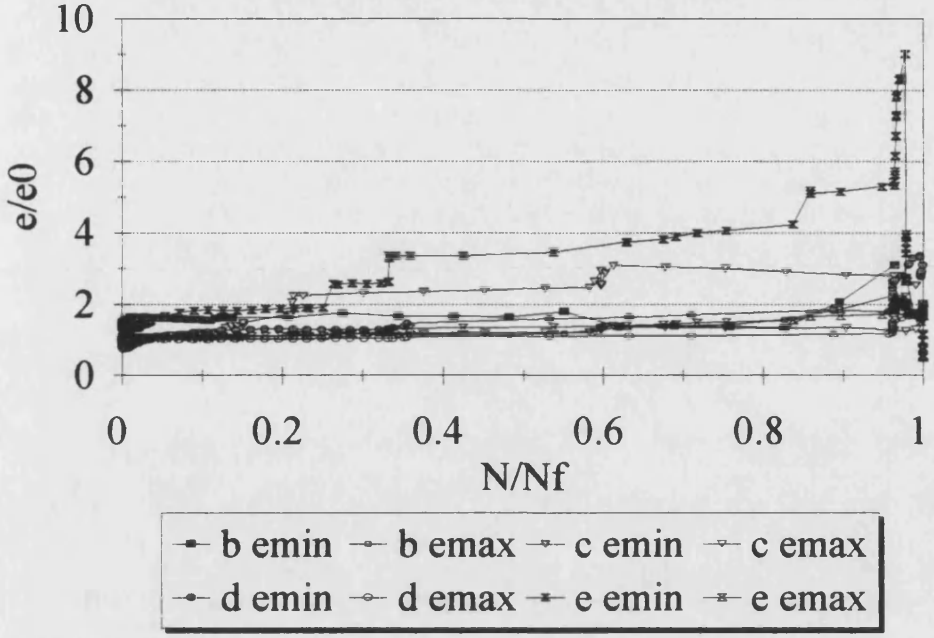

Fig.10.22b. Normalised max. and min. strains vs. normalised fatigue life, R=0.1, Smax=55 MPa

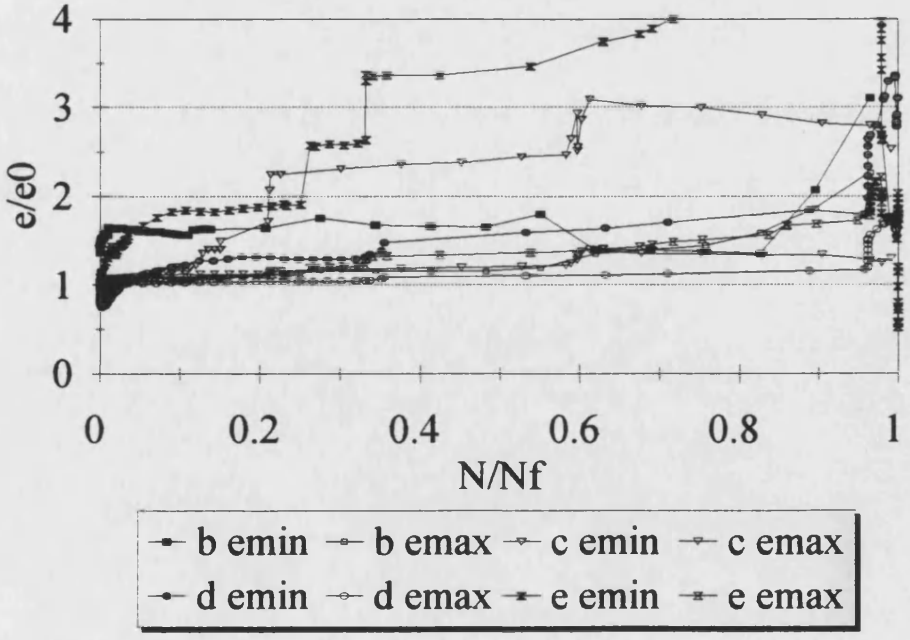

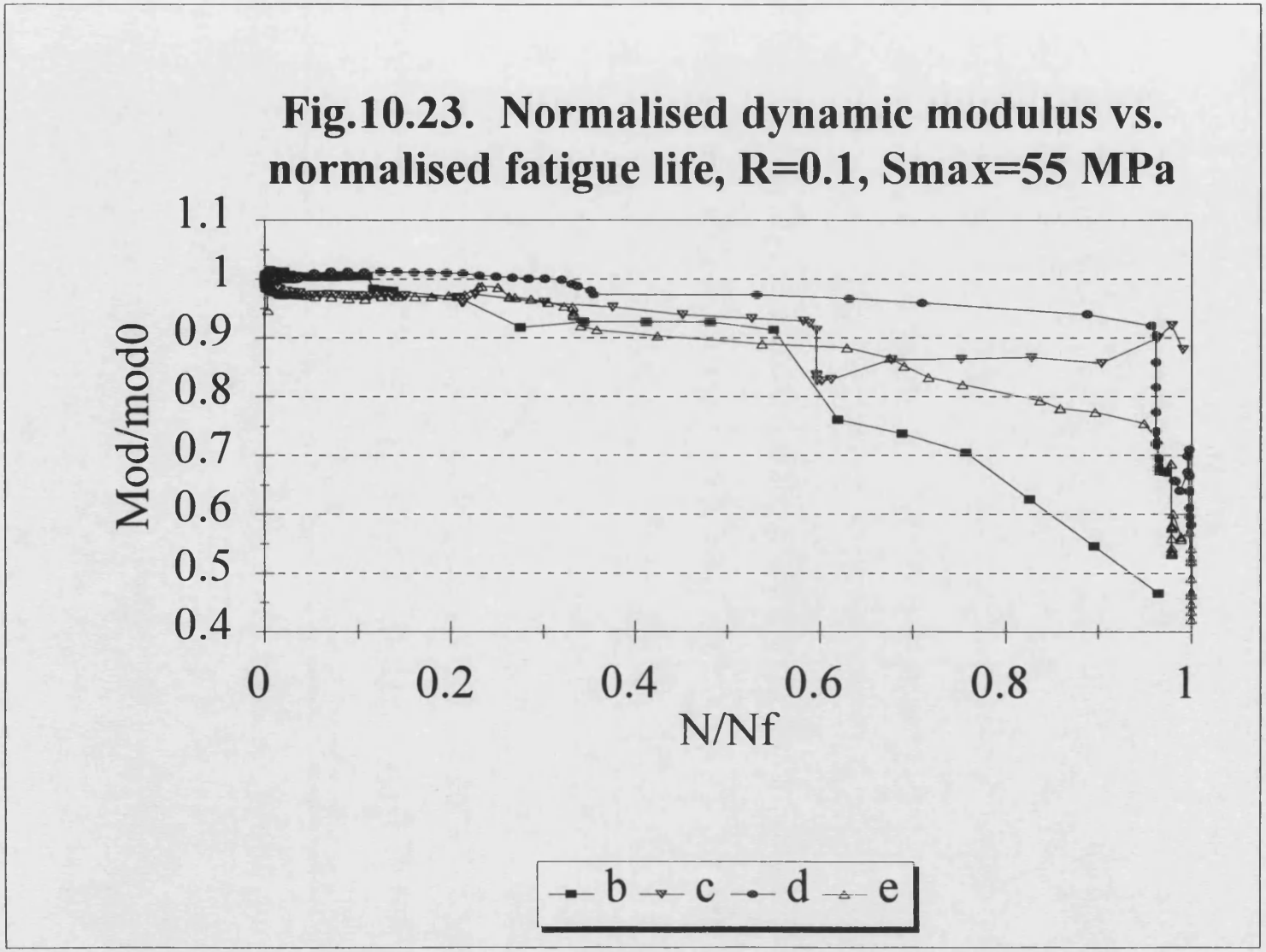
Fig.10.23. Normalised dynamic modulus vs. normalised fatigue life, R=0.1, Smax=55 MPa
Mod/mod0
1.1
1
0.9
0.8
0.7
0.6
0.5
0.4
0
0.2
0.4
0.6
0.8
1
N/Nf
b
c
d
e

Fig.10.24a. Normalised hysteresis loop area vs. normalised fatigue life, R=0.1, Smax=55 MPa

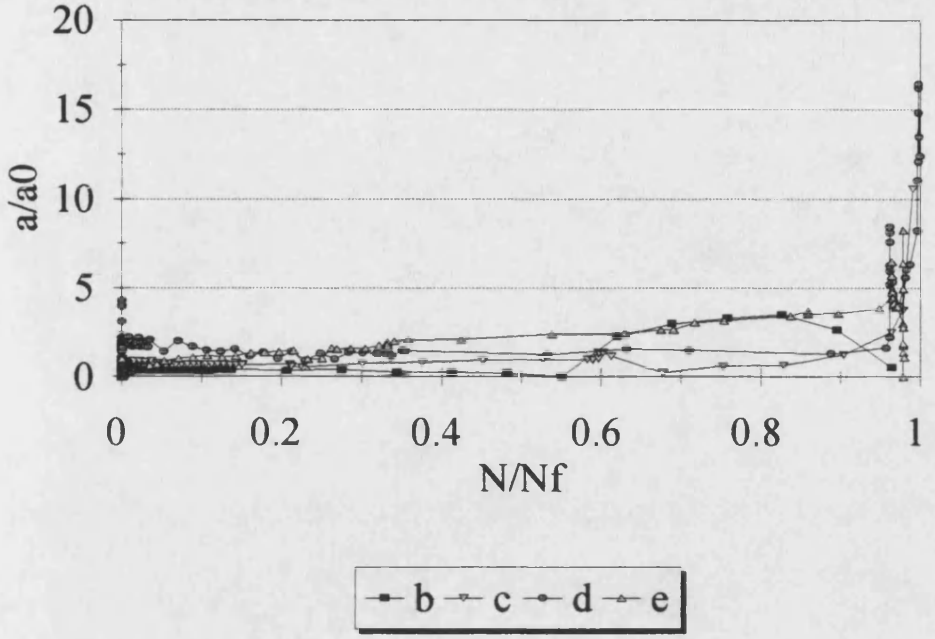

Fig.10.24b. Normalised hysteresis loop area vs. normalised fatigue life, R=0.1, Smax=55 MPa

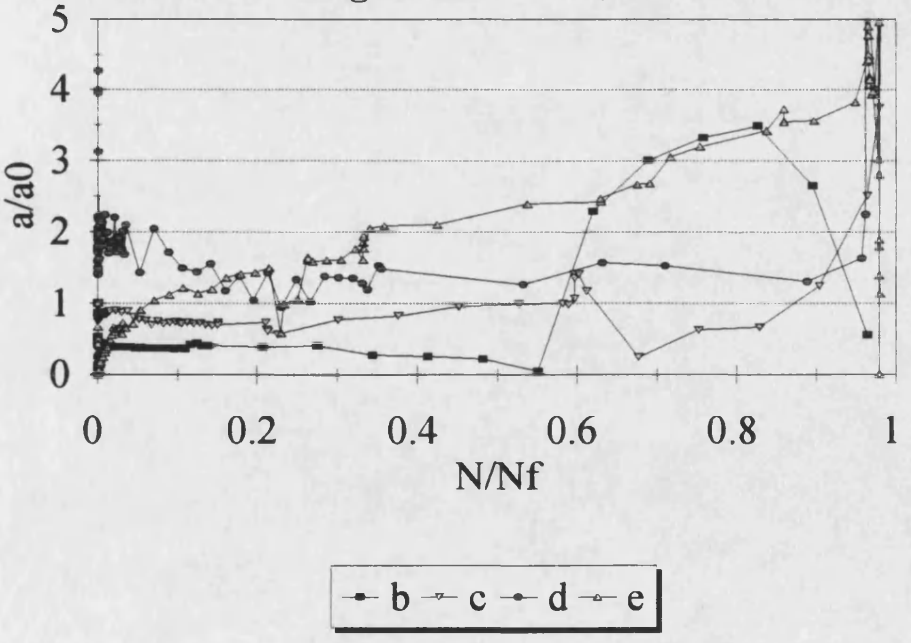

Fig.10.25a. Normalised max. and min. strains vs. normalised fatigue life, R=-1, Smax=35 MPa

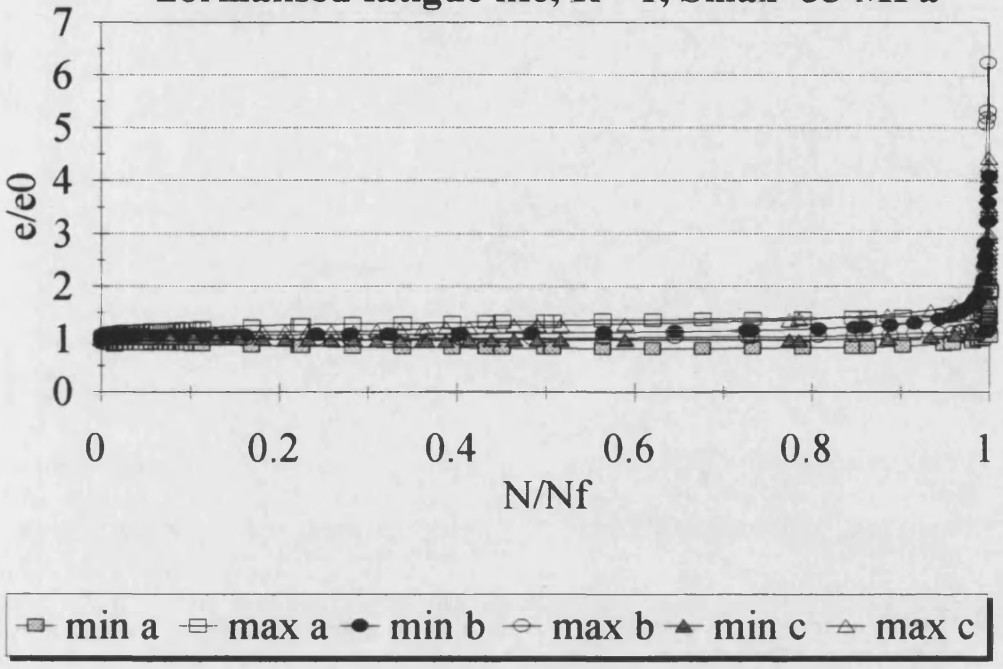

Fig.10.25b. Normalised max. and min. strains vs. normalised fatigue life, R=-1, Smax=35 MPa

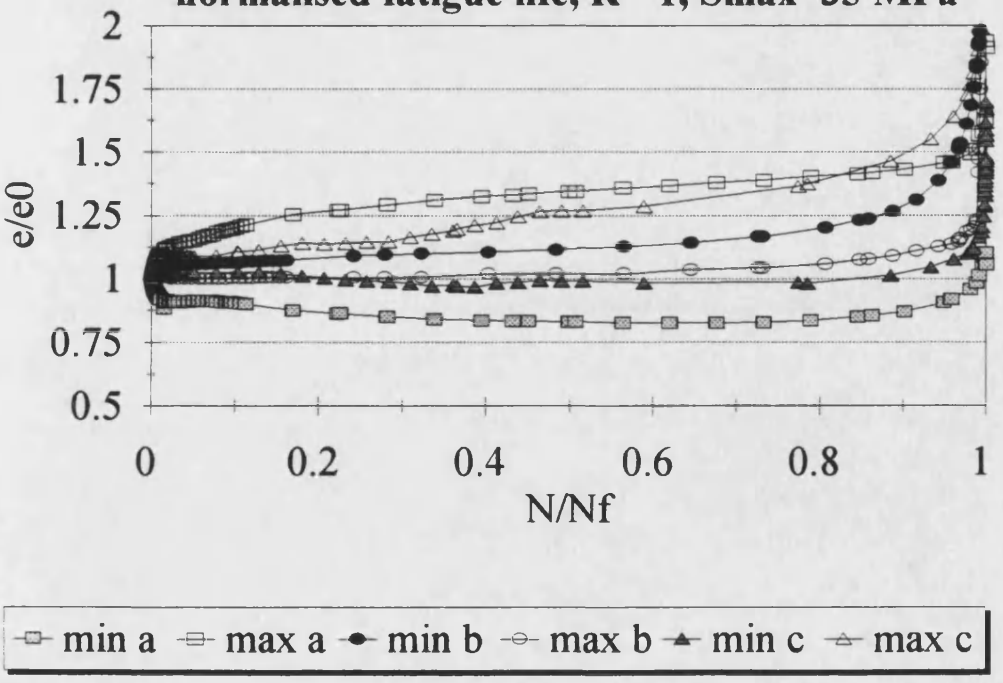

Fig.10.26a. Normalised dynamic modulus vs. normalised fatigue life, R=-1, Smax=35 MPa

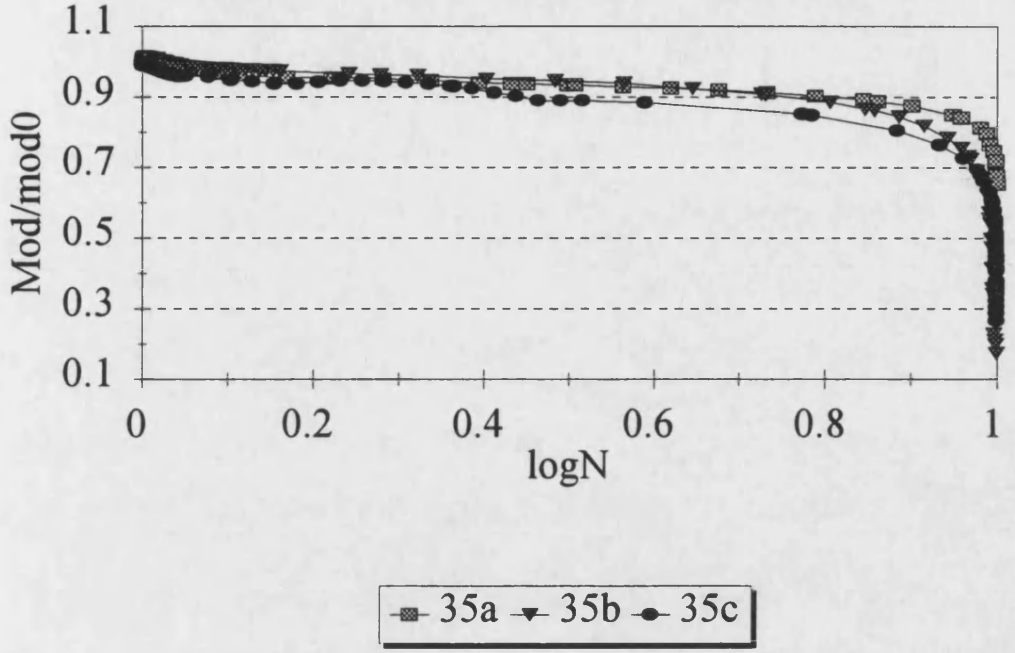

Fig.10.26b. Normalised dynamic modulus vs. normalised fatigue life, R=-1, Smax=35 MPa

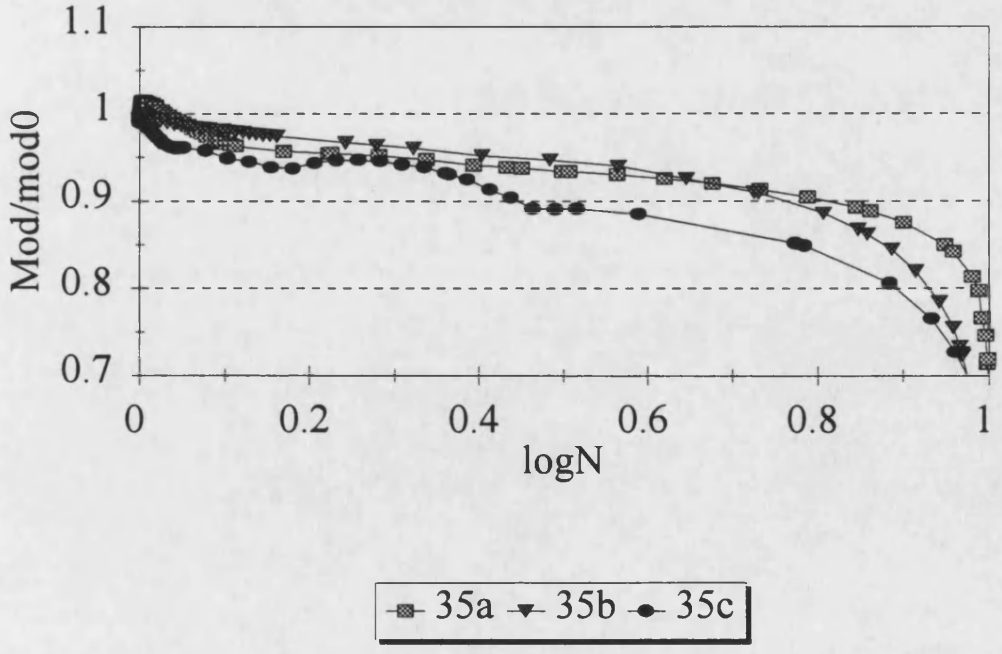

Fig.10.27a. Normalised hysteresis loop area vs. normalised fatigue life, R=-1, Smax=35 MPa

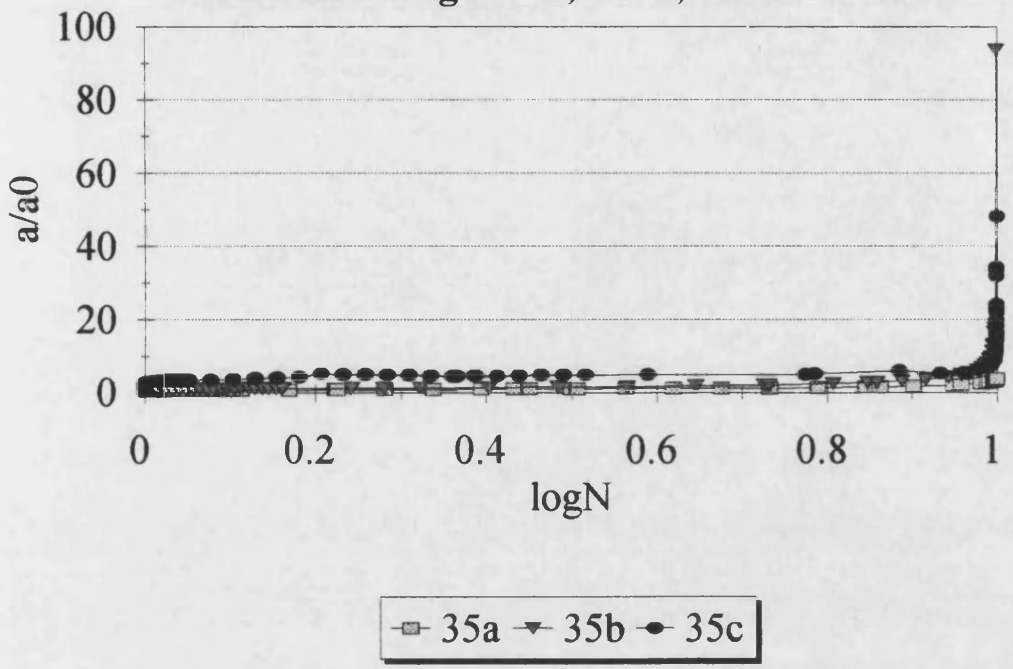

Fig.10.27b. Normalised hysteresis loop area vs. normalised fatigue life, R=-1, Smax=35 MPa

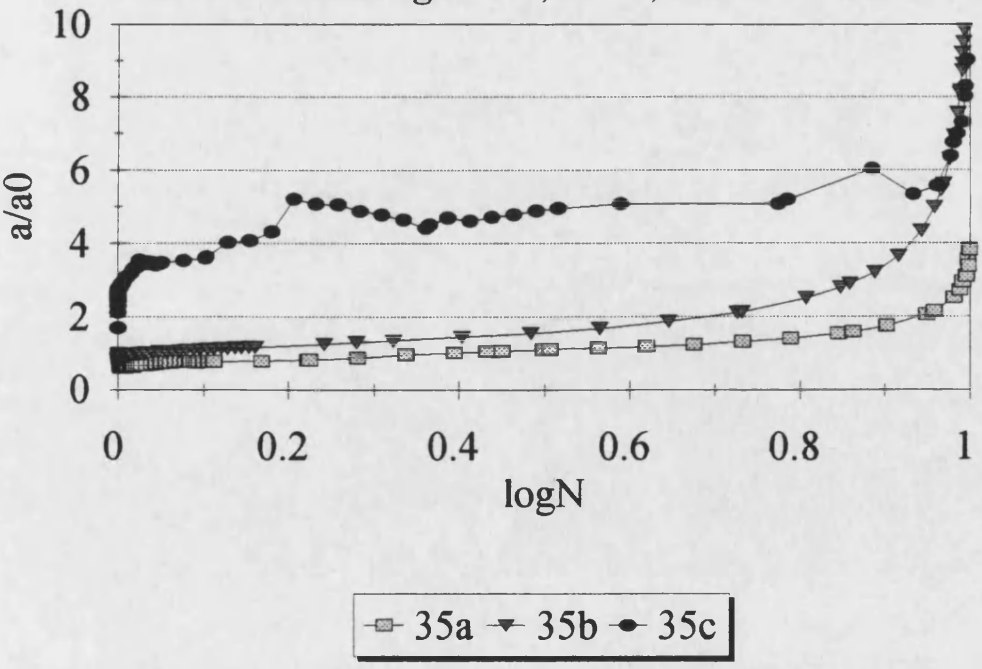

Considering the normalised modulus vs. N/N_f plots, figs.10.20, 10.23 and 10.26 the same trends emerge:

- R=10. Two types of response. One shows very little change up to failure and a second shows an initial rapid decrease followed by a steady linear change, probably followed by a rapid change prior to failure. If there is a rapid decrease immediately before failure it does not show up because the window trips were not working at the time of testing.
- R=0.1. Stepped changes in modulus starting as early as 20% of life, with big differences between samples.
- R=-1. A three stage decrease. Stage 1, a rapid change in modulus, lasting up to between 5 and 10% life; stage 2, a gradual linear change for up to 85% of life followed by the rapid decrease to failure, stage 3.

The normalised loop area plots are presented in figs. 10.21, 10.24 and 10.27. In compression fatigue all samples show a decrease in area during the first 2 to 10%. In two samples the loop area then increases to failure, albeit very slowly; two decrease and fail at 50% the original value and one increases rapidly to 6.5 times the starting value during the last 10% of life. The trends in tension fatigue are muddled with particularly rapid variations in the first and last 5% life. At R=-1 two samples show a linear increase for approximately 80% life followed by a rapid increase and one sample exhibits a three stage fatigue response with an initial rapid increase [up to 7% life], a semi-linear portion and another rapid increase to failure in the last 10%.

10.3. Loading and unloading moduli at R=-1

If the hysteresis loop was a straight line, enclosing no area, then it would be expected that the gradient of the stress strain response for loading and unloading in tension and compression would be the same. In practice this is never the case although in some instances they are indistinguishable at the start of the test Fig.10.28 shows schematically the different loading and unloading moduli and how they are likely to change under reverse loading fatigue. The dynamic modulus, E, is plotted as well to show how it falls in the middle of the tensile and compressive loading and unloading moduli at the start of the test.

The tensile and compressive loading moduli were calculated and plotted for all samples tested at R=-1. The data were examined and the observed trends tabulated (table 10.1). Fig.10.29 is a typical example of the most common trends observed.

In the third column of table 10.1 capital letters denote the most common order of the moduli before and after loop bending; "/" divides moduli where the first and second are similar and noticeably higher than the third and fourth. In the fourth column the number of cycles at which the loops begin to bend is expressed as a ratio of the number of cycles to failure. The final order of the loop moduli is presented, where possible, in column five.

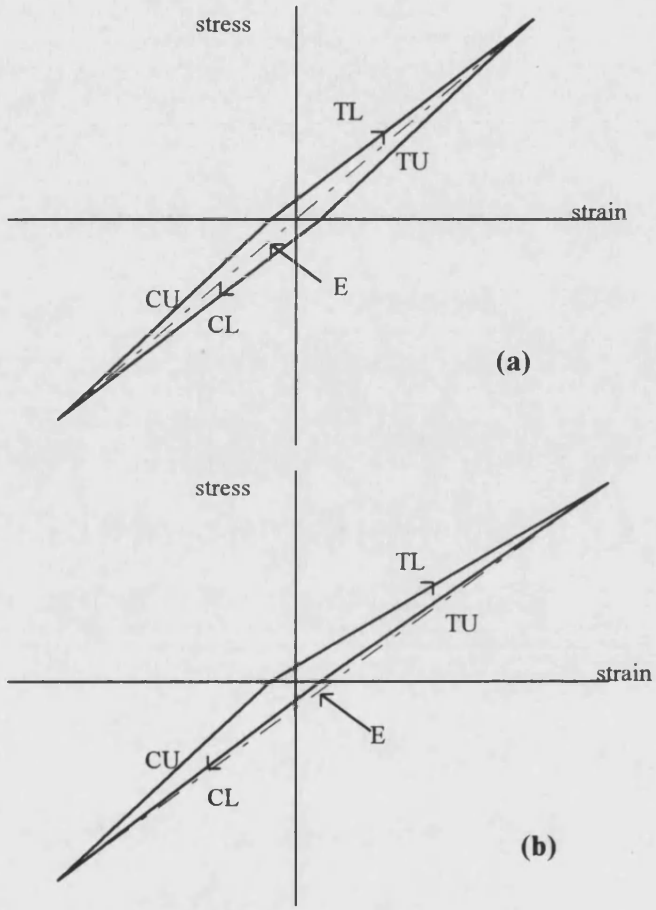

TL	tensile loading modulus
TU	tensile unloading modulus
CL	compression loading modulus
CU	compression unloading modulus
E	Dynamic modulus

In general, TU, CU > E > TL, CL at start of test.

Fig.10.28. Schematic diagram showing the different loading and unloading moduli,(a) at start of test, (b) after loop bending has occurred.

Sample	Max. stress, MPa	Highest-lowest moduli values	Splitting of the curves, N/N_f	Comments - final order
RM125a	25	TU, CU / TL, CL	no	all of very similar shape
RM130c	30	TU, CU / TL, CL	0.5	tu, tl, cu , cl
RM130f	30	tu, tl, cu, cl	0.72	CU, CL, TU, TL
RM130g	30	TU, CU / TL, CL	0.55	CU, CL, TU, TL
RM130h	30	TU, CU, TL, CL	0.45	CU, CL, TU, TL
RM135a	35	TU, CU / TL, CL	no	---
RM135b	35	TU, CU, TL, CL	no	---
RM135c	35	TU, CU / TL, CL	0.575	CU, CL, TU, TL
RM140a	40	cu, tu / tl, cl	no	---
RM140b	40	TU, CU TL, CL	0.2	CU, CL, TU, TL
RM140e	40	TU, CU / TL, CL	no	---
RM145a	45	TU, CU, TL, CL	no	---
RM145b	45	tu, cl, tl, cu	0.95	indistinguishable
RM145c	45	TU, CU, TL, CL	no	---
RM150a	50	cu, tu, / cl, tl	no	---
RM150b	50	tu, cl, tl, cl	no	---
RM150c	50	TU, CU, TL, CL	no	---

Table 10.1. Summary of tensile and compressive loading and unloading moduli.

The majority of loops have the highest modulus in tensile unloading (TU), followed by the compressive unloading (CU), tensile loading (TL) and compressive loading (CL) moduli. The gradient of the complete loop falls in between the compressive unloading and the tensile loading moduli. When the loops begin to bend the order of the moduli changes to CU, CL, TU and TL in the majority of cases as tensile damage causes significant changes in the tensile moduli but not the compression moduli. This occurs most commonly at between 0.4 and 0.6 of the samples life. In approximately 50% of the cases loop bending does not occur.

If the data in table 10.1 is compared with that in table 11.3 [see Chapter 11] it can be appreciated that there is not the clear correlation between the changes in tensile and compressive moduli and the various fatigue responses described for reverse loading. This is probably because other factors such as loop fattening affect the tensile and

Fig.10.29. Tensile and compressive loading and unloading moduli, R=-1, Smax=30 MPa

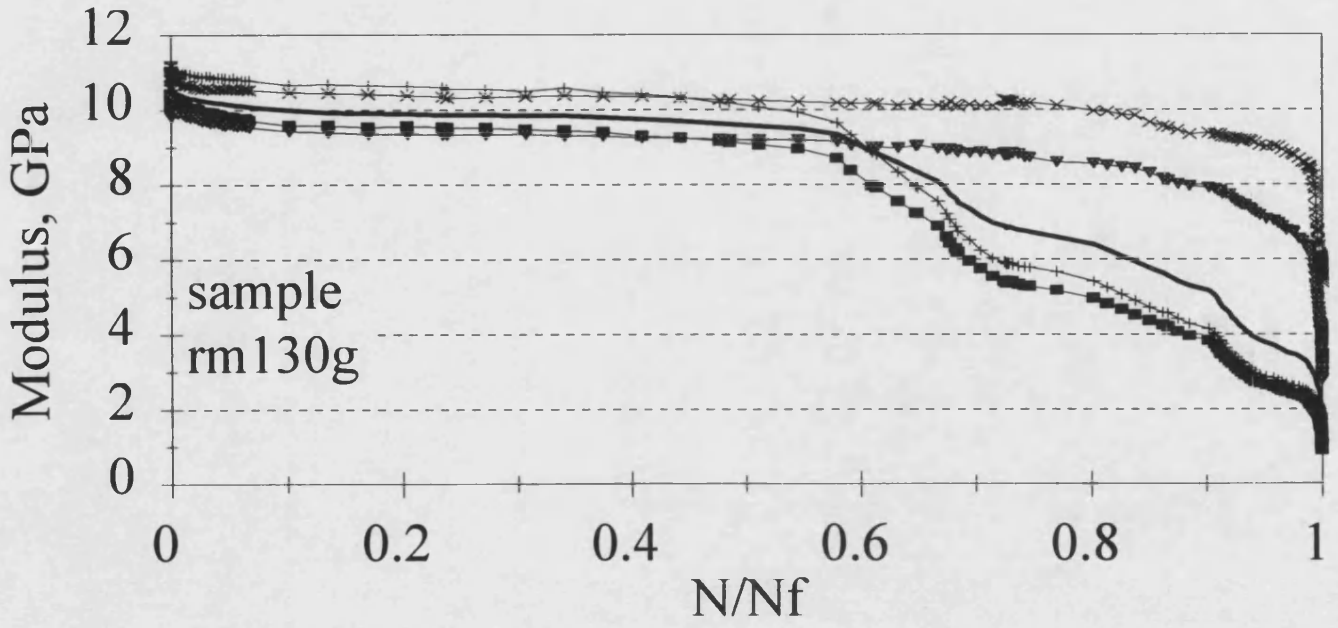

compressive moduli values, masking the expected changes in all but the most prominent cases. However, it can be said that for all samples showing a compression fatigue response no changes in the order of the TL, TU, CL and CU moduli were observed which indicates that no loop bending had occurred, as might be expected. Changes in moduli order were more common at lower stress levels.

10.3. Conclusions

Property changes as a function of log(N) have been generated for all samples tested in compression, tension and reverse loading fatigue. Both similarities and differences have been observed in the wood composite's fatigue response under the different loading regimes. The following general trends were observed:

- the strain increases in the direction of the applied stress
- the significant changes in strain occur at the end of a sample's fatigue life
- the dynamic modulus decreases
- the loop area increases
- the loop area decreases at the start of a test before increasing to failure
- during the initial part of the fatigue life the property remains unchanged or varies in a linear fashion.

The following differences in fatigue response were observed:

- creep is most significant at R=10
- a decrease in modulus is most significant at R=0.1
- the change in properties is not smooth but occurs in steps due to the accumulation and growth of tensile fatigue cracks at R=0.1
- loop bending occurs only at R=-1
- the most marked changes in properties occur at R=-1.

Normalising the data by dividing by the initial property value allows better comparison between samples of an inherently variable material. It was clear that:

- at R=10 the normalised strain increases and modulus decreases approximately linearly throughout the sample's life
- at R=0.1 and R=-1 the main changes in relative strain and modulus occur in the last half decade of cycles before failure

Plotting N/N_f as the x axis yields information on when in a sample's fatigue life the changes in properties occur.

- R=10. The samples tested at this R ratio showed two fatigue responses. The first had a rapid initial change in strains, moduli and areas up to 5-10% life followed by a gradual, semi-linear, change up to 90% of life after which the properties changed rapidly. The second showed very little change throughout their fatigue lives.
- R=0.1. There was large variation between samples and step changes in properties began as early as 20% of life.
- R=-1. All samples showed a three-stage change in strains and moduli. An initial rapid change during the first 5% of life was followed by small changes until 80% of life when properties changed rapidly again. The samples, however, exhibited either two- or three-stage changes in loop area. The two stage response consisted of a linear increase up to approximately 80% of life followed by rapid change to failure. The three-stage response comprised rapid change in the first 5% and last 20% of life with little change in between.

Tensile and compressive loading and unloading moduli have been calculated for reverse loading samples. The most common initial order of the moduli from highest to lowest was tu, cu, tl, cl, but after loop bending had occurred changed to CU, CL, TU, TL as tensile damage accumulated and caused a reduction in the tensile stiffness of the composite. This occurred most frequently between 40 and 60% life. However, no distinct correlation was observed between the fatigue damage response described in Section 3, probably due to the changes being affected by other factors such as loop fattening.

11. INITIAL PROPERTIES

One of the simplest methods of using stress-strain hysteresis loop data is to consider the property values at the start of a test and to relate them to the number of cycles to failure. This has been done for tests carried out at R=10, 0.1 and -1.

11.1. R=10

Figs.11.1 to 11.3 show the relationships between fatigue lifetime and initial strain, modulus and loop area.

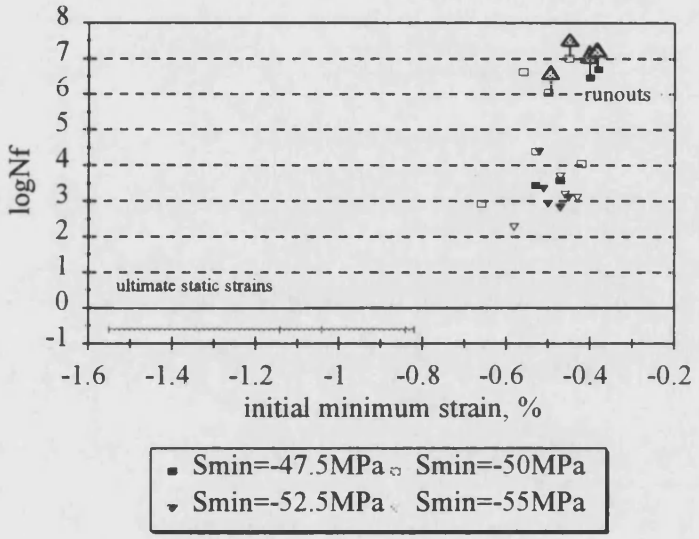

Fig.11.1. The relationship between initial dynamic modulus and sample lifetime at R=10.

In figs.11.1 and 11.2 values have been included from 5 static tests for comparison with the fatigue results. It is clear that there is a large amount of scatter in the results, which is to be expected due to the variable nature of the fatigue response of composite materials. Fig.11.2 shows the widest amount of scatter and there in no obvious relationship between the initial dynamic modulus and fatigue life, even when considering samples all tested at the same stress level. This is not entirely surprising as the static compressive Youngs moduli values span almost the same range as the dynamic moduli values. There is a better correlation between the number of cycles to failure and the strain, fig.11.1, and loop area, fig.11.3. In general, the samples with the lowest maximum fatigue strain have shorter lives than the ones with higher fatigue strains and the samples with high loop areas also fail the most rapidly. In fig.11.1 the strain data tend to form a cluster of between -0.4 and -0.55% with a few data points falling outside this group. This clustering is not surprising as all the sampler were tested within a strain range of only 10MPa [S_{min} = -45 to -55MPa].

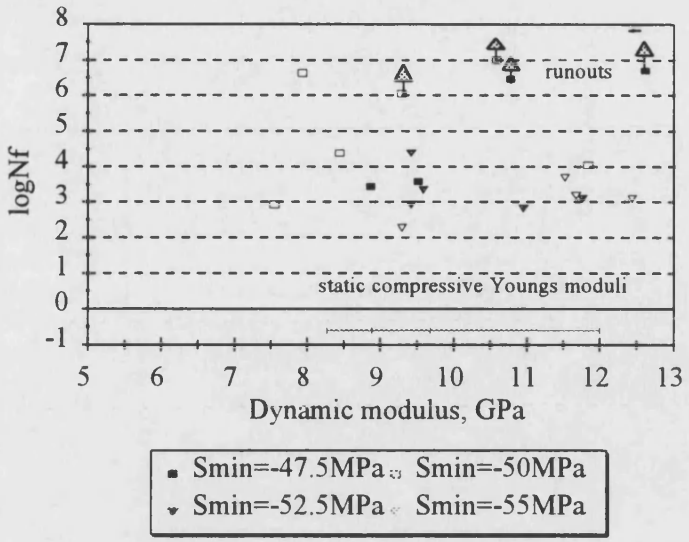

Fig.11.2. The relationship between initial dynamic modulus and sample lifetime at R=10.

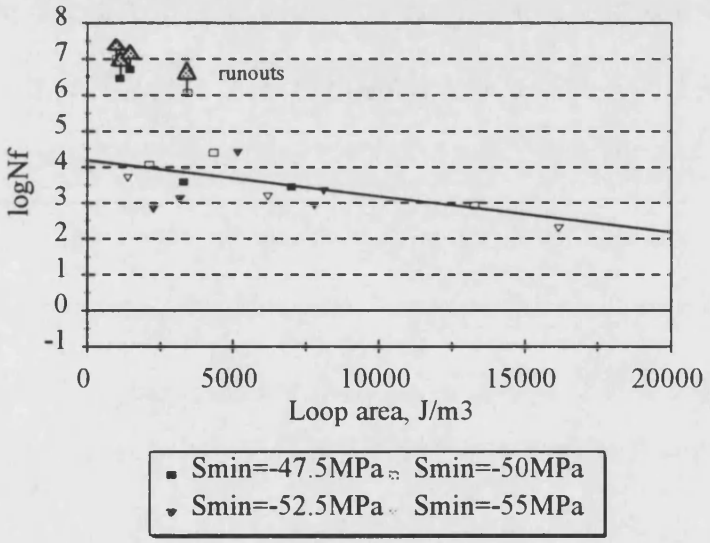

Fig.11.3. The relationship between initial hysteresis loop area and sample lifetime at R=10.

11.2. R=0.1

Figs.11.4 to 11.6 show the initial properties and the effect they have on fatigue life at R=0.1, tension fatigue. In comparison to the data for R=10, compression fatigue, the trends are better defined.

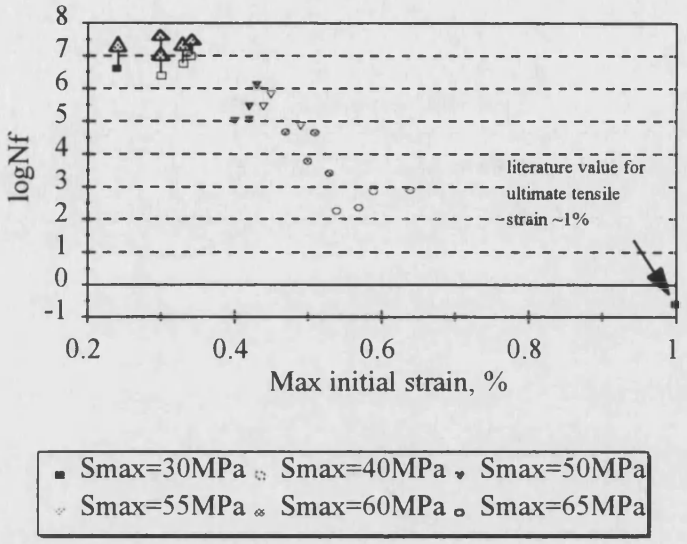

Fig.11.4. The relationship between initial maximum fatigue strain and sample lifetime at R=0.1.

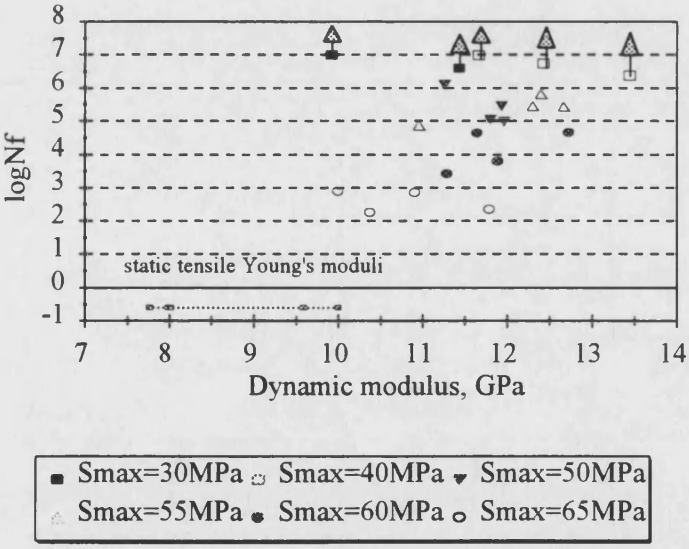

Fig.11.5. The relationship between initial dynamic modulus and sample lifetime at R=0.1.

Fig.11.4 shows the relationship between initial maximum strain and the number of cycles to failure. All the samples with a strain of less than 0.4% have not failed and as the strains increase log(N_f) decreases. The approximate ultimate static tensile strain (Dinwoodie, 1981) has also been included. If a curve was to be fitted through this point and the non-runout fatigue data points a line of the form log(N_f) = k/(max initial strain)

where k is a constant would give the best fit, suggesting that there is a fatigue limit in tension fatigue.

Data for dynamic modulus are presented in fig.11.5, and are distinctly different from those in fig.11.2 at R=10. Again the static tensile Youngs moduli values have been included for comparison. With the exception of two fatigue points all the initial fatigue moduli are higher than the static values, and the overall trend is for samples with higher moduli to survive the longest. This is not the case with the runout samples whose modulus values span the range of samples which failed. Dinwoodie (1981) states that in tension wood behaves elastically up to 60% UTS and Sun (1993) found the departure from linearity to be lower at 45±5%. The stress levels of the runout samples correspond to 35% and 47% UTS, close to or below the elastic limit. The marked difference in behaviour of the runout samples compared with those which failed suggests that fatigue damage does not build up in samples cycled below the elastic limit.

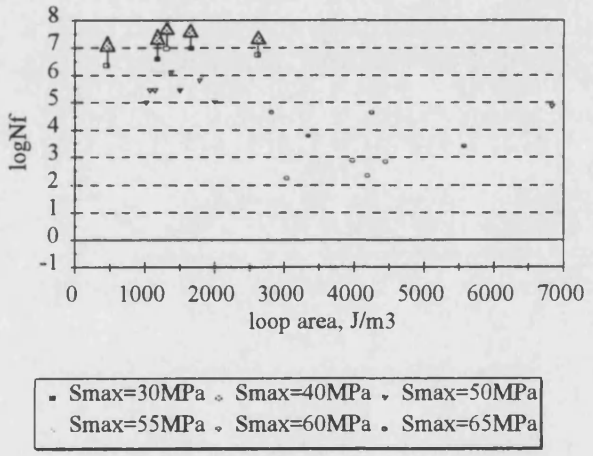

Fig.11.6. The relationship between initial hysteresis loop area and sample lifetime at R=0.1.

The loop area data in fig.11.6 can be split into three regions: the runout samples; those with a loop area of less than $2000Jm^{-3}$ and ones with an area greater than $2000Jm^{-3}$. All the samples with the low areas have a fatigue life of above 10^5 cycles, whereas those with areas above $2000Jm^{-3}$ show a much larger scatter in both areas [3000 to $7000Jm^{-3}$] and lifetimes [10^2 to 10^5 cycles].

11.3. R=-1

Figs.11.7 to 11.9 show the initial properties and the effect they have on fatigue life at R=-1, reverse loading fatigue. Like the R=0.1 data, in comparison to the data for R=10, the trends are more defined.

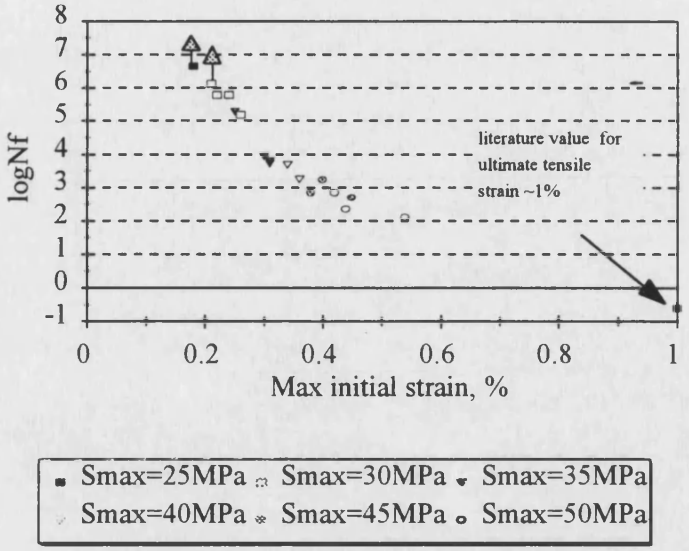

Fig.11.7. The relationship between initial maximum fatigue strain and sample lifetime at R=-1.

Fig.11.7 shows the clear relationship between the maximum initial strain and the fatigue lifetime, where samples with high initial strains have the shortest fatigue lives. As in tension fatigue, a curved line passing through the approximate static tensile strain best fits the data. This suggests the presence of a fatigue limit for reverse loading where strains of ±0.1% are unlikely to cause failure of the composite in under 10^8 or 10^9 cycles.

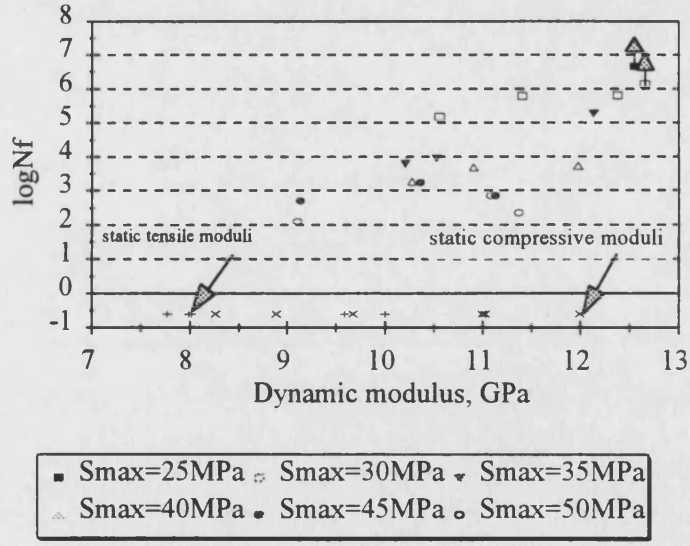

Fig.11.8. The relationship between initial dynamic modulus and sample lifetime at R=-1.

The initial dynamic moduli values are presented in fig.11.8 along with the tensile and compressive Youngs moduli obtained from static tests. As in fig.11.5 the general trend is that samples with higher moduli have the longest fatigue lives. This trend is also

observed when considering the behaviour at individual stress levels, but it is less marked and there is more scatter at the highest stress levels [45MPa and 50MPa]. This is not surprising because, as has been shown in Chapters 9 and 10, the samples loaded at the highest stress levels at R=-1 accumulate fatigue damage and fail in a compressive manner but the lower stress levels tend to cause tension-dominated fatigue damage. Fig.11.2 shows that there is no relationship between the initial modulus and fatigue lifetime at R=10 and this behaviour is reflected in the greater levels of scatter in the high stress level tests at R=-1. It is also clear that there is a much larger variation in compressive Young's modulus than the tensile modulus, a characteristic also reflected in the compression-dominated samples (fig.11.2) and the tension-controlled samples (fig.11.5) respectively.

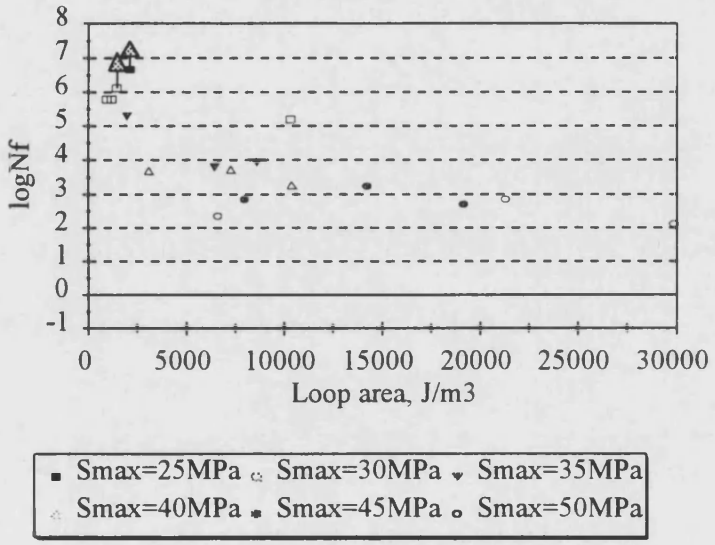

Fig.11.9. The relationship between initial hysteresis loop area and sample lifetime at R=-1.

Fig.11.9 presents the relationship between initial loop area and fatigue lifetime. The relationship between loop area and $\log(N_f)$ is similar to that observed in compression fatigue (fig.11.3), with the high loop area samples surviving the lowest number of fatigue cycles.

11.4. Conclusions

At R=10 the fatigue response was characterised by a large amount of scatter and compressive creep due to the proximity of the minimum applied stress to the UCS. The minimum fatigue strains were all similar and fell into a cluster when plotted with $\log(N_f)$ because of the small range of minimum stresses tested. Consequently there was no clear relationship linking minimum initial strain and life. Dynamic modulus provided no link to fatigue life with large scatter in both the static and dynamic values.

The relationship between initial loop area and fatigue life was fairly good with samples generating a large loop area having the shortest fatigue life.

The trends are more defined in tension fatigue with strain and $\log(N_f)$ showing the best relationship. All samples with a maximum fatigue strain of less than 0.35% were runouts. The fact that a curved line best fits the data suggests that there is a fatigue limit at R=0.1. Most initial dynamic moduli were found to be higher than the static values and samples possessing higher moduli tended to have a longer fatigue life. At lower stress levels the degree of scatter was much higher. This was also the case for loop areas and it is likely that this feature is related to fatiguing below the elastic limit of the wood composite.

The dependence of fatigue lifetime on initial parameters such as loop area and maximum initial fatigue strain was most marked for reverse loading fatigue. The strain-$\log(N_f)$ relationship had very low scatter and its curve fit suggests the possible presence of a fatigue limit. At low stress levels the modulus-$\log(N_f)$ plot was similar to that at R=0.1 but at high stress levels there was greater scatter and the data were more similar to the compression fatigue results. This reinforces the idea that at R=-1 high stress level tests are controlled by compression fatigue and at the lower levels tension fatigue dominates. The loop area response was found to be similar to the compression fatigue response.

12. SUMMARY OF CHANGES IN PROPERTIES

In Chapter 10 we saw the way in which the composite's properties [such as loop area and maximum or minimum strains] changed as a result of fatigue damage accumulation. The volume of data associated with these tests is large and it is important to be able to distinguish trends in property changes in a straightforward manner.

In order to identify these changes and the effect of R-ratio on the fatigue response of the composite the general trends were tabulated, see tables 12.1 to 12.3. The sample numbers correspond to the maximum, or minimum, stress applied to the sample. [ro] is an abbreviation of 'runout' and indicates that the sample did not fail in the duration of the test. Next to each sample number are shown the changes in dynamic modulus, hysteresis loop area and creep strain. For clarity they are shown as an increase or decrease in that property and a tensile or compressive creep and as such are unmasked by a multitude of figures. A property which changed by less than ±5% is shown to have undergone no change. To further highlight the property changes, any modulus or area showing a decrease is shaded grey, and an increases is indicated by a double edged box.

The first and last property values were presented graphically and the complete set is given in Appendix D. Fig.12.1 serves as an example (p.194).

12.1. R=10

The data presented in table 12.1 contains summarised results for the tests carried out at R=10.

The only consistent behaviour observed in table 12.1 is that all samples showed compressive creep under the influence of a mean compressive stress. However, a number of observations can be made despite the apparent lack of trends in dynamic modulus and loop area.

1. Approximately 50% of the samples showed no change in modulus, and 50% showed a decrease.
2. Approximately 50% of the sample exhibited an increase in loop area and 50% showed a decrease.
3. In all but one case, the samples showing a decrease in modulus also show an increase in loop area.
4. The samples showing an increase in modulus also show a decrease in loop area.

5. Of those showing no change in modulus all but three show a decrease in loop area.

Sample number	dynamic modulus	loop area	creep
47a	no change	decrease	C creep
47b	decrease	increase	C creep
47c [ro]	decrease	increase	C creep
47d [ro]	no change	decrease	C creep
50a [ro]	no change	decrease	C creep
50b [ro]	no change	decrease	C creep
50d	increase	decrease	C creep
50f	decrease	increase	C creep
50g [ro]	no change	no change	C creep
50h	no change	increase	C creep
52a	increase	decrease	C creep
52b	decrease	increase	C creep
52c	decrease	decrease	C creep
52d	no change	decrease	C creep
52f	decrease	increase	C creep
55a	no change	increase	C creep
55b	decrease	increase	C creep
55c	decrease	increase	C creep
55d	no change	decrease	C creep

Table 12.1. Overall property changes for samples tested at R=10.

In the samples where dynamic modulus increased or loop area decreased the property changed, on the whole, by less than 10% but where modulus decreased and loop area increased the changes tended to be more significant. Typically, the modulus decreased to between 90% and 80% of its original value and the loop area might increase by over 10 times. It is unclear why the expected trends of a decrease in dynamic modulus and an increase in loop area (Bonfield, 1991) as a result of damage accumulation are not consistently apparent.

12.2. R=0.1

The way in which the wood composite properties change in tension fatigue are summarised in table 12.2. The same conventions have been adopted as in table 12.1.

Four different regions in the table were identified at various stress levels where certain property changes are the most consistent feature, as follows:

1. A decrease in loop area
2. A decrease in modulus
3. Tensile creep
4. A decrease in loop area

Sample	gradient	area	creep	characteristic features			
				1	2	3	4
30a [ro]	no change	decrease	C	X			
30b [ro]	no change	decrease	C	X			
40a [ro]	increase	decrease	C	X			
40b [ro]	no change	decrease	T	X			
40c [ro]	no change	decrease	T	X			
50d	increase	increase	C		X		
50h	decrease	decrease	C		X		
50i	decrease	increase	T		X		
50j	decrease	increase	C		X		
55b	decrease	decrease	T		X	X	
55c	decrease	increase	T		X	X	
55d	decrease	increase	T		X	X	
55e	decrease	increase	T		X	X	
60a	increase	decrease	T			X	
60d	decrease	increase	T			X	
60e	no change	no change	T			X	
60f	no change	decrease	T			X	
65a	no change	decrease	none				X
65b	increase	decrease	T				X
65c	no change	decrease	T				X
65d	no change	decrease	C				X

Table 12.2. Overall property changes for samples tested at R=0.1.

In region 1 all hysteresis loops decreased in area and in the majority of cases there is no change in dynamic modulus. Over half the samples tested showed compressive creep which is surprising as the mean fatigue stress is tensile. These are the samples cycled at

below their elastic limit where, it is suggested, no fatigue damage occurs. Any changes in properties are most likely to be caused by the sample's moisture content decreasing slowly over the several weeks test duration [despite being enclosed in a constant relative humidity environment] or the operation of some form of work hardening mechanism.

At stresses of 50MPa and 55MPa a decrease in modulus was the most prevalent feature. It was accompanied by an increase in loop area in all but 2 samples and all but 3 exhibited tensile creep. This group overlapped with samples where tensile creep was the most noticeable feature [S_{max}=55 and 60MPa]. Of these samples half exhibited the expected decrease in dynamic modulus and increase in loop area. At the highest stress level the composite's behaviour became similar to that of the runout samples with loop thinning as the prevalent feature. The majority showed no change in dynamic modulus.

The changes in properties are shown clearly when the first and last value for each property is plotted. Fig.12.1 shows how this illustrates the trends in change in dynamic modulus, particularly highlighting the stress levels where the changes in dynamic modulus are most dramatic.

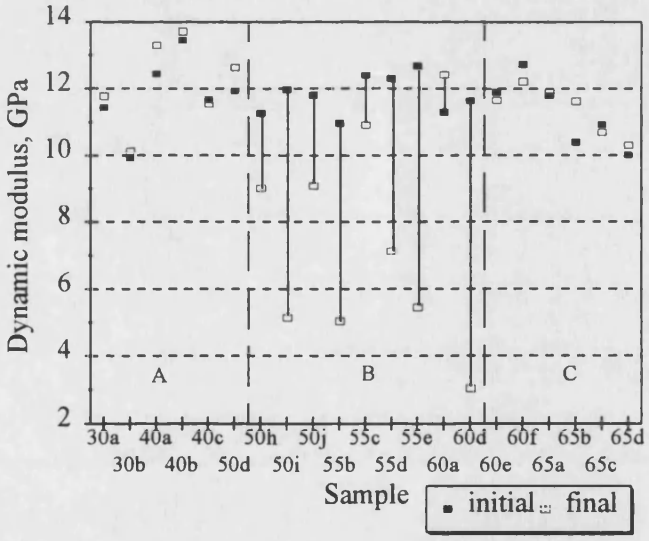

Fig.12.1. Initial and final dynamic moduli for all samples tested at R=0.1.

12.3. R=-1

The changes in properties of the Khaya epoxy wood composite under reverse loading fatigue are the most complicated of all three loading regimes investigated, not surprisingly, as it incorporates the effects of both tensile and compressive fatigue damage. The results of analysis of hysteresis loops are summarised in table 12.3. Four

different types of fatigue response were identified, tension dominated, compression dominated, a combination of the two and an intermediate response:-

Sample	gradient	area	creep @S=0MPa	loop bending	behaviour type
25a [ro]	no change	decrease	none		ro
30c	increase	increase	C		int
30f [ro]	decrease	decrease	T		ro
30g	decrease	increase	none	T&C	both
30h	decrease	increase	T	T	T
35a	decrease	increase	T		T
35b	decrease	increase	none	T&C	both
35c	decrease	increase	T	T&C	both
40a	decrease	increase	T		T
40b	decrease	increase	T		int
40e	decrease	increase	none	C	C
45a	decrease	increase	none		C
45b	decrease	increase	T	T	T
45c	decrease	increase	none	C	C
50a	decrease	increase	none		int
50b	decrease	increase	none	C	C
50c	decrease	increase	none	C	C

Table 12.3. Overall property changes for samples tested at R=-1.

With the exception of three low stress tests, two of them runouts, the gradients and loop areas show a consistent pattern of increasing area and decreasing dynamic modulus. Given that both tensile and compressive strains can change to different degrees the creep strain was taken at zero load. Whether loop bending was observed is also indicated. The behaviour type was determined by examining the hysteresis loops. All samples where loop bending had occurred in the compressive loading region were classified as exhibiting a compressive fatigue response. Those showing tensile creep were classified as showing a tensile fatigue response. Those with loop bending in the tensile and compressive loading regions were said to exhibit both of the above and samples with an 'intermediate' classification showed characteristics which were not well defined enough to fall into any of the previous groups.

12.4. Conclusions

At R=10 all samples showed compressive creep, all but two showed no change or a decrease in modulus and the loop area showed an equal tendency to increase or decrease in the course of a compression fatigue test.

At R=0.1 the fatigue response depended on stress level with different fatigue responses becoming dominant at different stresses. The runout samples, the lowest stress level tests, showed a decrease in loop area. Intermediate stress levels caused a decrease in modulus and/or tensile creep and the high stress level sample's predominant response was similar to the runout tests where loop area decrease prevailed.

The changes in properties of the Khaya epoxy wood composite under reverse loading fatigue are the most complicated of all three loading regimes as it incorporates the effects of both tensile and compressive fatigue damage. Four different types of fatigue response were identified, tension dominated, compression dominated, a combination of the two and an intermediate response.

13. FATIGUE MODULUS

13.1. Introduction

Wood composites are successful materials for wind turbine blade construction and they compete favourably with glass reinforced plastics and have excellent fatigue properties. One aim of the research carried out on the fatigue properties of wood composites at the University of Bath in conjunction with Wind Energy Group Ltd. is to increase understanding of how damage accumulates in a wood composite during fatigue. It is well known (Bonfield and Ansell, 1991) that fatigue causes damage throughout the bulk of the material, resulting in a gradual decrease in material stiffness. Fatigue is often accompanied by creep as a result of the mean fatigue load and it is the combination of these two processes which leads to eventual failure.

Stress-strain hysteresis loops have been captured during fatigue tests performed at R=10 (compression fatigue) and R=0.1 (tension fatigue) on Khaya epoxy wood composites. A fatigue modulus approach, proposed by Hwang and Han in 1989, has been applied to the data and a relationship established between the initial change in fatigue modulus and fatigue life. By following changes in fatigue modulus during the first 100 test cycles it is possible to predict the life of the sample, allowing rapid evaluation of the fatigue performance of wood composites.

A fatigue modulus approach was first introduced by Hwang and Han (1989) in their investigation of the fatigue of carbon reinforced plastic materials. The concept of a fatigue modulus is illustrated in fig 13.1 for a compression fatigue test. The gradients of the stress versus strain hysteresis loops decrease and shift to the left with time, indicating that fatigue and compressive creep are occurring simultaneously. The fatigue modulus F(N) is defined as the gradient of the line from the starting point of loading, K, at the beginning of a test to the stress-strain maximum for each hysteresis loop, M_1, M_N and M_L. It incorporates the effect of creep and fatigue in a way that dynamic modulus or mean strain alone do not.

Hwang and Han (1989) used the fatigue modulus approach applied to previously proposed fatigue life prediction methods in conjunction with a strain failure criterion to predict the number of cycles to failure for single and multi -stress level tests. The strain failure criterion states that fatigue failure will occur when the maximum fatigue strain reaches the ultimate static strain, see figs.5.8 and 5.9.

Yang, Lee and Sheu (1992) and Lee, Yang and Sheu (1993) applied the fatigue modulus approach in conjunction with appropriate failure criteria to predict the behaviour of matrix dominated composite laminates. Their failure criterion stated that failure would occur when the fatigue modulus fell by a certain amount and this correlated well with experimental results.

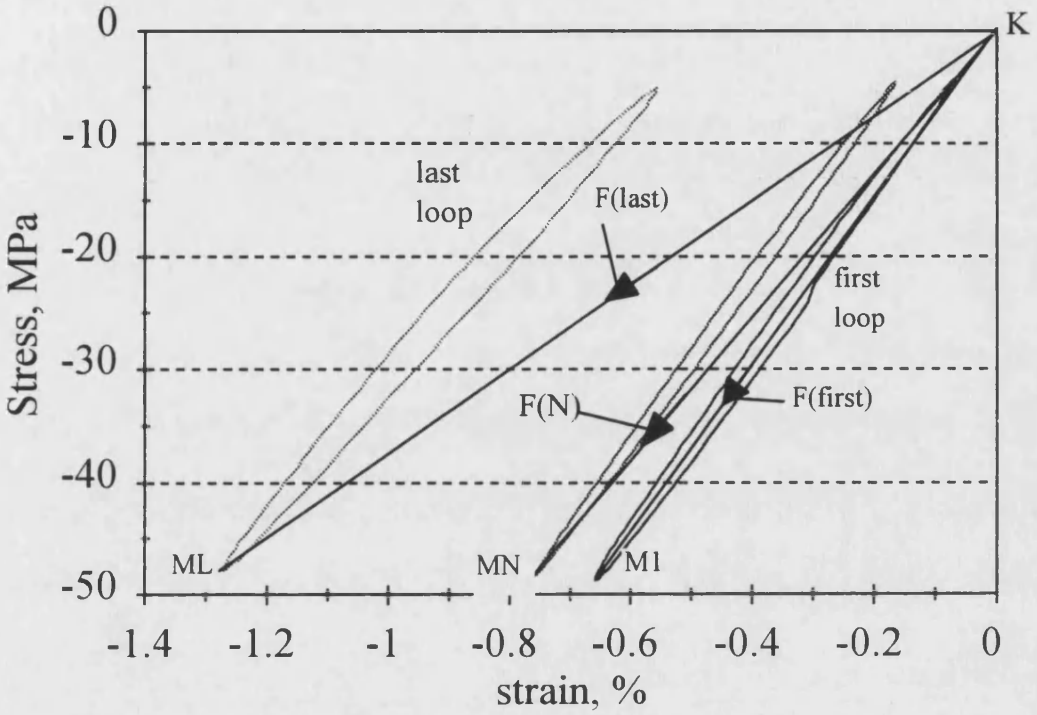

Fig.13.1. The concept of fatigue modulus. F(N) = fatigue modulus at the Nth cycle.

The fatigue modulus approach has been applied to wood composites under conditions of constant amplitude and complex loading so that life prediction can be attempted.

13.2. Life prediction at R=10

Fig 13.2 shows the changes in normalised fatigue modulus with log cycles for samples tested at a minimum stress of -55MPa. Each sample exhibits a gradual decrease in fatigue modulus until failure occurs. This, however is not always the case and some samples failed without any gradual modulus change and were labelled 'sudden death' samples. It was noticed that, with the exception of samples failing by 'sudden death', the samples exhibiting the most rapid decrease in fatigue modulus also failed after the least number of fatigue cycles.

In the cases of the samples which fail by 'sudden death' it is not possible to predict when they will fail because there are no changes in modulus to suggest that failure is imminent. A fatigue modulus analysis was, therefore, only applied to the samples

which failed after a progressive decrease in fatigue modulus. The fatigue moduli versus log cycles of all the samples which failed in this way are presented in fig 13.3.

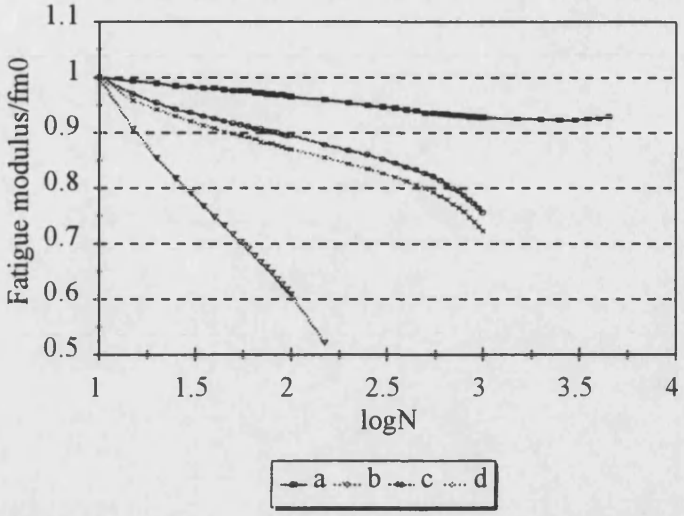

Fig.13.2. Fatigue modulus normalised by the initial fatigue modulus (fm_0) for samples tested at R=10, S_{min}=-55MPa.

The decrease in fatigue modulus falls into three regions. After an initial rate of decrease the fatigue modulus decreases more slowly before decreasing rapidly to failure. It can be appreciated from figs 13.2 and 13.3 that in general the samples which failed at the lowest number of cycles are the ones whose fatigue modulus decreased most quickly.

In order to determine any link between the rate of decrease in fatigue modulus and the number of cycles to failure the gradients of the first and second stages of fatigue modulus change were calculated from the graph by fitting straight lines to each curve, table 13.1. The first modulus corresponds to the tangent modulus at fm/fm_0=1.

In order to determine the equation relating the change in fatigue modulus and the number of cycles to failure the data were plotted and a logarithmic curve fit applied, figs.13.3 and 13.4.

The equations which best fit the first and second fatigue moduli data are given in equations 13.1 and 13.2 respectively.

$$LogNf=1.062-3.481*\log|FM1| \qquad \text{eq.13.1.}$$

$$LogNf=0.397-2.875*\log|FM2| \qquad \text{eq.13.2.}$$

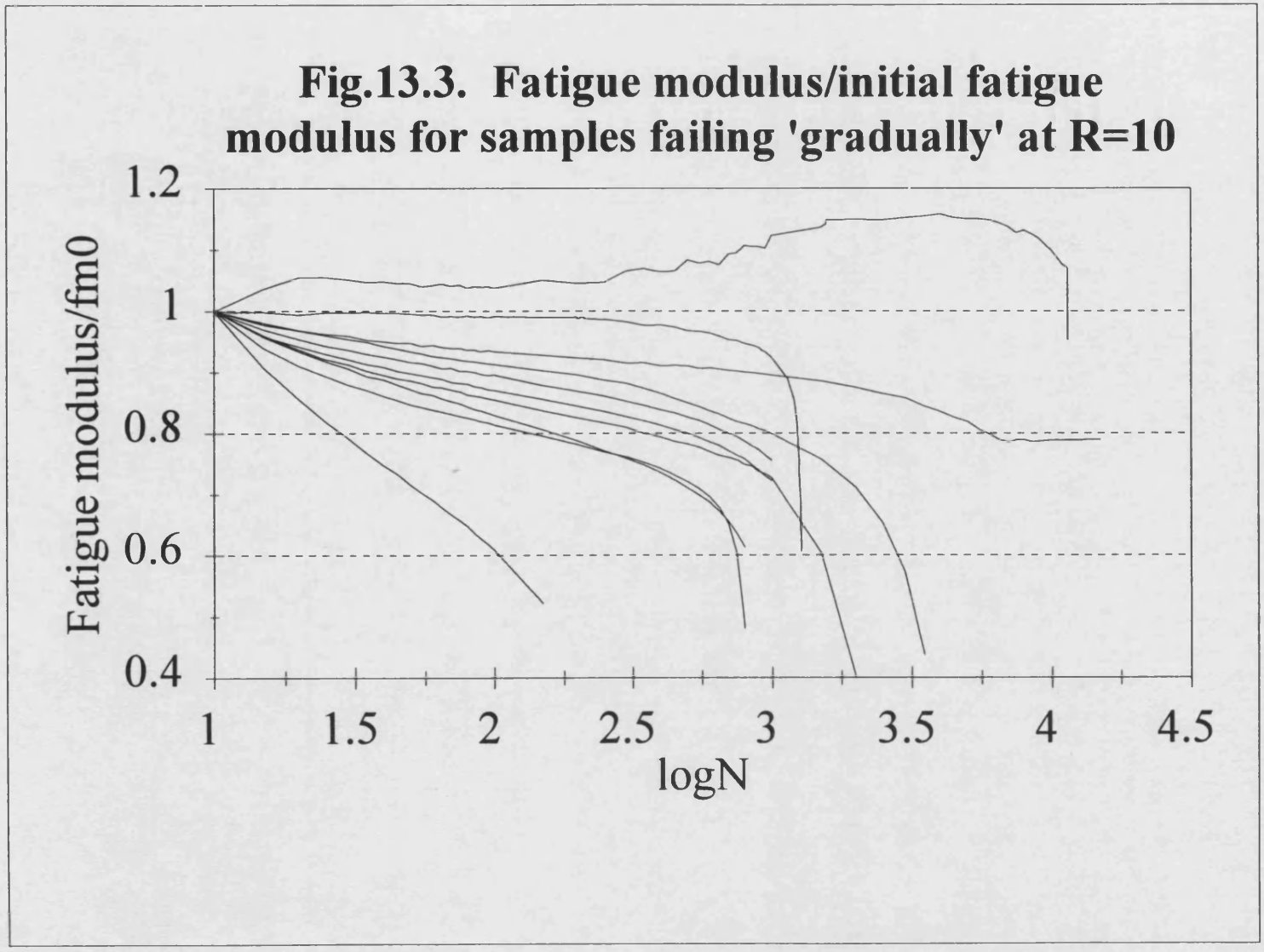
Fig.13.3. Fatigue modulus/initial fatigue modulus for samples failing 'gradually' at R=10
Fatigue modulus/fm0
1.2
1
0.8
0.6
0.4
1
1.5
2
2.5
3
3.5
4
4.5
logN

Sample	gra(FM1) $(\log \text{cycles})^{-1}$	gra(FM2) $(\log \text{cycles})^{-1}$	$\log N_f$ $(\log \text{cycles})^{-1}$
R1055b	0.536	0.347	2.28
R1052b	0.364	0.112	2.93
R1050f	0.253	0.141	2.93
R1055d	0.238	0.0906	3.09
R1052c	0.232	0.103	3.34
R1055c	0.198	0.0817	3.11
R1047b	0.138	0.0529	3.57
R1052a	0.127	0.0394	4.4
R1050a (runout)	0.0458	0.0188	6.06

Table 13.1 The magnitude of measured gradients of the first and second stages of fatigue modulus decrease and log cycles to failure.

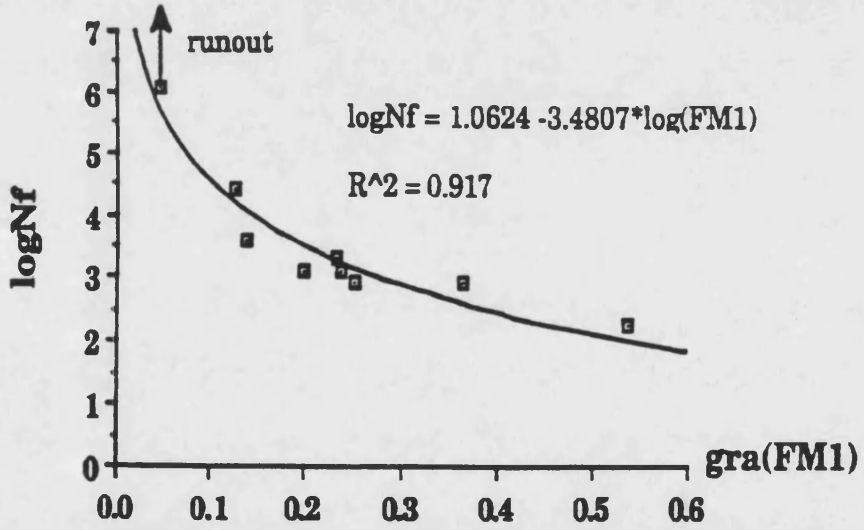

Fig.13.4. Logarithmic curve fit to the first modulus versus cycles to failure data [gra(FM1)= magnitude of the gradient of the first portion of the fatigue modulus curve].

The curves fitting the first and second fatigue modulus data are similar in shape and fit the data closely. However, the first fatigue modulus gradient is likely to be the better parameter with which to predict the number of cycles to failure. Firstly it can be calculated within the first 100 cycles of a test (see fig.13.3) thus giving the most rapid prediction of fatigue life. Secondly the range of gradient values is wider and has a more even distribution than is the case for the second fatigue modulus. Most of the

second fatigue modulus gradients are clustered together between values of 0.05 and 0.15 with a corresponding range in lifetime of about 1 decade. This suggests that this modulus is less reliable to extrapolate for values outside this small range.

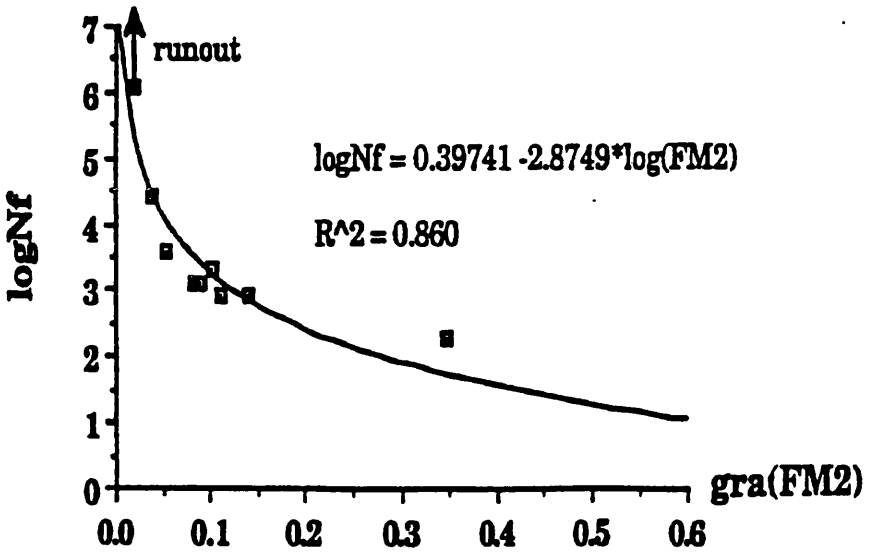

Fig.13.5. Logarithmic curve fit to the second fatigue modulus versus cycles to failure data [gra(FM2) = magnitude of the gradient of the second portion of the fatigue modulus curve].

13.3 Life prediction at R=0.1

The fatigue modulus has also been calculated for tests carried out in tension fatigue, at R=0.1. Fig.13.6 shows the results for all samples tested. The general trend is for the fatigue modulus to remain fairly constant up to approximately log(N)=4 before decreasing in an irregular manner. In some cases the calculated modulus actually increases. It is likely that this increase and the irregularity in the rate of decrease of the fatigue modulus are due to the formation of wood splinters which initiate on the sample surface and progressively grow into the veneers during fatigue. These splinters follow the tangential-longitudinal plane and are particularly noticeable where the grain in a surface veneer is not parallel to the axis of the sample. A splinter may grow across more than half of the sample surface without causing failure. Such a splinter cannot carry any load so when the sample sees a high tensile stress, the splinter lifts away from the bulk composite and can lift the extensometer away from the sample. In such cases as the size of the splinter increases, the strain measured by the extensometer decreases and consequently the fatigue modulus appears to increase. In comparison with the results for samples at R=10 (fig.13.3) the fatigue modulus gradient changes very little at the start of a test which makes it unsuitable for predicting the fatigue life of a sample.

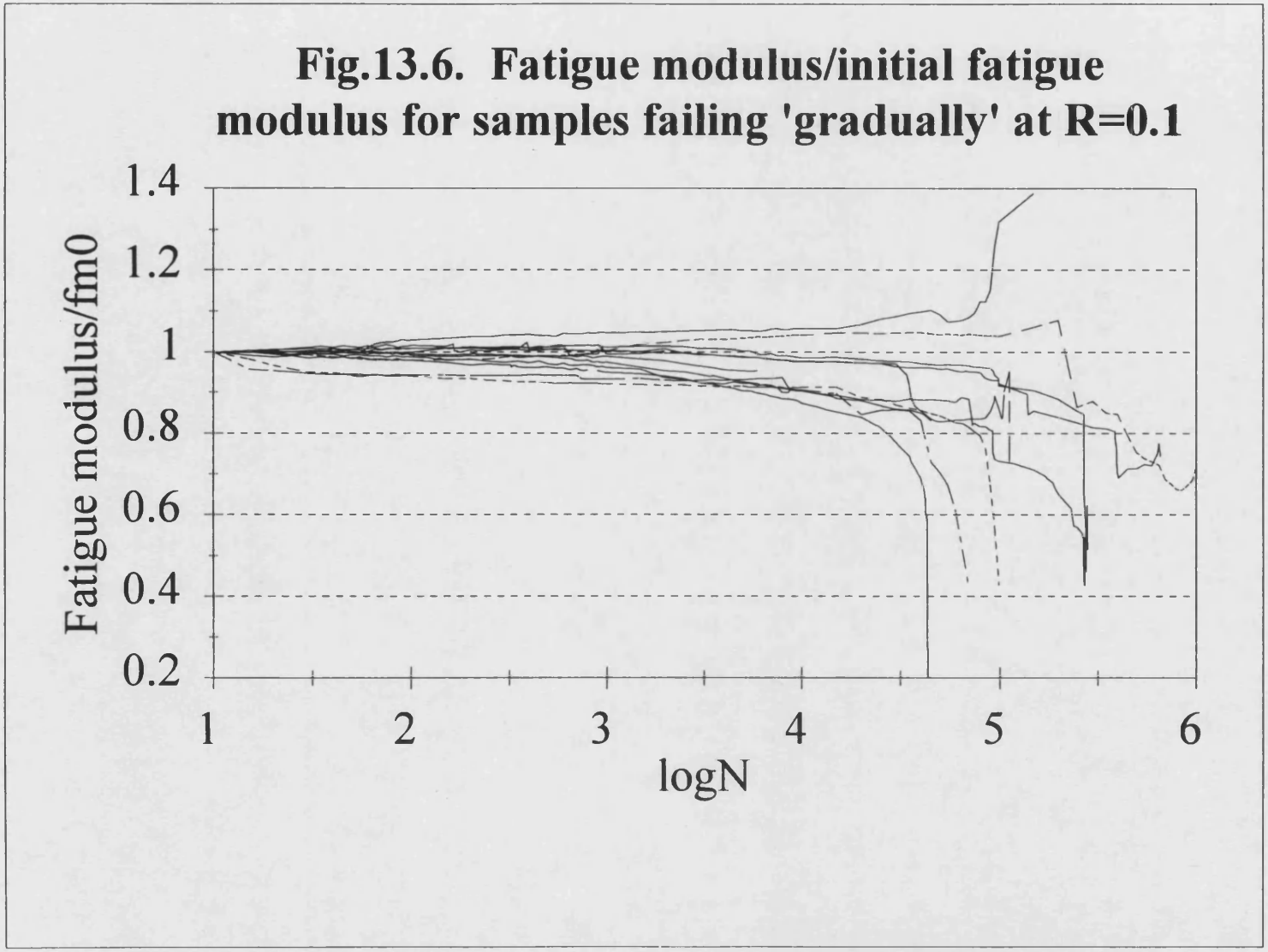
Fig.13.6. Fatigue modulus/initial fatigue modulus for samples failing 'gradually' at R=0.1
Fatigue modulus/fm0
1.4
1.2
1
0.8
0.6
0.4
0.2
1
2
3
4
5
6
logN

13.4 Complex load-time histories

This fatigue modulus approach has also been applied to the data obtained from complex load-time history tests. Data collected from an instrumented WTG blade was used to investigate the behaviour of the wood composite under typical operating conditions. These tests, and the results obtained from them, are presented in Chapter 15.

13.5. Conclusions

A fatigue modulus approach has been applied to wood composite data for samples tested at R=10 and R=0.1. In compression fatigue a good relationship was established between the initial fatigue modulus gradient and the number of cycles to failure. It is possible that this relationship could be used to predict the fatigue lifetime of a sample after about 100 cycles thus reducing the testing time required to evaluate a wood composite material.

In constant amplitude tension fatigue the fatigue modulus was found not to decrease sufficiently to be able to measure the initial gradient of the curve and predict the fatigue lifetime from it.

14. DECREASE IN STIFFNESS DAMAGE MODELS

14.1. Introduction

Change in material stiffness as a result of fatigue damage accumulation has been widely investigated and used in the fatigue life prediction of fibre-reinforced composite materials (Hashin, 1985, Rotem, 1988, Ye, 1989). Change in stiffness is an informative property to follow during fatigue because it is the cumulative result of microscopic damage events in the bulk of a composite material which are, in themselves, difficult to measure and complicated to model. In contrast, stiffness is also simple to measure.

The application of such methods, commonly used in fibre reinforced composites, has not been done for wood and wood composites. In this chapter one method of treating change in stiffness data has been applied to Khaya-epoxy wood composite.

14.2. The damage parameter, D

When a material is undamaged the level of damage, D is zero. As fatigue proceeds damage accumulates in the form of microcracks [fibre breaks, matrix cracks, delaminations] until a critical level of damage, $D_{critical}$, has accumulated and failure occurs (Jessen and Plumtree, 1991). As the number and size of the microcracks increases during fatigue the effective cross-sectional area of the sample is decreased and the actual stress sustained by the uncracked material is higher than the nominal applied stress. Consequently, the sample shows a decrease in modulus. It is to be expected that the critical level of damage $D_{critical}$ is dependent on the toughness of the material and its critical crack length at a particular stress level.

D is defined as:

$$D = 1 - \frac{E}{E_0} \qquad \text{eq.14.1}$$

where E is the instantaneous modulus [dynamic modulus] and E_0 is the initial dynamic modulus. Fig.14.1 shows typical plots of E/E_0 and D_c against proportion of fatigue life (Ye, 1989). The decrease in modulus plot has three stages. Although this three staged decreases is observed in wood composites a two staged decrease is the more common, see Chapter 10, figs.10.2, 10.5 and 10.8. The damage curve in fig.14.1 has been divided into only two sections. In the first the rate of increase in damage is gradually decreasing, whereas in the second it is increasing rapidly to failure. The transition between the two sections is defined as D_c [not to be confused with Jessen and Plumtree's, definition (1991) of $D_{critical}$ as the damage density at failure].

Stinchcomb (1986) portrays a characteristic damage state (CDS) which is a laminate property and equals the damage level when the matrix contains a regularly spaced pattern of cracks, fig.4.17. Once the matrix is saturated with cracks fibre breakage and debonding occurs. This appears to coincide with the end of the first stage of the decrease in modulus plot, fig.14.1.a. These observations were made on a graphite epoxy laminate and it is clear that the same damage phenomena will not necessarily occur in wood composites because of their different microstructure. For example, in wood the matrix of lignin is so intimately interlinked with the cellulose microfibrils that it is not possible to resolve it in a microscope, let alone determine whether it cracks in a regular pattern. The fact that the cellulose microfibrils are helically wound within the cell wall and that the overall structure is also cellular in nature further indicates that the damage mechanisms will be different.

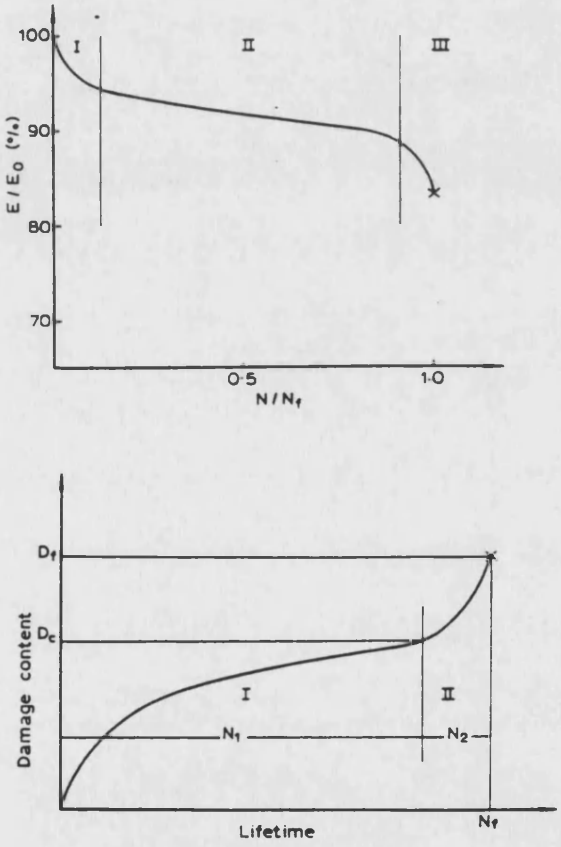

Fig.14.1. (a). Typical normalised stiffness reduction curve for composite materials.
(b). Fatigue damage development in composite materials (Ye, 1989).

Bangyan and Lessard, (1994) used theories of damage tolerance, residual-modulus degradation and residual strength degradation to propose a method of predicting progressive stiffness loss and increase in matrix crack density in tension fatigue for general laminates containing 0° plies as a function of fatigue load and number of cycles. Fig.14.2 shows the comparison between experimental results and the calculated

decrease in modulus and increase in crack damage, D_4, for a $[0/90]_{sl}$ E-glass epoxy laminate.

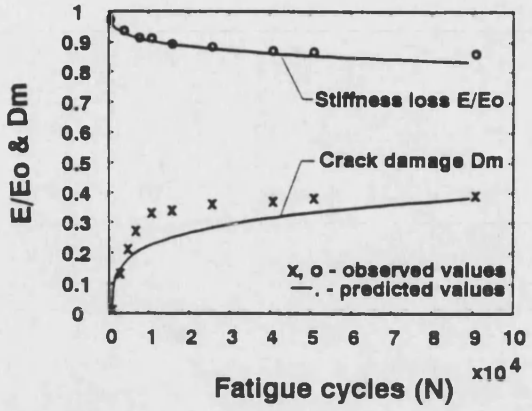

Fig.14.2. Variation of longitudinal stiffness and crack damage with number of fatigue cycles for a $[0/90]_{sl}$ E-glass epoxy laminate (Bangyan and Lessard, 1994).

14.3. Results

D has been calculated for all tests carried out at R=10, R=0.1 and R=-1 and an example from each R ratio is presented in figs.14.3, 14.4 and 14.5 respectively. The full set of plots are contained in Appendix D They have been plotted against logN so that changes in D can be seen for the runout samples as well as those that failed. All the samples which failed have also been plotted and typical graphs are presented in figs.14.6 to 14.8 of D against N/N_f for R=10, 0.1 and -1 respectively.

Some samples show the expected increase in D, for example, samples b, c and in fig.14.3, sample i in fig.14.4 and the samples in fig.14.5. In the case of many of the runout samples the damage state decreases and becomes negative, fig.14.5 sample d. Certainly, a considerable number of tests resulted in indeterminate damage curves. An idealised damage curve is presented in fig.14.9 and the important points on the curve identified. The 'critical damage state' as defined by Stinchcomb (1986) corresponds to the value of D at the first knee in the curve at N/N_f=A. Ye's D_c (1989) where the damage variable begins to increase rapidly to failure is found at N/N_f=B. Jessen and Plumtree's critical damage factor is denoted as D_f and is the value of D at failure where N/N_f=1.

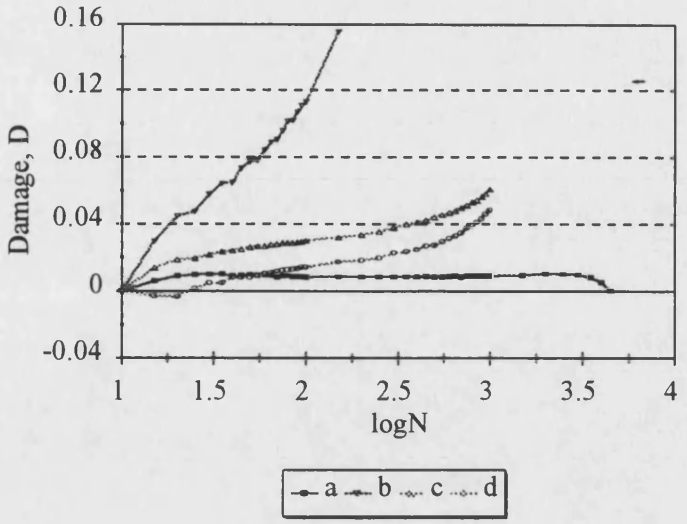

Fig.14.3. Damage parameter, $D=1-E/E_0$ for samples tested at R=10 and S_{min}=-55MPa.

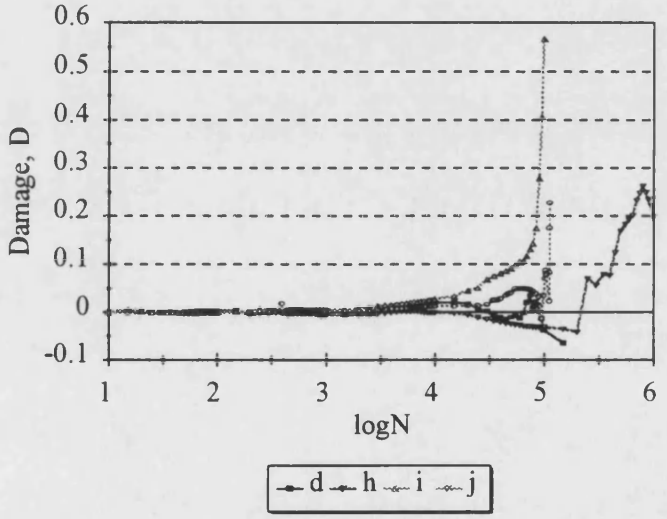

Fig.14.4. Damage parameter, $D=1-E/E_0$ for samples tested at R=0.1 and S_{max}=50MPa.

All damage curves have been inspected and values for A, B, D_A D_B and D_f estimated by eye. As is to be expected there is considerable variation in the results, and it is not possible to determine the location of all of these points in an appreciable number of samples. The values of A, B, D_A D_B and D_f are presented in tables 14.1 to 14.3 along with some general observations. The positions of A, B, D_A D_B and D_f are shown schematically in fig.14.9.

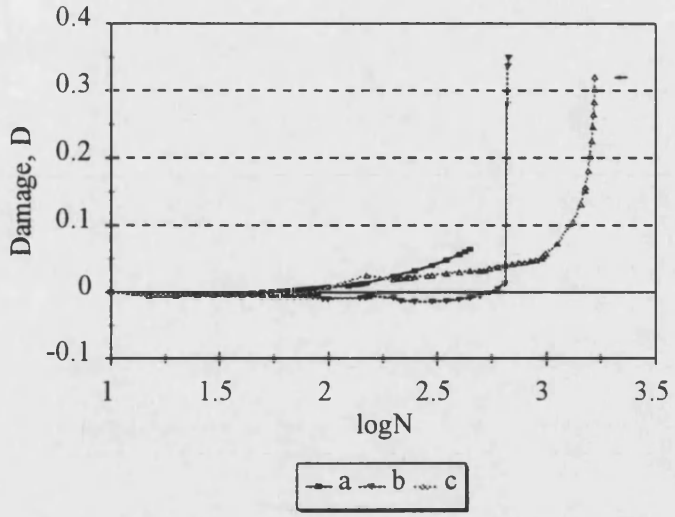

Fig.14.5. Damage parameter, $D=1-E/E_0$ for samples tested at R=-1 and S_{max}=45MPa.

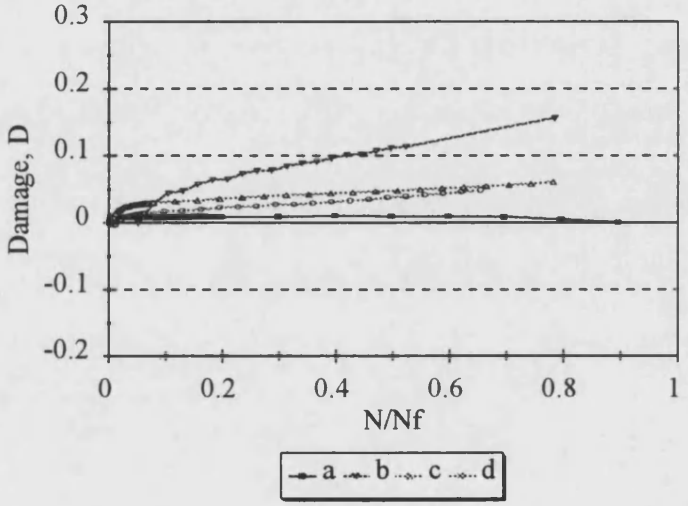

Fig.14.6. Damage parameter, $D=1-E/E_0$ versus N/N_f for samples tested at R=10 and S_{min}=-55MPa.

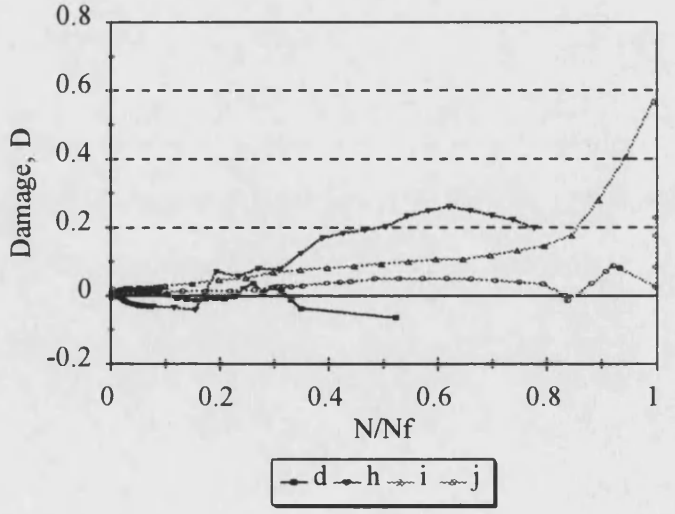

Fig.14.7. Damage parameter, $D=1-E/E_0$ versus N/N_f for samples tested at R=0.1 and S_{max}=50MPa.

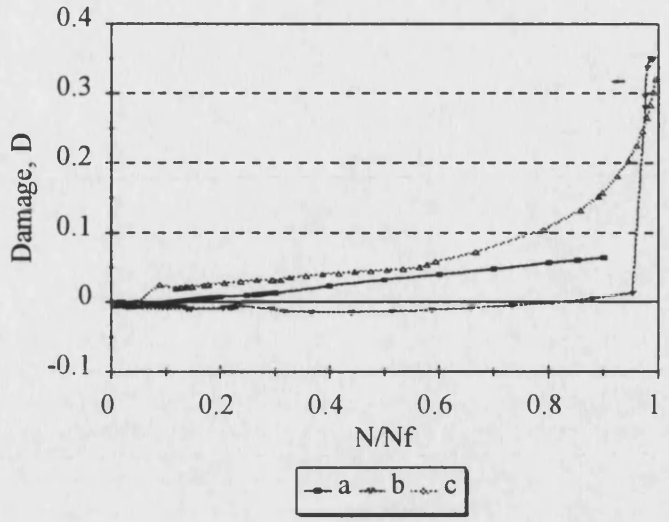

Fig.14.8. Damage parameter, $D=1-E/E_0$ versus N/N_f for samples tested at R=-1 and S_{max}=45MPa.

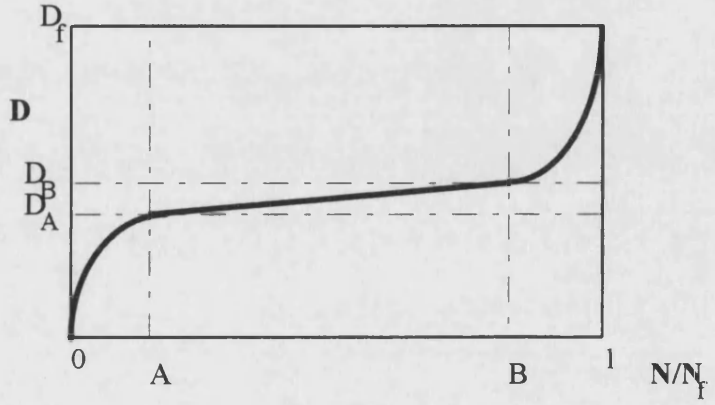

Fig.14.9. Schematic representation of the characteristic damage states.

The following trends can be drawn from tables 14.1 to 14.3:

At R=10, table 14.1.

- A is approximately 2% for half of the samples where A could be measured. This low value of A is most common for the lower stress level tests.
- For the other half of the samples where A could be measured it ranged from 5% to 22% of life. These values were more common for the higher stress level tests.
- The knee at A occurred in less than the first 250 cycles for all samples.
- With the exception of one sample the value of D_A was equal to, or less than, 0.03.
- In all but four cases the position of B could not be identified. In the cases where it could, D_B occurred at between 50 and 90% life.
- The most common value of D_f was between 0.16 and 0.22, although one sample showed a rapid increase in D to 0.99 and some showed negative damage at failure.
- The lowest stress level test (-55MPa) tended to show a linear relationship between N/N_f and D between N/N_f=A and failure.

valid tests	Nf	% life A	% life B	D_A	D_B	D_f	comments
r1047a	2750	D -ve from start of test until failure				-0.02	
r1047b	3750	2	54	0.018	X	0.19	undefined start of B region.
r1047c	2864773	runout				X	
r1047d	5007214	runout				X	
r1050a	1144386	runout				X	
r1050b	25002	runout				X	
r1050d	4300000	D -ve from start of test until failure				-0.17	
r1050f	845	2	57	0.02	X	0.22	undefined start of B region.
r1050g	10000000	runout				X	
r1050h	11465	2.5	X	0.015	X	0	decreased to 0 at 95% life
r1052a	25002	1	X	0.0025	X	---	undefined start of B region.
r1052b	845	12	X	0.03	X	0.08	undefined start of B region.
r1052c	2203	5	68	0.015	0.07	0.16	
r1052d	654	D near zero throughout test				-0.02	
r1052f	1288	X	90	X	0.025	0.99	-ve at start of test
r1055a	5000	1	X	0.01	X	0	linear until last capture (N/N_f)
r1055b	191	22	X	0.065	X	---	linear until last capture (N/N_f)
r1055c	1278	8	X	0.03	X	---	linear until last capture (N/N_f)
r1055d	1027	7	X	0.014	X	---	linear until last capture (N/N_f)

X indicates that it is impossible to determine the location of point B, eg. fig.14.10.

--- indicates that the last hysteresis loop was not captured in the last 10% of life and, therefore, cannot be regarded as necessarily close to D_f

Table 14.1. Damage parameter results at R=10

valid tests	Nf	% life A	% life B	D_A	D_B	D_f	comments
rp130a	4036009	runout. D decreased throughout test.					
rp130b	10000000	runout. D decreased throughout test.					
rp140a	5758720	runout. D decreased throughout test.					
rp140b	2464614	runout. D decreased throughout test.					
rp140c	10000000	runout. D near zero throughout test.					
rp150d	286528	no defined pattern					
rp150h	1286427	no defined pattern. Decreased at start of test					
rp150i	100572	13	85	0.03	0.15	0.57	
rp150j	113286	8	X	0.01	X	0.25	no B region. rapid increase at100% life to 0.25
rp155b	72588	X	62	X	0.25	0.54	D decreased at start.
rp155c	664156	7	X	0.025	X	0.12	no pattern at end of test
rp155d	281600	7	96	0.028	0.07	0.42	
rp155e	278744	X	96	X	0.25	0.58	D decreased at start.
rp160a	2629	X	X	X	X	---	D decreased at start.
rp160d	43631	22	96	0.03	0.2	0.72	
rp160e	6126	X	X	X	X	0.018	D decreased at start.
rp160f	45260	20	92	0.018	0.024	0.042	
rp165a	227	D decreased throughout test.					
rp165b	178	D decreased throughout test.					
rp165c	716	X	97	X	0.02	0.41	D decreased at start.
rp165d	778	X	96	X	-0.027	0.29	D decreased at start.

Table 14.2. Damage parameter results at R=0.1

valid tests	Nf	% life A	B	D_A	D_B	D_f	comments
rm125a	4527983	runout. D decreased throughout test.					
rm130c	613554	2	X	0.03	X	-0.01	decreased from 50% life
f	1349103	runout					
g	156481	1.5	50	0.055	0.09	1	stepped increase to D=1 after B
h	631441	5	50	0.06	0.08	1	stepped increase to D=1 after B
rm135a	8880	13	87	0.035	0.12	0.38	
b	6195	7	87	0.015	0.14	0.99	
c	193667	5	86	0.04	0.15	0.99	
rm140a	5198	2	X	0.0025	X	0.075	all increased linearly. No evidence of D_B
b	4751	18	X	0.025	X	0.175	
e	1799	7	X	0.005	X	0.11	
rm145a	499	23	X	0.008	X	---	
b	683	X	96	X	0.02	0.36	D -ve at start
c	1683	10	80	0.02	0.1	0.32	
rm150a	678	linear throughout to failure				0.08	
b	222	27	92	0.05	0.11	0.25	
c	125	linear throughout to failure				---	

Table 14.3. Damage parameter results at R=-1

At R=0.1, table 14.2.

- In all the runout tests D decreases.
- D decreases at the start of the test in over half of the tests where failure occurred. In the remainder of the samples A was located between 7 and 22% life.
- D_A ranged between 0.01 and 0.03.
- The second knee at N/N_f=B was evident in over half the tests and the most common value was between 85 and 97% of life.
- D_B ranged from 0.07 to 0.25 except for the highest stress level tests where D_A was much lower, or negative.
- The most common value of D_f was approx.0.4, although two tests at Smax=60MPa were much lower.

At R=-1, table 14.3.

- D_A ranged from 0.0025 to 0.06 and occurred between 1.5 and 27% of life.
- D_B was found between 50% and 96% life with the most common occurrence at about 96% life. The two samples with B at N/N_f=50% exhibited a stepped increase with N/N_f as crack growth took place.
- The most common value of D_B was around 0.1 with one sample with a value of 0.02.
- D_f was seen to be close to one for four samples tested with S_{max} between 30 and 35MPa.
- Five samples showed a linear increase of D with N/N_f and had D_f =0.1.
- The four remaining samples had a damage curve with both A and B clearly defined and D_f close to 0.3.

The mean and standard deviations of each variable have been calculated in both the x and y directions and plotted in fig.14.10. The range of D_A and D_B consist of a rectangle with sides of twice the standard deviation in length centred on the mean value. The mean value of D_f has been plotted along with the ±2 std. dev values.

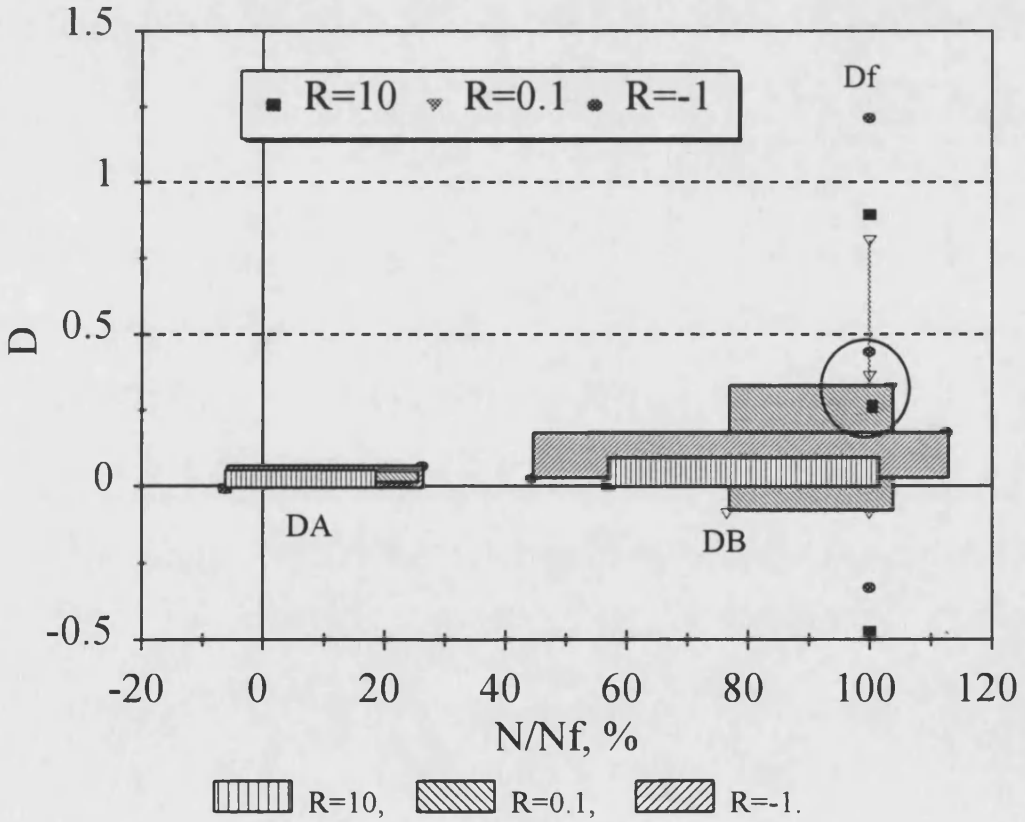

Fig.14.10. Mean values of A, B, D_A D_B and D_f for samples tested at all three R ratios. The shaded regions represents ±2 standard deviations in both the x- and y-directions. The three points inside the circle are the mean values of D_f.

Fig.14.10 illustrates very clearly the range in scatter of the data. The values of D_A for R=10 and R=0.1 all fall within the range [mean ± 2 std. dev. in x- and y-directions] of the R=-1 values. The mean values are all very similar, with the R=-1 value falling between the 10 and R=0.1 data points. In all cases the damage parameter, D, shows a similar range of values and the mean value of D_A varies by only 5%. The damage response at R=-1 appears to be a combination of the purely tensile and compressive responses.

Differences are more apparent for D_B with the shaded regions for each R ratio having different shapes. D_B shows the largest increase at R=0.1 and the smallest change at R=10. Again R=-1 falls in between the two. However, the shaded region is more similar in shape to the R=10 region which implies that compression damage tends to dominate reverse loading towards the end of a sample's fatigue life. The fact that the greatest changes are seen at R=0.1 suggests that cracking of the wood composite (typical tensile fatigue damage) cause the greatest increase in D.

At failure the order is reversed and R=-1 samples show the highest final values of D. The R=10 values of D_f are still the lowest which means that compression fatigue causes the least decrease in modulus. However, when tension and compression fatigue are combined in a reverse loading test the changes in modulus are much more significant, suggesting that the accumulation of compression damage at the same time as tensile damage causes a higher degree of longitudinal splitting along the grain of the wood composite.

14.4. Discussion

The questions which must be asked are:

- What is happening in the wood composite during each stage of damage accumulation, and
- How does this vary between the different stress levels and R ratios.

The fatigue damage accumulation in fibre reinforced composites has been extensively investigated (Ye, 1989 and Stinchcomb and Reifsnider, 1979). The basic failure mechanisms are matrix cracking, fibre breaking, debonding and delamination. These different mechanisms occur both independently and interactively according to the material variables and testing conditions.

As suggested by Stinchcomb (1986) for fibre-reinforced plastic composites, different types of damage development are associated with each stage of change in the damage

parameter, D. Fig.4.17 illustrates this for a graphite-epoxy multi-ply laminate with several off-axis plies. At the start of a fatigue test damage accumulates in the matrix in the form of matrix cracking. The initiation of matrix cracks does not occur instantaneously and depends on the local stress distribution in the laminate and local variations in strength. These cracks build up until there is a regularly spaced crack distribution throughout the off-axis laminates and is defined as the characteristic damage state [CDS]. This CDS corresponds to the point (A, D_A). Matrix cracks change the local stress distribution and initiate interfacial debonding, delamination and fibre breakage. These damage mechanisms continue until $D=D_f$ when failure occurs.

In the case of short fibre composite materials Ye (1989) states that up to $N/N_f=A$ the prevalent form of damage is matrix cracking along the fibres in the plies; in stage 2 [fig.14.1] the rate of damage build-up decreases because the cracks are stopped by off-axis fibres and in stage 3 there is a sudden coalescence of microcracks and rapid crack growth leading to catastrophic failure.

A different approach is suggested by Talreja, 1987, who classifies the different damage mechanisms in terms of the strains seen by the composite, see fig.4.13. However, this approach cannot be easily applied to wood, particularly when it is loaded in compression as well as tension as the mechanisms of damage are different.

Application to wood composites

It has been shown that a damage parameter, D, based on stiffness changes can be calculated for wood composites as well as fibre reinforced plastics (FRPs). However, to analyse the parameter has proved a complex task because of the wide range in the shape of the damage curves produced. This highlights the problems of variability encountered when working with a construction material, rather than carefully prepared laboratory specimens.

However, differences have emerged which are similar in magnitude to those observed in FRPs. Ye (1989) showed a 6% decrease in modulus [equivalent to a corresponding increase in D] at A=10% of life, and a further decrease between B and N_f from 90% to 84% of the original modulus value. Stinchcomb (1986) observed his CDS to occur at 20% of life and equal half the damage parameter recorded at failure.

In compression fatigue D_A was approximately 3% at A which was found to occur within the first 250 loading cycles. Unlike the results of Ye (1989) and Stinchcomb (1986) A did not occur after a particular fraction of life but within a few hundred loading cycles, independent of the minimum compressive fatigue stress. Given that the

minimum compressive stress is below the compressive elastic limit for all tests at R=10 it is likely that during this initial stage small amounts of localised compression kinking are occurring in regions of weakness in the structure until the stress state has reached an equilibrium. In general the onset of a rapid increase in damage to failure is not apparent in compression fatigue and it is likely that progressive localised cell wall kinking occurs at an increasing rate until the formation of a macroscopic compression crease. The most common value of D_f ~0.18 is close to the value found by Ye (1989).

In tension fatigue, at R=0.1, D decreases and becomes negative for all of the runout samples and over half of the samples which fail. This suggests that under the application of a fatigue load the wood fibres become better aligned which results in an increase in tensile stiffness. It is possible that this is partly due to the flattening of ray cells thus reducing the curvature in the fibres adjacent to them (see Chapter 16, section 16.5.2). In the samples where it was possible to determine the position of A an increase of ~3% was observed after at least 9000 loading cycles. This number of cycles is probably higher than for R=10 due to the lower relative values of the maximum fatigue stresses to the UTS. The point B was much more prominent in tension fatigue and occurred at ~85% of life, similar to Ye's composites (1989). In composites this corresponds to delamination and localised fibre breaking (Stinchcomb, 1986). In wood this could correspond to the onset of both localised and macroscopic R-L and T-L cracking. The most common value of D at failure was ~0.4, twice the value found by Ye (1989). This suggests that wood has twice the damage tolerance of the FRP composites cited.

In reverse loading fatigue A was much more evident that at R=0.1, with all but three samples showing an initial decrease of ~3% within the first ~1.5 to 27% of fatigue life. However, unlike at R=10 this did not correspond to a certain number of cycles and as the load levels increased the number of cycles to A decreased, suggesting that this initial damage is more stress-dependent in reverse loading. Clearly fibre alignment is not occurring. Values of D_f fell into two groups, four samples where D_f=1 and the remainder where $0.1<D_f<0.4$. The former group of samples had been loaded at an intermediate stress level and corresponded to those where high degrees of hysteresis loop bending were observed (fig.9.6).

14.5. Conclusions

D has been calculated for all R ratio tests. It was found to show considerable variation.

However, the following conclusions can be drawn:

- Differences in the damage parameter between the R ratios were evident.

- At R=0.1 the fatigue response was dominated by a decrease in D, either at the start of a test or throughout its duration. All the runout samples showed the latter behaviour and highlights the probable occurrence of fibre alignment within the wood structure as a result of tensile fatigue loading.
- The most common value of D_A was ~3% for all R ratios [where it could be determined]. In the case of compression fatigue A occurred within the first 250 loading cycles, independent of the stress level. In tension fatigue A did not occur under 9000 cycles, but was also seen to be independent of stress level. In reverse loading fatigue, however, the position of A was dependent on stress level and occurred after fewer cycles at the higher stresses.
- In general D_B could not be distinguished for R=10 tests but was most prominent for R=0.1 tests. This suggests that at R=10 the damage mechanism does not change but at R=0.1 damage accumulates rapidly in the form of RL and TL cracking.
- At R=-1 no fibre alignment occurs.

15. COMPLEX LOADING

15.1. Introduction

Although the majority of fatigue testing is carried out by laboratories using constant amplitude loading regimes the in-service fatigue loads experienced by any component are invariably complex. This means that the stress amplitude constantly varies with each loading cycle. Typical examples include aircraft, cars and other transport vehicles. In these cases components are primarily metallic so metal fatigue is the main concern. Fatigue life prediction is mainly based on Miner's linear damage accumulation rule but its application to a complex loading situation is not always accurate. Work hardening and softening, sequence effects and strain overloads are all likely to affect the fatigue life of a metallic component.

As composite materials are increasingly used in the production of high performance aircraft and automotive components their response to complex loading is also of importance. It has been shown by several workers that Miner's rule fails to predict composite fatigue life under spectrum loading (Yang and Du, 1983). Consequently, other methods of life prediction must be explored.

In the wind energy industry the evaluation of blade materials under complex loading has been made using the spectrum called WISPERX, a generalised spectrum produced from data gathered from 12 WTGs. It has been used to evaluate a fatigue life prediction method based on Miner's rule for wood composite fatigue developed by Bonfield (1991) (see Chapter 5). Although this spectrum has allowed the evaluation of life prediction models developed from constant amplitude fatigue data it does not provide any data concerning a wood composite's response to particular in-service loading conditions.

In order to determine the response of wood composites to actual loading conditions, load-time histories were supplied by WEG from an instrumented blade in service.

15.2. The load time histories

The actual loading conditions which are of particular interest to designers are those which are severe and consequently most likely to cause damage to the wood composite in the blades. Such events include benign and emergency stopping of the WTG and operation in turbulent wind conditions.

Variable amplitude load-time (l-t) histories for these conditions were supplied in the form of 10 minute campaigns taken from a WEG MS3A machine at Myers Hill in July 1992. They were in the form of ASCII code and contained 16386 data points each. After they had been converted into digital form using nCode software, peak-valley extraction was applied with a filter of 1 or 2 Volts to remove noise and to reduce the length of the signal to a more manageable level. This removed the data points in between the signal peaks as well as any cycle which was less than 1 or 2V in magnitude. Figs.15.1 to 15.3 show the load-time histories used for normal running conditions, a benign stop and an emergency stop respectively. All have been plotted on the same scale for comparison. The number of turning points in a l-t history is $P_{(l\text{-}t\ h)}$ and is equal to twice the number of cycles in the l-t history. Data associated with each l-t history are presented in table 15.1.

	w12_7p normal running	**w12_3s benign stop**	**w9_4es emergency stop**
Windspeed, ms^{-1}	12.7	12.3	9.4
Turbulence intensity, %	10.8	15.7	15.0
r.p.m.	45	45⇨0⇨45	45⇨0
V_{max}	56.886	61.954	52.363
V_{min}	25.00	-21.92	-25.41
V_{mean}	42.34	37.94	29.47

Table 15.1. Data for complex load-time histories

By comparing figs.15.2. and 15.3 it can be seen that the emergency stop is more immediate than the benign stop with the load going from the maximum value to its minimum within 20 cycles. This is ten times more quickly than the benign stop. It is also clear that the turbulence levels in the benign stop and the emergency stop are similar and higher than is the case for normal running conditions. These comparisons highlight the difficulties with using real l-t histories because it is impossible to isolate one feature for consideration from the others which will also affect fatigue life.

Extra points were added at the start of each sequence to ramp the load up from zero to the first recorded value in order to avoid the possibility of shock loading at the start of a test causing the sample to pull out of the machine grips. In addition, short blocks of five constant amplitude cycles were added at various points throughout each load-time history in order to allow repeatable and comparable hysteresis loop capture. The position and magnitude of these cycles were chosen so that they fitted into the spectrum

Fig.15.1. Load-time history for normal running conditions

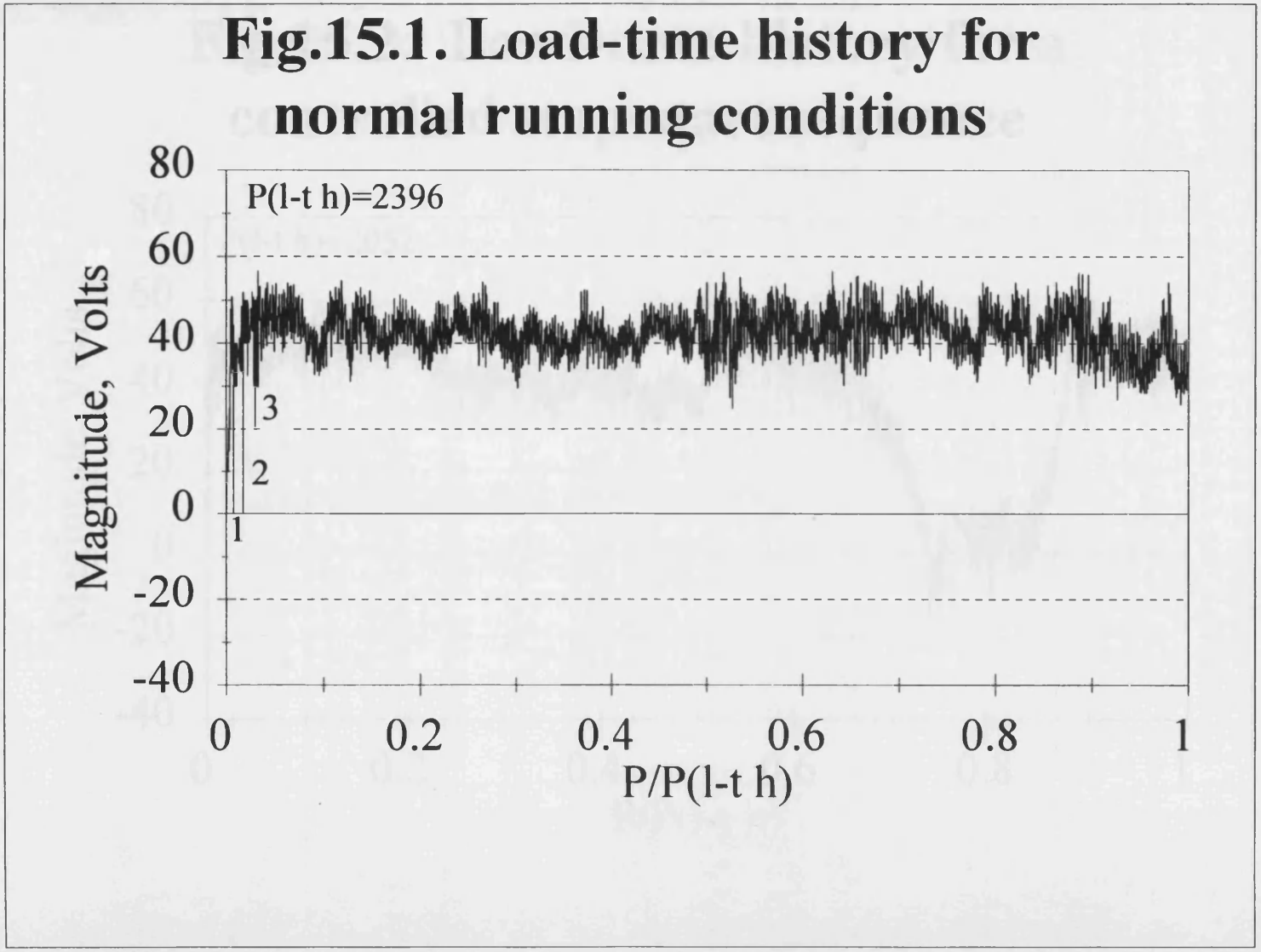

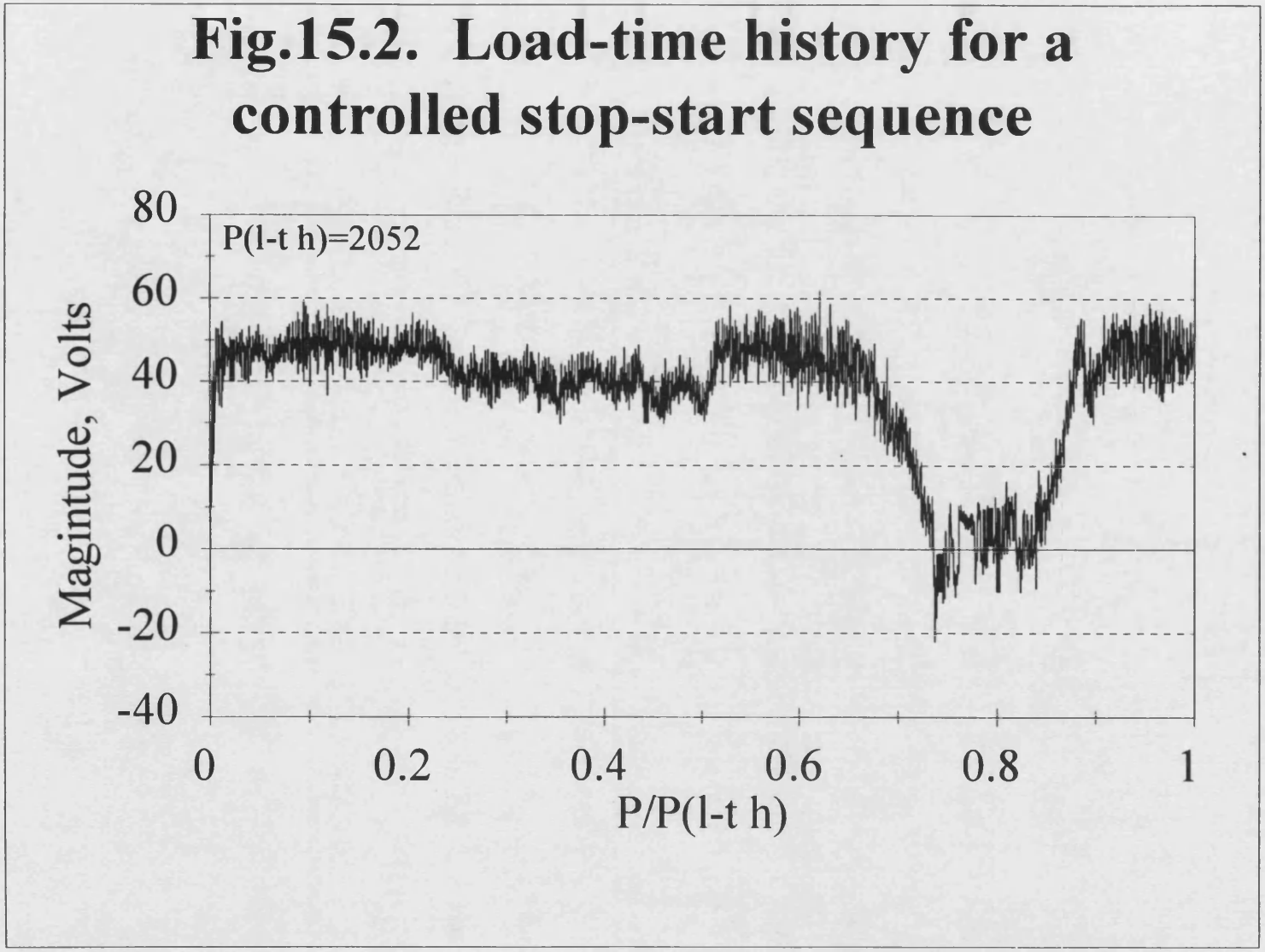

Fig.15.2. Load-time history for a controlled stop-start sequence

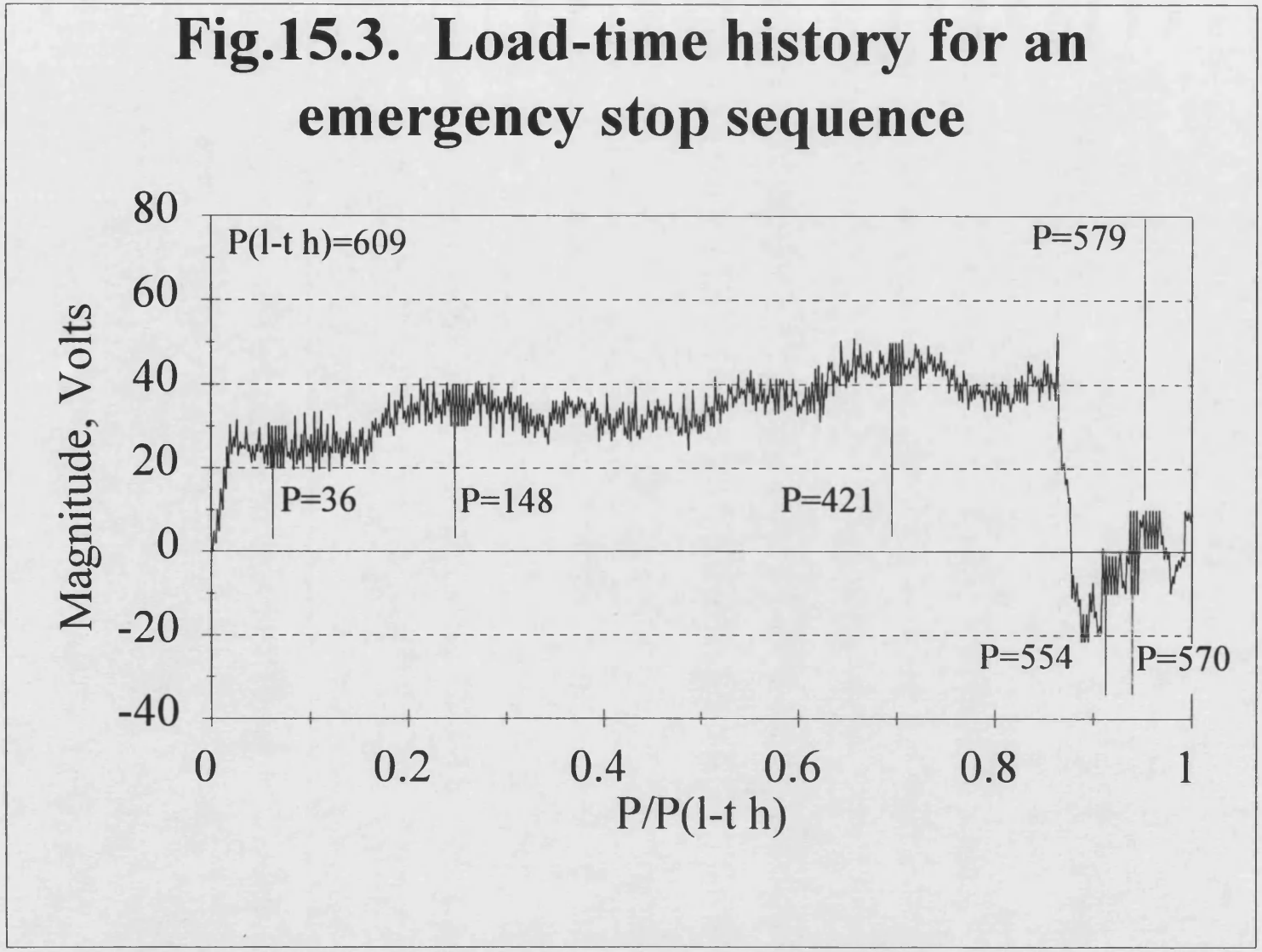
Fig.15.3. Load-time history for an emergency stop sequence
80
60
40
20
0
-20
-40
Magnitude, Volts
P(l-t h)=609
P=579
P=36
P=148
P=421
P=554
P=570
0
0.2
0.4
0.6
0.8
1
P/P(l-t h)

without appreciably changing its profile but would yield hysteresis loops with different R ratios. Details of these extra cycles are presented in figs.15.4 to 15.6. In the case of the normal running condition three blocks of constant amplitude loops were added at the start of the test, fig.15.4. For the controlled stop-start sequence five blocks were added, two at the start of the regime and three once the WTG had stopped, fig.15.5. These latter corresponded to R ratios of 10, 0.1 and -1, as used in the constant amplitude tests (Chapter 8). In some cases more loops were captured to determine in more detail where in the l-t history the most damage was occurring. Identical blocks were added on either side of the minimum spike (in compression testing) and after the WTG had been restarted, fig.15.6. However, the extra loops were only captured in a few tests because of the large volume of data it generated. The aim of capturing data at these points was to investigate which part of the l-t history caused the most damage in the wood composite and possibly to quantify the damage. The cycles inserted in the emergency stop regime can be seen in fig.15.3.

15.3. Experimental design

Unjointed Khaya-epoxy samples were tested in the Mayes fatigue machines using the above l-t histories in both tension and compression fatigue at three or four different stress levels. Only one sample was tested at each stress level because of time constraints in both the testing and data analysis.

Dartec's 'Profile' program was used to drive the tests and loop capture was triggered using the 'Advanced capture' option as explained in Chapter 6. The l-t history was scaled so that the maximum voltage gave the desired peak stress, S_{peak}, typically 45MPa, 50MPa, 55MPa or 60MPa for tension and -47.5MPa, -50MPa, -52.5MPa or -55MPa for compression. The tests were run at a constant loading rate of $400MPa.s^{-1}$, the same as for the constant amplitude loading tests. Stress-strain hysteresis data were captured at the desired cycles at the required number of passes until failure. The loops were then processed using nCode's LPA program and imported into 'Quattro Pro' for manipulation and analysis.

15.4. Basic results

The basic results for all tests are presented in table 15.2. From the number of points to failure, P_f, [except for the runout samples] the number of passes to failure has been calculated. In addition the actual position of failure during the last pass has also been calculated to determine which part of the l-t history caused failure. The mean stress for each test has also been calculated for comparison. The mean stress at a peak stress level of 55MPa has been highlighted by a double box in order to show how the mean stress varies between the l-t histories.

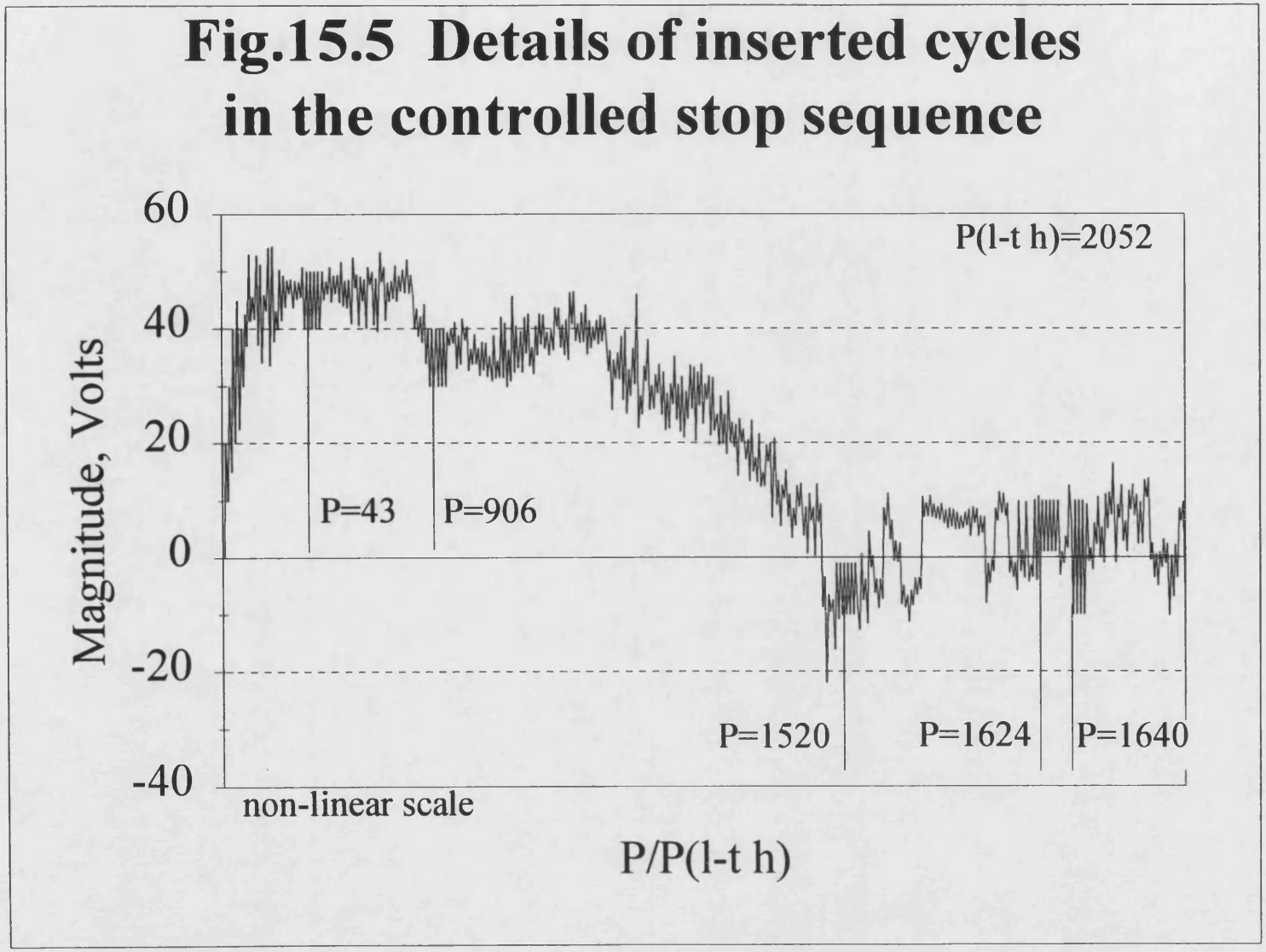
Fig.15.5 Details of inserted cycles in the controlled stop sequence
60
40
20
0
-20
-40
Magnitude, Volts
P(l-t h)=2052
P=43
P=906
P=1520
P=1624
P=1640
non-linear scale
P/P(l-t h)

Fig.15.4. Details of inserted cycles in the normal running sequence

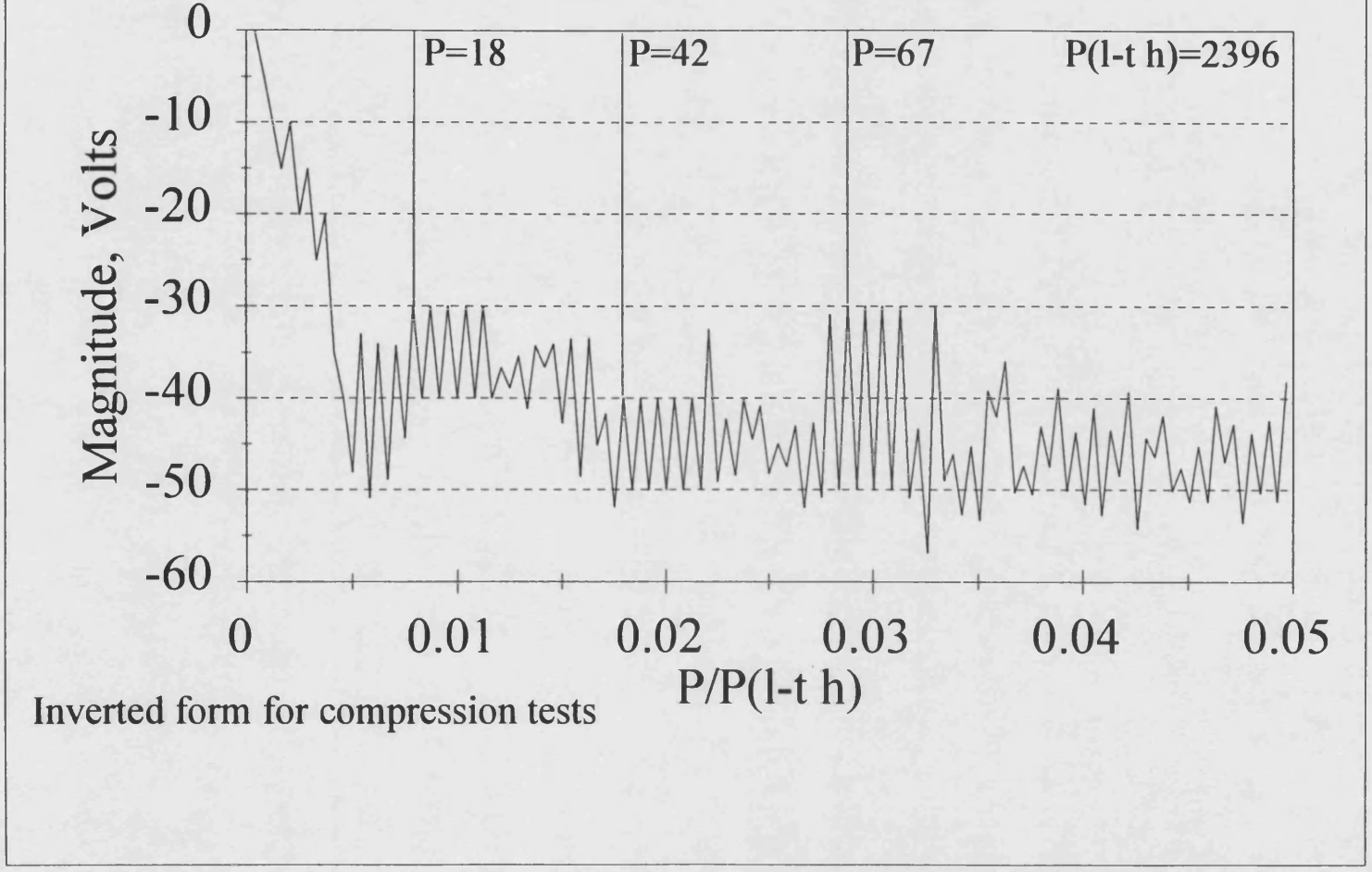

Inverted form for compression tests

Fig.15.6. Details of inserted cycles in the controlled stop-start sequence

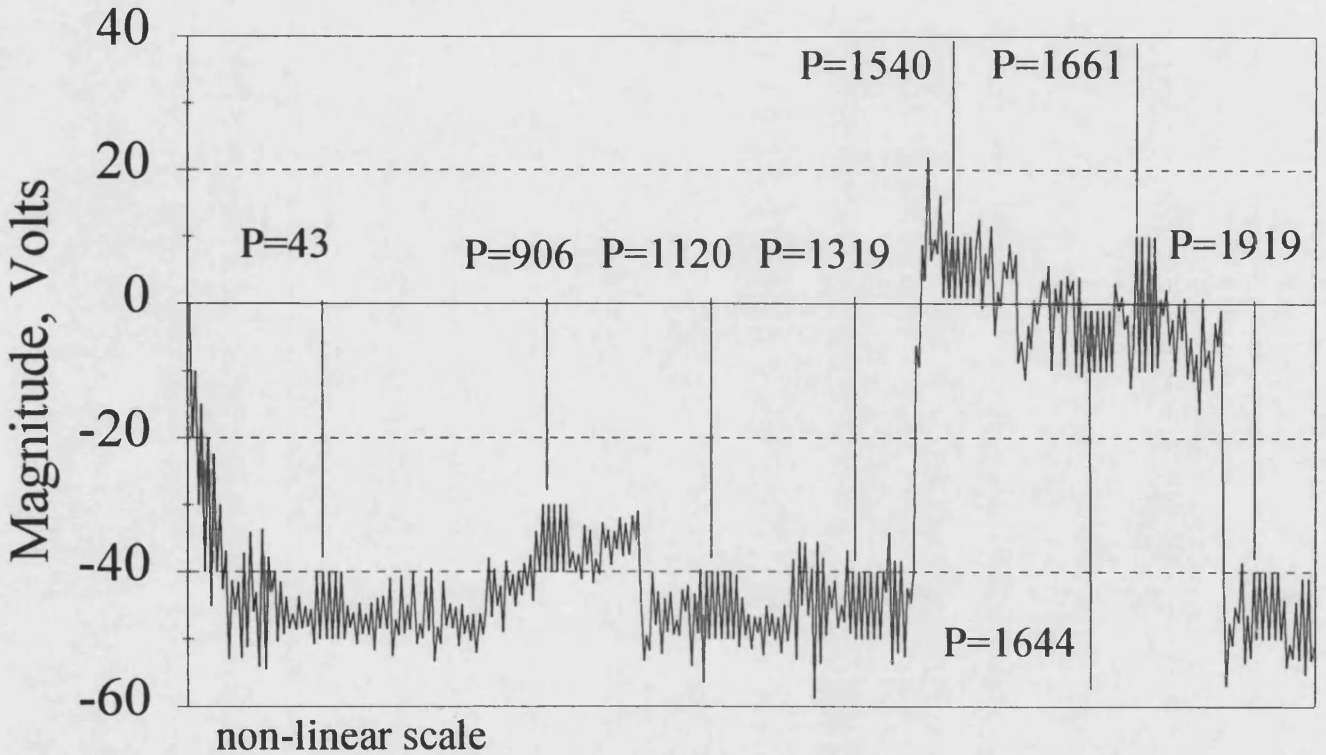

Sample	Peak stress MPa	Mean stress, MPa	P_f	Passes to failure	Point of failure
nm_45_t	45	33.66	9939665	4148.40	runout
nm_50_t	50	37.32	4950215	2066.03	79
nm_55_t	55	40.87	101834	42.50	1202
nm_60_t	60	44.43	319913	133.52	1245
nm_50_c	-50	-36.96	23331963	9737.88	runout
nm_50_c2	-50	-36.39	1233613	514.86	2069
nm_52_c	-52.5	-38.21	297217	124.05	113
st_40_t	40	24.61	19216886	9230.01	runout
st_45_t	45	27.94	10904893	5237.70	runout
st_50_t	50	30.91	221979	106.62	1287
st_55_t	55	34.08	55419	26.62	1287
st_47_c	-47.5	-28.52	9521251	4573.13	265
st_50_c	-50	-32.92	5776776	2774.63	1308
st_52_c	-52.5	-31.5	2885310	1406.10	198
st_55_c	-55	-33.04	474255	231.12	243
es_40_t	40	23.18	4778657	7846.73	runout
es_45_t	45	26.11	115627	189.86	526
es_50_t	50	28.88	170307	279.65	396
es_55_t	55	31.65	1010	1.658	401
es_45_c	-45	-24.94	773215	1269.6	394
es_47_c	-47.5	-27.13	9521251	15634.24	runout
es_50_c	-50	-28.25	3470	5.6979	425
es_52_c	-52.5	-28.83	516	0.847	516

Sample descriptions:

nm = normal running test

st = controlled stop-start test

es = emergency stop test

The number equals the peak stress

t = tension fatigue

c = compression fatigue

For example, es_55_t is an emergency stop sequence with the spectrum scaled to a peak tensile stress of 55MPa.

Table 15.2. Complex load-time history results.

The positions of each failure in the l-t history are presented in figs.15.7 to 15.9. The vertical lines mark the point at which failure occurred. In fig.15.7 the positions of failures during the normal running tests are given. Failure has occurred in three different parts of the spectrum, all of which are associated with some of the more extreme loading cycles. However, there is little difference between them as all are the result of normal turbulence. In the case of the controlled stop-start tests, fig.15.8, failure is associated with two high stress regions of the l-t history, one at the start of the test and the other at the maximum peak before the stop. Both samples which failed in tension did so at 1287 cycles, the overall maximum, fig.15.8. All samples failing under the emergency stop sequence did so as the stress levels increased towards the point of emergency shut-down, fig.15.9.

The data presented in table 15.2 have been used to produce S-logN diagrams in figs.15.10 to 15.12. In all cases the stresses on the y-axis have all been normalised by the static tensile or compressive strengths as appropriate. The compression tests results all appear higher on the y-axis than the tension test results because the stresses needed to cause failure in compression are a much higher proportion of the UCS than is the case for tension (see Chapter 8).

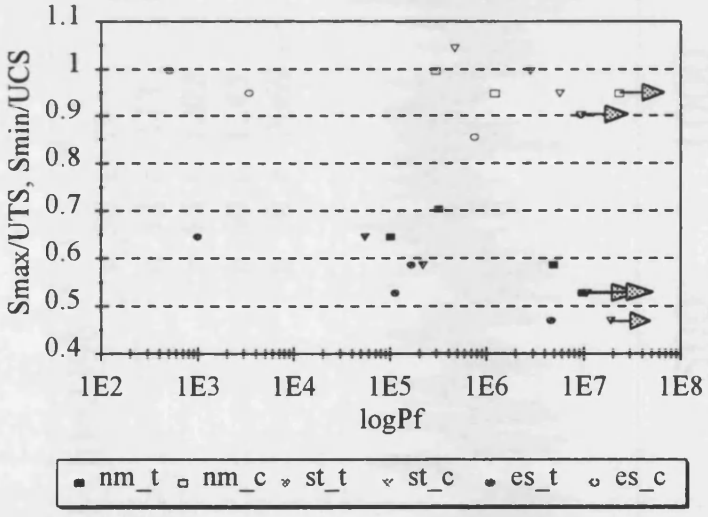

Fig.15.10. S_{max}-logP_f curves for complex load-time history tests.

The first question which must be addressed is how to plot the results. Although the peak stresses are similar it is clear from table 15.2 that the mean stresses vary considerably. At a peak stress of 55MPa the normal l-t history has a mean stress of 40.87MPa, the stop-start l-t history has a mean of 34.08MPa and the emergency stop l-t history has the lowest mean of 31.65MPa [see double edged boxes in table 15.2]. If, as in fig.15.10, the normalised peak stresses are used as the y-axis the fatigue response of the composite under the benign stop and normal running conditions appear to be

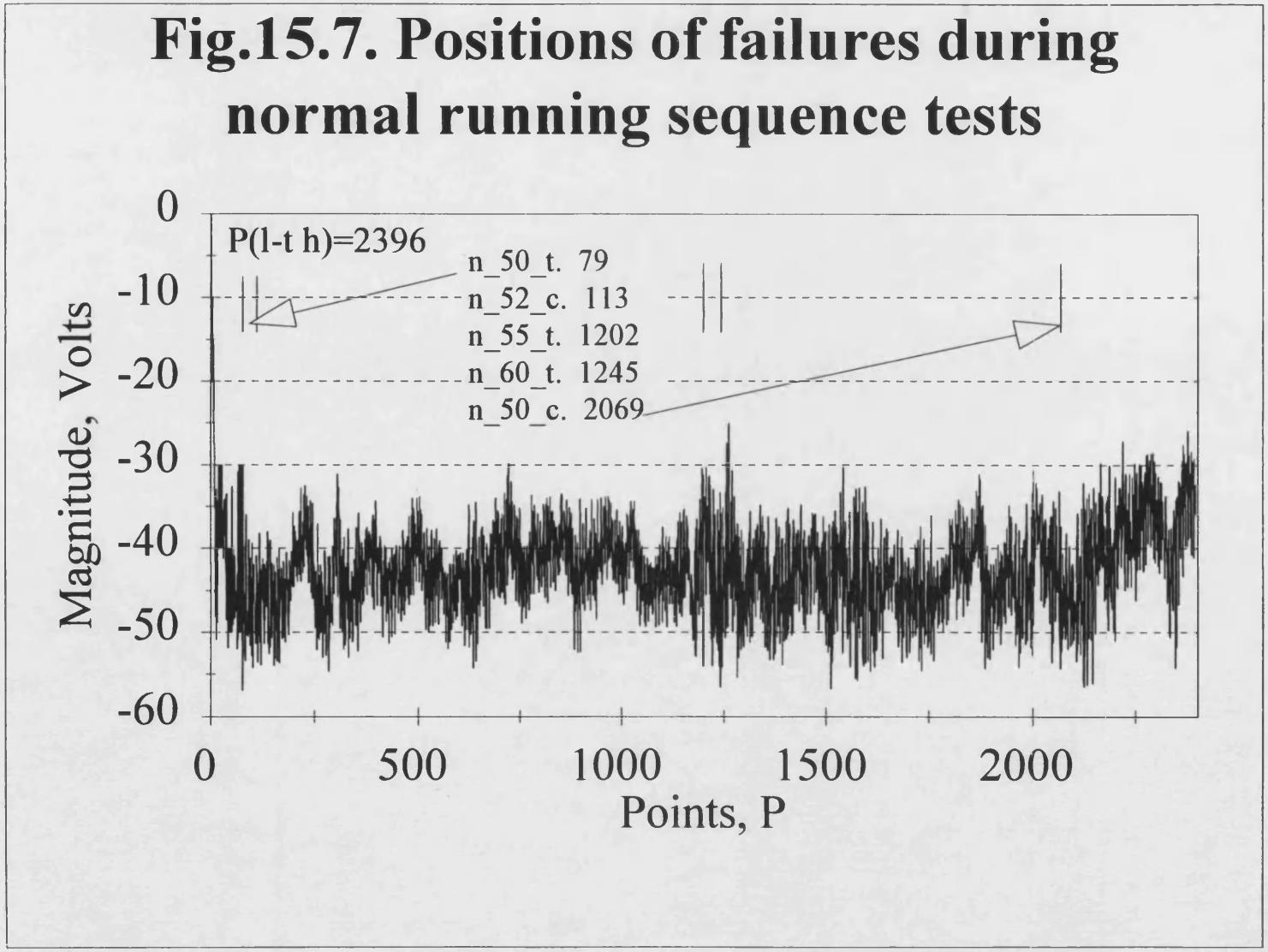
Fig.15.7. Positions of failures during normal running sequence tests
P(1-t h)=2396
n_50_t. 79
n_52_c. 113
n_55_t. 1202
n_60_t. 1245
n_50_c. 2069
Magnitude, Volts
0
-10
-20
-30
-40
-50
-60
0
500
1000
1500
2000
Points, P

Fig.15.8. Positions of failures during controlled stop-start sequence tests

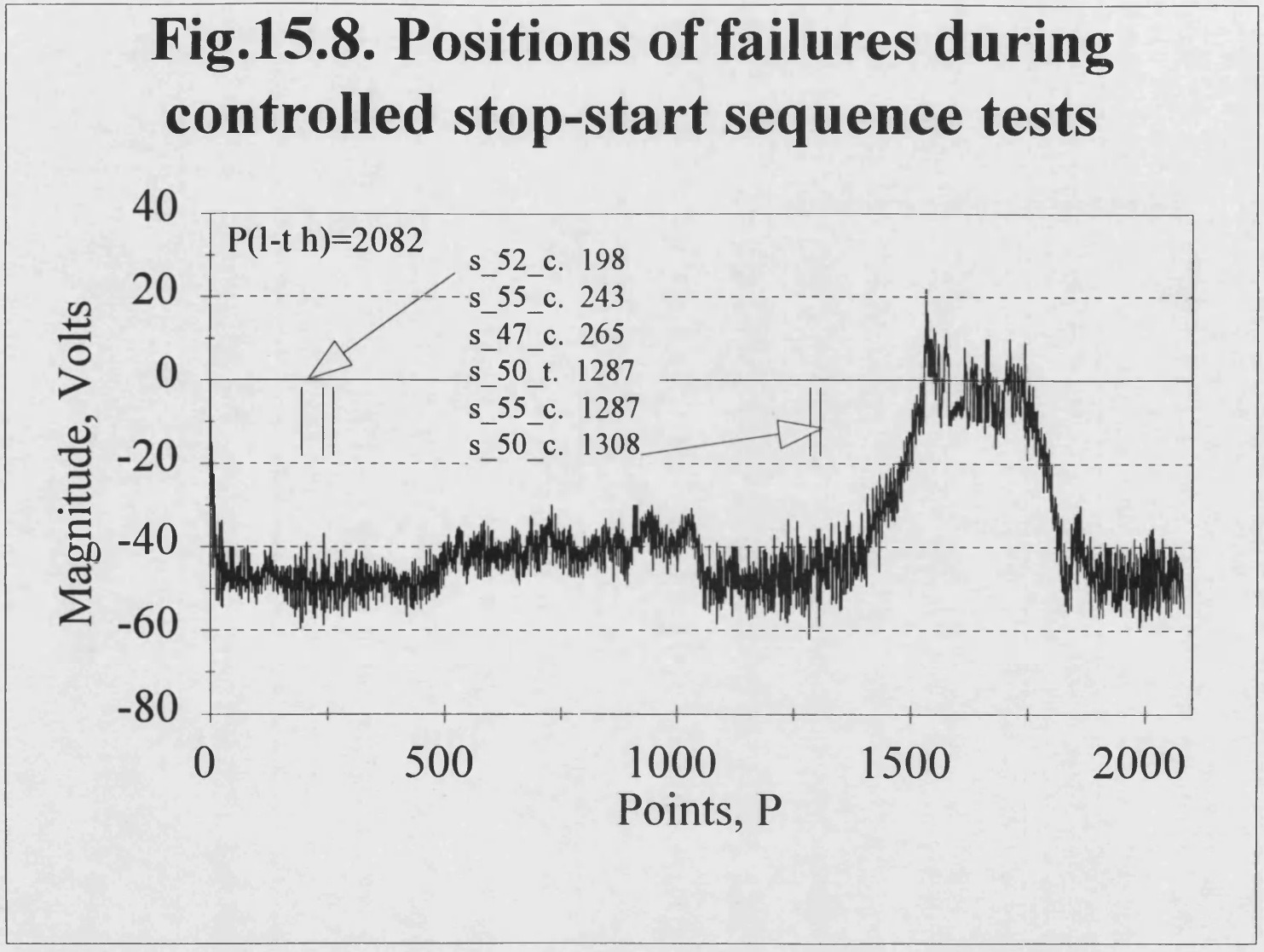

Fig.15.9. Positions of failures during emergency stop sequence tests

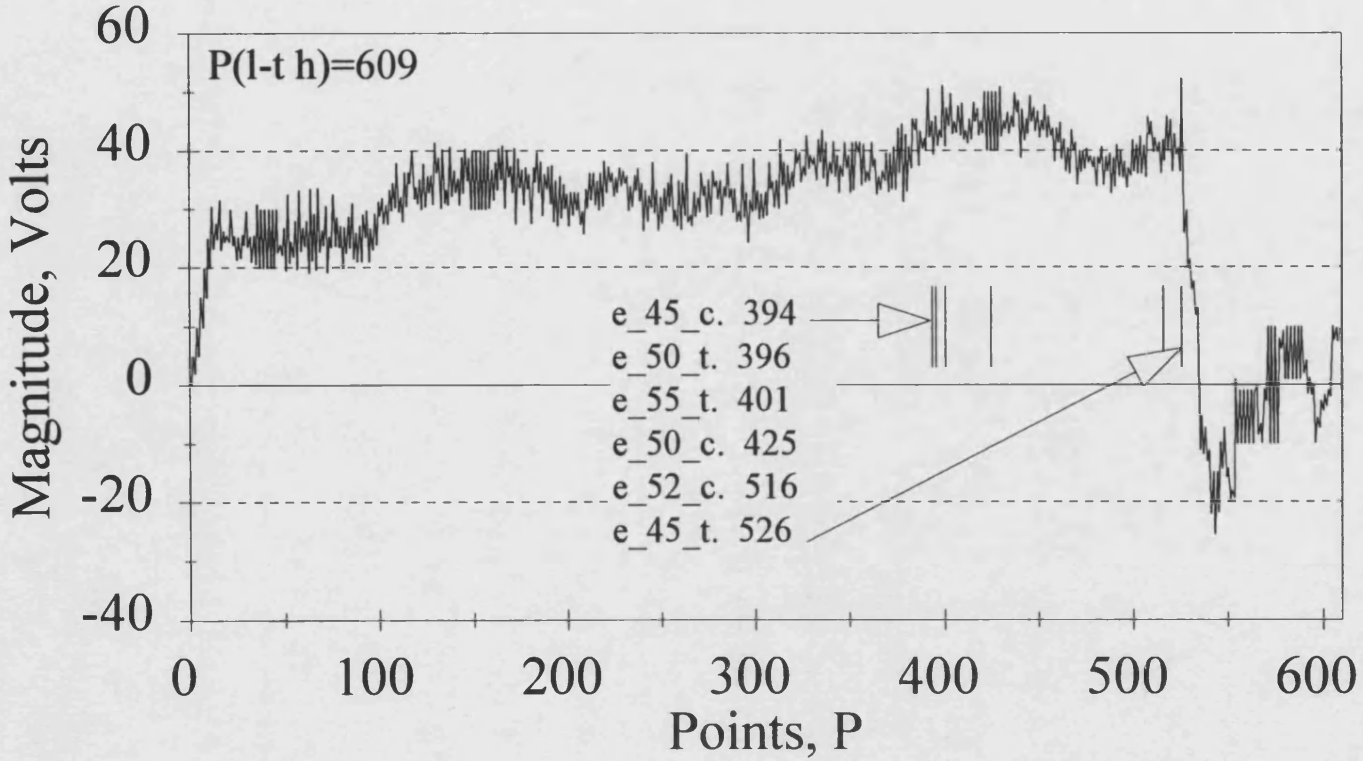

similar. However, when the normalised mean stress is used, the normal operation l-t history appears to have a less damaging effect. In both cases the emergency stop condition causes the most rapid failure of the composite.

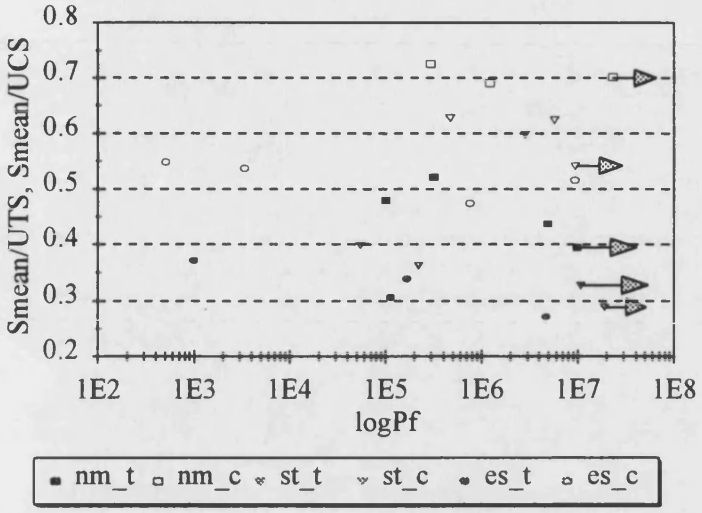

Fig.15.11. S_{mean}-logP_f curves for complex load-time history tests.

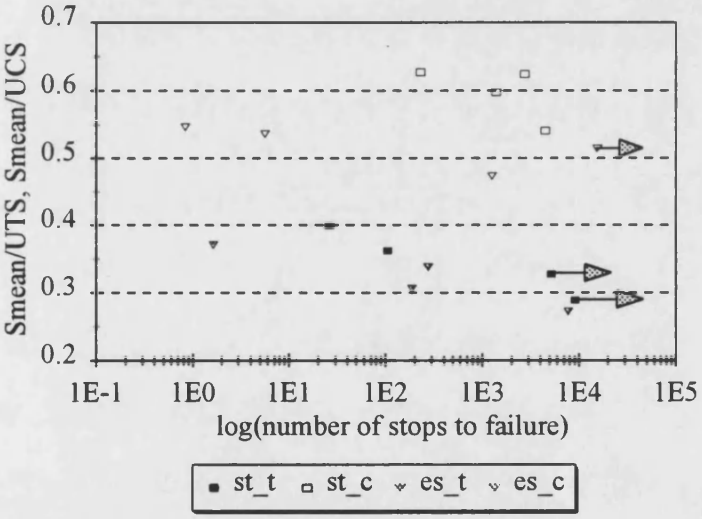

Fig.15.12. S_{mean}-log(number of stops to failure) curves for complex load-time history tests.

As each l-t history has a significantly different number of points, $P_{(l\text{-}t\ h)}$, the number of points to failure, P_f, has been plotted rather than the number of passes in figs.15.10 and 15.11. However, a more direct comparison of the effects of the two different types of stop can be made if stress is plotted against the number of passes which is clearly equal to the number of stops, fig.15.12. As expected the emergency stops are more damaging to the composite than the benign ones. However, it is interesting to note that in tension (the solid symbols) the effect on life of both regimes is much more similar than in compression.

15.5. Stress-strain hysteresis loops from complex loading tests

Typical loops from the first and last captured pass are presented in this section. An example is given for normal operation, controlled- and emergency-stop l-t histories.

Fig.15.13 shows loops captured during the first and 100th pass of the normal operation l-t history. The number of each loop corresponds to the number of the inserted cycles in fig.15.1. Only the first two loops captured during the first pass have been plotted so that they can be distinguished from each other. All three loops have been plotted for the 100th pass and it can be seen that they overlay each other and are difficult to identify. This is because they all lie on the same stress-strain curve for the loading response of Khaya, fig.15.14, which changes only slowly under the action of the applied load.

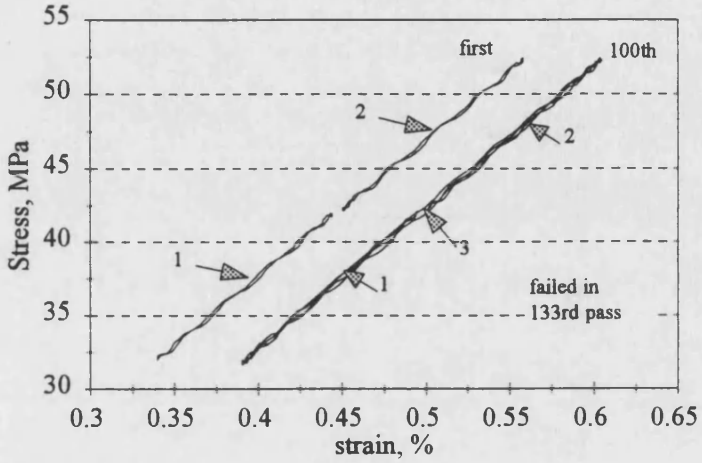

Fig.15.13. First and last group of hysteresis loops for normal operation test nm_60_t, S_{peak}=60MPa.

The loops in fig.15.13 are wavy because they are small and variations in load readings from the load cell on the Mayes can be resolved. This is because the load cell is mounted on the upper grip of the machine causing vibrations in output. The actual load seen by the sample does not vary in this manner (Thompson, 1994).

The loops from the 100th pass have moved to the right along the strain axis showing that tensile creep has occurred. It is also apparent that there is little change in the wood composite's stiffness over the duration of the test. The sample failed in the 133rd pass.

The schematic diagram in fig.15.15 illustrates the relative sizes of each loop. In this diagram the loops have been displaced from the line of the stress-strain characteristic so they can be distinguished from each other.

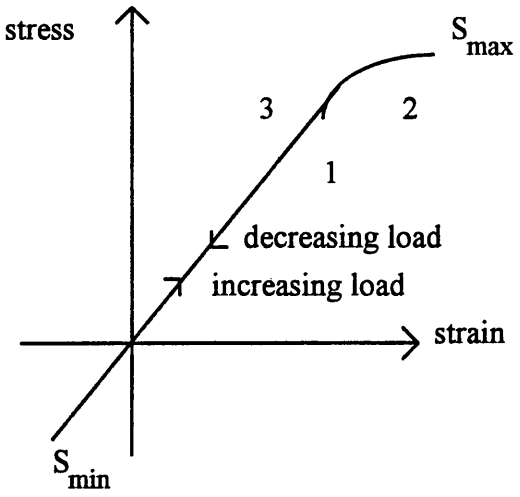

Fig.15.14. Schematic representation of stress-strain curve for Khaya composite during complex l-t history loading showing how the hysteresis loops are superimposed on top of each other [loop width has been exaggerated].

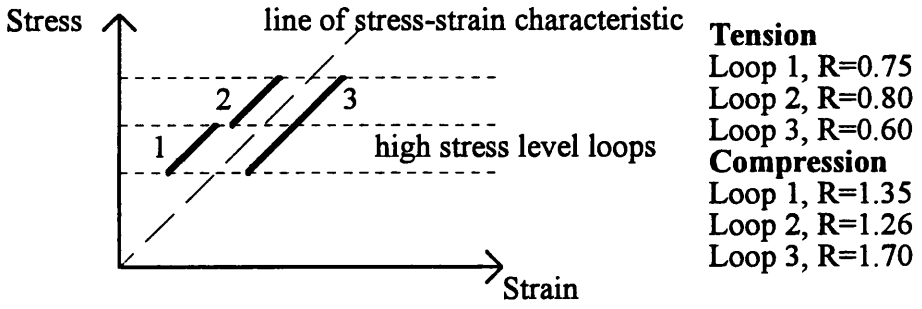

Fig.15.15. Schematic representation of loop capture in normal operation l-t history.

Loops from a controlled stop-start test in compression are shown in fig.15.16. As is the case for the normal l-t history the loops tend to overlay each other. They have also been displaced along the axis to the left between the first and last set of loop captures as a result of compressive creep. Fig.15.17 is a schematic of the relative positions of the loops.

It is difficult to determine whether there are any noticeable changes in the hysteresis loops when they are so small on the graph. However, some differences can be seen when the first and second loops [the low stress level loops] are plotted alone, fig.15.18. It is clear that the loops from the last capture have greater loop areas than those from the first pass of the l-t history. The gradients, however, are identical.

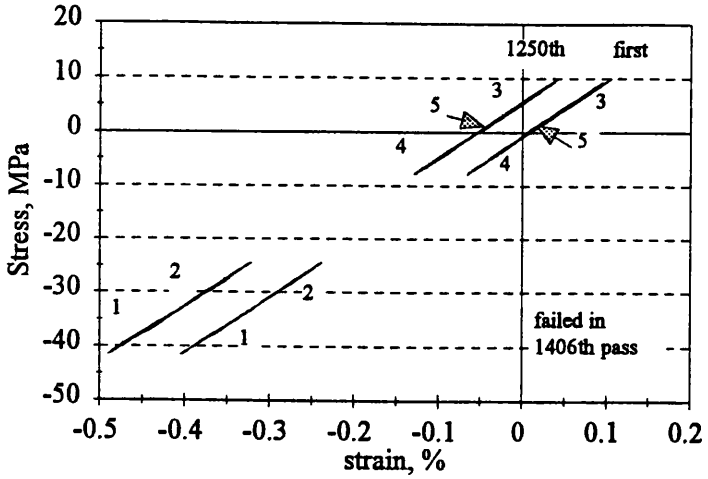

Fig.15.16. First and last hysteresis loops captured for controlled stop-start test st_52_c, S_{peak}=-52.5MPa.

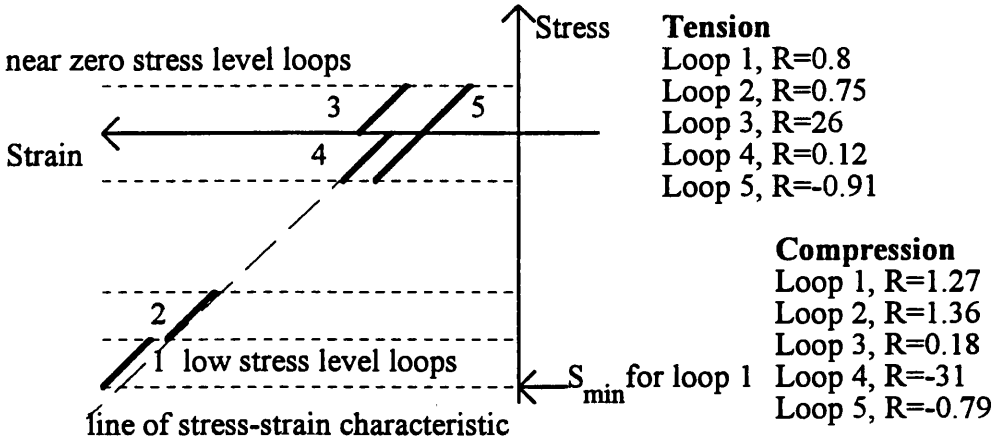

Fig.15.17. Schematic representation of loop capture in a controlled stop-start l-t history.

It is important to bear in mind the fact that for complex tests it is not possible to use the window trips as the loops of interest are not those with the extreme strains which can be used to trigger capture when the properties of the composite start to change rapidly at the end of a test. In fig.15.16 for example, the last capture was at the 1250th pass but failure occurred during pass number 1406. Therefore no capture has occurred in the last 10% of the sample's life where the most marked changes are to be expected.

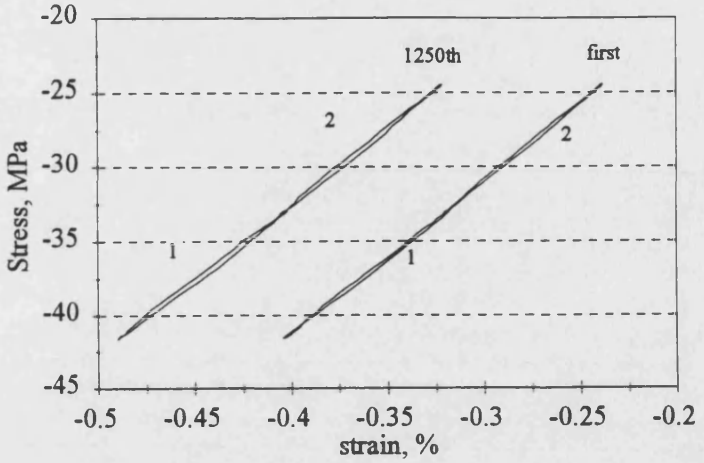

Fig.15.18. First and last hysteresis loops captured for controlled stop-start test st_52_c, S_{peak}=-52.5MPa. Low stress level loops.

Loops taken from a compressive emergency stop test are presented in fig.15.19. Only the loops captured close to zero stress have been plotted so the differences can be distinguished. How they fit into the full set of captures is shown schematically in fig.15.20.

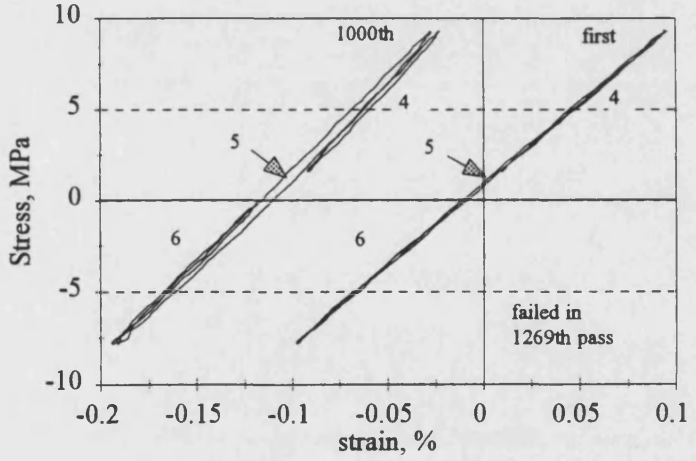

Fig.15.19. First and last hysteresis loops captured for emergency stop test es_45_c, S_{peak}=-45MPa. Near zero stress level loops.

The loops captured during the first pass all overlap each other closely, whereas those in the 1000th capture do not. In addition to the creep which has occurred over the 1000 passes this shows that creep is occurring within a single pass. The 6th loop is displaced to the left more than the 5th and 4th. It can also be seen that the last set of loops are much fatter than the first with the 5th loop showing the greatest increase. Contrary to

what one might expect, the loops from the 1000th pass have higher gradients than at the start of the test.

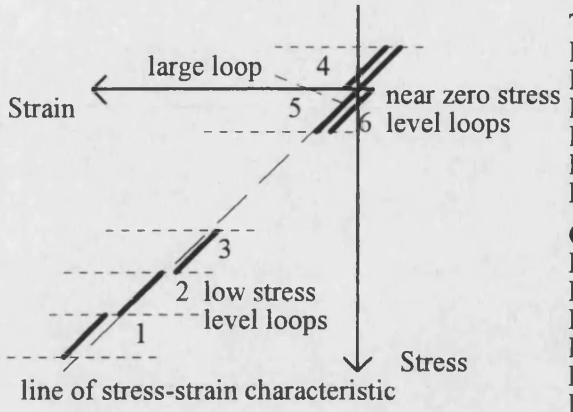

Fig.15.20. Schematic representation of loop capture in an emergency stop l-t history.

15.6. Changes in properties of the Khaya epoxy composite under the different load-time histories

Once imported into 'Quattro Pro' the data from each sample were sorted by R ratio so that similar loops could be compared. Strain, modulus and area data were plotted against logP (the number of points, rather than cycles). Normalised plots of these properties were also plotted where the data for each R ratio were normalised by dividing by the initial value at that R ratio. For example the third loop captured in the desired passes of the l-t history was normalised by the first value measured for the third loop.

A full compliment of the plots for all loading conditions are presented in Appendix E.

When the maximum (for tensile tests) or minimum (for compression tests) strains were normalised by the initial strain very large changes were observed for the loops with S_{max} or S_{min} close to zero. This is because the mean stress which causes creep is much higher than these loop stress levels, leading to a disproportionately large change in strain. Therefore the change in strain, $\Delta\varepsilon$, was plotted which is equal to the current strain minus the initial strain for each R ratio in order to give a better appreciation of the creep strains which were occurring.

When plotting loop area it was apparent that the loop in each pass with double the stress range, eg. loop 3 in the normal l-t history and the loops ~ R=-1, had, as would be expected, much higher areas. Therefore the loop area was normalised by the stress range, $A\text{-}S_{range}$, for a clearer comparison.

It was also noticed that in some samples there appeared to be a dependence of modulus and loop area values on the stress level at which the loop had been captured. In order to determine any such relationship the modulus and area values were also plotted against the maximum (for tensile tests) or minimum (for compression tests) stress level of the loop.

The volume of data associated with these tests at first appears bewildering. In order to make them more digestible they have been condensed into tabular form with one table for each l-t history. The data from the tensile and compressive tests are given in adjacent columns so ready comparisons between property changes can be made.

The schematic representations of the relative positions of loop captures presented in figs.15.15, 15.17, and 15.20 relate the loop numbers to the R ratios and clarify some of the descriptions used in these tables. Difficulty arises in comparing loops from tensile and compressive tests and the meaning of 'high' and 'low' stresses in each case. To avoid confusion the following scheme has been adopted: in tensile tests loops captured at high tensile stresses are called 'high stress level loops' and low stress level loops are termed 'near zero stress level loops'. In compression loops captured at high compressive stresses are termed as 'low stress level loops' and those captured at lower compressive stresses are called 'near zero stress level loops'. In this way confusion over which loop is being discussed is avoided.

A second distinction must also be made between the maximum or minimum stress in one pass of a l-t history and the maximum and minimum stresses in a hysteresis loop. To avoid confusion the former has been defined as the peak stress, S_{peak}, and its magnitude is the number which appears in the name which characterises a particular test [eg. es_45_t is an emergency stop l-t history, peak stress=50MPa, tensile test]. In this way the distinction can be drawn between property trends which are dependent on the stress level of the test, ie the peak stress, and those which depend on the stress level at which the hysteresis loop was captured.

15.6.1 Normal operating conditions

The property change data for tests carried out using the normal operating condition l-t history are presented in table 15.3. The names of each test have been further abbreviated to save space in the table as follows: test nm_45_t becomes n45t. In certain boxes of the table approximate average values of a property have been estimated from the full set of graphs and are presented to illustrate trends across the samples tested.

The abbreviations in the 'Property' column are as follows: $\varepsilon/\varepsilon_0$, strain normalised by initial strain; M/M_0, modulus normalised by initial modulus; A/S_{range}, loop area divided by stress range; $\Delta\varepsilon=(\varepsilon-\varepsilon_0)$ change in strain; $M\text{-}S_{max}$, modulus plotted against stress level and $A\text{-}S_{max}$,area plotted against stress level.

Property	Tension	Compression
Strain, %	Increases in all samples, up to ~0.5% (0.6% for n60t)	Decreases in all samples, to between -0.55% and -2%
Modulus, GPa	Increases in all samples. 1st loop has highest gradient. 1st & 2nd similar. n45t [runout] shows a dramatic increase at end of test.	Tends to decrease. 3rd loop has lowest gradient. 1st highest, & 2nd intermediate.
Area, Jm^{-3}	Very variable. Trends not distinct. 3rd loop largest because it has twice the stress range of the others.	
	Areas increase with peak stress. S_{peak} 45 50 55 60 (MPa) 1 & 2 50 75 100 150 3 200 250 300 450 In all but 60t the difference in area between small and large loops decreases with P.	No clear trends except in n50c. Large loop increases in size with P only in n50c: 1 & 2; 100-200 3 300-500
$\varepsilon/\varepsilon_0$	Highest for 1st loop. Similar for 2nd & 3rd loops (same S_{max}). Decreases with increasing S_{peak}: S_{peak} 45 50 55 60 (MPa) 1 2 1.2 1.095 1.12 2 & 3 1.7 1.15 1.07 1.08	Highest for 1st loop. Similar for 2nd & 3rd (same S_{min}). Increases with S_{peak}: S_{peak} -50b -50 -52 (MPa) 1 1.55 3.1 3.25 2 & 3 1.45 2.25 2.5
M/M_0	2-20% increase during sample life	-4-20% decrease during sample life
A/S_{range} (dimensionless quantity)	No trend with logP, except n60t where 3rd loop increased during the sample's life: S_{peak} 45 50 55 60 (MPa) 10 10 12 15 1,2,& 3. -- -- -- 20-30 3 (n60t only)	No trend with logP, except n52c. S_{peak} -50 -50 -52 (MPa) 15 20 10-27 1,2,& 3. -- -- 20-50 3 (n52c) Values for large and small loops overlap more closely than in tension.
$\Delta\varepsilon$, %	Mean creep strain of ~0.06% (except n45t with a higher creep strain of 0.3%)	Creep strain increases with stress level: S_{peak} -50b -50 -52 (MPa) -0.175 -0.7 -0.8.
$M\text{-}S_{max}$	Even scattering of modulus values at all S_{max}	
$A\text{-}S_{max}$	Even scattering of modulus values at all S_{max}	A is possibly higher at the higher stress levels. Only marginal.

Table 15.3. Results for normal operating conditions l-t history

Plots of results from test n52c are presented to show some of the trends observed in the data. Figs.15.21 and 15.22 show how the dynamic modulus and loop area change with logP (P = the number of turning points experienced).

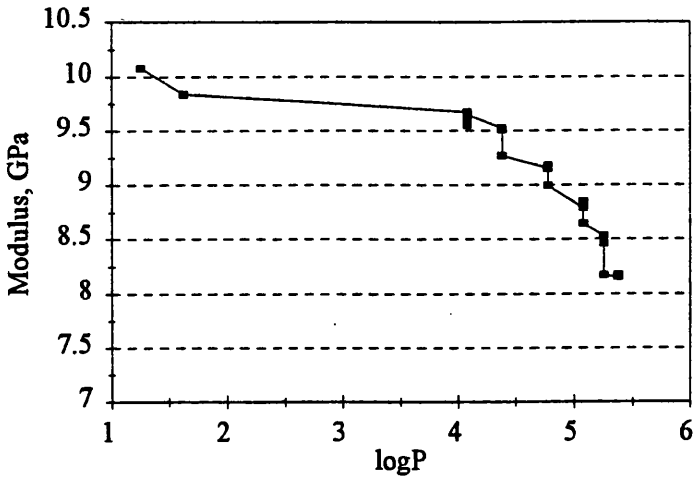

Fig.15.21. Change in modulus with logP for normal operation l-t history in compression, S_{peak}=-52.5MPa.

Even when the different R ratio loops have not been separated it is clear that there are differences in moduli values between loops 1, 2 and 3.

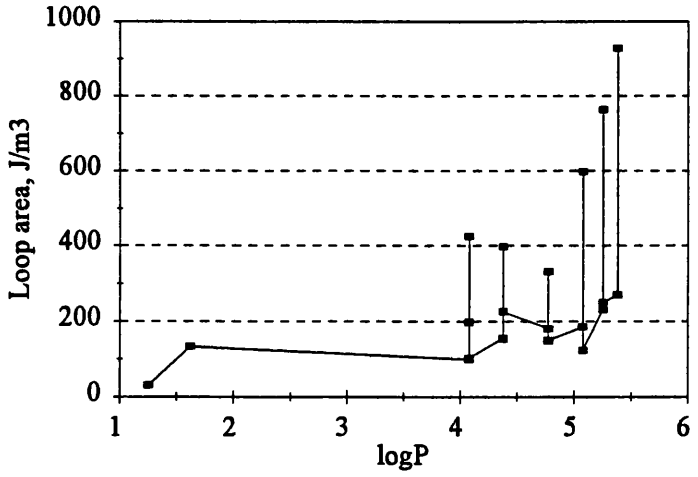

Fig.15.22. Change in loop area with logP for normal operation l-t history in compression, S_{peak}=-52.5MPa.

The most obvious difference in area between the loops captured is highlighted by the high peaks on the curve which tend to increase with logP. These curves correspond to

the third loop captured with double the stress range of the first two loops. It is these loops which also show the greatest increase with logP as damage accumulates.

In fig.15.23 minimum strain values have been plotted against logP. The minimum strains for each loop have been separated into curves for each R ratio.

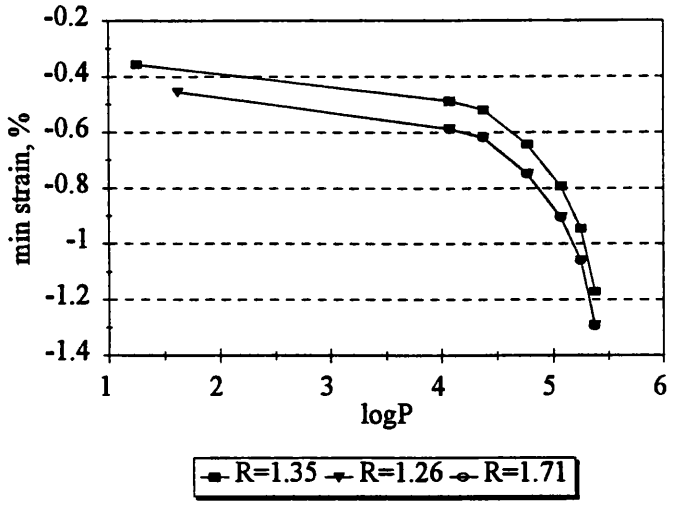

Fig.15.23. Minimum strains for loops at each R ratio in compression. Test n52c.

The R ratio R=1.35 corresponds to the first loop [see fig.15.14], R=1.26 to the second and R=1.71 to the third. The minimum strains for the second and third loops overlay each other because their minimum strains are the same [loop captures 2 and 3 in fig.15.15]. Compressive creep is clearly occurring as the strains all become more negative.

In fig.15.24 the modulus has been split into the different R ratios. It is clear that the first loop has the highest modulus and that the second and third loops have a slightly lower value. All have decreased in the course of the test by 20%. This is an appreciable amount, given that in constant amplitude compression fatigue the modulus typically decreased by 10 to 20% of the initial value.

The loop area values have been split up into the different R ratios in fig.15.25. The peak values seen in fig.15.22 correspond to the highest curve in fig.15.25, which belongs to the R=1.70 loops. These are the ones with double the stress range of the loops captured at R=1.35 and 1.26. The area values for the first two loops [R=1.35 and 1.26] are similar, with a slightly higher value for the second loop.

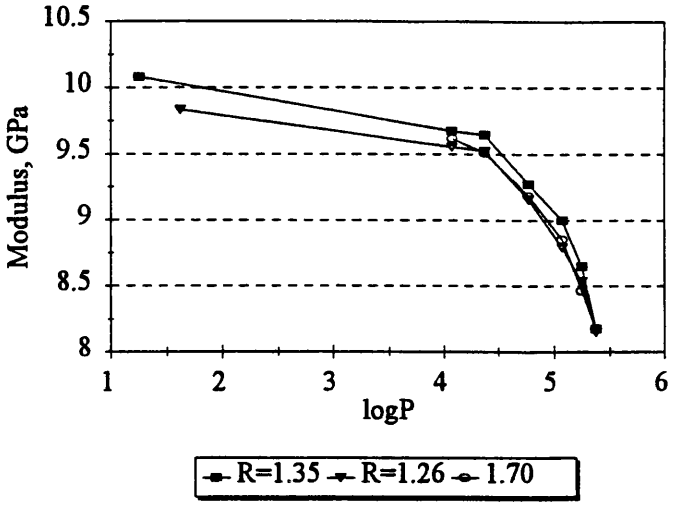

Fig.15.24. Dynamic modulus for loops at each R ratio in compression. Test n52c.

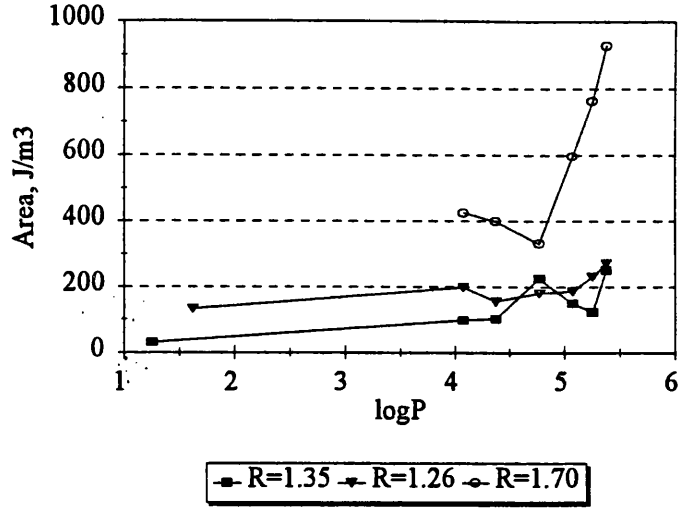

Fig.15.25. Hysteresis loop area for loops at each R ratio in compression. Test n52c.

An example of the plots obtained for tensile tests using the normal operation l-t histories is presented in fig.15.26. Loop area has been plotted against logP. Again it is clear that the third loop [corresponding to R=0.60] with the largest stress range has the highest area. The first and second loop areas are similar but the loop corresponding to R=0.75 [the first loop] has a slightly higher area.

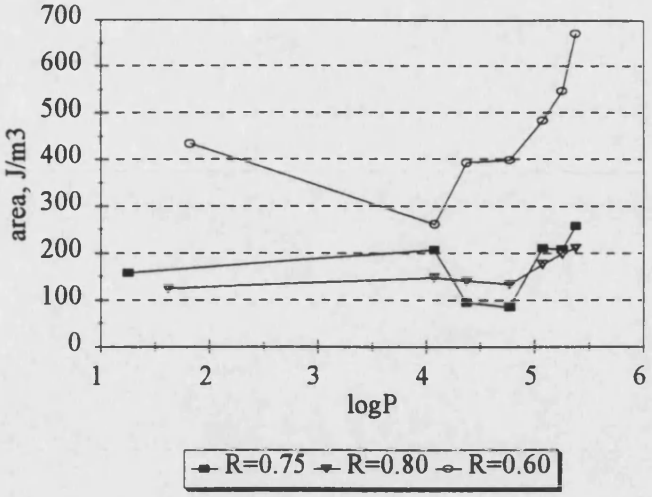

Fig.15.26. Example of property changes in tensile loading using the normal operation l-t history. Loop area for each R ratio. Test n60t.

15.6.2. Controlled stop-start conditions

Property change trends for tests using the controlled stop-start l-t history are presented in table 15.4. The abbreviations are the same as explained for table 15.3 at the start of section 15.6.1. Test names have been abbreviated, for example, st_47_c is written s47c.

Data obtained from test s50t are presented in the following figures as examples of the property changes observed using the controlled stop-start l-t history. In figs.15.27 and 15.28 the dynamic modulus and loop areas have been plotted without splitting the data into R ratios. In fig.15.27 it can be seen that the modulus decreases and then increases. As more loops are captured in the controlled stop l-t history tests it is difficult to determine which loops are the ones with the significantly lower modulus values.

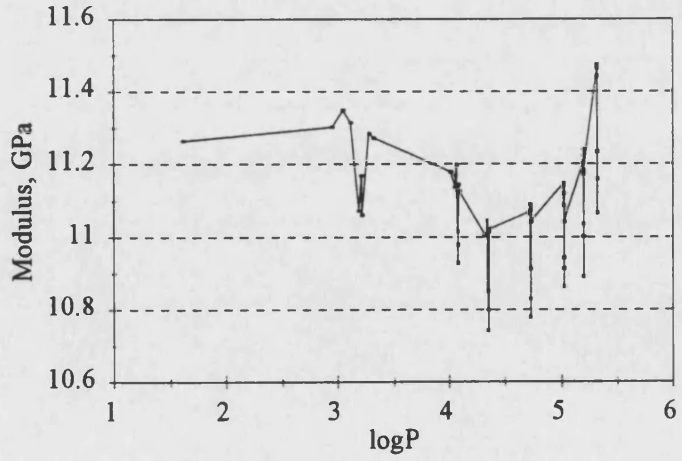

Fig.15.27. Change in modulus for controlled stop-start l-t history, S_{peak}=50MPa

Property	Tension	Compression
Strain, %	Two samples show an increase followed by a decrease, the other a slight increase.	All showed a marked decrease. In all but s47c the R=0.18 loop turned negative because of creep.
Modulus, GPa	Increased in all samples. Near-zero stress loops have the lower mods. s45t [runout] shows a dramatic increase at end of test.	Decreases (except s47c). Near zero stress loops have the higher mods. s47c: mod similar at all stress levels till logP=5.5 when mod of near zero loops decrease by ~2%.
Area, Jm^{-3}	Loop area for R=-0.79 (large loop) increases more dramatically than other loops. S_{peak} 45 50 55 (MPa) 1. 75 125 125 2. 100→500 275→350 200→500 1. approx area of small loops 2. inc in area for large loop R=-0.79.	Loop area increases dramatically for R=-0.84. S_{peak} -47 -50 -52 -55 50 100 150 100 100→250 200→800 200→600 0→900 Can only distinguish difference in areas between small loops for s52c: large loop > low stress loops > near zero stress loops.
$\varepsilon/\varepsilon_0$	R=30 loop shows rapid decrease (S_{mean} >> than S_{max} & causes tensile creep). Other loops near zero showed a more marked increase than high stress loops.	R=0.18 shows dramatic decrease (S_{max} >> than S_{mean} & causes compressive creep). Loops near zero showed a more marked increase than those at high stresses.
M/M_0	2-20% increase during sample life	6-15% decrease during sample life (except s47c which showed little change)
A/S_{range}	No trend with logP. S_{peak} 45 50 55 (MPa) 10 17 17.5 for all loops. R=30 is just distinguishable as the lowest and R=-0.84 the highest.	Increases observed in s52c and s55c S_{peak} -47 -50 -52 -55 (MPa) 6 12 15-30 9-40 for all loops. R=-0.79 shows greatest increase. In s52c A/S_{range} is lower for the near zero stress level loops than for the low ones.
$\Delta\varepsilon$	Not helpful	Creep strains between -0.1 and -0.7%. Near zero stress level loops show less creep than low level loops.
$M\text{-}S_{max}$	s45t: no relationship between mod and stress level. s50t, s55t: mod and range tend to increase with S_{max}.	s47c: no relationship. s50c, s52c and s55c: lower mod at lower stress levels.
$A\text{-}S_{max}$	s45t: no relationship. s50t, s55t: area and range tend to increase with S_{max}	Not possible to determine a correlation between area and S_{min}.

Table 15.4. Results for controlled stop-start l-t history

Fig.15.28 shows loop area values for the same test as shown in fig.15.27. The high values of loop area correspond to the loop with double the stress range of the others [see fig.15.17]. Some loops have much lower areas, but which ones they are cannot be resolved from this figure.

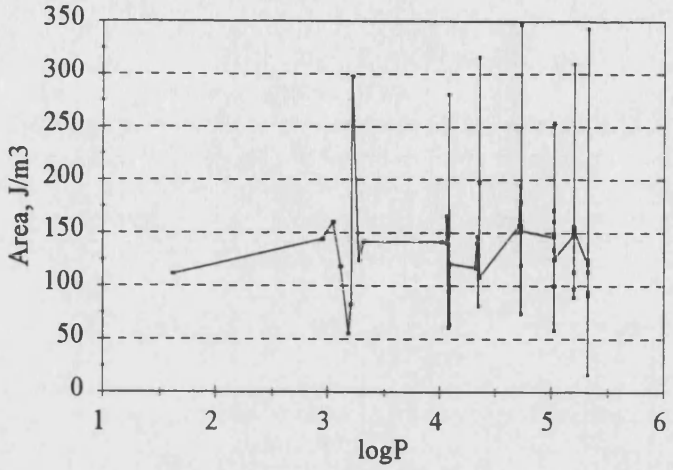

Fig.15.28. Change in loop area with logP for controlled stop start l-t history. S_{peak}=50MPa.

In test s50t nine loops have been captured during the desired passes of the l-t history [contrary to the five illustrated in fig.15.17] in order to determine whether any part of the l-t history had a particular influence on the property changes in the composite. All the additional loops had an R ratio of 0.8 and were inserted into the l-t history immediately before and after the peak value, after the controlled stop-start and right at the end of the history. The last loop at R=0.8 was captured at the same point as the first in the subsequent pass so the effects of one pass could be determined. Fig.15.6 shows the relative positions of the cycles in the l-t history. They have been investigated in section 15.7.

The maximum strains for each loop from test s50t have been plotted against logP in fig.15.29. As expected, all loops with R=0.8 overlay each other, as do the curves for R=0.12 and R=-0.91. All strains increase with logP as tensile creep occurs. The curve for R=26 changes from a negative to a positive strain as a result.

When the moduli are plotted for each R ratio in fig.15.30 it becomes clear which loops have the much lower modulus values observed in fig.15.27. The moduli for all the high stress level loops overlay each other fairly closely. The loops captured close to zero stress all have a much lower stiffness. R=-0.91 is the lowest, followed by R=0.12 and

R=26. R=-0.91 is the loop captured when the composite undergoes a load reversal. R=0.12 corresponds to a low stress level tensile loop and R=26 corresponds to an all compressive loop. This suggests that this sample has higher stiffness in compression than in tension. However, the opposite has been seen to be true for sample s55t. In both cases the stiffness of the R=~-1 loop was approximately the mean value of the near zero tensile and compressive loops.

No loop bending in the R=-0.91 loop was seen to occur as the test proceeded.

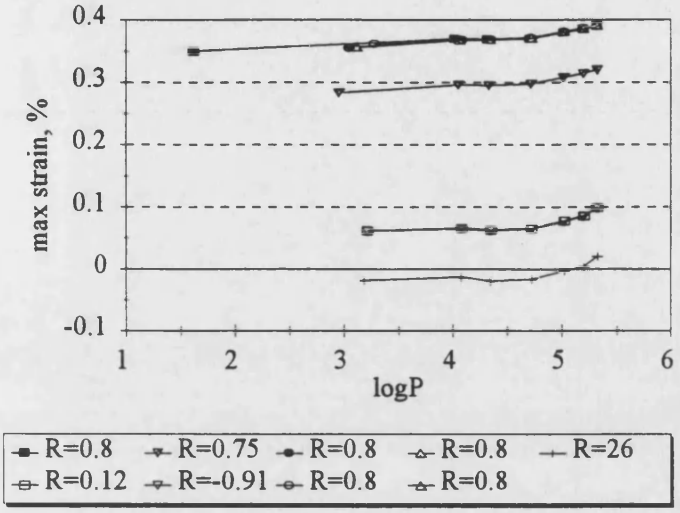

Fig.15.29. Change in maximum strain with logP for each R ratio. Sample s50t.

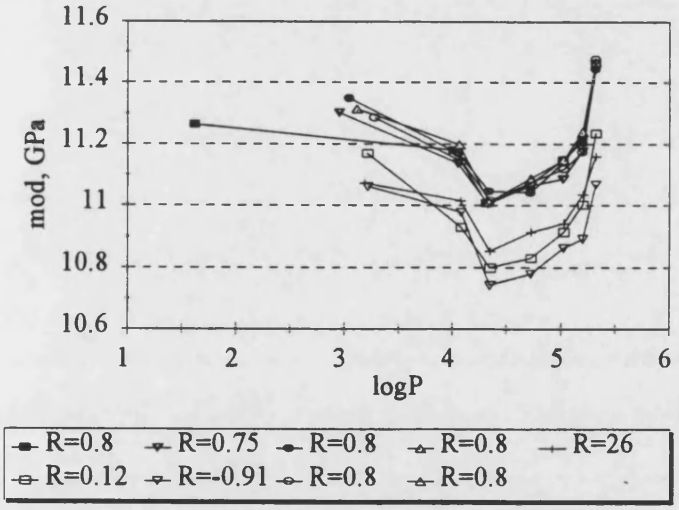

Fig.15.30. Dynamic modulus vs. logP for all R ratios. Test s50t.

In fig.15.30, the moduli all change in the same manner throughout the test with an initial decrease followed by an increase to failure. This has also been observed in most tensile complex tests and in over half of the constant amplitude tests at R=0.1.

Fig.15.31 shows how the loop area varies for each R ratio. It is immediately clear that there is appreciable variation in the measured values for loops of the same size. As usual, the loop area is much larger for the R=-0.91 loop with double the stress range. It can just be distinguished that the other near zero loops have the lowest values of loop area, with R=26 being the lowest.

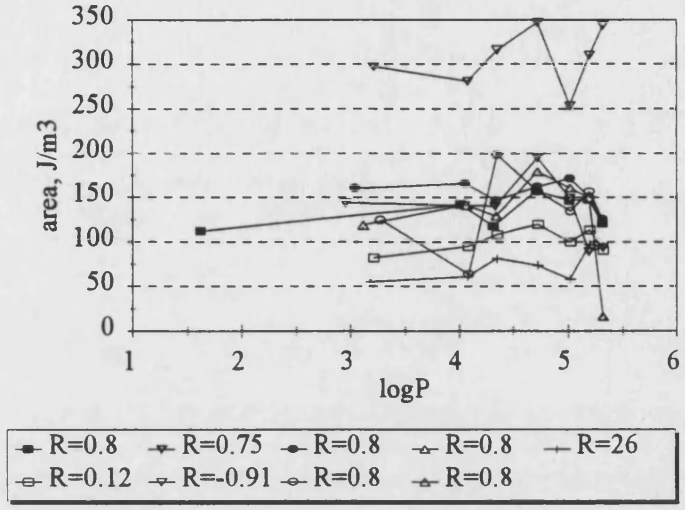

Fig.15.31. Loop area vs. logP for all R ratios. Test s50t.

Once the loop areas are normalised by the stress range of the loop the R=-0.91 line falls into the cluster of R=0.8 curves and cannot easily be distinguished, fig.15.32. R=26 emerges more clearly as the lowest followed by R=0.12.

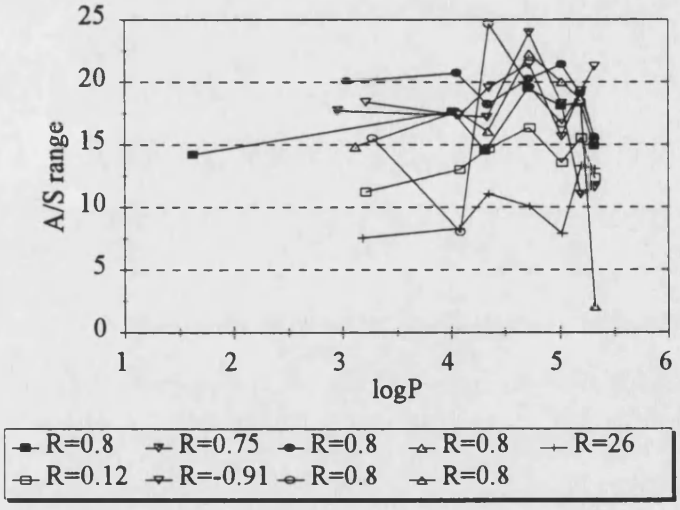

Fig.15.32. Loop area/(stress range) for all R ratio. Test s50t.

In order to establish whether there was any dependence of modulus and area on stress level, these properties were plotted against the maximum loop stress. They are

presented in fig.15.33 and 15.34 respectively. The range in data at each stress level is due to the changes in property which occurred during the test.

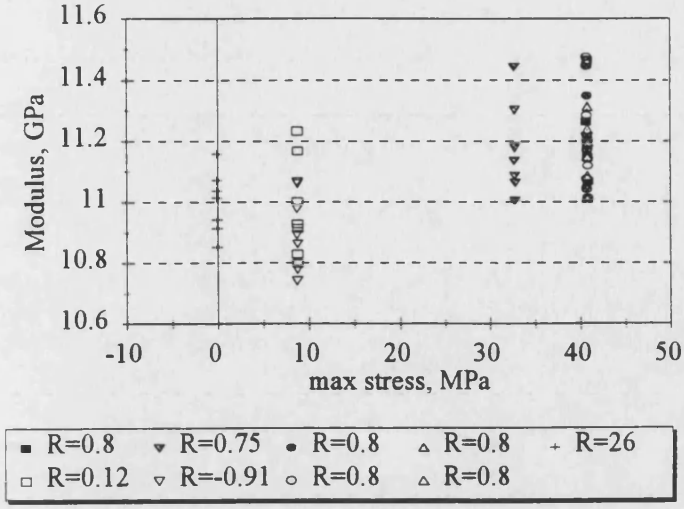

Fig.15.33. Plot of dynamic modulus against maximum loop stress for all R ratios. Test s50t.

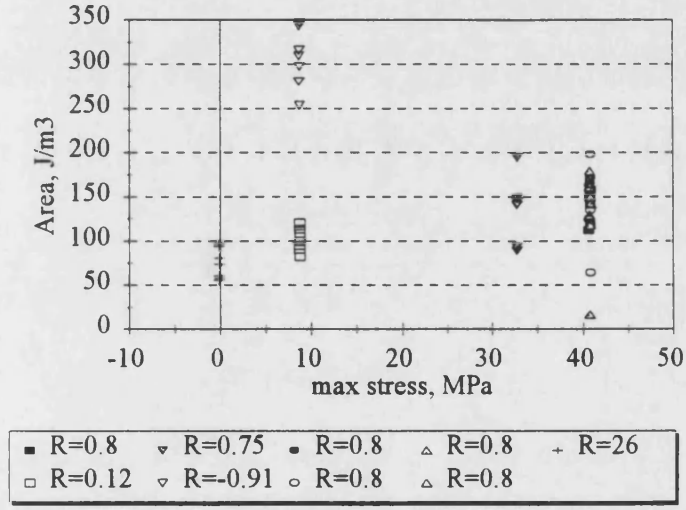

Fig.15.34. Plot of loop area against maximum loop stress for all R ratios. Test s50t.

In the case of the dynamic modulus, fig.15.33 shows that at higher stress levels the wood composite has greater stiffness. Similarly for loop area, fig.15.34 shows that the higher stress level loops tend to have the higher loop areas. The R=-0.91 areas cannot be considered in the comparison because they have double the stress range.

As examples from a compressive controlled stop-start test, two strain-based plots are presented in figs.15.35 and 15.36. In fig.15.35 the strains at each R ratio have been normalised by the initial strains measured on the first pass of the l-t history. In all but the R=0.18 line the curves increase, showing that the strains are becoming more

negative as the test proceeds. The near zero curves show a higher increase than those for low stress level loops. This difference arises because the minimum stress of the near zero loops is well above the mean stress causing compressive creep. Therefore, when the strain is normalised by the initial strain the amount of change appears high. Conversely, the low stress level loops are captured below the mean stress for the l-t history so when normalisation is carried out the changes appear much less significant. In the case of the R=0.18 loop the minimum strain is only ~0.025% and an overall creep strain of ~-0.3% occurs during the test (see fig.15.36). When subsequent minimum strains are normalised the change appears vastly exaggerated. It also changes sign because the minimum strain becomes negative as compressive as creep occurs.

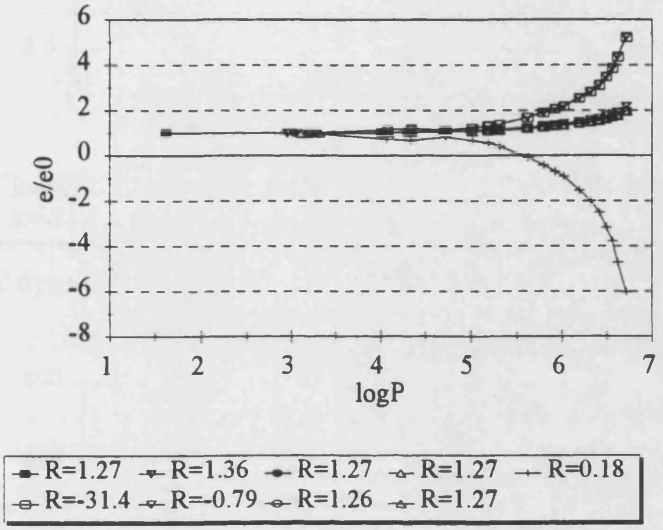

Fig.15.35. Minimum strain normalised by the minimum strain measured during the first pass of the l-t history for each R ratio. Test s50c.

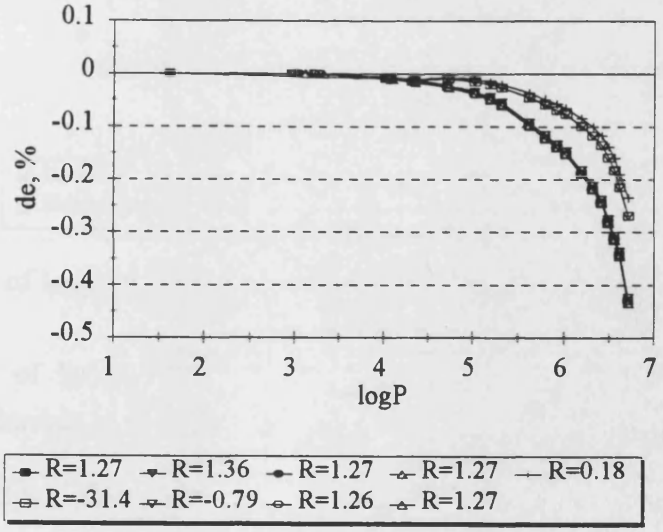

Fig.15.36. Change in minimum strain for each R ratio. This is equal to the creep strains developed during the test. Test s50c.

In contrast to the data presented in figs.15.33 and 15.34, the relationship between dynamic modulus and stress level are different in compression. At low stress levels the compressive tests show lower moduli values than for the near zero tests, fig.15.37. The loop area is also slightly higher at the low stress levels, fig.15.38.

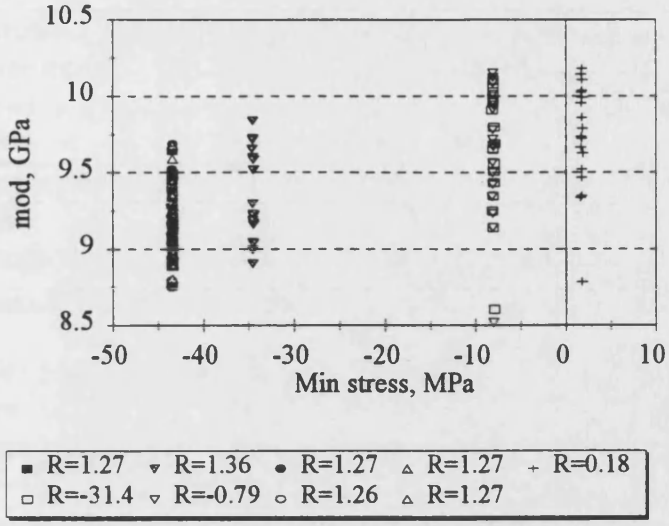

Fig.15.37. Plot of dynamic modulus against minimum loop stress for all R ratios. Test s50c.

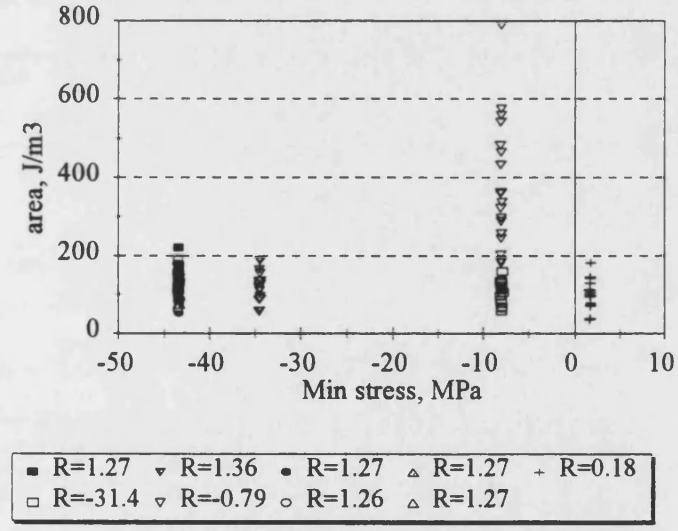

Fig.15.38. Plot of loop area against minimum loop stress for all R ratios. Test s50c.

The difference of behaviour in tension and compression suggests that the wood composite is behaving in different ways under each loading regime.

15.6.3. Emergency stop conditions

Property change trends for tests using the emergency stop l-t history are presented in table 15.5. The abbreviations are the same as explained for table 15.3 at the start of section 15.6.1. Test names have been abbreviated, eg., es_47_c is written e47c.

Property	Tension	Compression
Strain, %	e40t - increase at end of life e45t - [runout] decrease & increase e50t - little change	All showed a marked decrease. e45c had a 2 stage decrease where the rate was higher in the 2nd stage.
Modulus, GPa	Little change, perhaps a slight decrease. Near zero loops have the lower mods. Sample e40t [runout] shows a dramatic increase in mod at R=-0.85 at end of test.	Sample e45t - increase in mod, particularly dramatic for near zero stress loops. Sample e47t- decrease in mod. Near zero stress loops tend to have the higher mods.
Area, Jm^{-3}	Loop area for R=-0.85 (large loop) higher than other loops. No major change in area with P. S_{peak} 40 45 50 (MPa) 75 100 125 e50t - high stress level loops tend to have higher area than near zero stress level loops.	Little change in loop area for small loops. R=-0.84 shows dramatic increase. S_{peak} 45 47 1. 200 100 2. 200→1000 200→500 1. small loops 2. increase in R=-0.84 loops
$\varepsilon/\varepsilon_0$	R=~10 loop shows rapid change (S_{mean} >> than S_{max} & causes tensile creep). Loops near zero showed more marked increase than ones at low stresses in 2/3 tests.	R=0.17 shows dramatic decrease (S_{max} >> than S_{mean} & causes compressive creep). Loops near zero showed more marked increase (up to 2 times) than ones at low stresses.
M/M_0	Little change for the majority of life. e40t and e50t showed increase at end of life.	e45c - near zero loops showed greatest increase in M/M_0 e47c - [runout] near zero loops showed no change whilst lower stress level loops showed ~2% dec.
A/S_{range}	No trend with logP S_{peak} 40 45 50 (MPa) 10 15 17.5 for all loops. e40t, e50t, R=0.18 and -11 is just distinguishable as the lowest and R=-0.85 the highest.	No trend, except in e45c S_{peak} 45 47 (MPa) 1. ~20 ~15 small loops 2. 10→60 ----- R=-0.84.
$\Delta\varepsilon$	Not helpful	Creep strains of -0.05 and -0.15%. Near zero stress level loops show less creep strain than low level loops.
$M\text{-}S_{max}$	Sample e40t: no relationship between mod and stress level. e45t & e50t: as S_{max} increases mod and range tend to increase.	As S_{min} decreases so does the modulus
$A\text{-}S_{max}$	Increase in S_{max} leads to increase in loop area for all samples.	Slight relationship between S_{min} and loop area: decrease in S_{min} leads to an increase in loop area.

Table 15.5. Results for emergency stop l-t history

Data from emergency stop tests are presented in figs.15.39 to 15.49. Examples are taken from tests e50t (tension, S_{peak}=50MPa) and e45c (compression, S_{peak}=-45MPa). In figs.15.39 and 15.40 the modulus and area are plotted against logP respectively for the tension test. The shape of each curve is similar in form to those observed with the controlled stop start l-t history in tension, figs.15.27 and 15.28.

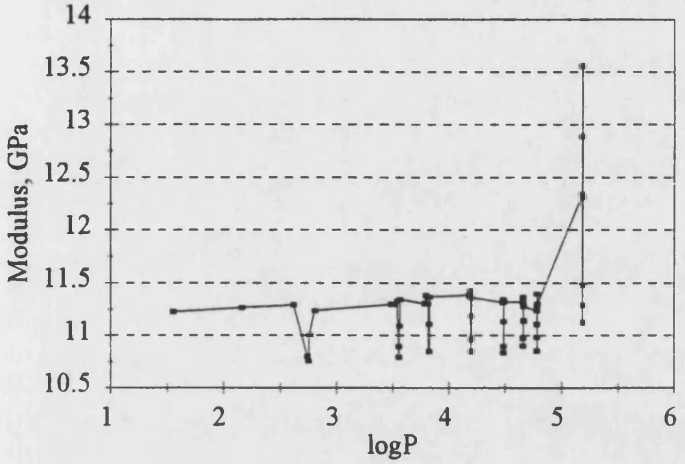

Fig.15.39. Change in modulus with logP for emergency stop l-t history. S_{peak}=50MPa.

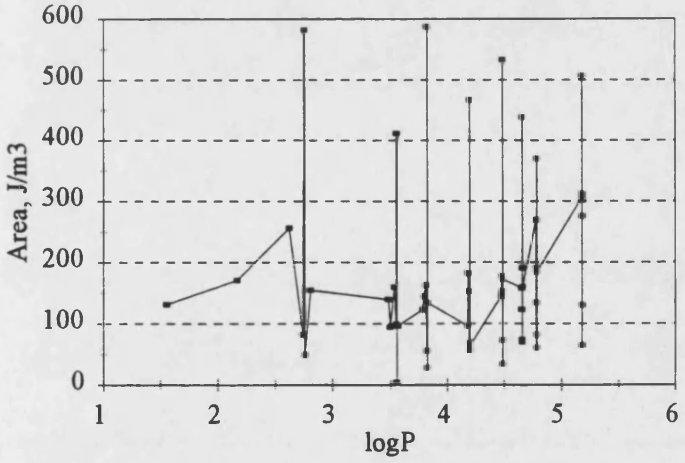

Fig.15.40. Change in loop area with logP for emergency stop l-t history. S_{peak}=50MPa.

The lowest modulus values correspond to the near zero loops (fig.15.39) and the highest loop area values belong to the loops where load reversal occurs (fig.15.40).

In fig.15.41 the modulus values have been plotted for test e45c. It can be seen that the modulus increases overall during the test, with some loops consistently showing the

largest increases. In addition to the high values, there are some smaller downward 'spikes' on the curve. Fig.15.42 separates the R ratios and shows that the greater changes belong to the near zero stress level loops, with R=0.17 the most pronounced. There is also an order discernible in the low stress level loops where it can be seen that the lower the R ratio, and minimum stress, the lower the dynamic modulus. This trend in the low stress level cycles was not visible in the controlled stop start l-t history compression tests.

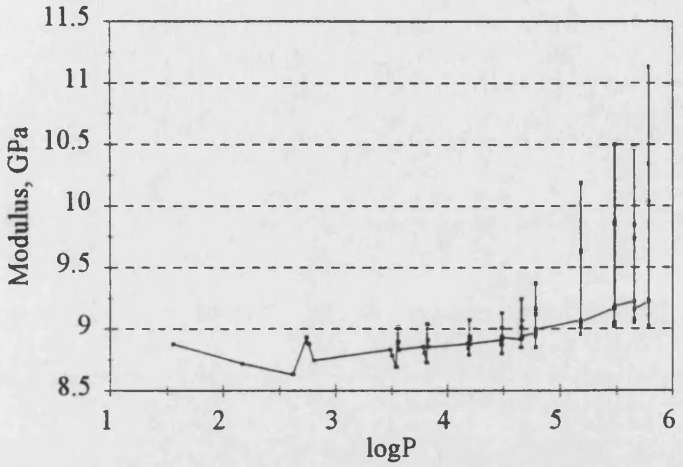

Fig.15.41. Change in modulus with logP for emergency stop l-t history. Test e45c.

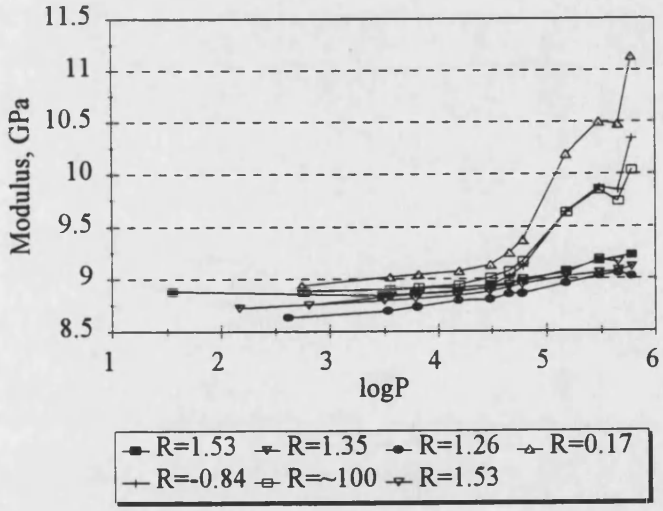

Fig.15.42. Change in modulus with logP for all R ratios. Test e45c.

If figs.15.43 and 15.44 are compared some differences in the loop area response of the composite to tensile and compressive loading can be seen. The first thing to notice is the relative scales of the y-axes, with the tension test (fig.15.43) having half the range of the compression test (fig.15.44). This is due to the fact that in compression the R=-0.84 loop increases in area five times in the course of the test. In contrast, the R=-0.85

loop in tension maintains a fairly constant loop area of ~400-600J.m^{-3} throughout the test. In both cases the near zero stress level tests have the lowest area values. In tension, all the small loops show an increase in loop area over the last three data captures, except the compression loop at R=~11, which does not change. In the compression test however, the area values for the small loops all converge to close to 200Jm^{-3} and show a slight decrease, if anything.

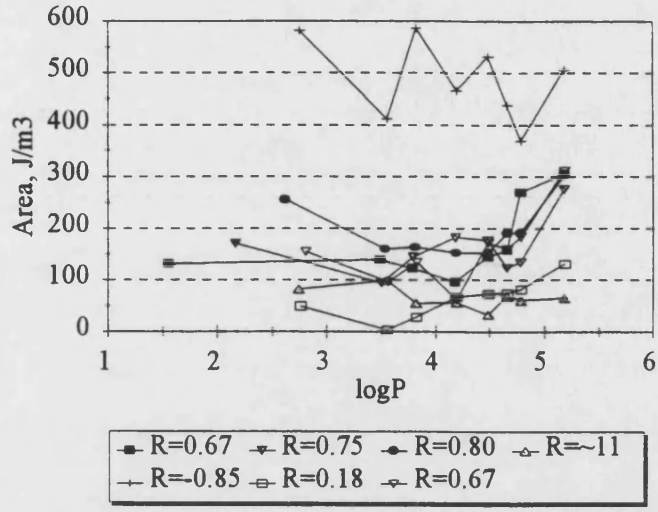

Fig.15.43. Change in loop area for each R ratio. Test e50t.

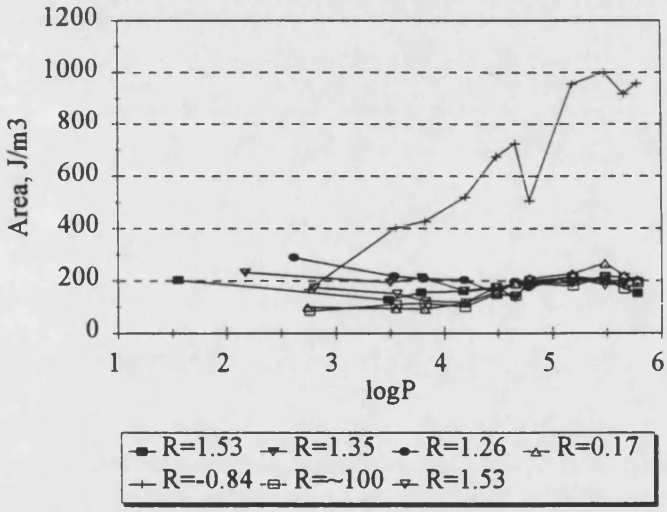

Fig.15.44. Change in loop area for each R ratio. Test e45c.

A comparison will now be made between the dependence of modulus and area on stress level for both tension and compression tests in figs.15.45 to 15.48. Firstly the dynamic modulus plots are given in figs15.45 and 15.46 for tension and compression respectively.

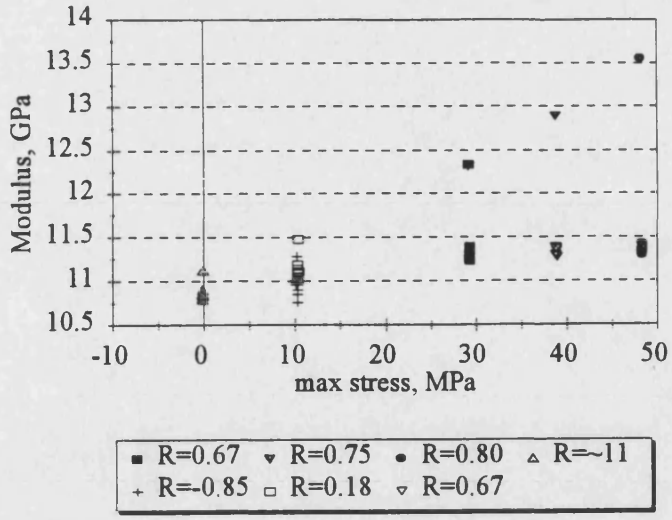

Fig.15.45. Plot of dynamic modulus against maximum loop stress for all R ratios. Test e50t. [Tension].

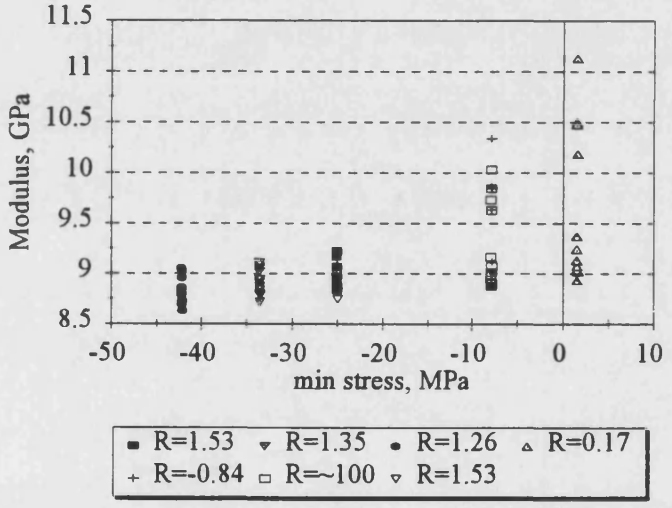

Fig.15.46. Plot of dynamic modulus against minimum loop stress for all R ratios. Test e45c. [Compression].

In fig.15.45 the maximum modulus points for each stress level correspond to the values recorded during the last recorded loop capture of the test. It is clear that these moduli values increase with stress level. If the other values are considered it can be seen that, although the dependence on stress level is much less marked, there is still the same relationship. As was also observed in the controlled stop start tests, the opposite is true in compression. Fig.15.46 shows that as the stress level decreases the modulus also decreases. The near zero stress level loops have the highest moduli values and the greatest scatter in values.

The loop area vs. stress level plots are presented in fig.15.47 for tension and fig.15.48 for compression. Ignoring the R=-0.85 area values on account of their larger stress range, fig.15.47 shows that as the maximum stress increases so does the loop area. This is the converse of what is observed for compression in fig.15.48. The lower the minimum stress level of the loop captured, the higher the loop area values. In both cases the near zero loops have the lowest areas.

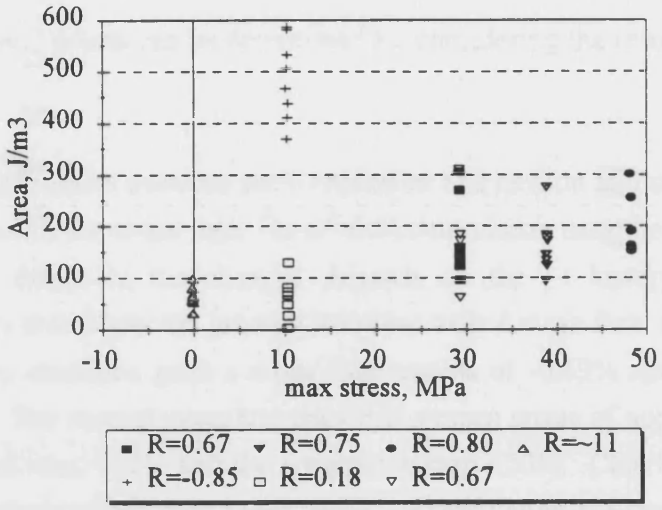

Fig.15.47. Plot of loop area against maximum loop stress for all R ratios. Test e50t. [Tension].

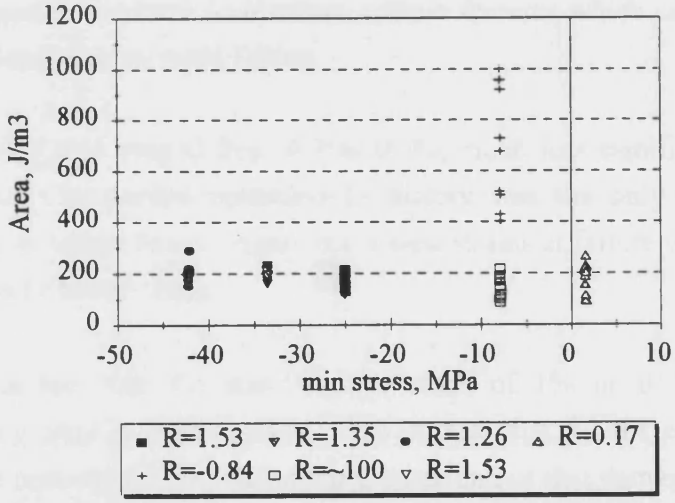

Fig.15.48. Plot of loop area against minimum loop stress for all R ratios. Test e45c. [Compression].

15.6.4. Discussion

It is clear from the figures presented in this section, and in appendix E and in the results tables that there is a high degree of variability and complexity associated with these results. However, they do contain some interesting information.

The issues to be addressed in evaluating the data include:

- differences between the l-t histories
- differences between T&C loading
- differences between stress level of loops captured

In addition, the data can be compared to the constant amplitude results.

The following general points can be determined by considering the results in tables 15.3 to 15.5:

- Strains. Differences between the l-t histories and tension and compression tests can be distinguished in the strain data. In all the compression tests the minimum strain decreases but the extent of the changes depends on the l-t history. The normal operation l-t history tests show the greatest decrease with a mean final strain of -1.02%. The controlled stop condition gave a mean final strains of -0.69% and the emergency stop only -0.52%. The normal operation tests had a mean stress of approximately 70% UCS, the controlled stop, ~60% and the emergency stop ~50%. Clearly, the final level of compressive strain is in line with these values. These values are similar to the R=10 constant amplitude final strains of between -0.5% and -1.2%. The fact that the controlled and emergency stop tests fail with lower degrees of creep than the normal operation tests suggests that these l-t histories contain features which cause other forms of damage which lead to more rapid failure.

In tension the final strains ranged from 0.3 to 0.6%, much less significant than in the compression tests. The normal operation l-t history was the only one to show a consistent increase in tensile strain. Again the lowest strains at failure were observed in the emergency stop l-t history tests.

Failure occurred at less than the static failure strain of 1% in all but the normal operation l-t history tests in compression. This implies that for the remainder of the tests, failure is not controlled by a strain failure criterion but that damage caused by the loading reversals and tensile and compressive overloads initiates premature failure

- Dynamic moduli. There are exceptions to the rule but in general in the case of the tensile tests the modulus increases during a test whilst in compression the modulus decreases. The most mixed changes in modulus occur as a result of the emergency stop l-t history. In comparison with the constant amplitude tensile and compressive fatigue tests the pattern under complex loading is in fact more consistent. All the runout

samples from the tensile tests showed dramatic increases in modulus of 2 or 3GPa in the second half of a test.

- Area. The area is very variable with indistinct trends. Its main feature is that the R=-0.85 loops (reversed loading loops) are the largest because of their stress range which is double that of the other loops. These loops also tend to show the largest changes as a test proceeds for compression tests where the load reversal at the stop is tensile. In the case of the tensile stop tests the loop area is higher across the load reversal but it tends to stay constant rather than show the rapid increase. Clearly this points to differences between the effect of tensile and compressive excursions on the wood composite.

- $\varepsilon/\varepsilon_0$. In the case of the two stop l-t histories, the main feature observed when considering these graphs is the huge change in $\varepsilon/\varepsilon_0$ of the lowest stress level loop whose strain is very close to zero and much lower than the mean strain. In the case of the normal operation tests the first loop captured had the lowest $\varepsilon/\varepsilon_0$ values and the second and third, with the same maximum or minimum strains, were slightly higher. These two were the same as they had the same maximum or minimum strains and consequently were captured at the same distance from the mean stress level. In the tensile tests with the normal operation l-t history the higher peak stress level tests showed a smaller change in strains than the lower ones. This is likely to be because in tensile loading at high stress levels failure is caused by the catastrophic propagation of a flaw before creep and fatigue damage builds up and develop large strains in the composite.

- M/M_0. This parameter shows the relative changes in dynamic modulus more clearly. In tension the controlled stop and normal operation l-t history showed between a 2% decrease and 20% increase. The emergency stop l-t history showed little change. In the compression tests a decrease of up to 20% was observed and again the emergency stop sequence showed the smallest changes.

- A/S_{range}. As the loop area values themselves have a high degree of variation it is not surprising that the same is true when they are normalised by the stress range. In general all the loops have a normalised value of between 8 and 20. No trend is observed with P in the tensile tests but in the higher stress level compression tests an increase may be observed at the end of the sample's life. Where there is an increase with P, the loops which show the greatest increase tend to be the high stress range ones. This implies that the loop area is not linearly related to the stress range.

- $\Delta\varepsilon$. This shows up the changes in strain from the start of the test and can be thought of as an indication of the accumulation of creep strains.- However, it is not particularly informative in the tension tests because the strains do not change in a consistent manner. In compression creep strains of between -0.1% and -0.7% are observed for the normal operation and controlled stops with smaller strains of between -0.05% and -0.15% for the emergency stop tests.

- Modulus-S_{max} and Modulus-S_{min}. There is no correlation between the modulus and the maximum (T) or minimum (C) stress and the dynamic modulus for the normal operation l-t history. This is not surprising because loops have only been captured at two fairly close stress levels.

In the case of the normal and emergency stop tests the low peak stress level tests show no relationship but the high ones do for both tension and compression. Where there is a relationship, the high tensile stress loops have higher moduli values and greater scatter than the near zero loops. This variation is unexpected because all the loops have been captured well below the elastic limit of the wood composite and one would expect, therefore, that all moduli values would be the same. However, the tests where the high stress loops have the highest moduli are from tests where the peak stress does exceed the elastic limit. This implies that these tensile overloads are increasing the stiffness of the composite in some way.

For compressive tests the low stress level tests have lower moduli than the near zero loops. This behaviour is more expected because all the low stress level loops are captured at stresses which are greater than the elastic limit (taken to be ~80%UCS) above which the modulus decreases rapidly (See Chapter 7). If incipient compression creases are accumulating it is hardly surprising that a decrease in stiffness is observed.

- Area-S_{max} and Area-S_{min}. In the case of the normal operation l-t history tests the tensile tests showed no relationship between the area and the maximum stress level of a loop. However, in compression it is possible that the loop area is marginally higher at lower stress levels. This ties in with the dynamic modulus values and the fact that the loops captured at the lower stress level are above the elastic limit and those at the higher stress level are very close or overlap the limit. As would be expected, the wood structure would exhibit more hysteresis once loaded beyond the elastic limit.

For the controlled stop l-t history in tension, the area for low peak stress level tests showed no relationship with maximum stress but as the peak stress was increased to above the elastic limit the area values and scatter were seen to increase with stress level.

This appears to be contradictory to the modulus results where the tensile excursion above the elastic limit caused a stiffening in the composite. An increase in loop area suggests that there are more dynamic losses at the high stress levels, which might be expected to accompany a modulus decrease. Therefore, the fact that these two contrary property changes are occurring suggests that changes in loop area and dynamic modulus occur as the results of different mechanisms. These could include increased microfibrillar alignment at higher stress levels, leading to an increase in stiffness and greater viscoelastic movement in the matrix materials causing increases in loop area.

In compression, the controlled stop l-t history shows no relationship between area and stress level.

Area and stress level show a relationship for the emergency stop sequence for both tension and compression. In tension an increase in stress leads to an increase in loop area. In compression the relationship is rather more tenuous but a lower stress seems to lead to higher area values.

Overall, the area and minimum stress relationship is less obvious in compression than for tension. In addition to the apparent contradiction between modulus and area values, it is also interesting that for the emergency stop sequence in tension the increase in area with increasing maximum stress occurs for all peak stress level tests whereas the modulus only shows an increase at the higher stress levels. It can be seen that although the area values have no correlation with stress level at low peak stresses they do correlate at higher stress levels for the less damaging controlled stop sequence (from the S-logP curves). The least damaging normal operation l-t history shows no dependence of area on stress.

Similarly, the relationship between area and stress level is much weaker in compression than is the modulus-stress level relationship.

These results are summarised for a clearer comparison in table 15.6.

On further investigation of the modulus curves for the normal operation l-t history an unexpected phenomenon was observed. Given that the hysteresis loops were captured in the vicinity of the elastic limit of the composite it would be expected that the loop with the lowest minimum strain would have the lowest modulus, loop 2, followed by loops 3 and 1, as in fig.15.49. The gradient of loop 3 would be expected to be the mean of loops 1 and 2.

In fact it was observed that in two out of the three tests the large third loop had the lowest modulus, followed by 2 and 1. This suggests that the modulus of loop 2 is steeper than expected. In order to try and explain this anomaly the static compression stress-strain curves were investigated. For each static curve the stress levels of the loop capture were superimposed and the mean modulus calculated across the three stress ranges. In the majority of cases the relative stiffnesses were as expected in fig.15.49. However, sample c5 had the same relative stiffness values as seen in the complex loading tests (fig.15.23) where the 3rd loop had a gradient similar to, or lower than, the second. Fig.15.50 is a plot of modulus against stress level for that sample. The gradient of the stress-strain curve was calculated across stress intervals of about 2MPaand plotted as a function of stress level. The stress levels corresponding to the maximum and minimum stress levels of the loops captured have been superimposed and the mean moduli across each range calculated. The reason that the third loop has the lowest mean stress level is the increase in stiffness of the composite before the rapid decrease in modulus to failure.

	Normal operation		Controlled stop start		Emergency stop	
	T	C	T	C	T	C
Modulus	None	None	Low peak stress, none. High peak stress, mod increases with max stress.	Low peak stress, none. High peak stress, mod decreases with stress.	Low peak stress, none. High peak stress, mod increases with stress.	Low peak stress, none. High peak stress, mod decreases with stress.
Area	None	Weak. Low min stress, higher area.	Low peak stress, none. High peak stress, area inc as min stress decreases.	None	Area increases as min stress decreases.	Weak. Low min stress, higher area.

Table 15.6. Summary of the dependence of dynamic modulus and loop area on stress level.

The mean modulus between (a) and (b), loop 1 is 11.45GPa, between (b) and (c), loop 2, is 10.55GPa and between (a) and (c) is 10.3GPa. It can be seen that the small increase in modulus before the onset of rapid degradation has led to this unexpected result. This suggests that in both static and fatigue compression tests there might be a

small degree of stiffening in the composite before the elastic limit is passed in some samples.

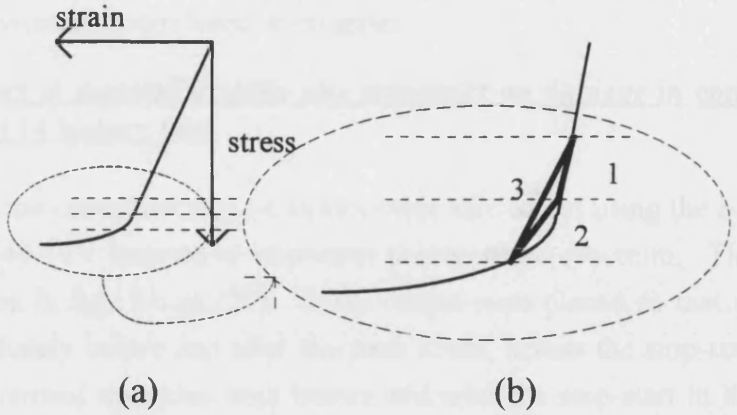

Fig.15.49. Position of the three loop captures in the vicinity of the elastic limit in compression and their expected relative gradients. (b) is an enlargement of the circled area in (a).

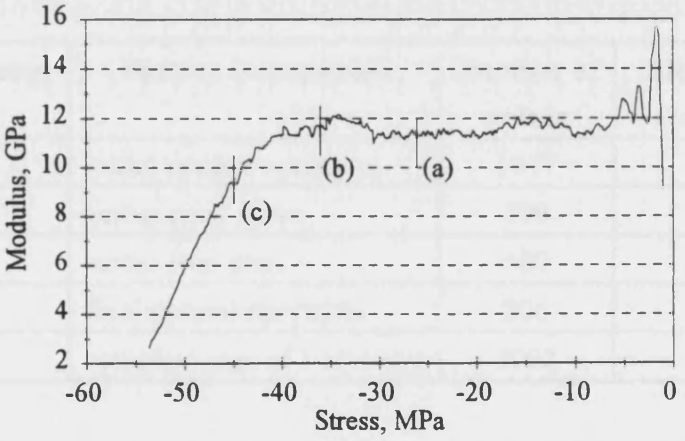

Fig.15.50. The relationship between modulus and stress level for static compression sample c5. (a) S_{max} for loops 1 and 3, (b) S_{min} for loop 1 and S_{max} for loop 2, (c) S_{min} for loops 2 and 3.

The near zero stress level tests were investigated for both controlled and emergency stops in tension and compression. It was found that there was a great variety of relative moduli across all the tests. However, the most common result was for the near zero tensile loop (R=~0.15) which had the highest modulus of the three in 7 out of 12 tests, the reverse loading loop R=-0.85 had an intermediate modulus and in 8 out of 12 tests the compressive loop had the lowest modulus. The difference in moduli values was typically only about 1.5%. The fact that the most common result was for the tensile

loop to have the highest modulus and the compressive loop to be the lowest suggests that some loop bending could be present in the R=-0.85 loop. However, loop bending was not observed in any of the reverse loading loops either at the start or end of the tests in which hysteresis loops were investigated.

15.7. Effect of maximum spike and stop-start on damage in controlled stop-start l-t history tests

Five tests using the controlled stop l-t history were carried out using the l-t history with extra cycles of 40-50V inserted at important points in the spectrum. The position of these can be seen in fig.15.6 (p.227). These cycles were placed so that data could be captured immediately before and after the peak stress, across the stop-start and across the portions of normal operation both before and after the stop-start in the l-t history. Table 15.7 provides more information on these captures. The mean value is given in volts because this value is factored for each test to give the desired peak stress. Clearly it is different for each stress level test. However, since all the points in the l-t history are factored by the same figure their relative values do not change and comparison between different parts of the sequence is simpler with fewer values.

Capture range	Feature investigated	Number of points	Mean voltage across range
43-1120	initial normal operation	1077	43.84
1120-1319	across peak stress	199	47.11
1319-1919	across stop-start	600	21.74
1919-2125	final normal operation	206	45.83
43-2125	complete pass of l-t history	2082	37.98

Table 15.7. Position of extra cycles added to controlled stop start l-t history to investigate the effect of different parts of the l-t history. The mean voltages in each part are also given.

Once the tests were complete [s45t, s50t, s55t, s47c, s50c] the data from the desired loops were removed and the change in maximum (T) or minimum (C) strain was calculated across each feature. These values were then plotted against the number of passes.

This was repeated for dynamic modulus and loop area values to determine whether these properties were affected by any particular part of the l-t history. Unfortunately no distinct trends could be detected for modulus and loop area so the plots were not useful to clarify the damage process and are not presented in this section.

15.7.1. Results

Changes in strain results are presented in figs.15.51 to 15.56.

The changes in strain per pass of the l-t history are small, as expected, typically less than 0.005%. Some show the trends observed more distinctly than others but in general a number of important observations can be made.

Figs.15.51 to 15.53 show results for tensile tests. In each case it is clear that the greatest changes in strain occur during the first pass of the l-t history. The change in strain for the complete pass is equal to the sum of the changes in strain of the individual parts. As may be expected from a tensile fatigue test these initial values are positive ($\varepsilon_{after}>\varepsilon_{before}$) with the largest value for the complete l-t history. Within the individual portions of the l-t history the first portion of normal operation causes the largest increase in strain. This can be attributed to the high mean stress in this part of the l-t history and the fact that it lasts for just over 50% of every pass.

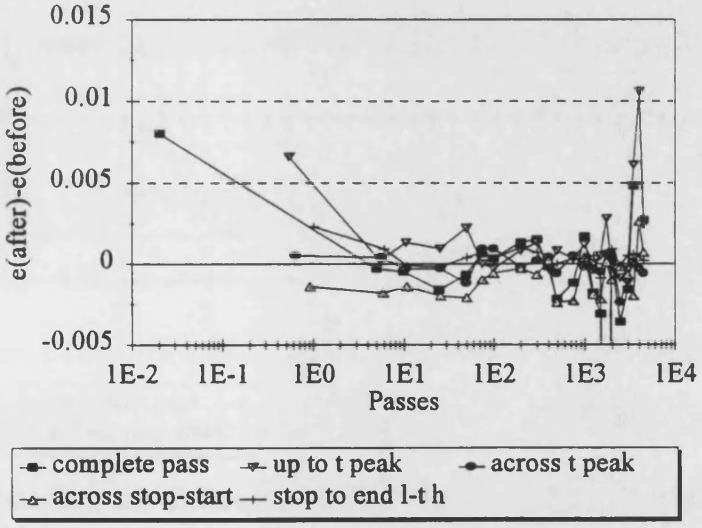

Fig.15.51. The effect of the different parts of the start-stop l-t history on strain for test s45t. S_{peak}=45MPa [runout].

Here the similarities in strain changes between the samples end, as the different parts of the l-t history have various effects. In fig.15.51, a runout test, the changes in the first pass all cause an increase in tensile strain with the exception of the stop start part which results in a decrease. It might be expected that all portions of the l-t history would cause an increase in strain because the mean stress for each part is tensile. However, the data show that this is not the case and the brief excursion into compression causes compression strain even though the number of cycles in compression is relatively small. At higher peak stresses, samples s50t and s55t, the stop-start portion of the l-t history causes a mean increase in strain, fig.15.52 and 15.53.

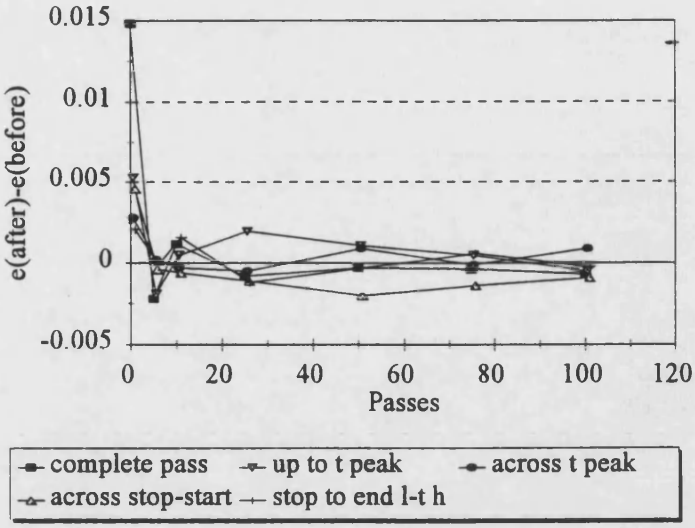

Fig.15.52. The effect of the different parts of the start-stop l-t history on strain for test s50t. S_{peak}=50MPa.

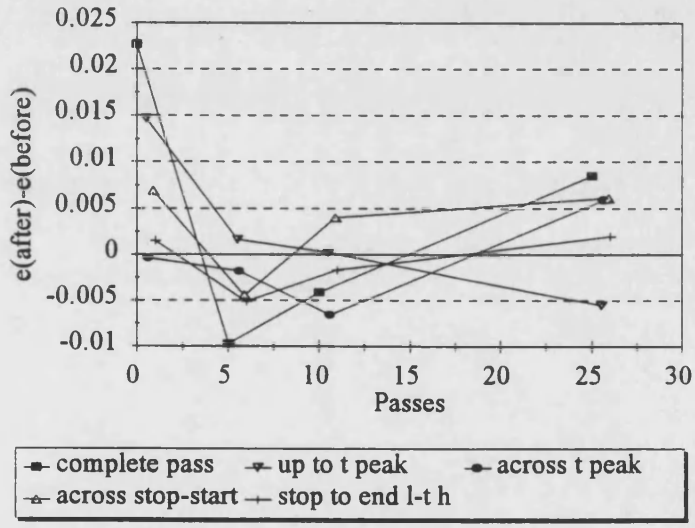

Fig.15.53. The effect the different parts of the start-stop l-t history on strain for test s55t. S_{peak}=55MPa.

After the initial pass through the l-t history the effect each part has on the overall strain is not always clear. In fig.15.51, the lowest stress level test [peak stress=45MPa], the stop-start part of the l-t history consistently causes a decrease in strain. In general the first, and largest, portion of normal operational conditions causes the greatest proportional increase in strain. The end portion of normal operation tends to cause an increase in tensile strain but the amount is much less pronounced because of its shorter length (10% of the whole l-t history). It is slightly surprising that across the tensile peak of the l-t history the change in strain is not always positive, but fluctuates between tensile and compressive strain.

At the two higher stress levels, figs15.52 and 15.53, after the initial increase in tensile strain over the first pass there is a decrease in strains for 5 to 10 passes before the effect of the l-t history on the wood composite causes an increase in strains again. In fig.15.52 the first portion of normal loading causes an increase in strain and the stop-start part causes a decrease. After an initial decrease the change in strain caused by the tensile peak increases slightly so that on the last capture it is the only one to cause an increase in tensile creep. In fig.15.53 the general trend in all parts of the l-t history, except for the initial normal operation part, is for the large increase in strain over the first pass to be followed by a change to compressive strains over the next 5 to 10 passes, after which the strains become tensile again.

The results from the compressive tests are presented in figs.15.54 to 15.56. In fig.15.54 it is clear that by far the largest changes occur during the first pass of the l-t history, with all except the compressive peak causing a decrease in strain. In order to distinguish any differences in strain changes over the rest of the test the data has been replotted in fig.15.55 with a different scale. Similar trends to those observed in tension become apparent. Both the first (up to the compressive peak) and last (from the stop to the end of the l-t history) portions of normal operation in the l-t history cause compressive strains. The stop-start part causes a tensile strain and the compressive peak causes either on what appears to be a fairly random basis.

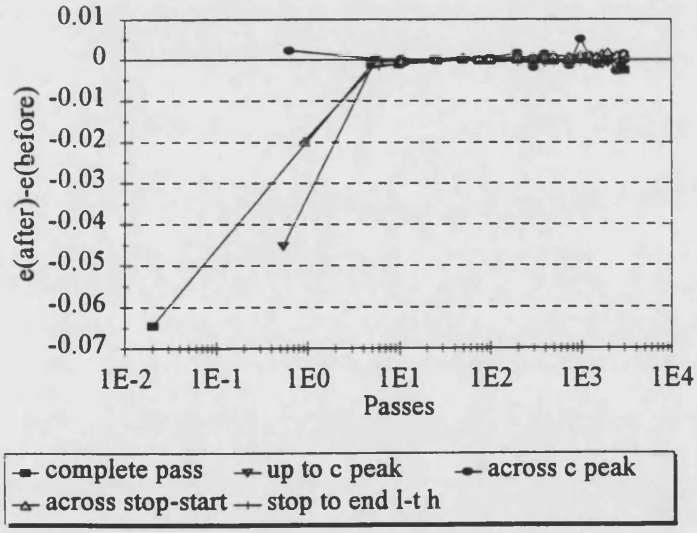

Fig.15.54. The effect the different parts of the start-stop l-t history on strain for test s47c. S_{peak}=-47.54MPa.

The trends exhibited by sample s50c in fig.15.56 are the most pronounced of all. It appears that the stop-start part of the l-t history has an opposite effect to the first part of normal operational conditions. The decrease in strain during the normal operation part

of the l-t history is balanced by the tensile strain caused during the stop-start part of the sequence, giving an overall change in strain per pass of close to zero.

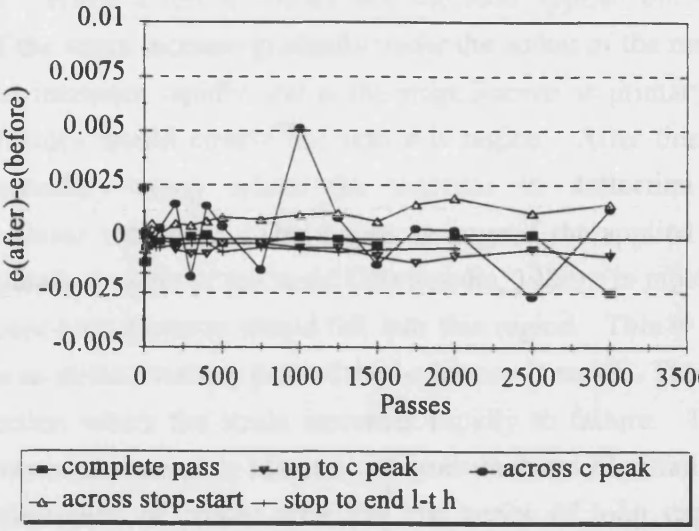

Fig.15.55. The effect the different parts of the start-stop l-t history on strain for test s47c. S_{peak}=-47.54MPa [enlarged scale].

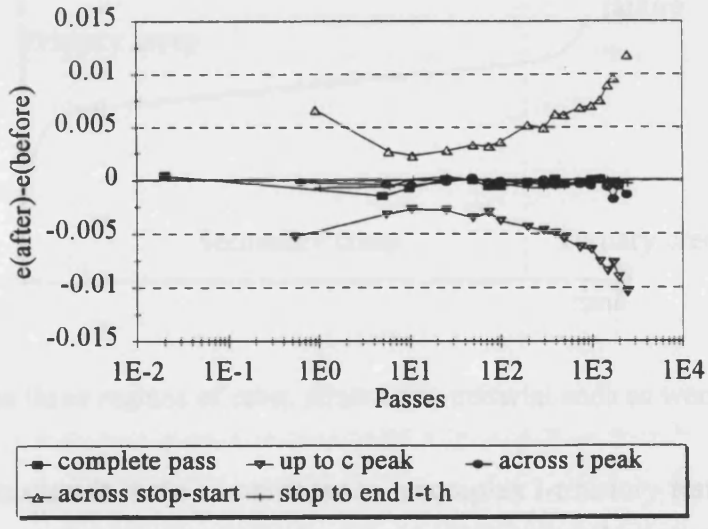

Fig.15.56. The effect the different parts of the start-stop l-t history on strain for test s50c. S_{peak}=-50MPa.

15.7.2. Discussion

The two main features observed in the results of these tests to be discussed are :

- the initial rapid change in strains
- the effect of the stop-start portion on the creep strains

The initial rapid changes in strains [tensile for the tensile tests and compressive for the compression fatigue tests] is what would be expected with any viscoelastic material such as wood. When a test is started and the load applied the elastic and plastic components of the strain increase gradually under the action of the mean stress. At first the creep strain increases rapidly and is the stage known as primary creep. The first pass of a l-t history would clearly fall into this region. After this there is a period known as secondary creep where the increase in deflection is gradual and approximately linear with time. This region is large if the applied stress is less than 50% of the ultimate strength of the wood (Dinwoodie, 1989). In most tests the majority of the subsequent loop captures would fall into this region. This is shown by the fact that the change in strain over any pass of the l-t history is small. There is a third region of creep deflection where the strain increases rapidly to failure. This occurs over a small proportion of the sample's life and can pass unobserved if failure occurs several hundreds or thousands of passes after the last series of loop captures. Fig.15.57 illustrates the manner in which a creep strain increases with time under the action of a constant load.

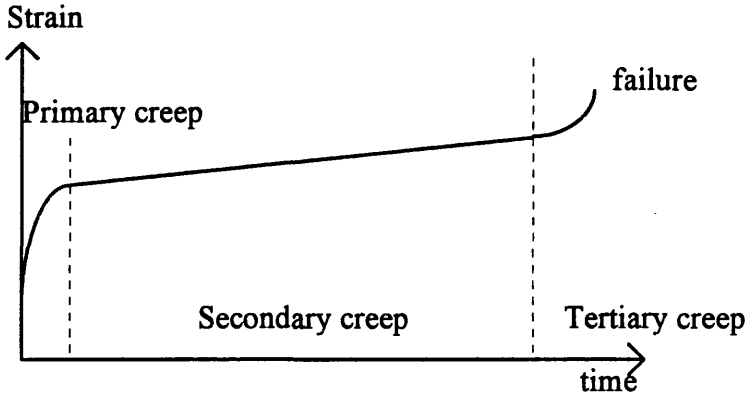

Fig.15.57. The three regions of creep strain for a material such as wood.

Clearly the situation is more complicated in a complex l-t history test than a creep test because of the cyclic component to loading in addition to the mean stress associated with the sequence. However, creep has been seen to play an important part in the response of the wood composite to all real load-time histories.

It has been seen in constant amplitude loading at R=10 and R=0.1 that fatigue failure will not occur if the peak stress is less than the stress level of the elastic limit of the composite (Chapter 8). In all cases the mean stress was less than 50% UTS, giving rise to a large region of secondary creep. Therefore, failure was determined by the peak stresses rather than by creep rupture. In the case of these controlled stop-start l-t history

tests in tension, the peak stress was close to, or above, the elastic limit in tension and the mean stress was always below the 50% UTS level. Therefore, as in constant amplitude loading, failure would have been determined by the peak loads exceeding the elastic limit, rather than by creep rupture. However, the peak stress was not seen to affect the strains seen by the composite, although it did cause failure in both tensile tests. In compression, the peak stresses were above the elastic limit and the mean stresses above the 50% UCS level. This implies that failure would have been caused by a combination of creep rupture and damage due to the peak loads.

The second feature of interest is the strain changes associated with the load reversal associated with the stop-start portion of the l-t history. For a tensile test, the mean stress over this portion of the sequence is between 18 and 23% UTS but with an overall minimum stress of 30-37% UCS. In all cases except s55t, where the stress levels were highest, this short and low magnitude reversal of stress causes an appreciable undoing of the creep strain developed during the first part of the l-t history. A possible explanation could be that the reversal disrupts any fibre alignment which has occurred under the action of the mean tensile load. This could involve the rupture of hydrogen bonds between cellulose microfibrils, and the hemicellulose and lignin matrix or the change in microfibrillar angle in the S_2 cell wall. It has been seen that the dynamic moduli of all near-zero stress level loops are lower than the high tensile stress level loops. This suggests that when the stress passes into compression in a predominantly tensile loading situation the improved fibre alignment which occurs under the action of purely tensile fatigue is disrupted and the improvement is lost in the resistance of tensile loads. Whatever the mechanism, once the high tensile load is reapplied to the sample the higher stiffness value is regained.

15.8. Fatigue modulus in complex loading situations

The fatigue moduli for all tests at each R ratio have been calculated. However, the curves produced for the near zero stress levels have not been included because they are very different from the higher stress level moduli curves. Fig.15.58 illustrates why. In addition, the fatigue modulus curves are more likely to be comparable with the constant amplitude results for the high stress level loops.

Figs.15.59 to 15.61 show a typical fatigue modulus vs logP plot for each of the l-t histories used to test the composite in tension. The only l-t history where the fatigue modulus shows a fairly consistent decrease is for the normal operation l-t history, fig.15.59. The final modulus was on average 20% lower than the initial modulus values. As is the case with the constant amplitude tests in tension (fig.13.6) the fatigue modulus varies in an erratic manner in the second half of the test. The fatigue modulus

response for the controlled and emergency stops in tension is rather more variable, with half the samples showing an increase in fatigue modulus, fig.15.60, and half showing a decrease, fig.15.61. The mean change for the controlled stop tests is an increase of 10% over the initial value of fatigue modulus. In the case of the emergency stop a mean decrease of only 2% was recorded.

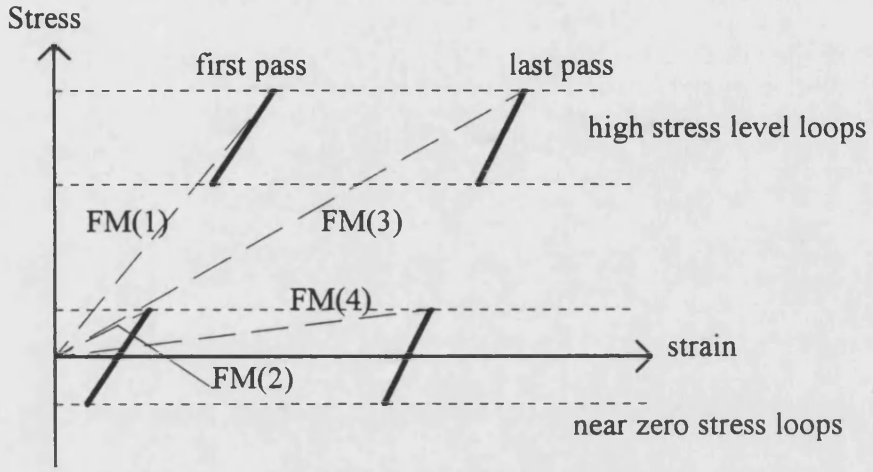

FM(1) Fatigue modulus for high stress level loop on first pass of l-t history
FM(2) Fatigue modulus for near zero stress level loop on first pass of l-t history
FM(3) Fatigue modulus for high stress level loop on last pass of l-t history
FM(4) Fatigue modulus for near zero stress level loop on last pass of l-t history

$$\text{Normalised fatigue modulus for last loop} = \frac{FM(last)}{FM(first)}, \qquad \frac{FM(4)}{FM(2)} >> \frac{FM(3)}{FM(1)}$$

Fig.15.58. Diagram illustrating the disproportionately large decreases in fatigue modulus for near zero stress level loops.

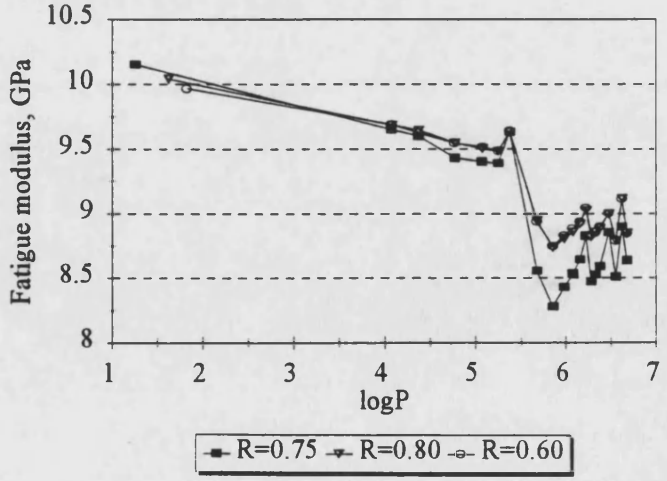

Fig.15.59. Fatigue modulus for all loops captured during a normal operation l-t history test. S_{peak} =50MPa.

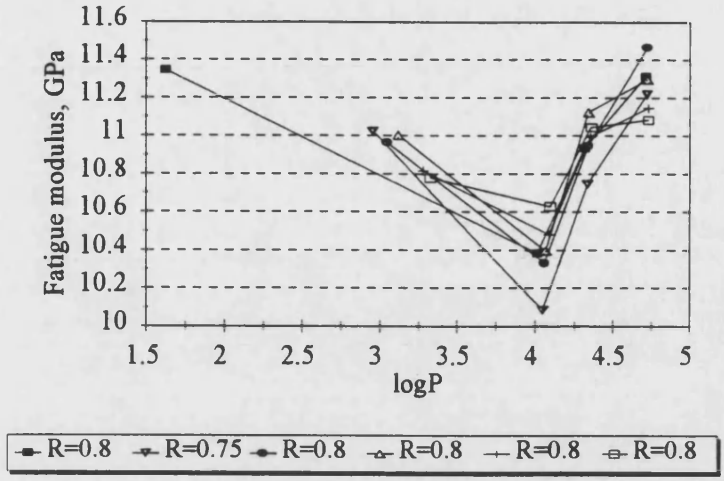

Fig.15.60. Fatigue modulus for all loops captured during a controlled stop l-t history test. S_{peak} =55MPa.

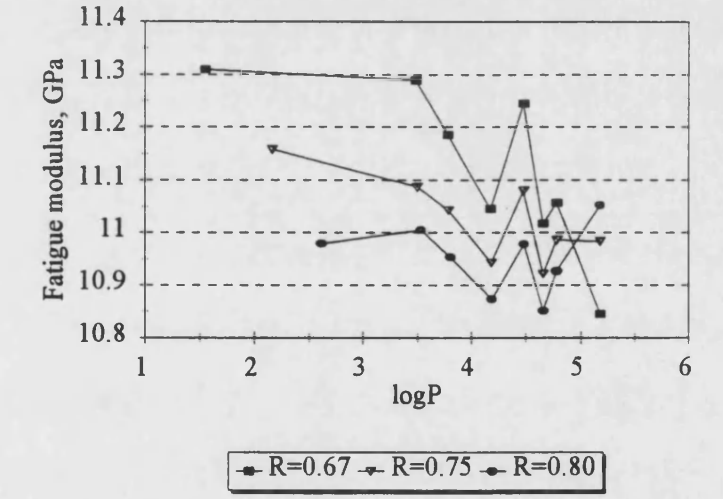

Fig.15.61. Fatigue modulus for all loops captured during an emergency stop l-t history test. S_{peak} =50MPa.

A full set of both tensile and compression plots are presented in Appendix E along with the other complex l-t history graphs.

As a result of the variable nature of the fatigue modulus in tensile complex l-t history tests it is not likely that the rate of change of this property could be used to predict the fatigue life of other such tests. This is the same conclusion which was drawn from the constant amplitude tensile tests where the fatigue modulus showed little change at the start of a test but then changed wildly (Chapter 13).

In the case of the complex l-t history tests in compression the change in fatigue modulus with logP decreases in every case in a generally more predictable manner than for the tension tests. This was also found to be the case with the constant amplitude fatigue tests at R=10. A feature which was not observed in the constant amplitude tests, however, is the knee in the curves which is present for the normal operation and emergency stop l-t sequence tests. Figs.15.62 to 15.64 show representative curves for the normal operation, controlled stop and emergency stop tests respectively. Because the fatigue modulus changes in a more predictable way the values have been normalised by the initial fatigue modulus in order to use the curves for fatigue life prediction. The normal operation l-t history showed the greatest decrease in mean fatigue modulus of 60%, followed by the controlled stop tests at 46% and the emergency stop tests at 25%.

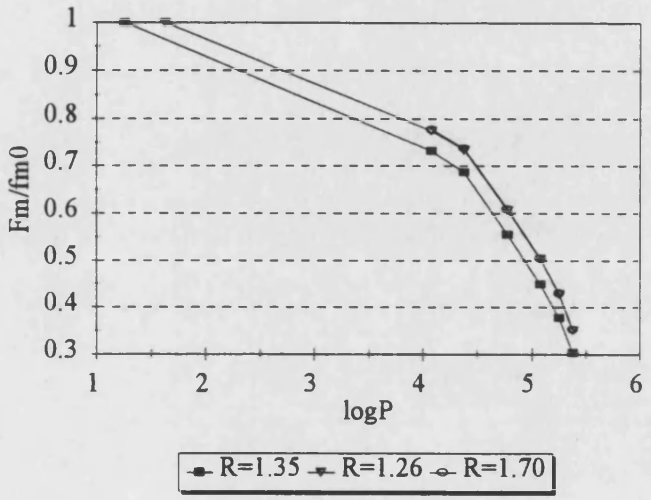

Fig.15.62. Normalised fatigue modulus for all loops captured during a normal operation l-t history test. S_{peak} =-52.5MPa.

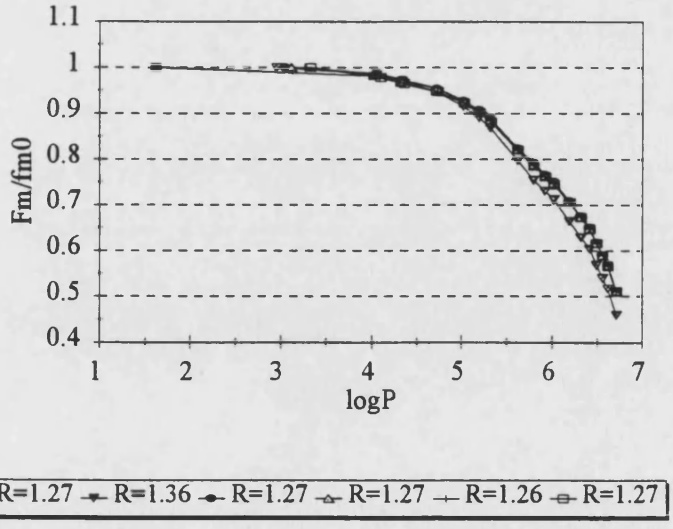

Fig.15.63. Normalised fatigue modulus for all loops captured during a controlled stop l-t history test. S_{peak} =-52.5MPa.

In constant amplitude compression fatigue at R=10 the initial gradient in the fatigue modulus curve was measured tangentially to the curve at the origin. Because the number of points recorded at the start of the test is small in comparison to the constant amplitude tests the gradient of the line between the first two data points for the first loop captured (R=1.27) was calculated using 'Quattro Pro'. In this way it was hoped to determine whether there is a relationship between the gradient of the fatigue modulus curve and fatigue life for complex l-t histories. The results of the analysis are presented in table 15.8 and represented graphically in fig.15.65.

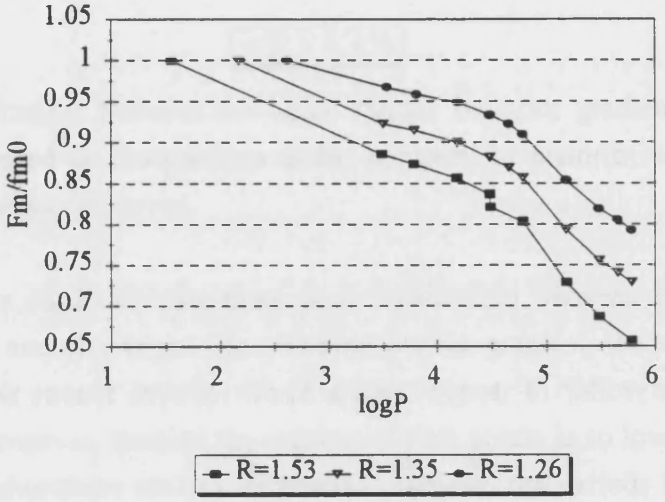

Fig.15.64. Normalised fatigue modulus for all loops captured during an emergency stop l-t history test. S_{peak} =-45MPa.

Sample	P_f	$\log P_f$	Gradient of FM curve
nm_50_c	23331963	7.37	-0.48 [ro]
nm_50_c2	1233613	6.09	0.09
nm_52_c	297217	5.47	-0.96
st_50_c	5776776	6.76	-0.08
st_52_c	2885310	6.46	-0.11
st_55_c	474255	5.68	-0.50
es_45_c	773215	5.89	-0.53
es_47_c	9521251	6.98	0.19 [ro]

Table 15.8. Initial gradients of the fatigue modulus curves for complex compression l-t history tests where the gradual change in modulus was observed.

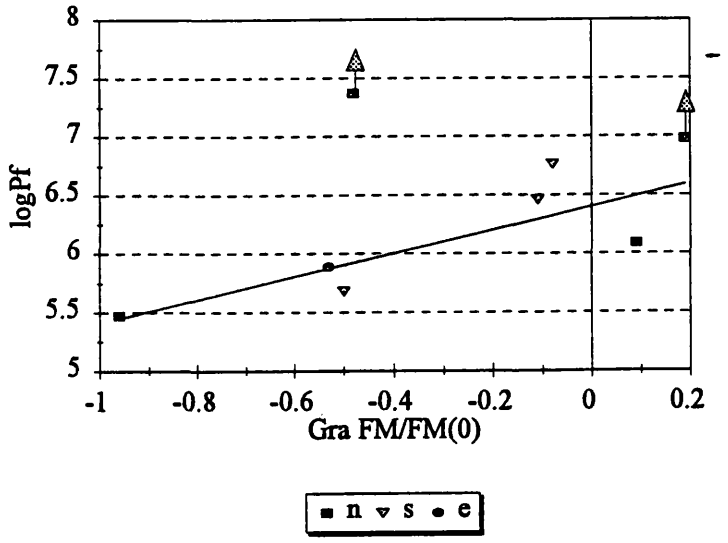

Fig.15.65. Relationship between the initial fatigue modulus gradient and the fatigue life of samples tested in compression under complex l-t histories where the gradual change in property was observed.

It can be seen in fig.15.65 that there is a relationship between the initial fatigue modulus gradient and the fatigue life. The steeper the gradient, the shorter the fatigue life, except for the runout samples which do not appear to follow the pattern of the other samples. However, because the number of data points is so low it is not possible to determine whether there are any differences between the various l-t histories. The line in fig.15.65 is the best linear fit to the data, excluding the runout samples. In the case of the constant amplitude fatigue tests at R=10 the relationship between the fatigue modulus gradient and the lifetime was a logarithmic one. With the small number of data points it is not possible to determine this at this stage.

15.9. Damage parameter based on change in stiffness

The damage parameter D where

$$D = 1 - \frac{E}{E_0} \qquad \text{eq.15.1.}$$

was calculated for the complex l-t history tests described in section 15.7. The aim was to determine whether the different parts of the controlled stop l-t history gave rise to different amounts of damage, and in particular, whether the stop-start part of the sequence produced the greatest increase in damage.

Unfortunately the results were inconclusive because in only one sample, s50c, showed the expected increase in damage with passes of the l-t history, fig.15.66. Even in this sample it was not possible to separate the damage curves for the different parts of the test.

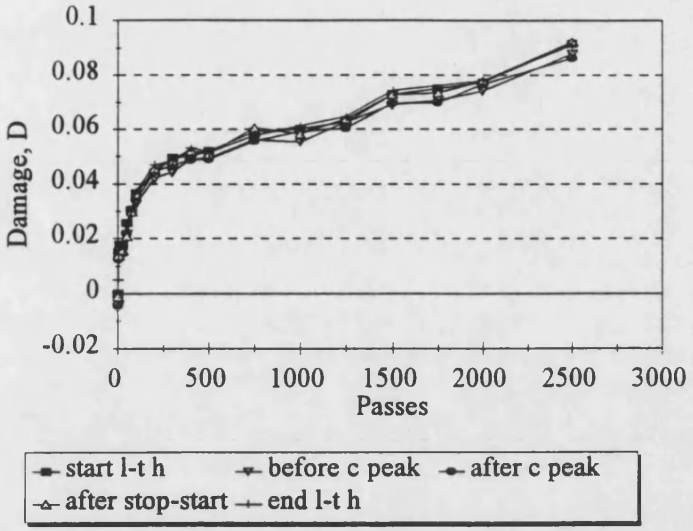

Fig.15.66. Damage parameter, D calculated for test s50c.

Because of the inconclusiveness of the investigation it was not pursued on the other samples and no conclusions could be drawn.

15.10. Conclusions

Complex load-time histories recorded from an instrumented WTG blade have been manipulated and used successfully to test Khaya-epoxy's response to real life fatigue loading conditions. Stress-strain hysteresis loops have been captured during tests using a normal operation, a controlled stop-start and an emergency stop l-t history.

S-logP plots showed that the emergency stop l-t history was the most damaging of the three, followed by the controlled stop-start l-t history.

Although the stress-strain hysteresis loops were much smaller than those captured during constant amplitude fatigue tests (Chapter 9) and variability was high, similar property changes for complex tension and compression fatigue were observed. They can be summarised as follows:

- Changes in strains were more significant in compression than in tension. In tension, tensile creep did not occur consistently but in compression, compressive creep was always evident.
- The modulus tended to increase for tensile fatigue and decrease for compression fatigue.
- Loop area was very variable but in tension it did not increases significantly during fatigue, whereas in compression an increase in loop area at the end of a test was sometimes observed.

Failure was not dependent on a strain failure criterion (failure occurs when the static failure strain is reached) for all tensile tests and compressive tests which included a load reversal.

Properties changed the least for the most damaging emergency stop tests, implying that failure occurred by rapid crack growth before the changes were able to occur.

In tension an excursion into compression causes no change in loop area at R=~-1 but in compression an excursion into tensile loading causes an increase in area for the R=~-1 loop. An explanation for this could be that when a compression test sample undergoes a tensile excursion, the compression creases in the cell walls are straightened and energy is absorbed. In tension fatigue, the magnitude of the compression excursion is too low to cause any compression damage.

There are no clear relationships between modulus and area and stress level for the normal operation l-t history because loops were only captured at two stress levels. However, relationships did exist for both controlled and emergency stop l-t histories.

Tensile overloads above the elastic limit of the wood appear to cause an increase in stiffness of the composite. It also seems that fibre alignment is better maintained at higher stress levels when tensile overloads cause stiffening.

When the peak stress is above the elastic limit of wood, a high maximum stress leads to higher loop area values.

It can be concluded that different mechanisms of damage accumulation in tensile loading conditions cause the changes in modulus and loop area. It has been suggested that for tensile loading microfibrillar alignment at higher stresses leads to an increase in stiffness, and greater viscoelastic movement in the matrix materials causes an increase in loop area.

In compression the stiffness of the wood composite decreases as the minimum stress approaches the UCS.

In compression the loop area's relationship with stress level is much weaker but the lower peak stress level tests show an increase in loop area with minimum stress.

This result is consistent with what would be expected with a decrease in dynamic modulus occurring at the same time as an increase in loop area. It suggests that in compression the accumulation of compression kinks within the cell walls determines the changes in both dynamic modulus and loop area.

Despite large amounts of variation in the near zero stress level loops it was most common for the tensile loop to have a higher modulus than the compressive loop, with a difference of about 1.5%.

The first pass of the controlled stop l-t history always caused the greatest changes in strain for both tensile and compressive tests.

The load reversal which was recorded when the WTG was stopped was seen to cause noticeable changes in strain. In all but the highest stress level tensile test, the excursion into compression caused a compressive strain, despite the mean tensile stress across this portion of the l-t history. In the compressive tests, the tensile excursion caused a tensile strain, despite the mean compressive stress. These results suggest that load reversals appear to 'undo' the strain developed in the majority of the pass, leading to a mean change in strain of near zero. This could be caused by the disrupting of fibre alignment or the straightening out of compression kinks.

A fatigue modulus approach was found not to be applicable to constant amplitude loading in tension, as was the case for the constant amplitude loading tests. In compression, however, the fatigue modulus varied in a more consistent way and a relationship was developed between initial fatigue modulus and life. However, the number of data points was too small to have full confidence in the results.

The damage parameter, D, based on stiffness changes in the composite was not found to show any consistent patterns which could be used in the development of a fatigue life prediction model for complex loading conditions.

16. ENVIRONMENTAL SCANNING ELECTRON MICROSCOPY (ESEM) OF FATIGUED WOOD

The aim of this section of work was to conduct an investigation into the static fracture characteristics of fatigued Khaya-epoxy composite at the cellular level or below. The ESEM was used because of its ability to image the formation of cracks and new surfaces in an insulating material such as wood. It was hoped that different patterns of crack development and growth would be evident in samples subjected to different constant amplitude fatigue loading regimes and the various mechanisms of fatigue damage accumulation could be elucidated.

16.1. Introduction

The microstructure of wood and wood composites can be successfully investigated using a conventional scanning electron microscope (SEM), see fig.3.13 (Tsai and Ansell, 1990) and figs.17.14-17.15. However, as it is an insulator and contains water it must be desiccated and covered in a conducting layer, typically gold, before it can be inspected in a SEM.

Desiccation is usually carried out by storing the samples in a desiccator containing dehydrated copper sulphate for at least a week prior to the coating process. The layer of gold is applied using a sputter coater which itself is a high vacuum process. This process serves to vacuum dry the wood before the coating is applied. Whilst desiccation is not a serious problem for wood, the removal of water from other types of samples containing higher proportions of water, eg biological tissues, will significantly affect their microstructure.

Gold is the conducting material used and the electrons from the SEM electron beam flow away from the insulating wood surface through it. However, the gold does not penetrate deep into the wood fibres and vessels and charge build-up may occur. This is observed as a bright glow and disrupts the formation of an image of the sample by the detector. It can be appreciated that if a dynamic in-situ loading test was to be carried out on wood in a SEM, the moment a crack was formed the gold coating would be disrupted, charge would build up and the most critical part of the image would be obscured.

It is in the case of wet and insulating materials that the ESEM can be used to overcome the problems associated with conventional SEM investigation. A literature search has shown an extensive range of applications for the ESEM in the investigation of wet and insulating materials. The majority of work is on the former. Applications have been

found in fields as diverse as the food industry, where bread mould (Danilatos, 1990) and the microstructure of a tortilla chip during deep fat frying (McÐonough et al, 1993) have been investigated, to materials science where polymer coatings and cement hydration have been explored. Other uses have been in archeological applications and pharmacology for studying the dissolution of drugs (Danilatos, 1990). In order to carry out many of these investigations hot or cold specimen stages and in-situ loading rigs have been developed.

16.2. Fracture and crack propagation in wood

The complex cellular structure of wood and the composite nature of the cell walls provide a multitude of weak interfaces along which a crack may grow. The investigation of fracture and crack propagation in wood is complicated by the anisotropic nature of wood. This results in a possible six different modes of crack propagation (Ashby et al, 1985). However, because wood is about ten times tougher across the grain than along it, cracks tend to be deflected so that they run along the grain. This reduces the most commonly investigated cracking directions to four.

Possible routes for a crack include:

- between individual cells
- between layers within the cell wall
- across a cell wall

Structural features such as ray bundles and vessels will also influence the crack path.

Which of the above mechanisms is favoured depends on the direction of crack propagation and the density of the wood. For woods of density less than 200kgm^{-3} crack advance is commonly by cell wall breaking in both the RT and RL orientations [first letter = direction normal to the crack plane, second letter = direction of crack propagation]. The cell wall bends initially and will then break by either plastic collapse or by fracture. This is shown schematically in fig.16.1.

For woods of higher density cracks advance by both cell wall breaking and cell wall peeling. Cell wall peeling involves the separation of two cells by debonding along the central lamella. Cell wall peeling predominates in the TR crack orientation which suggests that it requires less energy than cell wall breaking in this direction (Gibson and Ashby, 1988). This is shown schematically in fig.16.2. As the density of Khaya is in the order of 530kgm^{-3} it is to be expected that some cell wall peeling will occur.

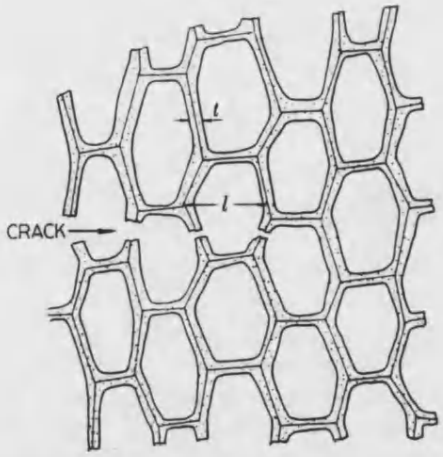

Fig.16.1. Schematic drawing of crack advance by cell wall breaking of balsa in RT loading (Gibson and Ashby, 1988).

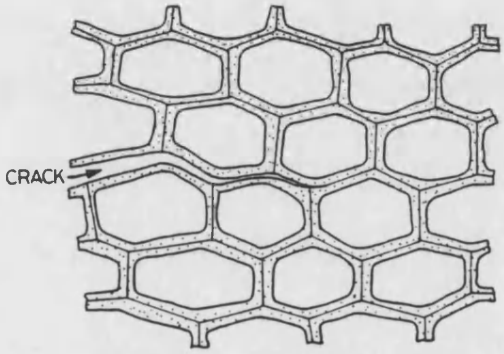

Fig.16.2. Schematic diagram of crack advance by cell wall peeling for ash under TR loading (Gibson and Ashby, 1988).

Gibson and Ashby (1988) also observed that vessels can act as crack arresters. The crack tends to deviate towards a vessel and either enter it or run partly around its periphery and stop. It was also observed that a crack often jumped from one vessel to another, arresting at each jump. These two responses are represented in figs.16.3 and 16.4.

Bentur and Mindess (1986) studied load-induced cracks along the grain (RL) in balsa using compact tension specimens inside the chamber of a conventional SEM. They were able to resolve failure mechanisms including the slippage of microfibrils, buckling of cell walls and intracellular fracture within different parts of the cell wall.

The most frequently observed feature was crack bridging by fibres which suggests that load was transmitted across the crack. This bridging was seen to be caused by cell rupture along its axis leading to strands of microfibrils bridging the crack. Cell rupture perpendicular to the cell in the form of a straight break was also observed. Damage was

detected in clear wood ahead of the main crack tip. In a second sample a group of ray cells was seen to cause the crack to deviate and arrest the crack. When the load was increased the crack passed through the ray cells. A vessel was also seen to make the crack deviate and cause a discontinuity in the crack by the occurrence of bridging.

It was concluded that the larger part of crack propagation was associated with splitting within cell walls.

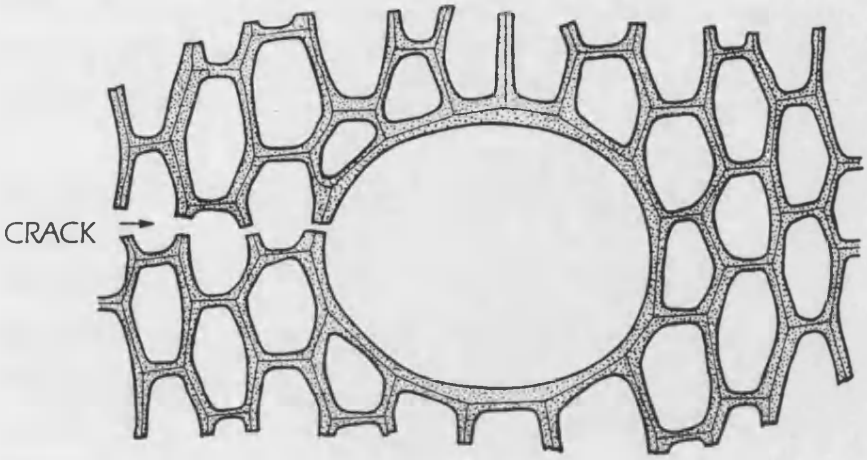

Fig.16.3. Schematic diagram of a crack breaking into a vessel for a wood in the TR direction (Gibson and Ashby, 1988).

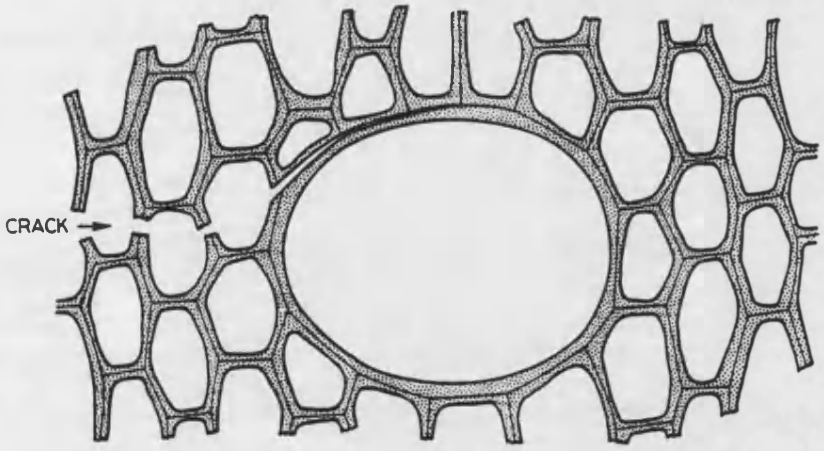

Fig.16.4. Schematic diagram of splitting in a vessel wall for wood in the TR direction (Gibson and Ashby, 1988).

Zimmerman et al (1994) conducted bending tests on spruce at different rates of loading and investigated the tensile fracture surfaces. At high loading rates (impact bending) flat brittle failures perpendicular to the loading direction were observed but at lower rates (long term loading) the fracture surfaces were tufted and clumps of microfibrils were seen to have been pulled out from the S2 cell wall. Delaminations were observed

within cell walls between the middle lamella and the S1 layer and also between layers S1 and S2. Weak elements of spruce in tension included the ray cells and the fringe of the bordered pits.

16.3. Operation of the ESEM

The ESEM was originally designed to enable the investigation of truly wet specimens. It is defined as a SEM capable of maintaining a minimum water vapour pressure of at least 609Pa in its specimen chamber. This pressure corresponds to the saturation pressure of water at 273K and constitutes a natural threshold, above which water can be maintained in its liquid phase (Danilatos, 1990).

The gas which is present in the specimen chamber, typically air or water vapour, is ionised by the electron beam and forms a cloud of positive ions around the sample. This prevents the build-up of charge on an insulating sample which can consequently be observed without the application of a conductive coating. The presence of the gas is also used in the formation of the image and serves to amplify the image signal.

Whilst the specimen chamber is maintained at a low vacuum (between 1 and 20torr), the electron gun must be maintained at high vacuum of 10^{-7}torr. This is achieved by using a series of differential pressure zones in the column of the microscope, fig.16.5.

The zones are separated by pressure limiting apertures and are evacuated by a system of pumps. The electron beam passes through these apertures which are small enough to enable the differences in pressure between the zones to be maintained.

Although some electrons from the beam are scattered by the gas in the environmental and specimen chambers a significant proportion remain in the central focused beam. The scattered electrons contribute to the background noise in the microscope but the central portion of the beam remains focused and is used for imaging.

The image of the sample may be formed using back-scattered electrons or secondary electrons. It is the amplification effect of the ionised gas in the specimen chamber which enables the latter to be used. The secondary electrons from the specimen surface drift towards the anode of the detector biased to a few hundred volts. As they do so they create an avalanche of additional radiation and the resulting current flow is used to create the image.

The main limitations of the ESEM are problems associated with beam damage of the sample and sample evaporation problems which might occur if the optimised pump-

down routines are not followed. In the case of wood composites some beam damage was observed when the magnification was high and the electron beam concentrated on a small area.

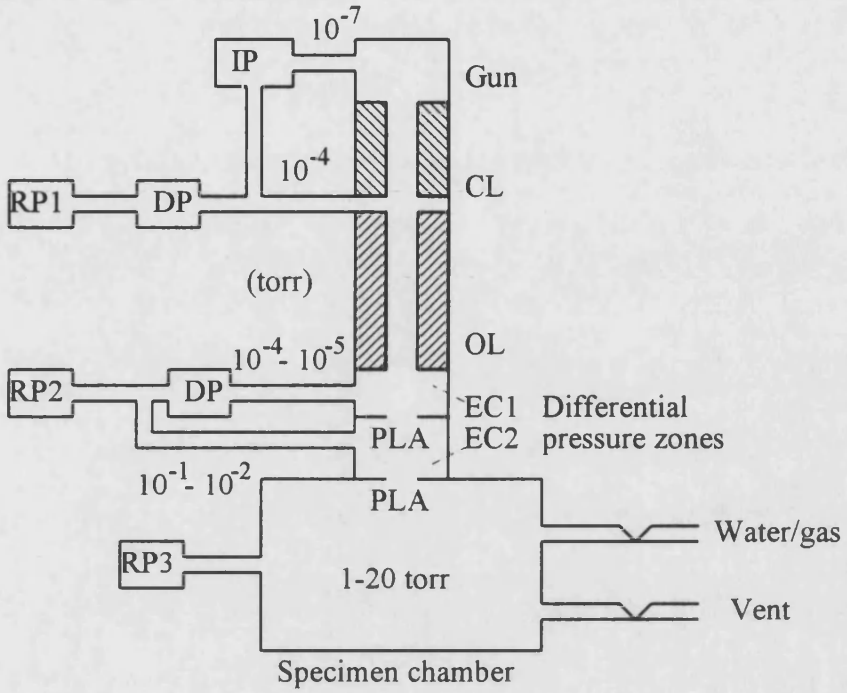

Fig.16.5. A schematic diagram of the differential pumping system in the Electroscan ESEM. IP=ion pump, DP=diffusion pump, RP=rotary pump, PLA=pressure limiting aperture, EC=environmental chamber, CL=condenser lens, OL=objective lens (Cameron, 1994, Danilatos, 1990).

16.4. Experimental technique

The use of an Electroscan environmental SEM was arranged with Dr. Svend-Ib Thor and Dr. Hans Lilholt from Risø National Laboratory, Roskilde, Denmark. The ESEM is run by Dr. Andy Horsewell and the work was carried out over a period of about two weeks and was carried out as a joint investigation.

An in-situ loading jig had recently been supplied by Alan Hever of the Engineering Department at the University of Cambridge, fig.16.6. The principal components of the jig are a screw-driven vice in which the specimen is mounted and a strain-gauged beam used to calculate the loads applied to the sample. The jig can be used for both tension and compression tests, depending on the set of grips employed. The strain-gauged beam was calibrated prior to the tests so the load on the sample could be calculated. The screw was turned by coupling it to one of the motors usually used to operate the x-z tilt of the microscope stage.

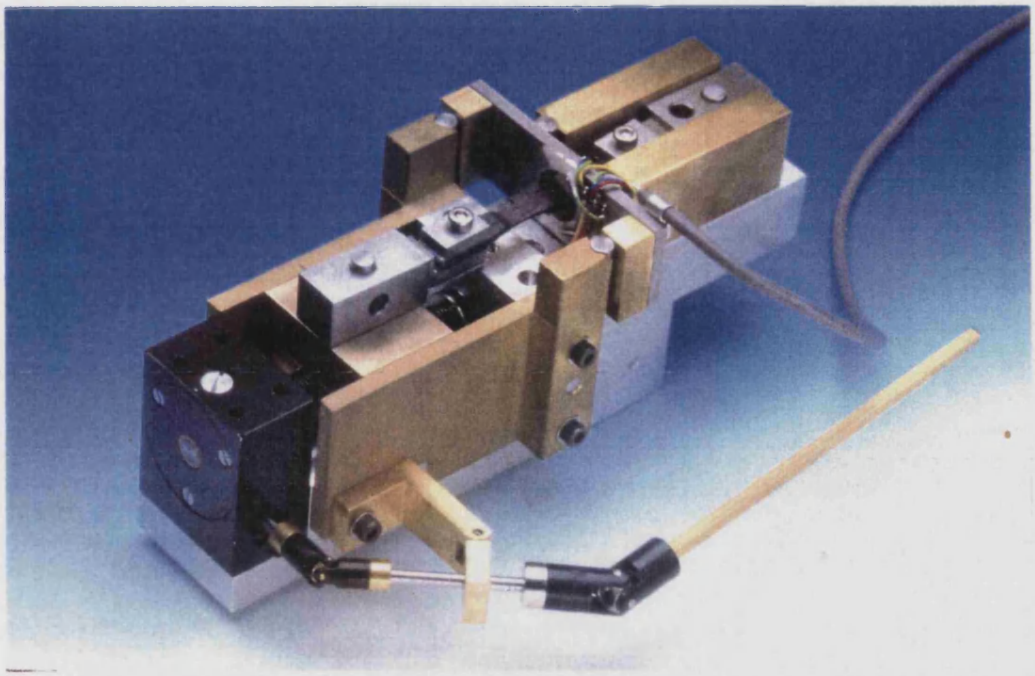

Fig.16.6. In-situ loading jig (Slide supplied by Dr. Andy Horsewell).

Samples of Khaya-epoxy composite for tensile testing were prepared to the dimensions shown in fig.16.7. They were produced by cutting thin slices of veneer, approximately 1mm thick, from a large fatigue specimen, as in fig.6.1. The longitudinal axis of the sample was parallel to the wood grain and the flat surface was the tangential section (or TL plane) , see fig.3.7. Slices of veneer were taken from an unfatigued sample and ones which had failed as a result of fatigue at R=10, R=0.1 and R=-1. In the case of the fatigued samples, the veneers were cut from the sample gauge length in the vicinity of the failure. This was likely to be the most damaged region of the sample and therefore the most likely to show damage mechanisms in the ESEM related to the type of fatigue damage in the wood.

The dog-bone shaped ESEM samples were then cut using a single edged razor blade from these pieces of veneer. The necked portion of the sample was made by cutting with a razor bent into a curve. The sample was thinned at the centre of the necked portion using the razor. A small notch was cut on one side to create an initiation point for failure. The notch was cut so that the direction of crack propagation would be LT, using the notation discribed by Gibson and Ashby (1988), and would force the crack to grow across the grain in the tangential direction. It was essential to initiate crack growth because it would have been very easy to miss the first cracks which are small with respect to the width of the sample. Immediately prior to testing a final thin cut was made across the top of the sample with a fresh razor to create a clean surface on which to observe the fracture processes. The notch was also lightly scored with a fresh

razor to ensure that the notch was sharp. It can be appreciated that with the small size of the samples this was a very delicate operation. The holes fitted over posts in the tensile test grips to aid stress transfer between the grip surfaces and the sample. The sample was not symmetrical about the necked portion because the region for inspection had to be offset from the centre to prevent it being obscured by part of the loading jig.

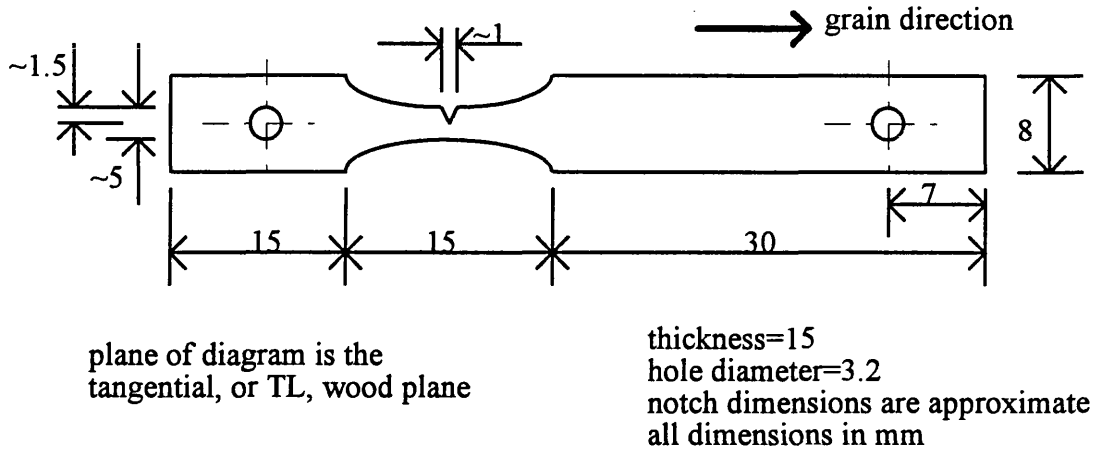

Fig.16.7. Sample dimensions for tensile tests in the in-situ loading jig.

The ESEM was operated at a chamber pressure of about 5 torr and the image was produced using secondary electrons which are plentiful in natural materials. This enabled effective imaging of a material such as wood which has high levels of surface topography. The pressure used and the distance from the detector were balanced to give optimum contrast and intensity in the image.

As the tests proceeded the load levels were noted and the fracture stresses calculated. Stress-strain curves were not produced because the tests were slow, taking several hours, and the load was applied in stages because it had to be held constant during image capture.

16.5. Results

Table 16.1 shows the failure stresses of each sample tested. Usually a crack propagated in steps through the sample until the maximum stress was reached. Once this had occurred the load dropped and small increments in load were sufficient to cause further crack growth and rapid failure. This is to be expected in a crack growth type of test using a notched sample, where crack growth causes a progressive reduction in cross-sectional area of the sample.

Sample	Ultimate stress, MPa
Unfatigued Khaya 1	109.05
Unfatigued Khaya 2	14.3
Fatigued Khaya [R=0.1]	66.15
Fatigued Khaya [R=10]	22.35
Fatigued Khaya [R=-1]	51.33

Table 16.1. Ultimate strength of samples tested in the ESEM.

These values are as expected with the exception of the second unfatigued Khaya test where the ultimate stress is extremely low. This is possibly due to damage introduced into the sample whilst mounting it in the loading jig because fracture was observed to have occurred from the un-notched side of the sample. The second tensile test on unfatigued Khaya showed a failure stress at the top end of the results obtained in Chapter 7. This high result emphasises Khaya's high notch insensitivity as its presence does not reduce the UTS for this sample at all. For the fatigued samples, all failed below the unnotched UTS [~85MPa], which is as might be expected for pre-damaged material. The sample produced from a fatigue sample tested at R=10 has a very low tensile strength because failure occurred along the line of the macroscopic compression crease which was present in the sample approximately 7mm away from the notched region of the sample.

Differences were observed in the way in which the samples responded to in-situ static loading. This implies that the samples contained damage which was related to the type of fatigue loading the wood had undergone. Micrographs from each test are presented and discussed in the following subsections.

16.5.1. Unfatigued Khaya

Two tensile tests were carried out on unfatigued Khaya. The features observed in these tests clearly are not a result of fatigue damage and as such are a control so that features due to fatigue damage in later tests can be separated from behaviour which is common in undamaged Khaya.

In the first test the notch was cut so that it ended in a group of ray cells. Initial rapid crack growth occurred at a stress level of 12.4MPa, fig.16.8. It can be seen that the crack has deviated from the cut notch and moved in the TL direction, through the first ray bundle and into the next. One fibre (a) which crosses from above the first bundle

(1) to the second bundle (2) has fractured diagonally. The adjacent three fibres (b) between the major crack and another ray bundle (3) have fractured perpendicular to their length. The failed fibre ends are jagged. A crack is also visible between the end of the first bundle (1) and the third (3).

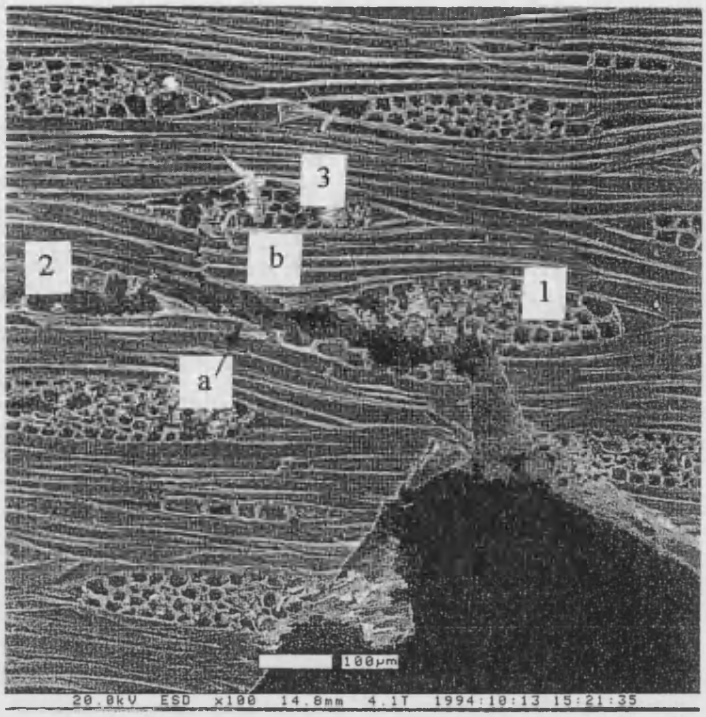

Fig.16.8. Tensile loading of unfatigued Khaya. Initial crack growth along and between ray bundles.

The same process is occurring in fig.16.9 for another pair of ray bundles at an applied stress level of 13.7MPa. Failure is evident in both bundles. Fibre bridging can also be seen. One fibre (a) is damaged but still intact and bridging the crack between the two ray bundles. The other (b) has fractured diagonally and longitudinally and thin strands of microfibrils can be seen still bridging the crack.

Fig.16.10 was taken at the ultimate load of the test, 14.6MPa, and is a detail of the fibre bridging in fig.16.9. The strands of microfibrils still bridge the crack even though it has opened considerably since fig.16.9. Although some microfibrils were seen to have failed in tension, others continued to peel away from the fractured fibre wall as the crack widened. The bridging fibre (a) has been bent to the point where a crack has propagated across it (i). The fibre below it (ii) has also partially cracked. Soon after the image was recorded the load started to drop and catastrophic failure followed. Rapid fracture occurred as a result of a massive crack growing across the sample from the un-notched side. However, although the load levels were low the test did clearly show the mechanisms of longitudinal crack growth between ray bundles.

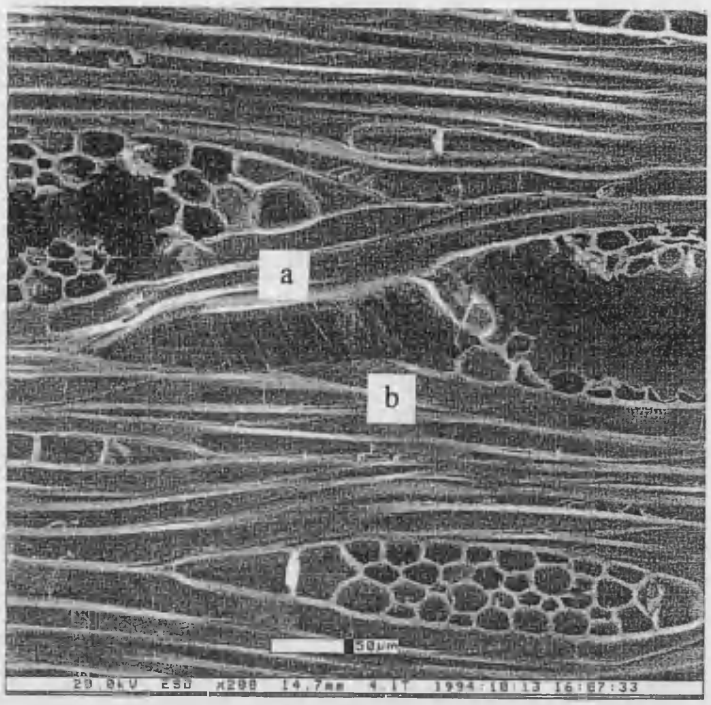

Fig.16.9. Tensile loading of unfatigued Khaya. Fibre bridging across crack between two ray bundles.

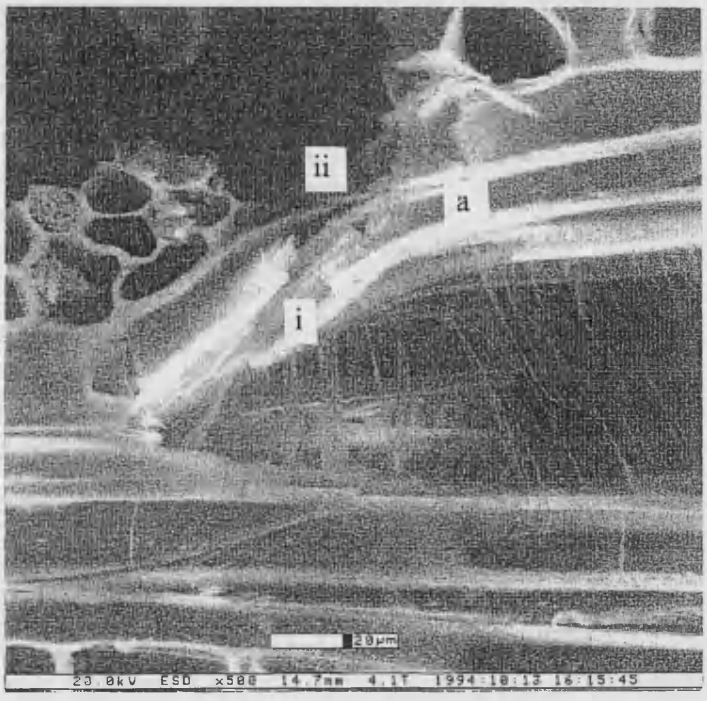

Fig.16.10. Tensile loading of unfatigued Khaya. Fracture of bridging fibres and 'unpeeling' of microfibrils from failed cell wall.

In the second unfatigued Khaya test the notch ended at a vessel. The crack first propagated into the vessel at a stress of 8.3MPa, fig.16.11. It is clear that it

immediately deviated from the LT to the TL direction. The speckled appearance of the vessel lumen is caused by ridges and small perforations on the surface. They were present in varying amounts in about 60% of the vessels observed and are slit-like pits, known as scalariform pits. They are arranged in rows with their long axis close to the transverse axis of the vessel (Meylan and Butterfield, 1972). The diagonal white line across the vessel is known as a simple perforation plate and is where the cell ends of the vessel cells have been formed and then dissolved away so that liquid can be easily transported along the length of the vessel (Meylan and Butterfield, 1972).

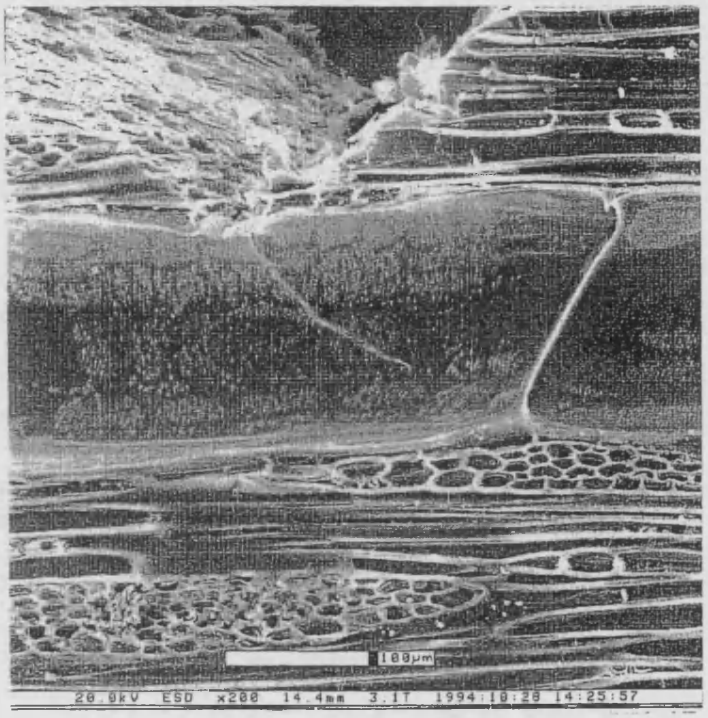

Fig.16.11. Tensile loading of unfatigued Khaya. Second test. Crack propagating along vessel.

As it is unlikely that the wood immediately behind the vessel contains any ray bundles to provide weak fracture paths it can be imagined that the fracture path behind the vessel must be complex and involve only the fracture of fibres. This is supported by the complex pattern of cracks in the vessel wall which have developed up to a load of 39.9MPa. The original crack has opened considerably and secondary cracks have developed travelling along the vessel in the opposite direction. Two cracks have appeared across the perforation plate and are not connected to the main crack in the vessel wall. They could, however, be connected via cracks in the fibres behind the vessel. The crack moving in the opposite direction is highly branched and tortuous which suggests that the wood is being very effective in its resistance to crack propagation, displaying high toughness and energy absorption. A crack parallel to the starter crack is visible in the bottom right corner of fig.16.12 which passes through

about seven fibres. On the sample surface it does not have any connection to the cracking in the vessel.

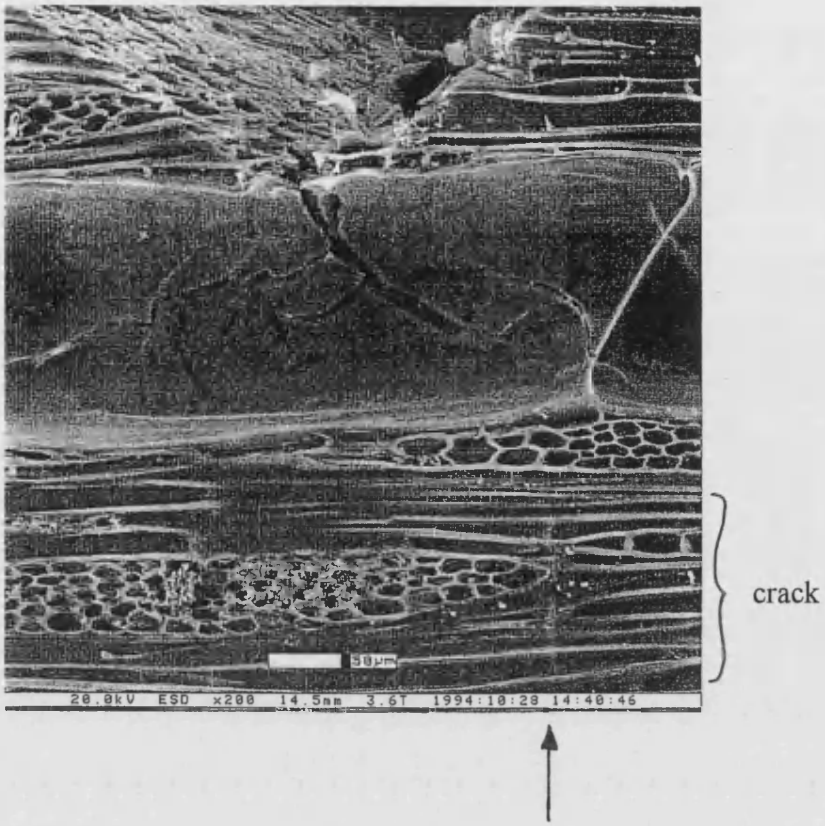

Fig.16.12. Tensile loading of unfatigued Khaya. Sample 2. Extensive cracking in the vessel at the crack tip and a remote crack across a group of fibres.

In fig.16.13 the fibres behind the vessel have sheared along the TL direction causing the vessel to rupture along its length. The tear in the vessel wall is very jagged. The fibres below the vessel have a hairy appearance, suggesting that fracture along the cell wall has occurred and microfibrils have been peeled up from the fracture surface across the crack. The fact that microfibrils remain attached to both sides of the crack suggest that diagonal cracking along the microfibrillar winding direction must have occurred ahead of the crack. This would have occurred until the stress was high enough, and the microcracking severe enough, for fracture to occur.

The influence of a ray bundle on the crack path is apparent since the crack leaves the vessel at the end of a ray bundle and passes along its length (1). An evenly spaced array of cracks across fibres is visible between the first and second vessels. The crack spacing is about 300μm. This can roughly be equated to the length of the ray bundles. The main crack at the left hand side of the figure extends beyond the second vessel into a ray bundle. Other hairline cracks can also be seen in this vessel. The stress level was 53.2MPa.

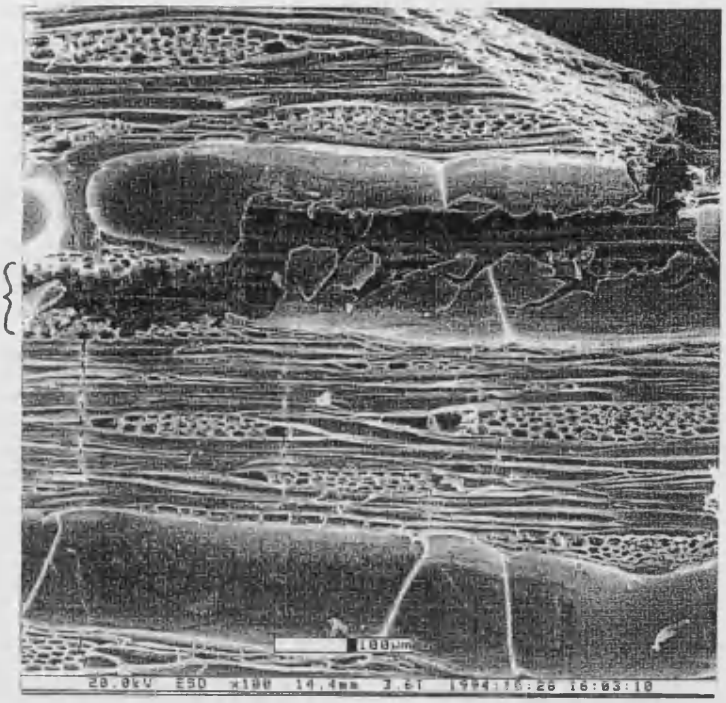

Fig.16.13. Tensile loading of unfatigued Khaya. Second sample. After rapid crack propagation through the first vessel. A regular array of cracks are present in the fibres below it.

As the load was increased cracks grew both parallel to the fibre direction and across the fibres. Fracture occurred at the high stress of 110.9MPa and involved the shearing of fibres along their length, leaving a very jagged fracture surface. Clearly large amounts of work were done in the fracture process, which explains why such a high strength was obtained.

16.5.2. Khaya fatigued at R=0.1

Micrographs are presented for the tensile test of Khaya, prefatigued at R=0.1 (tensile fatigue), in figs.16.14 to 16.22. Before in-situ loading was started the sample surface was inspected thoroughly for damage already present in the wood structure. Several types were observed. In fig.16.14 a longitudinally split ray bundle is shown. Three were found across the sample. It is clear that the individual ray cells have separated along the middle lamella and that no cell wall fracture is observed. This corresponds to the cell peeling behaviour observed by Gibson and Ashby (1988) and shown in fig.16.2. This type of damage is likely to have been caused by the repeated squeezing together of the ray cells during fatigue loading causing progressive weakening of the middle lamella. It was also noticed that the ray cell ends appeared very papery, unlike in the unfatigued state. However, it is possible that this feature could have been produced during sample production. A second type of damage found extensively was in the form

of helical cracks along many of the fibres, fig.16.15. They are particularly evident in the fibre under the micron bar (a) and two above it (b). The damage takes the form of a series of small cracks very close together (i) or longer cracks, slightly farther apart (ii). The angle of the cracks was measured and found to be 12.5° and 19°. This falls within the range of the expected helical angle of the S2 layer [10°-30°], see fig.3.5, which makes up 50% of the cell wall thickness and is responsible for wood's high strength in tension.

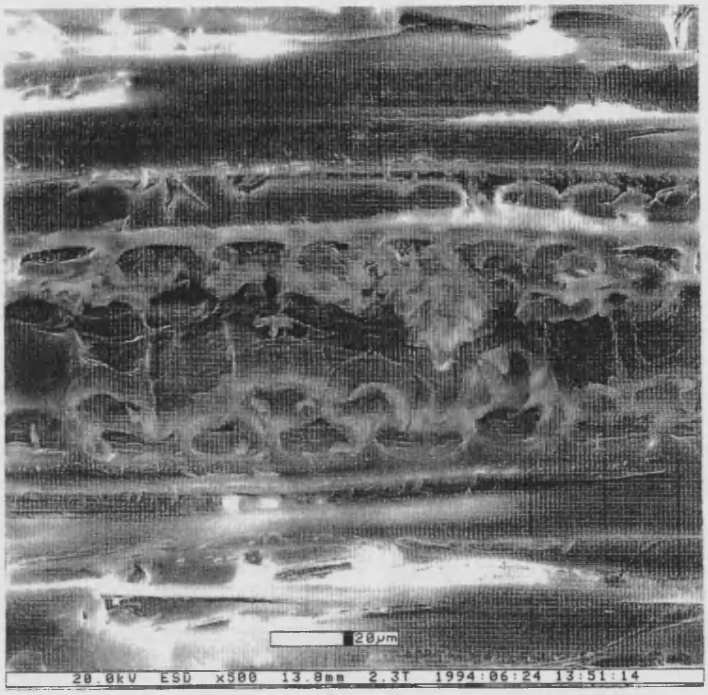

Fig.16.14. Khaya pre-fatigued at R=0.1 (tension). Damage present prior to in-situ loading test. Delamination of middle lamella.

The circular feature in fig.16.15 is a section through a bordered pit which functions as a valve through which sap can pass. The secondary cell walls of the adjoining fibres are raised over the torus and margo which can be seen as a thin dividing line between them, fig.16.16. Bordered pits may be found in hardwoods but the simple pits, which have also been identified in Khaya are more common.

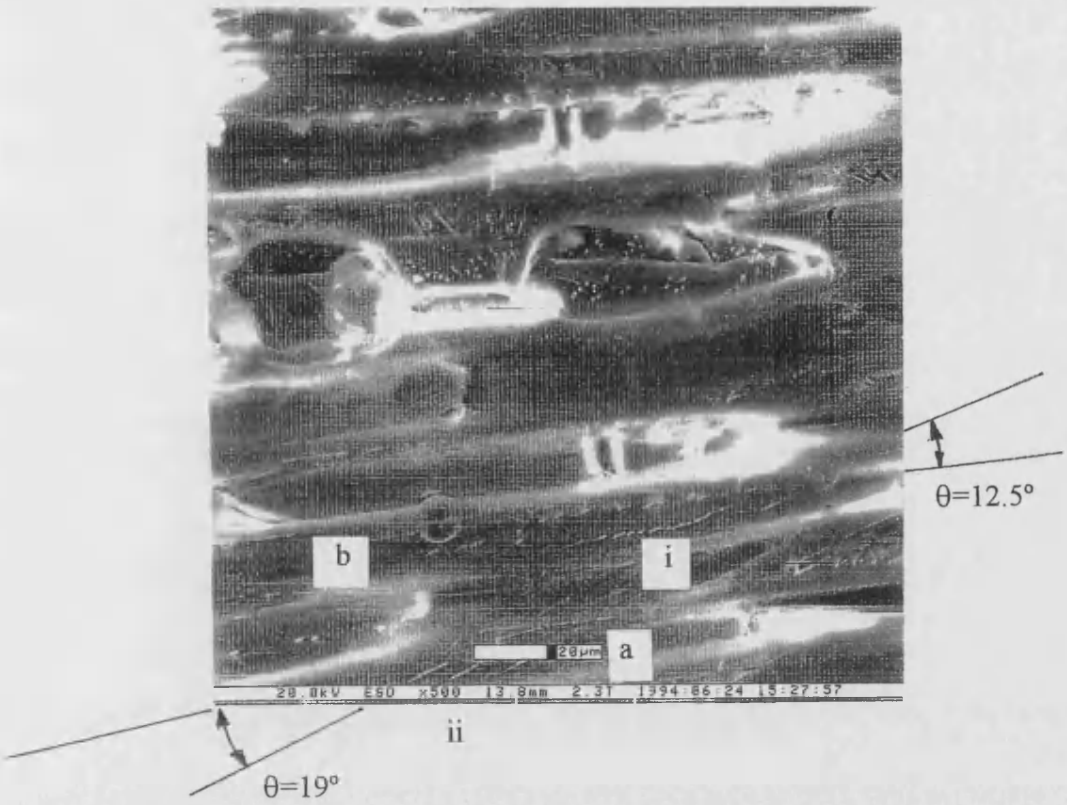

Fig.16.15. Khaya pre-fatigued at R=0.1 (tension). Damage present prior to in-situ loading test. Cracking of S2 cell wall.

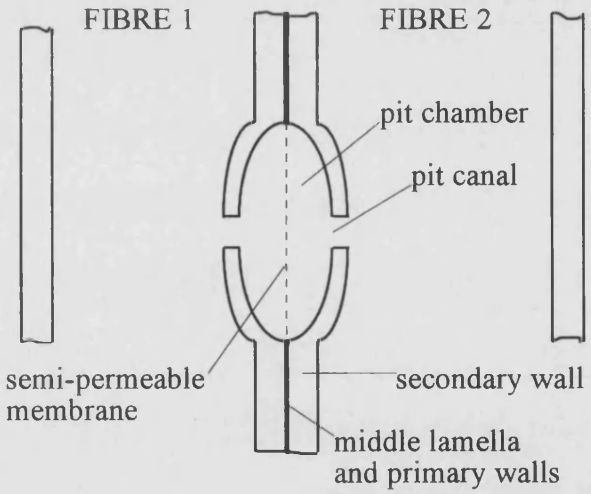

Fig.16.16. Schematic diagram of a bordered pit (Meylan and Butterfield, 1972).

The notch tip had been cut into a group of fibres and on loading the first fibre soon failed at a stress of 18MPa. Fig.16.17 shows this. It can also be seen that the ray cells immediately below the cracked fibre are already cracked in a direction perpendicular to the fibre crack. In fact the ray bundle had cracked completely along its length. This is

not altogether unexpected based on observations of this behaviour in unfatigued Khaya. In the leftmost ray cell an inner warty layer on the cell lumen can be seen.

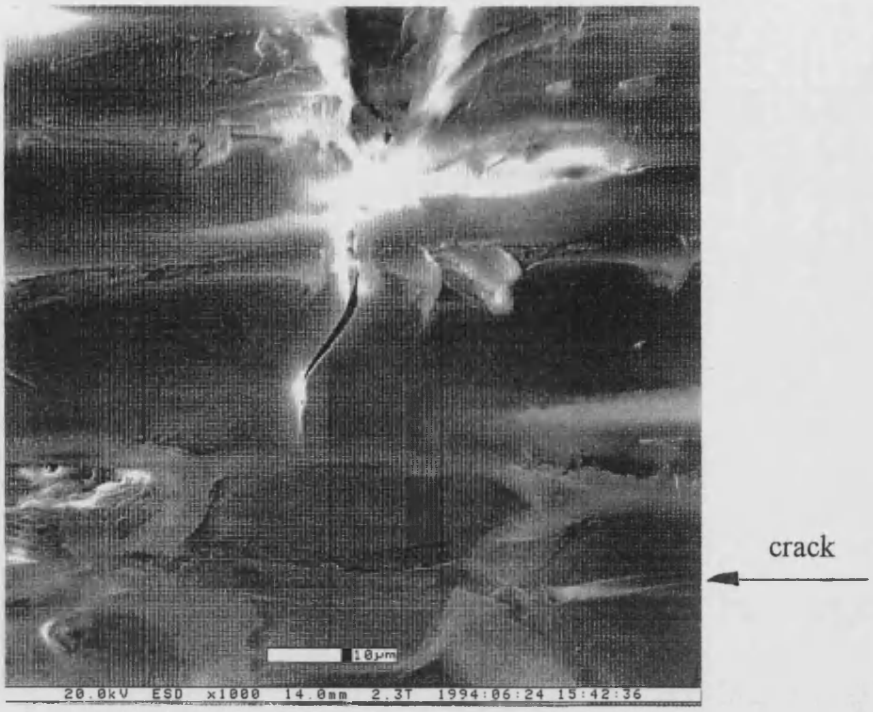

Fig.16.17. Khaya pre-fatigued at R=0.1 (tension). First fibre crack at 18MPa. Longitudinal crack in ray cells.

Fig.16.18 shows how the crack had grown at ~28MPa. From the notch tip it runs through the first ray bundle (1) through a group of fibres where it stops at a second ray bundle (2). The ray bundle deflected the crack in the TL direction until a stress of over 35MPa had been reached.

As the stress level was increased further damage accumulated in the second ray bundle (2) and it fractured along its length. Damage was also seen to accumulate in the fibres immediately below the ray bundle, but without the outer cell walls of the ray actually failing. At about 44MPa the crack broke through the ray cell wall and at the same time a new major crack appeared from the end of the ray bundle (2) which spanned about seven fibres, fig.16.19. The damage ahead of the crack which entered the ray bundle was in the form of several diagonal splits in one fibre and a fibre break about 50µm to the right of the crack through the ray cell. Several small cracks are visible which span only a single fibre and are typically between 20µm and 40µm apart. These more dispersed cracks had not been present in the unfatigued samples. Only the large ones which spanned a group of fibres had been found. A second long crack through fibres also developed between ray bundles (3) and (4).

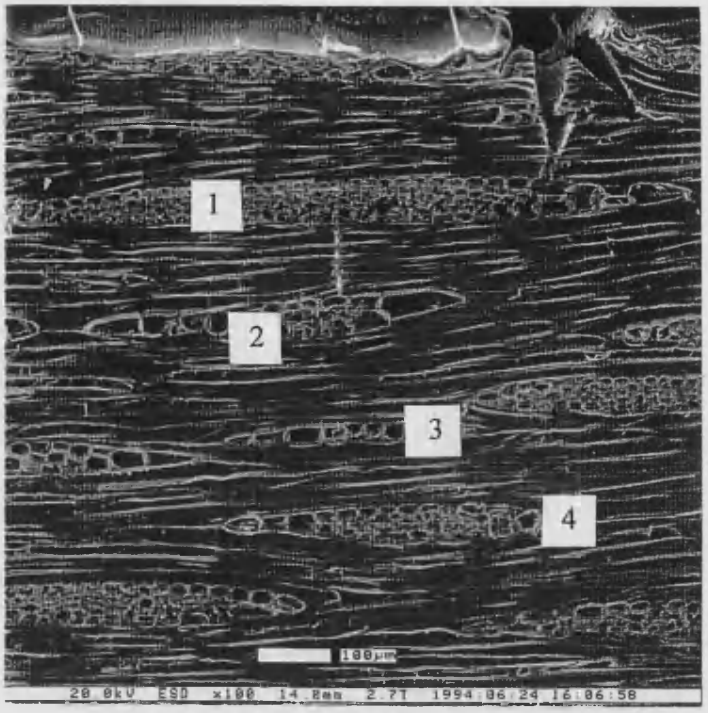

Fig.16.18. Khaya pre-fatigued at R=0.1 (tension). Crack which runs from notch tip, along first ray bundle, through some fibres to the second ray bundle.

Further detail of the diagonal cracking is given in fig.16.20. It can be seen that immediately next to the fractured ray cell wall that there is a region of plastic deformation in the cell wall which extends part of the way across the fibre. This appears to blunt the crack and deflect it so that it propagates a distance of 60µm, and four diagonal splits, further along the fibre. The distance between each split is 3µm, equivalent to between 300 and 1000 microfibrils. Delamination can also be detected between the split fibre and the ray cell wall. As the load was increased the split sections of fibre continued to bridge the crack until a load of approximately 60MPa was reached when it fractured completely.

The overall situation at a stress of 63MPa is given in fig.16.21. The crack at the end of the notch has grown to over 50µm wide. It is then deflected through part of an unusually long ray bundle (1), ~0.8mm in length, before continuing across the sample via a series of cracks across fibres and along ray bundles. Some of these cracks are fairly straight and pass from one fibre to the next whilst others are jagged as the fibres fractured in a more dispersed manner. Beyond ray bundle (5) the cracking is particularly dispersed. Several thin diagonal cracks can also be seen in the vessel at the bottom of the picture. Above this level of loading fracture occurred rapidly. The crack opened suddenly in several stages until 66MPa was reached when a further ray bundle

cracked longitudinally, the vessel at the bottom of fig.16.21 collapsed and failure ensued.

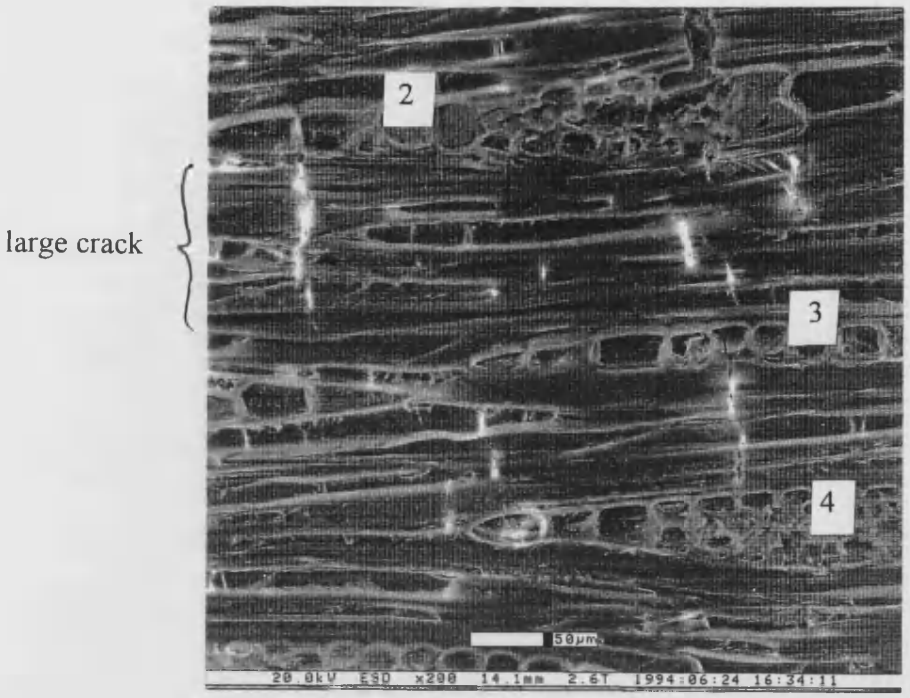

Fig.16.19. Khaya pre-fatigued at R=0.1 (tension). Long cracks between ray bundles and dispersed cracks across fibres.

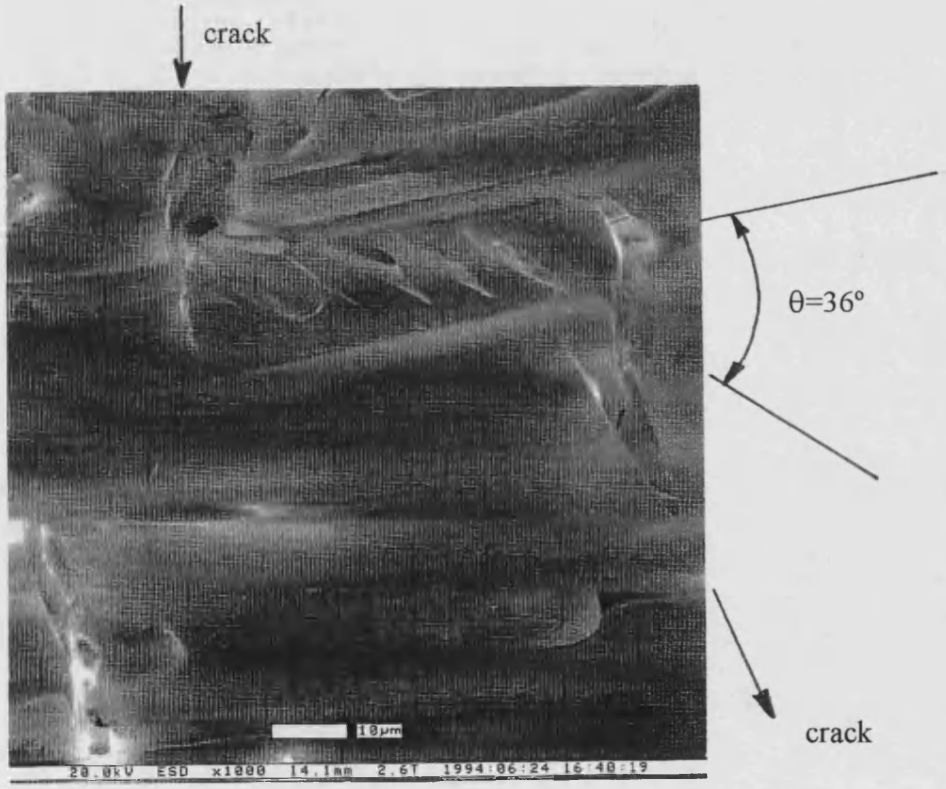

Fig.16.20. Khaya pre-fatigued at R=0.1 (tension). Detail of diagonal cracking and plastic cell wall deformation below a fractured ray cell.

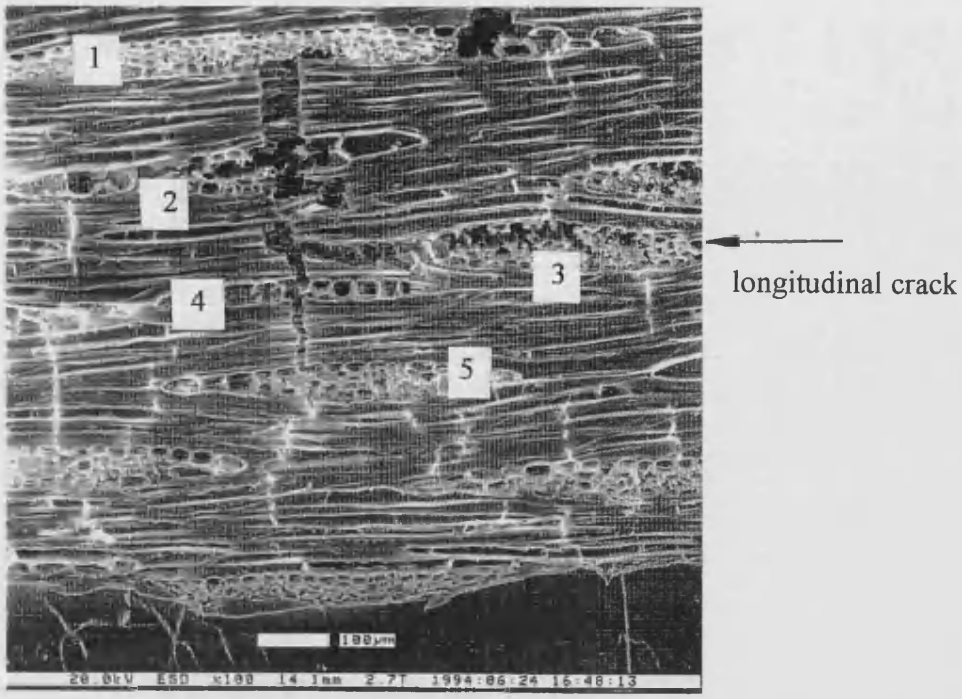

Fig.16.21. Khaya pre-fatigued at R=0.1 (tension). Dispersed cracking just prior to failure.

16.5.3. Khaya fatigued at R=10

Micrographs taken from the test on Khaya pre-fatigued at R=10 are presented in figs.16.22 to 16.32. The sample contained a compression crease several mm away from the notch and although initial crack growth occurred from the notch, final failure occurred along the compression crease. Before loading the sample was inspected for damage both away from and in the vicinity of the compression crease.

Fig.16.22 is of wood about 2-3mm away from the crease which contained a compression kink between two ray bundles. This suggests that, whilst compressive failure occurs in a very localised manner with one large instability propagating rapidly across the wood, there are other minor instabilities which also develop as the load level is increased which do not coalesce to form part of the main crease. The crease in fig.16.22 was measured and found to cross the fibres at an angle of 51° to their axis. This is perpendicular to the angle of the kink in each cell wall and falls within expected values of 45° to 60° (Dinwoodie, 1981). The crease does not pass through the ray bundle (1) at this angle but moves straight across it perpendicular to the fibre direction.

The vessel surface in the middle of the picture has a high degree of surface texture. This is shown in more detail in fig.16.23 and appears to be helical thickening of the cell wall, behind which the pit openings are visible.

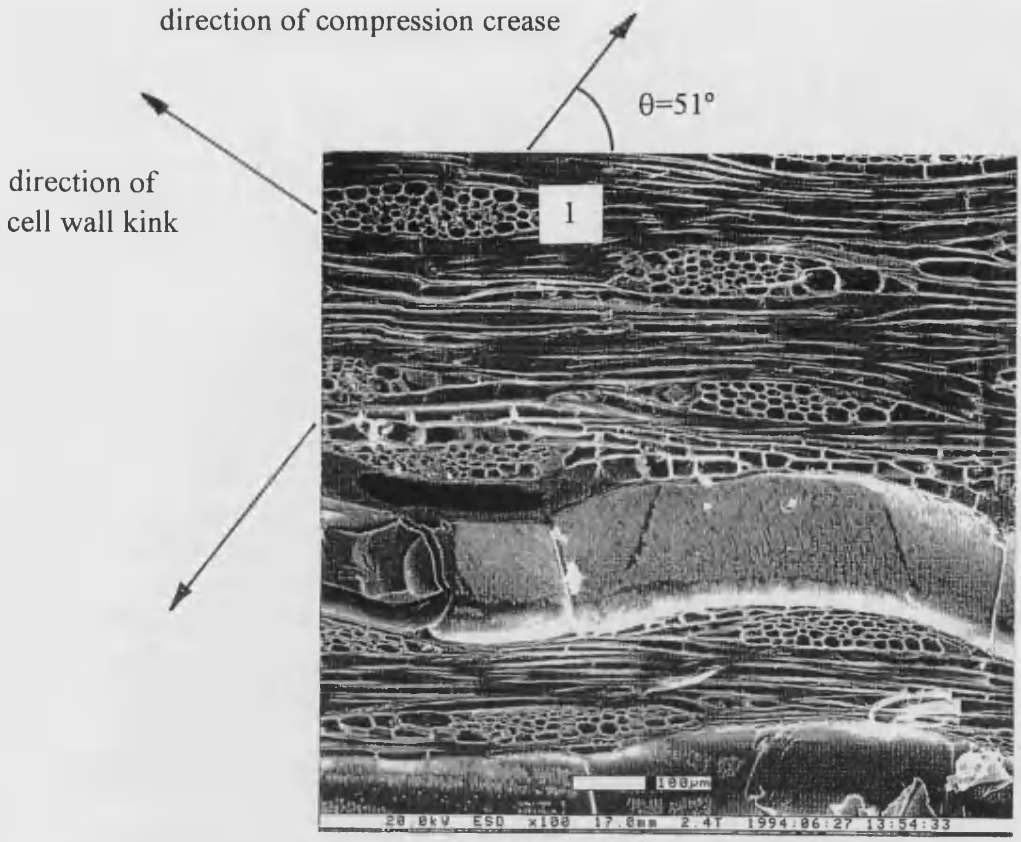

Fig.16.22. Khaya pre-fatigued at R=10 (compression). Before in-situ loading. Small compression crease remote from the main crease.

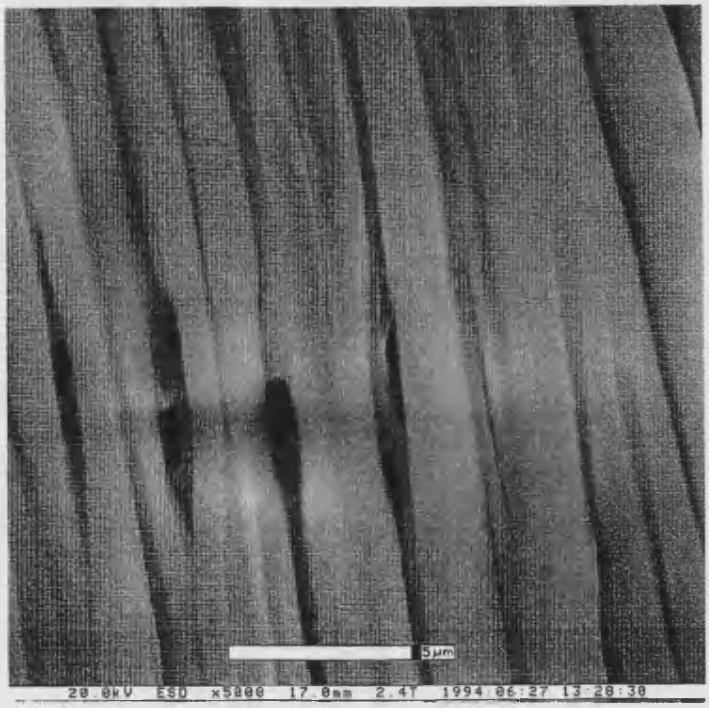

Fig.16.23. Khaya pre-fatigued at R=10 (compression). Before in-situ loading. Detail of texture on vessel lumen in fig.16.23.

Another type of damage which was observed away from the compression crease is shown in fig.16.24. It takes the form of marks on the surface of a fibre which are not complete cracks. The largest is at an angle of 30° to the fibre axis, the two smaller ones are at angles of 9° and 18°. Although the high angle feature falls outside the expected S2 angle range of between 10° and 30° it is considerably lower than the expected S1 angles of between 50° and 70°. The two lower values are similar to the crack angles measured in the R=0.1 fatigued sample, fig.16.16.

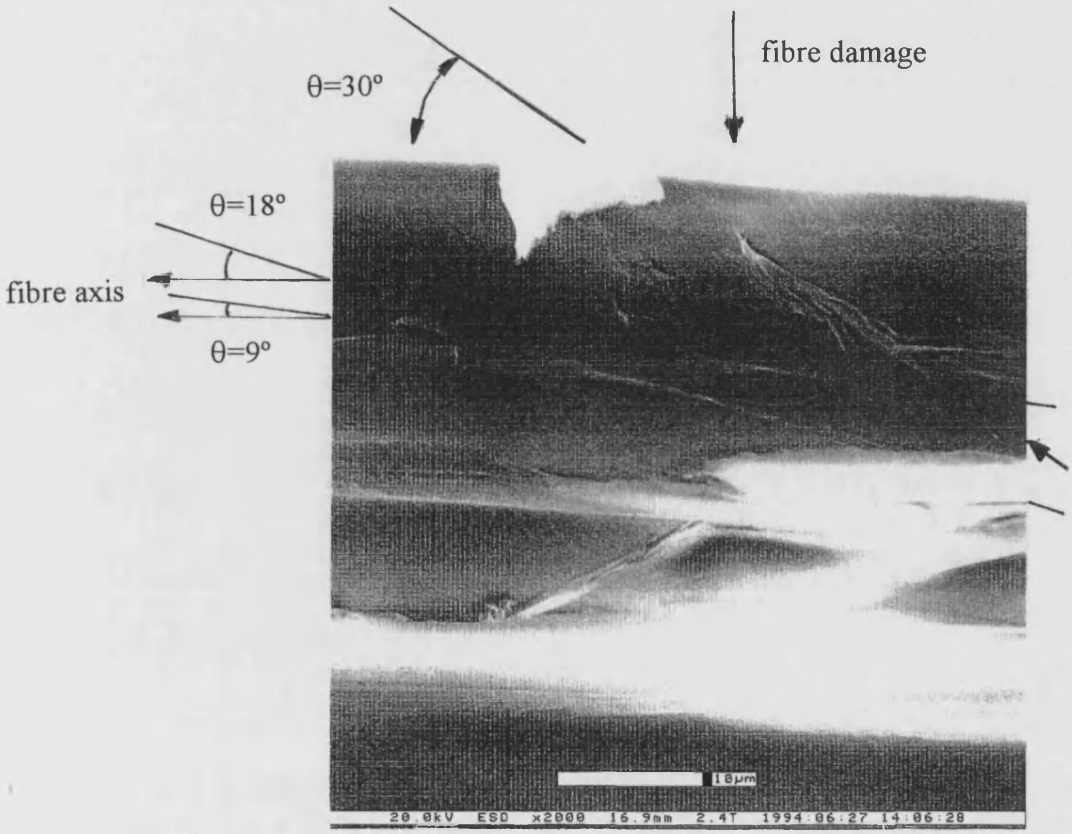

Fig.16.24. Khaya pre-fatigued at R=10 (compression). Before in-situ loading. Detail of damage on outer surface of a fibre.

Other forms of damage observed remote from the compression crease were occasional fibre breaks and associated delamination between adjacent fibres along the fractured fibre.

A portion of the macroscopic compression crease is presented in fig.16.25. The wood structure has deformed enormously. Ray bundles present in the crease have been flattened and/or sheared along their length. The vessel visible in the bottom left hand corner of the picture has completely collapsed at the start of the crease. The edges of the fibres are wavy and full of coalesced compression creases. The fibres in region (a)

show how compression kinks have built up between two ray bundles, (1) and (2), slightly ahead of the main crease. The fibres appear undamaged for a distance of about 75μm between the small and main crease.

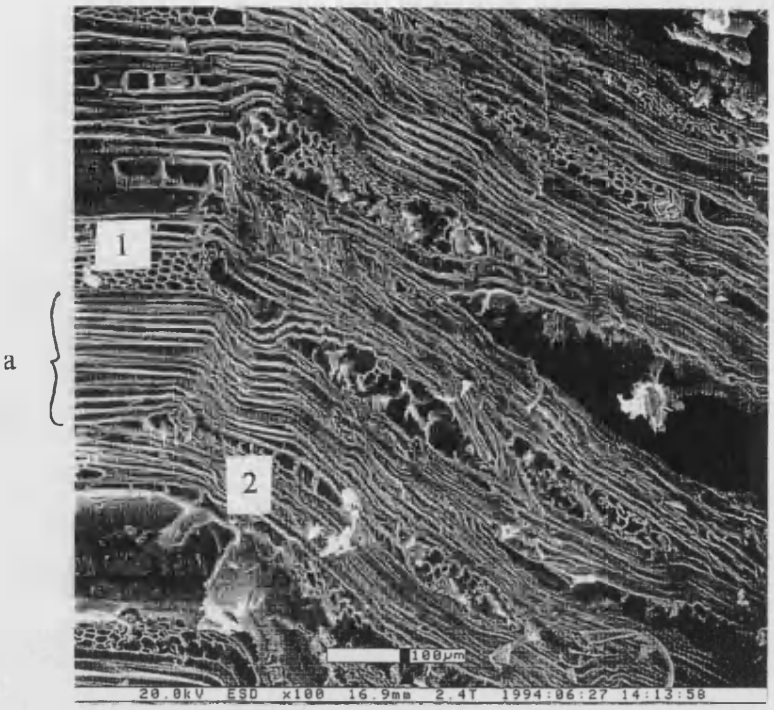

Fig.16.25. Khaya pre-fatigued at R=10 (compression). Before in-situ loading. View of the macroscopic compression crease showing crushed and uncrushed regions.

Ray bundle (1) shows particularly clearly how a compression crease grows and destroys the structure of a ray. The crease in the fibres below the ray, see fig.16.25, is putting the bottom of the ray bundle into tension whilst the fibres above it are impacting the undamaged wood causing a shearing action across the ray bundle. The effect of this on the individual ray cells is shown more clearly in a similar ray bundle in Fig.16.26. The left-most ray cells, farthest from the crease have a regular hexagonal structure with straight sides. In the second row the long sides of the cells are curved or kinked. The third row appears to have sustained little damage but the one after has very bent cell walls and cracks can be seen between the individual ray cells. Beyond this point the regular hexagonal structure is unrecognisable as the cells are deformed further and pulled apart.

Fig.16.27 shows clearly the gross plastic deformation present in the fibres within the compression crease as a result of the coalescence of compression creases.

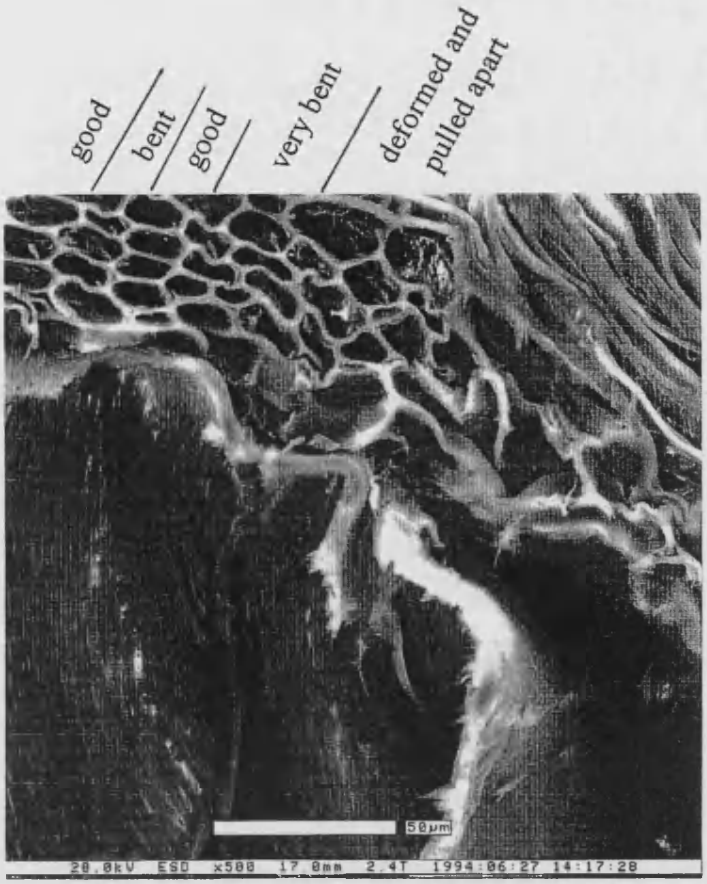

Fig.16.26. Khaya pre-fatigued at R=10 (compression). Before in-situ loading. Damage of ray bundle at edge of compression crease.

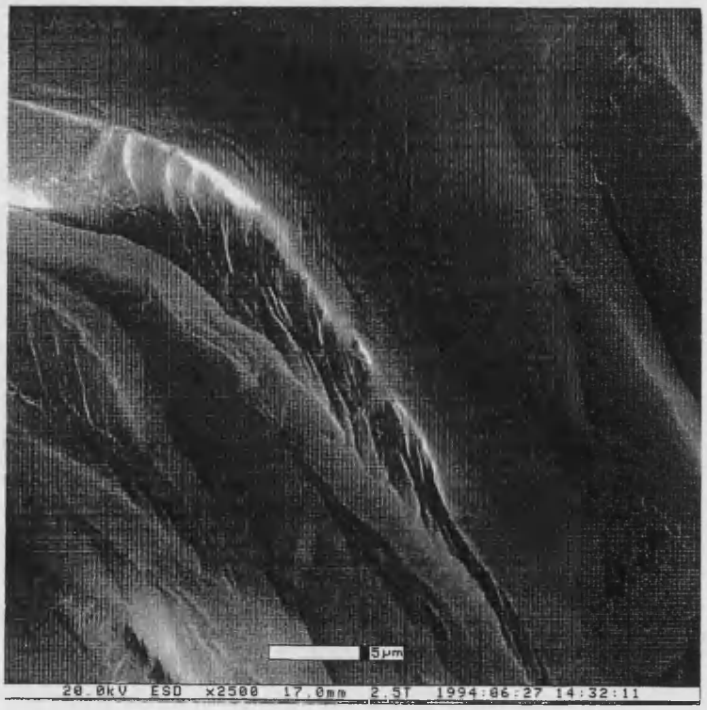

Fig.16.27. Khaya pre-fatigued at R=10 (compression). Before in-situ loading. Fibre damage in compression crease.

The effect of an instability in a ray cell wall in the initiation of a compression crease is shown clearly in fig.16.28. The triangular end ray cell in ray (1) has buckled under the axial compressive force. The fibre next in line also buckles under the additional compressive stress it now sees. However, its displacement is constrained by straight, undamaged, fibres so that rather than bowing out, it fails by kinking in two distinct steps, ⎯╱‾‾╲⎯. As it does so, stress is transferred to its neighbour and the kink is perpetuated. In this way compression creases grow in pairs, becoming increasingly far apart and centring on the initiation site. This is represented schematically in fig.16.29.

This has caused the fibres immediately above and below to buckle. The fibre next in line also buckles in two steps so that the fibre accommodates the buckle in the first by buckling itself in two places in opposite directions. This initiates this double buckling in the next fibres and in this way two compression creases grow away from the original instability, becoming increasingly far apart. High degrees of delamination are visible between the fibres which no doubt reduces the structure's coherence and ability to withstand further buckling.

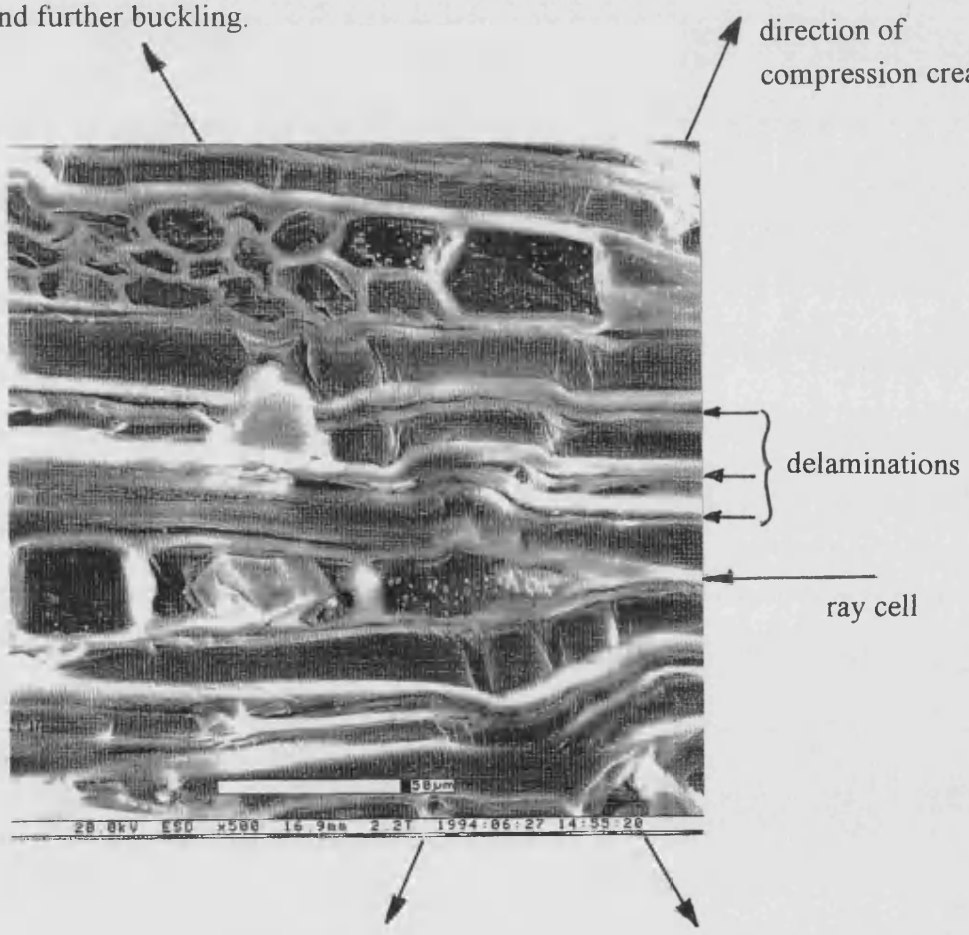

Fig.16.28. Khaya pre-fatigued at R=10 (compression). Compression crease originating from the end cell in a ray bundle.

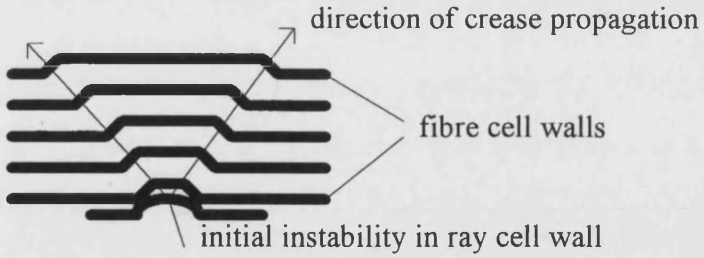

Fig.16.29. Schematic diagram of compression crease initiation and propagation.

Loading was then begun. At 7.6MPa the crack at the notch tip began to grow and propagated along a ray bundle and through some fibres. Fig.16.30 shows the end of the crack tip in the fibres. At the bottom of the picture bridging across the crack is visible where a fibre has ruptured. The cracks across the next two fibres are smooth and straight. The crack is just growing into the next fibre. This fibre appears to have split along its length. The top part has reduced in thickness. It has ligament-like features and part of the surface of the fibre is lifting away. The fracture surface which can be seen above the top half of the fibre has a different, fibrous structure as opposed to an essentially smooth surface.

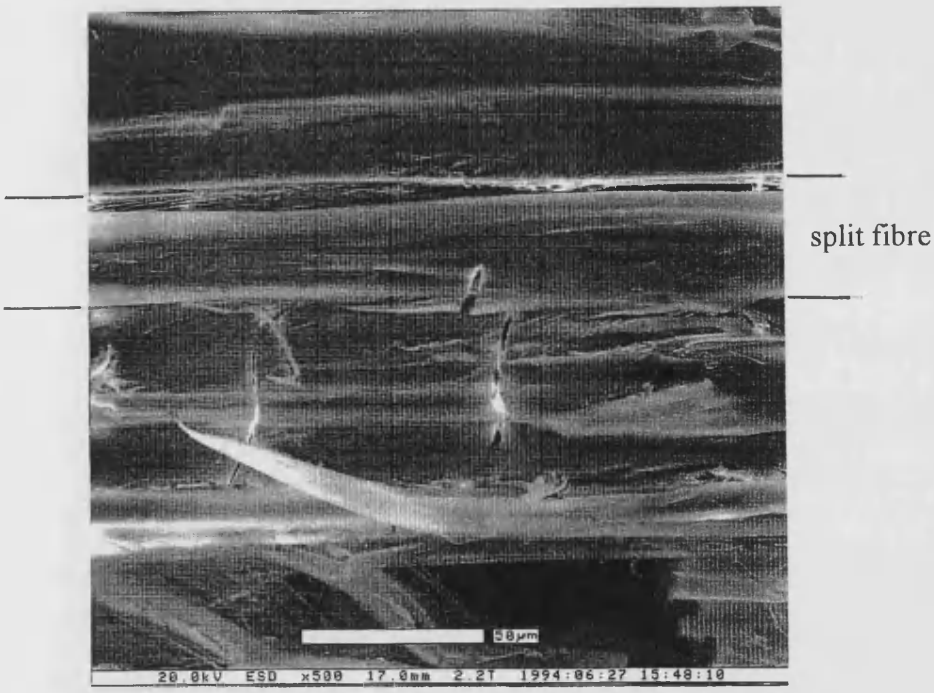

Fig.16.30. Khaya pre-fatigued at R=10 (compression). Longitudinally split fibre.

As the load was increased this fibre fractured along with its neighbours. When the crack reached another ray bundle it fractured a fibre at the end of the bundle along its length, as in fig.16.30. Bundles of microfibrils were seen to bridge the crack. The crack continued to grow by fracturing fibres perpendicular to the cell axis. As the load

was increased crack growth continued by LT direction fracture of fibres and RL direction splitting of ray bundles and adjacent fibres. When the load reached 22.35MPa the crack rapidly grew back to the macroscopic compression crease and caused the sample to fail. Fig.16.31 shows the macroscopic compression crease which has been pulled straight under the action of the applied load.

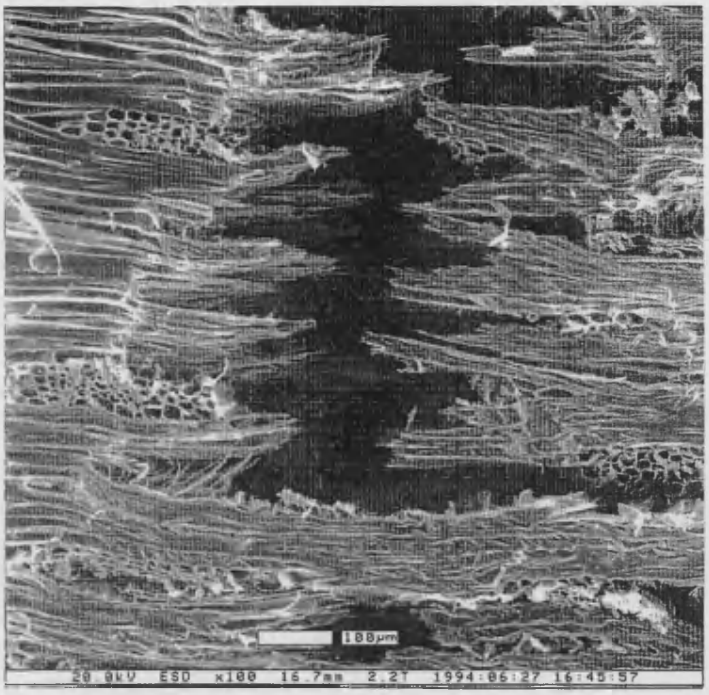

Fig.16.31. Khaya pre-fatigued at R=10 (compression). Compression crease which has been pulled apart in the course of the in-situ loading test.

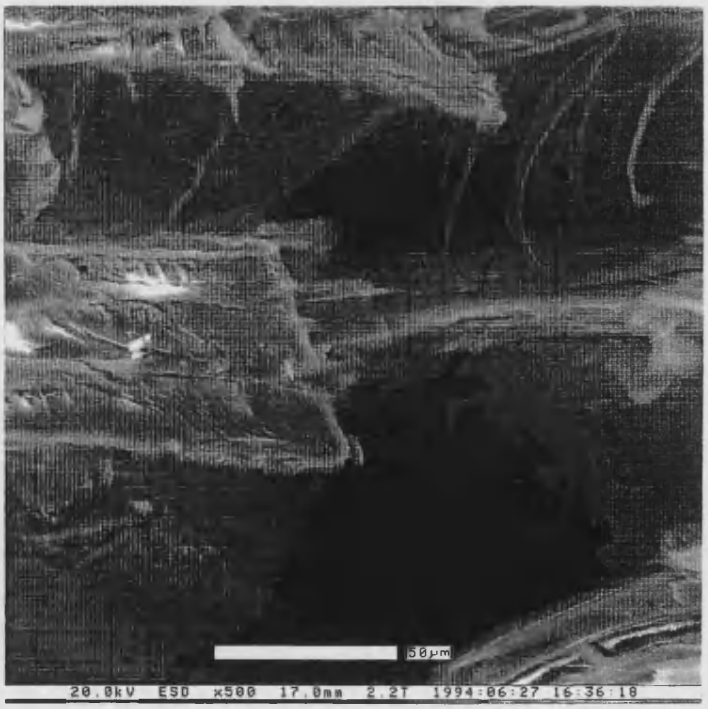

Fig.16.32. Khaya pre-fatigued at R=10 (compression). Blunt failure of fibres in the compression crease.

The fracture is jagged with fibres protruding in clumps from both sides of the failure. At the base of each protrusion of fibres is the remains of a ray bundle. Some of the fibre ends were blunt and wedge-shaped, suggesting that they had failed at the site of a compression crease across them, fig.16.32, whilst others were wispy, indicating that there had been a high level of pull-out of microfibrils from the cell walls as they fractured, fig.16.33.

Fig.16.33. Khaya pre-fatigued at R=10 (compression). Wispy failure of fibres in the compression crease.

16.5.4. Khaya fatigued at R=-1

As the sample had seen both tensile and compressive loading in the course of its initial fatigue test it was expected that the sample would contain types of damage which had been observed in the R=0.1 and R=10 samples. In fact signs of tensile damage were the most obvious of the two with many fibre cell walls containing series of small diagonal cracks along the fibre, as in fig.16.15. In addition, a much higher proportion of ray bundles had been split along their length by debonding between individual ray cells, as in fig.16.14. In terms of compression damage, no compression creases were observed but occasionally fibres were seen to have irregular surface markings or a fibre break. The markings were similar to those shown in fig.16.24 but they were less directional and branched in both directions along the fibre.

One feature which was present in the sample before loading was a crack through a vessel wall, fig.16.34. The crack runs from top to bottom of the vessel, approximately perpendicular to its axis. The crack is kinked and there is a hairline crack adjacent to the main crack which it joins at the kink. Beneath it a longitudinally debonded ray bundle is visible.

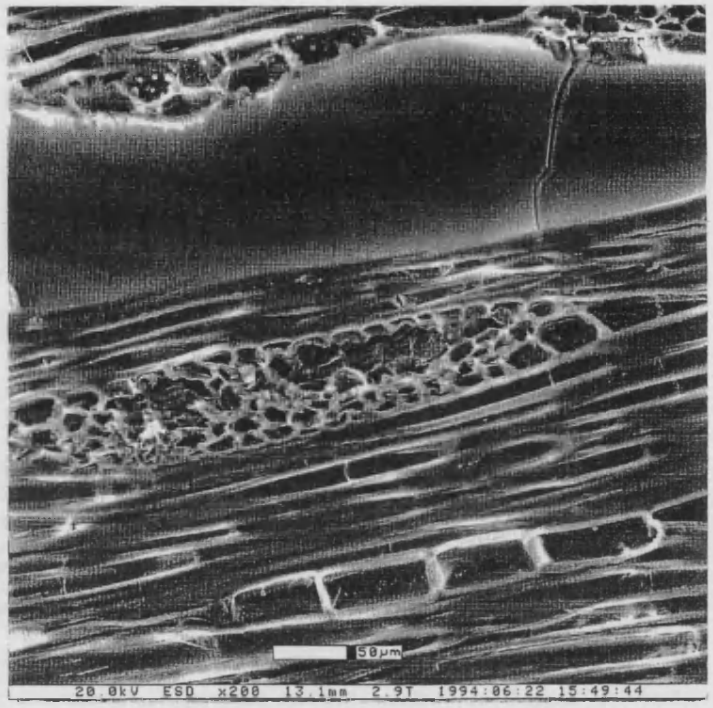

Fig.16.34. Khaya pre-fatigued at R=-1 (reversed loading). Before in-situ loading. Cracked vessel.

The crack is shown at higher magnification in fig.16.35. Before the kink, the surfaces of the crack look completely smooth and thin fibres can be seen bridging the crack underneath. Because of the shallow angle of the bridging material it is likely that they are microfibrils from the S1 layer. The clean cleavage of the cell wall suggests that the S2 layer has fractured in a brittle manner without following the S2 microfibrillar winding angle. At the site of the kink fibre bridging can be seen inside the crack. This is shown more clearly in fig.16.36.

In fig.16.36 it can be seen that there is material spanning the crack in two places. The S1 microfibrils have also been obscured and the crack appears to have a 'floor' to it. It is possible that this is also a bunch of microfibrils which are bridging the crack. The edges of this part of the crack are also rougher than the rest. Once the crack returns to its original direction again, at the bottom of the picture, the cell wall is cracked right through and the S1 microfibrils can be seen again.

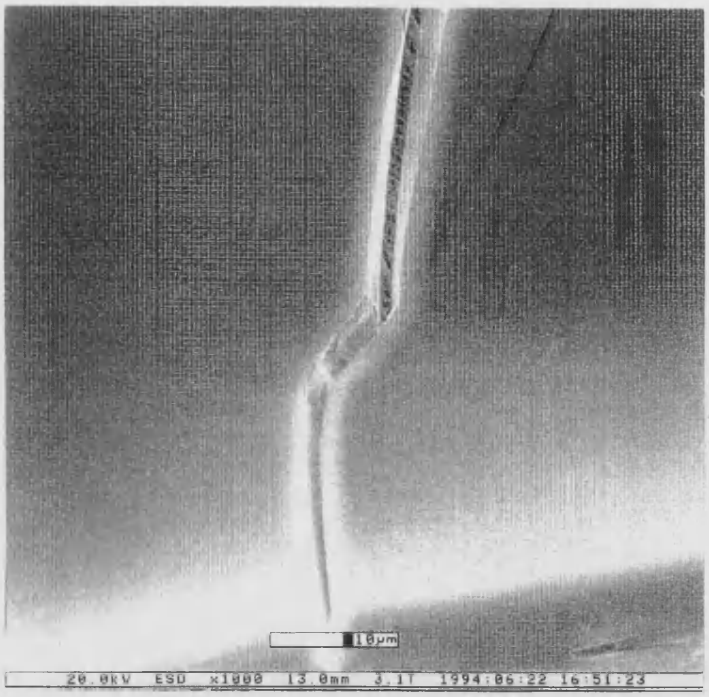

Fig.16.35. Khaya pre-fatigued at R=-1 (reversed loading). Before in-situ loading. Cracked vessel, detail of kink.

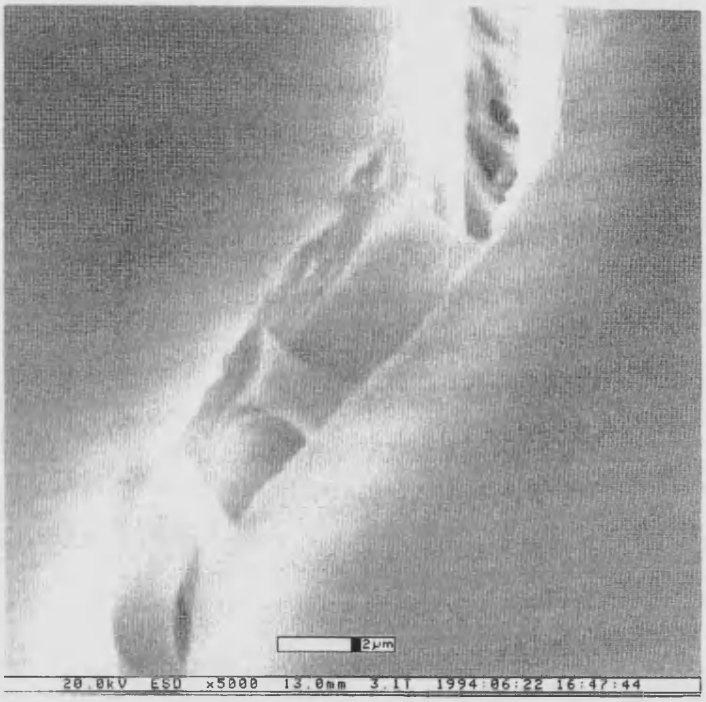

Fig.16.36. Khaya pre-fatigued at R=-1 (reversed loading). Before in-situ loading. Cracked vessel, inside the kink.

When the sample was prepared the vessel wall was cut, revealing a cross-section of the cell wall containing the crack. This is shown in fig.16.37. The crack does not pass

completely through the cell wall thickness but stops just over half way through with a region of delamination within the cell wall, probably between the S1 and S2 layers. The delamination crack is very convoluted which suggests that it absorbed much energy when it was formed. It also suggests that whilst the boundary does have an inherent weakness, the two cell wall layers are well cemented.

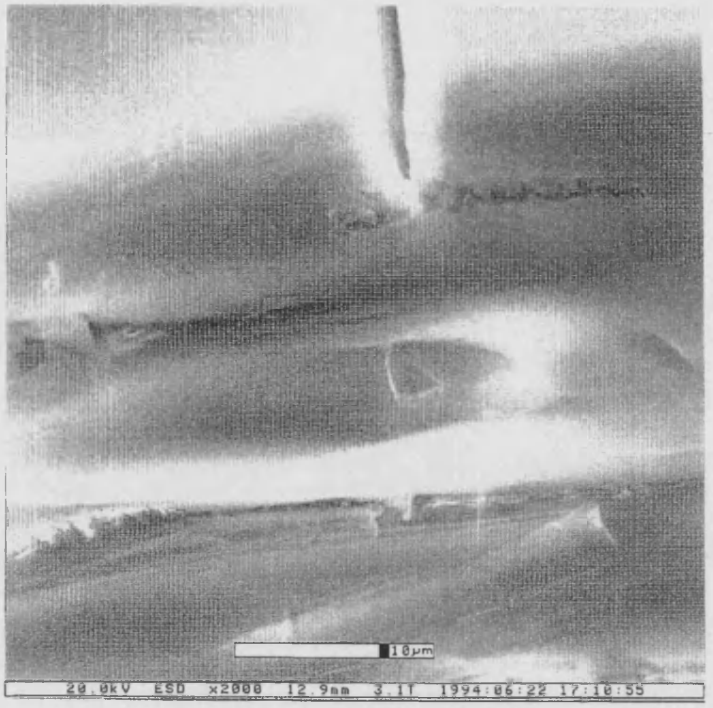

Fig.16.37. Khaya pre-fatigued at R=-1 (reversed loading). Before in-situ loading. Delamination between S1 and S2 cell wall layers in a vessel.

The notch tip was situated in a vessel and as the load was increased cracks developed along its length, fig.16.38. Initially the cracks grew to the right and in the first cell adjacent to the crack they roughly followed the longitudinal fibre direction. In the next vessel the cracks were predominantly diagonal with an angle of about 70.5°, clearly relating these cracks to the S1 layer. The wispy lines, approximately 1-2µm thick, visible in the vicinity of the perforation plate appeared soon after loading had begun. It is possible that they are strands of microfibrils which became detached from the cell wall as a result of cutting during sample preparation.

As the load was increased the crack moved in the opposite direction along the vessel. This is shown in fig.16.39 at 34.15MPa. The cracks are predominantly diagonal, at the same angle as can be seen in fig.16.38. Around the cracks are pale grey regions which suggest that there is intracellular delamination associated with them. One of these cracks breaks across the adjacent ray bundle. No longitudinal cracking along its length

is evident, in contrast to the other samples where the ray bundles served to deflect the crack from growing in the LT to the TL direction.

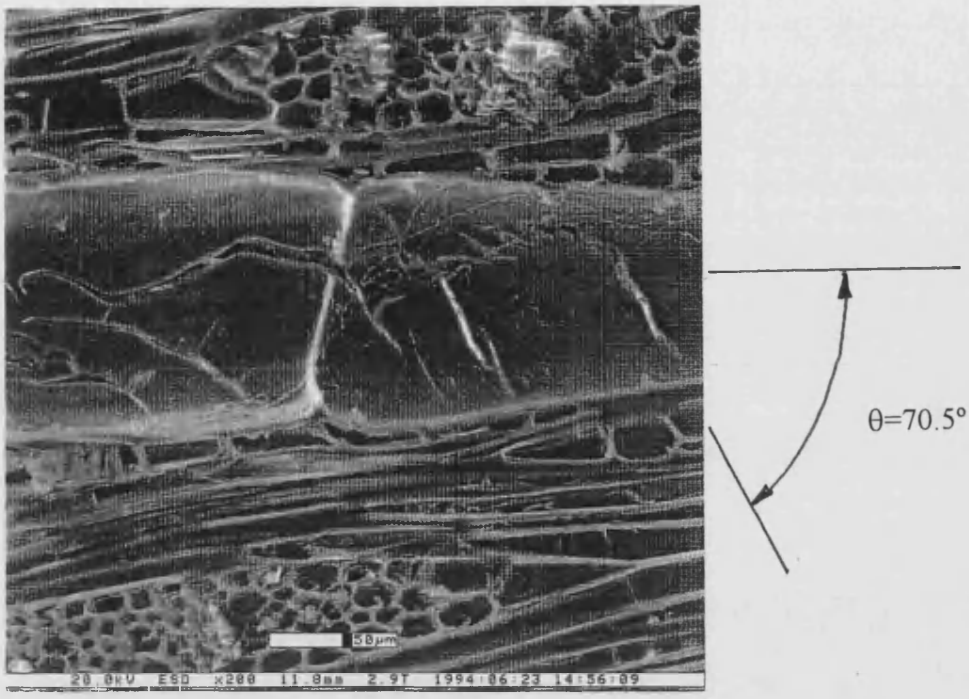

Fig.16.38. Khaya pre-fatigued at R=-1 (reversed loading). Cracking along the vessel to the right of the notch.

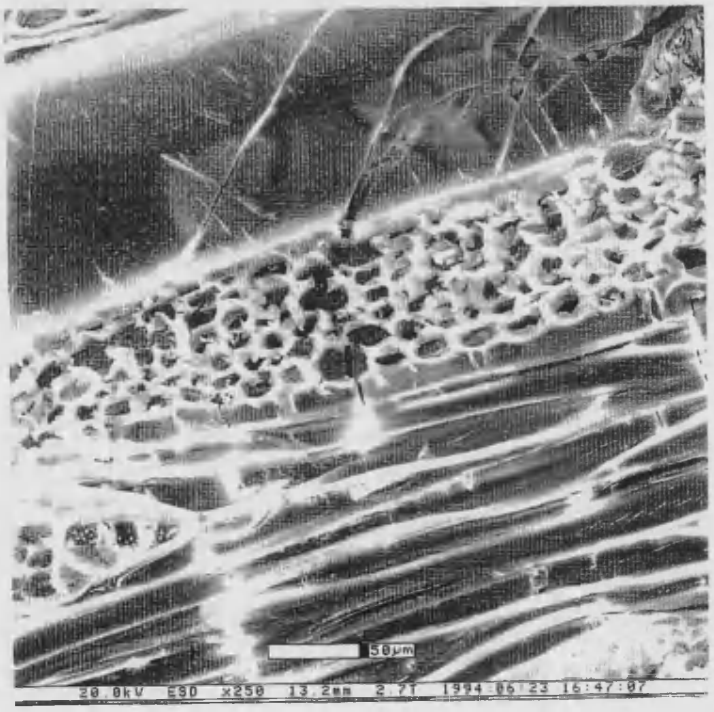

Fig.16.39. Khaya pre-fatigued at R=-1 (reversed loading). Cracking along the vessel to the left of the notch.

Fig.16.40 shows the sample a short time later when the load has been increased by about 2MPa and the second vessel is starting to crack. The first vessel has cracked along its length, in a similar way as the unfatigued Khaya sample in fig.16.14. However, by comparison the edges of the vessel in the R=-1 sample are much smoother and less deformed. No crack propagation along the ray bundles is evident, despite the occurrence of a high proportion of delaminated ray cells along the bundle. It must be assumed that the reversed loading fatigue seen by the sample before in-situ loading has weakened the fibres so that it requires less energy to form a crack across them than along a ray bundle.

Once the load had reached the maximum of 51.33MPa the crack suddenly started to increase in width and sample failure followed rapidly.

Fig.16.40. Khaya pre-fatigued at R=-1 (reversed loading). Extensive cracking close to failure of the sample.

16.6. Summary and conclusions

- Differences in initial damage were observed between the prefatigued samples as summarised in table 16.2. It is clear that different types of damage are associated with tension and compression fatigue and that both are present in the reversed loading situation.

- All prefatigued samples failed at stresses below the mean UTS of Khaya, as measured in Chapter 7. The valid result for unfatigued Khaya was over 109MPa, a

high result even for unnotched Khaya. This results suggests that fatigue reduces the strength of wood, which is as expected.

R ratio	Major damage	Occasional damage
R=0.1	Helical cracking of fibres associated with S2 layer of cell wall.	Longitudinal splitting of ray bundles.
R=10	Small compression creases.	Plastic type deformation on some fibres. Fibre breaks.
R=-1	Helical cracking of fibres associated with S2 layer of cell wall. Longitudinal splitting of ray bundles.	Plastic type deformation on the surface of some fibres. Fibre breaks. S1/S2 intracellular cracking in vessels

Table 16.2. Summary of initial damage states of prefatigued samples.

- The levels of crack growth before failure were much higher in the prefatigued samples. This suggests that fatigue loading also reduces the wood's insensitivity to notches.

- It is likely that fatigue loading reduces the inherent strength of the fibres and lowers the interfacial strength of the middle lamella.

- The unfatigued Khaya showed a typical tensile failure. The crack extended only twice before failure, which involved the shearing of the fibres. A regular array of cracks approximately 300μm apart, crossing several fibres, was observed before failure. The fracture path was only slightly influenced by the ray bundles.

- For the sample prefatigued at R=0.1, fracture along the length of ray bundles was a characteristic feature. The cracking of fibres was more dispersed. This implies that tensile fatigue weakens the middle lamella, reducing its shear strength and ability to transfer stress. Therefore failure of individual fibres occurs at their weakest points.

- Conclusions cannot be drawn for the sample prefatigued at R=10 because failure was controlled by the macroscopic compression crease. However, it was possible to confirm that compression creases initiate from ray bundle ends where the lateral support is at its lowest.

- Compression creases were seen to contain flattened ray bundles, collapsed vessels, gross plastic deformation of fibre cell walls and debonding between fibres.

- The sample prefatigued at R=-1 was the only one to exhibit intracellular failure between the S1 and S2 layers. This is because the relative motion of the two layers is likely to be at its highest where the loading direction is reversed. The S2 layer is responsible for the wood's high tensile strength and the S1 layer provides its compression resistance.

- The crack was not deflected by ray bundles after fatigue at R=-1, even though the majority had been split along their length.

- Cracks tended to cross several fibres, with a spacing of approximately 100μm, as opposed to the more dispersed mode for the R=0.1 sample. Over 50% of these cracks started from the end of a ray bundle. This suggests that the sites of fibre cracking have been determined by the presence of compression damage.

17. ALTERNATIVE ADHESIVES FOR WIND TURBINE BLADES

One of the major objectives of this work was to investigate cheaper materials for the manufacture of wind turbine blades. The approach is two-fold: firstly, the investigation of cheaper constituent materials, namely the adhesives and wood veneers, and secondly, the application of cheaper or more efficient manufacturing methods such as improved methods of joining veneers end-to-end.

17.1. Introduction to adhesives used in wind turbine blades

The adhesives used in the construction of wood composite wind turbine blades is of critical importance to the performance and life of the finished blade. Epoxy has been used successfully in the manufacture of wind turbine blades both in the USA and the UK. At present WEG use about 200kg of two part, room temperature curing structural adhesive in an 18m blade, costing approximately £1000 per blade.

Epoxies have excellent cohesive strength and will adhere well to most materials, including wood. Their moisture resistance makes them suitable for the harshest of outdoor applications. However, they are not a widely used wood glue because of their high cost in comparison to other glues which have adequate properties, table 17.1.

Adhesive	Cost per mixed kg, £
Epoxy	5
PRF	2.6
MUF	1.5
UF	1.0
PVA (1 part)	1.4

PRF= phenol resorcinol formaldehyde
MUF= melamine urea formaldehyde
UF= urea formaldehyde
PVA= poly vinyl acetate

Table 17.1. The cost of various adhesives. (From data supplied by manufacturers, Appendix F)

The bond epoxy forms with *Khaya ivorensis* is stronger than the wood itself and the laminate has been seen to perform well in fatigue. However, epoxy is used in wind turbine blade manufacture because it was originally used in the USA where the technology was developed and where it is considerably cheaper. As the blades

consistently over-perform there is clearly scope for making cost savings by switching to a lower performance, less expensive adhesive system.

The range of adhesives which may be used with wood is extensive and includes elastomers, thermoplastics and thermosetting resin systems, table 17.2. It is important with such a wide range of adhesives that the correct one is used in a particular application. The bond must meet the strength requirements and survive the environmental conditions it will experience without weakening (Hansone, 1975). It must also be compatible with the manufacturing process.

Of the list of adhesives in table 17.2 the ones which are used most commonly with wood are the amino (UF) or phenolic (PF) resins, their derivatives and PVA. Slightly less common ones include isocyanates and epoxy. The other adhesives listed have wide ranging applications but in terms of volumes consumed per year are much less significant.

	Thermoset Resins									Elastomers					Thermoplastics			Other
	Urea-formaldehyde	Melamine/urea-formaldehyde	Phenol-formaldehyde	Resorcinol/phenol-formaldehyde	Tannin-phenol-formaldehyde	Tannin-formaldehyde	Sulfite liquor	Diisocyanate	Cross-linked polyvinyl acetate	Polychloroprene (contact)	Polychloroprene (gap)	Polyacrylonitrile-styrene	Styrene-butadiene rubber	Neoprene	Ethylene vinyl acetate	Polychloroprene latex	Polyvinyl acetate emulsion	Cement
Standard Abbreviation	UF	MUF	PF	RF	TPF	TF	SL	MDI	PVA				SBR				PVA	
Laminated beams Prefabricated trusses	4	4	1	1	1	1												
Boat building		2	1	1														
Window frames Exterior doors		2	1	1	1	1			2									
Joinery on site	3	2							2		3	3	3	3			3	
Interior doors	3								2								3	
Furniture	3	2									4				3		3	
Wood veneering	3	2							2	3					3	3	3	
Waferboard manufacture		1	1															
Particleboard manufacture	3	2	1	1	1	1	1	1-3										1
Plywood manufacture	3	2	1	1	1	1												
MDF manufacture	3																	
Wood wool cement slab manufacture																		1

1. suitable for full exposure to weather or water immersion
2. suitable for intermediate conditions between 1 and 3
3. Suitable for use inside heated and ventilated buildings, and environments where the equilibrium moisture content of softwood does not exceed 18% and the bond line remains below 50°C.
4. Could be suitable in special cases but not used in general practice.

Table 17.2. Adhesives for bonding wood to wood (Pizzi, 1983).

The basic chemistry of the major systems is outlined in section 17.2.

17.2. Adhesive bonding of wood

The bonding of wood has been an important process since the times of ancient Egypt where decorations of inlaid wood veneer glued with animal glue were made for the Pharaohs. Since then adhesives have been widely used with wood in both structural and decorative applications. Until the 1930s the adhesives were mostly natural, being based on substances such as casein (milk protein), starch (vegetable carbohydrate) and fish and animal proteins. These have now been completely replaced by synthetic polymeric adhesives with superior properties, particularly in terms of moisture and temperature resistance.

Glued wood products range from fibreboard, where moist fibres fibres are sprinkled with droplets of resin and compressed by heat and pressure into a board, to huge structural laminated members such as glulam roof arches. The performance of glued wood products is influenced by temperature and humidity along with the wood particle size and geometry and the manufacturing process employed. It is important to consider all these when chosing an adhesive to produce a successful wood composite or structural joint.

17.2.1. Mechanisms for adhesion in wood composites

Before an adhesive wood joint can be formed the adhesive must wet the surface of the wood. At the start of the bonding process the adhesive's viscosity needs to be such that it can flow controllably over the rough surfaces of the wood and wet, penetrate and be absorbed into the wood fibres. Strong adhesive forces between the wood fibres and the adhesive are necessary if the adhesive is to displace contaminants and adhere to the wood fibres. If the wetted adherends are held in close contact and the polymerization process is promoted, either by the application of heat or by catalysis, a sound bond should develop.

The actual bonding between the wood and the adhesive is attributed to a combination of three mechanisms:

1. *Mechanical interlocking*. This involves the intertwining of wood fibres and polymer molecules. It occurs when the adhesive wets the wood and penetrates beyond the damaged fibres at the wood surface. It is thought that penetration between two and six fibres deep into the wood and penetration of fibre walls is necessary for durable structural bonds (Slaats, 1979).

2. *Physical attraction.* The formation of hydrogen (H) bonds and van der Waals forces cause strong physical attraction between wood fibres and adhesive. Physical adsorption, especially between polar -OH groups on the fibre wall and the adhesive's polar groups can be particularly strong. It is considered by many chemists to be the primary bonding mechanism and since it causes the first step of bonding, namely the wetting and adsorption of the polymer into cell walls, it is undeniably important.

3. *Covalent chemical bonding.* The formation of covalent bonds by the sharing of electrons between wood fibres and adhesive molecules is likely to occur in cross linking systems. However, the importance of covalent bonds in terms of producing waterproof bonds is uncertain.

17.2.2. Factors influencing bond formation

Several thermodynamic and kinetic factors influence the process of bond formation between the fibre and adhesive, eg. surface wetting and adhesive penetration into the substrate. A problem with any factor could result in an unsatisfactory bond.

Good wetting is synonymous with close molecular contact between substrate and adhesive. In general, if the Gibbs free surface energy of an adherend is higher than that of the adhesive system, wetting is likely to occur. The free energy of wood is difficult to measure because it is influenced by factors such as extractives, porosity and surface roughness. It is maximised, however, by using a freshly cut wood surface free from non-polar extractives. Adhesive systems containing aqueous OH- or phenol groups will cause swelling of the wood fibres which increases surface wetting and penetration.

Once the wood surface has been wetted, penetration of the fibres and cellular structure must occur and this is a diffusion-based process. In the case of water-based systems or thermosetting condensation polymers such as PRF or UF, where water is a by-product of cure, the water at the glueline will also diffuse into the wood, taking low molecular weight polymer fractions into the wood microstructure. If the water cannot diffuse away the formation of a good bond will be impaired.

It is important that the adhesive is applied evenly without regions being starved of resin. The required temperature and pressure must then be applied to enable the adhesive to cure fully and reach its maximum strength.

17.2.3. Wood as a substrate

The structure of a wood surface is always rough as a result of its cellular structure. Growth rings present different regions of density, porosity and penetrability. The

preparation of wood surface for bonding will involve a variety of mechanical or thermomechanical processes, all of which cause gross damage to the cell structure and increase the overall surface roughness. Such irregularities could hinder adhesive bonding since the adhesive must penetrate undamaged wood fibres for good bonding. Also the wood to wood contact must be less than the diameter of a fibre for durable adhesive bonds to form (Pizzi, 1983).

The wood surface is not only texturally rough but chemically heterogeneous as well. A cut wood surface will contain cell cavities, severed cell walls and middle lamella surfaces. The chemistry of each type of surface could be critical to bonding in certain situations. The carbohydrate in cell walls is highly polar whereas lignin is less so and could be wetted less extensively by a polar adhesive. The presence of extractives could also interfere with the bonding process by preventing resin penetration or by disrupting cure (Skeist, 1989).

17.3. Adhesive systems

The chemistry of the major wood adhesives are outlined in this section. They include, amino resins, phenolic resins and polyvinyl acetate. Two less common, but important, adhesives which have wood gluing applications are also presented, namely isocyanates and epoxies.

17.3.1. Amino resins

Amino resins are prepared by reacting formaldehyde with a compound containing the amino group, $-NH_2$. The most commonly used amino compounds are urea and melamine, fig.17.1.

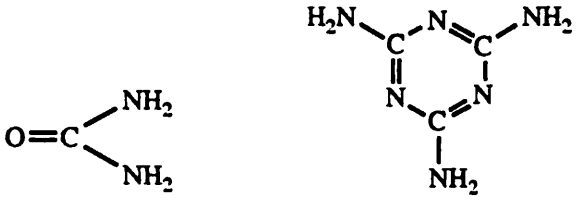

urea melamine

Fig.17.1. The structure of urea and melamine.

Amino resins are widely used in the production of particleboard, plywood and in the assembly of furniture. They are water soluble before curing which makes them easy to apply to a substrate. Other advantages include colourlessness, hardness, good solvent and heat resistance as well as low cost. However, they may release toxic formaldehyde during and after curing. Water resistance is a problem for products made with UF as it

is susceptible to hydrolytic degradation, especially at high temperature (Pizzi, 1983). MF resin is much more resistant to moisture and is used successfully in outdoor conditions. MF is more expensive than UF so it is diluted with UF to produce a resin with intermediate properties and cost, MUF.

Two major chemical reactions are involved in the bonding of amino compounds with formaldehyde to produce a cured amino resin. Firstly, formaldehyde adds to the amino group which introduces the hydroxy-methyl group (methylol) group, eq.17.1.

$$RNH_2 + HCHO \rightarrow R\text{-}NH\text{-}CH_2OH \qquad \text{eq.17.1}$$

Secondly, the hydroxy-methyl group combines with an active hydrogen to release a molecule of water, eq.3.2. Depending on the degree of polymerization this will produce a dimer, trimer, a polymer chain or a vast polymer network.

$$R\text{-}NH\text{-}CH_2OH + H_2NR \rightarrow RNH\text{-}CH_2\text{-}NHR + H_2O \qquad \text{eq.17.2.}$$

These reactions must be carefully controlled to produce a successful amino resin. The first reaction occurs during the manufacture of the resin and will occur in either acid or basic conditions whilst the second is the curing reaction and is catalysed by acid. The resin is part cured during production to prevent crystallisation of the monomeric methylol compounds. Once the desired degree of polymerization has been achieved the resin is dried by vacuum distillation to give a liquid of the desired viscosity, or a solid which can then be ground to a powder and stored until it is needed. The amino resin is used as an adhesive by reactivating the curing reaction with an acid catalyst at the site of the joint (Pizzi, 1983, 1989, Landrock, 1985, and Skeist, 1989)

17.3.2. Phenolic resins

A phenolic resin is one which has been formed between phenol or substituted phenols during condensation with formaldehyde. Phenol formaldehyde (PF) is the most commonly used adhesive in plywood and waferboard production. 98% of softwood plywood was bonded with PF in the USA in 1980 (Paxton, 1992). It is also used in the manufacture of glulam beams and wooden boats. There are two types of phenolic resin, namely resols and novolacs. A resol is formed in the molar ratio of formaldehyde to phenol is greater than one, and a novolac is formed if this ratio is less than one. The chemical reaction conditions can be controlled to produce resins with a huge range of different properties for diverse applications.

Novolac resins are generally referred to as two step resin systems since another reactive component must be present in order to effect a cure. This can be a resol, an aminophenol or, most frequently, hexamethylene tetramine (HMTA). The reaction mechanism depends on the pH of the medium in which it occurs. The formaldehyde dissociates, eq.17.3, and reacts with phenol to produce methylol phenol, eq.17.4. This is a fast reaction in a strongly acid medium.

$$HO\text{-}CH_2\text{-}OH + H^+ \leftrightarrow {}^{\cdot}CH_2\text{-}OH + H_2O \qquad \text{eq.17.3.}$$

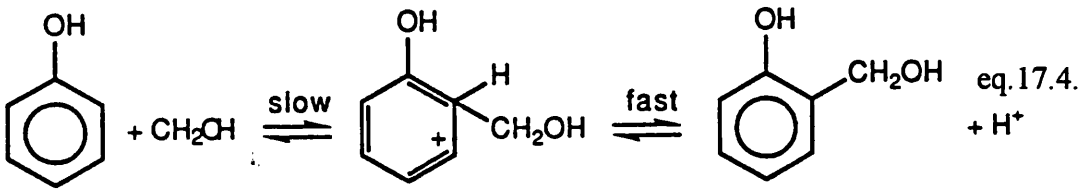

eq.17.4.

The methylol group is then converted to a carbonium ion, eq.17.5, which will readily react with phenol to form a dihydroxydiphenylmethane, eq.17.6.

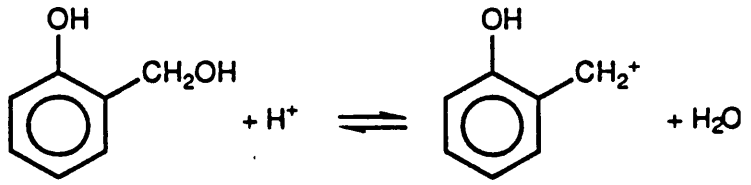

eq.17.5.

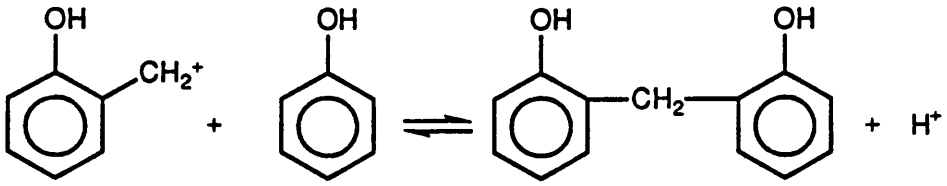

eq.17.6.

Such molecules are stable to molecular weight gain because they do not contain any active methylol groups.

HMTA cures the resin under the action of heat and moisture by breaking down to produce ammonia and formaldehyde. Whilst most of the ammonia escapes, the formaldehyde forms methylene bridge linkages in the resin. This converts the novolac resin from a low molecular weight thermoplastic into a cross-linked thermoset resin. The principle application of novolac resins is for the bonding of oriented strand board, OSB (Paxton, 1992).

In contrast to novolacs, resols contain methylol end groups and are very reactive. They are one stage thermosetting resins which are irreversibly cured by the application of heat and pressure. The majority of resols are reacted in a basic medium and are dependent on the nature of both the phenol and the formaldehyde. The two main reaction mechanism steps are methylolation, eq.17.7, and condensation, eq.17.8.

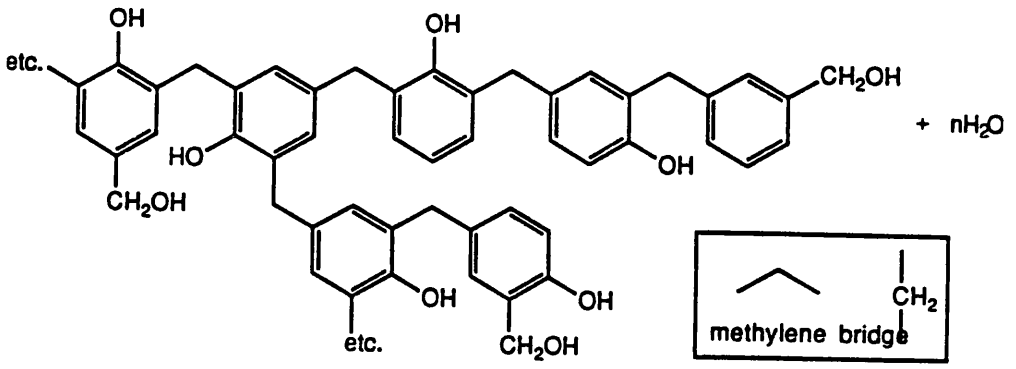

eq.17.7.

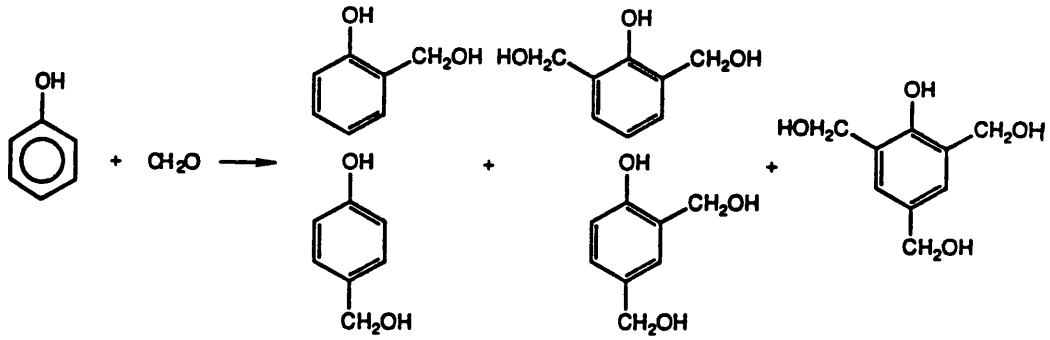

eq.17.8.

The combination of addition and condensation reactions produces a polymer network which is the basis of the resin system.

Resorcinol is a derivative of phenol with a higher reactivity. It is used to partially replace phenol in a resin in order to increase the resin cure rate. PRF is used in applications such as lumber laminating where ambient temperature curing is required. It forms bonds which are water- and heat-resistant and are rated for outdoor applications (Pizzi, 1983).

17.3.3. Polyvinyl acetate

Polyvinyl acetate is a thermoplastic polymer which is capable of producing strong and durable bonds between woods and wood derived composites. It is versatile and widely used, readily available and of low cost. It adheres to most surfaces and has a fast setting speed. This is because it has a high solids content which means that only a small amount of water is required to give it a suitably low viscosity for applying to the substrate.

The vinyl acetate monomer from which it is produced is synthesized from ethylene and acetic acid in a vapour phase reaction. Typically, the polymer is produced from the monomer by emulsion polymerization methods and for the production of wood adhesives the PVA particle size is controlled so it is relatively large. Once applied as an emulsion to a wood substrate the bond develops by the loss of water from the joint to form a continuous film of PVA. The polymer chains are of high molecular weight and are usually linear, fig.17.2.

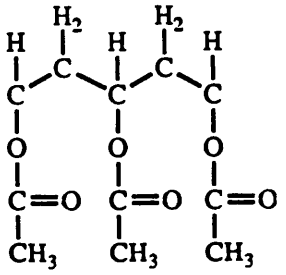

Fig.17.2. The structure of PVA.

In this form PVA has a low creep resistance and can only be used for non-structural applications such as bonding veneers (Paxton, 1992). Properties can be improved if the polymer is made to branch during polymerization (Skeist, 1989) or if extensive cross-linking is induced during drying (Pizzi, 1983). Both of these changes can be induced by the addition of a catalyst to the adhesive mixture. Branched and cross-linked PVAs have increased tensile strength and toughness as well as water and creep resistance. However, Pizzi (1983) states that creep can still occur in cross-linked PVA even after 14 days when the full strength has developed. He suggests that its use should be restricted to non-structural applications.

Fully cross-linked PVA adhesives are available in one and two part systems. The two part systems have superior mechanical properties and are the more water resistant. However, they are considerably more expensive and require mixing before use.

17.3.4. Isocyanates

Until recently there has been no serious commercial interest in isocyanate adhesives because of their high cost, hazardous nature and problems such as their ability to bond to metal platens during the pressing of board products (Paxton, 1992). The demand for high quality particle board which does not emit formaldehyde, along with recent technical developments, has led to the production of isocyanate binders for particleboard manufacture. The adhesive properties of isocyanates are based mainly on the reactivity of the NCO groups and their ability to covalently bond with -OH groups in the cellulose in wood cell walls. This bond is very strong and resistant to water and dilute acids.

However, isocyanates are extremely expensive and are generally used where their impressive properties enable the quantity of adhesive to be reduced considerably, thus offsetting their high cost.

17.3.5. Epoxies

Epoxy resins are high performance structural adhesives and are used in applications where high strength and endurance properties are essential. Because of this epoxies are the most widely used thermosetting plastic available. They can be obtained either as two part room temperature curing or one part high temperature curing systems. The range of resin types, hardeners and modifiers is considerable and must be selected according to the anticipated service conditions. Such high performance characteristics are usually considered unnecessary for epoxies to be widely used in applications involving wood. Cheaper phenolics or amino resins are generally used instead. However, because it is an epoxy which is used in the production of wood composite wind turbine blades, an outline of the chemistry and properties of epoxies will be given below.

In the unhardened state an epoxy resin's chemical structure is characterised by the epoxide group, fig.17.3.

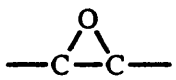

Fig.17.3. An epoxide group.

The most widely used epoxy resins are based on Bisphenol A and epichlorohydrin. Its chemical structure is shown in fig.17.4.

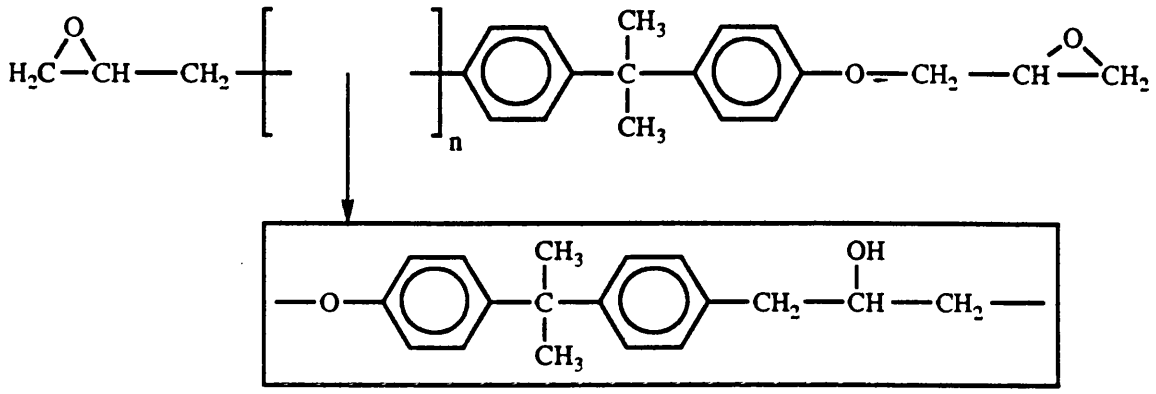

Fig.17.4. The structure of an epoxy resin molecule.

An epoxide group is present on each end of the molecule which remains difunctional as its molecular weight increases during polymerization. Because epoxies are 100% reactive, no volatiles are produced and no shrinkage occurs during cure. The polymerization reaction is exothermic and measures must be taken to avoid heat build-up in the pot by mixing only small batches of resin, mixing in shallow containers or by cooling the mixture. If the temperature of the resin is allowed to rise it will cure in the pot in an unstable manner. In general pot life ranges from a few minutes to several hours. The adhesive then takes up to 24 hours to cure at room temperature and as little as 20 minutes at 100°C. The hardener used determines the curing schedule and also affects the solid resin's properties and consequently must be chosen with care. Hardeners used for bisphenol A epoxies are most commonly polyamides and anhydrides.

17.4. Experimental techniques

In service, the laminating gluelines experience mainly shear forces as a result of the bending of the blade. Consequently it was decided that the shear strength of the glueline was an appropriate property with which to compare alternative adhesive systems.

Adhesive manufacturers were approached and samples of phenol resorcinol formaldehyde, PRF, melamine urea formaldehyde, MUF, urea formaldehyde, UF, cross-linked poly vinyl acetate, PVAc, and phenol formaldehyde, PF, were obtained. A sample of the epoxy used in blade manufacture was also obtained from WEG. Details of how to use each adhesive system are presented in table 17.3.

As a first attempt a simple lap shear method was used, fig.17.5. The joint is loaded in tension and the adhesive layer experiences a shear stress as it transfers the load from one substrate to the other. However, the application of the load is not symmetrical and

the joint bends as the load is applied, fig.17.6 (Bullen and Van der Straeten, 1986). Tensile forces are set up which tend to peel the joint apart. The stress concentrations at the end of the glueline is very high and leads to premature failure of the joint. The stress concentration for various lap joint designs are presented in fig.17.7. It is clear that the single lap joints, fig.17.5, have the highest shear stress concentrations at each end.

Adhesive and Supplier	**Name**	**Components**	**Mixing ratio**	**Assembly time at 20°C**
Epoxy SPS	SP110/210 standard curing rate	Resin hardener microfibre filler	3 wt 1 wt 25% vol	20 mins
PRF Borden	Casocphen Resorcinol	Aqueous resin solution, powdered hardener	5 wt 1 wt no extra filler	70 mins
PRF Dyno	Aerodux 500	Liquid resin Liquid hardener	1 wt 1 wt optional extra filler	2 hrs (medium speed)
MUF Dyno	Aerolite 308 Hardener GPBX or GBQX	MUF powder Hardener (formic acid solution)	100 wt 30-35 wt water 12 wt GBPX or 16 wt GBQX	1 hr
UF Dyno	Aerolite 306 Hardener GPBX or GBQX	UF powder Hardener (formic acid solution)	2 wt 1 wt water Hardener applied to adherend	15 mins
PVA Britannia	--	White liquid	--	not given
PF BP Chemicals Ltd.	Cellobond J2027L	Red resin Phencat 10 catalyst	6% wt catalyst	18 mins
UF Humbrol	Cascamite	White powder water	2 wt powder 1 wt water	1hr 30 mins

Table 17.3. Data for the adhesives tested.

Adhesive and Supplier	Mixing and application	Closed time	Pressure	Comments
Epoxy SPS	Mix resin and filler, add hardener, mix and apply.	8 hrs	Not specified	Clean up with acetone. WBP gap filling.
PRF Borden	Mix and stand to deaerate. Apply, leave to soak into wood for 70 mins before closing joint.	4 hrs	Sufficient to exclude air and maintain close contact	Clean up with water. WBP gap filling.
PRF Dyno	Mix and apply.	5 hrs	As above	Clean up with water. WBP gap filling.
MUF Dyno	Add water to powder, stir and stand. Add hardener.	1.5 hrs	Not specified	Clean up with water. BR gap filling.
UF Dyno	Mix resin and water, stand and apply to one adherend. When tacky apply hardener to other joint. Close.	2.25 hrs	Sufficient to firmly position joint	Clean up with water. MR gap filling. Avoid iron contamination.
PVA Britannia	Apply and close joint.	not given	Not given	Intermediate
PF BP Chemicals Ltd.	Add catalyst to resin slowly. Stir. Apply and close joint.	17 hrs	Not given	This phenolic is essentially for production of fibre reinforced composites.
UF 'Cascamite' Humbrol	Mix 1pt water to resin, mix, add 2nd part water.	6 hrs	Not given	Standard off the shelf wood working adhesive. Water and damp resistant.

WBP = Weather-proof and boil-proof

BR = boil resistant

MR = moisture resistant and moderately weather resistant

Intermediate = Properties between WBP and MR (BS 1204, 1979, BS 5442, 1979)

Table 17.3 continued. Data for the adhesives tested.

From the single lap shear tests the shear strength of the joints was found to be approximately 4MPa. All the samples had failed in the wood adjacent to the glueline. However, given that the shear strength of *Khaya ivorensis* was found to be 9.6MPa

(Bonfield, 1991) it was clear that additional forces were acting on the glueline and causing failure at much lower stress levels.

In order to measure the shear strength of the various adhesive joints in the absence of large stress concentrations and peel forces the method of block shear testing was adopted.

The aim of the static block shear testing was to identify suitable adhesives for use in fully laminated samples. Adhesives which were eliminated from the investigation at this stage were either of low strength or were incompatible with the manufacturing process.

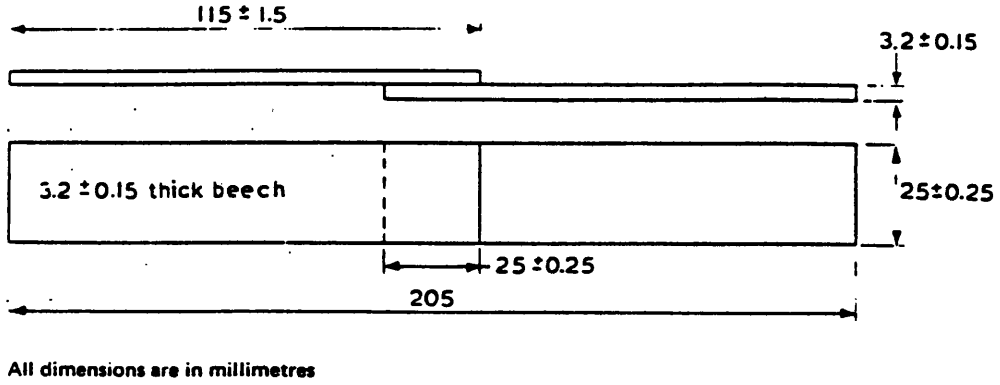

Fig.17.5. Simple lap shear close contact joint. BS 1204: Part 1 (1979).

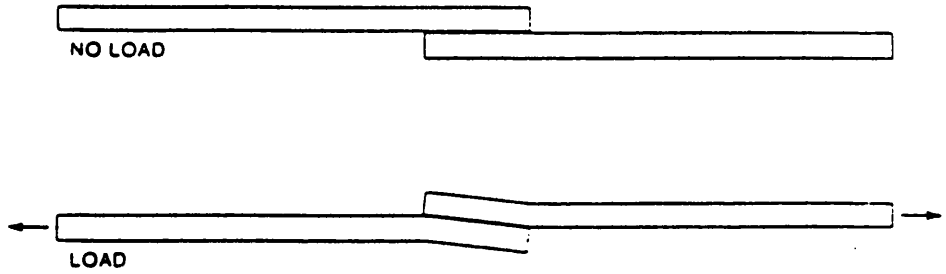

Fig.17.6. Asymmetric loading of a simple lap joint (Bullen and Van der Straeten, 1986).

17.4.1. Block shear testing

Laminated blocks of Khaya were bonded together as shown in fig.17.8 and a shear force applied to the glueline using a jig as specified in BS 4169 (1988), fig.17.9. An Instron 1195 was used to apply a load with a cross-head speed of 1mm min^{-1}. The maximum load applied to the sample was recorded by the Instron and from this the shear strength of each sample was calculated. Four or eight samples were tested for each adhesive and the mean shear strength calculated.

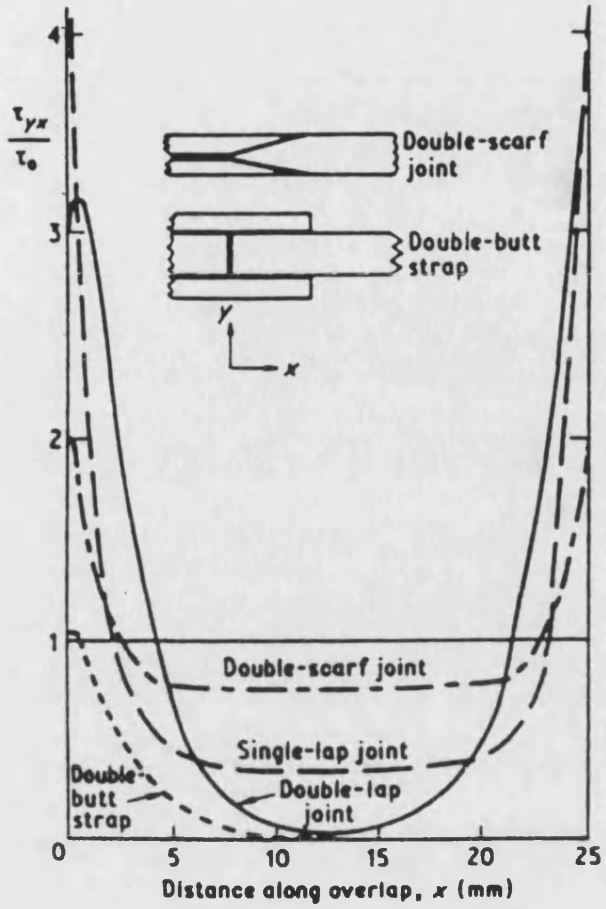

Fig.17.7. Shear stress concentrations for various lap joint designs (Kinloch, 1987).

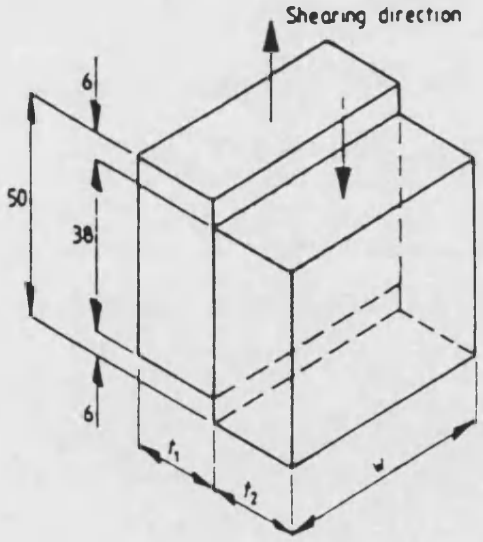

t_1 and t_2 are the thicknesses ≥ 20mm, w is the width ≥50mm

All dimensions are in mm

Fig.17.8. Dimensions of test specimens for glueline block shear test, BS 4169 (1988).

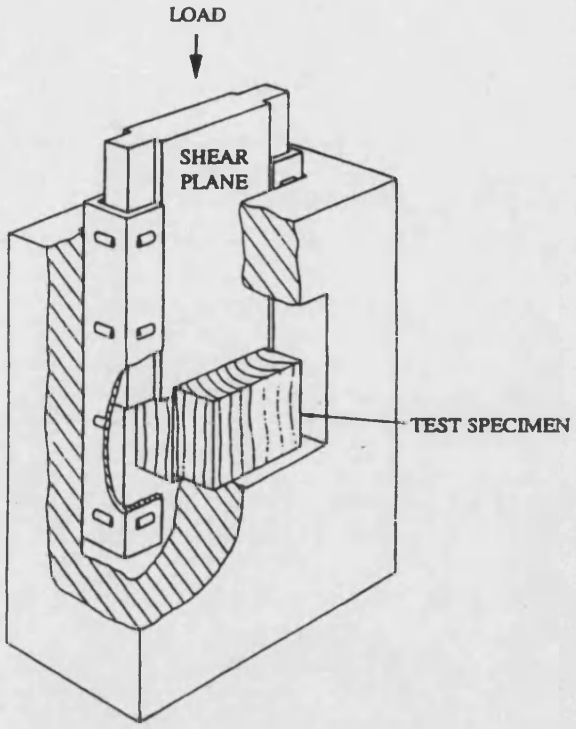

Fig.17.9. Block shearing jig. BS 4169 (1988).

All the surfaces of failed block shear samples were investigated under an optical microscope. Photomicrographs were taken of typical fracture faces. Small samples of each type of adhesive glueline were prepared for investigation in a scanning electron microscope (SEM). 5mm cubes were cut from the block shear samples and a smooth surface through the glueline was prepared by soaking the cubes in water and microtoming them. They were then dried and sputter-coated with gold. Electron micrographs were then taken in the Jeol T330 SEM.

17.4.2. Static and fatigue testing

The adhesives which were of sufficiently high performance and were compatible with the manufacturing process were used in the production of fully laminated samples. These comprised five pre-scarfed Khaya veneers with an outer glass-epoxy coating and were cut to the shape shown in fig.17.10.

Static and fatigue testing were carried out on the Mayes 20 tonne servohydraulic fatigue rig. Five samples of each type were used to obtain mean values for the ultimate tensile strength. Valid tensile failures were obtained in the necked part of the sample. Once the static testing was complete fatigue tests were carried out to generate S-N data at R=-1 for each adhesive system. A constant loading rate of 400MPa.s^{-1} was used and

the moisture content of the sample kept constant at 65%RH. The number of data points obtained was limited by the small number of samples available.

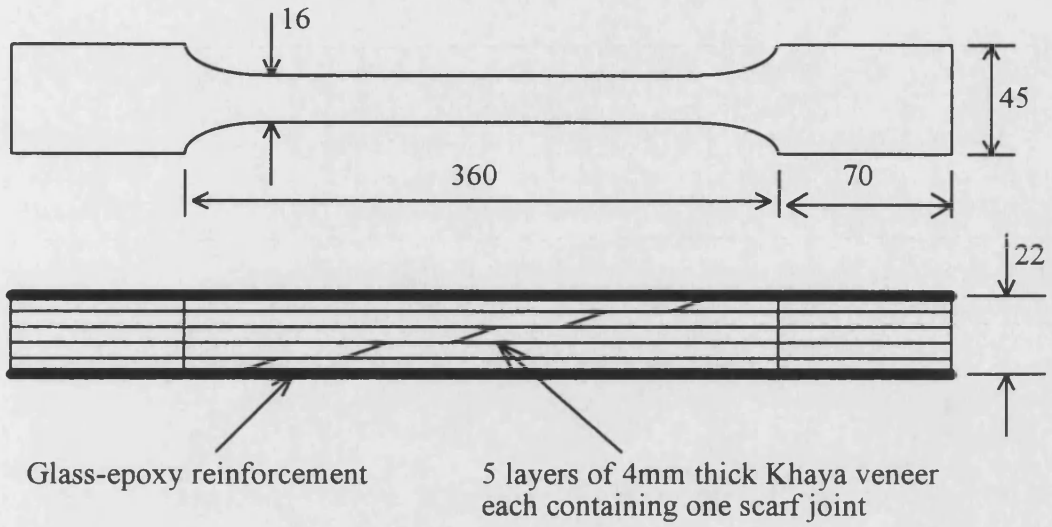

Fig.17.10. Sample geometry of fully laminated samples for static and fatigue testing.

17.5. Results

The shear strengths of the different adhesive joints measured by the block shear method are presented in table 17.4, with values ranging from 6.2MPa for PRF (Borden) to 13.0MPa for Cascamite. It was observed that the samples failed by wood shear away from the glueline (deep wood shear), wood shear adjacent to the glueline (thin wood shear) or by shearing in the adhesive itself. Figs.17.11 to 17.13 are photographs illustrating each type of failure. Fig.17.14 illustrates the different types schematically. In some of the adhesives tested a mixture of the above failure types was observed, but usually one particular type predominated. The adhesives which failed predominantly by deep wood shear were epoxy, PRF (Dyno) and Cascamite. The only adhesive joint to fail by adhesive shear alone was PF (BP) and the remainder failed by thin wood shear.

Micrographs taken through the glueline are presented in figs.17.15 and 17.16. The sections through the glueline were very similar for each adhesive system.

Sample (Supplier)	Block shear strength (Standard deviation) MPa
Epoxy (SPS)	12.5 (1.2)
PRF (Borden)	6.2 (1.6)
PRF (Dyno)	9.1 (0.9)
MUF (Dyno)	9.9 (1.7)
PVA (Britannia)	7.6 (0.8)
PF (BP)	10.7 (1.3)
UF - Cascamite (Humbrol) UF	13.0 (2.1)

Table 17.4. Block shear strengths.

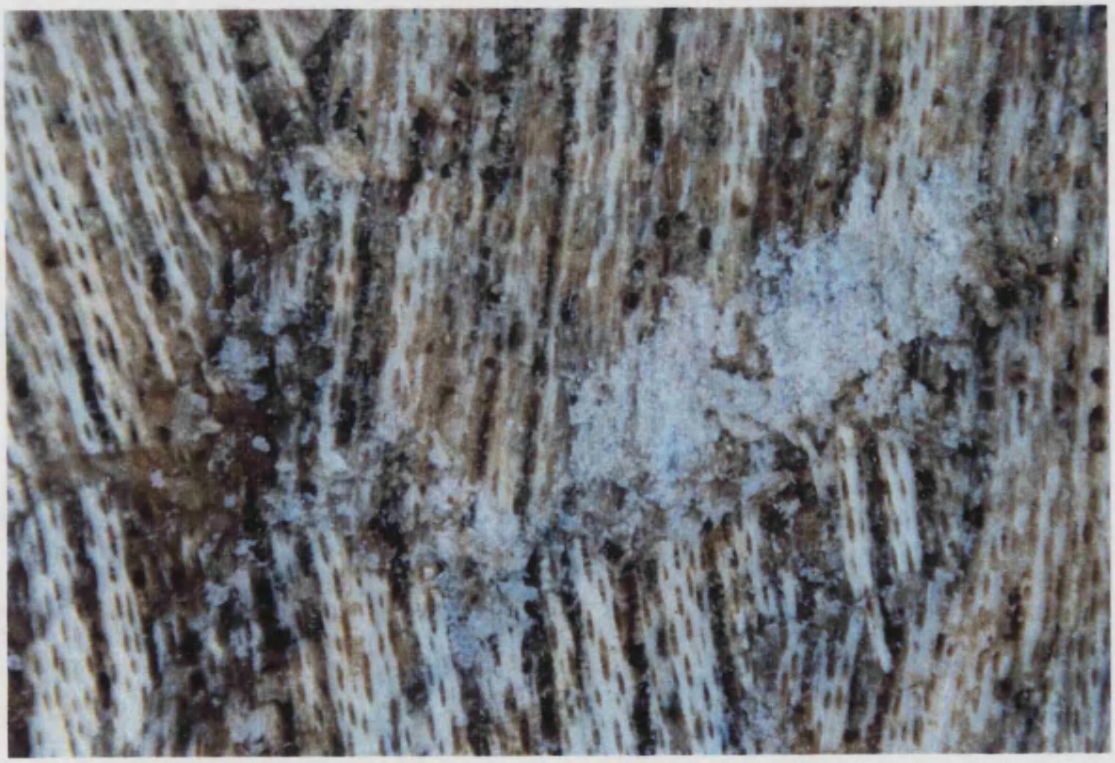

Fig.17.11. Deep wood shear. Epoxy glueline. Regions of deep wood shear are visible, along with white regions of failed epoxy [X 6.5].

Fig.17.12. Thin wood shear failure. PRF (Dyno) glueline. The dark PRF is visible through a thin layer of wood cells [X 6.5].

Fig.17.13. Mixed failure. Adhesive failure alternates with deep wood shear. PRF (Dyno) glueline [X 6.5].

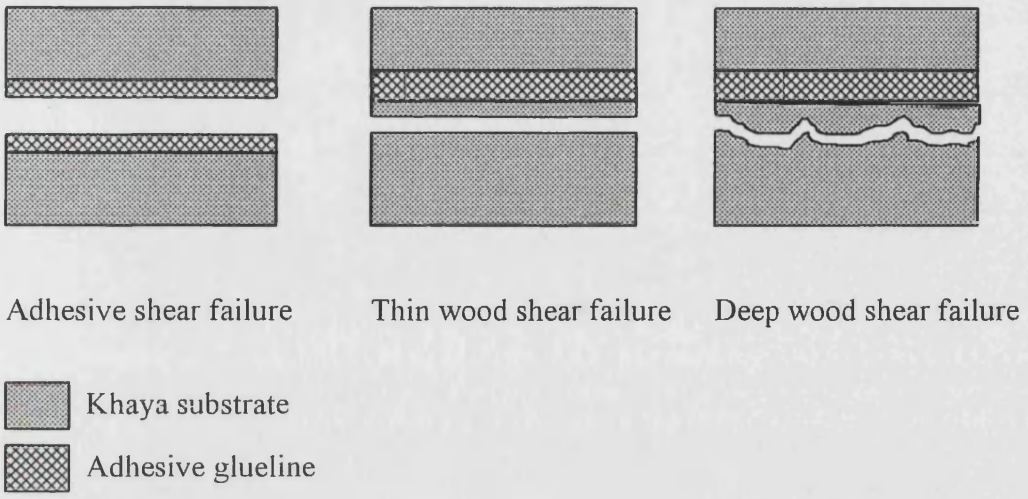

Fig.17.14. Block shear failure types.

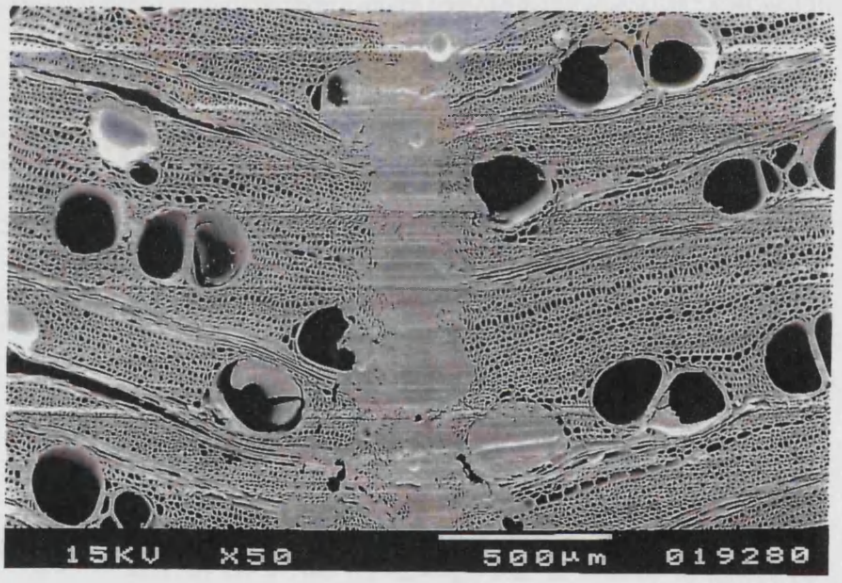

Fig.17.15. Epoxy glueline

Table 17.5 contains in decreasing order the static tensile strengths measured for the fully laminated samples produced with the alternative adhesives. Standard deviations have been calculated although with only 7 samples they are not strictly statistically valid. However, they do give and indication of the scatter in the results. As expected the all epoxy samples are the strongest. However, based on the block shear results it was not expected that the all PVA samples were stronger than the MUF and PRF ones. The fracture morphology of the failed samples was observed and any differences were noted.

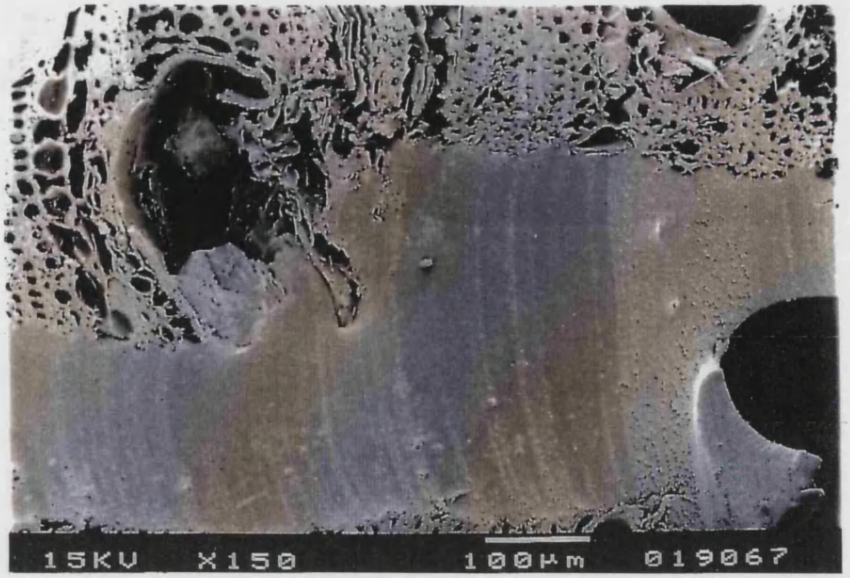

Fig.17.16. PVA Britannia glueline with a very damaged wood substrate.

Adhesive	**UTS (Std. Dev.) MPa**
Epoxy	67.2 (10.11)
PVA/Epoxy	64.4 (8.68)
PVA	56.2 (9.1)
MUF	54.45 (8.4)
PRF	48.5 (1.8)

Table 17.5. Static tensile results for fully laminated samples.

S-logN data for all the fully laminated samples tested in fatigue are presented in fig.17.17. The error bar on the static strengths is equal to the range of all the static data points. A best fit linear regression line was applied to each group of data and the equations of these lines are presented in table 17.5 and illustrated graphically in fig.17.18.

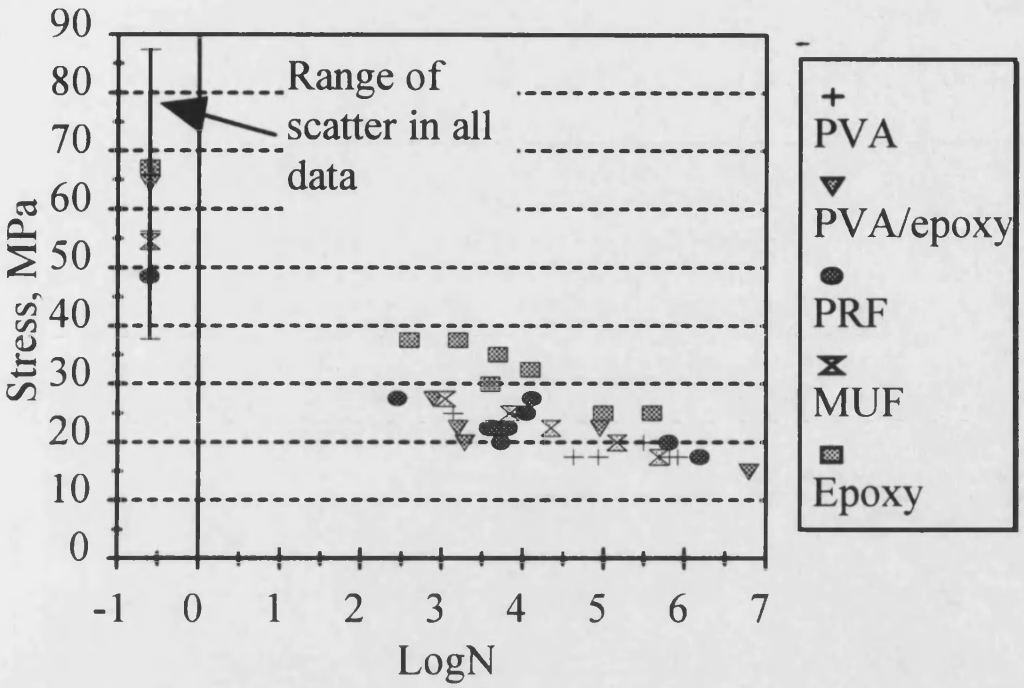

Fig.17.17. S-logN data for all the adhesives tested. R=-1, Khaya veneers.

Sample (Supplier)	**Tensile strength of fully laminated samples (Standard deviation) MPa**	**S-logN equation**
Epoxy (SPS)	67.2 (10.1)	S=50-4.8logN
PRF (Dyno)	48.6 (1.8)	S=37-3.1logN
MUF (Dyno)	54.5 (8.4)	S=40-3.8logN
PVA (Britannia) [epoxy scarf joints]	64.4 (8.7)	S=32-2.4logN
[PVA scarf joints]	56.2 (9.1)	S=31-2.1logN

Table 17.6. Fatigue test results.

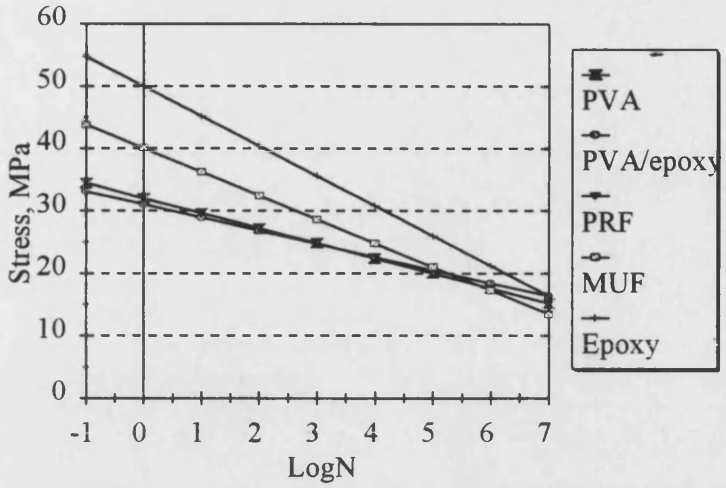

Fig.17.18. The best line fit for each adhesive system. Plotted without the data points.

17.6. Discussion

Block shear testing provided an effective way of comparing various Khaya-adhesive joints without additional forces masking the important results. When considering the values obtained in table 17.4 it is important to bear in mind the fact that the shear strength of Khaya in the L-T plane was found to be 9.6MPa (Bonfield, 1991). Consequently, it can be seen that in some cases (epoxy, MUF, PF and Cascamite) the joint formed was stronger than the substrate. This can be attributed to the infiltration of the wood by the adhesive having a reinforcing effect on the wood in the vicinity of the joint (Slaats, 1979). The remainder had lower shear strengths than Khaya and it can be assumed that no reinforcing effect took place.

17.6.1. Failure by deep wood shear

The adhesives which failed predominantly by deep wood shear tended to have the highest shear strengths. These included epoxy, PRF (Dyno) and Cascamite. The failure path in these samples passed through one or both adherends up to 3mm away from the glueline. Fig.17.11 illustrates failure by deep wood shear. The two veneers on either side of the glueline have slightly different grain angles so it can be seen clearly that failure has passed through both adherends. Although deep wood shear predominated in the epoxy samples some adhesive failure was also observed. This can be seen on the right side of fig.17.11 as a white region. Such regions were usually associated with voids in the glueline. This highlights the importance of a defect-free adhesive layer to obtain the best possible gluelines.

Fig.17.13 clearly illustrates the way in which the Khaya always tended to shear along the L-T and L-R planes in deep wood shear failure. This resulted in a ridged failure

with the ridges running parallel to the direction of shear. The flat surface with the elliptical groups of ray cells visible is the L-T plane and the plane perpendicular to it is the L-R plane. This plane is less easily visible in the photograph because it is nearly perpendicular to it. However, the shear failure can be seen to run through and between the ray cells. On the lower edge of each of the four bands of wood in fig.17.13 strips of ray cells have been pulled up as shear failure occurred.

PRF (Dyno) also failed predominantly by deep wood shear with a small amount of thin wood shear and mixed failure modes. Its shear strength was found to be slightly below that of Khaya (9.1MPa) but this was not thought to be a problem because the deep wood shear failure mode showed that the joint was as strong as the wood [the adherends could have had a lower mean shear stress than those measured by Bonfield (1991)].

Cascamite could prove to be a suitable candidate for laminating wind turbine blades since its open and closed times are acceptable and the joint strength is high enough. It is safe to use but there are two manufacturing considerations which prevented it being used to produce fully laminated samples. These were, firstly, the difficulty of mixing large quantities of powder and, secondly, its high price (>£4 per mixed kg). If it could be obtained at closer to £1 per mixed kg it would warrant further investigation. It is also less environmentally stable than PRF or MUF. However, this is not necessarily a problem because the glass-epoxy outer layer on the blade is thought to provide a very effective barrier to moisture penetration.

17.6.2. Failure by thin wood shear

Fig.17.12 shows a typical thin wood shear fracture face with particular clarity because of the dark colour of the adhesive. The failure surface is smooth with a thin layer of cells adhering to the PRF (Dyno). The dark lines which cross the picture from top to bottom are vessels which were open to the glueline and became filled with resin when the joint was formed. The adhesives which failed predominantly in this way were MUF (Dyno), PVA (Britannia) and PRF (Borden). Their shear strengths were 9.9MPa, 8.2MPa and 6.2MPa respectively.

PRF (Borden) had a particularly low strength because complete bonding over the surface did not occur. This was because the instructions recommended that the joints should be left open for a period of time before closure and this caused the adhesive to soak into the wood and dry before the joint was formed. As it was also recommended that the resin should be applied to both faces of the joint, an unacceptable condition in blade manufacture, the test with this adhesive was not repeated.

17.6.3. Failure by adhesive shear.

Fig.17.13 shows a portion of a PRF (Dyno) sample where adhesive shear failure had occurred in between ridges of wood shear failure. The PRF has been pulled up into small scales.

The only adhesive to fail entirely in the glueline was BP's cold curing PF with a shear strength of 10.7MPa. Failure occurred in the resin itself or at the wood-adhesive interface. It was observed that samples with higher than average shear strengths had the adhesive distributed more evenly between the two substrate surfaces, whereas on the weaker samples the adhesive remained mainly on the surface to which it had been applied. This indicates that the interface is likely to be the weak point in the joint. It is surprising that although the mean shear strength of the joint is higher than that of Khaya very little wood shear failure of any kind was observed in the fracture faces.

17.6.4. Cross-sections of gluelines

Figs.17.15 and 17.16 illustrate two features which were commonly observed in all the adhesive gluelines inspected in the SEM. Fig.17.15 is an epoxy glueline and it can be seen that the adhesive has infiltrated some of the vessels adjacent to the glueline. There is evidence of the adhesive being drawn into the Khaya up to a depth of 0.5mm as a filled vessel can be seen in the top left hand corner of the photograph. Such infiltration into the wood is beneficial as it reinforces the wood in the vicinity of the joint. Fig.17.16 shows a PVA (Britannia) glueline where the wood is very damaged and crushed cell debris has prevented the adhesive filling vessels next to the glueline.

Slaats (1979) suggested that damaged wood at the glueline behaves as a weak boundary layer between the sound wood and the adhesive. Furthermore, damaged cells block vessels open to the glueline and prevent them being infiltrated with resin. The combination of these two effects causes serious weakening of the bond and the use of a higher performance adhesive will not compensate for a poor adherend. Consequently, it is important to have a clean-cut, debris-free surface for adhesive bonding. However, the substrates used in this investigation were prepared by the same method of machining so the wood surface finish was similar and would not have caused undue differences in adhesive performance. None the less, thin wood shear failure was observed in several different adhesives. This implies that there is a weak layer of wood immediately adjacent to the glueline and this serves as a fracture path in some cases. Therefore, it is likely that the adhesives with high shear strengths are the ones which are able to penetrate the wood, damaged or undamaged, most effectively and have a strong

reinforcing effect. If the adhesive does not do this the layer of damaged wood remains the weakest link and provides a path for failure at a low stress.

17.6.5. Adhesive selection for fully laminated samples

The following adhesives were chosen for use in the production of fully laminated samples for static and fatigue testing:

- MUF (Dyno)
- PRF (Dyno)
- PVA (Britannia)

The first two were chosen because of the high strength of the bond they formed with Khaya. Both were compatible with the manufacturing schedule of wind turbine blades and had much shorter closed times. This would reduce the time required in the mould per blade by several hours, particularly in the case of MUF, see table 17.3. PVA (Britannia) was also selected because of its low cost, ease of use and complete safety. It undoubtedly forms a glueline which was weaker than the substrate (7.6MPa) but the implications for the manufacturing process would be significant enough to warrant further investigation. Savings of £3.60 could be made per kg adhesive, time taken to mix the adhesive would no longer be necessary, and clean-up afterwards could be done with water alone. Two configurations of fully laminated PVA samples were produced. One contained only PVA and the other contained epoxy scarf joints and used PVA as the laminating adhesive. The latter was prepared because the most critical part of a fully laminated sample is the joints and as epoxy is stronger it was decided that this would be an optimum solution.

The following adhesive were rejected:

- PRF (Borden)
- UF (Dyno)
- PF (BP)

All were rejected on the grounds of incompatibility with the manufacturing process. PRF (Borden) was rejected, as explained earlier, because it required application to both surfaces of the joint and could not be joined immediately. UF (Dyno) was rejected even before the block shear testing stage because the hardener was a formic acid solution which again had to be applied to the opposite surface to the resin. In the case of PF the catalyst could not be used to give the desired pot life and open and closed joint times.

17.6.6. Static testing of fully laminated samples.

The average tensile strengths of the PVA, PVA/epoxy and epoxy samples were 56.2, 64.4 and 67.2MPa respectively, with the strength decreasing as the content of the

weaker PVA adhesive increased. However, if the range of the results is taken as ±2 std. dev. the difference between the three types of sample is much less clear, particularly between the all epoxy and the PVA/epoxy samples.

In both the PVA and PVA/epoxy samples there was very little delamination of the PVA gluelines. The difference between the two lay in the way the scarf joints failed. In the case of the PVA samples, failure had occurred at the wood-adhesive interface leaving all the adhesive attached to one side of the joint. In the PVA/epoxy samples the scarf joints failed by brittle fracture leaving a shiny cleavage plane and epoxy adhering to both sides of the joint. Often the failure was associated with the presence of large voids in the joint. In both sample types the presence of low quality joints caused a weakening of the laminate as they appeared to be the sites of initiation of failure.

Although the static strengths of the samples made with PRF and MUF adhesives were lower than the epoxy and PVA samples, failure did not involve delamination of the gluelines. Failure occurred away from the gluelines in the wood. When bonding with PRF the scarf joints were not involved in the failure but with MUF adhesive some samples exhibited fracture paths passing through the scarf joints.

17.6.7. Fatigue testing

The data for all the fatigue tests carried out at R=-1 are presented in fig.17.16 but it is difficult to distinguish the relative fatigue performances of each sample type beyond the fact that epoxy samples consistently perform the best. However, the difference in fatigue performance is more distinguishable in fig.17.17 where the best fit linear regression lines have been plotted for each adhesive. The equations of each line further distinguish between the fatigue performance of each system. The equation which fits the epoxy data is seen to have the highest intercept value and steepest gradient. The all PVA equation has the lowest intercept and gradient and consequently, the poorest fatigue performance. The sequence in which the intercept and gradient values increase is the same as the order in which the shear strengths of the different gluelines increase.

If the equations of the lines are plotted they all converge towards 10^7 cycles and consequently the differences in the fatigue performance of each adhesive system are much less distinct. As wind turbine blades are designed to last over 10^8 cycles it would appear that for such low stress and long life applications the choice of adhesive does not significantly affect the composite's performance and consequently costs might be reduced by switching to a cheaper adhesive system. However, there is a range of other factors which must be investigated before such a significant change in blade material can be made. In addition to determining the composite's creep performance and the

importance of environmental stability, manufacturing issues must be addressed. It will be necessary to determine the adhesive's compatibility with the current blade production process and the viability of any modifications which might be required for its successful use. For example, the adhesive must be compatible with other materials in the blade, such as the epoxy used to make the scarf joints, and the blade production rate must be maintained.

17.7. Conclusions

- The shear strength of Khaya adhesive joints has been measured for a range of possible alternative adhesives to the epoxy currently used in blade manufacture. The adhesives tested were: Epoxy, PRF (Borden), PRF (Dyno), MUF (Dyno), PVA (Britannia), PF (BP) and UF - Cascamite (Humbrol).

- The shear strengths measured ranged from 6.2MPa for PRF (Borden) to 13.0MPa for Cascamite. Four resin systems produced joints with shear strengths higher than the Khaya substrates themselves - epoxy, MUF (Dyno), PF (BP) and Cascamite. On a strength basis alone all four could make a suitable alternative to the epoxy. However, due to incompatibility with the manufacturing process the PF and Cascamite were not used to make fully laminated samples for testing.

- Of the adhesives which performed less well than unjointed Khaya, MUF was made into fully laminated samples because the difference in shear strength was marginal and PVA was also used because of its cheapness and ease of use. The PRF (Borden) was not pursued because of incompatibility with the manufacturing process.

- Three types of failure were observed in the sample fracture faces. Failure occurred by either the shearing of the substrate deep in the wood away from the glueline, by shear wood failure close to the glueline of by failure of the adhesive. The adhesives with the highest shear strengths tended to fail by deep wood shear.

- Static and fatigue testing of fully laminated samples has been carried out and the fatigue performance of the different systems evaluated.

- The fatigue performance of samples produced with the epoxy system currently used in blade manufacture is superior to that of the samples laminated with possible alternative adhesives (MUF, PRF and PVA).

- Although the fatigue performance of the samples laminated with MUF, PRF or PVA is, on the whole, fairly similar the resin systems can be distinguished from each other and listed in order of decreasing fatigue performance: epoxy, MUF, PRF, PVA with epoxy scarf joints and PVA. This is the same as the order in which the shear strengths of the adhesives decreases.

- The fatigue performance of all the adhesive systems converges at around 10^7 cycles and consequently are indistinguishable at this point. In a low stress, long life application such as a wind turbine blade which is designed to last over 10^8 cycles it would appear that the choice of adhesive is not going to affect the performance of the blade. However, other factors such as the adhesive's creep behaviour might become significant in limiting a blade's life.

- Once any production issues have been addressed, potential cost savings could be made by selecting a cheap, safe and easy to use adhesive system such as PVA for the laminating adhesive in wood composite wind turbine blades.

18. DISCUSSION

The aim of this discussion is to draw the work together and to extract common ideas connecting the discoveries made in the individual Chapters.

The two main areas of discussion are, firstly how damage accumulates in wood, and secondly, how this relates to the changes in properties observed in the wood composite under the different types of fatigue loading investigated. In addition, these aspects will be related to the property changes seen under different loading modes and the effectiveness of alternative life prediction methods.

18.1. Damage mechanisms

Starting at a basic level, the application of cyclic loads causes a decrease in strength of metals, wood and composite materials. This is shown in the form of S-N diagrams, eg figs.4.3 and 4.21. The mechanisms differ from material to material because their molecular structures are different. Furthermore, different loading regimes cause damage at different rates and stress levels, fig.4.27.

In metals, fatigue causes damage by the initiation and growth of a single main crack which extends progressively with each load application, fig.4.24. Fibre reinforced materials, however, are resistant to crack growth because they contain crack-stopping interfaces and a single crack cannot grow unhindered. Because of this, fatigue damage initiates in many places and accumulates through the bulk of the material, causing progressive weakening until the cracks coalesce and failure results. Damage builds up in the form of matrix cracks, fibre breaks, interfacial debonding between the matrix and fibres and delamination between plies. These forms of damage can be quantified and related to the fatigue performance by counting individual damage events (eg. number of fibre breaks or matrix cracks) throughout the fatigue life.

Wood is a fibre-reinforced polymeric material comprising cellulose microfibrils in a hemicellulose and lignin matrix, and fatigue damage also accumulates in a progressive manner. However, wood has a cellular structure which causes an additional level of complexity. In addition, the fibres and matrix are so intimately linked that it is not possible to resolve them, except following fracture. Therefore, traditional techniques used in following fatigue damage in other composites cannot be used for wood. The use of bulk property changes, such as those used in this work, must be used to follow damage accumulation.

18.2. Fatigue and strength reduction in wood composites

The S-N diagrams which are presented in Chapter 8 illustrate the dependence of the fatigue strength of Khaya-epoxy wood composite on stress level and loading mode. When loaded in compression fatigue, the peak stress must be within the range of scatter in the static strength values for fatigue to occur, fig.8.3. The S-N curve is very flat, implying that the fatigue lifetime of a particular sample has more to do with its static strength than the number of cycles it survives until failure. The S-N curve is steepest in reverse loading where tensile and compressive damage modes combine to weaken the wood at the most rapid rate, fig.8.6. The rate at which the strength of the wood composite decreased with each decade of loading cycles was found to be better than for fibre reinforced plastics which show a decrease of ~10% of the ultimate strength per decade. For wood in tension fatigue this value was 4.4%, and in compression it was even lower at 2.8%, table 8.4. As expected, the value was higher for reversed loading fatigue: 7.3% when normalised by the UTS and 11.8% when normalised by the UCS.

In the case of S-P diagrams (number of load reversals, P, not cycles, N) presented in figs15.10 to 15.12 for the complex load-time (l-t) history tests, similar observations can also be made. In order for the compressive samples to fail, the peak stress level has to be a higher proportion of the ultimate strength than is the case for the tensile tests. It is also clear that the l-t history itself has a significant effect on fatigue life. The l-t history tests for normal operation are the least damaging and the emergency stop, with the largest load reversal, is the most damaging. This also confirms that the effect of load reversals is to accelerate the rate of damage accumulation.

From the ESEM tests it was found that the overall effect of the fatigue damage present in the wood was to reduce its notch sensitivity when loaded axially in tension. The unfatigued Khaya was completely notch insensitive, with a UTS a few MPa higher than any of the notched samples tested in Chapter 7. The tension fatigued sample had a UTS equal to 75% of the mean value measured in Chapter 7 and the reversed loading sample, 60%. Unfortunately, a value could not be calculated for the compression-fatigued sample because failure was controlled by the macroscopic compression creases.

The damage zone which developed in unfatigued Khaya consisted of two parts: a region in which intracellular shear failure of the fibres occurred in the vicinity of the notch, and the remainder of the sample where a regular array of cracks across groups of fibres developed, fig.16.13. In the pre-fatigued samples the zone of shear failure in the vicinity of the notch was not observed. This suggests that fatigue weakens the individual fibres, reducing their ability to withstand cracking.

In the reverse loading sample, the failure path did not follow the ray bundles, despite the fact that all the ray bundles were cracked. This implies that even more severe fibre weakening had occurred. The fact that a high proportion of the cracks tended to run from the ends of ray bundles, suggests that the position of the cracks had been determined by the presence of compression fatigue damage. This is clearly an example of the combination of compression and tensile damage leading to the most rapid rate of damage accumulation.

18.3. Macroscopic and microscopic damage mechanisms

Macroscopic fatigue damage can be seen in Khaya-epoxy composite in the course of fatigue, depending on the R ratio and stress level used for the test. In tension, at intermediate stress levels, this may take the form of large amounts of longitudinal splitting, fig.8.8 which often occur at as early as 50% of the sample's life. At high stress levels splitting is not observed before failure occurs. In compression, the formation of a compression crease only occurs at the point of failure, fig.8.9. There is no damage visible on the sample surface to suggest that failure is imminent. In reverse loading a combination of tensile and compressive types of damage are observed, with the balance between the two depending on the stress level of a particular test, fig.8.10.

The way in which the tension and compression fatigue damage combine was made clear in the controlled stop tests where stress-strain hysteresis loops were captured at the same R ratio before and after the portion of the l-t history which contained the load reversal. The effect of the load reversal is to reverse the strain developed during the first part of the l-t history up to that point, see fig.15.51 (tensile l-t history test) and fig.15.56 (compressive l-t history test). In a tensile test the strain developed across the compressive peak is negative, despite the fact that the mean stress of this part of the l-t history is tensile, fig.15.51. The magnitude of the compressive load is not sufficient to cause the formation of compression creases. In a compression test with a tensile load reversal, fig.15.56, the mean stress is still negative and the tensile load level is not sufficient to cause tensile damage, yet tensile strain occurs. The low stress levels of the reversals imply that rather than causing new damage, the load reversal is acting on the damage caused by the first part of the l-t history.

At a microscopic level, it has been shown that in tension fatigue, the microfibril winding angle may be reduced and fibres straightened. Therefore, it is likely that the compressive loading excursion undoes the alignment developed during the first part of the l-t history. In the case of a predominantly compressive test, the tensile excursion will straighten out compression kinks developed in the wood cell walls (although it will

not heal them). Further evidence of these changes is given by changes in loop area for the complex l-t history tests. In a predominantly tensile test, the area of the loop captured close to R=-1, across the reversal does not increase with time, fig.15.43. This shows that the same amount of energy is absorbed throughout the test as microfibrils and fibres are unstraightened. This behaviour is in contrast to the compressive l-t history tests where the loop area increases progressively throughout a test, fig.15.44, showing that the energy absorbed also increases. As the peak stress levels are higher than the elastic limit in compression, compression kinks would develop progressively, and the increase in area reflects the increasing amount of energy absorbed as the damaged wood structure is pulled in tension.

In the fully reversed constant amplitude loading tests the stress level of the reversal would be high enough to cause some levels of damage. The tensile strength of a macroscopic compression crease was found to be very low in the ESEM tests, and it is, therefore, likely that an individual compression kink in a cell wall is also weak. Therefore, a compression crease formed during one part of the loading cycle is likely to be further weakened, or even pulled apart, in the next. Clearly, this would contribute to the high rate of damage accumulation observed at R=-1. However, the S-P diagrams for the complex l-t history tests show that, even though the magnitude of the load reversal is small, it does significantly reduce the fatigue life of a sample. Therefore, it must be assumed that the undoing of the predominant damage state must produce other weakening effects in the wood structure. Such a mechanism could be a reduction in strength of the middle lamella, as was seen to be the case in the ESEM tests.

All forms of fatigue damage seen in the tension- and compression-fatigued samples were observed in the reverse loading fatigue sample. The tensile forms of damage predominated and were more frequent than in the tension fatigue sample. All the ray bundles were split and a higher proportion of fibres contained diagonal cracks. This shows how compression loading acts on the tensile damage, resulting in more severe tension fatigue damage accumulation. It can be appreciated that the rays, in addition to being squeezed together will also be forced apart when the load is reversed. In the case of helical cracking, a compressive stress will increase the shear strain range on the matrix material between the microfibrils leading to more extensive S2 cracking between microfibrils.

This increase in relative movement between microfibrils is also likely to be evident at the interface between cell wall layers with different winding angles. In fact, cracking within vessel walls at the S1/S2 interface was only seen in the reverse loading sample.

The main difference in loading response for the samples fatigued in tension and reverse loading was the importance of ray bundles and the dispersion of fibre cracks. In the tension fatigue sample, crack growth progressed along ray bundles and fibre cracking was more dispersed, with individual fibres breaking rather than the crack fracturing a larger bundle of fibres. This implies that the fibres have some resistance to cracking and that the weakest path is through ray bundles, some of which were seen to have split before loading in tension was begun. The more dispersed nature of the cracking implies that the shear strength of the middle lamella layer had decreased, thus reducing the shear stress transfer and enabling the fibres to fracture at their weakest sites.

18.4. Strain changes

The ultimate static strain for wood in both tension and compression was found to be about ±1%, for example fig.7.6 (Chapter 7). However, in the fatigue tests the ultimate strains shown by the Khaya-epoxy composite were sometimes smaller than this, fig.10.1. In certain circumstances they were higher, see fig.10.7. As might be expected, the general trend observed for most constant amplitude and complex l-t history tests was for the strains to increase in the direction of the applied stress. In tension, the changes were small and not always predictable and in some of the R=0.1 tests a compressive creep strain was observed, table 12.2. The reason for this is not known. However, the changes were much larger in magnitude and more consistent for the compressive fatigue tests, table 12.1.

As the stress levels used in the compression tests were close to the UCS it was not surprising that the fatigue strains were also large. Usually, the minimum strain was seen to decrease linearly throughout a sample's life, fig.10.1. As explained earlier, this change is due to the progressive accumulation of compression creases causing the minimum strain to decrease. In some cases, however, no such decrease was observed before failure occurred. These samples were defined as 'sudden death' samples because compressive collapse was instantaneous, without any progressive accumulation of compression kinks.

In the complex fatigue tests, the only test which showed a final fatigue strain of about 1% were the l-t history tests for normal operation in compression. In these tests, the mean stress was high and there were no damaging loading reversals. Therefore, creep and creep rupture are likely to play an important rôle in the failure of these samples. For these tests a strain failure criterion possibly could have been used to predict the fatigue life [fatigue failure occurs when the fatigue strain equals the static failure strain]. For the tests containing a load reversal, the failure strains were much less significant, as fatigue failure occurred before compressive creep strains could develop.

Clearly, failure was not controlled by the level of creep strain in these tests, but by the accumulation of fatigue-related damage.

During constant amplitude fatigue tests at R=0.1, the maximum strain was seen to change very little until about the last half decade of loading cycles [the second half of the sample's life]. It then increased in irregular steps, rather than in the smooth manner seen in all the compression tests, fig.10.4. In samples where the changes in strain were large, [samples b and d in fig.10.4] this corresponded to the onset of visible cracking of the sample along the grain of the wood. These step increases are therefore likely to be due to the initiation and growth of these cracks. In the complex l-t history tests the step-wise increase in strain was less obvious The strains at failure tended to decrease with the increasing severity of the l-t history and the peak stress level.

It is possible that the initiation of cracking along the grain of the wood was determined by the damage state of the ray bundles as the cracks appeared to split them in half. In the ESEM investigation of the tension-fatigued sample, some of the ray bundles were observed to have split along their length. This suggests that fibre alignment occurs under the action of a tensile load. Fibres are most curved as they pass around a ray bundle and as they are pulled, the ray would be compressed. It is possible that under the repeated stress application the ray parenchyma are plastically deformed and permanently compressed. As the load is removed, a resultant tensile force pulls the cells apart along the middle lamella. In this way a weak path would be developed for longitudinal splitting. This might also explain why very little changes in the wood's properties were seen until the second half of fatigue life, where cracking along the grain began to occur.

18.5. Effects of stress level

The effect of the stress level applied in constant amplitude loading tests depends on the loading mode. At R=10, if the stress is below the range of UCS values, failure will not occur. At R=0.1 there are two threshold stress levels. The lower one is approximately equal to the elastic limit, below which failure will not occur. The higher one does not have a physical significance, but above it failure occurs without any significant property changes. It was seen in the ESEM tests that fatigue damage reduced the notch sensitivity of the wood and it is likely that at the high stress levels the fatigue damage accumulates rapidly until the notch sensitivity is increased and a crack propagates catastrophically causing failure without property changes. This would also explain the low strain changes seen in the tensile complex l-t history tests. The most damaging emergency stop sequence would cause the fastest increase in notch sensitivity and hence the smallest changes in properties as a result of fatigue.

Stress-strain hysteresis loops for a compression test are presented in fig.9.1. It can be seen that the minimum stress is close to the UCS, and that large degrees of compressive creep have occurred in the course of the test. Stress-strain hysteresis loops for two tests in tension are presented in figs.9.2 and 9.3. The former failed without large property changes and the latter exhibited significant changes. It can be appreciated from these two figures that a large change in strain is also accompanied by a large increase in loop area. The dynamic modulus has also reduced. All these changes can be attributed to the development of longitudinal cracks.

In reverse loading the effect of stress level on fatigue damage and the accompanying property changes is less clear (see table 12.3). The main reason for this is the sensitivity of compression fatigue damage to the minimum stress level, with respect to the UCS. For compression damage to accumulate the minimum stress must be within the range of scatter of UCS values. As there is inherent variation in the static UCS, of two samples tested at the same stress level, one might rapidly accumulate compression damage and the other be virtually unaffected. When the minimum stress is close to the UCS the sample's fatigue response is compression-dominated. This tends to happen at the highest stress level tests, for example, fig.9.4. The last loop is much fatter in the compression loading part of the cycle and the minimum strain has become more negative, whilst the tensile portion of the last hysteresis loop has hardly changed at all. In some tests tensile damage dominates, fig.9.5, and in others both types of damage are evident, resulting in the bending of the hysteresis loops, fig.9.6, as the accumulation of cracks along the grain increases the strain much more significantly than the compression damage decreases the strain in compression.

The stress level of the peak stress in a complex l-t history test also played an important part in the fatigue response of the wood composite. In all but the normal operation l-t history tests in compression, the mean stress was well below the elastic limit. In the remainder of the compression tests, the peak (but not the mean) stress was above the elastic limit. In tension, about half of the peak stresses (for the higher stress level tests) were above the elastic limit. In these samples it was seen that the hysteresis loops captured at a higher maximum stress were stiffer than those captured at a slightly lower stress level, fig.15.30 and 15.33. This implies that the occurrence of a tensile overload on a sample has the effect of enabling an increase in stiffness with load level, which does not occur without loading beyond the elastic limit. It was also observed that whilst the stiffness increased, the loop area increased with stress level for these samples, fig.15.34. This appears contradictory as a decrease in modulus is usually accompanied by an increase in area in the constant amplitude tests, eg. the R=0.1 tests where

longitudinal cracking occurs, fig.9.3. In order to explain the co-existence of the two property changes, it must be assumed that two different mechanisms are causing the changes.

ESEM inspection of the Khaya pre-fatigued at R=0.1 showed that the most widespread form of damage was helical cracking in fibre walls, associated with the S2 microfibrils, see fig.3.5 and 16.15. These are the ones responsible for the tensile strength of wood. It is likely that under a repeated tensile stress, these microfibrils are pulled straighter along the fibre axis, leading to shear stresses between microfibrils which eventually cause failure of the matrix material. When the microfibrils are in a more aligned orientation, under the influence of a tensile stress, it is not surprising that the cell has greater stiffness. In order for the microfibrils and fibres to become progressively more aligned damage in the matrix material of the cell walls and the middle lamella must accumulate. This could explain the increase in loop area whilst the dynamic modulus also increases. In addition, it explains why in complex loading the stiffness of the wood composite is higher for hysteresis loops captured at the higher stress levels.

A feature which is not explained by the occurrence of tensile overloads is the significant increase in dynamic modulus half way through the test for all the runout samples, Appendix E. Clearly these did not see a tensile overload above the elastic limit.

In the case of the compression l-t history tests the increase in modulus with stress level was not detected. In fact, as the stress level became more negative the dynamic modulus decreased, as might be expected with the progressive accumulation of compression kinks. As the modulus decreased, so did the area, implying that energy was absorbed as the kinks were formed, or coalesced. Although the peak stress was below 80% UCS in all the tests, the higher peak stress level tests did not show this relationship, table 15.6.

The damage characteristic of compression-fatigued wood was much less obvious in the ESEM. It was not possible to identify compression kinks within the cell walls as this required polarised light microscopy of microtomed sections (Tsai and Ansell, 1990), or transmission electron microscopy (Hoffmeyer, 1991). However, it must be assumed that the cell walls contained compression kinks because it has been shown that they accumulate throughout the fatigue life of wood (Tsai and Ansell, 1990).

18.6. Modulus changes

The presence of S2 helical cracking in Khaya failed at R=0.1 explains why in tension fatigue (both constant amplitude and complex loading conditions), so many samples

showed an increase in stiffness. In tension fatigue at R=0.1 all samples exhibited a slight decrease in the damage parameter, D, which is based on stiffness values, eq.14.1. This points to a universal improvement of microfibril and/or fibre alignment under the action of tensile fatigue.

The main difference in stiffness changes between the constant amplitude loading modes is that at R=10 compression damage accumulates progressively right from the start of the test, fig.14.3, but in tension and reverse loading fatigue the changes in the early part of the fatigue life are much less significant, figs.14.4 and 14.5. As was also observed in both the dynamic and fatigue modulus trends, the changes in tension fatigue are much less predictable than in compression. The step-wise increments which occur after a period of what appears to be no change, do not make fatigue life prediction in tension possible using property change techniques, fig.13.6. Because of the unpredictable nature of the modulus changes, it would appear that the initial properties provide the most reliable means of estimating fatigue life in tension and reverse loading fatigue (Chapter 11). It was seen that there was a good relationship between the initial strain and the fatigue lifetime for both R=0.1 (fig.11.4) and R=-1 (fig.11.7).

The fatigue modulus was particularly beneficial for fatigue life prediction in compression, fig.13.3, because it combined the small changes in dynamic modulus with the important creep strains to produce a parameter which could be followed easily by hysteresis loop capture, enabling fatigue life prediction. This prediction method was based on the fact that fatigue damage accumulated from the start of the test in a gradual fashion and it is possible that it could be used to estimate the fatigue life of a sample after only 100 fatigue loading cycles. Clearly this would afford enormous savings in testing time.

18.7. Summary of observations

The inter-relationships between macro- and microscopic damage and the fatigue loading mode is complex but broad trends have emerged which have improved the understanding of the response of wood to fatigue. These trends are summarised in the next chapter.

19. CONCLUSIONS

(a) The measured static strengths and stiffnesses of *Khaya ivorensis*-epoxy laminates are close to values reported in the literature. In tension along the grain the mean ultimate strength (UTS) is 85.4MPa and the Young's modulus is 8.7GPa. In compression along the grain the mean ultimate strength (UCS) is 52.7MPa and the Young's modulus is 10.8GPa.

(b) Stress versus log cycles to failure (S-N) plots have been produced at R ratios of 0.1 (tension fatigue), 10 (compression fatigue) and -1 (reverse loading fatigue). At R=0.1 the fatigue strength decreases at a rate of 4.4% per decade of loading cycles at between 50% and 75% of the UTS. At R=10 the fatigue strength decreases at a rate of 2.8% per decade of loading cycles at between 50% and 75% of the UTS. At R=-1 the fatigue strength decreases at the fastest rate of 7.3% per decade of loading cycles when normalised by the UTS so reversed loading is the most damaging mode.

(c) The macroscopic appearance of fracture is dependent on R ratio. At R=0.1 there is typically a high degree of longitudinal splitting. At R=10 a macroscopic compression creases runs diagonally across the sample. At R=-1 fatigue failure comprises both tension and compression damage.

(d) Property changes have been followed by capturing hysteresis loops at all stages of the fatigue tests at all three R ratios. The property variables were strain, dynamic modulus and loop area. At R=0.1 the fatigue response depended on stress level. At the lowest stress levels, the run-out samples, there was a decrease in the loop area. At intermediate stresses there was a decrease in modulus and/or tensile creep but at high stress levels behaviour was similar to run-out samples. At R=10 all samples experienced compressive creep but there were no definite trends in the change in dynamic moduli and loop areas. Under reverse loading four different fatigue responses were observed which incorporate tensile and compressive features of fatigue damage.

(e) A fatigue modulus approach has been applied to wood composites at R=0.1 and R=10. Changes in the fatigue modulus with cycles at R=0.1 were unpredictable and life could not be predicted from the initial gradient. In compression fatigue a good relationship was achieved between the initial gradient of the fatigue modulus versus cycles characteristic and the life of each sample.

(f) The damage parameter, D, has been calculated at all three R ratios. The development of damage, measured in terms of D, depends on R ratio, but the overall picture is complex and depends on the development of physical damage.

(g) Complex load versus time histories have been imposed on wood composites in order to simulate normal operation, controlled stop-start and emergency stop load sequences in operational wind turbine blades. Property changes have been followed by hysteresis loop capture during these tests. Stress versus log passes through each load history (S-logP) plots demonstrate that the normal operation history is the least damaging and the emergency stop history is the most damaging.

(h) Trends in property changes in complex loading are complicated. In broad terms, it is suggested that tensile changes in dynamic modulus are a function of microfibrillar realignment and changes in loop area depend on viscoelastic deformation of the molecular matrix surrounding the microfibrils. In compression it is suggested that the accumulation of compression kinks within the cell walls determines changes in the dynamic modulus and loop area.

(i) The application of the fatigue modulus approach and the evaluation of the damage parameter D provided little insight into the prediction of life under complex load. However, in compression, the change in fatigue modulus showed some promising trends for life prediction.

(j) Productive use of environmental scanning electron microscopy (ESEM) was made to establish fatigue damage accumulation mechanisms at the three R ratios. Sections were taken from fatigue specimens and they were extended in tension in the ESEM to reveal fatigue damage. At R=0.1 the major damage mechanism was helical cracking of fibres associated with the S2 layer of the cell wall. At R=10 small compression creases were the major feature of fatigue damage. At R=-1 helical cracking of fibres associated with the S2 layer of the cell wall was also observed in conjunction with the longitudinal splitting of ray bundles.

(j) The performance of alternative adhesives systems was assessed in fatigue. The epoxy resin system currently used for the manufacture of blades is superior in fatigue to melamine urea formaldehyde (MUF), phenol resorcinol formaldehyde (PRF) and poly vinyl acetate (PVA) systems in that order. The fatigue performance of all adhesive systems converges at about 10^7 cycles so turbine blades with a design life of over 10^8 cycles can be manufactured using any of these resin systems as long as the creep of the adhesive or environmental stability does not limit its application.

(k) The mechanical response of wood composites to fatigue loads is dependent on R ratio and the form of complex load versus time histories and additional factors such as the adhesive system. The results of this research demonstrate that under predicted service conditions wood composites provide a highly effective design solution for the design of wind turbine blades.

20. REFERENCES

Adam, T, Fernando, R.F. Dickson, H., Reiter, H. and Harris, B. (1989). Fatigue life prediction for hybrid composites. *Int. J Fatigue*, 11, No.4, pp233-237.

Anderson, J.C., Leaver, K.D., Rawlings, R.D. and Alexander, J.M. (1989). Materials science. 3rd edition. Van Nostrand Reinhold (UK) Co. Ltd.

Andreä, A. (1993). Development and test of an extruded aluminium rotor blade for horizontal axis wind turbines and cost minimizing series production. In proceedings of the CEC European Community Wind Energy Conference, Lübeck-Travemünde, Germany, 8-12 March 1993, pp.156-159.

Ansell, M.P., Hancock, M. and Bonfield, P.W. (1991). Wood composites - the optimum fatigue resistant materials for commercial wind turbine blades. Proceedings of the 1991 International Timber Engineering Conference, London. Vol 4. pp.194-202.

Ashby, M.F., Easterling, K.E., Harrysson, R. and Maiti, S.K. (1985). The fracture and toughness of woods. Proc. Royal Soc. London A 398, pp.261-280.

Ashby, M.F. and Jones, D.R. (1987). Engineering materials. An introduction to their properties and applications. First edition 1980. Pergamon International Ltd., UK.

Aubrey, C. (1994). Something new in the air: the sounds of approval. *The Daily Telegraph*, 19.2.94.

Bach, P. (1993). The effect of moisture on the fatigue performance of glass fibre reinforced polyester in bolted joints. In proceedings of the CEC European Community Wind Energy Conference, Lübeck-Travemünde, Germany, 8-12 March 1993, pp.180-183.

Bathias, C. (1989). La fatigue des matériaux composites à hautes performances. In proceedings of the International Conference 'Advanced materials. Composite. Ceramic. Polymer. Les matériaux avancés'. Ed Gosh, S.K.. Institute for Industrial Technology Transfer International, Gournay-sur-Marne, France. pp.138-159.

Benner, J.H. (1993). Impact of wind turbines on birdlife. An overview of existing data and lacks in knowledge. In proceedings of the CEC European Community Wind Energy Conference, Lübeck-Travemünde, Germany, 8-12 March 1993, pp.20-23.

Bentur, A. and Mindess, S. (1986). Characterisation of load-induced cracks in balsa wood. *Journal of Materials Science*, 21, pp.559-565.

Berrie, T.W. (1992). Electricity economics and planning. Peter Perigrinus Ltd on behalf of the Institution of Electrical Engineers, London.

Bodig, J. and Jayne, B.A. (1982). Mechanics of wood and wood composites. Van Nostrand Reinhold Company Inc., New York, USA.

Bond, I.P. (1994). The fatigue design of commercial wood composite wind turbine blades. PhD thesis, University of Bath.

Bond, I.P. and Ansell, M.P. (1994). Fatigue testing of wood composites for aerogenerator rotor blades. Part X. Life prediction and variable amplitude testing using extreme 'in service' load conditions. In Wind Energy Conversion. Proceedings of the Sixteenth BWEA Wind Energy Conference. 15-17 June, Stirling. Ed. Elliott, G.. pp.199-204.

Bond, I.P., Hacker, C.L. and Ansell, M.P. (1992). Optimising and standardising the fatigue design of commercial wood composite turbine blades. First progress report for the Department of Energy (Contract No.E/5A/6111/2818).

Bonfield, P.W. (1991). Fatigue evaluation of wood laminates for the design of wind turbine blades. PhD thesis, University of Bath.

Bonfield, P.W. and Ansell, M.P. (1988). Fatigue testing of wood composites for aerogenerator rotor blades. Part III - axial tension/compression fatigue. In Wind Energy Conversion. Proceedings of the Tenth BWEA Wind Energy Conference. 22-24 March, London. Ed. Milborrow, D.J.. pp.377-384.

Bonfield, P.W. and Ansell, M.P. (1989). Fatigue testing of wood composites for aerogenerator rotor blades. Part IV - shear, size effect, modulus change and block loading. European Wind Energy Conference and Exhibition. 10-13 July, Glasgow. Peter Perigrinus Press Ltd., Part 1, pp.406-410.

Bonfield, P.W. and Ansell, M.P. (1990). Fatigue testing of wood composites for aerogenerator rotor blades. Part V - Life prediction analysis and hysteresis. In Wind Energy Conversion. Proceedings of the Twelfth BWEA Wind Energy Conference. 27-30 March, Norwich. Eds. Davis, D., Halliday, J.A. and Palutikof, J.P.. pp.19-24.

Bonfield, P.W. and Ansell, M.P. (1991). Fatigue properties of wood in tension, compression and shear. *J. Mater. Science*, **26**, pp.4765-4773.

Bonfield, P.W., Bond, I.P., Hacker, C.L. and Ansell, M.P. (1992). Fatigue testing of wood composites for aerogenerator blades. Part VII. Alternative wood species and joints. In Wind Energy Conversion, proceedings of the 1992 Fourteenth BWEA Wind Energy Conference. 25-27 March, Nottingham. Ed. Clayton, B.R. Mechanical Engineering Publications Ltd., London. pp.243-249.

Bonfield P.W., Hacker C.L., Ansell M.P. and Dinwoodie J.M. (1993). Fatigue and creep of chipboard. Part 1. R=0.01. *Wood Science and Technology*. 28, pp.423-435.

Bonnee, W.J. (1989). Constant amplitude fatigue tests on pre-stressed bolted joints in glass reinforced polyester. European Wind Energy Conference and Exhibition. 10-13 July, Glasgow. Peter Perigrinus Press Ltd., Part 1, pp.400-405.

BS 1204: Part 1: 1979. Synthetic resin adhesives (phenolic and aminoplastic) for wood. Specification for gap filling adhesives.

BS 3518: Part 1: 1962. Methods of fatigue testing. General principles.

BS 4169: 1988. Manufacture of glued-laminated timber structural members.

BS 5442: Part 3: 1979. Adhesives for construction. Adhesives for use with wood.

Bullen, C.J. and Van der Straeten, E. (1986). The design and construction of glued joints. *J. Inst. Wood Science*, 10, 6, pp.220-228.

Butterfield, B.G. and Meylan, B. (1980). 3-dimensional structure of wood - an ultrastructural approach. 2nd edition. Chapman and Hall, London.

Calvert, N.G. (1979). Windpower Principles. C. Griffin & Co. Ltd, High Wycombe, UK.

Cameron, R.E. (1994). Environmental SEM: Principles and applications. *Microscopy and Analysis*, May 1994, pp11-13.

Carswell, W. (1985). Hysteresis and damage in composite materials. In proceedings of the First European Conference on Composite Materials, Sept 1985, Bordeaux, France. Eds., Bunsell, A.R., Lamicq, P. and Massiah, A.. pp.391-402.

Carver, H.A. and Page, D.I. (1994). Public attitudes to the Cemmaes wind farm. In Wind Energy Conversion, proceedings of the 1994 sixteenth BWEA Wind Energy Conference. 15-17 June 1994, Stirling. Ed. Elliott, G. Mechanical Engineering Publications Ltd., London. pp.237-240.

Chesshire, J. (1993). Environmental impacts of electricity generation: some public policy dimensions. IEE PROCEEDINGS-A, Vol 140, N 1, pp.47-52.

Clarke, A. (1991). Wind energy. Progress and potential. *Energy Policy*, October 1991, pp.742-755.

Conners, T.E. and Medvecz, P.J. (1992). Wood as a bimodular material. *Wood and Fibre Science*, n.24, v.4, pp.413-423.

Corbett, D. (1993). Investigation of materials and manufacturing methods for wind turbine blades. Contract report for the Energy Technology Support Unit, no. ETSU W/44/00261/REP.

Curtis, P.T. (1989). The fatigue of organic matrix composite materials. In NASSA IAA Conference proceedings Issue 05 Advanced NCED Composites. pp.331-367.

Danilatos, G.D. (1991). Review and outline of environmental SEM at present. *Journal of Microscopy*, V. 162, Pt. 3, pp.391-401.

Davidson, R. (1994). Environmentalists say stop. *Windpower Monthly*, Vol.9. No.10, p.28.

Desch, H.E. and Dinwoodie, J.M. (1981). Timber, its structure, properties and utilisation. 6th edition, revised by Dinwoodie, J. The Macmillan press Ltd, London.

Dinwoodie, J. (1981). Timber, its nature and behaviour. Van Nostrand Reinhold Co., Wokingham.

Dinwoodie, J. (1989). Wood: Nature's cellular, polymeric fibre composite. The Institute of Metals.

Dietz, (1949). Materials of construction. Wood, plastics, fibres. Macmillan and Co., London.

Dutton, A.G., Irving, A.D. and Lipman, N.H. (1992). Infra red condtion monitoring of wind turbine blade fatigue tests. In Wind Energy Conversion, proceedings of the 1992 Fourteenth BWEA Wind Energy Conference. 25-27 March, Nottingham. Ed. Clayton, B.R. Mechanical Engineering Publications Ltd., London. pp.221-228.

Everett, A. (1994). Materials. Mitchell's building series. 5th edition. Longman Scientific and Technical, Harlow.

Everett, R.A. (1986). A comparison of fatigue life prediction methodologies for rotorcraft. NASA Technical memorandum 102759. AVSCOM technical report 90-B-011.

Fengel, D. and Wegener, G. (1984). Wood. Chemistry, ultrastructure, reactions. Walter de Gruyter, Berlin, Germany.

Freris, L., Ed. (1990). Wind energy conversion systems. L.L. Prentice Hall, UK Ltd.

Gardener, K.H. and Blackwell, J. (1974). The structure of native cellulose. *Biopolymers*, pp.1975-2001.

Garrad, A. (1991). Time for action. Wind energy in Europe. The European Wind Energy Association.

Gibson, L.J. and Ashby, M.F. (1988). Cellular solids: structure and properties. Pergamon Press, Oxford

Gillie, O. (1994). Plans to generate electricity from alternative sources have split local communities and environmentalists. *The Independent*, 26 February 1994. p.6.

Gipe, P. (1991). Wind energy comes of age. California and Denmark. *Energy Policy*, October 1991. pp.756-767.

Gipe, P. (1993). Wind power for home and business. Renewable energy for the 1990s and beyond. Chelsea Green Publishing Company, Vermont, USA.

Goddard, W. and Goddard, C. (1993). A comparative study of the total environmental costs associated with electrical generation systems. *Renewable energy*, Vol 3, No. 2-3, pp.113-120.

Hacker, C.L. (1993). Wood Composites - properties and performance in fatigue. Presented at the American Wind Energy Association's Conference, San Francisco, 12-16 July 1993.

Halliday, J.A. (1993). Wind energy: an option for the UK? IEE PROCEEDINGS-A, Vol 140, N 1, pp.53-62.

Hansone A.P. (1975). Choice of glues for wood. Building Research Establishment Digest, n.175. pp.1-4.

Harris, B (1986). Engineering Composite Materials. Institute of Metals, London.

Harris, B., and Bunsell, A.R. (1977). Structure and properties of engineering materials. Longman Inc., New York.

Hashin, Z. (1985). Cumulative damage theory for composite materials: Residual life and residual strength methods. *Composite Science and Technology*, 0266-3538/85/$0.30 Elseiver Applied Science Publishers Ltd., England.

Heuler, P. and Schutz, W. (1986). Assessment of concepts for fatigue crack initiation and crack propagation life prediction. *Z. Werkstofftech.* 17, pp.397-405.

Hoffmeyer, P. (1991). Non-linear creep as a result of slip plane formation. COST 508 -Wood mechanics. Workshop on fundamental aspects on creep in wood, 20-21 March, pp.57-70.

Hull, D (1981). An introduction to composite materials. Cambridge University Press, Cambridge.

Hwang, W, and Han, K.S. (1985). Fatigue of composites-Fatigue-modulus concept and life prediction. *J. Composite Materials*, v.20, pp.154-165.

James, B. (1993). Evaluation of photoelastic stress analysis and its applications to wood composites. School of Materials Science. Final Year Project.

Jamieson, P., Jaffrey, A., Wei, J. and Gow, G. (1994). In Wind Energy Conversion, proceedings of the 1994 sixteenth BWEA Wind Energy Conference. 15-17 June 1994, Stirling. Ed. Elliott, G. Mechanical Engineering Publications Ltd., London. pp.41-46.

Jefferson, M. (1993). Energy in tomorrow's world. In Wind Energy Conversion, proceedings of the 1993 Fifteenth BWEA Wind Energy Conference. 6-8 October 1993, York. Ed. Pitcher, K.F. Mechanical Engineering Publications Ltd., London. pp.15-21.

Jessen, S.M. and Plumtree, A. (1991). Continuum damage mechanics applied to cyclic behaviour of a glass fibre composite pultrusion. *Comopsites*, 22, 3, pp.181-190.

Kinloch, A.J. (1987). Adhesion and adhesives science and technology. First edition. Chapman and Hall, New York.

Knight, S. (1993). Balancing the energy budget. *Windpower Monthly*, Vol.10. No.2, pp.15-16.

Kohara, M. and Okuyama, T. (1993). Mechanical responses of wood to repeated loading. 6. Energy loss partitioning scheme to predict tensile fatigue lifetime. *Mokuzai Gakkaishi*, v.39, n.11., pp.1226-1230. [in Japanese]

Landrock, A.H. (1985). Adhesives technology handbook. Noyes Publications, Park Ridge, USA.

Le Gougiérès, D. (1982). Wind power plants. Theory and design. Pergamon press, Oxford.

Linde, L. and Henderson, P.J. (1992). Thermo-mechanical fatigue of an oxide dispersion strengthened Ni-Cr alloy and its effect on hysteresis loop shape. *Scripta Metallurgica and Materiala*, 26, pp.1687-1692.

Lindley, D. (1994). Wind energy - current status in the UK. In Wind Energy Conversion, proceedings of the 1994 sixteenth BWEA Wind Energy Conference. 15-17 June 1994, Stirling. Ed. Elliott, G. Mechanical Engineering Publications Ltd., London. pp.1-8.

Lindley, D. (1994b) (Ed). Major wind energy projects in the UK (end September 1994). *Wind Directions*, Vol XIV, No.1, October 1994, p9.

Leipholtz, H.H. (1992). Fatigue and accoustics. Prediction of metal fatigue using Miner's rule. NASA STAR Conference paper issue 13. Shock and Vibration bulletin part 2. Modal test and analysis techniques.

Liu, S-Y. and Chen, I-W. (1992). Fatigue deformation mechanisms of zirconia ceramics. *J. Am. Ceram. Soc.*, v.75, n.5, pp.1191-1204.

Lowe, G. A. and Satterly,N. D. (1993). Fatigue properties of wingblade materials and components manufactured by the transverse filament winding process. In proceedings of the CEC European Community Wind Energy Conference, Lübeck-Travemünde, Germany, 8-12 March 1993, pp.191-194.

Luke, A. (1994). Bird deaths prompt rethink on windfarming in Spain. *Windpower Monthly*, Vol.10, No.2, pp.14-16.

Mann, J.Y. (1967). Fatigue of materials. Melbourne University Press, Australia.

Massy, J. (1994). Minister pacifies objectors with wind farms limit. *Windpower Monthly*, Vol 10, No.4. p.12.

Massey, J. (1994b). The battle for Britain. *Windpower Monthly*, Vol 10, No.6. pp.23-26.

Matthews, R. (1994). The rise and rise of global warming. *New Scientist*, 26 November 1994, No.1953. p.6.

McDonough, C., Gomez, M.H., Lee, J.K., Waniska, R.D. and Rooney, L.W. (1993). Environmental scanning electron microscopy evaluation of tortilla chip microstructure during deep-fat frying. *Journal of Food Science*, v.58, n.1, pp.199-213.

Meylan, B.A. and Butterfield, B.G. (1972). Three dimensional structure of wood. A scanning electron microscope study. Syracruse University Press, New York.

Milborrow, D.J. (1993). Energy generation costs - now and for the year 2000. In Wind Energy Conversion, proceedings of the 1993 Fifteenth BWEA Wind Energy Conference. 6-8 October 1993, York. Ed. Pitcher, K.F. Mechanical Engineering Publications Ltd., London. pp.15-21.

Miner, M.A. (1945). Cumulative damage in fatigue. Trans ASME, Vol 67, A159.

Morrow, J.D. (1970). Laboratory simulation of structural fatigue behaviour. ASTM STP 4625.

O'Brien, K.T., Rigamonti, M. and Zanotti, C. (1989). Tension fatigue analysis and life prediction for composite laminates. *Int. J. Fatigue*, 11, 6, pp.379-393.

O'Callaghan, P.W. (1993). Energy Management. A comprehensive guide to reducing costs by efficient energy use. McGraw-Hill, London.

Ozturk, A. and Moore, R.E. (1992). Tensile fatigue behaviour of tightly woven carbon/carbon composites. *Composites*, v.23, n.1, pp.39-46.

Page, D.I. (1991). UK review of wind energy activities during 1990/91. In Wind Energy Conversion, proceedings of the 1991 Thirteenth BWEA Wind Energy Conference. DATE/PLACE. Eds. Quarton, D.C. and Fenton, V.C. Mechanical Engineering Publications Ltd., London. pp.15-20.

Panshin, A.J. and De Zeeuw, C. (1970). Textbook of wood technology. Volume 1. 3rd edition. McGraw-Hill book Co., New York, USA.

Paxton, B.H. (1992). Wood composites - adhesives. In Handbook of Adhesion, Ed. Packham, D.E.. Longmans, London.

Picasso, B. and Priolo, P. (1988). Damage assessment and life prediction for graphite-PEEK quasi-isotropic composites. American Society of Mechanical Engineers, Pressure Vessels and Piping, V146, pp.183-188.

Pizzi, A., Ed. (1983). Wood adhesives, chemistry and technology. Vol.2. Marcel Decker Inc., New York, USA.

Poore, R.Z. and Lynette, R. (1991). Wind energy cost reductions: potential technological contributions. ASME Solar Division. Vol.11. 10th ASME Wind Energy Symposium.

Poppen, M. and Bach, P. (1989). Fatigue testing of glass fibre reinforced epoxy using the WISPER sequence. FFA Technical Report TN 1989-45, Flygtekniska Försökanstalten - The Aeronautical Research Institute of Sweden.

Poursartip, A. and Beaumont, P.W.R. (1986). The fatigue damage mechanics of farbon fibre laminate. Part 1, Development of the model. *Composite Science and Technology*, 25, pp.283-299.

Reinhart, T.J., technical chairman (1988). Engineered Materials Handbook Volume 1. Composites. First edition 1987. ASM International, USA.

Reifsnider, K.L., Ed. (1991). Volume 4, Composite Materials Series Fatigue of composite materials. Elseiver Science Publishing Company Inc, New York, USA.

Reiter, H. (1992). Fatigue phenomena in composites. Presented at 'Fracture and fatigue of polymer based composites'. A specialist 1 day seminar, 15.5.92, Bath.

Richardson, R.D. (1993). Wind energy systems. Proceedings of the IEEE, Vol 81, N 3, pp.378-388.

Rink, H.D. and van Delft, D.R. (1994). Fatigue behaviour of wood-epoxy laminates for wind turbine rotor blades. Presented at the European Wind Energy Conference, 10-14 October, Thessaloniki, Greece.

Rotem, A. (1988). Residual strength after fatigue loading. *Int. J Fatigue*, 10, 1, pp.27-31.

Seoane, I., Ed. (1992). COST 508. State of the art wood mechanics research. CEC Report.

Simpson, P.B. (1994). Developments in wind turbine technology. In Wind Energy Conversion, proceedings of the 1994 sixteenth BWEA Wind Energy Conference. 15-17 June 1994, Stirling. Ed. Elliott, G. Mechanical Engineering Publications Ltd., London. pp.29-40.

Skeist, I., Ed. (1989). Handbook of adhesives, 3rd edition. Van Nostrand Reinhold, New York, USA.

Slaats, M.A. (1979). Eliminating glueline failure in bonding hardwood. *Adhesive Age*, 22, 6, pp.18-22.

Smallman, R.E. (1985). Modern physical metallurgy. 4th edition, Butterworth and Co. Ltd., London.

Spera, D.A., Esgar, J.B., Gougeon, M. and Zuteck, M. (1990). Structural properties of laminated Douglas fir/epoxy composite material. NASA Reference publication 1236. DOE/NASA/20320-76.

Spearing, S.M. and Beaumont, P.W. (1992a). Fatigue damage mechanisms of composite materials. I. Experimental measurement of damage and post fatigue properties. *Composite Science and Technology*, 44, pp.159-168.

Spearing, S.M. and Beaumont, P.W. and Ashby, M.F. (1992b). Fatigue damage mechanisms of composite materials. II. A damage growth model. *Composite Science and Technology*, 44, pp.169-177.

Spearing, S.M. and Beaumont, P.W. (1992c). Fatigue damage mechanisms of composite materials. Part III: Prediction of post fatigue strength. *Composite Science and Technology*, 44, pp.299-307.

Spearing, S.M. and Beaumont, P.W. (1992d). Fatigue damage mechanisms of composite materials. Part IV: Prediction of post fatigue stiffness. *Composite Science and Technology*, 44, pp.309-317.

Spruce, C. (1988/89). Wind Energy Group MS-3 Prototype Wind Turbine. *Windirections*, 8, 3 pp.20-22.

Still, D., Little, B., Lawrence, S.G. and Carver, H. (1994). The birds of Blyth harbour. In Wind Energy Conversion, proceedings of the 1994 sixteenth BWEA Wind Energy Conference. 15-17 June 1994, Stirling. Ed. Elliott, G. Mechanical Engineering Publications Ltd., London. pp.241-248.

Stinchcomb, W.W. (1986). Nondestructive evaluation of damage accumulation processes in composite laminates. *Composite Science and Technology*, 44, pp.169-177.

Stinchcomb, W.W. and Reifsnider, K.L. (1978). Fatigue damage mechanisms in composite materials. A review. Fatigue mechanisms, Proceedings of an ASTM-NBS-NSF symposium, Kansas City, Mo. May 1978. Ed. Fong, J.T., ASTM STP 675, pp.762-787.

Sun, W.M.H. (1993) Elastic properties of wood composites with and without joints. Final year project, The School of Materials Science.

Talreja, R. (1987). Fatigue of composite materials. Technomic Publishing Co. Inc., Pensylvania, USA.

Taylor, R.H. (1983). Alternative energy sources for the centralised generation of electricity. Adam Hilger Ltd., Bristol.

Thompson, R.J.H. (1994). Second progress report on the High frequency cyclic loading of structural grade chipboard. For the Department of the Environment, Building Research Establishment. Contract Reference no. F3/2/482. In BRE Library, Watford.

Trinick, M. (1994). Best practice in planning for wind energy development. In Wind Energy Conversion, proceedings of the 1994 sixteenth BWEA Wind Energy Conference. 15-17 June 1994, Stirling. Ed. Elliott, G. Mechanical Engineering Publications Ltd., London. pp.155-157.

Tsai, K.T. (1987). An investigation into the fatigue behaviour of wood laminates for wind energy convertor blade design. PhD thesis, University of Bath.

Tsai, K.T. and Ansell, M.P. (1985). Fatigue testing of wood composites for aerogenerator rotor blades. Part II. Effect of moisture and R-ratio- In Wind Energy Conversion 1985. Ed. Garrad, A. Mechanical Engineering Publications Ltd., London. pp.285-292.

Tsai, K.T. and Ansell, M.P. (1990). The fatigue properties of wood in flexure. *J. Mater. Science*, 25, pp.865-878.

Underhill, W. (1993). The winds of change blow loud and long. *The Daily Telegraph*, 28.9.93.

Watts, S. (1992). Low targets set for 'green' energy. *The Independent*. 7.11.92.

Weightman, F. (1994). Beyond the bogbrush - establishing community support for wind power. In Wind Energy Conversion, proceedings of the 1994 sixteenth BWEA Wind Energy Conference. 15-17 June 1994, Stirling. Ed. Elliott, G. Mechanical Engineering Publications Ltd., London. pp.231-235.

Weltner, K., Grosjean, J., Schuster, P. and Weber, W.J. (1986) Mathematics for Engineers and Scientists. Stanley Thornes (Publishers) Ltd., Cheltenham.

Xiao-yan, T., De-jun, W and Hao, X. (1989). Investigation of cyclic hysteresis energy in fatigue failure process. *Int J Fatigue*, 11, 5, pp.353-359.

Yang J.N. and Du, S. (1983). An exploratory study into the fatigue of composites under spectrum loading. *J. of Composite Materials*, 17, pp.511-524.

Yang, J.N., Lee, L.J. and Sheu, D.Y. (1992). Modulus reduction and fatigue damage of matrix dominated composite laminates. *Composite Structures*, 21, pp.91-100.

Ye, L. (1989). On fatigue damage accumulation and material degradation in composite materials. *Composite Science and Technology*, 36. pp.339-350.

Zimmerman, T., Sell, J. and Eckstein, D. (1994). Rasterelectronmikroskopische Untersuchungen an Zugbruchflächen von Fichtenholz. *Holz als Roh- und Werkstoff*, 52, pp.223-229.